# The 4th Japan – Greece Workshop

# Seismic Design of Foundations, Innovations in Seismic Design, and Protection of Cultural Heritage

Special Issue: The 2011 East Japan Great Earthquake

October 6–7, 2011 Kobe, Japan



## Volume 2

Edited by T. Tazoh and G. Gazetas

Co-chairperson: T. Okada
G. Gazetas

Secretariat General: T. Tazoh

## Organizing Committee

Y. Goto
K. Maebayashi
T. Sato
K. Wakamatsu
T. Kaneyoshi
N. Yoshida
T. Asano
F. Miura
A. Mikami
H. Kimata
K. Horikoshi
M. Saitoh
N. Funaki
P. Dakoulas
M. Panagiotou
N. Gerolymos
I. Anastasopoulos
R. Kourkoulis

Organized by:

- Earthquake Engineering Committee of Japanese Society of Civil Engineers
- Kobe Gakuin University
- Hellenic Society for Earthquake Engineering, Technical Chamber of Greece
- Laboratory of Soil Mechanics of National Technological University of Athens
- Project DARE funded by ERC
- Project PERPETUATE funded by EC FP7

Supported financially by:

- Japan Society of Civil Engineers
- Kobe Gakuin University
- ATTIKES DIADROMES, ATTIKI ODOS, J&P AVAX, OMETE

# Contents

# Volume 1



## Invited papers

## Submitted papers

# Volume 2

## Volume 3

# Submitted Papers

# Earthquake-Resistant Tall Reinforced Concrete Buildings Using Seismic Isolation and Rocking Core-Walls

Vladimir Calugaru and Marios Panagiotou
*University of California, Berkeley, USA*

ABSTRACT: This paper investigates the seismic response of five 20-story tall reinforced concrete core-wall buildings. The first two buildings are conventionally designed. The first building is designed to develop plasticity anywhere along its height while in the second building all inelastic deformations are concentrated in a single plastic hinge at its base. The third building uses an isolation plane, consisting of elastomeric bearings, at the base of the building below the ground level. The fourth building uses a core-wall designed to rock at the ground level. The last building uses both the isolation plane and the rocking core-wall of the third and fourth building, respectively. The rocking core-walls include unbonded steel and post-tensioning tendons. The buildings are subjected to 14 strong pulse-type near-fault ground motions. The response is presented in terms of floor accelerations, forces, displacements, material strains, and deformation of the bearings. In comparison with the conventionally designed buildings the building with a single isolation plane did not prevent the formation of a plastic hinge at the core-wall, while the building designed with a rocking core-wall did not reduce floor accelerations and forces in comparison with the conventionally designed buildings. The building with both the isolation plane and the rocking core-wall demonstrated superior performance, significantly reducing floor accelerations, forces, and preventing the formation of a plastic hinge at the core-wall.

## 1 INTRODUCTION

Construction of tall buildings in the United States (U.S.) and around the world is increasing due to the rapid growth of cities and their dense inner cores (CTBUH 2011). Construction of 20- to 60-story tall buildings has increased significantly. This trend has been slower in regions of high seismicity, but numerous tall buildings are being planned or designed in regions vulnerable to earthquakes. Currently, two hundred buildings taller than 120 m (394 ft) are proposed or under construction in U.S. with 21 of them in highly seismic regions: 7 in Los Angeles, 8 in San Francisco, and 6 in Seattle (CTBUH 2011).

Considerable damage to tall buildings due to earthquakes has a decades-old history. In the U.S. during the last forty years, the 1971 M6.6 San Fernando, the 1989 M6.9 Loma Prieta, and the 1994 M6.7 Northridge earthquakes resulted in the most damage to infrastructure, with the largest number of fatalities equal to 65, 63, and 60, respectively (USGS 2011). In the Loma Prieta earthquake, the major cities of San Francisco and Oakland were at considerable distance from the epicenter (~100 km), resulting in low excitation and almost no damage to tall buildings (Celebi 1992a, 1992b). In the case of the San Fernando and Northridge earthquakes, a combination of the relatively large distance of the epicenter from downtown Los Angeles (35 and 31 km, respectively), and minor fault rupture directivity, for downtown Los Angeles, resulted in moderate excitation and minor damage of tall buildings (Naeim 1994, 1998). Outside the U.S. in the 1985 M8.0 Mexico earthquake, which caused around 10,000 fatalities, at least 15 tall buildings (14 to 18-stories tall) at a distance of 350 km from the epicenter suffered major

damage or collapsed in Mexico City due to amplification of the long-period content of the ground motions by deep and soft soil deposits (Otani 1999). In the 1995 M6.9 Kobe, Japan, earthquake, 40% of the 10 to 12 stories buildings were heavily damaged or collapsed (Otani 1999). In the 1999 M7.6 Chi-Chi, Taiwan, earthquake more than twenty-five 10 to 20-stories reinforced concrete (RC) frame buildings collapsed (Tsai 2000). In the recent 2010 M8.8 Chile earthquake, one 15-story tall building collapsed, a 21-story tall building partially collapsed, see Fig. 1, and at least 15 other buildings between 12- and 23-stories tall suffered significant, and in some cases irreparable, damage (Carpenter et al. 2011, Lew et al. 2011, Rojas et al. 2011, Youssef et al. 2011). Finally during the very recent M6.3 2011 Christchurch, New Zealand, earthquake, the tallest structure in the city, a 26-story tall hotel, experienced significant damage, resulting in large permanent tilt of the building (Kam 2011). These recent large earthquakes raised a significant question for urban planners. Commercial and residential buildings in the immediate shade of the heavily damaged tall buildings had to be evacuated until the damaged buildings to be demolished, which can be problematic. Demolition of buildings that are in precarious condition is not as simple as of those that are in sound condition.

Current codes (ICC 2009) have been calibrated for low- or moderate-rise construction using standard construction materials and without regard to post-earthquake damage, economic losses, and reparability. This is becoming a major concern in the seismic design of tall buildings – particularly those using high-performance materials and employing nonconforming structural systems and details – which may not achieve performance expectations (Lew 2006). *Ad hoc* procedures have been developed, with several groups in the process of developing a consensus on minimum performance expectations, design, and analysis requirements, and to streamline performance-based seismic assessment of tall buildings as they are currently designed (LA TBSDC 2005, SEAONC 2007, Moehle et al. 2007, Wilford 2008, TBI 2010). None of these guidelines address how to reduce post-earthquake damage in a tall building to enhance their seismic resilience.

Figure 1. Partially collapsed of O'Higgins building, tallest in Conception, during the 2010 M8.8 Chile Earthquake, threatens the surrounding built environment. Courtesy of J. Restrepo.

Many tall buildings in highly seismic regions are now designed with RC core-walls as the main lateral force resisting system. Based on current practice RC core-wall buildings are designed to develop nonlinear deformations in regions defined as plastic hinges located at the base of the core-walls (Moehle et. al. 2007, Panagiotou & Restrepo 2009). Numerical studies have shown that when these buildings undergo strong pulse-type near-fault ground shaking experience high acceleration and force demands along their entire height with significant contribution from the second and higher modes of response (Panagiotou & Restrepo 2009, Panagiotou et al. 2009). For walls designed to restrict all the inelastic deformations in a single plastic hinge at their base, studies have shown that large bending moment demands develop around mid-height (Moehle et al. 2007, Panagiotou & Restrepo 2009) and a large amount of longitudinal reinforcement is required for elastic response of these regions (Panagiotou et al. 2009). To avoid the development of large bending moments on the upper part of the wall some designs allow plasticity to develop anywhere along the height of the wall which requires special detailing over the entire wall height in order for these regions to be able to accommodate possible inelastic deformations (Panagiotou & Restrepo 2009). Panagiotou & Restrepo (2009) proposed a design concept with two flexural plastic hinges, one at the base and another at the mid-height of the wall to reduce second and higher modes of response in this type of buildings. This design though cannot eliminate damage and may also result in residual deformations after an earthquake.

Seismic isolation can be very effective in reducing demands and post-earthquake damage in tall buildings and has been used in their design. Traditionally seismic isolation has been considered most effective for relatively short and stiff structures by elongating their fundamental period, thus reducing the accelerations and forces they develop. For tall buildings the main goal of seismic isolation is not to increase the already long fundamental period. Seismic isolation appears to have great potential for advancing the earthquake-protective and resilient design of tall buildings by concentrating deformations in a few robust locations that are easily replaceable, reducing the contribution of higher modes in response, and reducing structural demands (accelerations, forces, displacements) that may cause structural and nonstructural damage. Such strategy facilitates re-occupancy, and allows for flexibility in architectural and structural design, and reduces the sensitivity of the response of the building to uncertainties in ground motion.

Japan is currently the leading proponent of applying seismic isolation in tall buildings. One third of all recorded isolated buildings built in Japan after 1990 are over 40-m tall (Pan et al. 2005), with the tallest being 41-stories (Komuro et al. 2005). Incorporating isolation in the upper part of buildings has been also proposed or used (Kawamura et al. 1998, Ziyaeifar & Noguchi 1998, Tsuneki et al. 2009, Calugaru & Panagiotou 2010, 2011, Chey 2010).

The tallest isolated building in the world is located in Los Angeles. Large elastomeric bearings, e.g. with 1.5 m diameter, required to isolate tall buildings are currently available (DIS 2011) and they have been studied experimentally under combined lateral and vertical loading (Fujita 1991, Kawamura et al. 1998, Muramatsu et al. 2001, Kato 2003, Komuro et al. 2005). Large friction bearings also exist (THK 2011, EPS 2011).

Another strategy to address the response of tall buildings to strong ground motion is rocking walls under gravity (Nielsen 2009), designed with unbonded steel and post-tensioning tendons (Wiebe & Christopoulos 2009), or walls with buckling restrained braces or viscous dampers (Munir & Warnitchai 2011) which have been studied numerically. Wiebe & Christopoulos (2011) proposed a design including multiple rocking planes along the height of a rocking wall to reduce the contribution of second and higher modes of response. Munir & Warnitchai (2011) proposed a design with multiple plastic hinges along the height of the wall. The authors are not aware of any tall building that uses a rocking wall. Mechanical detailing, use of external mild steel dampers, and post-tensioning tendons can significantly facilitate inspection, repair and adaptability of rocking walls (Marriot et al. 2008). The combination of base isolation and rocking, which is investigated in this paper for a tall building, has also been investigated numerically for a rigid block subjected to pulse-type ground excitations (Vassiliou & Makris 2011).

This study investigates numerically the seismic response of tall RC core-wall buildings that use either an isolation plane consisting of elastomeric bearings or a rocking core-wall, or combination of the two. The latter design is considered for the first time as an earthquake-resistant strategy for a tall building. The buildings were subjected to 14 strong near-fault earthquake ground motions. The responses of the buildings that use isolation planes or rocking core-wall were compared to conventionally designed buildings in terms of different response parameters.

## 2 DESCRIPTION AND DESIGN OF BUILDINGS

Five 20-story buildings are considered in this study. A reinforced concrete core-wall provides all the lateral force resistance above ground, see Figure 2. Figure 3 shows the common floor plan view of the buildings above ground. The five designs differ in response to the locations where the majority of deformations develop. The first two are fixed at the ground level, see Figure 2, the third uses one isolation plane below ground, the fourth a core-wall designed to rock at the ground level, and the fifth both the isolation plane and the rocking core-wall of the third and fourth building, respectively. Table 1 lists the main characteristics of the buildings. The following sections describe the design of the five buildings.

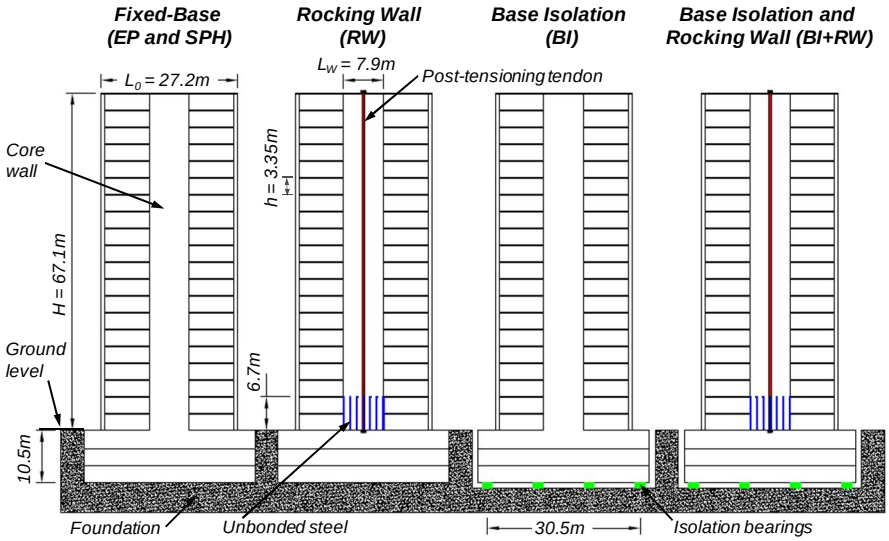


Figure 2. Elevation view of the five buildings considered.

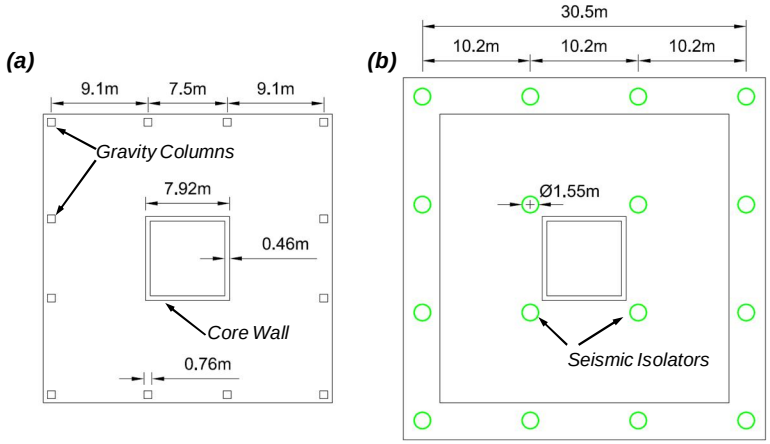


Figure 3. Plan view of: (a) floor above ground, and (b) isolation plane below ground.

Table 1. Building characteristics.

| | EP | SPH | RW | BI | BI+RW |
|---|---|---|---|---|---|
| Bonded steel in stories 3 – 20, $\rho_{3\text{-}20}$ (%) | 0.8 | 3.0 | 2.4 | 2.4 | 2.4 |
| Bonded steel in stories 1 and 2, $\rho_{1\text{-}2}$ (%) | 0.8 | 0.8 | 2.4 | 2.4 | 2.4 |
| Un-bonded steel, $\rho_{UB}$ (%) | - | - | 0.4 | - | 0.4 |
| Post-tensioning steel, $\rho_{PT}$ (%) | - | - | 0.4 | - | 0.4 |
| Axial load ratio at the base of the core-wall due to gravity $P_{cw} / (f'_c A_g)$ | | | 0.09 | | |
| Seismic weight / floor $w$, kN | | | 7123 | | |
| Seismic weight / underground floor $w_{ug}$, kN | - | - | - | 10685 | 10685 |
| Expected base flexural strength $M_{b,y}$, kN·m | 398500 | 398500 | 394486 | 760600 | 394486 |
| Curvature at $M_{b,y}$, $\varphi_{b,y}$, rad/m | 4.2E-4 | 4.2E-4 | - | 4.2E-04 | - |

### 2.1 *Fixed-base buildings (EP and SPH)*

Modal response spectrum analysis (MRSA), based on the requirements of ASCE-7 (ASCE 2006), with a response modification factor of $R$ = 5 was used to obtain design forces for the fixed-base buildings for a site in downtown Pasadena, California, for soil type C, corresponding to very dense soil and soft rock. Figure 4 depicts the design basis earthquake (DBE) and

maximum considered earthquake (MCE) acceleration and displacement spectra for the site considered. An effective section moment of inertia $I_e = 0.5I_g$ was used for the core-walls along their entire height for the MRSA where $I_g$ is the gross section moment of inertia of the core-wall.

The design bending moment, $M_u$, and shear force, $V_u$, envelopes are shown in Figure 5, where the MRSA bending moment and shear force envelopes are labeled *MRSA*. The $MRSA_{Mb,o}$ envelopes, shown also in Figure 5, are the *MRSA* envelopes scaled by $1.25\frac{M_{b,y}}{M_{b,MRSA}}$, where 1.25 is the base flexural overstrength factor, $M_{b,MRSA}$ is the *MRSA* base bending moment, and $M_{b,y}$ the expected flexural strength at the base of wall computed by moment-curvature analysis.

In the first considered fixed-base design, referred to as extended plasticity (EP), plasticity is allowed to develop in any region along the height of the wall. The amount longitudinal steel is uniform along the height of the building with a longitudinal steel ratio $\rho_l = 0.8\%$. This design assumes that adequate transverse and confinement reinforcement is provided along the height of the wall to ensure the development of inelastic deformations without strength degradation.

The second fixed-base design is referred to as single plastic hinge (SPH) and is designed to form a single flexural plastic hinge extending over the bottom two stories of the building, see Figure 2. The reinforcing steel ratio in the plastic hinge region is equal to $\rho_b = 0.8\%$. A high longitudinal steel ratio $\rho_E = 2.4\%$ above the plastic hinge is provided to ensure elastic response of this part of the wall. The curvature, $\varphi_{b,y}$ at $M_{b,y}$ is also presented in Table 1.

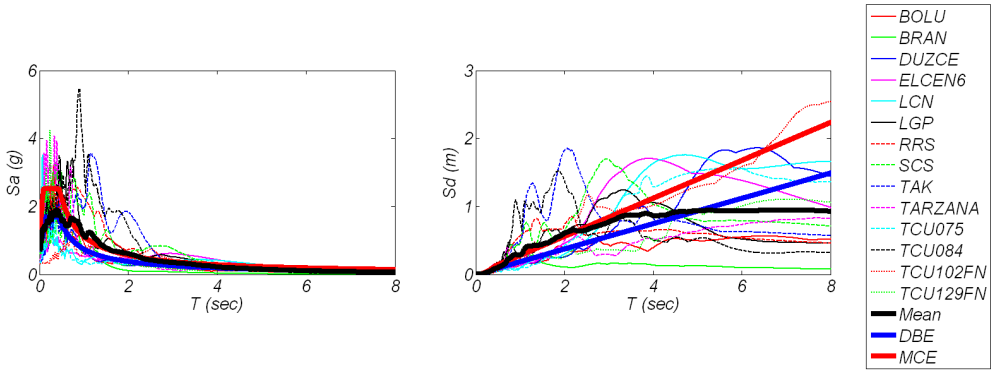


Figure 4. Absolute acceleration and relative displacement response spectra of the 14 considered ground motions, and mean response spectra for 2% damping, as well as DBE-, and MCE-level design spectra.

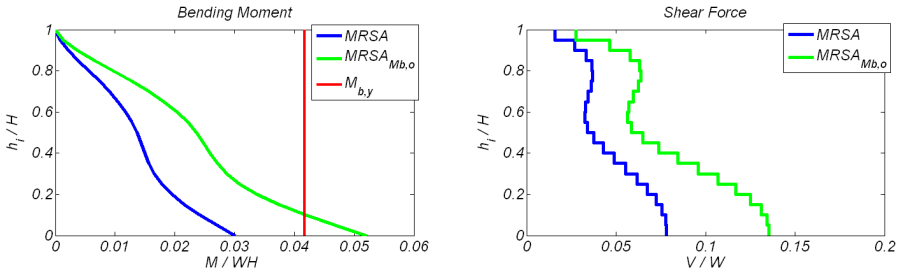


Figure 5. MRSA design envelopes for the fixed-base buildings.

## 2.2 *Rocking wall (RW) building*

In contrast with the EP and SPH buildings this building uses a rocking core-wall designed to rock at the ground level to avoid the formation of a flexural plastic hinge at the base of the wall. Unbonded longitudinal steel reinforcement over the lower two stories, and post-tensioning steel along the entire height of the building was used, see Figure 2. It is assumed that the tendons are placed around the centroid of the core-wall to achieve the maximum deformation capacity of the

wall without yielding them. Proper detailing of the regions where the tendons are anchored is required to distribute the post-tensioning force to the core-wall. Alternatively twice the area of tendons can be distributed in the perimeter of the core-wall and post-tensioning at half stress to achieve the same post-tensioning force, and similar deformation capacity without yielding them.

In addition to achieving a similar bending moment strength at the base of the wall to the EP and SPH buildings, the design objectives (Restrepo & Rahman 2007) were as follows to: i) control the sliding shear; ii) control the neutral axis depth to be less than $0.15L_w$ to ensure hysteretic and geometrical stability of the wall , iii) ensure that the post-tensioning tendons remain elastic, as well as that the gravity plus the post-tensioning force is enough to re-center the core-wall after reaching its ultimate roof lateral displacement, and iv) limit the peak tensile strain in the unbonded reinforcement to 4%. The steel ratio of both the unbonded reinforcement ($\rho_{UB}$ ) and the post-tension ($\rho_{PT}$), was equal to 0.4%, see Table 1. The initial stress of the tendons due to post-tensioning was equal to 414 MPa. The $M_{b,y}$ reported in Table 1 is at first yield of the outer un-bonded steel.

Assuming a dynamic coefficient of friction equal to 0.6 the minimum sliding shear resistance, accounting only for the gravity and the initial post-tensioning force, of the wall is calculated as 50218 kN corresponding to a base shear to total seismic weight ratio V / W = 0.35. A number of passive methods can be used to enhance the sliding resistance of the wall at its base (Restrepo & Rahman 2007). The neutral axis depth at a roof displacement of 2 m was computed, using the first mode lateral force profile, equal to $0.06L_w$. The rotation of the rocking plane at yielding of the tendons, as well as at 4% strain of the outer unbounded steel was computed equal to 3.6%.

### 2.3 *Base isolated (BI) building*

The third design, referred as BI, used a single isolation plane of 16 low-damping laminated elastomeric bearings. This isolation plane was located at the base of the building below ground to achieve the maximum plan view length and ensure that the bearings did not experience tension. For this type of bearings the isolation plane has essentially a linear force-displacement behavior.

The main objective of this design was to reduce floor accelerations and forces, eliminating the inelasticity at the base of the wall, without exceeding the deformation capacity of the bearings. To achieve the latter the stiffness and thus the period of the building needs to be controlled to avoid large displacements associated with excitations with strong low-frequency content.

Aiming at the largest possible deformation capacity the bearings had a diameter D = 1.55 m and a maximum allowed displacement $\Delta_{b,u}$ = 0.9 m, corresponding to $\Delta_{b,u}$ / D = 0.6. Each bearing had thirty alternating layers of rubber and steel plates with thicknesses $t$ = 12.7 mm and $t_s$ = 3.2 mm, respectively. The total height of rubber, and of the bearing was thus $t_r$ = 38 cm, and $H_b$ = 44.1 cm, respectively. For these properties and a rubber shear modulus $G_r$ = 483 kPa, the lateral, vertical (compression), and rotational stiffnesses of each bearing was $K_h$ = 2392 kN/m, $K_v$ = 6661 MN/m, and $K_\theta$ = 104320 MN/rad, respectively. Bearings with these dimensions and properties are commercially available (DIS 2011).

The core-wall in this case is heavily reinforced with $\rho_l$ = 2.4% to prevent the formation of a plastic hinge at core-wall at the ground level. Based on pushover analysis using the first mode lateral force profile the displacement of the bearings, and the roof displacement at which the flexural strength of the wall at the ground level is reached was calculated equal to 0.45 m, and 1.05 m, respectively. At this level of displacement the ratio of the shear force at the ground level to the seismic weight above the ground level was computed to be $V / W$ = 12%. At the first mode period $T_{l,1}$ = 4.61 sec, see section 5 below, the elastic spectral displacement demand for the MCE level is equal to 1.3 m. Thus yielding of the wall at the ground level was expected for motions with elastic displacement demand close or higher than the MCE spectrum in this period range.

The case of reducing the stiffness of the isolation plane and thus increasing the period of the building was investigated but this proved inadequate; despite the smaller stiffness, the development of larger bearing displacements resulted in a similar level of lateral forces, and similarly when the stiffness of the isolation plane was increased. In this case, the smaller

developed displacements of the bearings in combination with the larger stiffness of the isolation plane resulted in similar level of lateral forces.

To address this issue, the BI+RW system was developed to combine the beneficial effects of an isolation plane in reducing accelerations and lateral forces, and a rocking core-wall that eliminates inelastic deformations and thus post-earthquake damage at ground level of the wall.

### 2.4 *Building with base isolation and rocking wall (BI+RW)*

The BI+RW design uses both the isolation plane and the rocking core-wall of the BI and RW buildings, respectively. In this design the rocking plane serves as a safety valve to control the maximum deformation of the bearings. By controlling the moment strength of the rocking plane, the base shear force is controlled, thereby limiting the amount of lateral displacement the bearings will experience. This design combines the beneficial features of the BI design - which controls the force and deformation at the isolation plane consisting of bearings by also reducing second and higher modes - as well as the benefits of the RW by avoiding the formation of a flexural plastic hinge at the ground level of the wall. Here, deformations are distributed between the displacement of the bearings, the rotation of the wall at the rocking plane, and the elastic deformations of the core-wall above the rocking plane.

The stability of the bearings, under the maximum considered displacement, and the combined axial / shear force had to be ensured (Kelly & Takhirov 2004, DIS 2011). Based on pushover analysis, using the first mode lateral force profile, at the 0.9 m displacement of the bearings the ratio of the vertical compressive load P to the critical vertical load $P_{cr}$ (Kelly & Takhirov 2004) was computed equal to 0.17, a value that ensures the stability of the bearings under combined shear deformations and compressive loads.

## 3 NUMERICAL MODELING

The Open System for Earthquake Engineering Simulation (OpenSees) software was used in this numerical study. Nonlinear beam-column elements with fiber sections were used to model the RC walls. One element per story was used. The material models Concrete03 and Steel02 were used for concrete and steel, respectively (OPENSEES 2011). The initial concrete modulus was $E_c$ = 35.2 GPa, while the concrete compressive strength $f_c^{'}$ = 48 MPa. The confined concrete strength was $f_{cc}^{'}$ = 68 MPa at a strain of 0.4%. The steel modulus, the yield stress, and the strain-hardening ratio were $E_s$ = 200 GPa, $F_y$ = 455 MPa, and $b$ = 0.02, respectively.

Linear vertical, horizontal, and rotational zero-length springs were used to model the force-displacement behavior of each isolator in the corresponding direction. The vertical force, shear force, and bending moment interaction (Ryan et al. 2005) were not considered in this study. The vertical stiffness of the isolators in tension was modeled five times smaller than the compressive stiffness (Fujita 1991, Kato 2003) even though the isolators did not undergo tension in this numerical study. The slab above the isolation plane and the walls of the three underground floors were modeled with beam-column elements of high flexural and axial rigidity, see Figure 6.

The rocking plane was modeled with a short nonlinear beam-column element with fiber section as described above. The confined concrete material model - described above - with zero tensile strength was used for this element. The unbonded steel was modeled as seven steel truss elements equally spaced along the width of the core-wall, see Figure 6. A frame element of high flexural and axial rigidity was used at the second-story level to represent the width of the wall and connect the ends of the elements representing the unbonded steel. The post-tensioning was modeled with an elastic corotational truss element, spanning from ground to the top story, and an initial strain material (InitStrainMaterial) resulting in initial stress of the tendons equal to 414 MPa.

The gravity system and the floor slabs were not modeled. Based on tributary area considerations, vertical mass equal to 0.43 of the lateral mass was modeled above ground. For the BI and BI+RW buildings the gravity load resisted by the gravity columns at the base was

modeled as concentrated vertical forces. Rayleigh damping with 2% damping in the first and the third mode was used.

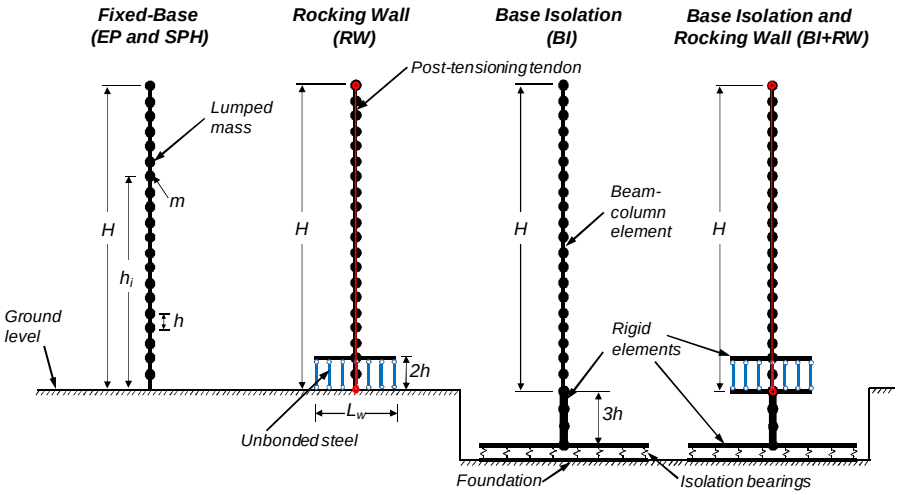


Figure 6. Elevation view of the numerical models.

## 4 GROUND MOTIONS

Fourteen strong pulse-type near-fault ground motions from the Imperial Valley (1979), Loma Prieta (1989), Landers (1992), Northridge (1994), Kobe (1995), Chi-Chi (1999), and Duzce, Turkey (1999) earthquakes were used in this study. The elastic absolute acceleration and relative displacement spectra for 2% damping are presented in Figure 4. The ground motions were selected to have pulses with different predominant frequency content. Table 2 lists the peak acceleration (PGA) of the ground motions. This table also presents the period of the predominant pulses contained in these motion. These periods were calculated as the periods $T_{pi,Sv}$, and $T_{pi,Sa}$ at which the elastic velocity, and absolute acceleration spectra, respectively, had a distinct local peak. As Table 2 shows, up to four distinct pulses with different predominant frequency content were identified in some of the ground motions.

As shown in Figure 4, the mean spectrum closely matches the MCE-level design spectrum between $T$ = 0.7 and 3.5 sec. The mean spectrum is close to the DBE-level in the constant acceleration period range. The MCE spectrum exceeds the mean spectrum for T larger than 3.5 sec. Individual motions included in the study (DUZCE, ELCEN6, LCN, TCU075, TCU102) exceed the MCE spectrum over different period ranges for T larger than 3.5 sec.

Table 2. Location and characteristics of the fault-normal ground motions used in this study.

| Record | Earthquake Location, Year | PGA (g) | $T_{p1,Sv}$ (sec) | $T_{p2,Sv}$ (sec) | $T_{p3,Sv}$ (sec) | $T_{p1,Sa}$ (sec) | $T_{p2,Sa}$ (sec) | $T_{p3,Sa}$ (sec) | $T_{p4,Sa}$ (sec) |
|---|---|---|---|---|---|---|---|---|---|
| BOLU | Duzce, Turkey, 1999 | 0.68 | 2.44 | 0.95 | - | - | - | 0.30 | - |
| BRAN | Loma Prieta, CA, 1989 | 0.63 | 0.80 | - | - | - | 0.40 | - | - |
| DUZCE | Duzce, Turkey, 1999 | 0.36 | 5.62 | 0.80 | - | 5.22 | 0.80 | - | - |
| ELCEN6 | Imperial Valley, CA, 1979 | 0.44 | 3.33 | - | - | 2.99 | - | - | - |
| LCN | Landers, CA, 1992 | 0.77 | 4.13 | - | - | 4.03 | - | - | - |
| LGP | Loma Prieta, CA, 1989 | 0.65 | 3.23 | 1.69 | 0.75 | 2.74 | 1.54 | 0.45 | - |
| RRS | Northridge, CA, 1994 | 0.89 | 1.00 | - | - | 0.75 | - | - | - |
| SCS | Northridge, CA, 1994 | 0.59 | 2.94 | 1.14 | - | 2.94 | 1.10 | - | - |
| TAK | Kobe, Japan, 1995 | 0.68 | 2.09 | 1.29 | - | 1.94 | 1.24 | - | - |
| TARZANA | Northridge, CA, 1994 | 1.33 | 4.38 | 2.09 | 0.70 | - | 2.09 | 0.70 | - |
| TCU075 | Chi-Chi, Taiwan, 1999 | 0.33 | 4.13 | - | - | - | - | - | - |
| TCU084 | Chi-Chi, Taiwan, 1999 | 1.15 | 4.83 | 1.74 | 0.90 | - | - | 0.90 | 0.45 |
| TCU102 | Chi-Chi, Taiwan, 1999 | 0.30 | 9.50 | 2.64 | - | - | 2.49 | - | - |
| TCU129 | Chi-Chi, Taiwan, 1999 | 1.02 | 4.13 | 1.59 | - | - | - | 0.25 | - |

## 5 RESULTS OF NUMERICAL ANALYSIS

Table 3 presents the periods of the first three lateral modes ($T_{L,i}$), as well as the first vertical ($T_{V,1}$) of the buildings. Base isolation increased the first, and second mode of the fixed-base and RW buildings by 2.5 and 4.3 times, respectively.

Table 3. Modal periods of studied buildings.

| Period (sec) | SPH | EP | RW | BI | BI+RW |
|---|---|---|---|---|---|
| $T_{L,1}$ | 1.81 | 1.88 | 1.80 | 4.61 | 4.61 |
| $T_{L,2}$ | 0.28 | 0.30 | 0.28 | 1.25 | 1.24 |
| $T_{L,3}$ | 0.10 | 0.11 | 0.10 | 0.24 | 0.24 |
| $T_{V,1}$ | 0.12 | 0.12 | 0.12 | 0.13 | 0.13 |

Figure 7 presents mean response envelopes of the buildings to the 14 near-fault ground motions. All the envelopes are presented in terms of the height, $h_i$, of floor $i$ from the ground level, normalized to the building height above ground, $H$. Presented are the bending moment, $M$,

normalized to the total building's seismic weight above ground, *W*, times *H*, curvature ductility, $\mu_\varphi$, of the core-wall, which is the ratio of peak curvature to the section yield curvature, see Table 2, shear force, $V_i$, normalized to *W*, floor acceleration, *A*, normalized to the PGA, lateral displacement relative to the ground, *D*, and interstory drifts (*ID*) responses. Table 4 presents the mean values as well as the peak values, of different response parameters. The floor accelerations and shear forces presented are filtered with a low-pass filter with a 10 Hz cut off frequency.

The response of the fixed-base EP and SPH buildings, resulted in large mean value of base shear force equal to 0.24W and 0.25W, with the peak value reaching the excessive value for a 20-story building of 0.34 and 0.43W, respectively, see Table 4. For these designs, large curvature ductility, and large tensile strains developed at the base of the wall corresponding to significant structural damage at the base, see Table 4. In the EP building, some inelastic deformations developed also around mid-height of the wall. Also significant were the floor accelerations for both fixed-base buildings, which were close to or larger than PGA along about 70% of the building height.

The RW building experienced similar floor accelerations, forces and displacements compared to the fixed-base buildings. The RW building prevented the formation of a plastic hinge at the base of the wall, compared to the fixed-base buildings with the peak strain in the bonded reinforcement to be less than 0.1%. Compared to the EP and SPH buildings, however, the RW building developed higher moments on the upper part of the building. The mean uplift at the rocking plane of the wall was 9.6 cm, and the peak 20.2 cm, corresponding to a rotation of the rocking plane of about 2.6%.

The BI and BI+RW designs resulted in significant reduction of the shear forces and floor accelerations by about 50%, in comparison with the fixed-base and rocking wall designs. These designs reduced the bending moments on the upper half of the buildings by about 35%.

As expected for a mean displacement of the isolation bearings equal to 0.65 m, the base isolated building resulted in exceeding the flexural strength of the wall at the ground level, despite the large amount of longitudinal steel in the wall (2.4% longitudinal steel ratio), and developing significant inelastic deformations strains in the steel, see Table 4. The mean value of $\mu_\varphi$ for the BI design was 4.9, with the peak value to be 12.5.

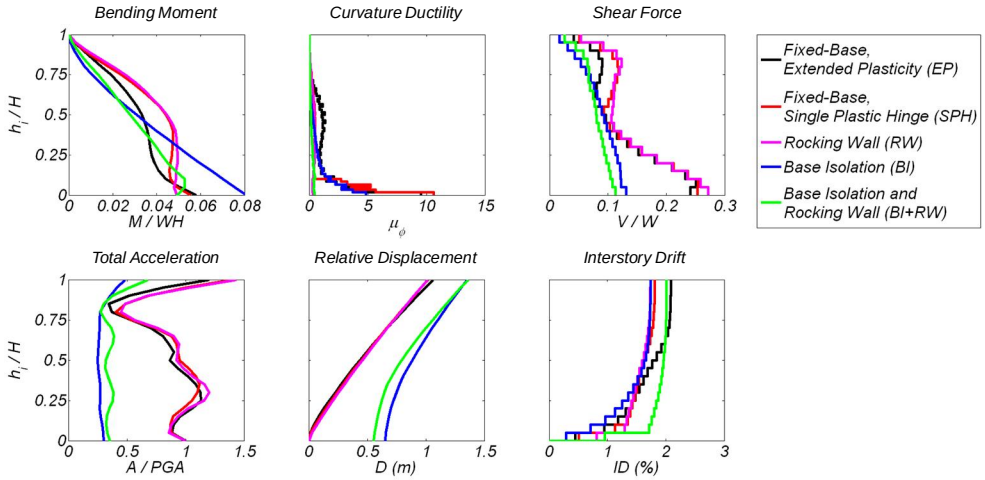


Figure 7. Mean response envelopes.

The BI+RW building was able combine the beneficial effects of an isolation plane with bearings in reducing accelerations and lateral forces, and a rocking plane that eliminated inelastic deformations and thus post-earthquake damage at the base of the wall, see Figure 7 and Table 4. Compared to the fixed-base designs, it reduced the shear forces and floor accelerations by a factor of 2, while it avoided the formation of plastic hinge at the core-wall. The bearing displacements were also less than 80 cm for all motions, with the mean displacement to be equal to 56 cm, see Table 4. The mean and peak uplift at the rocking plane of the wall was 12.5 cm,

and 29.7 cm, respectively corresponding to a rotation of the rocking plane of about 1.7%., and 4.0%, respectively.

The response envelopes to the 14 individual ground motions, for the response parameters described above, are presented in Figure 8. The bending moment at the ground level for the buildings without an isolation plane consisting of bearings is controlled by the bending moment strength of the wall at this level as well as the level of hardening this section experiences.

Table 4. Mean, and peak (in parenthesis) values of response parameters over 14 ground motions.

| | EP | SPH | Rocking Wall (RW) | Base Isolation (BI) | Base Isolation and Rocking Wall (BI+RW) |
|---|---|---|---|---|---|
| Midheight bending moment, $M_{0.5H}$ / $WH$ | 0.033 (0.046) | 0.044 (0.069) | 0.045 (0.067) | 0.031 (0.045) | 0.028 (0.035) |
| Base shear, $V$ / $W$ | 0.24 (0.34) | 0.25 (0.43) | 0.27 (0.42) | 0.13 (0.22) | 0.11 (0.16) |
| Roof acceleration $A_r$ / $PGA$ | 1.4 (3.1) | 1.6 (2.3) | 1.6 (2.6) | 0.6 (1.2) | 0.9 (2.1) |
| Base curvature ductility, $\mu_{\varphi b}$ | 9.6 (13.7) | 10.6 (16.4) | 0.3 (0.4) | 4.9 (12.5) | 0.5 (0.8) |
| Peak tensile strain at 0.3m from the ground level, $\varepsilon_b$ (%) | 2.9 (4.2) | 3.3 (5.1) | 0.03 (0.05) | 1.4 (3.7) | 0.07 (0.15) |
| Uplift of wall at ground level (cm) | - | - | 9.6 (20.2) | - | 12.5 (29.7) |
| Isolator Displacement (cm) | - | - | - | 65 (92) | 56 (80) |

Significantly larger variation of this moment is observed for the buildings with a base isolation plane consisting of bearings which is due to its dependence on the displacement and thus on the force it develops. As a result of the predominant frequency content of the ground motion, significant variation on the shape of the bending moment envelope of the buildings without base isolation was observed. For example, the TCU084 ground motion resulted in significant excitation of the second mode of response for the EP, SPH, and RW buildings and the bending moment envelope had a local peak around the mid-height of the structures. This motion contains multiple strong pulses with $T_{p3,Sa}$ about 0.45 sec, see Table 3, which causes significant excitation of the second mode of response. The base-isolated buildings show significantly smaller sensitivity to the frequency content of the ground motions in terms of shape of the bending moment envelope. A nearly linear bending moment envelope for all the ground motions is noted, demonstrating the efficiency of base isolation in reducing the second and higher modes of response.

As noticed for the bending moment envelopes, the shear force envelopes, follow the first mode shear force profile for BI and BI+RW buildings, while for SPH, EP, and RW buildings showed significant contribution of the second mode of response for some ground motions, see the local peak of shear force at 0.75H.

Similarly, the trend regarding the sensitivity of floor accelerations to the frequency content of the motions is observed. Acceleration envelopes of BI and BI+RW were nearly constant over the height of the buildings for all fourteen ground motions and below PGA, except for three motions for the BI+RW building, while those of SPH, EP, and RW buildings were significantly affected by the second and higher modes of response, with roof accelerations reaching three times the PGA in some cases.

The displacement and interstory drift ratio envelopes for all buildings were dominated by the first mode of response. The peak roof displacement for all buildings occurs for the ELCEN6 motion. As it can be seen from the elastic displacement spectra this motion results in displacements larger than 1 m for period larger than 2.7 sec. Similarly this is also observed in

the displacement demand that the LCN motion imposes for all buildings. While expected for the base isolated buildings, it is assumed that this response for the fixed base buildings occurs because the low-frequency predominant pulse results in significant amplification of the elastic displacements and thus to significant inelastic displacements.

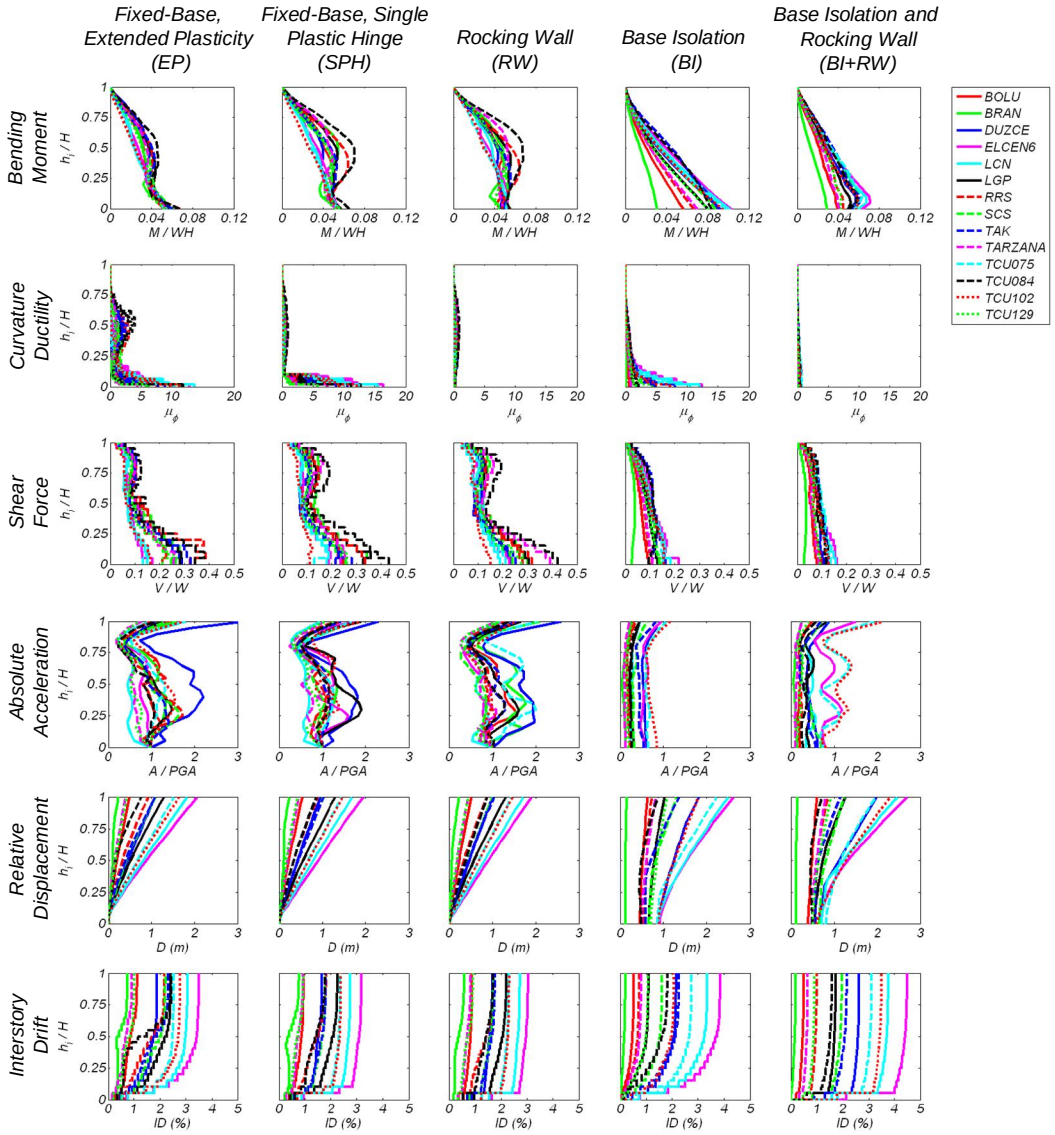


Figure 8. Response envelopes to individual ground motions of the five buildings studied.

## 6 SUMMARY AND CONCLUSIONS

This paper investigated the seismic performance of five tall reinforced concrete wall buildings. The first two buildings were conventionally designed to develop the majority of inelastic deformation in a flexural plastic hinge at the base of the core-wall. The third building used an isolation plane, consisting of elastomeric bearings, at the base of the building below the ground level. The fourth had a core-wall designed to rock at the ground level. The last building included both the isolation plane and the rocking core-wall of the third and fourth building. The response of these buildings subjected to 14 strong pulse-type near-fault ground motions was compared in terms of floor accelerations, forces, displacements, and material strains. The following conclusions were drawn:

1) The building with a core-wall designed to rock at the ground level avoided the formation of a flexural plastic hinge at the base of the wall without reducing the floor accelerations and forces when compared to conventionally designed buildings.
2) The buildings with base isolation below ground developed about 2 times smaller mean, as well as peak, accelerations and shear forces in comparison with the buildings without isolation bearings.
3) The building with base isolation and without a rocking core-wall was not able to prevent the formation of a plastic hinge at the core-wall.
4) The performance of the BI+ROCKING building that combined the isolation plane with bearings of the BI building and the rocking core-wall of the RW building exhibited a superior performance. This building reduced about 2 times on average accelerations, and shear forces while eliminated the formation of a flexural plastic hinge at the base of the core-wall above the ground.
5) The buildings designed with seismic isolation demonstrated significantly less sensitivity to the ground motion characteristics in terms of the shape of the bending moment, shear force, and floor acceleration envelopes.

## REFERENCES


ASCE 7-05. 2006. *Minimum Design Loads for Buildings and Other Structures.* American Society of Civil Engineers.

Calugaru, V. & Panagiotou, M. 2010. Seismic isolation using single and dual shear hinging of tall cantilever wall buildings subjected to near fault ground motions. *Proceedings, 9th U.S. National and 10th Canadian Conference on Earthquake Engineering, Toronto.*

Calugaru, V. & Panagiotou, M. 2011. Seismic isolation of tall cantilever wall buildings using one or more isolation planes. *Proceedings, 8th International Conference on Urban Earthquake Engineering, March 7-8, 2011, Tokyo Institute of Technology, Tokyo*.

Carpenter, L. D., Naeim, F., Lew, M., Youssef, N. F., Rojas, F., Saragoni, G. R., Schachter Adaros, M. 2011. Performance of tall buildings in Viña del Mar in the 27 February 2010 Offshore Maule, Chile earthquake. *Structural Design of Tall and Special Buildings* 20:17-36.

Celebi, M. 1992a. Highlights of Loma Prieta responses of four tall buildings. *Proceedings, Earthquake Engineering Tenth World Conference, Rotterdam, Holland.*

Celebi, M. 1992b. The Loma Prieta, California, earthquake of October 17, 1989 – building structures. *U.S. Geological Survey Professional Paper 1552-C*.

Chey, M.H., Chase, J.G., Mander, J.B., Carr, A.J. 2010. Semi-active tuned mass damper building systems: application. *Earthquake Engineering & Structural Dynamics* 39(1):69-89.

Council on Tall Buildings and the Urban Habitat (CTBUH). 2011. *Tall Building Database*. http://www.ctbuh.org/Resources/WorldsTallest/tabid/123/Default.aspx.

Dynamic Isolation Systems (DIS). 2011. http://www.dis-inc.com/index.html.

Earthquake Protection Systems (EPS). 2011. http://www.earthquakeprotection.com/.

Fujita, T. 1991. Seismic isolation rubber bearings for nuclear facilities. *Nuclear Engineering and Design* 127:379-391.

International Code Council (ICC). 2009. *International Building Code.*

Kam, W.Y. 2011. Critically damaged multi-storey RC buildings. *Day 03 Field Report, Christchurch 22 Feb 2011 6.3Mw Earthquake.* http://www.eqclearinghouse.org/2011-02-22-christchurch.

Kani, N. 2009. Current state of seismic-isolation design. *Journal of Disaster Research* 4(3): 175-181.

Kato, R. 2003. The tensile tests of natural rubber bearings focused on the effect of the steel flange plates. *Proceedings, ASME Pressure Vessels and Piping Conference, Cleveland.*

Kawamura, S., Ogura, K., Tanaka, S., Yajima, A. 1998. Base and mid-story seismic isolation retrofit of middle rise RC buildings. *Proceedings, Second Japan-Turkey Workshop on Earthquake Engineering, Istanbul*; 383-394.

Kelly, J.M. & Takhirov, S.M. 2004. Analytical and numerical study on buckling of elastomeric bearings with various shape factors. *Earthquake Engineering Research Center Report, UCB/EERC-2004/03.*

Komuro, T., Nishikawa, Y., Kimura, Y., Isshiki, Y. 2005. Development and realization of base isolation system for high-rise buildings. *Journal of Advanced Concrete Technology* 3(2):233-239.

Lew, M. 2006. Design of tall buildings in high-seismic regions. *Structural Design of Tall and Special Buildings* 16:537-541.

Lew, M., Naeim, F., Carpenter, L. D., Youssef, N. F., Rojas, F., Schachter Adaros, M., Saragoni, G. R. 2010. Seismological and tectonic setting of the 27 February 2010 Offshore Maule, Chile earthquake. *Structural Design of Tall and Special Buildings* 19:838-852.

Los Angeles Tall Buildings Structural Design Council (LA TBSDC). 2005. *An Alternative Procedure for Seismic Analysis and Design of Tall Buildings Located in the Los Angeles Region.* LA TBSDC.

Marriott, D., Pampanin, S., Bull, D.K., Palermo, A. 2008. Dynamic testing of precast, post-tensioned rocking wall systems with alternative dissipating solutions. *Bulletin of the New Zealand Society for Earthquake Engineering* 41(2):90-102.

Moehle, J., Bozorgnia, Y., Yang, T.Y. 2007. The Tall Buildings Initiative. *Proceedings SEAOC Convention*; 315-324.

Munir, A., Warnitchai, P. 2011. Optimal reduction of inelastic seismic demands in high-rise reinforced concrete core wall buildings using energy-dissipating devices. Published online, *Structural Design of Tall and Special Buildings*, May.

Muramatsu, Y., Nishikawa, I., Kawabata, I., Takayama, M., Kimura, Y. 2001. Tensile property of large-sized natural rubber bearing. *Journal of Architecture and Building Science* 116(1466):53-56.

Naeim, F. 1994. Implications of the 1994 Northridge earthquake ground motions for the seismic design of tall buildings. *The Structural Design of Tall Buildings* 3:247-267.

Naeim, F. 1998. Performance of 20 extensively-instrumented buildings during the 1994 Northridge earthquake. *Structural Design of Tall Buildings* 7:179-194.

Nielsen, G.M. 2009. Performance of rocking core walls in tall buildings subjected to severe seismic demands. *Master's Thesis*, University of California, Berkeley.

Open System for Earthquake Engineering Simulation (OpenSees). 2011. opensees.berkeley.edu

Otani, S. 1999. RC buildings damage statistics and SDF response with design seismic force. *Earthquake Spectra* 15(3):485-501.

Pan, P., Zamfirescu, D., Nakashima, M., Nakayasu, N., Kashiwa, H. 2005. Base-isolation design practice in Japan: introduction to the post-Kobe approach. *Journal of Earthquake Engineering* 9(1):147-171.

Panagiotou, M., Calugaru, V., Visnjic, T. 2009. Higher mode effects on the seismic response of tall cantilever wall buildings subjected to near fault ground motions. *Proceedings, Structural Engineers Association of California Convention, San Diego*; 345–357.

Panagiotou, M., Restrepo, J.I. 2009. Dual-plastic hinge design concept for reducing higher-mode effects on high-rise cantilever wall buildings. Published online, *Earthquake Engineering and Structural Dynamics*, February.

Restrepo, J.I., Rahman, A. 2007. Seismic performance of self-centering structural walls incorporating energy dissipaters. *Journal of Structural Engineering, ASCE*, November; 1560-1570.

Rojas, F., Naeim, F., Lew, M., Carpenter, L. D., Youssef, N. F., Saragoni, G. R., Schachter Adaros, M. 2011. Performance of tall buildings in Concepción during the 27 February 2010 moment magnitude 8.8 Offshore Maule, Chile earthquake. *Structural Design of Tall and Special Buildings* 20:37-64.

Ryan, K.L., Kelly, J.M., Chopra, A.K. 2005. Nonlinear model for lead–rubber bearings including axial-load effects. *Journal of Engineering Mechanics*, December; 1270-1278.

Structural Engineers Association of Northern California (SEAONC). 2007. Seismic design and review of tall buildings using non-prescriptive procedures. *Recommended Administrative Bulletin, San Francisco*, April 23.

Tall Building Initiative (TBI), Pacific Earthquake Engineering Research Center (PEER). 2010. *Guidelines for Performance-Based Seismic Design of Tall Buildings.* PEER Report No. 2010/05.

THK. 2011. http://www.thk.com/us/products/class/sliderail/index.html

Tsai, K.C., Hsiao, C.P., Bruneau, M. 2000. Overview of building damages in 921 Chi-Chi earthquake. *Earthquake Engineering and Engineering Seismology* 2(1):93-108.

Tsuneki, Y., Torii, S., Murakami, K., Sueoka, T. 2009. Middle-story isolated structural system of high-rise building. *Journal of Disaster Research* 4(3):229-238.

Vassiliou, M.F. & Makris, N. 2011. Analysis of the rocking response of rigid blocks standing free on a seismically isolated base. Published online, *Earthquake Engineering and Structural Dynamics*, April.

U.S. Geological Survey (USGS). 2011. http://earthquake.usgs.gov/earthquakes/states/historical.php.

Wiebe, L., and Christopoulos, C. 2009. Mitigation of higher mode effects in base-rocking systems by using multiple rocking sections. *Journal of Earthquake Engineering* 13(1):83-108.

Willford, M., Whittaker, A., Klemencic, R. 2008. Recommendations for the seismic design of high-rise buildings. *Council on Tall Buildings and the Urban Habitat, Draft for Comment*, February 21, 2008; 28.

Youssef, N. F., Tunick, D., Naeim, F., Lew, M., Carpenter, L. D., Rojas, F., Saragoni, G. R., Schachter Adaros, M. 2011. Performance of the Torre Bosquemar and Olas Buildings in San Pedro de la Paz and the Pedro de Valdivia Building in Concepción in the 27 February 2010 Offshore Maule, Chile earthquake. *Structural Design of Tall and Special Buildings* 20:65-82.

Ziyaeifar, M. & Noguchi, H. 1998. Partial mass isolation in tall buildings. *Earthquake Engineering and Structural Dynamics* 27(1):49-65.

# Seismic Behavior of Batter-Pile Foundation: Centrifuge Tests and Analytical Study

T. Tazoh
*Institute of Technology, Shimizu Corporation, Japan*

M. Sato
*National Research Institute for Earth Science & Disaster Prevention, Japan*

J. Jang & Y. Taji
*Institute of Technology, Shimizu Corporation, Japan*

H. Kimata & N. Kobayashi
*Civil Engineering Division, Shimizu Corporation, Japan*

G. Gazetas
*National Technical University of Athens, Greece*

ABSTRACT: We carried out centrifuge tests to clarify the seismic behavior of batter-pile foundations. A vertical-pile foundation and a batter-pile foundation without the presence of a superstructure were installed parallel to each other in a soil container filled with dry sand, and were excited simultaneously. Through a comparison of the acceleration and displacement response of the footing, as well as the bending and axial strain of the piles for the two pile foundations, the seismic behavior of the batter-pile foundation was experimentally and analytically investigated.

## 1 INTRODUCTION

The lateral stiffness of a pile foundation can be increased by adopting batter piles, which is why they are commonly used in landing piers that are subject to large lateral forces. However, batter piles are seldom used for buildings or civil engineering structures even in the case of large lateral forces for the following reasons:

1) When soil settlement occurs, not only the safety of the pile foundation but also that of the structure as a whole system may be threatened by settlement-induced vertical loads acting on the batter piles.
2) During an earthquake, the piles in a batter-pile foundation may be subject to excessive axial compression and pullout forces, which are not generated in a vertical-pile foundation.
3) The strength of concrete piles is reduced by decreasing the compressive force acting on the piles due to rocking motions induced by the adopted batter piles.
4) Since infinite lateral ground planes cannot be assumed for batter piles, they cannot be expected to have the same horizontal subgrade reaction as that of vertical piles.
5) In urban areas, the use of batter piles is constrained by the boundary lines of adjacent land.

The 1995 Great Hanshin Earthquake in Japan has increased the demand for pile foundations with high seismic performance, as well as lower cost and easier construction. Batter piles can be used with little additional expense, no special design, and relatively easy construction. Therefore, the seismic behavior of batter piles has recently attracted much research interest, as has research and development related to easy and accurate methods of installing batter piles (Bhattacharya, S., et al., 2009, Deng, N., et al., 2007, Gerolymos, N., et al., 2008, Giannakou, A., et al., 2007, 2009, Escoffier, S., et al., 2008, Pinto, P., et al., 1997, Poulos, H. G., 2006, Razavi, S. A., 2007, Tazoh, T., et al., 1987, 1988, 2005, 2007, 2009).

In this study, we carried out centrifuge shaking table tests to clarify the seismic behavior of batter-pile foundations. A vertical-pile foundation and a batter-pile foundation were installed parallel to each other in a soil container filled with dry sand, and were excited simultaneously (Tazoh, T., et al., 2005, 2007, 2009). As our objective was to investigate the fundamental characteristics of the seismic behavior of batter piles, none of the pile-foundation models had a superstructure. This study focused on the kinematic interaction of batter piles (Fan, K., et al., 1991, Mylonakis, G., et al., 1997, Mylonakis, G., 2001, Nikolaou, S., et al., 2001, Sica, S., et., al., 2007, Tazoh, T., et al., 1987). Through a comparison of the acceleration and displacement response of the footing, as well as the axial and bending strain of the piles for the two pile foundations, the seismic behavior of the batter-pile foundation was experimentally and analytically studied.

## 2 CENTRIFUGE TESTS

The most direct and effective way to quantitatively and qualitatively investigate the seismic behavior of batter piles is to compare the seismic behavior between a vertical-pile foundation and a batter-pile foundation under the same input motions. Each test for each model must be carried out under nearly identical conditions with respect to input motions, soil conditions, and soil behavior. Note, however, that it is impossible to achieve complete similarity between shaking table tests due to the difficulty of reproducing the input motion and nonlinear behavior of the soil. Therefore, a vertical-pile foundation and a batter-pile foundation without the presence of a superstructure were installed parallel to each other in a soil container, as shown in Figure 1, and were excited simultaneously.

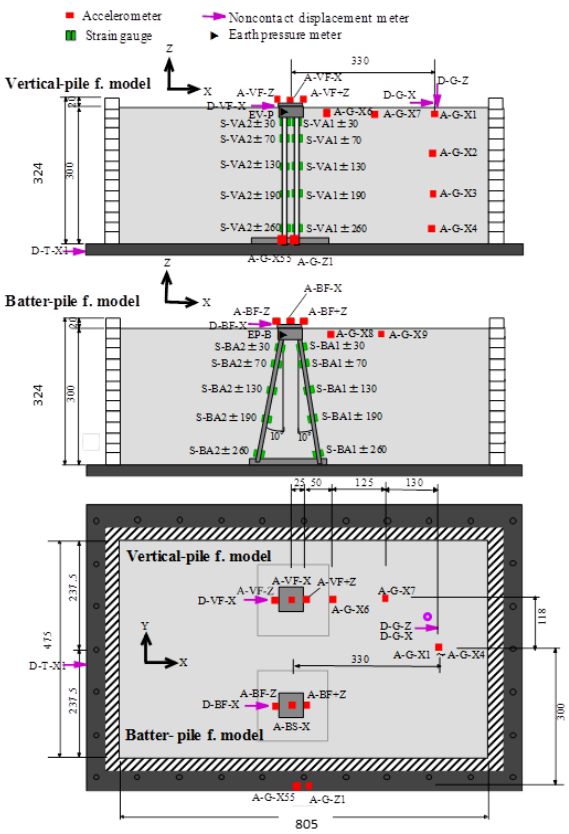


Figure 1 Longitudinal sections and plan of the 1/30-scale centrifuge model
(Scale unit: mm, for the prototype dimensions: multiply by 30. A vertical-pile foundation and a batter-pile foundation without the presence of a superstructure were installed parallel to each other in a soil container which was filled with dry sand, and were excited simultaneously.)

A laminar box was used as the soil container to allow shear deformation of the soil deposit as in the free field. Actually, installing two models that behave differently in a laminar box is not an appropriate testing method because the behavior of the models might influence each other. However, considering the inconsistency of the input motion and the difficulty of reproducing the soil conditions and nonlinearity, we believe that this method is more reasonable than individually testing the vertical-pile foundation and batter-pile foundation separately.

The interior of the soil container was 805 mm in length, 475 mm in width, and 324 mm in height. All tests were conducted at centrifugal acceleration of 30 g on a 1/30-scale model. Table 1 shows the scaling ratios of the models.

Table 1 Scaling ratios of the test model

| Item | | Symbol | Unit | Centrifuge model | Prototype | Scale |
|---|---|---|---|---|---|---|
| Sand stratum | Depth | H | m | 0.3 | 9 | $1/\lambda$ |
| | Density | $\rho_t$ | $KN/m^3$ | 15.0 | 15.0 | 1 |
| Structure | Width | W | m | 0.05 | 1.5 | $1/\lambda$ |
| | Height | H | m | 0.04 | 1.2 | $1/\lambda$ |
| | Mass | M | kg | 0.785 | 21,195 | $1/\lambda^3$ |
| Footing | Width | W | m | 0.05 | 1.5 | $1/\lambda$ |
| | Height | H | m | 0.03 | 0.9 | $1/\lambda$ |
| | Mass | M | kg | 0.58875 | 15,896 | $1/\lambda^3$ |
| Pile | Diameter | D | m | 0.01 | 0.3 | $1/\lambda$ |
| | Thickness | t | m | 0.0002 | 0.006 | $1/\lambda$ |
| | Young's modulus | E | $MN/m^2$ | 2.06E+05 | 2.06E+05 | 1 |
| | Area | A | $m^2$ | 6.16E-06 | 5.54E-03 | $1/\lambda^2$ |
| | Moment of inertia of area | I | $m^4$ | 7.40E-11 | 5.99E-05 | $1/\lambda^4$ |
| | Normal stiffness | EA | MN | 1.27E+00 | 1.14E+03 | $1/\lambda^2$ |
| | Bending stiffness | EI | $MN\text{-}cm^2$ | 1.52E-09 | 1.23E-03 | $1/\lambda^4$ |
| Acceleration | Centrifuge | *g* | *g* | 30 | 1 | $\lambda$ |
| | Earthquake | $\alpha$ | Gal | 6000 | 200 | $\lambda$ |
| Other parameters | Displacement | $\delta$ | m | 1 | 30 | $1/\lambda$ |
| | Force | F | N | 1 | 900 | $1/\lambda^2$ |
| | Stress | $\tau$ | KPa | 1 | 1 | 1 |
| | Strain | $\gamma$ | | $1x10^{-6}$ | $1x10^{-6}$ | 1 |
| | Time | t | s | 1 | 30 | $1/\lambda$ |
| | Frequency | f | Hz | 30 | 1 | $\lambda$ |

The vertical-pile foundation and the batter-pile foundation each had four piles, and the pile heads and pile tips were rigidly connected to the footing and the base of the soil container, respectively. The batter piles were identically inclined at a 10° angle. The soil deposit was a uniform layer consisting of dry silica sand No. 7 (mean particle diameter $D_{50}$ = 0.147 mm; soil density $\rho_s$ = 26.35 $KN/m^3$; maximum dry density $\rho_{max}$ = 15.39 $KN/m^3$; minimum dry density $\rho_{min}$ = 12.06 $KN/m^3$). Thickness and relative density of the soil deposit were 300 mm (prototype: 9 m) and Dr = 60%, respectively.

Figure 2 shows the grain size accumulation curve of silica sand No. 7. Table 2 shows the materials and size of the experimental model used in the tests and Photograph 1 shows the test model. Sixty monitoring channels in total were installed, with the sensors comprising fifteen accelerometers, five non-contact displacement meters, and forty strain gauges (Table 3). The test was conducted a total of twelve times, varying the input motion and maximum acceleration as shown in Table 4.

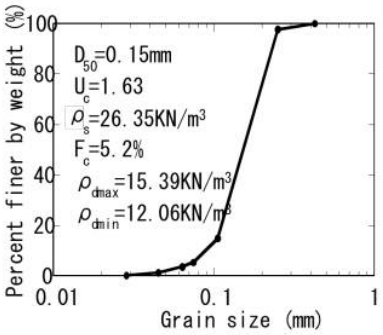


Figure 2 Grain size accumulation curve of silica sand No. 7
(Mean particle diameter $D_{50}$ = 0.15 mm, Soil density $\rho_s$ = 26.35 KN/m$^3$,
Maximum dry density $\rho_{max}$ = 15.39 KN/m$^3$, Minimum dry density $\rho_{min}$ = 12.06 KN/m$^3$)

Table 2 Materials and dimensions of the test model

| Parts | Material & size |
|---|---|
| Laminar box | 805 mm, 475 mm, 324 mm (Inner size: length, width, depth) |
| Soil deposit | Dry sand: Silica No. 7 (Dr = 60%), Thickness: 300 mm |
| Vertical pile | Stainless steel<br>No. of piles: 4 (2×2), Inclination angle: 0°<br>Length: 270 mm, Diameter: 10 mm, Thickness: 0.2 mm |
| Batter pile | Stainless steel<br>No. of piles: 4 (2×2), Inclination angle: 10°<br>Length: 274 mm, Diameter: 10 mm, Thickness: 0.2 mm |
| Footing | Steel<br>Thickness: 30 mm, Plan size: 50 mm×50 mm |

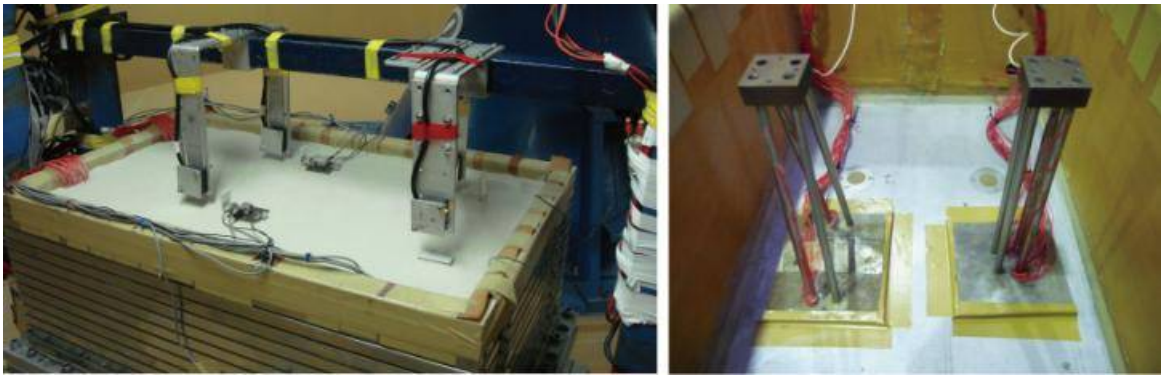

Photograph 1 Test model
(The pile foundations have four piles.)

While the purpose of this study was to clarify the kinematic interaction of the batter piles, the effects of the mass of the footing (made of steel, size: 3×5×5 cm) must also be considered. The results might include inertial interaction caused by the inertial force of the footing because the footing has 43% of the total mass of the pile-footing model, which consequently may not represent perfect kinematic interaction. We evaluated the degree of influence of the inertial interaction analytically by the finite element method, as shown in the Appendix.

Table 3 Installed sensors
(60 monitoring channels were installed, with the sensors comprising 15 accelerometers, 5 non-contact displacement meters, and 40 strain gauges.)

| Transducer | Location | Direction | Number | Subtotal | Total |
|---|---|---|---|---|---|
| Accelerometer | Batter pile | X | 1 | 15 | 60 |
| | | Z | 2 | | |
| | Vertical pile | X | 1 | | |
| | | Z | 2 | | |
| | Ground | X | 6 | | |
| | Base | X | 1 | | |
| | Table control | X | 1 | | |
| | Centrifugal acc. | Z | 1 | | |
| Non-contact displacement meter | Batter pile | X | 1 | 5 | |
| | Vertical pile | X | 1 | | |
| | Ground | X | 1 | | |
| | | Z | 1 | | |
| | Base | X | 1 | | |
| Strain gauge | Batter pile | Pile-BA1 | 10 | 40 | |
| | | Pile-BA2 | 10 | | |
| | Vertical pile | Pile-VA1 | 10 | | |
| | | Pile-VA2 | 10 | | |

Table 4 Test cases

| Input motion | Freq. of input motion (Hz) | Max. acc. of input motion (Gal) | Test case No. |
|---|---|---|---|
| Sweep test motion | 1.7–10 Hz | 5 | 1-1 |
| | | 15 | 1-2 |
| | | 30 | 1-3 |
| Sinusoidal excitation | 3.5 Hz | 50 | 2-1 |
| | | 100 | 2-2 |
| | | 200 | 2-3 |
| Sinusoidal excitation | 7.0 Hz | 50 | 3-1 |
| | | 100 | 3-2 |
| | | 200 | 3-3 |
| El Centro record | El Centro record N-S component | 50 | 4-1 |
| | | 100 | 4-2 |
| | | 200 | 4-3 |

## 3 CENTRIFUGE TESTS

### 3.1 *Dynamic behavior of the ground*

Figure 3 shows the frequency transfer function calculated by the acceleration records between the soil surface and the input motion of the sweep test. The predominant frequency of the ground is 3.5 Hz in the case of maximum acceleration of input motion at 5 Gal. The predominant frequencies are 3.2–3.3 Hz and 3.0–3.1 Hz, and also the peak acceleration amplification factors decrease corresponding to the increase in maximum acceleration of the input motion to 15 Gal and 30 Gal.

Figure 4 shows the frequency transfer function between the ground surface and input motion obtained from El Centro record excitation. The predominant frequency of the ground is 3.4 Hz in the case of maximum acceleration of input motion at 50 Gal. The predominant frequencies are 2.8–2.9 Hz and 2.4–2.5 Hz, and also the peak acceleration amplification factors decrease according to the increase in maximum acceleration of the input motion to 100 Gal and 200 Gal. These phenomena were obviously produced by the nonlinearity of the soil.

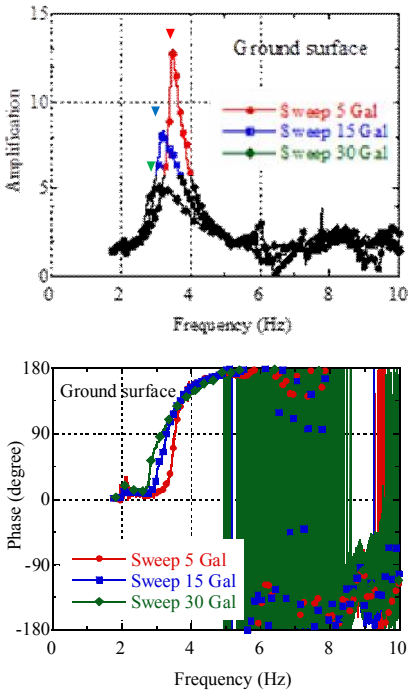


Figure 3 Frequency transfer function of the ground surface obtained from sweep test (5 Gal, 15 Gal, 30 Gal)

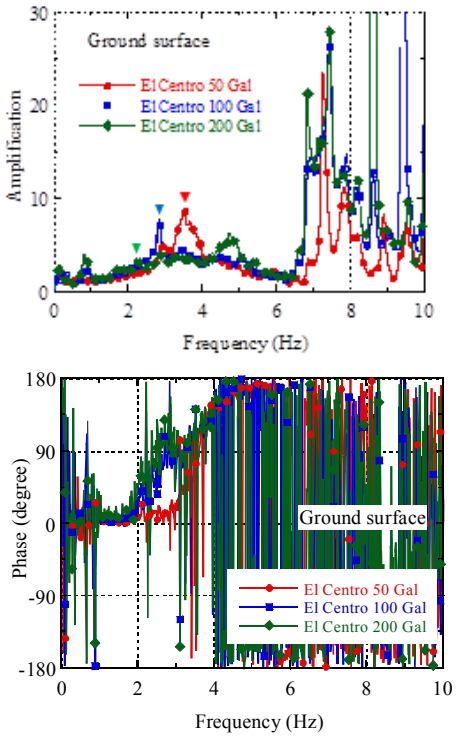


Figure 4 Frequency transfer function of the ground surface obtained from the El Centro record excitations (50 Gal, 100 Gal, 200 Gal)

### 3.2 *Rotational characteristics of the footing*

Figure 5 shows the relationship between horizontal displacement and rotational angle of the footing based on the data from sinusoidal excitation of 3.5 Hz, in order to investigate the rotational characteristics of the footing of the vertical-pile foundation and the batter-pile foundation. The rotational angle is calculated by dividing the difference in the vertical displacement based on the data of the accelerometers installed at both sides of the footing by the distance between the two accelerometers.

The fact that there is no phase difference between the sway and rocking motions indicates that the response of the footing to motion to the right is counterclockwise rotation, as shown in Figure 6. There is no phase difference between the sway and rocking motions of the vertical-pile foundation; on the other hand, anti-phase behavior can be seen in the data for the batter-pile foundation.

Figure 7 shows the data obtained from El Centro record excitation at the maximum acceleration of 200 Gal. The same trend as seen in the case of sinusoidal excitation can also be found in Figure 7. The phenomena of the opposite phase between the sway and rocking motions of the vertical-pile foundation and the batter-pile foundation can be found in all of the other test data. From Figures 5 and 7, it can also be seen that the rotation angles of the batter-pile foundation are almost two times larger than those of the vertical-pile foundation. This causes the larger strains of the batter piles compared with those of the vertical piles as shown in the next section.

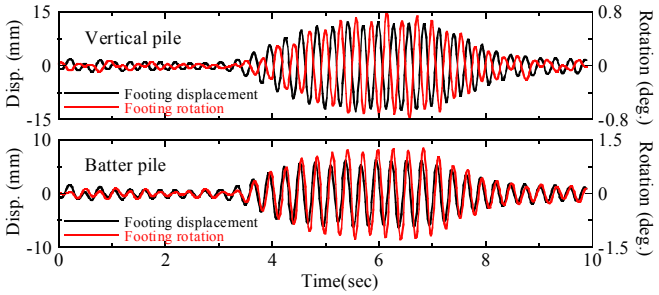


Figure 5 Comparisons of horizontal displacement and rotational angle of the footings between the vertical-pile foundation and the batter-pile foundation (Sinusoidal excitation: 3.5 Hz, 200 Gal)

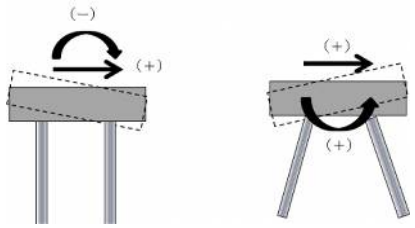


Figure 6 Kinematic responses of footings

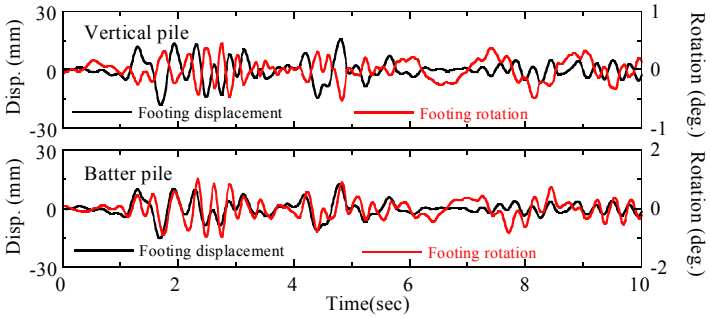


Figure 7 Comparisons of horizontal displacement and rotational angle of the footings between the vertical-pile foundation and the batter-pile foundation (El Centro record: 200 Gal)

### 3.3 *Bending and axial strains of the piles*

Figure 8 shows the maximum-value distribution of the bending and axial strains of the piles in the vertical-pile foundation (pile-VA1) and the batter-pile foundation (pile-BA1) obtained from sinusoidal excitation of 3.5 Hz. The frequency of 3.5 Hz closely corresponds to that of the predominant frequency of the ground as shown in Figure 3. The largest values were obtained at the pile heads, and the bending and axial strains of the batter-pile foundation were larger than those of the vertical-pile foundation in all cases, as shown in Figure 8.

Figure 9 shows the maximum-value distribution of the bending and axial strains of the piles in the vertical-pile foundation (pile-VA1) and the batter-pile foundation (pile-BA1) obtained from El Centro record excitation. The largest values were obtained at the pile heads, and the bending and axial strains of the batter-pile foundation were larger than those of the vertical-pile foundation, likely due to the sinusoidal excitation.

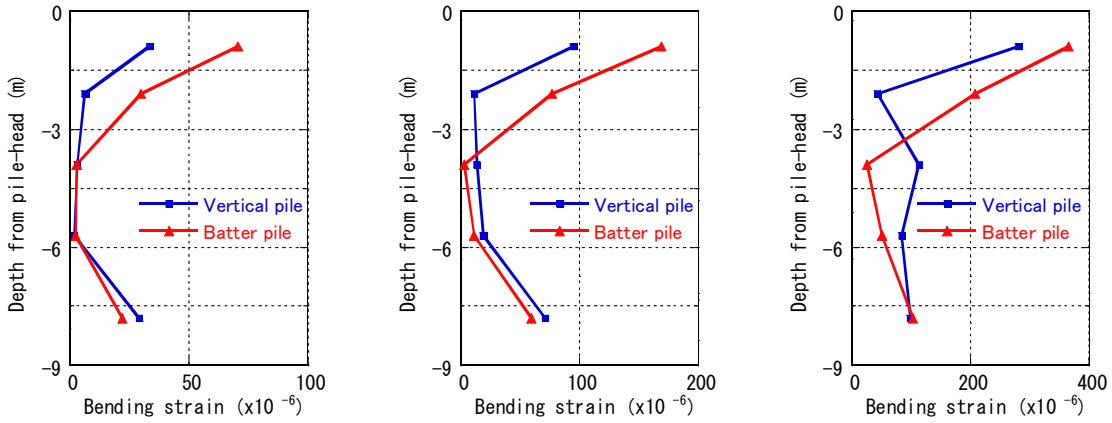


a) Bending strain

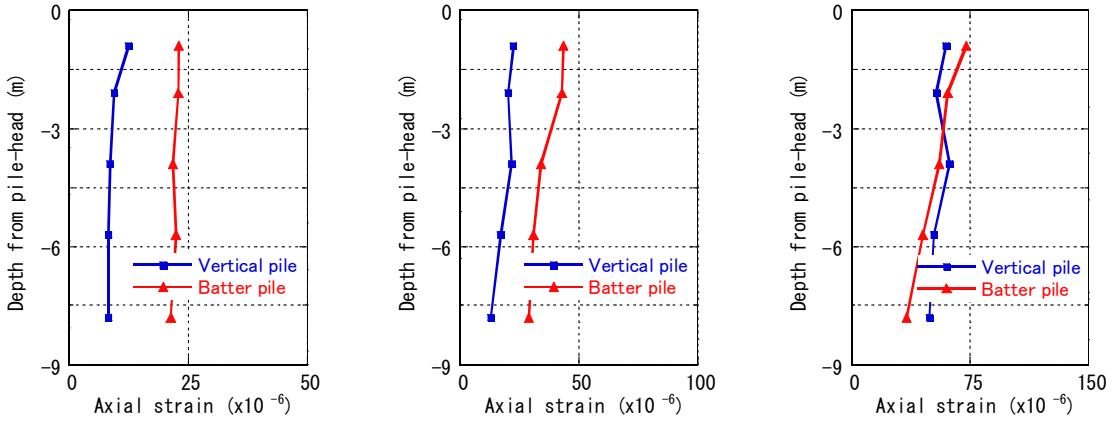


b) Axial strain

Figure 8 Bending and axial strain distributions of the vertical-pile foundation (pile-VA1) and the batter-pile foundation (pile-BA1) obtained from the sinusoidal excitation of 3.5 Hz (50 Gal, 100 Gal, 200 Gal)

### 3.4 *Maximum responses of the footing, the ground surface and the bending and axial strains at the pile head*

Figures 10 and 11 show the maximum values for acceleration of the footings and the ground surface, and the bending and axial strains at the pile heads corresponding to the increments in maximum acceleration of the input motion. From the figures, it can be seen that the maximum acceleration of the footing of the vertical-pile foundation is larger than that of the batter-pile foundation

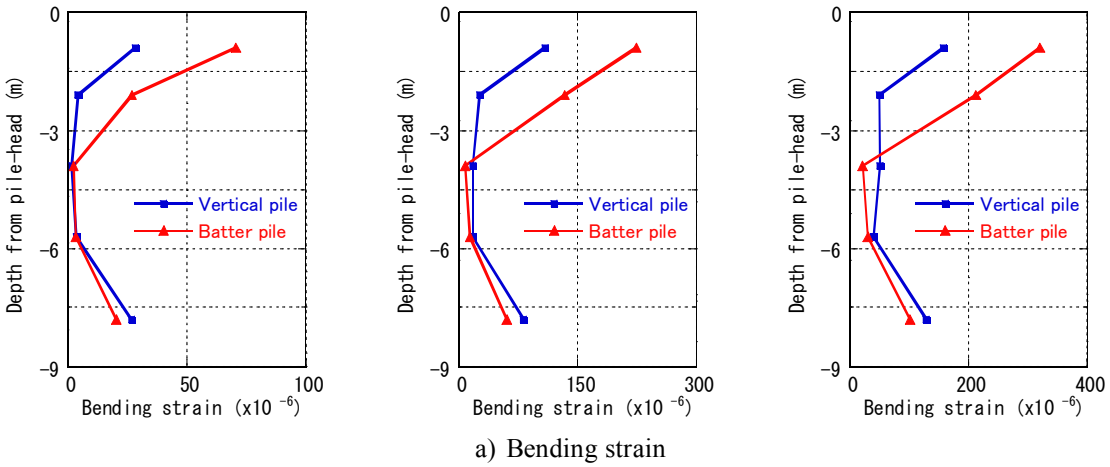


a) Bending strain

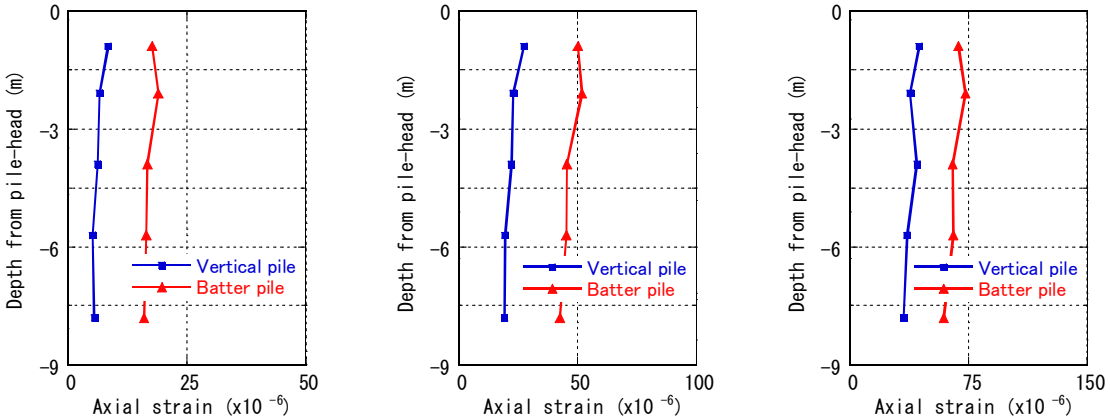


b) Axial strain

Figure 9 Bending and axial strains distributions of the vertical-pile foundation (pile-VA1) and the batter-pile foundation (pile-BA1) obtained from El Centro record (50 Gal, 100 Gal, 200 Gal)

and that both the bending and axial pile strains of the batter-pile foundation are larger than those of the vertical-pile foundation in both the sinusoidal and El Centro record excitations.

### 3.5 *Aseismicity of batter pile*

Figures 12 and 13, and Figures 14 and 15 show the frequency transfer functions of the horizontal acceleration of the footing and input motion, and of the bending and axial strains of the piles and input motion, respectively, between the vertical-pile foundation and the batter-pile foundation obtained from the sweep test and El Centro record excitation. In Figures 12 and 13, the difference between the frequency transfer functions of the two pile foundations, the vertical-pile foundation and the batter-pile foundation, represents the aseismicity of the batter-pile foundation. From these figures, it can be elucidated that the batter-pile foundation has a certain level of aseismicity in almost all of the frequency ranges. From Figures 14 and 15, it can be seen that the bending and axial strains of the batter piles are larger than those of the vertical piles. It is therefore considered that batter piles require large cross-sectional capabilities to compensate for their aseismicity.

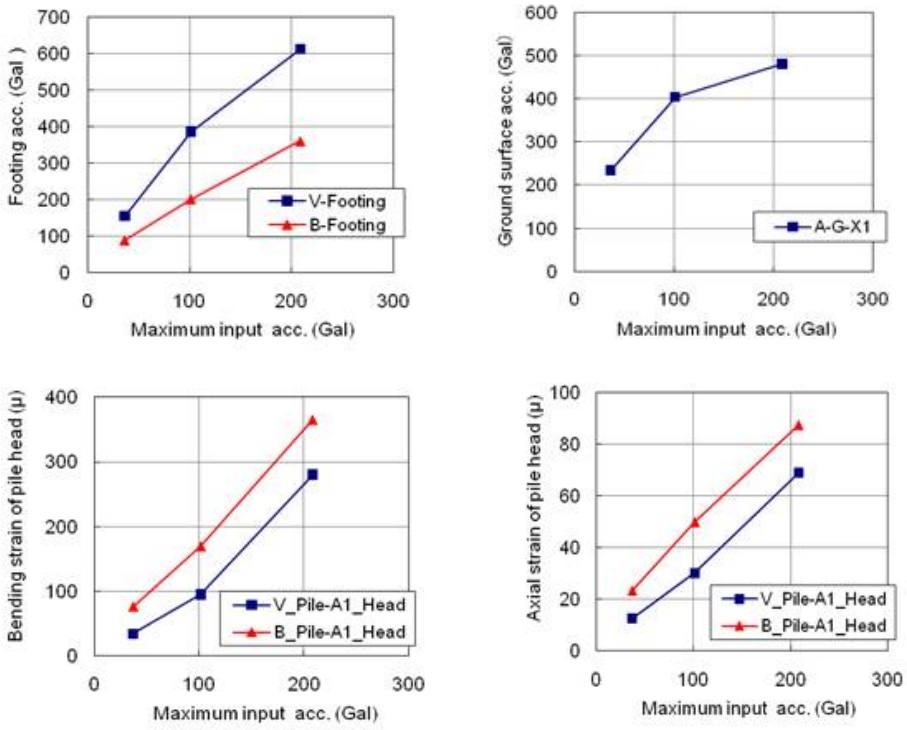


Figure 10 Maximum values of the accelerations of the footings and the ground surfaces, and the bending and axial strains at the pile heads (Sinusoidal excitation: 3.5 Hz)

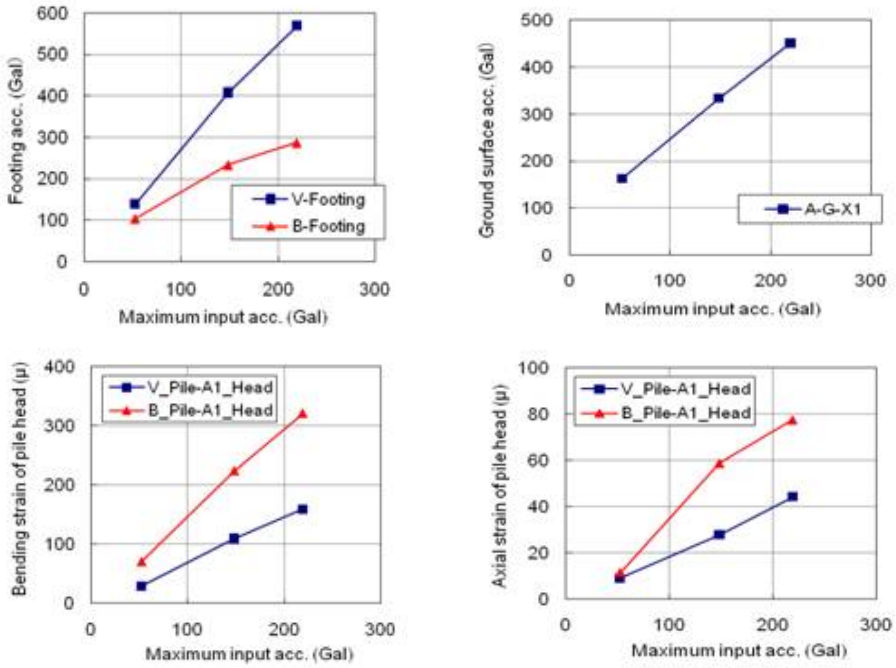


Figure 11 Maximum values of the accelerations of the footings and the ground surfaces, and the bending and axial strains at the pile heads (El Centro record)

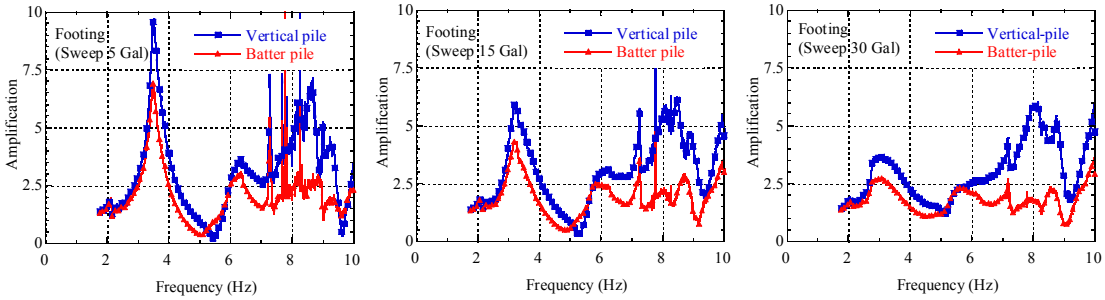


Figure 12 Aseismicity of the batter-pile foundation: Comparison of the frequency transfer function between the horizontal acceleration of the footing and input motion in the vertical-pile foundation and the batter-pile foundation obtained from sweep tests (5 Gal, 15 Gal, 30 Gal)

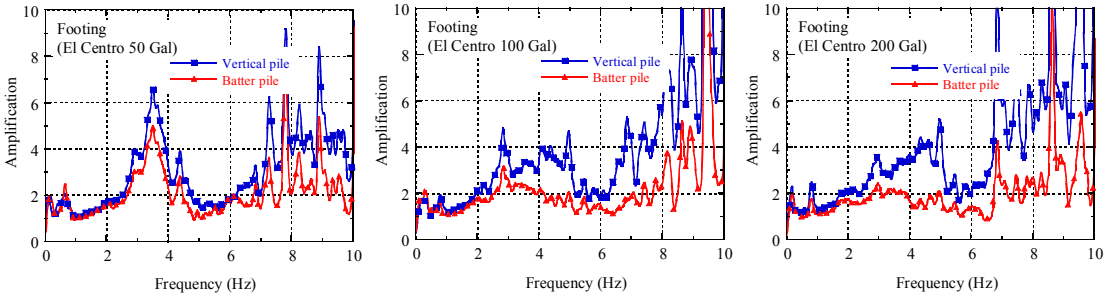


Figure 13 Aseismicity of the batter-pile foundation: Comparison of the frequency transfer function between the horizontal acceleration of the footing and input motion in the vertical-pile foundation and the batter-pile foundation obtained from El Centro record (50 Gal, 100 Gal, 200 Gal)

Figures 16 and 17 show the transfer function ratios of the vertical-pile foundation to the batter-pile foundation calculated based on the transfer functions in Figures 13 and 15 which were obtained from El Centro record excitation. The magnification of the difference between the lateral line of 1.0 and each curve of the transfer function ratio in Figure 16 represents the aseismicity of the batter-pile foundation and those in Figure 17 represent the compensation for the aseismicity of batter piles.

From the variation of the three curves of 50 Gal, 100 Gal, and 200 Gal in these figures, it can be seen that the effect of the aseismicity of the batter-pile foundation increased as the maximum acceleration of the input motion increased. However, the bending and axial strains at the pile head of the batter pile appear to approach those of the vertical pile as the maximum acceleration of the input motion increased. It is considered that these results are caused by the soil nonlinearity, which becomes significant as the maximum acceleration of the input motion increases.

### 3.6 *Numerical Analysis*

To clarify the phenomena shown in Figures 16 and 17 that the effect of the aseismicity of the batter-pile foundation can be increased, and the bending and axial strains at the pile head of the batter pile approach those of the vertical pile as the maximum acceleration of the input motion increased, we carried out numerical analyses based on a simple model of two-dimensional finite element analysis.

Figure 18 shows the analytical model. The soil, pile and footing are modeled by solid and beam elements, respectively. The analytical constants are shown in Table 5. The linear response analyses were carried out by varying the shear wave velocity of soil as 80 m/s, 100 m/s, and 120 m/s.

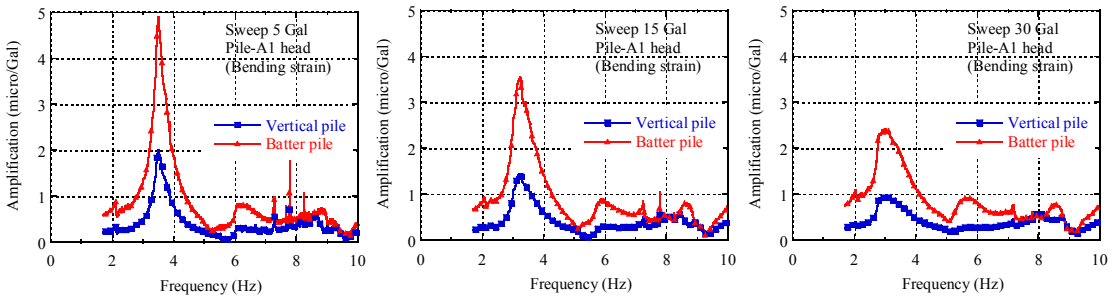


a) Bending strain

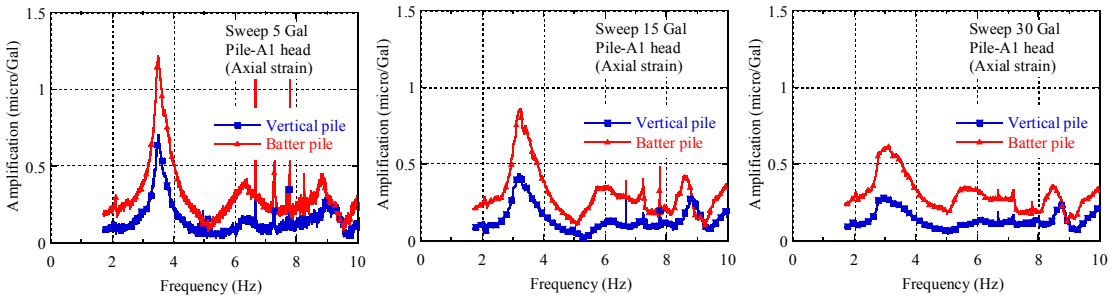


b) Axial strain

Figure 14 Comparisons of the frequency transfer functions of the bending and axial strains of the piles and input motion between the vertical-pile foundation and the batter-pile foundation (sweep tests)

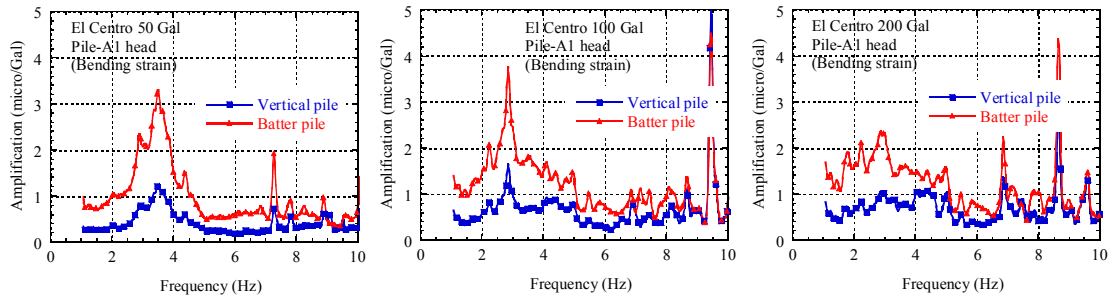


a) Bending strain

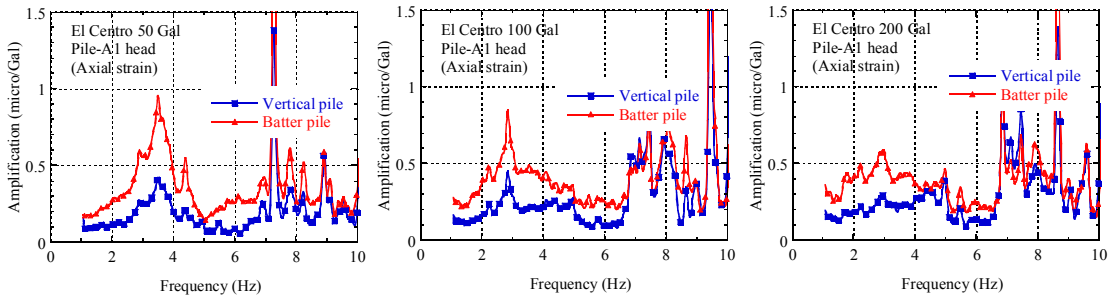


b) Axial strain

Figure 15 Comparisons of the frequency transfer functions of the bending and axial strains of the piles and input motion between the vertical-pile foundation and the batter-pile foundation (El Centro record)

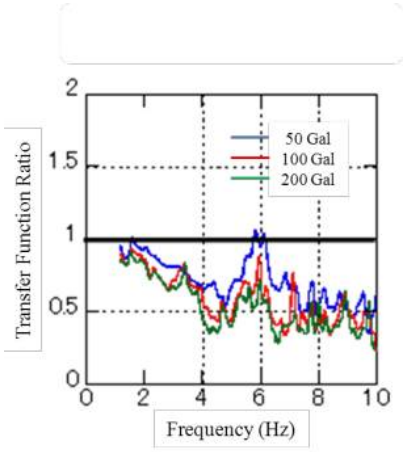


Figure 16 Transfer function ratio of the vertical-pile foundation to the batter-pile foundation of the horizontal acceleration of the footing

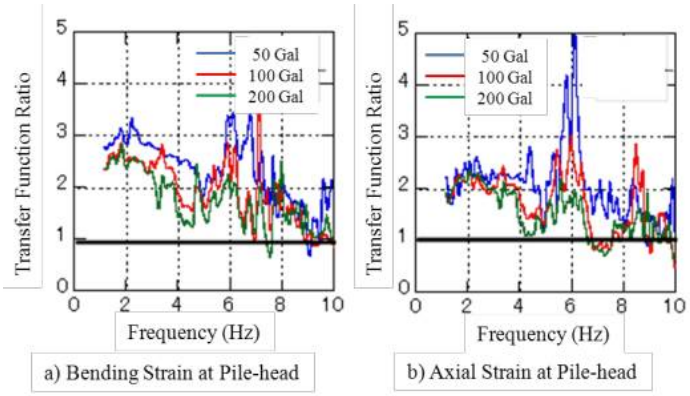


Figure 17 Transfer function ratios of the vertical-pile foundation to the batter-pile foundation of the bending and axial strains of the piles at the pile head

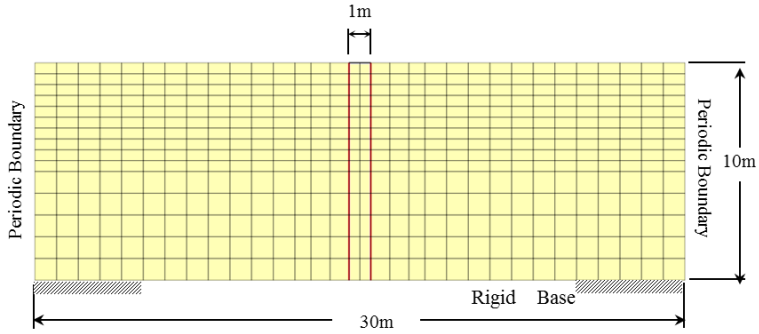


a) Vertical-pile foundation model

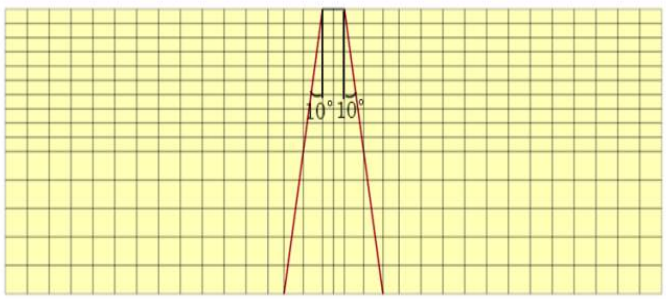


b) Batter-pile foundation model

Figure 18 Analytical models of vertical-pile and batter-pile foundations for 2D FEM analysis

Table 5 Analytical constants

| | Soil (Vs＝100m/s) | Pile (φ300) | Footing (Rigid Body) |
|---|---|---|---|
| Unit Weight ρ (kN/m$^3$) | 15.0 | 78.5 | 78.5 |
| Poisson's Ratio ν | 0.45 | – | – |
| Young's Modulus E (kN/m$^2$) | $4.439\times10^4$ | $2.1\times10^8$ | $2.1\times10^{10}$ |
| Sectional Area A (m$^2$) | – | 0.006 | 0.006 |
| Moment Inertia I (m$^4$) | – | $6.0\times10^{-5}$ | $6.0\times10^{-5}$ |
| Damping Constant h | 0.20 | 0.20 | 0.20 |

These are modeled based on the concept of equivalent linearization to simplify and clarify soil nonlinearity as the stiffness reduction of soils. Figure 19 represents the analytical result in the same form as Figures 16 and 17. A comparison of these figures shows consistency of the magnitude correction of the three curves in the frequency region higher than 4.0 Hz, suggesting that the phenomena are related to soil nonlinearity.

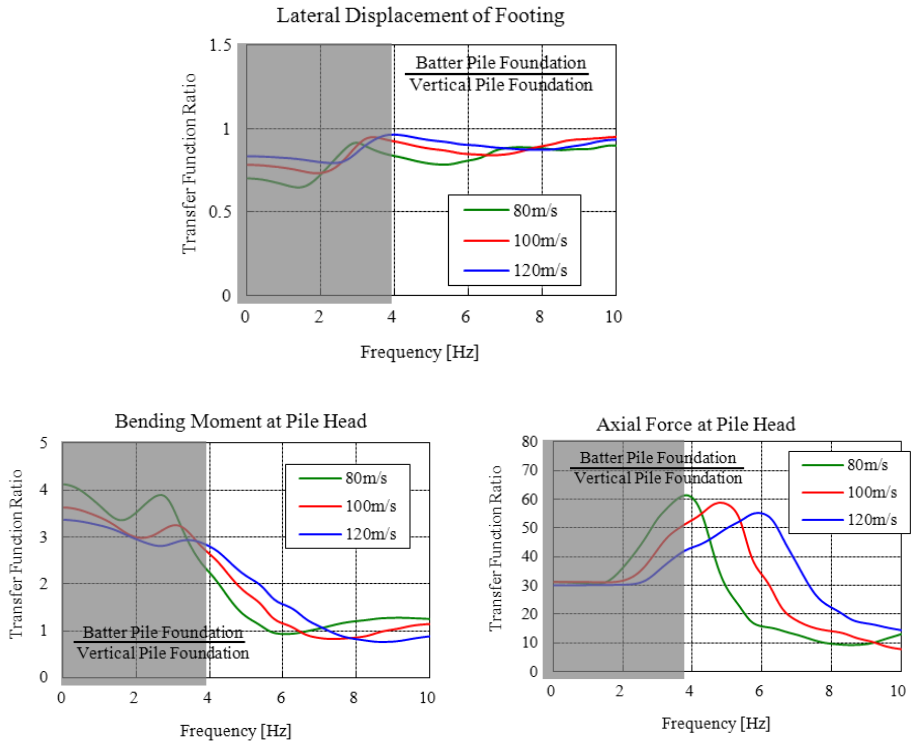


Figure 19 Analytical results obtained from 2D linear response analysis

## 4. CONCLUSIONS

The main conclusions of the study are as follows:

1) The response of the footing of the vertical-pile foundation to motion to the right is counter-clockwise rotation. On the other hand, that of the batter-pile foundation is rotation in the opposite direction to that of the vertical-pile foundation.
2) Bending and axial strains attain the largest values at the pile heads in both the vertical-pile foundation and batter-pile foundation.
3) The aseismicity can be improved by using batter piles in almost all frequency ranges.
4) Bending and axial strains of the batter-pile foundation are larger than those of the vertical-pile foundation. In other words, batter piles require large cross-sectional capabilities to com-

pensate for their aseismicity.

5) The effect of the aseismicity of the batter-pile foundation increased and the bending and axial strains at the pile head of the batter pile approached those of the vertical pile as the maximum acceleration of the input motion increased. These phenomena are considered to be related to soil nonlinearity.

## 5. ACKNOWLEDGEMENT

We would like to express our sincerest gratitude to Mr. Katsumi Yoshinari for his invaluable help with the centrifuge tests.

## 6. REFERENCES

Bhattacharya, S., Tazoh, T., Jang, J., and Sato, M., 2009. A Study on the Behavior of Raked Piles in Seismically Liquefiable Soils, Proceedings of the 3rd Greece-Japan Workshop on Seismic Design, Observation and Retrofit of Foundations, 1–19.

Deng, N., Kulesza, R., and Ostadan, F., 2007. Seismic Soil-Pile Group Interaction Analysis of a Battered Pile Group, 4th International Conference on Earthquake Geotechnical Engineering, Paper No. 1733.

Fan, K., Gazetas, G., Kaynia, A., Kausel, E., and Ahmad, S. 1991. Kinematic seismic response of single piles and pile groups, *Journal of Geotechnical Engineering*, 117, 1860–1879.

Fscoffier, S., Chazelas, J-L., and Garnier, J., 2008. Centrifuge Modelling of Raked Piles, Bull. Earthquake Engineering, Vol. 6, No. 4, 689–704, Springer.

Gerolymos, N., Giannakou, A., Anastasopoulos, I. and Gazetas, G., 2008. Evidence of Beneficial Role of Inclined Piles: Observations and Summary of Numerical Analyses. Bulletin of Earthquake Engineering, Vol. 6, No. 4, 705–722, Springer.

Giannakou, A., Gerolymos, N., and Gazetas, G., 2009. Kinematic and Inertial Behavior of Raked Piles, Proceedings of the 3rd Greece-Japan Workshop on Seismic Design, Observation and Retrofit of Foundations, 36–50.

Giannakou, A., Gerolymos, N., and Gazetas, G., 2007. Kinematic Response of Groups with Inclined Piles, and Inertial Behavior of Raked Piles, 4th International Conference on Earthquake Geotechnical Engineering, Paper No. 1256.

Mylonakis, G., Nikolau, S., and Gazetas, G. 1997. Soil-pile bridge seismic interaction: kinematic and inertial effects. Part I: Soft soil, *Earthquake Engineering and Structural Dynamics*, 26, 337–359.

Mylonakis, G., 2001. Simplified model for seismic pile bending at soil layer interfaces, *Soils and Foundations*, 41, 4, 47–58.

Nikolaou, S., Mylonakis, G., Gazetas, G., and Tazoh, T., 2001. Kinematic pile bending during earthquakes: analysis and field measurements, *Geotechnique*, 51, 5, 425–440.

Pinto, P., McVay, M., Hoit, M., and Lai, P., 1997. Centrifuge Testing of Plumb and Battered Pile Groups in Sand, Transportation Research Record, Vol. 1569.

Poulos, H.G., 2006. Raked Piles–Virtues and Drawbacks, Journal of Geotechnical and Geoenvironmental Engineering, ASCE, 795–803.

Razavi, S.A., Fakher, A., and Mirghaderi, S. R., 2007. An Insight into the Bad Reputation of Batter Piles in Seismic Performance of Wharves, 4th International Conference on Earthquake Geotechnical Engineering, Paper No. 1423.

Sica, S., Mylonakis, G., and Simonelli, A. L., 2007. Kinematic bending of piles: Analysis vs. code provisions, *Proceedings of the 4th International Conference on Earthquake and Geotechnical Engineering* (ICEGE), Thessaloniki, Greece, on CD-ROM.

Tazoh, T., Shimizu, K., and Wakahara, T., 1987. Seismic observations and analysis of grouped piles. Geotechnical Special Publication No. 11, *Dynamic Response of Pile Foundations*, ASCE, 1–20.

Tazoh, T., Wakahara, T., Shimizu, K., and Matsuzaki, M., 1988. Effective Motion of Group Pile Foundations, Proceedings of Ninth World Conference on Earthquake Engineering, Vol. 587–592.

Tazoh, T., Sato, M., and Gazetas, G., 2005. Centrifuge tests on pile-foundation structure systems affected by liquefaction-induced flow due to quay-wall collapse, *Proceedings of the 1st Greece-Japan*

*Workshop on Seismic Design, Observation and Retrofit of Foundations*, Athens, Greece, 79–106.
Tazoh, T., Sato, M., Jang, J., and Gazetas, G., 2007. Centrifuge tests on remedial measure using batter piles against liquefaction-induced soil flow after quay wall failure, *Proceedings of the 2nd Greece-Japan Workshop on Seismic Design, Observation and Retrofit of Foundations*, Tokyo, Japan, 431–439.
Tazoh, T., Sato, M., Jang, J., Taji, Y., and Gazetas, G., 2009. Kinematic Response of Batter Pile: Centrifuge Tests. Proceedings of the 3rd Greece-Japan Workshop on Seismic Design, Observation and Retrofit of Foundations, 20–35.

## Appendix: Influence of the inertial interaction caused by the mass of the footing on the test results

The results showing good agreement between the analytical results by using two-dimensional FEM earthquake response analysis and the test results are presented first. Figure A1 shows the analytical model, which is a prototype when the test model is conducted 30 times. The footing and piles are modeled by using elastic beam elements. The bottom boundary of the model is rigidly connected to the base and periodic boundary conditions were imposed on both sidewall boundaries of the model because the tests were conducted using a laminar box to allow shear deformation of the soil deposit as in the free field. The soil was modeled by nonlinear solid elements taking into account the confining pressure dependency of initial shear stiffness. The Ramberg-Osgood model (R-O model) was used for modeling soil nonlinearity. The reference strain $\gamma_{0.5}$ and the maximum damping coefficient $h_{max}$ were defined by fitting to the stiffness reduction and the damping ratio curves obtained from the cyclic hollow cylinder torsion tests of silica sand No. 7 as shown in Figure A2. The record obtained for the base of the shaking table was used as the input motion for the analysis. The analysis was performed for a width of 1.5 m in the out-of-plane direction, which is the same length as the out-of-plane direction of the footing.

The analytical results are shown in Figure A3. A comparison of Figures 16, 17 and A3 reveals good agreement between the analytical results and the test results. Thus, it is considered that the numerical analysis simulates the test results adequately.

The mass of the footing in the test was 43% of the total mass of the pile foundation model used in the test, so we evaluated the influence of the inertial interaction caused by the inertial force of the footing mass on the test results. Nonlinear response analyses were performed with a massless footing for the pile foundation model shown in Figure A1. Figure A4 shows the resulting responses of the two pile foundations either with or without the mass of the footing.

A difference of about 10% in the maximum bending moment only at the pile head of both of the batter piles and the vertical piles can be observed, and a difference of about 10% in the maximum axial strain can be seen in the whole length of the batter piles, but there was a 50% difference in the vertical piles. Except for the axial strain of the vertical piles, these are not remarkable differences, and so the test results reasonably reflect the seismic behavior generated by the kinematic interaction.

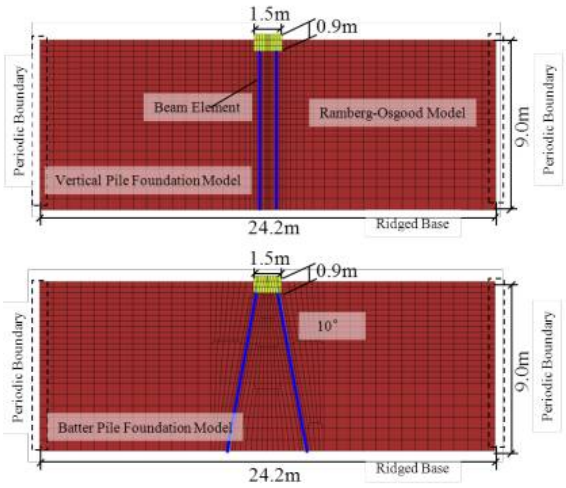


Figure A1 Analytical models for 2D nonlinear response analysis

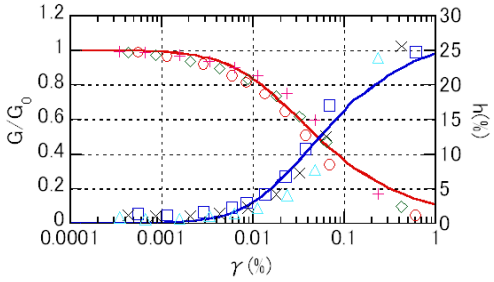


Figure A2 Fitting to the stiffness reduction and the damping ratio curves obtained from the cyclic hollow cylinder torsion tests of silica sand No. 7

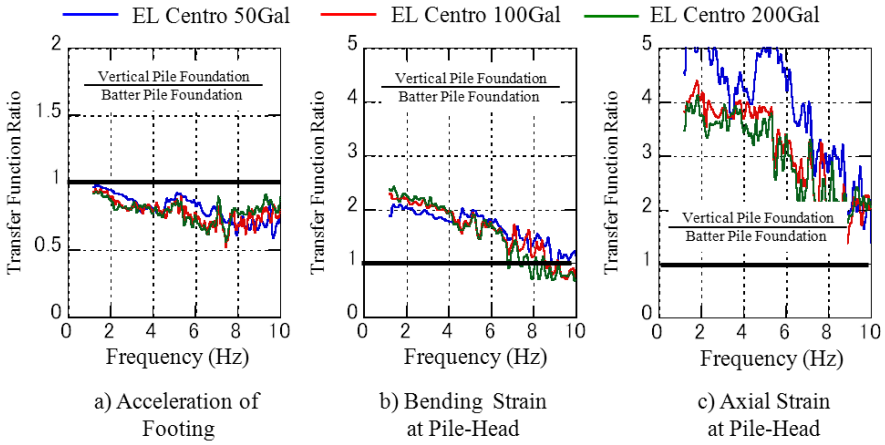


Figure A3 Analytical results of transfer function ratio of the vertical-pile foundation to the batter-pile foundation

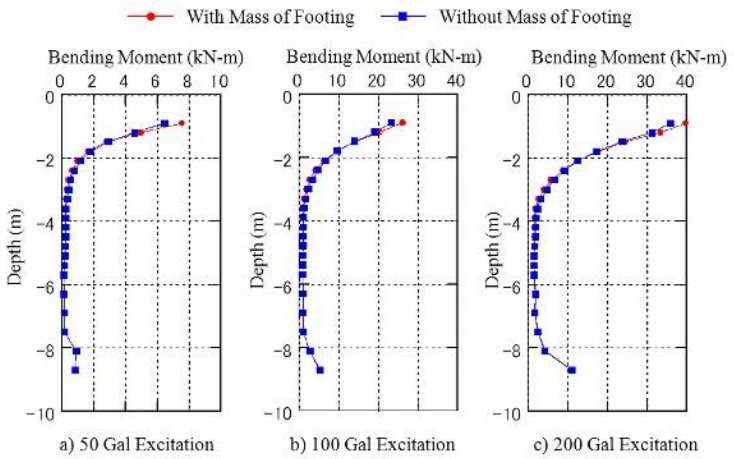


a) Bending moment of batter pile

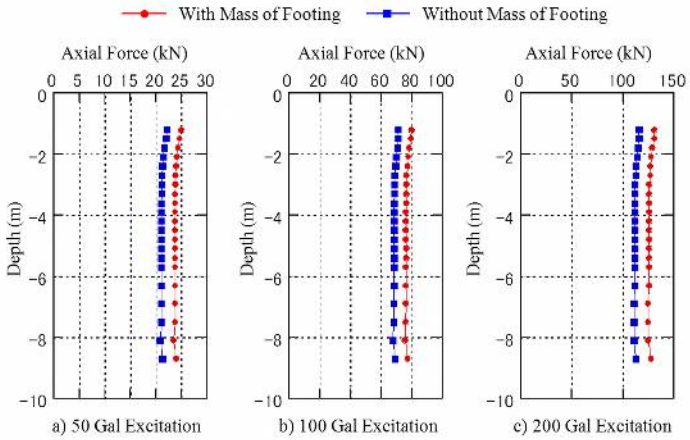


b) Axial force of batter pile

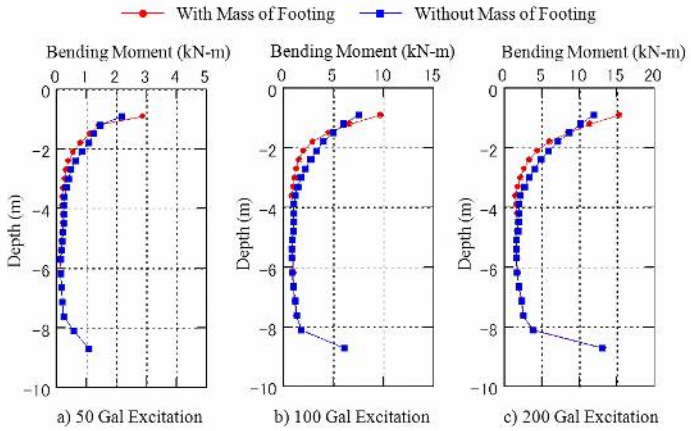


c) Bending moment of vertical pile

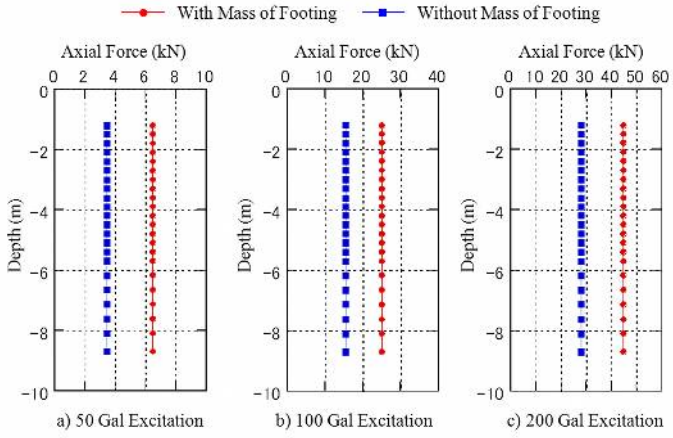


d) Axial force of vertical pile

Figure A4 Analytical results obtained from 2D nonlinear response analyses

# Amplitude dependent response for three-story moment-resistant building during earthquakes

S. Kataoka
*Associate professor, Hirosaki University, Japan*

ABSTRACT: To study an amplitude dependency of building response, temporal seismic observation data in three-story building is used. Two seismometers were placed at the ground floor and third floor. Identification for the natural frequency and damping factor was performed in the time domain. To do this identification systematically, a grid search method was used. Response of SDOF system with an arbitrary combination of natural frequency and damping factor is calculated from ground floor motion then fitness to the third-floor response is evaluated. Best fir combination is the estimated value. Estimated natural frequency and damping factor is changed during a shaking. When the response becomes large, natural frequency becomes lower and damping factor becomes larger. However, when shaking ends those become previous values.

## 1 INTRODUCTION

It is often said that vibration characteristics such as natural frequency and damping factor of a building depend on amplitude of input motion or response. However, we do not have enough data to discuss amplitude dependency. To study such characteristics, a large amount of data those amplitudes have a large variety is needed and ordinary it takes a long time.

To obtain a large amount of data, aftershock recording might be a good way. Author installed seismometers in a building where large PGA and high Japanese seismic intensity was recorded during the 2008 Iwate-Miyagi nairiku earthquake. Fifty-three event records were obtained successfully. Using this data set, we study amplitude dependent characteristics.

## 2 OUTLINE OF THE BUILDING

A target building shown in photo1 has a moment- resistant frame with spread foundation. This building was constructed in 1964. The plans of first and third floor of this building are shown in Figure 1. As shown in Figure 1, this building has four spans in transverse direction, and its length is 14.4 meters. However, at the third floor, the building is set back with one span. In longitudinal direction, length is 23.75 m, and it is covered by 6 span frames. Story height is 3.63m, 3.25m, and 3.25m from the first floor, respectively. So, that the third floor is 6.88m high from the ground level.

During the 2008 Iwate-Miyagi Nairiku earthquake, PGA that was recorded very closed to this building is about 1600cm/s/s, but damage of this building was not severe. Horizontal and vertical cracks have been seen in walls. Depths of cracks were almost the same to the cover concrete. Some parts of cover concrete of columns fell out.

**Photo 1 Apperance of the target building**

## 3 RESULT OF AMBIENT VIBRATION TEST

Natural frequency of the building is estimated by ambient vibration test during the temporal seismic observation. Two three-component sensors are placed ground floor and third floor respectively. Places are the same to the seismometer described in later chapter.

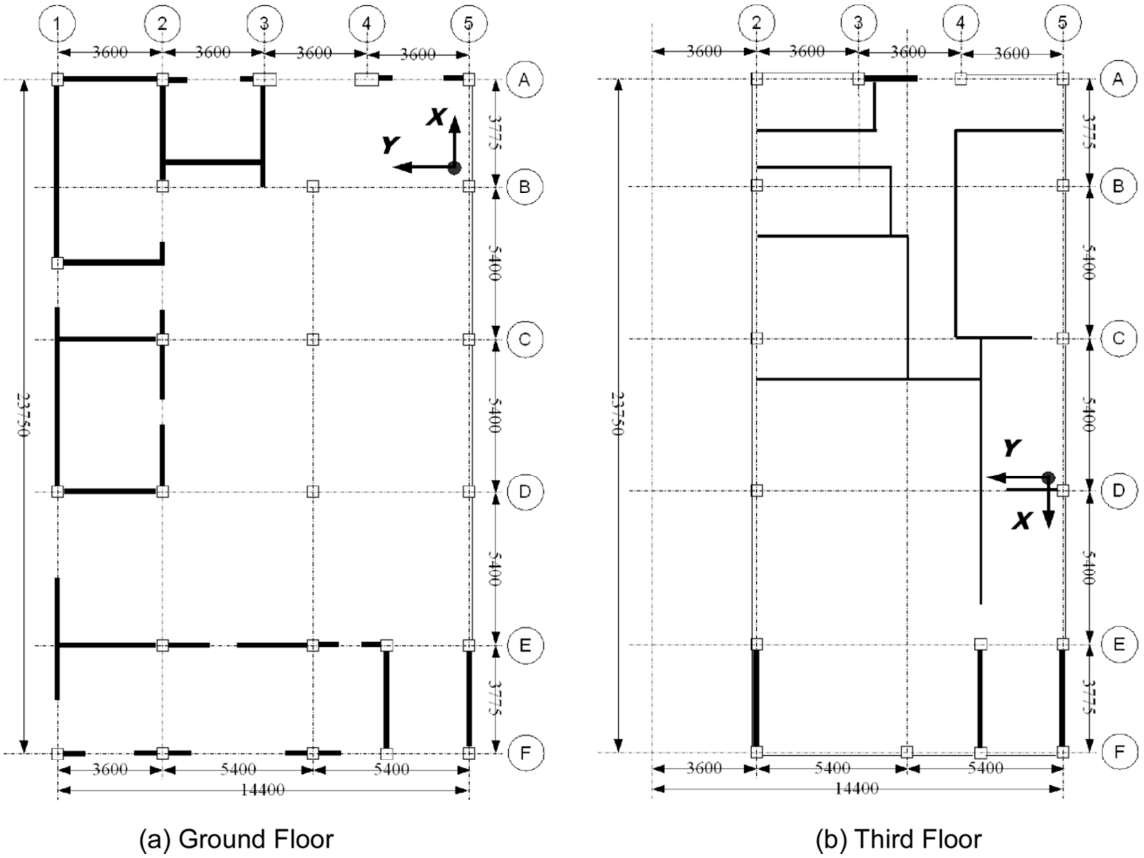


**Figure 1 Plan of the building. Solid circles indicate seismometer location.**

Spectral analysis was performed using recorded ambient noise. Frequency response function (hereafter, FRF) in the transverse direction that is Y direction in Fig.1 is illustrated in Figure 2. Spectral ratio between third and ground floor is also shown in Fig.2. From the figure, we can see that natural frequency is about 4Hz and damping factor is about 0.02. There is no figure in longitudinal direction, but natural frequency is about 3.6 Hz and damping factor is 0.015.

## 4 OUTLINE OF TEMPORAL SEISMIC OBSERVATION SYSTEM

One accelerometer was installed on the ground floor just next day of the main shock of the 2008 Iwate-Miyagi Nairiku earthquake. The sampling frequency of this seismometer is 100 Hz. This was removed six months later. Fifty-three events are recorded successfully. The location of the seismometer is shown in Fig.1. Another accelerometer was installed on the third floor on June 26. The sampling frequency is also 100 Hz. Observation duration of this seismometer is about 40 days.

As these two seismometers placed independently and there is no connecting line between them, they start independently. Additionally, these two are different type seismometer, so that the positive direction of one horizontal direction is opposite.

## 5 IDENTIFYING NATURAL FREQUENCY AND DAMPING FACTOR

### 5.1 *Method*

The natural frequency $f$ and damping factor $h$ are identified in the time domain. The FRF of ambient vibration test shows that relation between motions those are obtained at ground floor, and third floor is modeled by SDOF input-output system in a certain frequency range. So that,

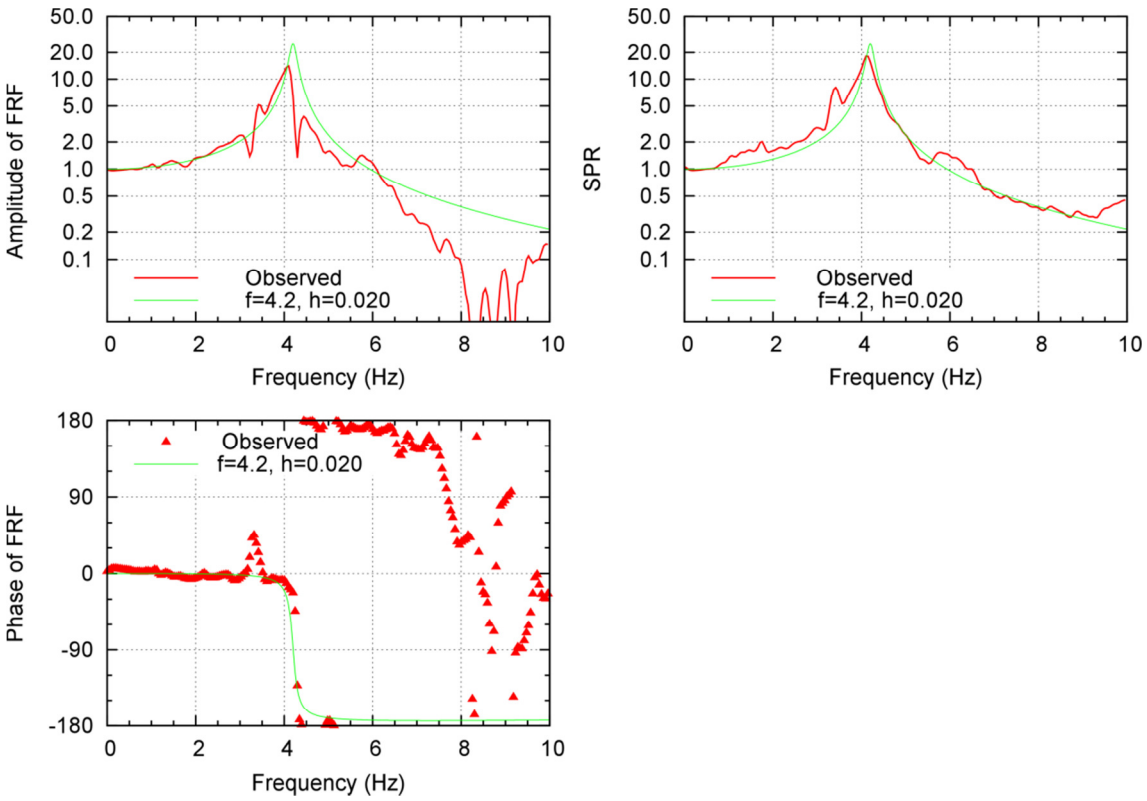


**Figure 2 Frequency respsonse function in transverse direction of the building (left hand side). Spectral ratio of the ground floor and third floor (right hand side).**

we focus on the SDOF system response with input of acceleration obtained at ground floor. When we use an adequate combination of *f* and *h*, observed response will be simulated by a SDOF response. To find the best combination of *f* and *h* systematically, a grid search method was adopted. Additionally, the best combination of *f* and *h* is evaluated in one record to divide a record by short duration time segment. In the method, a combination of *f* and *h* minimizing following misfit is the estimated time varying natural frequency and damping factor

$$\text{Misfit(j)} = \frac{\sum_{i=1}^{N}\left(X_{ist+i}^{(obs)} - X_{j+i}^{(cal)}\right)^2}{\sum_{i=1}^{N}\left(X_{ist+i}^{(obs)}\right)^2}, j = 0,1,2\cdots \quad (1)$$

In equation (1), $x^{(obs)}$ means observed acceleration at the third floor and $x^{(cal)}$ means absolute acceleration response calculated from assumed a combination of *f* and *h*, where input motion is observed acceleration at the ground floor. In the equation, *ist* is the start time of the target time segment and N is a data number for the time segment. Starting time of each seismometer is different each other, we should find out the correct timing. The *j* in the equation indicates the timing.

### 5.2 *Data and Search conditions*

Ten events records are chosen to evaluate vibration characteristics. Some parameters of these events are listed in Table 1. Eight events among them are aftershocks of the 2008 Iwate-Miyagi Nairuku earthquake. Those magnitudes are not large and duration times are short. Magnitudes of another two events are large. These two were occurred distance location. The largest PGA among them is 241 cm/s/s. This was induced by an event that occurred July 24, 2011. Despite of this record, PGAs of another records are below 100 cm/s/s.

**Table 1 Parameters of the event those are used to evaluate vibration characteristics**

| No. | Year | Date | Hour | lat. | | Long. | | Depth | Mag. | Hypo dist | PGA@1F | PGA@3F |
|---|---|---|---|---|---|---|---|---|---|---|---|---|
| | | | | deg. | min. | deg. | min. | (km) | | (km) | (cm/s/s) | (cm/s/s) |
| EQ1 | 2008 | 06/26 | 15:51 | 39 | 4.9 | 140 | 58.2 | 7 | 4.6 | 12 | 18 | 37 |
| EQ2 | 2008 | 06/29 | 15:53 | 38 | 53.1 | 140 | 44.0 | 7 | 4.3 | 34 | 17 | 26 |
| EQ3 | 2008 | 07/05 | 14:21 | 39 | 3.9 | 140 | 56.9 | 9 | 4.0 | 14 | 30 | 67 |
| EQ4 | 2008 | 07/07 | 15:14 | 39 | 2.1 | 140 | 53.2 | 10 | 4.0 | 19 | 26 | 38 |
| EQ5 | 2008 | 07/19 | 11:39 | 37 | 31.2 | 142 | 15.8 | 32 | 6.9 | 201 | 13 | 28 |
| EQ6 | 2008 | 07/20 | 03:58 | 39 | 6.2 | 140 | 50.4 | 12 | 3.9 | 24 | 35 | 19 |
| EQ7 | 2008 | 07/23 | 12:54 | 38 | 59.7 | 140 | 51.6 | 10 | 4.2 | 21 | 27 | 38 |
| EQ8 | 2008 | 07/24 | 00:26 | 39 | 43.9 | 141 | 38.1 | 108 | 6.8 | 141 | 241 | 474 |
| EQ9 | 2008 | 07/29 | 16:27 | 39 | 3.7 | 140 | 51.6 | 10 | 4.3 | 21 | 28 | 33 |
| EQ10 | 2008 | 07/29 | 16:35 | 39 | 3.7 | 140 | 51.7 | 10 | 4.6 | 21 | 70 | 51 |

As ambient vibration test indicates that natural frequency is about 4.2 Hz, the search range for natural frequency is from 2.2 Hz to 4.2 Hz. The search range for damping factor spans from 0.02 to 0.10. In both two parameters, candidate values are derived from division of each range by 40 equally. The identification was performed every 1.25 second at the beginning of response. Length of each time segment set to be 2.5 seconds.

## 6 RESULT AND DISCUSSION

### 6.1 *Example of result*

A result comes from event 8 is shown in Figure 3. Observed acceleration, time varying natural frequency, damping factor and estimated maximum deformation is illustrated in the figure. The maximum deformation is the absolute maximum value of relative displacement response. At the beginning, natural frequency is around 3.2 Hz. It decreases with increasing response amplitude or maximum deformation. At around 25 seconds, it arises with decreasing response amplitude. During a most severe response, the natural frequency falls to 2.4Hz. It is about 60 % of the original value. A feature of change of damping factor is contrast to natural frequency. It increases with increasing response amplitude. Figure 4 shows observed and calculated acceleration. Theoretical response and observed record looks similar each other. However, theoretical one does not reproduce some ripples. In this fitting process, SDOF system is assumed, while the actual response is the MDOF system response. Investigating the ambient vibration test, we found out that higher mode can be seen. So that the discrepancy comes from the assumption of this procedure and there is no help to discuss any more.

### 6.2 *Nonlinear elasticity*

Relation of relative displacement and natural frequency is studied. Figure 5 shows the resultant of event 5 and event 8. In the figure, number by mark indicates the time segment number, so that natural frequency starts at high value and becomes low with increasing deformation. After it arrives at the maximum deformation point, natural frequency becomes large. This phenomenon is so called nonlinear elasticity. It is said that nonlinear behavior appears during a large deformation but in this case deformation is thought to be small. That is about 1 cm. Elevation of third floor is about 6.85m. A drift angle is about 1 over 700. In conventional seismic design, structure behaves elastically under such a small drift angle.

All the result except event 5 and 8 are shown in Figure 6. The same tendency can be seen. At the beginning, natural frequencies are almost the same to about 3.8Hz. Then they decrease with increasing deformation. After a response reaches to the maximum value, then it becomes higher. Additionally, the end of event 8, the natural frequency is about 2.8Hz. On the other hand, at the beginning of event 9, it is 3.8Hz. It recovered to the ordinal value. Therefore, we can say that this building responds nonlinearly but elastically.

### 6.3 *Amplitude dependency for damping factor*

Figure 7 shows a relation of maximum deformation and damping factor. An amplitude-dependency can be seen but weakly comparing to natural frequency. One reason why the tendency is weak attribute to the estimation method. In the method, vibration characteristic is estimated by fitting the theoretical response for observed one. Response wave form is not affected by damping factor strongly but the natural frequency. And damping factor will have wide variety value. To search exact damping factor, more precise treatment is needed.

## 7 CONCLUDING REMARKS

To study an amplitude dependency of building response, temporal seismic observation data in three-story building is used. The observation was performed just after the 2008 Iwate-Miyagi Nairiku earthquake. Ten events records are chosen to evaluate vibration characteristics. PGAs are ranged from 13 to 241 cm/s/s. Almost PGAs are below 50cm/s/s. Identification for the natural frequency and damping factor was performed in the time domain. Followings are pointed out.

A) Calculated SDOF response simulated observed response at the third floor well.
B) At the beginning of the response, natural frequency is 3.8Hz, this is little smaller than the value that estimated from ambient vibration.

C) Natural frequency decreases with increasing response even if maximum deformation is below 1 mm. 1 mm of maximum deformation corresponds to a drift angle of 1 over 7000.
D) Maximum deformation in this study is estimated about 1 cm.
E) Natural frequency recovers original value, even if it suffered 1 cm deformation.
F) Damping factor increases with increasing response. However, we cannot find out the strong relation between them.

From facts described above, this building behaves nonlinearly but elastically during earthquakes. The author has one more example (Kataoka, 2008). Kashima et al. (2005) and Nakamura (2003) pointed out same tendency. This kind structural behavior in small deformation might be general one.

## REFERENCES


Kashima T., Y. Kitagawa, 2005, Dynamic characteristics of buildings estimated fron strong motion records, AIJ J. Technol. Des., Bo.22, 163-166. (in Japanese with English abstract)

Kataoka S., 2008, Evaluation for dynamic characteristics of 8th floor building through aftershock records, Summaries of technical papers of annual meeting, AIJ, 159-160, 2008. (in Japanese)

Nakamura M., 2003, Amplitude dependence evaluation of modal parameters through earthquake observation on a SRC high-rise building, Summaries of technical papers of annual meeting, AIJ, 949-950, 2003. (in Japanese)

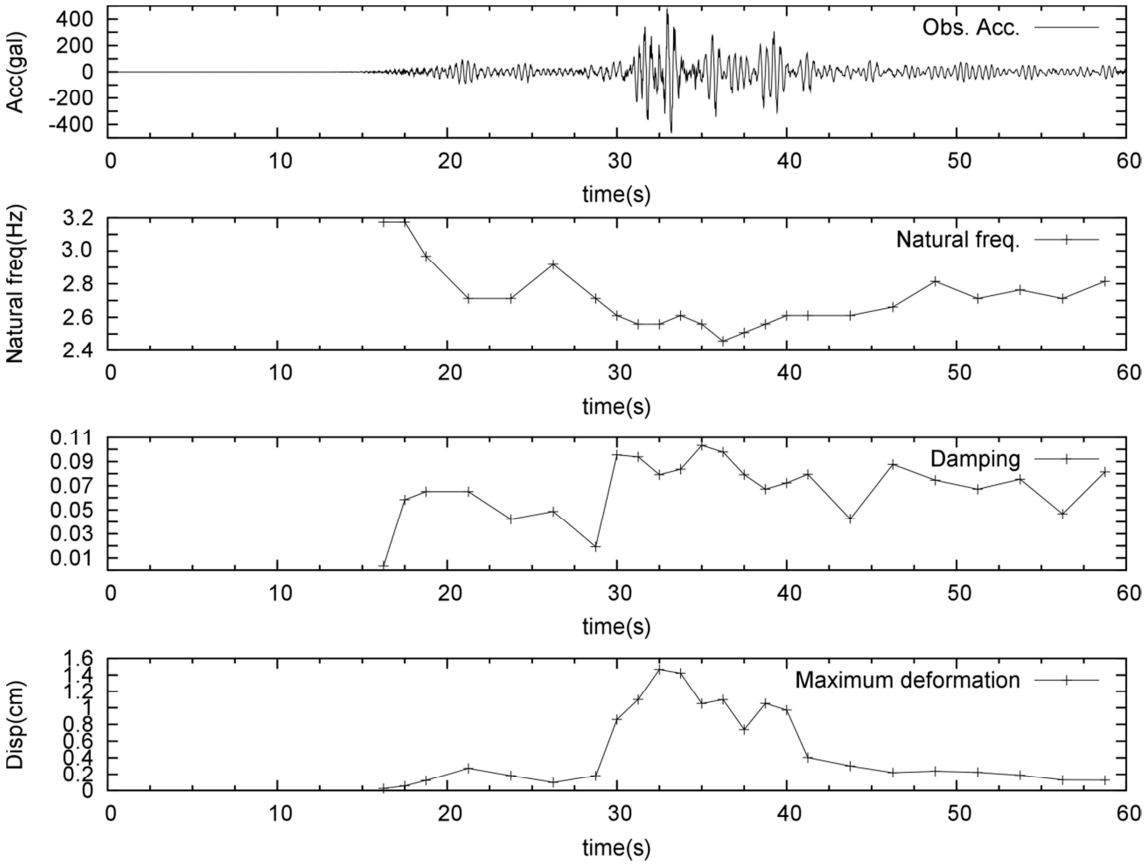


**Figure 3. An example of the estimation. From the top observed acceleration, time varying natural frequency, damping factor and estimated relative displacement is illustrated**

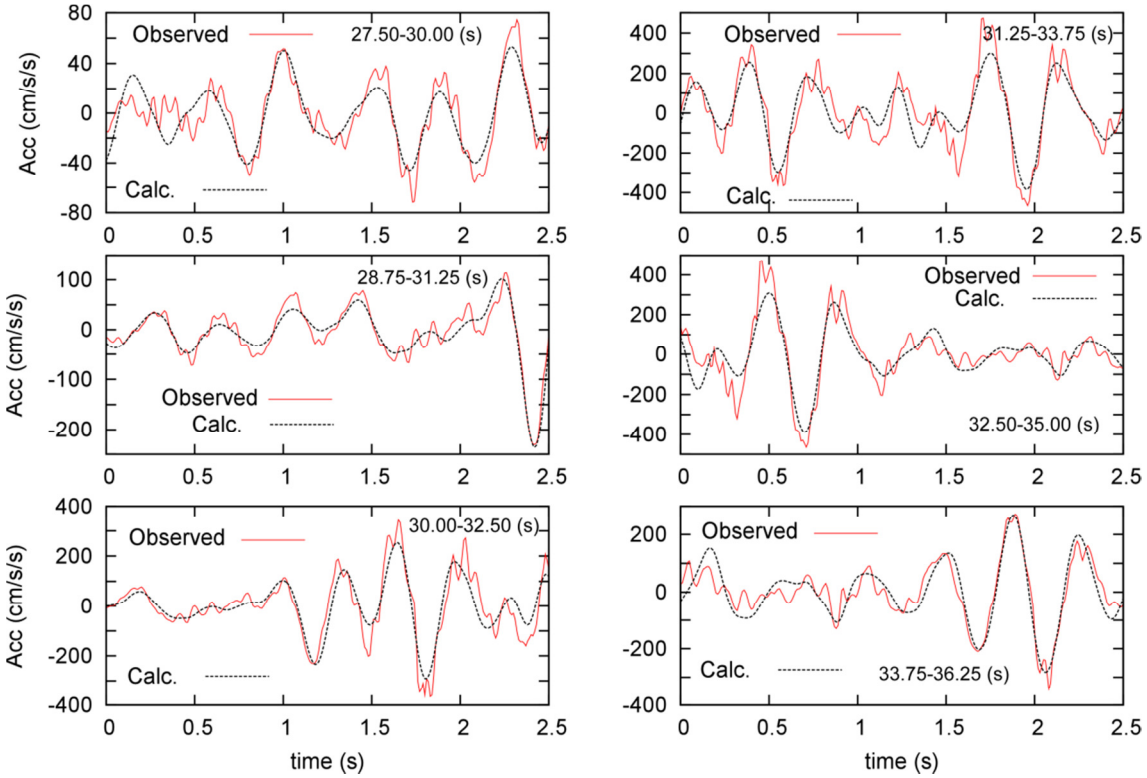


**Figure 4. Fitting result. Each plate indicates each time segment. Correspondent time segment is shown in each plate.**

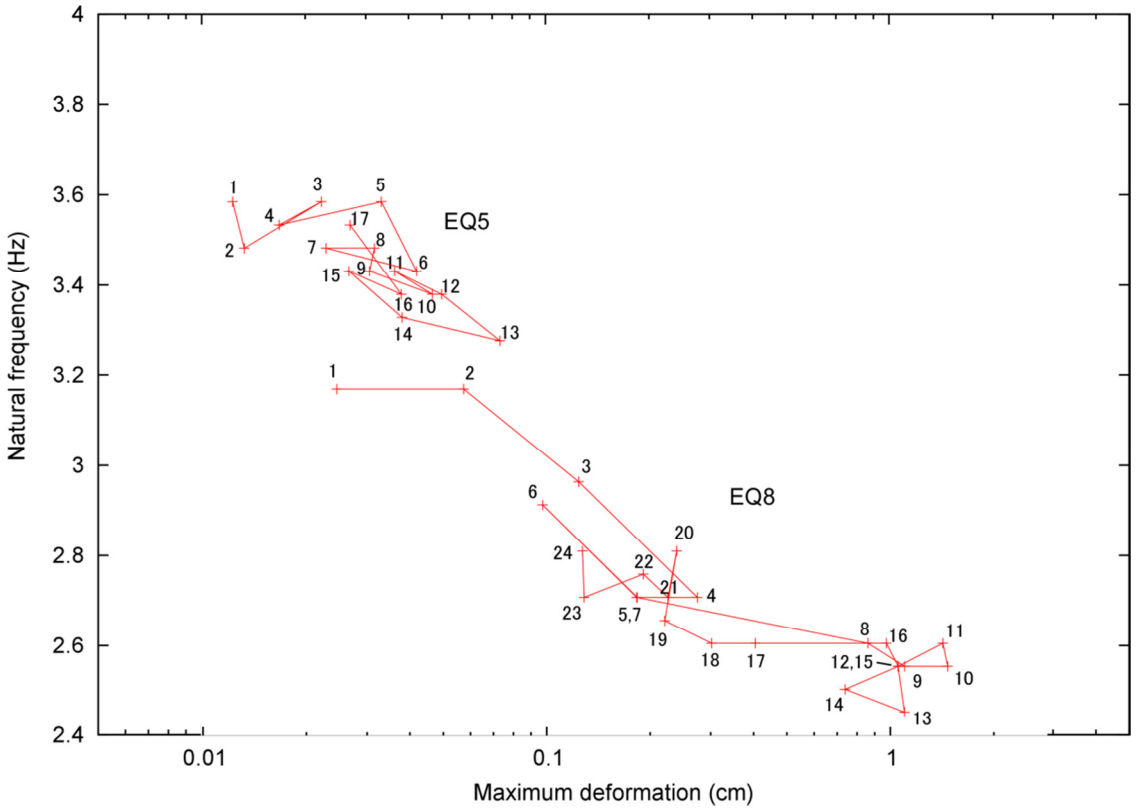


**Figure 5. Relation of maximum deformation and natural frequency for the case of event 5 and 8.**

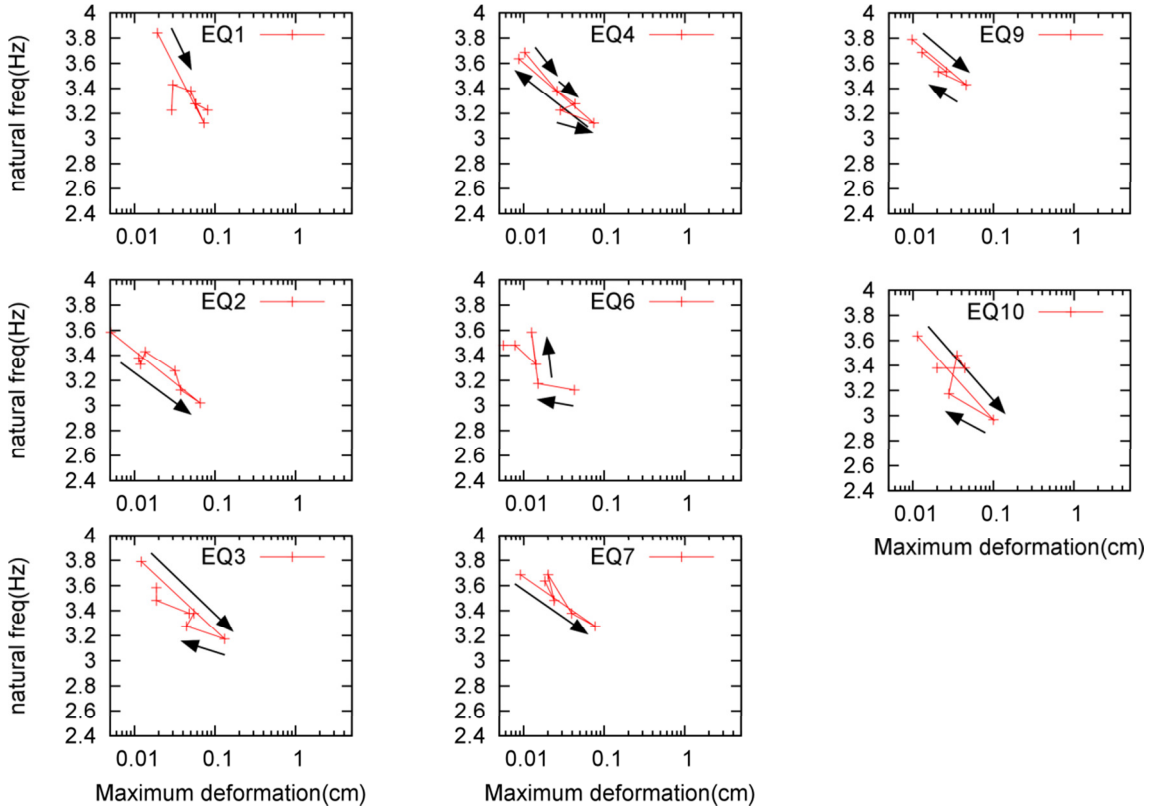


**Figure 4. Relation between maximum deformation and natural frequency for another 8 cases.**

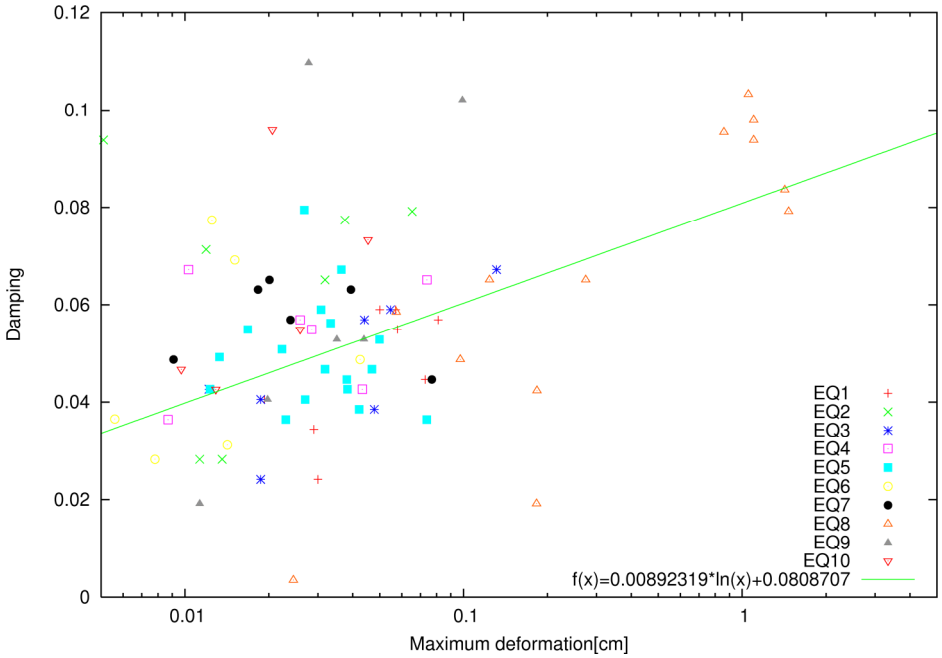


**Figure 7. Relation between maximum deformation and damping factor**

# Shaking Table Test of Bridge Pile Foundation in Liquefied Ground Focused on Section Force to the Intermediate Part of Pile

K. Uno & M. Mitou
*Institute of Technology, Penta-Ocean Construction Co., Ltd., Japan*

H. Otsuka
*Professor, Department of Civil and Structural Engineering, Kyushu University, Japan*

ABSTRACT: In seismic design, in general, the pile bearing capacity of the inertial force of a superstructure is checked, but the design does not give significant importance to the soil-pile-structure interaction. However, during an earthquake, the pile foundation is heavily damaged at the boundary division of the ground types, liquefied ground and non-liquefied ground, and there is a possibility of the collapse of the piles. In this study, we conduct a shaking table test and an effective stress analysis of the influence of liquefied ground and the seismic inertial force exerted on the pile foundation. When the intermediate part of the pile, there is at the boundary division, is subjected to section force, this part increases in size as compared to the pile head in certain instances. Further, we clarify that the action of the seismic inertial force leads to an increased risk of collapse of the piles during liquefaction.

## 1 INTRODUCTION

The pile foundation in liquefaction is heavily damaged at the boundary division of ground classification—liquefied ground and non-liquefied ground—during an earthquake because of the inertial force of a superstructure, liquefaction, and lateral flow, and there is a possibility that the piles will collapse. This agrees with results of the damage surveys conducted for past earthquakes.

In the 2011 earthquake that occurred off the Pacific coast of Tohoku (March 11), liquefaction occurred in Urayasu-shi, in the Tokyo Bay Area, and in Miyagi, Fukushima, and Tochigi Prefectures. This liquefaction seemed to damage the pile foundation. In Onagawa-cho (Miyagi Prefecture) the pile was torn out of the soil by a tsunami. The main cause of the collapse and fall was the tsunami, but it was believed that the pile's resistance to the tsunami was low because the ground was loose.

With respect to the seismic characteristics of the pile foundation, a study on the soil-pile-structure interaction is in progress. Murono *et al.* developed a seismic design by considering the dynamic interaction of the soil-pile-structure, ground displacement, and the inertial force during an earthquake.

Tanimoto *et al.* applied a response displacement method to the seismic performance check of the bridge foundation. They estimated the displacement of the liquefied ground, evaluated the inertial force exerted on the superstructure during liquefaction, decreased the coefficient of soil constants and the horizontal resisting force of the ground, and combined the inertial force and the ground displacement.

However, because of the liquefaction countermeasure of the pile foundation, the ground improvement is considerable. Further, the structural countermeasure, increase in the pile size, and the use of a sheet pile are some factors that increase the section force during an earthquake.

We conduct a shaking table test with the pile to understand the damage mechanism of the pile and the effects of the soil liquefaction and the inertial force of the pile. Moreover, we confirm that a local section force is exerted on the pile at the layer boundary.

In this study, we develop a seismic resistance method for a pile foundation using seismic isolation rubber; the section force is exerted on the intermediate part of the pile.

## 2 REFERENCE BRIDGE PILE FOUNDATION

We first conduct a test with a normal pile and then, compare the results of the pile test using seismic isolation rubber with those of the test conducted with the normal pile.

In this experiment, we hope to achieve an almost real model and build a scale model of this almost real model by reference to the existing literature. A detailed drawing of the pier and the foundation of this model is given in Figure 1. The material of the pile is steel. The section performance of a steel pipe pile is shown in Table 1.

We consider a liquefied ground, and hence, the soil physicality of the literature is not applicable to our case.

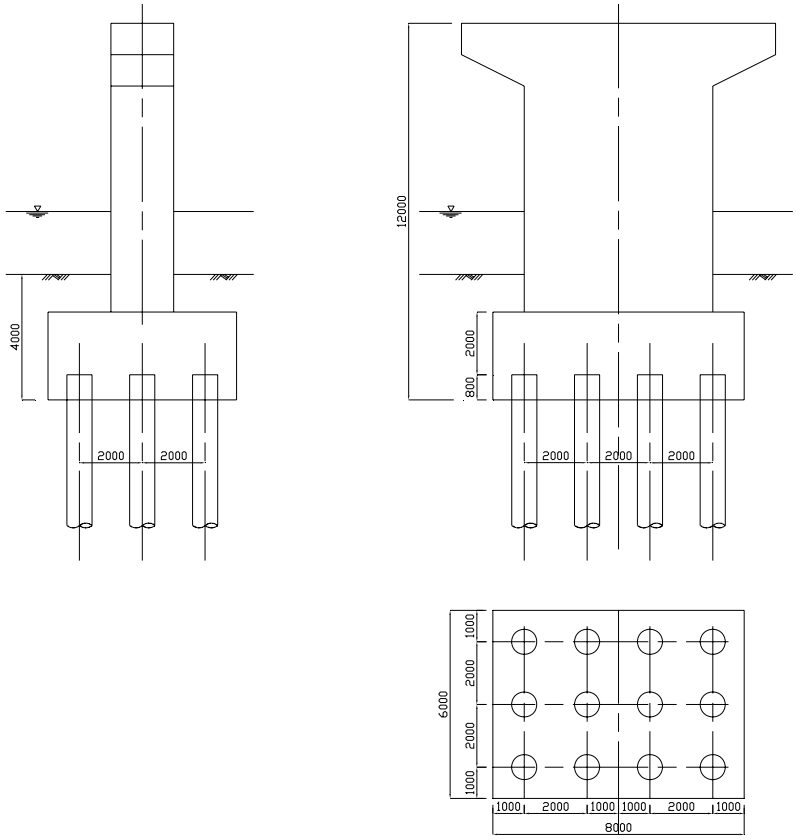


Figure 1. Reference drawing of pile and foundation (unit: mm)

Table 1. Section performance of a steel pipe pile

| mejor diameter | (mm) | 800 | |
|---|---|---|---|
| pipe pile wall thickness | (mm) | 12 | 9 |
| corrosion allowance | (mm) | 2.0 | |
| cross-section area | ($cm^2$) | 246.9 | 173.5 |
| second moment of area | ($cm^4$) | 190000 | 135000 |
| section modulus | ($cm^3$) | 4790 | 3390 |

## 3 OUTLINE OF EXAMINATION

### 3.1 *Scale size and similarity rule*

A cross-section drawing of the test model is shown in Figure 2. With respect to the previous test, the seismic isolation rubber at the intermediate part of the pile is not set, but the other properties are the same as those described in the following sentences. The scale size of the model is 1/20, considering the modeling area and the size of the tank. A similarity rule as that for a 1G gravitational field, proposed by Iai, is used (as mentioned in Table 2). This similarity rule is calculated on the basis of the equation that rules the material phenomenon. This rule is divided roughly into the equation of the saturated ground, the equation of the structure such as a normal pile or a sheet pile, and the equation of water. The parameter of length is assumed to be a standard of the reduced scale among similarity rules requested by these equations, and the reduced scale ratio of the other parameters is calculated. The similarity rule to the soil fraction particle frame of the ground in this case corresponds to the result of the study conducted by Kagawa and Kokusho *et al.*.

In the case of a scale model, the use of water in the experiments is investigated. The effect of the viscosity of water on the water penetration in the ground is determined by observing the dispersal of the pore water pressure for a certain period of time after the shaking test. The experimental results reveal that the viscosity of water does not considerably influence the water penetration during the shaking test. Therefore, water is used in the experiments.

Table 2. List of scaling law

| Parameter | Scaling law | prototype/model |
|---|---|---|
| length | $\lambda$ | 20 |
| density | 1 | 1 |
| time | $\lambda^{0.75}$ | 9.46 |
| stress | $\lambda$ | 20 |
| water pressure | $\lambda$ | 20 |
| siaplacement | $\lambda^{1.5}$ | 89.4 |
| acceleration | 1 | 1 |
| strain | $\lambda^{0.5}$ | 4.47 |
| permeability | $\lambda^{0.75}$ | 9.46 |
| bending stiffness | $\lambda^{4.5}$ | 715,542 |
| axial stiffness | $\lambda^{2.5}$ | 1,789 |

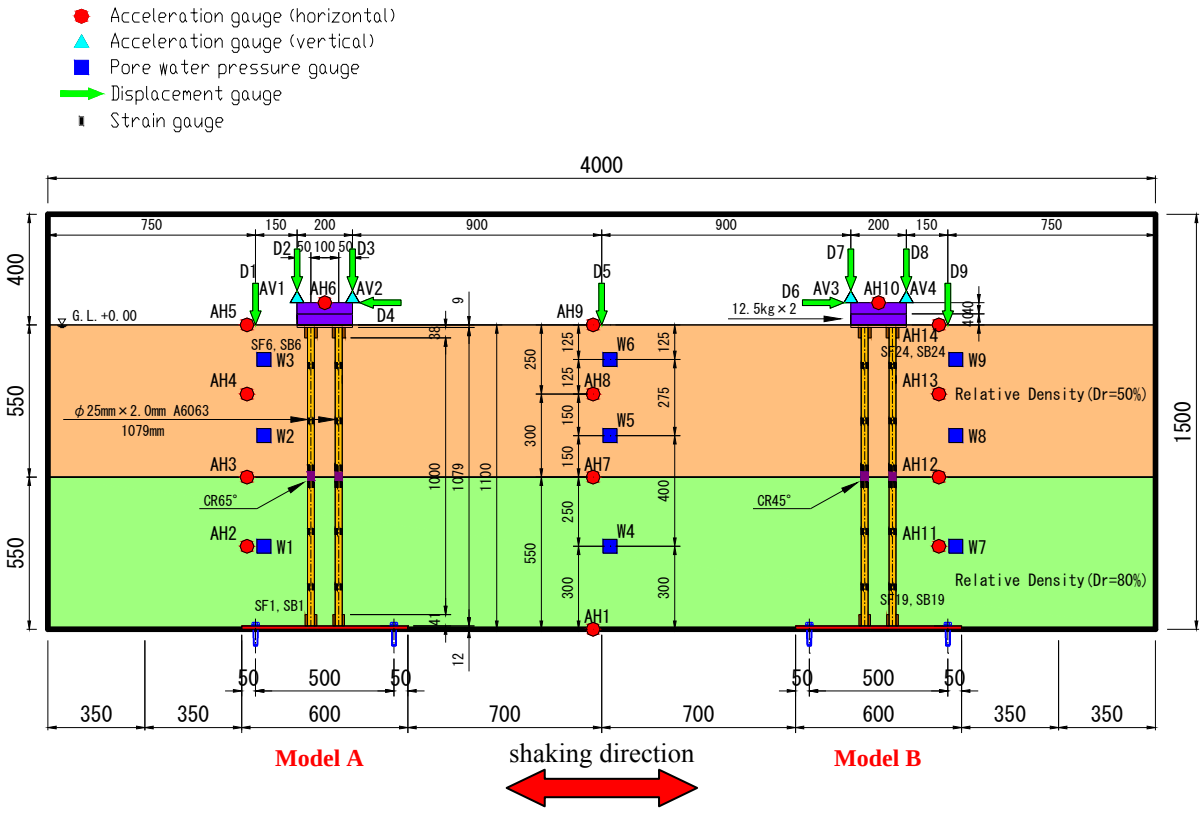


Figure 2. Cross-section drawing of the experiment model

To observe the behavior of the pile during the shaking experiment, the number of piles is adjusted to four. The length of the pile is decreased because of the restriction of the experiment equipment, though, the length requirement of the similarity rule. An aluminum pipe is used for the pile.

Moreover, in order to observe the influence of behavior from the inertial force during an earthquake, the weight considered for obtaining the desired pile load shear ratio of the superstructure and the substructure of the bridge is set as 25 kg.

### 3.2 *Underwater shaking table and earth bank*

A large-scale underwater shaking table having a diameter of 5.5 m is used as the shaking test device. The experimental earth tank has a box-type steel frame having a length of 4.0 m, height of 1.5 m, and depth of 1.5 m. To prevent the water from flowing back to the earth tank, the outflow and the inflow of water in the earth tank boundary are enabled by an unwoven cloth attached to ExpandMetal at a right angle to the shaking direction.

### 3.3 *Development of model*

First, the plate and the shaking table installed in the pile in the earth tank are fixed with the bolt.

Then, the pile is inserted in the ring that is welded in the plate; it is fixed in two directions with bolts. Moreover, epoxy resin is injected into the space between the ring and the pipe. The setting situation of the pile foundation is shown in Photo 1.

Next, non-liquefied ground and liquefied ground are prepared using Soma-Sand. The non-liquefied layer reaches the prescribed height first at a relative density of 80%, and the soil is compacted and flattened out. The density of the sand is determined using the weight and the height of the ground for every 100-mm-thick layer.

The non-liquefied layer is prepared in air. Water is then poured to prepare the liquefied layer.

The liquefied layer is prepared using sand by the underwater sedimentation method. It has a relative density of 50%.

The list of the materials used for preparing the pile foundation and the soil is given in Table 3, and the size of the pile foundation model is given in Table 4. In Tables 3 and 4, the steel plate connected with the top of the pile (it is usually the bridge part of the footing) is considered the upper structure, and the steel plate that is fixed at the bottom of the pile and the shaking table is considered the lower structure.

Photo 1. Setting situation of the pile foundation

Table 3. List of the materials of the soil and the pile foundation

| item | | material | remarks |
|---|---|---|---|
| Liquefied ground | | Soma-Sand (underwater sedimential method) | Dr≒50% |
| Non-liquefied ground | | Soma-Sand (in air method) | Dr≒80% |
| Pile foundation | upper | steel plate | t=9mm |
| | lower | steel plate | t=12mm |
| | pile | aluminum pipe | φ=25mm, t=2.0mm |

Table 4. Size of the pile foundation model

| structure | detail | figure | material | measurement |
|---|---|---|---|---|
| Pile foundation | upper structure | plate | steel | PL-200×200×9 |
| | | ring | steel | 42(mejor diameter)×8(wall thickness)×38(height) (minor diameter: 26mm) |
| | lower structure | plate | steel | PL-1100×600×12 |
| | | ring | steel | 46(mejor diameter)×10(wall thickness)×41(height) (minor diameter: 26mm) |
| | pile | pile | aluminum | 25(major diameter)×2.0(wall thickness)×1079(length) (minor diameter: 21mm) |
| Weight | ----- | plate | steel | PL-200×200×4 |

### 3.4 *Seismic isolation rubber*

The seismic isolation rubber is installed in the intermediate part of the pile as shown in Figure 2. The configuration of the seismic isolation rubber and the installation method to the pile are shown in Figure 3. The seismic isolation rubber was not a laminated structure but a unit, and two kinds of hardness values (CR65° and CR45°) are obtained in the layer boundary part of the intermediate of the pile. Moreover, the pile and the rubber are fixed by using the adhesive. The pile that has a hardness of CR65° is called Model A, and the pile that has a hardness of CR45° is called Model B.

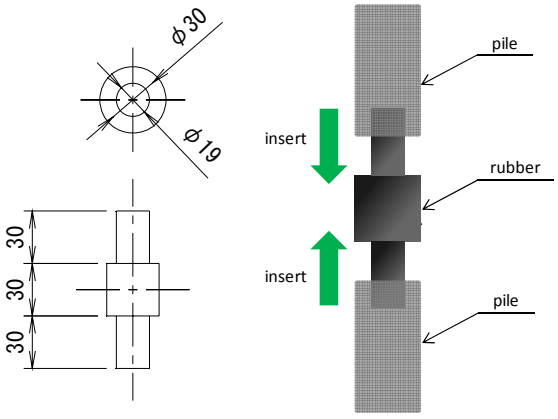


Figure 3. Configuration of the seismic isolation rubber and the installation method to the pile

### 3.5 *Shaking wave*

Shaking tests are conducted under the conditions of a 1G sinusoidal wave with a frequency of 10 Hz and wave numbers of 20. The frequency is set in consideration of the natural period of the pile foundation.

In the tests, we consider three cases—the case with 100 Gal (Case 1), the case with 350 Gal (Case 2), and the case with 700 Gal (Case 3). The shaking wave of 100 Gal is shown in Figure 4. The 100-Gal and 350-Gal input levels of the sine wave are considered the energy of the corresponding level 1 seismic ground motion and level 2 seismic ground motion. The maximum seismic ground motion is assumed for the case with 700 Gal. Each test wave has a taper installed in the first wave.

The horizontal axis shown in Figure 4 denotes the time from the beginning of the shaking of the table. All the time history data shown in since Figure 5 are the time from the beginning of the measurement recorded by using a recording device. The time for the beginning of the measurement is set to 3~3.5 s from the time of the beginning of the shaking of the table. Therefore, the data are displayed from 3 s after the beginning of the measurement as shown in since Figure 5.

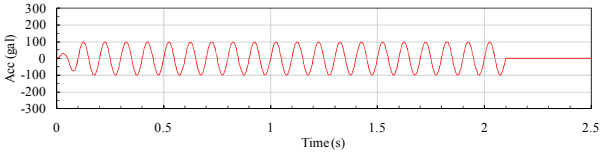


Figure 4. Shaking wave (100 Gal)

### 3.6 *Measurement point*

The list of the measurement points is given in Table 5. We use 18 accelerometers (horizontal direction: 14, vertical direction: 4), 9 pore water pressure gauges, 9 displacement gauges, 24 placements of the strain gauge with reference to the placement shown in Figure 2. As time histo-

ry data, we measure the displacement, acceleration, and strain of the pile foundation and the acceleration, pore water pressure, and surface displacement of the ground by using metering equipment.

Moreover, the residual displacement of the ground level is measured from the measurement result of the target coordinates before and after the experiment.

Table 5. List of the measurement points

| measurement item | measurement target | equipment |
|---|---|---|
| horizontal disp. | upper structure | disp. gauge |
| vertical disp. | upper structure, ground level | disp. gauge |
| horizontal acc. | upper structure, ground | acc. gauge |
| vertical acc. | upper structure | acc. gauge |
| excess pore water pressure | ground | pore water pressure gauge |
| strain | pile | strain gauge |
| residual disp. | ground level | target rivet |

## 4 EXPERIMENT RESULT

### 4.1 *Acceleration*

The time histories of the acceleration response in the pile head of Cases 1–3 is shown in Figures 5–7, respectively. The effect of the seismic isolation rubber is verified by the comparison with the response acceleration time histories of the pile head of the normal pile in the experiment. The upper structure acceleration response decreases because the natural period of the pile has become longer with the seismic isolation rubber when first paying attention to the result of Case1. However, because the time until liquefaction is longer in Case 1 than in Case 2 and Case 3, a rapid decrease in the response is observed after a considerable period of time. It is believed that the ground before liquefaction is not affected easily by the seismic isolation rubber because a considerable section force acts on the pile head as compared to the layer boundary part. Next, in the normal pile test, in Case 2, the response in the pile foundation decreases more naturally than in Case 1; further, in Models A and B that have countermeasures, the response is smaller in Case 2 than in Case 1. This is because the time until liquefaction is short and the effect of the rubber is demonstrated once as compared to in Case 1. As a result, when the pile foundation is designed considering the scale of level 2 ground motion, the effect of the seismic isolation rubber on a liquefied ground is very high. Next, the acceleration of the first wave in the pile with the seismic isolation rubber is larger than in the normal pile after the taper wave is recorded in Case 3. However, this acceleration decreases significantly when we consider the total energy of

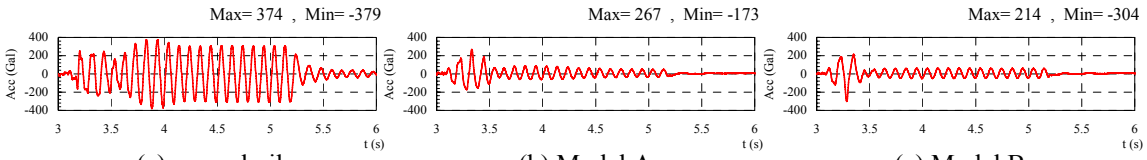


(a) normal pile (b) Model A (c) Model B

Figure 5. Time histories of the acceleration response in the pile head (Case 1)

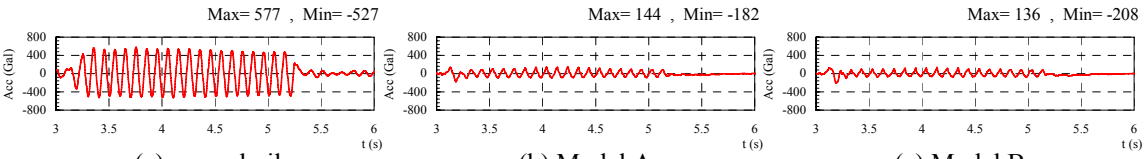


(a) normal pile (b) Model A (c) Model B

Figure 6. Time histories of the acceleration response in the pile head (Case 2)

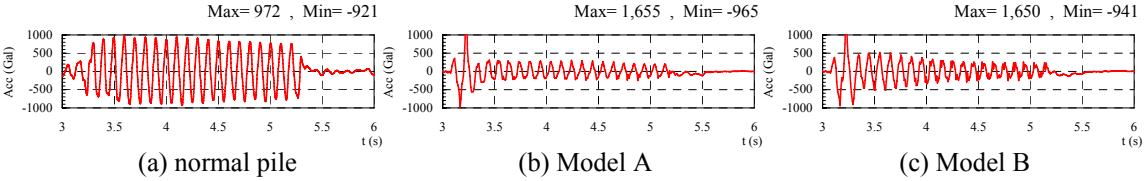


(a) normal pile (b) Model A (c) Model B

Figure 7. Time histories of the acceleration response in the pile head (Case 3)

an earthquake for the model. Whether the damage to the entire structure is caused by the amplitude of the first wave should be verified in the future.

From the above-mentioned results, we can conclude that the earthquake energy in all the considered cases decreased in the pile head. When liquefaction generates level 2 seismic ground motion, the effect of the seismic isolation rubber is demonstrated and the response is decreased. Hence, the proposed method is very effective as an earthquake resistance improvement plan of the pile foundation in the liquefied ground.

## 4.2 *Strain*

The time histories of the strain in the pile foundation are shown in Figure 8. This figure presents the results obtained in Cases 1–3. The left side of the figure is the normal pile, the center is Model A and the right is Model B. In the normal pile, the strain results are felt in six places because the strain gauge is attached to only one place on the pile intermediate part. In this figure, SF denotes the strain measured at the front of the pile and SB denotes the strain measured at the back. Further, averaged strain (SFB) excluding the pile head is calculated by using the proposed method to unite the gauge.

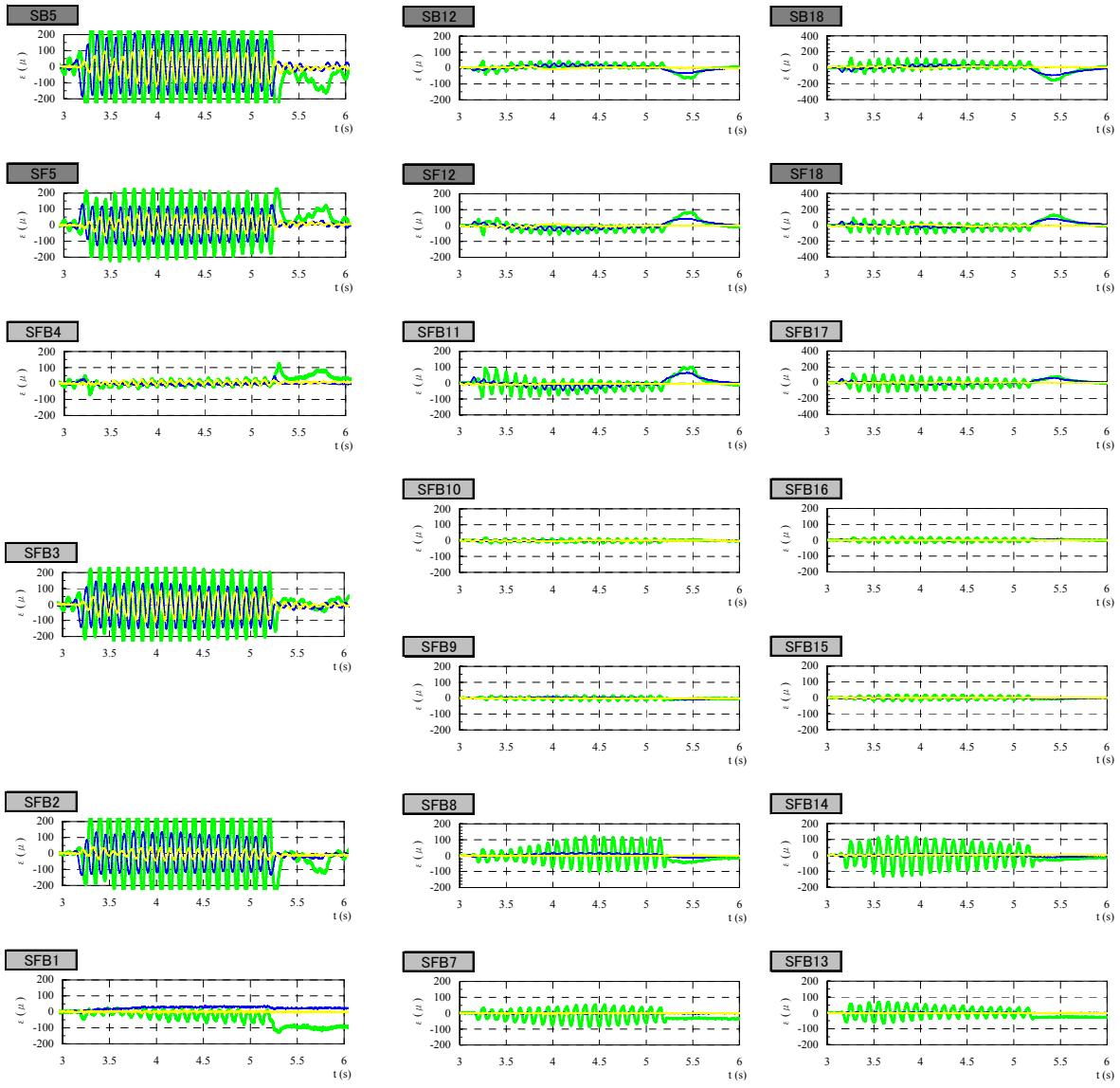


(a) normal pile (b) Model A (c) Model B

Figure 8. Time histories of the strain in the pile foundation

In the case of the normal pile, significant strain is generated by SF5, SB5 of the pile head, and SFB3 in the middle part of the pile. In particular, the maximum value of the strain is observed at 3.5 s. It is speculated that the response value is significant because the inertial force of the upper structure is exerted on the middle of the layer boundary after liquefaction.

In Case 1, the strain is not generated in almost all the parts of the pile. It is shown that hardly any strain is generated in Models A and B although the strain is generated in the case of the normal pile.

In Case 2, the countermeasure pile decreases as compared to the normal pile although some strains to the pile head are generated in the countermeasure pile. Moreover, hardly any strain is generated at intermediate part and the bottom of the pile.

In Case 3, it is possible to considerably decrease the strain as compared to that in the case of the normal pile although some strains are generated in the pile head. Moreover, a significant amount of strain is comparatively generated in the vicinity of the bottom of the pile. This is attributed to the fact that the layer boundary part moves downward because the shaking wave is large as mentioned above. Hence, the layer boundary part before shaking is liquefied. Therefore, it is speculated that the position where the seismic isolation rubber is installed moves downward if the assumed maximum seismic ground motion becomes a countermeasure.

### 4.3 *Deformation amount of seismic isolation rubber*

The maximum deformation, shear strain, and effective plane area of the seismic isolation rubber observed during the shaking test are given in Table 7. When focusing attention on the maximum deformation amount and the shear strain, it seems to be no problem for tearing rubbers in each case compared with the seismic isolation rubber bearing generally used because the shear strain is small. It can be said that there is still latitude when paying attention only to the deformation amount of the seismic isolation rubber because it designs the deformation of the seismic isolation rubber bearing by allowing less or equal 250% of the shear strain for level 2 seismic ground motion.

However, it is possible to calculate the bearing capacity shortage of the pile during shaking even if the shear strain is small (in an unstable state caused by the bending deformation of the seismic isolation rubber) by installing the seismic isolation rubber in the intermediate part of the pile. The effective plane area of the seismic isolation rubber during shaking is also given in Table 7. The effective plane area is the area where the distance of the seismic isolation rubber during an earthquake is measured. This shows that it can be expected that the pile is able to support the vertical force compared with before shaking. In Cases 1 and 2, approximately 60% or more of the plane area remains, and this area can maintain a steady vertical force. However, in Case 3, it is necessary to note that approximately 30%~40% of the plane area remains although a bending deformation is not generated during the experiment. Therefore, it is speculated that in this case, countermeasures such as securing each effective plane area by arranging two or more seismic isolation rubbers are necessary.

Table 6. Deformation of seismic isolation rubber

| | Case 1 (100Gal) | | Case 2 (350Gal) | | Case 3 (700Gal) | |
|---|---|---|---|---|---|---|
| | CR65° | CR45° | CR65° | CR45° | CR65° | CR45° |
| maximum deformation (mm) | 1.1 | 1.4 | 7.6 | 9.8 | 14.3 | 16.8 |
| shear strain (%) | 3.7 | 4.7 | 25 | 33 | 48 | 56 |
| effective plane area (%) | 95 | 94 | 68 | 60 | 42 | 33 |

### 4.4 *Bending moment*

The maximum bending moment distribution of the pile foundation in each case is shown in Figure 9. The maximum bending moment distribution of the normal pile is also displayed in the figure for the sake of comparison.

Firstly, from the result, we conclude that the section force decreases in all cases. In particular, it is possible to significant decrease the strain if the seismic ground motion level of Case 2 is considered. This consequently leads to a decrease in the section force of the pile head although the seismic isolation rubber is installed to decrease the responses of the intermediate part of the pile for the purpose.

In the case of a very large seismic ground motion such as Case 3, the section force is generated on the pile head and the bottom side of the pile even when the seismic isolation rubber is installed appropriately. In this case, we believe that the responses of the entire pile are decreased by moving the installation location of the rubber a little downward and increasing the installation number as mentioned above.

In this experiment, we demonstrate that the seismic isolation rubber is very effective when level 1 and level 2 seismic ground motions are targeted, but when the maximum ground motion as in Case 3 is targeted, we believe that the required seismic capacity can be attained if the designer and practitioner appropriately judge the disposition of the seismic isolation rubber on the basis of the experimental results.

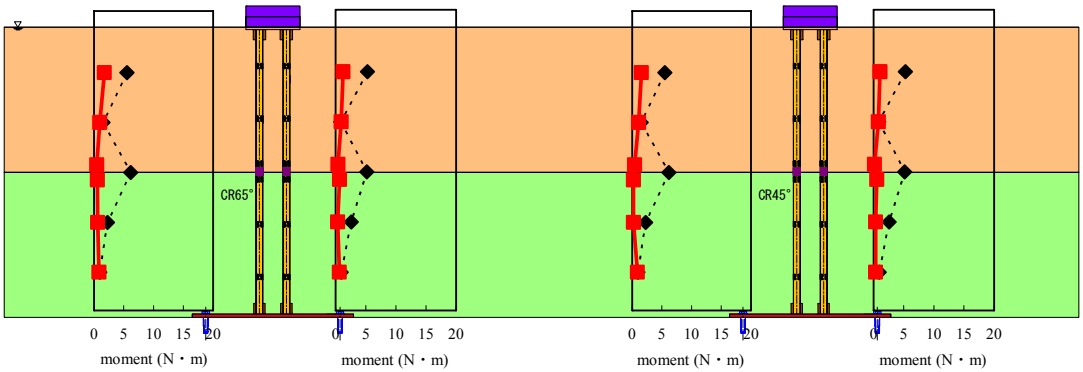


(a) Case 1

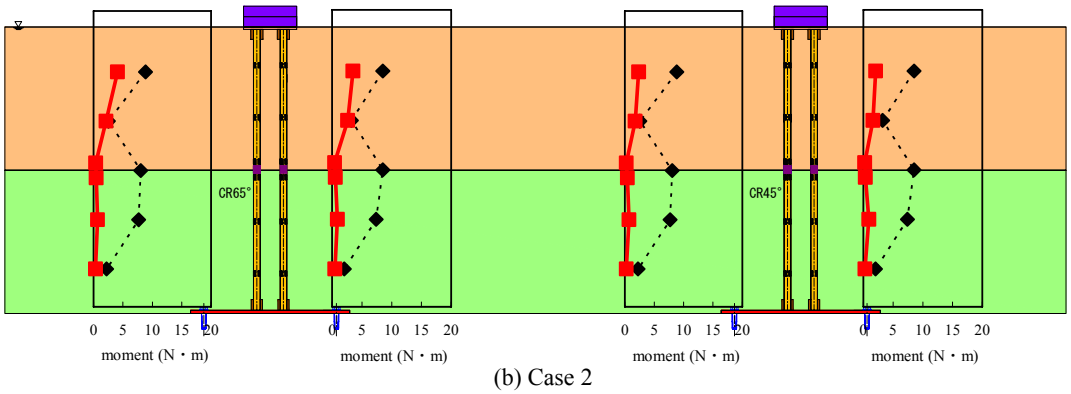


(b) Case 2

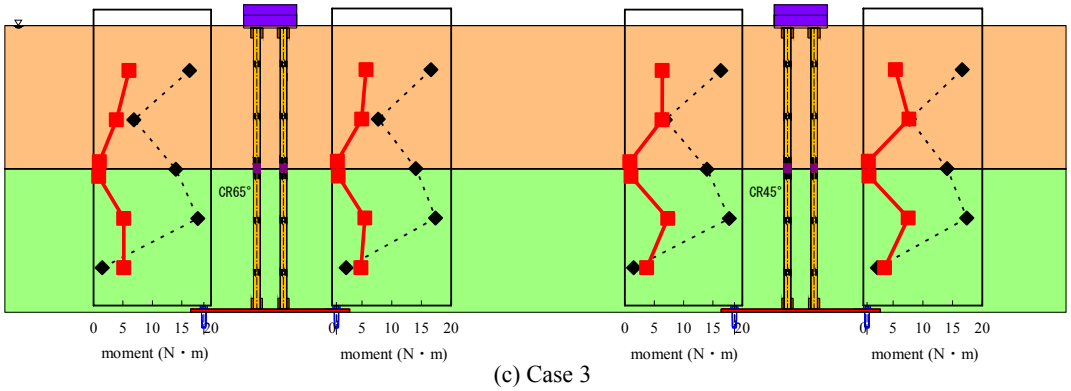


(c) Case 3

: Normal pile : Seismic isolation pile

Figure 9. Maximum bending moment distribution of the pile foundation

## 5 CONCLUSIONS

The following conclusions were drawn from the experiments.

- The countermeasures for the entire pile foundation were very effective because the pile foundation took a long time to form. Hence, the section force of the pile head could be decreased, although the generation of section force in the middle of the pile decreased because of the installation of the seismic isolation rubber.
- On the basis of the acceleration response, it was concluded that the seismic isolation rubber installed in the middle of the pile produced the desired effect during liquefaction.
- The layer boundary moved downward in the case when the shaking wave was large and the layer boundary before shaking was liquefied. Hence, it is necessary to consider the seismic ground motion for determining the installation position.
- Lastly, we need to understand the behavior of the pile with a special focus on the effective plane area of the seismic isolation rubber in order to ensure that the pile does not collapse because the seismic isolation rubber is usually installed in the intermediate part of the pile and not the bearing part. Moreover, the installation number and the rigidity of the seismic isolation rubber should be changed appropriately.

## ACKNOWLEDGEMENTS

About the characteristics of the seismic isolation rubber and shaking test method, the authors express our gratitude to Dr. Hiroo Shiojiri (Professor, College of Science and Technology, Nihon University) for his guidance and advice. We thank to Mr. Hamagami and Mr. Sasaki, The Yokohama Rubber Co., Ltd., for providing the experimental materials and supporting the experiments with seismic isolation rubber.

## REFERENCES

Kunihiko UNO, Hisanori OTSUKA and Masaaki MITOU (2011). The consideration about the seismic resistance improvement of the bridge pile foundation with the seismic isolation system in liquefied ground, *Japan Society of Civil Engineers 2011 Annual Meeting*, I-503 (in Japanese)

Kouichi TOMISAWA, Satoshi NISHIMOTO and Itaru HASHIMOTO (2004). Examples of bridge foundation pile deformation caused by the liquefaction of the Tokachi-oki earthquake in 2003, *Proceedings of the symposium on the pile behavior and design in liquefaction*, 217-220 (in Japanese)

Yoshitaka MURONO, Akihiko NISHIMURA and Shinji NAGATSUMA (1998). Seismic Response of Pile Foundation In Soft Ground And Its Application to Seismic Design, *JSCE Journal of Structural Engineering*, Vol.44A, 631-640 (in Japanese)

Shunsuke TANIMOTO, Hideki SUGITA, Akihiro TAKAHASHI and Kazuyuki HAYASHI (2004). Parametric Study on Seismic design Method of Bridge Foundation in Liquefiable Ground Considering Ground Displacement, *Proceedings of the symposium on the pile behavior and design in liquefaction*, 185-188 (in Japanese)

Kunihiko UNO, Hisanori OTSUKA and Masaaki MITOU (2011). Experimental study on influence of soil liquefaction and seismic inertial force on bridge pile foundation, *Annual Meeting of Kanto Branch of JSCE*, Part I, I-35 (in Japanese)

Japanese Technical Association for Steel Pipe Piles and Sheet Piles (2009). Steel Pile Piles –The Design and Construction- (in Japanese)

Susumu IAI (1988). Similitude for Shaking Table Tests on Soil-Structure-Fluid Model in 1g Gravitational Field, *Report of the Port and Harbour Research Institute*, Vol.27, No.3

Takaaki KAGAWA (1978). ON THE SIMILITUDE IN MODEL VIBRATION TESTS OF EARTH-STRUCTURES, *Proceedings of the Japan Society of Civil Engineers*, No.275, 69-77 (in Japanese)

Takaji KOKUSHO and Takahiro IWATATE (1979). SCALED MODEL TESTS AND NUMERICAL ANALYSES ON NONLINEAR DYNAMIC RESPONSE OF SOFT GROUNDS, *Proceedings of the Japan Society of Civil Engineers*, No.285, 57-67 (in Japanese)

Kenji ISHIHARA (1996). Soil Behaviour in Earthquake Geotechnics, OXFORD SCIENCE PUBLICATIONS

Japan Road Association (2004). Manual for Highway Bridge Bearing (in Japanese)

# Dynamic Centrifuge Model Test of Pile-Supported Building with Semi-Rigid Pile Head Connections in Liquefiable Soil

S. Ishizaki & T. Nagao
*Technology Center, Taisei Corp., Yokohama, Japan*

K. Tokimatsu
*Tokyo Institute Technology, Tokyo, Japan*

ABSTRACT: Dynamic centrifuge model tests were conducted to investigate the seismic behavior of buildings with semi-rigid pile head connections in liquefiable soil. The test results and analysis show that: (1) The semi-rigid pile head connections effectively reduce the bending moment of piles both before and during liquefaction; (2) The natural period of the soil-pile-structure system with semi-rigid pile head connections becomes longer than that with rigid pile head connections during liquefaction; (3) The hysteresis damping in the relation between inertia force of the structure and displacement of the foundation, with semi-rigid pile head connections, increases with larger displacement; and (4) The maximum acceleration of the superstructure with semi-rigid pile head connections is considerably smaller than that with rigid pile head connections in liquefied soil.

## 1 INTRODUCTUION

Various semi-rigid pile head connection methods for improved pile designs have been developed that permit the pile heads to rotate, and their effectiveness for reducing pile damage has been verified by structural tests (Hara et al. 2002, Ohtsuki et al. 2001, Hiraide et al. 2004). However, only the static structural properties of pile head connections have been studied; the effectiveness of semi-rigid pile head connection methods for reducing damage has not been studied using the whole building while considering the dynamic soil-pile-structure interaction. In our previous study, Ishizaki et al. 2006, shaking table tests of pile-supported building models in dry sand were conducted to investigate the seismic behavior of buildings with semi-rigid pile head connections. In this study, dynamic centrifuge tests are conducted using pile-supported building models in liquefiable soil to examine the effectiveness of the semi-rigid pile head connection method for reducing seismic damage to piles, and the effects on the response of the building.

## 2 TEST OUTLINE

Dynamic centrifuge model tests were performed at 50g centrifugal acceleration using a geotechnical centrifuge at the Technology Center of Taisei Corporation. Two soil-pile-structure models were used: a building model with either rigid pile head connections (Model R) or semi-rigid pile head connections (Model S). The models were prepared in a laminar shear box measuring 560×210×400mm (L×W×D).

## 2.1 *Models*

Figure 1 shows the soil-pile-structure model used in the tests. The soil models were created using Toyoura sand ($D_{50}$=0.18 mm), and consisted of two layers with different relative densities. The target relative density was set at 60% in the upper layer and 90% in the lower layer. The relative density of the upper layer before excitation was 65% in Model S and 60% in Model R, therefore the soil in Model S was denser than in Model R. The soil models were saturated with silicone oil 50 times more viscous than water.

The mass of the superstructure was 5.2 kg and that of the foundation was 2.7 kg. The natural period of the superstructure at small excitation was 0.003 s (0.15 s in the prototype scale). The pile groups consisted of 2×2 stainless steel pipes, each of 16 mm diameter and 1mm wall thickness. The elastic coefficient of the pipe was $1.97\times10^8$ kN/m$^2$. The pile tips were connected to the base of the laminar box with pin joints. The pile head connections are shown in Figure 2. The pile heads were connected to the foundation (pile cap) either rigidly or semi-rigidly. In Model R, the pile heads were sandwiched between divided sections of the foundation and fastened by bolts, while in Model S, the foundation was simply placed on the pile heads.

The rotation characteristics at the pile head connections were identified by preliminary static bending tests, using a cantilever beam composed of pile and foundation as a specimen (Fig. 3). The pile tip was subjected to loading and unloading perpendicular to the axis. The bending moment and rotation angle at the pile heads were measured. Several initial axial forces of 1 kN (2.5 MN in the prototype scale), 0.4 kN (1.0 MN) and 1.6 kN (4.0 MN) were applied to the semi-rigid pile head connection. Figure 4 shows the relations between the bending moment and rotation angle at pile heads for both types of pile head connections. In the semi-rigid pile head connection, the initial rigidity was small, and the rotation angle increased drastically as the bending moment increased. The relation curve was almost the same either in loading or unloading (non-linear elastic behavior). The maximum resistance of moment *Mu* is given by:

$$M_u = \frac{D}{2} N \tag{1}$$

where, *D* is pile diameter and *N* is axial force. *Mu* at each axial force is also shown in Figure 4. The bending moment at the semi-rigid pile head connections are close to *Mu* for the respective axial forces.

## 2.2 *Measurement parameters*

The measurement parameters are shown in Figure 1. The horizontal accelerations of the soil and structure, vertical accelerations of the foundation, strains in the piles, rotation angles of the pile heads, and pore water pressures of the soil were measured. The displacements of the structure and soil were calculated by double integration of the accelerations with respect to time.

## 2.3 *Input motion*

An artificial ground motion called a Rinkai wave, which is produced as an earthquake in the southern Kanto region in Japan, was used as an input base acceleration to the shaking table, with a maximum acceleration of 200 cm/s$^2$ in the prototype scale. The initial vibration characteristics of the soil-pile-structure models were identified under small excitation.

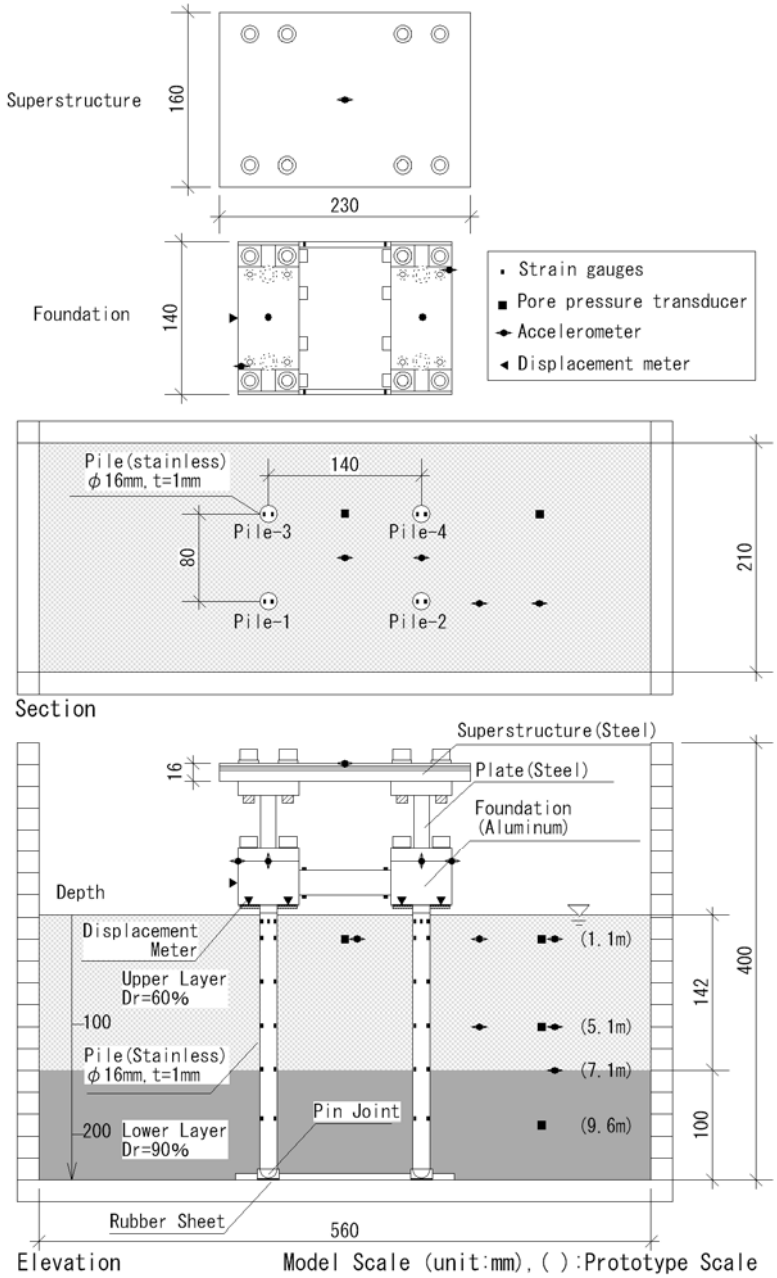


Figure 1. Model layout.

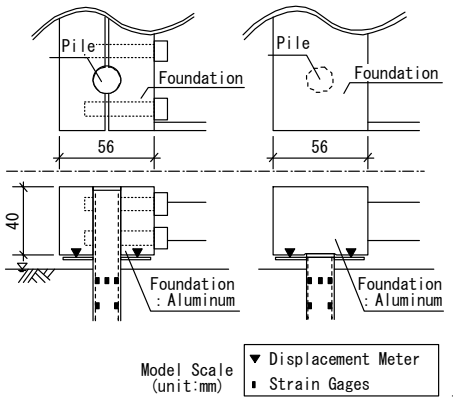


Figure 2. Models of pile heads.

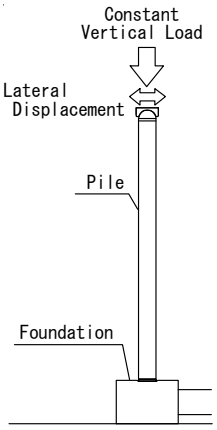


Figure 3. Specimen in preliminary test.

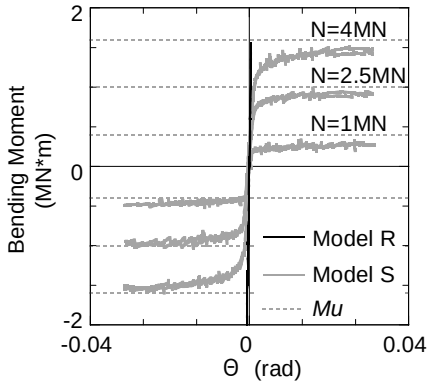


Figure 4. Rotation characteristics at pile heads in preliminary tests.

## 3 TEST RESULTS AND ANALYSIS

All data presented in this section are for the prototype scale. The results of excitation by the Rinkai wave with a peak input acceleration of 200 cm/s$^2$ were compared for Model R and Model S. The initial axial forces on the pile heads in Model S were almost the same (Table 1).

Table 1. Initial axial forces on pile heads in Model S.

| Pile | Initial Axial Force | Pile | Initial Axial Force |
|---|---|---|---|
| Pile-3 | 2,100kN | Pile-4 | 2,320kN |
| Pile-1 | 2,350kN | Pile-2 | 2,200kN |

### 3.1 *Time histories of responses of soil, building, and pile heads*

The time histories of accelerations of soil and shaking table, displacement of soil, and excess pore water pressures of soil are shown in Figure 5. The excess pore water pressures of soil at depths of 1.1 m and 5.1 m reach the respective initial effective vertical stresses, then the upper layers liquefy in both models. The excess pore water pressure of soil at 5.1 m depth in Model S rises later than in Model R, due to its higher relative density of the upper layer. Therefore, the acceleration of the soil in Model S decreases after 20 s, whereas that in Model R decreases after 12 s.

The soil displacements at 1.1 m depth in both models increase drastically during soil liquefaction, especially from 77 s to 88 s.

Figure 6 shows the time histories of acceleration of the superstructure, displacement of the foundation, and bending moment and rotation angle of the pile heads. The acceleration of the superstructure in Model S is the same or a little larger than in Model R before 20 s. But after 23 s, by when the soil in the upper layer has almost liquefied, the acceleration of the superstructure in Model S tends to decrease and be delayed compared with that in Model R. After 30 s, the maximum acceleration of the superstructure in Model S is 0.47 m/s$^2$, which is 40% of that in Model R (1.09 m/s$^2$).

The displacements of the foundation in the two models mostly agree before 20 s, but thereafter that in Model S increases and is delayed, especially from 77 s to 88 s. The displacement of the foundation in Model S corresponds to that of the soil at 1.1 m depth in the model after 20 s (Fig. 5b).

The bending moment at the pile heads in Model S already becomes smaller than in Model R before liquefaction, and almost reaches *Mu* at 13 s.

The rotation angle at the pile heads in Model S becomes larger with increasing pore water pressure and soil liquefaction, notably from 77 s to 88 s.

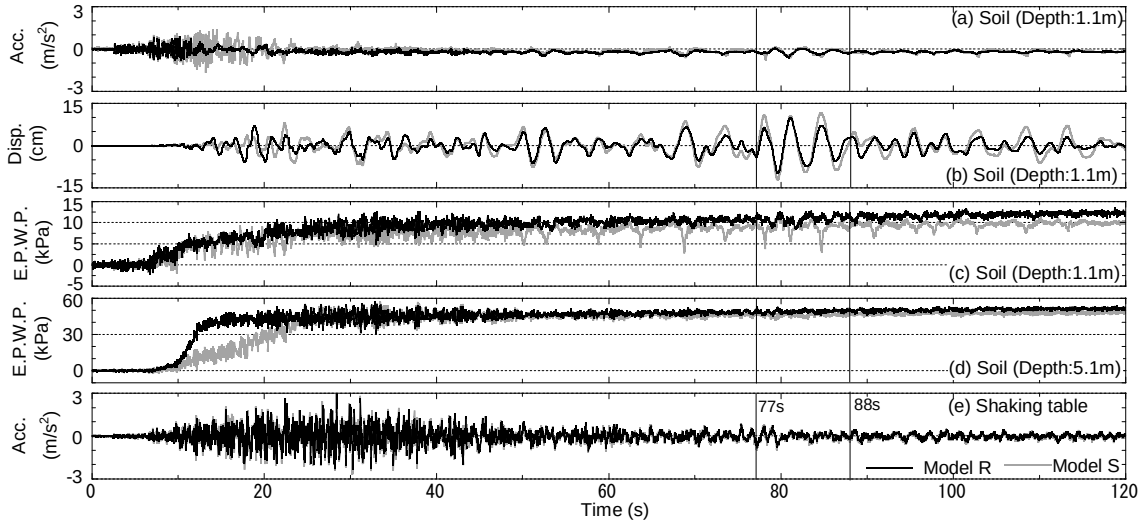


Figure 5. Time histories of acceleration, displacement, and excess pore water pressure of soil.

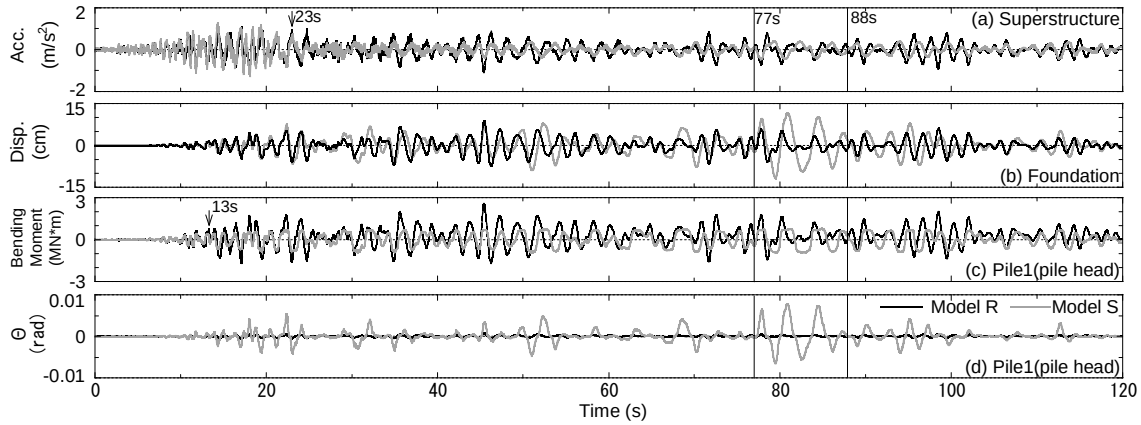


Figure 6. Time histories of acceleration of superstructure, displacement of foundation, bending moment and rotation angel of pile heads.

### 3.2 *Relations between bending moment and rotation angle at pile heads*

Figure 7 shows the relations between bending moment and rotation angle at the pile heads. Model S shows lower initial rigidity than in Model R as shown in the preliminary tests, and exhibits non-linear elastic behavior. The bending moment in Model S drops steadily below that in Model R. The axial forces on the pile heads varied due to overturning moment of the structure. Therefore, in Model S, the maximum bending moment in the pile subjected to compression becomes higher than that in the pile subjected to pullout force.

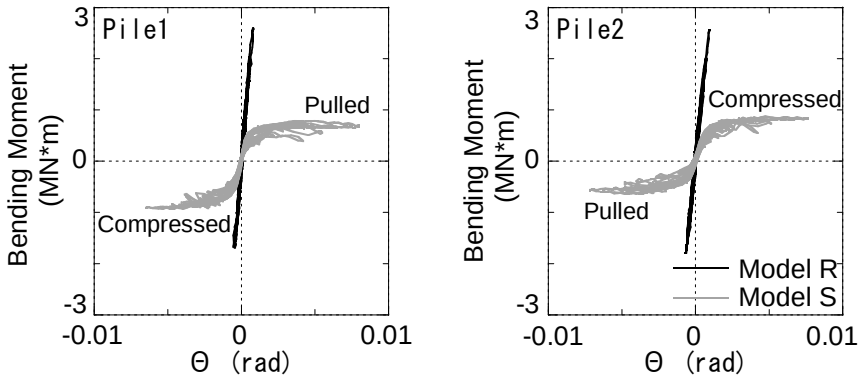


Figure 7. Relations between bending moment and rotation angle at pile heads.

### 3.3 *Distributions of Bending Moment along Piles*

Figure 8 shows the distributions of bending moment along piles at 18.0 s (before liquefaction). The inertia force from the structure is computed from the observed accelerations of superstructure and foundation. At this second, the inertia forces in both models are the same. In Model R, the maximum bending moment occurs at the pile heads. In Model S in which the pile heads can rotate, the bending moment at the pile heads is lower than that in Model R. The maximum bending moment in the soil in Model S is larger than in Model R, and occurs at a shallower depth.

Figure 9 shows the distributions of the maximum bending moment along the piles before liquefaction (0-25 s) and during liquefaction (25-120 s). Table 2 shows the maximum inertia forces for the respective periods.

Before liquefaction, in Model S, the bending moment in the soil is slightly larger than at the pile heads, and the bending moment at the pile heads is almost 50% of that in Model R.

During liquefaction, the maximum inertia force in Model R is almost the same as that before liquefaction, but the maximum inertia force in Model S is about 40% of that before liquefaction. The maximum bending moment in Model R is significantly larger than that before liquefaction due to the stiffness decrease of liquefying soil, because the inertia forces for the respective periods are the same. In Model S, in contrast, the maximum bending moment in the liquefied soil is lower than that before liquefaction. This is because the inertia force reduces not only in the state in which the pile head bending moment reaches *Mu* but also in the state in which the soil stiffness considerably decreases. As a result, through the whole time of shaking, the maximum bending moment in Model S decreases to 40% of that in Model R.

Table 2. Maximum inertia forces.

| Period | 0-25 s | 25-120 s |
|---|---|---|
| Model R | 1,056 kN | 1,074 kN |
| Model S | 1,200 kN | 439 kN |

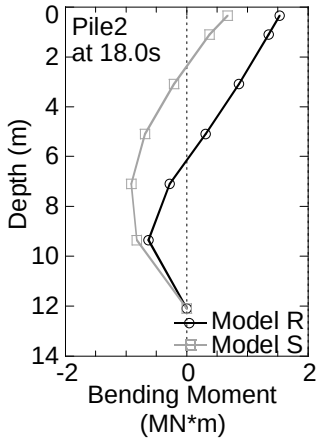


Figure 8. Distributions of bending moment along piles.

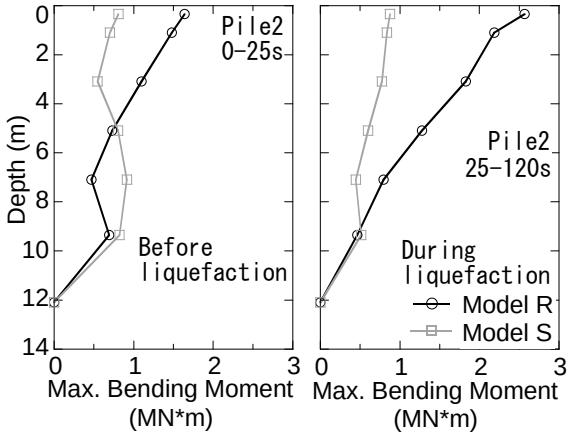


Figure 9. Distributions of maximum bending moment along piles.

### 3.4 *Natural periods of soil-pile-structure systems*

The ratios of Fourier spectrums of superstructure acceleration to shaking table acceleration at small excitation, in the period from 5.1 s to 18.0 s (early process of liquefaction), and in the period after 25.0 s (during liquefaction) are shown in Figure 10. To smooth the ratios, Hanning window with 0.14 s bandwidth was applied to the ratios except for the early process of liquefaction. At small excitation, the time (*T1*: natural period of the soil-pile-structure system) in which the ratio becomes a peak in Model S is 0.45 s, which is the same as that in Model R. In the early process of liquefaction, *T1* becomes longer than that at small excitation due to the reduction of effective stress of soil, but is the same in the two models.

However, during liquefaction, *T1* in Model R is 2.0 s but that in Model S is 2.7s. Thus, the natural period of the system in Model S becomes longer than in Model R. In the early process, the pile head bending moment in Model S becomes smaller than in Model R and reaches *Mu* (Fig. 6c). Accordingly, the effect of semi-rigid pile head connections on the behavior of the building becomes larger during liquefaction.

The Fourier spectrum ratio around *T1* in Model S is flatter than in Model R, which implies that the damping of the system is larger in Model S.

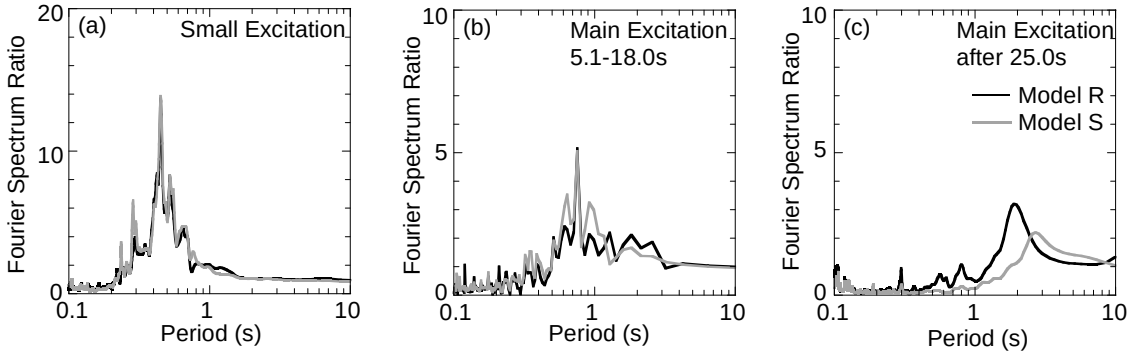


Figure 10. Fourier spectrum rations of superstructure acceleration to shaking table acceleration.

### 3.5 *Lateral resistance of soil-pile-foundation systems*

The relations between inertia force from the structure and displacement of the foundation in the period from 0.0 to 18.0 s (early process of liquefaction), in the period from 18.0 s to 25.0 s (later process of liquefaction), and after 25.0 s (during liquefaction) are shown in Figure 11. In the early process of liquefaction, the pile head bending moment in Model S reaches *Mu* (Fig. 6c), but the gradient (*Ks*) in the relation is almost the same or slightly larger than in Model R. In the later process of liquefaction, *Ks* decreases steadily with decreasing soil stiffness due to the reduction of effective stress, but *Ks* in both models is almost the same, even though in Model S the bending moment reaches *Mu* and the rotation angle at the pile heads increases (Figs. 6c, d). However, during liquefaction, *Ks* in Model S becomes smaller than in Model R according as the displacement of the foundation increases. These phenomena can be understood as follows. Before liquefaction, the subgrade reaction is large enough to resist the inertia force, whether semi-rigid pile head connections or not, and *Ks* in both models is almost the same. During liquefaction, the subgrade reaction is so small that the foundation can easily deform with semi-rigid pile heads rotating, and *Ks* in Model S becomes smaller. That is to say, the lateral resistance of the soil-pile-foundation system with semi-rigid pile head connections becomes smaller than that with rigid pile head connections only when the soil completely liquefies. And this causes the soil-pile-structure system to be long-period (Section 3.4).

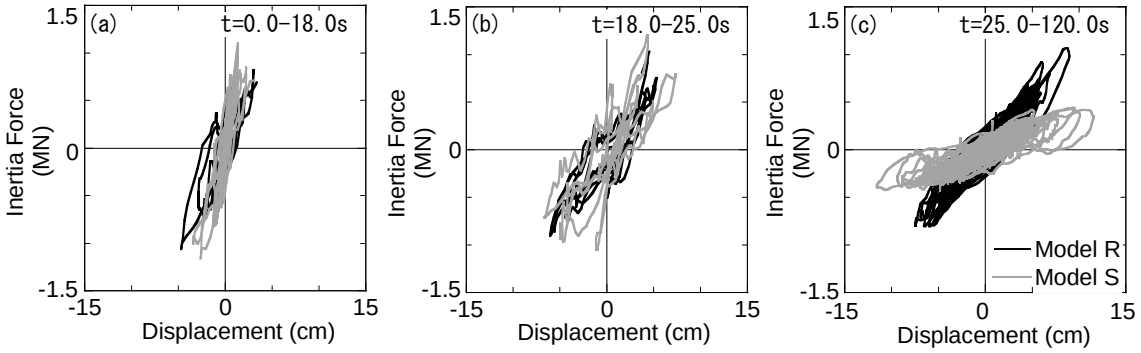


Figure 11. Relations between inertia force from structure and displacement of foundation.

### 3.6 *Hysteresis damping in soil-pile-foundation systems*

The relations between inertia force from the structure and displacement of the foundation in the period from 77 s to 81 s are shown in Figure 12. The force-displacement loop is spindle-shaped in Model R, but is parallelogram-shaped and tends to be swollen at large displacement in Model S. The hysteresis damping ratio in the loop is defined as the ratio of the energy absorbed in the loop over the elastic energy. The hysteresis damping in this loop is 13% in Model R and 27% in Model S. The hysteresis damping at semi-rigid pile head connections is very small because the relation between bending moment and rotation angle shows nonlinear-elastic behavior. The reason for the increase in hysteresis damping in Model S could be that the lateral resistance of the soil-pile-foundation system decreases with increasing displacement of the foundation. The hysteresis damping ratios were then calculated by each loop in the period from 60.0 s to 120.0 s during which the input motion mainly includes long-period waves. To remove the effect of short-period waves, a low-pass filter is applied to the inertia force and the displacement. Figure 13 shows the relations between hysteresis damping ratio and maximum displacement in each loop. The hysteresis damping in Model S increases with increasing displacement, while in Model R it is the same as in Model S at small displacement but smaller at large displacement. At large displacement, the lateral resistance of pile foundation with semi-rigid pile head connections is smaller than that with rigid pile head connections because the pile head bending moment with semi-rigid pile head connections reaches *Mu*, and then the absorbed energy generated by the dynamic interaction between the piles and the liquefied soil increases. Thus, the hysteresis damping in Model S increases at large displacement.

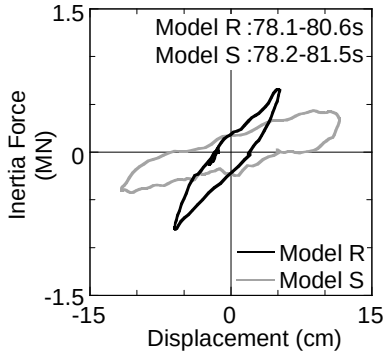


Figure 12. Relations between Inertia force from superstructure and foundation displacement.

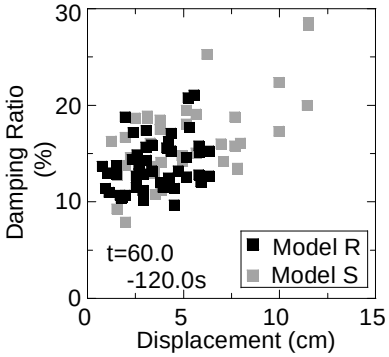


Figure 13. Relations between hysteresis damping and foundation displacement.

### 3.7 *Acceleration response spectrums and observed maximum acceleration of superstructure*

The acceleration response spectrums calculated using the accelerations at the shaking table after 25 s, with 15% damping in Model R and 30% damping in Model S based on Section 3.6, are shown in Figure 14. In this figure, the maximum accelerations of the superstructure are plotted at the respective periods of *T1*, which are the natural period of the soil-pile-structure system during liquefaction (Section 3.5). In both models, the observed accelerations are in accordance with the respective acceleration response spectrums. Therefore, the reason why the maximum acceleration of the superstructure in Model S decreases to 40% of that in Model R is that the natural period of the soil-pile-structure system becomes longer due to the reduction of lateral resistance of the soil-pile-foundation system, and that the hysteresis damping induced by the dynamic interaction between liquefied soil and piles becomes large at large displacement.

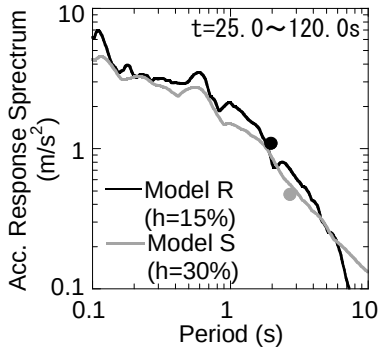

Figure 14. Acceleration response spectrums and observed maximum acclerations.

## 4 CONCLUSIONS

Dynamic centrifuge model tests were conducted to investigate the seismic behavior of buildings with semi-rigid pile head connections in liquefiable soil. The test results and analysis lead to the following conclusions:

1. Before liquefaction, the maximum bending moment along piles with semi-rigid pile head connections occurs in the soil, but is almost the same as that at the pile heads, and is about half of the maximum bending moment along piles with rigid pile head connections which occurs at the pile heads.

2. During liquefaction, the maximum bending moment along piles with rigid pile head connections is larger than that before liquefaction due to soil liquefaction. In contrast, in the case of semi-rigid pile head connections, the bending moment in the soil during liquefaction is lower than that in the soil before liquefaction. This is caused by the reduction of inertia force in the state in which the pile head bending moment reaches the maximum and the soil stiffness considerably decreases. And thus, the maximum bending moment along piles with semi-rigid pile head connections is about 40% of that with rigid pile head connections through the whole time of shaking.

3. The natural period of the soil-pile-structure system with semi-rigid pile head connections becomes longer than that of the system with rigid pile head connections during liquefaction. This is because the lateral resistance of the soil-pile-foundation system with semi-rigid pile head connections reduces during liquefaction.

4. In the case of semi-rigid pile head connections, during liquefaction, the hysteresis damping in the relation between inertia force from the structure and displacement of the foundation becomes large at large displacement. This is because the absorbed energy generated by the dynamic interaction between liquefied soil and piles with semi-rigid pile head connections increases at large displacement.

5. The acceleration of the superstructure with semi-rigid pile head connections is almost the same as that of the structure with rigid pile head connections before liquefaction. During liquefaction, on the contrary, the response of the superstructure with semi-rigid pile head connections tends to considerably decrease and be delayed compared with that of the structure with rigid pile head connections, for the reasons given in conclusions 3) and 4) above.

## REFERENCES

Hara, T. Yasuda, S. Kawabata, I. Komuro, T. Korenaga, T. Tatsuno, S. 2002. Development of Pile Head-Foundation Joint without Anchorage of Pile Rebar. Summaries of Technical Papers of Annual Meeting. AIJ. C-2. pp187-190 (in Japanese ).

Hiraide, T. Sugimura, Y. Ohsugi, F. 2004. Experimental Study on Mechanical Properties of Pile Head-joint for Prestressed High Strength Concrete Piles Using Unbonded Stud Bars. Journal of Structural and Construction Engineering. AIJ. No.581. pp71-78 (in Japanese ).

Ishizaki, S. Majima, M. Nagao, T. Funahara, H. Aoshima, K. 2006. Shaking Table Tests on Soil-Pile-Structure Models with Semi-Rigid Pile Head Connections. Journal of Structural and Construction Engineering. AIJ. No. 602. pp171-177 (in Japanese ).

Ohtsuki, A. Tazoh, T. Aoki, T. Mano, H. Isoda, K. Iwamoto, T. Arakawa, N. Ishihara, T. Ohkawa, M. 2001. A Pile-head Device with Spherical Contact-Surface for Decreasing the Bending Moment. Summaries of Technical Papers of Annual Meeting. AIJ. B-2. pp451-454 (in Japanese ).

# Effects of inertial and kinematic interaction on vibration of an apartment building based on earthquake observation records

M. Iiba
*Building Research Institute, Tsukuba, Japan*

K. Watanabe
*Urban Renaissance Agency, Yokohama, Japan*

ABSTRACT: In order to investigate effects of SSI on a response of building, the earthquake motions are analyzed which were recorded at the residential building. The building is a steel reinforced concrete structure with 11 stories with cast-in place piles of 22m in length. Accelerometers are installed in the building, at the pile, at several levels in the ground near and far from the building. The earthquake motions recorded at the building are analyzed. The results such as maximum acceleration, amplification of surface ground and characteristics of building including surface ground, kinematic and inertial interactions, are discussed.

## 1 INTRODUCTION

It is very important to evaluate a seismic action to structures during earthquake. The seismic action is dependent on characteristics of an incident wave at engineering bedrocks, surface soil amplification, an interaction between structure and soil, and a structure itself, etc. To incorporate the interaction effects in the seismic design, parametric study is necessary to clarify the effects of various factors on the response to the structures. Focused on the dynamic interaction, effects of combinations of soil and structural properties on the seismic response of the structure need to be discussed.

To propose a design methodology for pile foundations, many numerical and experimental researches have been carried out. Recently effects of soil deformation are incorporated in addition to inertial forces of superstructures. The effects of soil deformation to the piles are investigated in the experiments and analyses (Mizuno et al. 1988 and Sugimura et al. 1997). An evaluation way of seismic forces to pile foundations is proposed (Murono & Nishimura. 2000).

In the paper, to evaluate a seismic performance of buildings, effects of characteristics of surface ground, soil structure interaction (SSI) and building itself on building response should be examined. The SSI phenomena based on earthquake motion observation will be made clear. The earthquake motions are analyzed which were recorded at the residential building of 11-story steel reinforced concrete structure in Tokyo (BRI 1973 and BRI 1974). A soil deposit under the building is soft and the building has cast-in place piles of 22m in length. Accelerometers are installed in the building, at the pile, at several levels in the ground near and far from the building. The earthquake motions recorded at the building are analyzed, based on transfer functions (Fourier spectral ratios) between building and ground, etc. Following items are summarized.

a) Maximum acceleration distribution
b) Amplification of surface ground
c) Characteristics of building including surface ground, kinematic and inertial interactions

## 2 OUTLINE OF BUILDING AND SURFACE GROUND

### 2.1 *Outline of building*

The building is a residential apartment constructed in Tokyo. The building has the steel reinforced concrete structure with 11 stories and 2-story penthouse. Figure 1 shows a setting of buildings in the site and Photograph 1 presents the overall of the building. The building is the D-building which are connected to the C-building with an expansion joint (BRI 1973).

Figure 2 shows plan, elevation and fundamental dimensions (BRI 1973 and BRI 1974). The height of building is 30.95m and the dimensions of plan are 78m (15spans) and 8.35m (1 span). The direction of the short span (a transverse direction) is called a X (NS) direction, and the direction of the multi spans (a longitudinal direction) is called a Y (EW) direction. Piles are cast-in place ones and consist of $16\times1500\phi$、$16\times1200\phi$、$2\times900\phi$ with a length of 22m (the pile tips will be at the depth of 25m). And a embedment depth of foundation girders will be 2.45m.

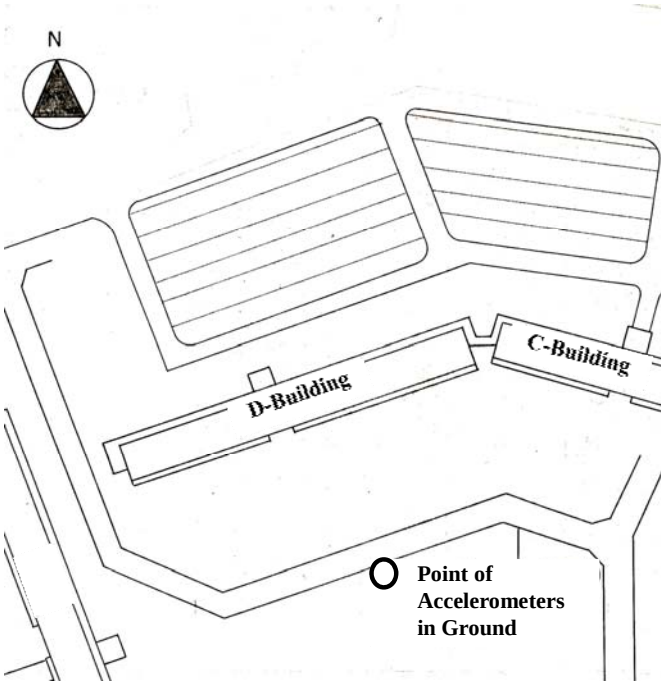


Figure 1. Building setting.

Photograph. 1. Overall of building.

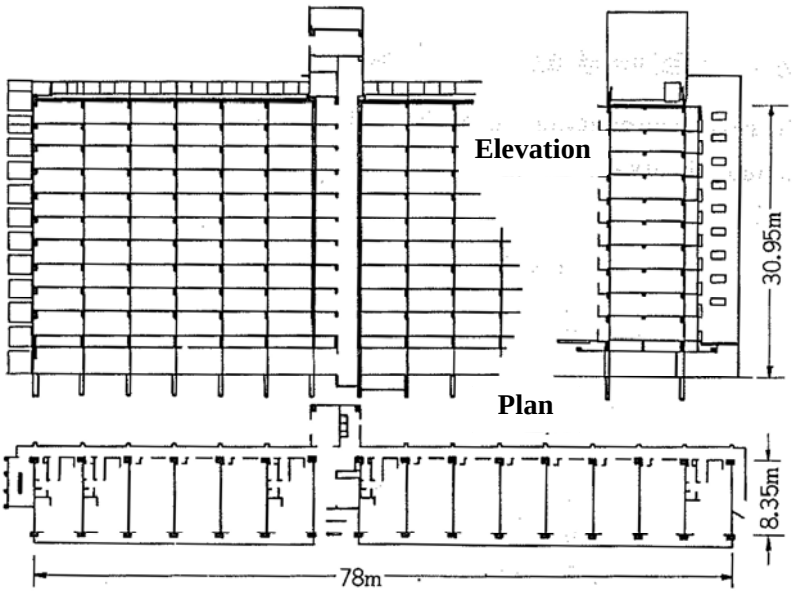


Figure 2. Plan and elevation.

## 2.2 *Characteristics of surface ground*

The soil condition for type, N-value and Shear wave velocity are summarized in Figure 3 (BRI 1974). The upper most layers to 1.7m (N-value is 11) is the surface soil. Until the depth to 17.9m, there is a soft silt ground with N-value of 0 to 1.Below the deposit, the clay layer leis. Below the depth of 31.4m, there is an engineering bed rock called the Tokyo gravel deposit. The pile tips are set on the gravel deposit. According to the distribution of S-wave velocity (Vs), until the layer of 17.9m, the Vs is about 100m/s. At the gravel deposit, the Vs is about 500m/s.

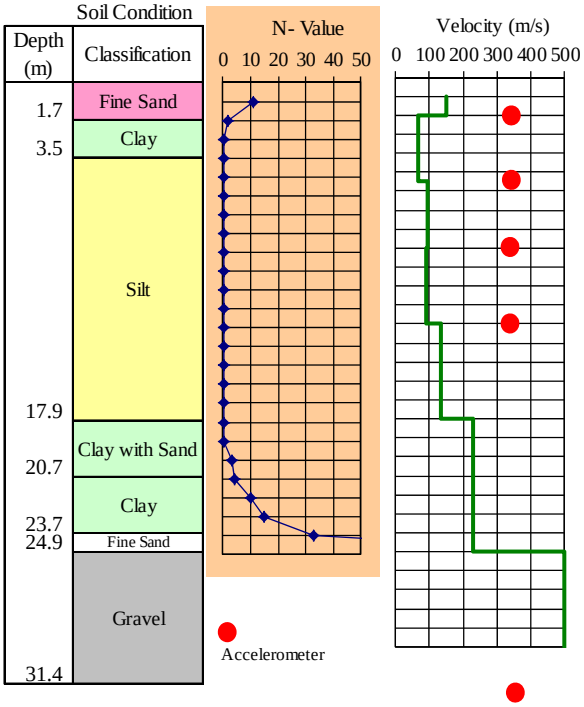


Figure 3. Soil condition.

## 3 EARTHQUAKE MOTION OBSERVATION AND RECORDS

### 3.1 *Installation of accelerometer*

An arrangement of the accelerometers in each direction of building is drawn in Figure 4 ((BRI 1974 and Ohta 1978). The accelerometers are installed in the center of the building. The three lines in a point means to measure accelerations of three components (X, Y and Z). The horizontal, diagonal and vertical lines mean the accelerometer in the X, Y and Z directions, respectively. A mark is set at each accelerometer; B, P, BS and S are the accelerometers in the building, at the piles, in the ground near and far from the building. Also PH, 1F and 1.7M mean the accelerometers at the penthouse, on 1st floor and at the depth in the ground.

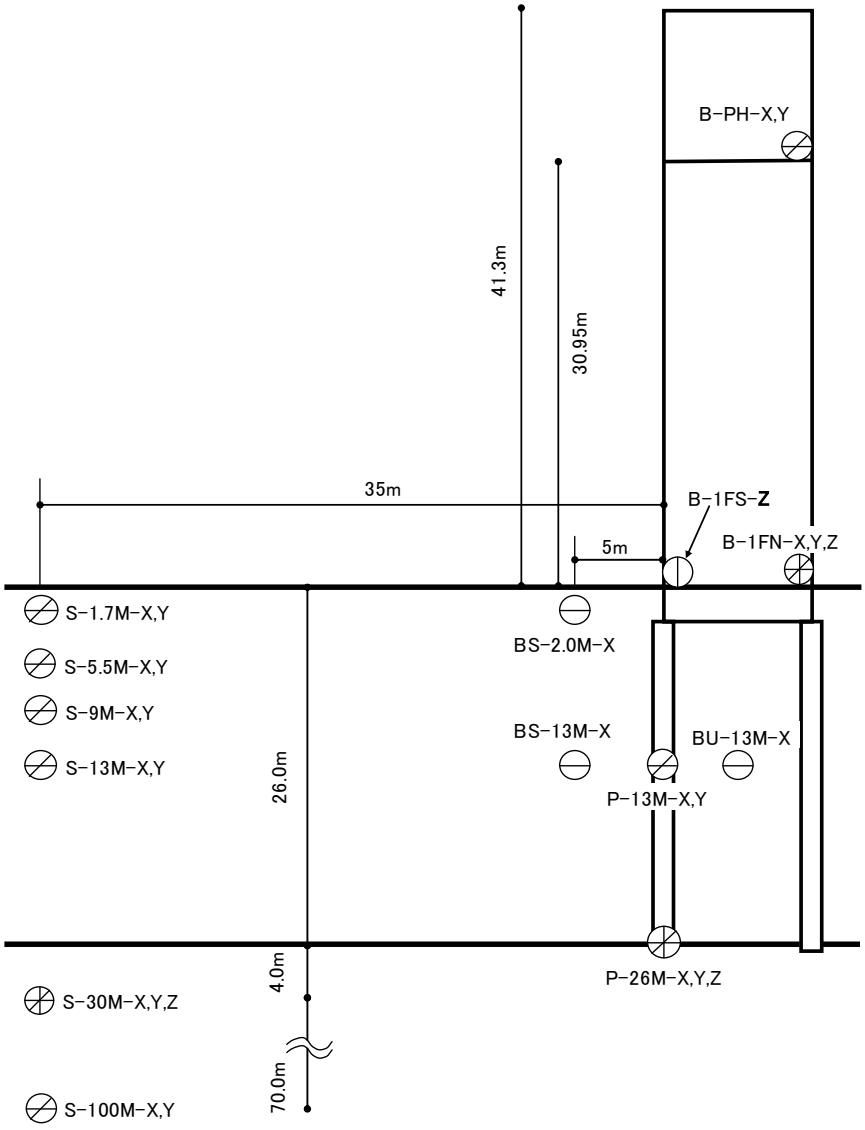


Figure 4. Arrangement of accelerometers.

### 3.2 *Situation of recorded data*

The earthquake motion observation had been continued since 1975. By aging, some of accelerometers have been down year by year. The effective observation data are summarized in Table 1. The data recorded in the period of 1975.12 to 1980.9 are very useful, as all and almost channels of acceleration were recorded. The information of earthquakes are summarized in Table 2. The data in the period of 1988.5 to 1991.1 are used for calculation of maximum acceleration.

Table 1. Effective acceleration data in observation periods (* means effective data).

| Period of Observation | | | 1975.12-1980.9 | 1988.5-1991.1 |
|---|---|---|---|---|
| No. of EQ motions | | | 8 | 108 |
| Soil Ground | S-1.7m | X | * | * |
| | | Y | * | * |
| | S-5.5m | X | * | |
| | | Y | * | |
| | S-9.0m | X | * | * |
| | | Y | * | |
| | S-13m | X | * | |
| | | Y | * | |
| | S-30m | X | * | |
| | | Y | * | * |
| | | Z | * | * |
| | S-100m | X | * | * |
| | | Y | * | * |
| Pile or | BS-2.0m | X | * | * |
| Near Building | BS-13m | X | * | * |
| | BU-13m | X | * | * |
| | P-13m | X | * | * |
| | | Y | * | * |
| | P-26m | X | * | * |
| | | Y | * | * |
| | | Z | * | * |
| Building | B-PH | X | * | |
| | | Y | * | * |
| | B1FN | X | * | * |
| | | Y | * | * |
| | | Z | * | * |
| | B1FS | Z | * | * |

Table 2. Information of eight earthquakes from 1975.12 to 1980.9).

| EQ No. | | EQ Name | Maximum. Seismic |
|---|---|---|---|
| Date | Time (Epicenter) | | Intensity OF JMA |
| 1975/12/15 | 09:45 | Central Chiba | 3 |
| 1976/05/13 | 20:00 | East of Tokyo | 3 |
| 1976/06/06 | 23:01 | East of Saitama | 4 |
| 1976/06/16 | 07:36 | East of Yamanashi | 4 |
| 1978/01/14 | 12:24 | Near Izu-Ohshima Island | 4 |
| 1978/02/20 | 13:36 | Off Miyagi Pref. | - |
| 1978/06/12 | 17:14 | Off Miyagi Pref. | 4 |
| 1980/09/25 | 02:54 | South-west of Chiba | 4 |

### 3.3 *Example of recorded acceleration data*

An example of acceleration time histories observed in 1976/June/16 is drawn at each observation arrays (Building-foundation-pile and ground arrays) in Figure 5.

### 3.4 *Maximum Acceleration of Building and Ground*

Figure 6a) presents maximum acceleration for superstructure, pile and ground and the amplification of maximum acceleration to the pile tip, based on the data observed in 1976/June/16. The amplitude of maximum acceleration on the surface ground and 1$^{st}$ floor to the pile tip is 3 to 5, and that on the top of building is 4 to 10. The maximum accelerations in the ground far from the building are larger, and those in the ground near the building and those at the pile are similar.

Almost all of the amplification of maximum acceleration to the pile tip are drawn in Figure 7. In the X-direction, the amplitudes at 1$^{st}$ floor and building top are 1 to 6, 4 to 13, respectively. The averages are 3.1 and 8.0, respectively. In the Y-direction, the amplitudes at 1$^{st}$ floor and

building top are 1 to 4, 3 to 12, respectively. The averages are 2.4 and 6.8, respectively. The average amplitude in X direction is a little larger than that in Y direction.

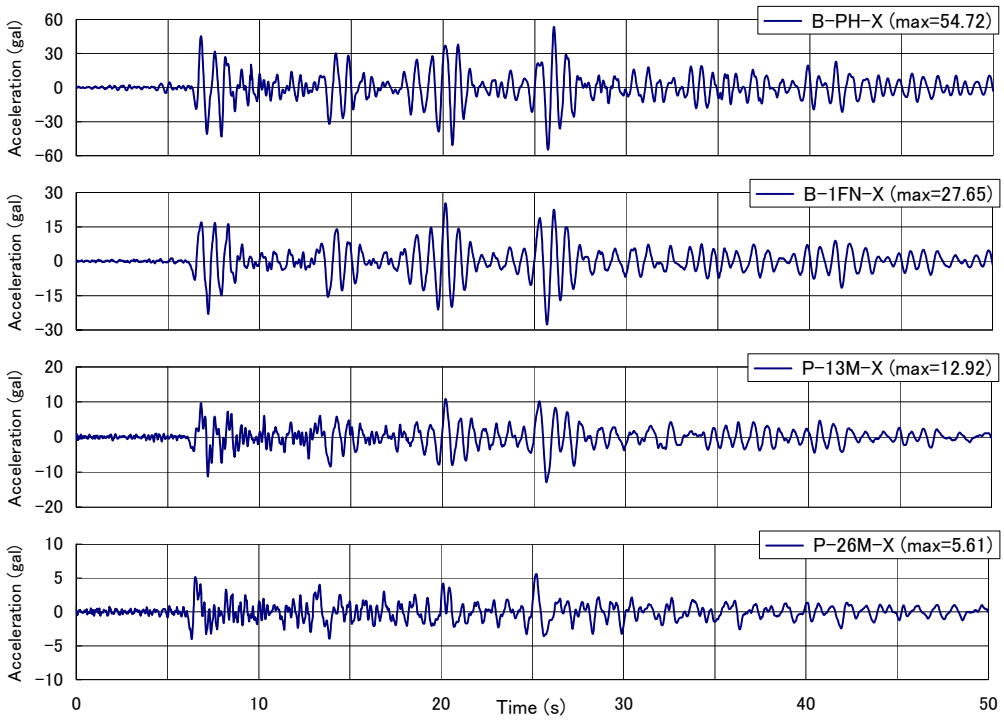


Figure 5a). Acceleration time history (building-foundation-pile array, X-direction).

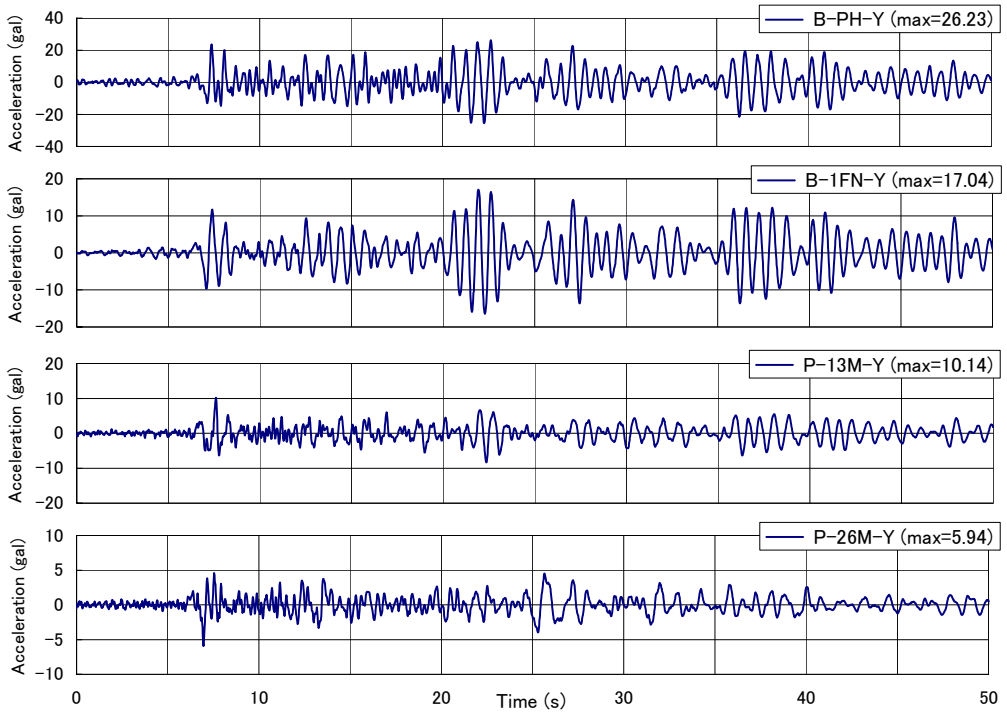


Figure 5b). Acceleration time history (building-foundation-pile array, Y-direction).

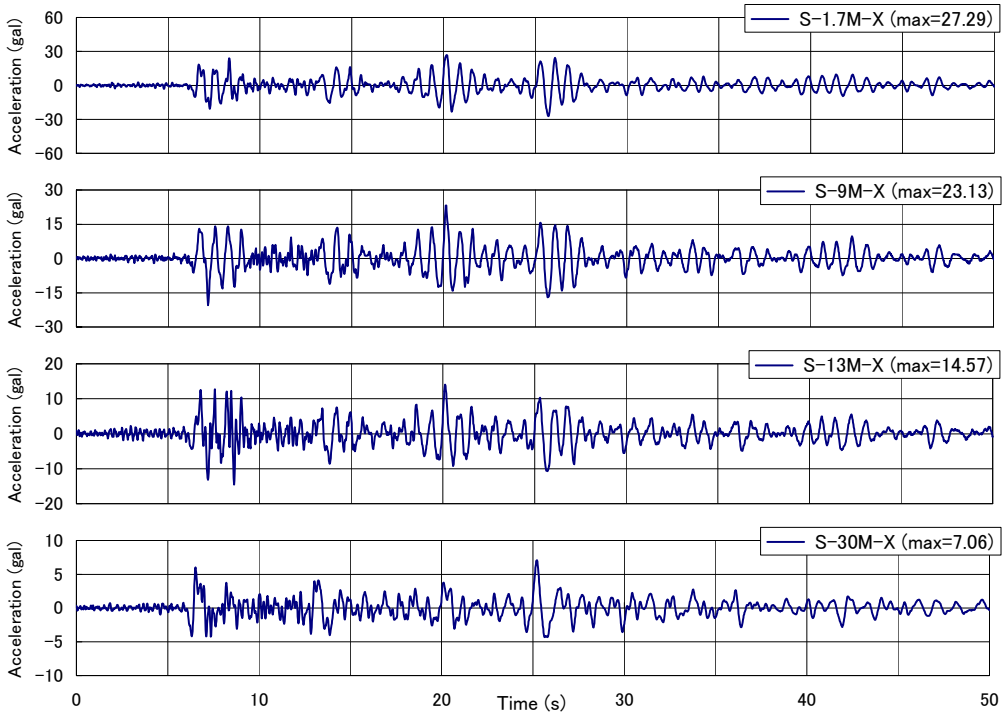


Figure 5c). Acceleration time history (ground array, X-direction).

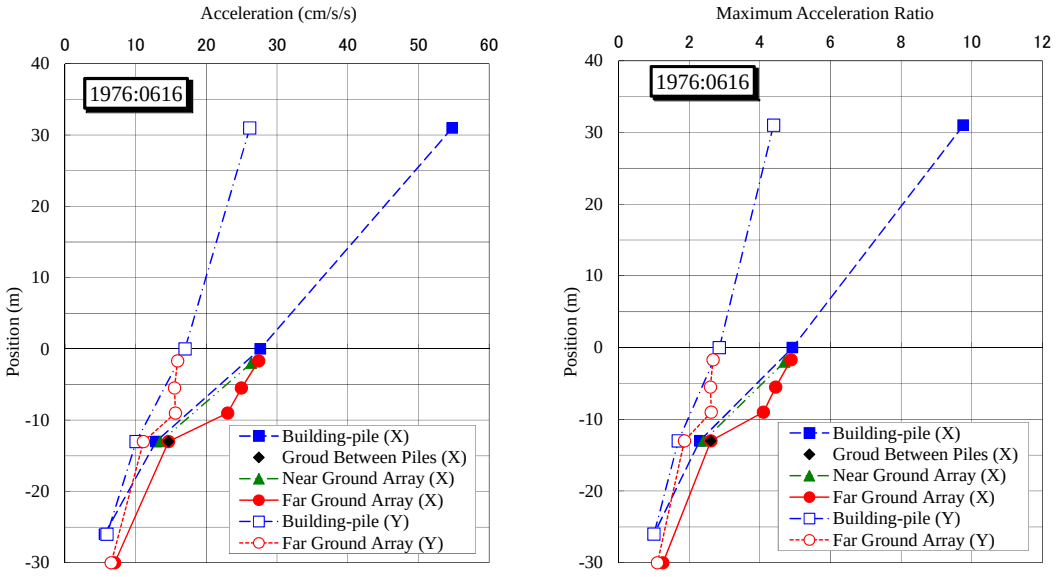


a) Maximum acceleration b) Amplification of maximum acceleration

Figure 6. Maximum acceleration distribution based on data observed in 1976/June/16.

Figure 8 shows the amplitude of maximum acceleration to the pile tip at the depth of 13m and 1.7m in the ground. There are different situation; the ground far from the building, near the building, between piles and pile. The amplitudes at the depth of 13m and 1.7m are 1 to 3 and 1 to 7, respectively. The amplitudes at the same depth are smaller with far ground, near ground, between pile and 1st floor (or pile). The maximum accelerations are smaller with smaller distance to building.

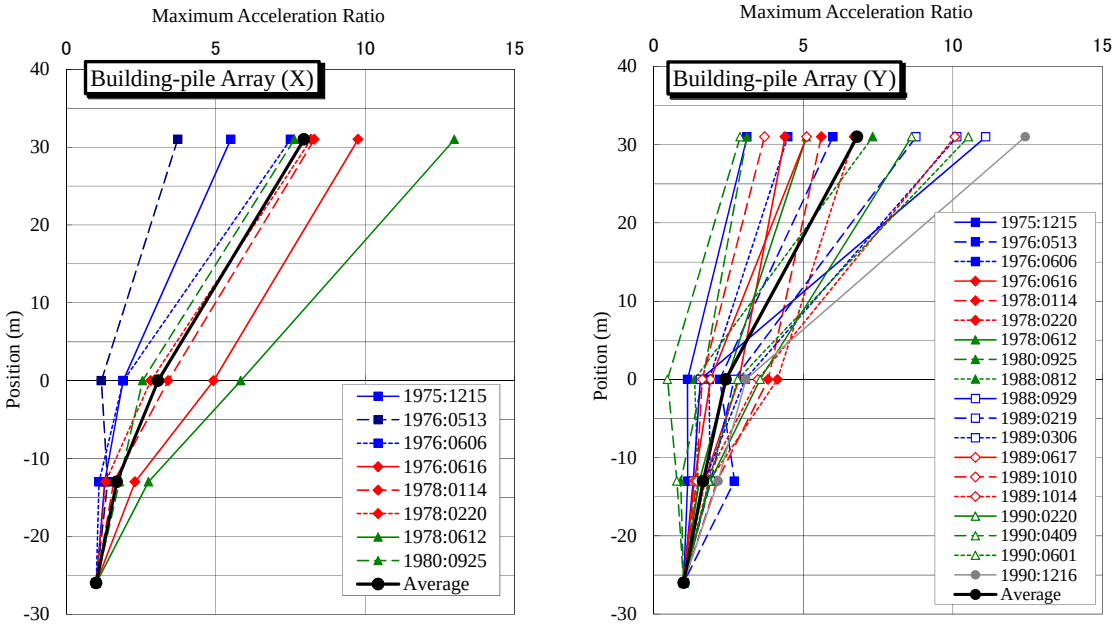


a) X direction b) Y direction

Figure 7. Amplification distribution of maximum acceleration based on almost all observed data.

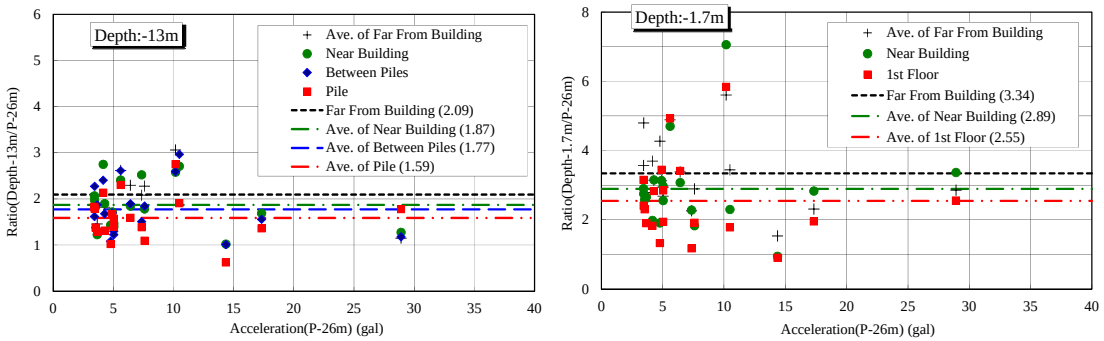


a) Ratio at depth of 13m b) Ratio at depth of 1.7m

Figure 8. Amplitude of maximum acceleration to pile tip.

## 4 EARTHQUAKE MOTION AT GROUND SURFACE AND AMPLIFICATION OF SOIL DEPOSIT

### 4.1 *Earthquake motion at ground surface*

Pseud velocity response spectra (damping factor 5%) of observed accelerations at the engineering bedrock in three directions are drawn in Figure 9. In the figure, the velocity response spectrum of horizontal earthquake motion for medium earthquake motion at outcropped engineering bedrock which is provided by the Building Standard Law in Japan is also drawn. The velocity levels of all earthquake motions are less than that of provided one. The earthquake motion observed in 1978/June/12 has large velocity response in period of 1-2 seconds. The earthquake motion observed in 1978/January/14 has large velocity response in long period region.

Pseud velocity response spectra (damping factor 5%) of observed accelerations at the ground surface in horizontal directions are drawn in Figure 10. In the figure, the velocity response spectrum of horizontal earthquake motions for medium earthquake motion at ground surface which is provided by the Building Standard Law in Japan is also drawn. The velocity level of the earthquake motion observed in 1978/June/12 has a similar velocity response in period of 0.6-0.8 seconds.

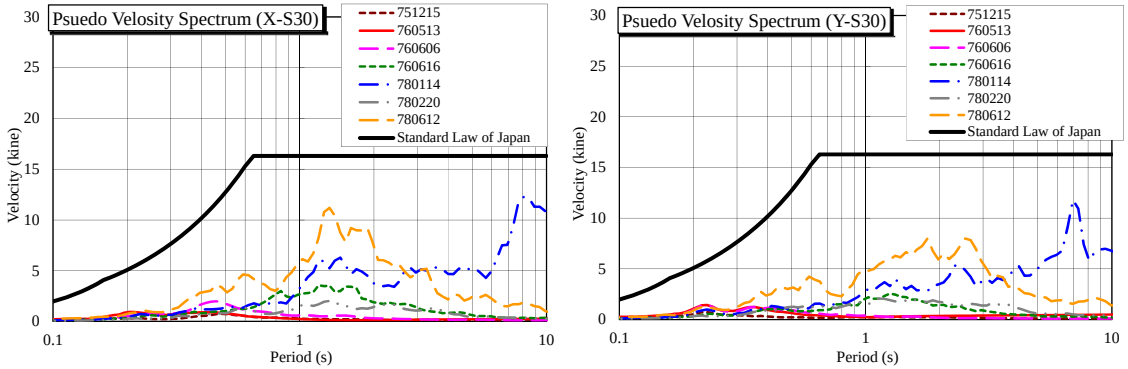


a) X direction b) Y direction

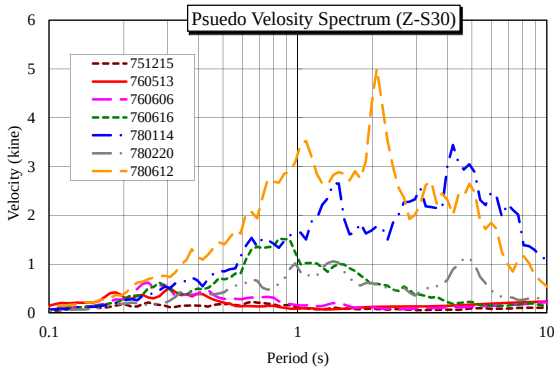


c) Z direction

Figure 9. Pseud velocity response spectra of observed accelerations at engineering bedrock (damping factor 5%).

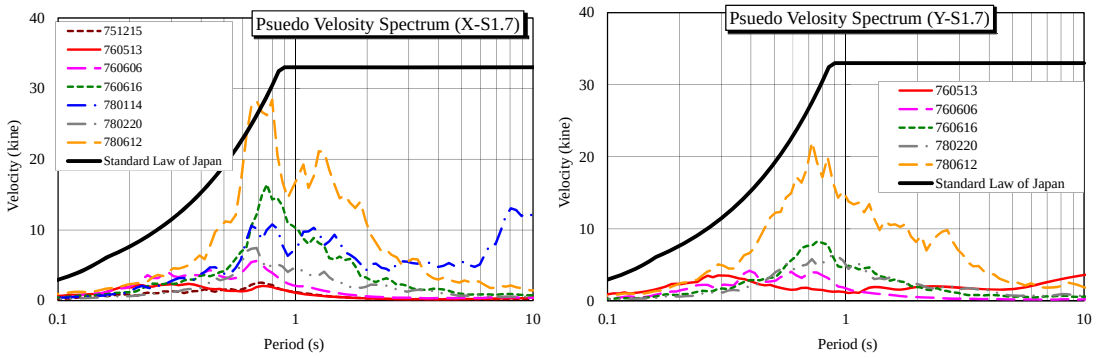


a) X direction b) Y direction

Figure 10. Pseud velocity response spectra of observed accelerations at ground surface (damping factor 5%).

## 4.2 *Amplification of surface ground*

Ratios of Fourier spectra of ground surface to engineering bedrock in X and Y directions are shown in Figures 11 and 12, respectively. The average of spectral ratios are also drawn in a) of both figures. And in figures b) the amplification factor of surface ground using one dimensional wave propagation theory is drawn. In the calculation, the damping of the ground is assumed to be hysteretic one with 4% damping factor. The spectral ratios have clear amplified peaks up to the first three modes. The predominant frequencies by one dimensional wave propagation theory have a good agreement on those of observed spectral ratios in the frequency range less than 4 Hz.

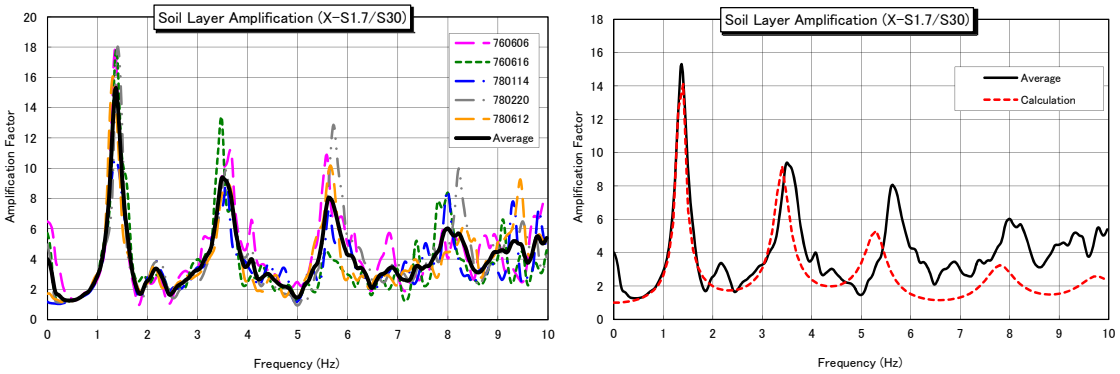


a) Observed spectral ratios and average ones b) Comparison of data for observation and theory

Figure 11. Ratios of Fourier spectra of ground surface to engineering bedrock (X direction).

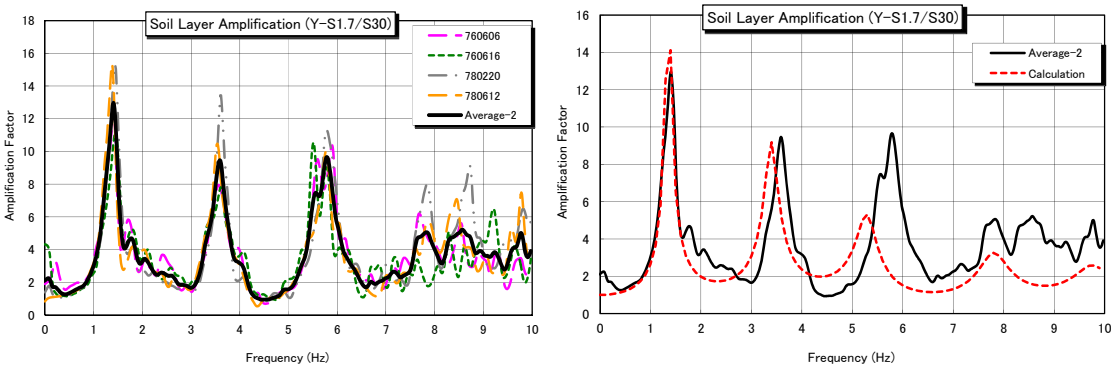


a) Observed spectral ratios and average ones b) Comparison of data for observation and theory

Figure 12. Ratios of Fourier spectra of ground surface to engineering bedrock (Y direction).

## 5 CHARACTERISTIC OF BUILDING WITH SOIL STRUCTURE INTERACTION (SSI)

### 5.1 *Amplification of building to engineering bedrock or pile tip (Characteristics including surface ground, kinematic and inertial interactions)*

Fourier spectral ratios of the acceleration at building top to that at engineering bedrock in soil ground are drawn in Figure 13. In the X (transverse) direction, the fundamental resonant frequency of the building-foundation-ground system is 1.3 to 1.4 Hz, and the amplitude at fundamental resonant frequency is 25 to 40. The second resonant frequency of the system is about 2.2 Hz and the amplitude at frequency of 3.5 to 4.0 Hz is larger. The fundamental resonant frequency is corresponding to the resonant frequency of surface ground as shown in Figure 11. Since the frequency of 2.2 Hz is not the resonant frequency of surface ground, it is related to the characteristics of building or SSI system. The frequency of 3.5 Hz is corresponding to the second resonant frequency of surface ground. On the other hand, in the Y (Longitudinal) direction, the fundamental resonant frequency of the building-foundation-ground system is 1.3 to 1.4 Hz, and the amplitude at fundamental resonant frequency is about 20. The second resonant frequency of the system is about 3.6 Hz. These frequencies are corresponding to the first and second resonant frequencies of surface ground. In both directions, the characteristics of building-foundation-ground system are affected by those of surface ground. The effect of Inertial interaction is not so remarkable.

Fourier spectral ratios of the acceleration at building top to that at pile tip in soil ground are drawn in Figure 14. The Fourier spectra of building top to pile tip is similar to that of building to engineering bedrock as shown in Figure 13. In detail, The peak frequencies of the building top to pile tip is larger by 0.1 to 0.2 Hz than that of the building top to engineering bedrock. Also the Fourier spectral ratios are a little different in frequencies more than 3 Hz.

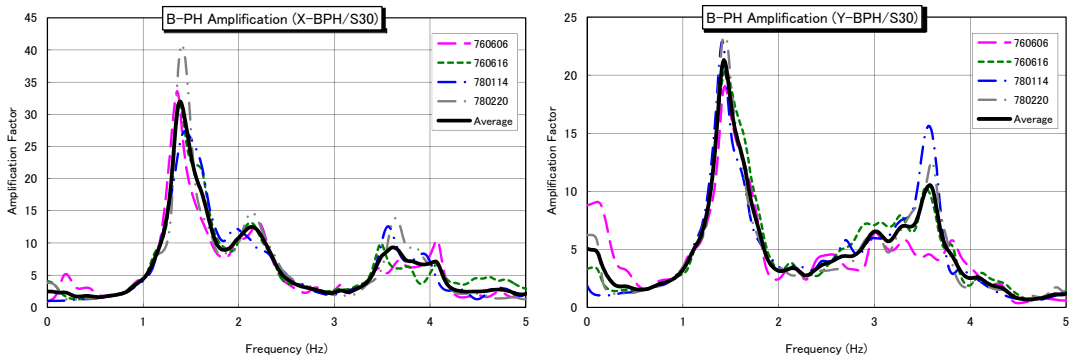


a) X direction b) Y direction

Figure 13. Fourier spectral ratio of building top to engineering bedrock in soil ground.

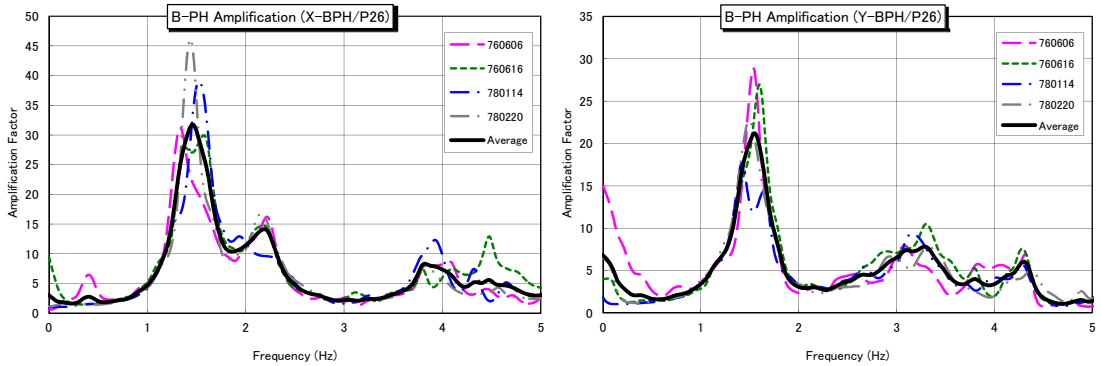


a) X direction b) Y direction

Figure 14. Fourier spectral ratio of building top to pile tip in soil ground.

## 5.2 *Amplification of 1st floor to ground surface (Characteristics of kinematic interaction)*

Fourier spectral ratios of the acceleration at 1st floor to that at surface ground far from and near the building in the X direction are drawn in Figure 15. Those at 1st floor to that at surface ground far from the building in the Y direction are drawn in Figure 16.

The peak of Fourier spectral ratios of the acceleration at 1st floor to that at surface ground far from the building is 1.6 to 2.0 Hz. The ratios are more than 1.0 in the frequencies less than 2.0 Hz and less than 1.0 in the frequencies larger than 2.0 Hz. The frequencies of 1.6 to 2.0 Hz seem to be the predominant frequency of the building with inertial interaction.

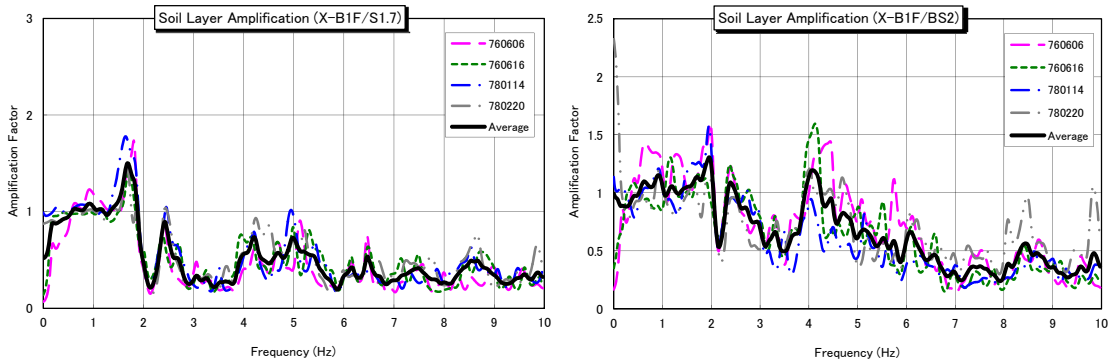


a) Surface ground far from building b) Surface ground near building

Figure 15. Fourier spectral ratio of 1st floor to surface ground in X direction.

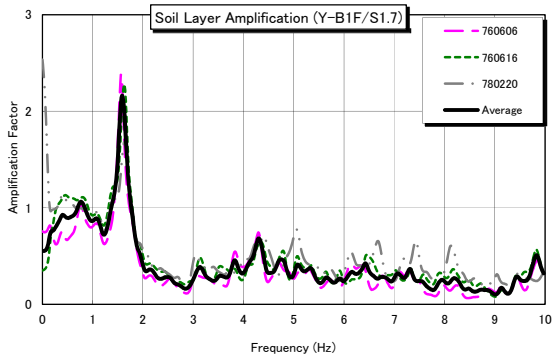


Figure 16. Fourier spectral ratio of 1st floor to surface ground far from building in Y direction.

### 5.3 *Amplification of building top to ground surface or 1st floor (Characteristics of inertial interaction)*

Following systems (Transfer functions) are defined (Stewart & Fenves 1998) ;

a) System of sway, rocking and building (SRB ; $u_t/u_g$) : Characteristics of building including kinematic interaction and inertial interaction of sway and rocking

b) System of rocking and building (RB ; $u_t/(u_g + u_f)$) : Characteristics of building including inertial interaction of rocking

c) System of building itself (B ; $u_t/(u_g + u_f + u_r)$) : Characteristics of building with base fixed condition

Where $u_t$ is the response of building top including a response of sway($u_f$) with kinematic interaction, rocking($u_r$) and building ($u_b$). $u_r$ is the horizontal displacement at building top, which is the product of rocking angle ($\theta$) at the 1st floor and equivalent height of the system ($H$) which is assumed to be the same height as total height of building in the paper.

Fourier spectral ratios of the acceleration at building top to that at ground surface are drawn in Figure 17. In the X (transverse) direction, the fundamental resonant frequency of the SRB system is about 1.8 Hz, and the amplitude at fundamental resonant frequency is 4 to 8. In the Y (longitudinal) direction, the fundamental resonant frequency of the SRB system is about 1.6 Hz, and the second resonant frequency of the SRB system is about 3.0 Hz.

Fourier spectral ratios of the acceleration at building top to that at 1st Floor are drawn in Figure 18. In the X direction, the fundamental resonant frequency of the RB system is about 2.1 Hz, and the amplitude at fundamental resonant frequency is 13 to 31. In the Y direction, the fundamental resonant frequency of the RB system is 2.7 to 3.0 Hz, and the amplitude at fundamental resonant frequency is 12 to 25.

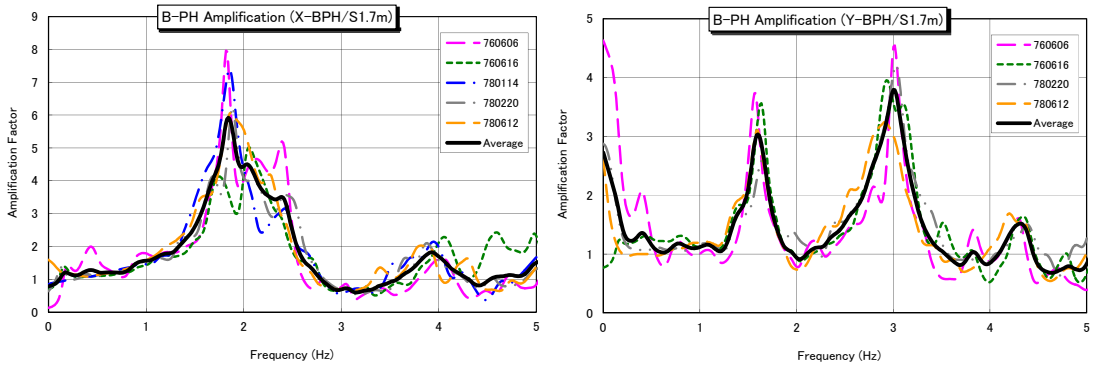


a) X direction b) Y direction

Figure 17. Fourier spectral ratio of building top to ground surface.

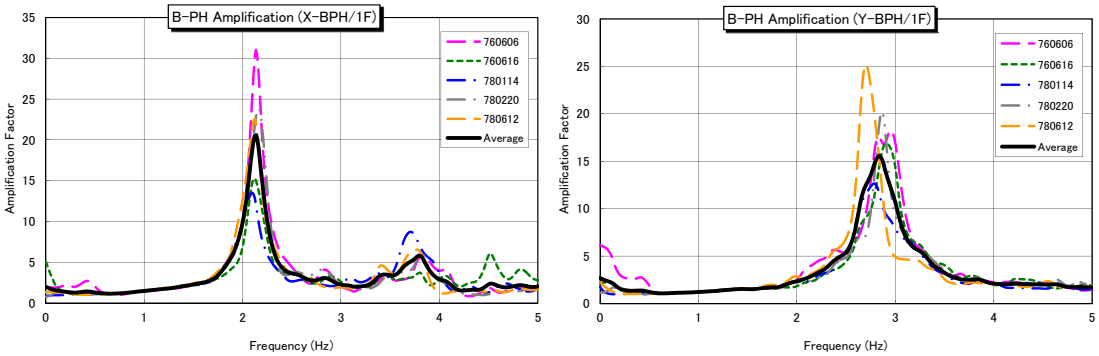


a) X direction b) Y direction

Figure 18. Fourier spectral ratio of building top to 1st floor.

## 6 CONCLUDING REMARKS

In order to investigate effects of SSI on the response of building, earthquake motions recorded at the residential building are analyzed. The results are summarized in the following;

1) Maximum acceleration distribution: In the X direction, the averages of amplitude at 1st floor and building top are 3.1 and 8.0, respectively. In the Y-direction, the averages of amplitude at 1st floor and building top are 2.4 and 6.8, respectively. The average amplitude in X direction is a little larger than that in Y direction.

2) Earthquake motion at ground surface: The velocity level of the earthquake motion observed in 1978/June/12 is similar to that in period of 0.6-0.8 seconds, for medium earthquake motion at ground surface which is provided by the Building Standard Law in Japan.

3) Amplification of surface ground: The amplification factor of surface ground using one dimensional wave propagation theory with the hysteretic damping factor of 4% has a good agreement on those of observed spectral ratios up to first two modes.

4) Characteristics including surface ground, kinematic and inertial interactions: Based on the Fourier spectral ratios of the acceleration at building top to that at engineering bedrock in the X direction, the fundamental resonant frequency of the building-foundation-ground system is 1.3 to 1.4 Hz, and the second resonant frequency of the system is about 2.2 Hz. The fundamental resonant frequency is corresponding to the resonant frequency of surface ground. On the other hand, in the Y direction, the fundamental resonant frequency of the system is 1.3 to 1.4 Hz, and the second resonant frequency of the system is about 3.6 Hz.

5) Characteristics of kinematic Interaction: The peak of Fourier spectral ratios of the acceleration at 1st floor to that at surface ground far from the building is 1.6 to 2.0 Hz. The ratios are more than 1.0 in the frequencies less than 2.0 Hz and less than 1.0 in the frequencies larger than 2.0 Hz. The frequencies of 1.6 to 2.0 Hz seem to be the predominant frequency of the building with inertial interaction.

6) Characteristics of inertial interaction: The fundamental resonant frequency, based on the Fourier spectral ratios of the acceleration at building top to that at ground surface in the X direction, is about 1.8 Hz. In the Y direction, the fundamental resonant frequency is about 1.6 Hz, and the second resonant frequency is about 3.0 Hz. The fundamental resonant frequency, based on the Fourier spectral ratios of the acceleration at building top to that at 1st Floor in the X direction, is about 2.1 Hz. In the Y direction, the fundamental resonant frequency is 2.7 to 3.0 Hz.

## 7 ACKNOWLEDGEMENT

Authors express their sincere thanks to Dr. Masanori Niwa, Kyowa Exeo corporation and Dr. Naohito Adachi, Kajima Corporation for providing the earthquake observation data and preparing the explanation of the data.

## 8 REFERENCES


Building Research Institute 1973. Earthquake motion observation in structure and surrounding soil deposit (Part 1), Report of project on comprehensive technical development (in Japanese)

Building Research Institute 1974. Earthquake motion observation in structure and surrounding soil deposit (Part 2), Report of project on comprehensive technical development (in Japanese)

Mizuno H., M. Iiba & S. K. Londono 1988. Scale model tests on inertial interaction and kinematic interaction of pile-supported buildings, Proceedings of 9th World Conference on Earthquake Engineering, Vol. III, pp. 569-574

Murono, Y. & A. Nishimura 2000. Evaluation of seismic force of pile foundation induced by inertial and kinematic interaction, Proceedings of 12th World Conference on Earthquake Engineering. Report No. 1496

Ohta T., M. Niwa & K. Ueno 1978. Seismic response characteristics of structure with pile foundation on soft subsoil layer, Proceedings of 5th Japan Earthquake Engineering Symposium, pp.561-568 (in Japanese)

Stewart J.P. & G. L. Fenves 1998. System identification for evaluating soil-structure interaction effects in buildings from strong motion recordings, Journal of Earthquake Engineering & Structural Dynamics, 27, pp.869-885

Sugimura Y., K. Fujiwara, T. Ohgi & M. B. Karkee 1997. Seismic behavior of piles supporting tall buildings and the consideration of ground response effects in design, Proceedings. of 4th Conference on Tall Buildings in Seismic Regions, Tall Buildings for the 21st Century, pp. 303-317

# Cyclic Pushover and Shake Table Testing of Bridge Pier with Foundation Uplifting and Soil Yielding

I. Anastasopoulos, M. Loli, V. Drosos, G. Gazetas

*Soil Mechanics Laboratory, National Technical University, Athens, Greece*

ABSTRACT: Recent studies have highlighted the beneficial role of foundation uplifting and the potential effectiveness of guiding the "plastic hinge" into the foundation soil by allowing full mobilization of bearing capacity during strong seismic shaking. With the inertia loading transmitted onto the superstructure being limited by the capacity of the foundation, such concept may provide an alternative method of "in-ground" seismic isolation: the so called rocking isolation. Attempting to unravel the effectiveness of such alternative design method, this paper investigates experimentally the nonlinear response of a surface foundation on sand and its effect on the seismic performance of an idealized slender 1-dof structure. Using a bridge pier as an illustrative prototype, three foundation design alternatives are considered, representing three levels of design conservatism. Their performance is investigated through static (monotonic and slow-cyclic "pushover") loading, and reduced-scale shaking table testing. It is shown that rocking isolation may constitute a valid alternative for the seismic protection of structures, providing encouraging evidence in favor of the innovative idea of moving foundation design towards a less conservative, even unconventional, treatment.

## 1 INTRODUCTION

Seismic design of structures recognizes that highly inelastic material response is unavoidable under strong seismic shaking (design earthquake motion). Ductility levels of the order of 3 or more are usually allowed to develop at bearing structural elements and “plastic hinging” is directed appropriately so as the overall stability is maintained (capacity design). By contrast, as reflected in the respective seismic codes, current seismic design practice demands a very conservative treatment of the foundation. Hence, increased safety factors and overstrength design ratios are adopted, lest "failure" be transferred below the ground level. However, this conservative treatment of the foundation, which is designed to retain "elastic" behavior even for extreme loading, conflicts modern research findings indicating that nonlinear foundation response : (i) may be highly probable even for seismic events of moderate intensity, (ii) may be favorable for the overall system performance, and (iii) may result in permanent deformations which could be restrained within acceptable limits thanks to the transient nature of seismic loading.

In the case of shallow foundations, nonlinearity manifests itself through alternating uplifting of the foundation (geometric nonlinearity), sliding at the soil–foundation interface (interface inelasticity), and/or mobilization of bearing capacity failure mechanisms in the supporting soil (soil inelasticity). When slender structures are considered, rocking motion prevails and the geometric component of nonlinearity dominates.

Earlier studies on rocking structures [Housner, 1963; Meek, 1975; Psycharis & Jennings, 1983; Chopra & Yim, 1985] have indicated the beneficial role of foundation uplifting on the performance of the supported structure, particularly during severe seismic shaking. Furthermore, allowing for foundation rocking has been proposed by several researchers as an effective

method of seismic isolation [e.g. Beck & Skinner, 1974; Huckelbridge & Ferencz, 1981; Priestley et al., 1996; Mergos & Kawashima, 2005; Chen et al., 2006; Sakellaraki & Kawashima, 2007] and has been applied in the design of modern bridges (e.g. the Rion Antirion Bridge : Pecker, 2005). However, in the last decade the research community has ventured one significant step further acknowledging that in a way similar to pure uplifting, concurrent inelastic soil response may also help to protect the superstructure against increased seismic demands [e.g. Martin & Lam, 2000; Pecker & Pender, 2000; Faccioli et al., 2001; Gajan et al., 2005; Harden et al., 2006; Gazetas et al., 2007; Paolucci et al., 2007; Anastasopoulos et al., 2010a].

This paper investigates experimentally the role of nonlinear foundation response on the seismic performance of a slender 1-dof structure. The configuration of the conceptual prototype problem is portrayed in Figure 1. It involves a bridge pier of moderate height founded upon a layer of dense sand through a square shallow foundation of varying width $B$. Three different foundation sizes were considered, designated as "large", "medium", and "small", representing a conservatively designed foundation, a less conservative one, and a seriously under-designed foundation, respectively. The performance of the three systems under static (monotonic and cyclic) and earthquake loading was thoroughly investigated through a series of 1-g physical tests and evaluated with respect to the effectiveness of their design concept regarding the prohibition or permission of foundation nonlinearity.

## 2 METHODOLOGY

A number of simplified bridge pier physical models with shallow foundations of various sizes (i.e. $FS$ values) were built at the Laboratory of Soil Mechanics of NTUA and tested against (vertical and horizontal) static and dynamic (shaking table) loading. A linear geometric scale of 1:20 was selected with regard to the shaking table capacity and the physical models dimensions and properties were appropriately scaled down according to the relevant scaling laws [Muir Wood, 2004].

### 2.1 *Soil Sample*

Dry Longstone sand [see, Anastasopoulos et al., 2010b] was used in the experiments. Nine identical soil specimens were constructed within a rigid container of dimensions160 x 90 x 75 cm (at model scale), upon which each one of the pier models was tested separately. The sand was placed into the container through an electronically-controlled sand raining system designed to produce soil samples of controllable relative density $D_r$ , ensuring repeatability. In the present study the initial soil sample was chosen to be of high density, $Dr \approx 85\%$ for all tests, to minimize soil densification during shaking. The effective soil friction angle was estimated as $\varphi' \approx 44°$ through a series of vertical pushover tests on three different foundation models making use of traditional bearing capacity equations [Meyerhof, 1951].

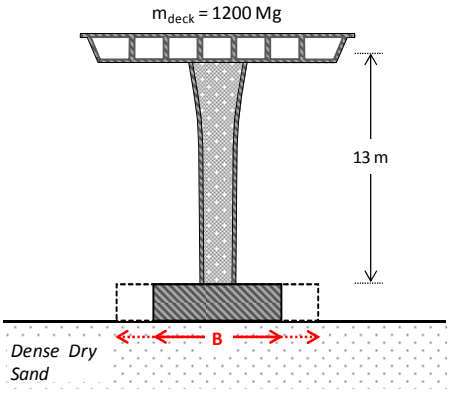

Figure 1. Problem definition : an idealized bridge pier on shallow foundations of varying dimensions.

## 2.2 *Pier–Foundation Model*

Figure 2 gives an overview of the pier model geometry. It is comprised of three parts: the deck (an assembly of steel plates with total weight of 150 kg), the column, and the foundation.

With the exception of the foundation size, the three tested pier models were identical. It may be readily observed that the very elongated shape of the foundation model is essentially different from the square shape considered in the conceptual prototype pier. The reason for this intentional discrepancy lies in the treatment of small scale effects originating from the pressure dependence of soil behavior. As the magnitude of the applied confining stress presumably depends on the geometric scale, reduced scale modeling unavoidably leads to misreproduction of the stress field in the soil model in comparison to the prototype and hence to misreproduction of the soil strength in terms of both magnitude and distribution. As a result, geometric scaling of the foundation size would result to incorrect scaling (actually overestimation) of its capacity.

Aiming to compensate for this limitation of small-scale modeling and achieve similitude between model and prototype regarding the foundation response it is essential to satisfy the following three conditions:

(i ) for similarity in the vertical direction to be preserved, the ratio of the total vertical load carried by the foundation to its vertical capacity ($N/N_u$) must be the same in model and prototype;

(ii) in the same way, the ratio of the lateral load to the lateral capacity ($Q/Q_u$, and $M/M_u$) should be instantaneously preserved;

(iii) lastly, as rocking response is controlled by the slenderness ratio (here equal to the height of the centre of mass $h$ divided by the foundation length in the direction of shaking $L$), it is essential that this parameter remains unchanged.

With regard to foundation design practice, the first two conditions basically reduce to preserving the Factors of Safety ($FS$) for vertical and combined-seismic loading ($FS_V$ and $FS_E$ respectively) in the model the same as in the prototype. Given the overestimation of the soil strength in the model, this may only be achieved by reducing the foundation area. However, doing so in both directions would violate the requirement for preservation of the slenderness ratio $h/L$. Therefore the foundation area was reduced by decreasing only the out-of-plane foundation dimension.

For stability in the out-of-plane direction the deck-mass was supported through a Π shaped column-foundation system with the two footings of breadth $B$ being in adequately large distance to prevent any interaction effects. $B$ was calculated with respect to the intended $FS$ values for each one of the two systems making use of common practice bearing capacity formulas for pure vertical loading [Meyerhof, 1951] and combined $N$–$Q$–$M$ loading [Butterfield & Gottardi, 1994] for an average pre-estimated effective soil friction angle of $\varphi' \approx 44°$. Table 1 summarizes the geometry, elastic properties of column sections, and design characteristics of the three pier-foundation systems.

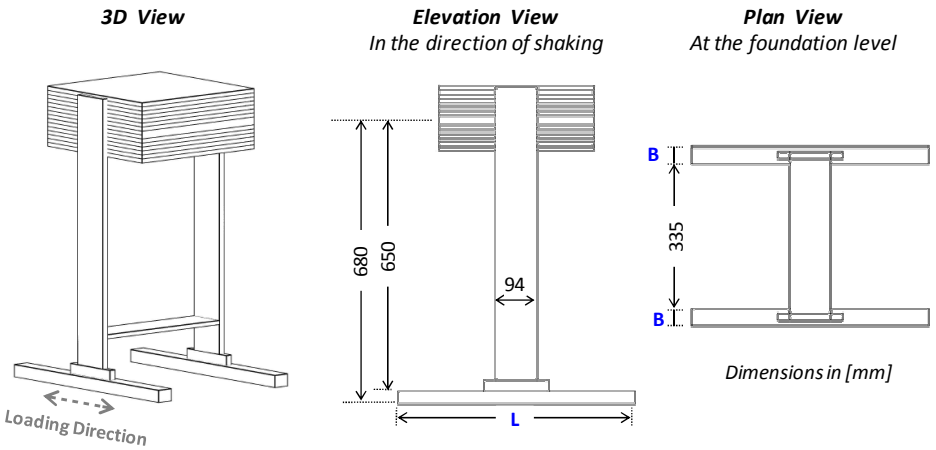


Figure 2. Geometry of the foundation–structure model.

Table 1. Summary of the pier models geometry and design characteristics (in prototype scale).

| PIER | | | | | | |
|---|---|---|---|---|---|---|
| *Deck Mass* | *Pier Height* | *Total Height* | *Column Section* | | | *Fix. base Period* |
| **M : Mg** | **$h_p$ : m** | **h : m** | **A : $m^2$** | **$I_x$ : $m^4$** | **E : kPa** | **$T_0$ : sec** |
| 1200 | 13 | 13.6 | 1.06 | 0.32 | 40 x $10^8$ | 0.16 |

| FOUNDATION | | | | | | | | |
|---|---|---|---|---|---|---|---|---|
| **size** | *Length* | *Width* | *Slenderness* | *Total Weight* | *Design Safety Factors* | | | |
| | **L : m** | **B : m** | **h/L** | **N : kN** | **$FS_V$** | | **$FS_E$** | |
| ***large*** | 11 | 1.70 | 1.2 | 14 362 | 7.49 | > 3 | 1.07 | > 1 |
| ***medium*** | 7 | 1.40 | 1.9 | 13 593 | 3.41 | > 3 | 0.55 | < 1 |
| ***small*** | 7 | 1.14 | 1.9 | 13 436 | 2.29 | < 3 | 0.43 | < 1 |

## 2.3 *Set-up and Instrumentation*

The experimental series involved three types of tests, namely: (i) vertical-push tests; (ii) monotonic and cyclic lateral pushover tests; and (iii) shaking table testing.

During monotonic and slow-cyclic push tests, load was applied in the horizontal or vertical direction through a servo-electric actuator, and measured by a load cell connected at its edge. Wire and laser displacement transducers measured vertical and horizontal displacements of the pier model. In the dynamic (shaking table) tests, the motion of characteristic points within the soil and on the structure were recorded by vertical and horizontal accelerometers. Strain gauges installed at the base of the column measured section bending strains and verified the results derived by the acceleration measurement of the deck-mass. Figure 3 displays the set-up and instrumentation for the three test types.

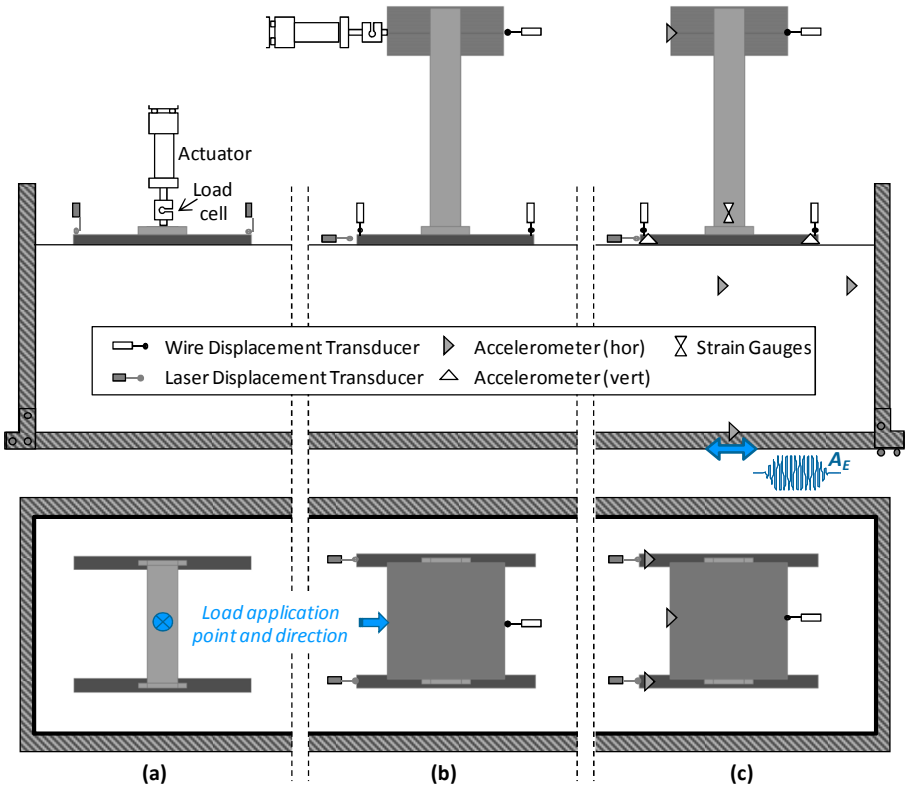


Figure 3. Experimental set up and instrumentation for : (a) vertical pushover, (b) horizontal pushover, and (c) shaking table tests.

## 3 PRESENTATION OF RESULTS

### 3.1 *Vertical Push*

Slow vertical push was applied by an actuator, which was placed precisely at the centre of the foundation area, as shown in Figure 3a. Successive loading–unloading cycles produced the load–settlement curves shown in Figure 4 for the three different foundations. The ultimate bearing capacity $N_{ult}$ is given in each case. The large footing carries an ultimate load of about 99 MN (corresponding to $FS_V \approx 6.9$), which is well above the current code requirements and exceeds the ultimate capacity of the medium and small foundation by a factor of 2.2 and 3.6, respectively. It should be noted that the measured foundation capacities are slightly lower than initially estimated (see design $FS_V$ values in Table 1). This is due to the postulation of a constant secant friction angle ($\varphi' = 44°$) made in the analysis — an unavoidable simplification of a more complex reality where φ' varies with the applied stress.

### 3.2 *Lateral Pushover*

Figure 5 summarizes the moment−rotation ($M-\theta$) and settlement−rotation ($w-\theta$) response of the three foundations during both monotonic and cyclic lateral pushover tests.

Foundation moment capacity primarily depends on foundation size, and hence it comes as no surprise that the large foundation transmits the greatest moment. In particular, when loaded monotonically it transmits approximately 2 and 2.4 times larger moment than the medium and small foundations, respectively, verifying their design (see Table 1).

Switching into cyclic mode has an important effect on the behavior as it leads to apparent overstrength especially for the small foundation. Comparison of cyclic $M-\theta$ response with the corresponding monotonic shows that whereas for the two larger footings the monotonic curves almost envelope the cyclic loops, with $M_{ult}$ being quite the same under monotonic and cyclic loading, the cyclic loops of the smaller foundation surpass appreciably the monotonic curve. As a result, when loaded cyclically, the small foundation bears significantly higher lateral loads than estimated in its design, thus appearing to transmit approximately the same peak moment as the medium-size foundation. It should be noted that the two smaller foundation systems have exactly the same slenderness ratio $h/L$, which appears to be the most decisive parameter for the ultimate lateral capacity of rocking systems, perhaps overshadowing the effect of $FS_V$.

Yet, $FS_V$ presumably plays a dominant role when foundation displacements are considered, this being elucidated by the settlement–rotation loops of Figure 5, where the cyclic movement of the foundation midpoint is depicted as a function of footing rotation. As expected, settlement increases consistently with reducing $FS_V$. Hence, although there is only a minor difference among the peak transmitted moments, the small foundation settles almost twice as much as the medium-size foundation.

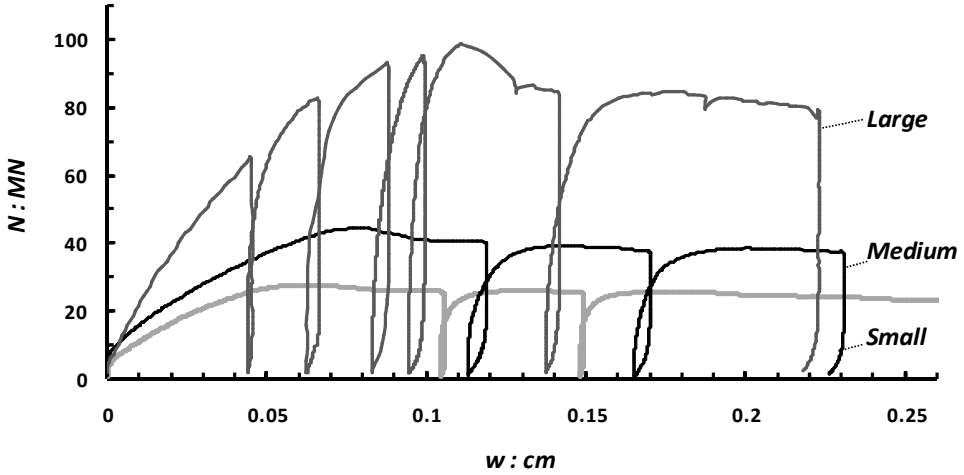


Figure 4. Vertical load – settlement curves for the three considered foundation systems.

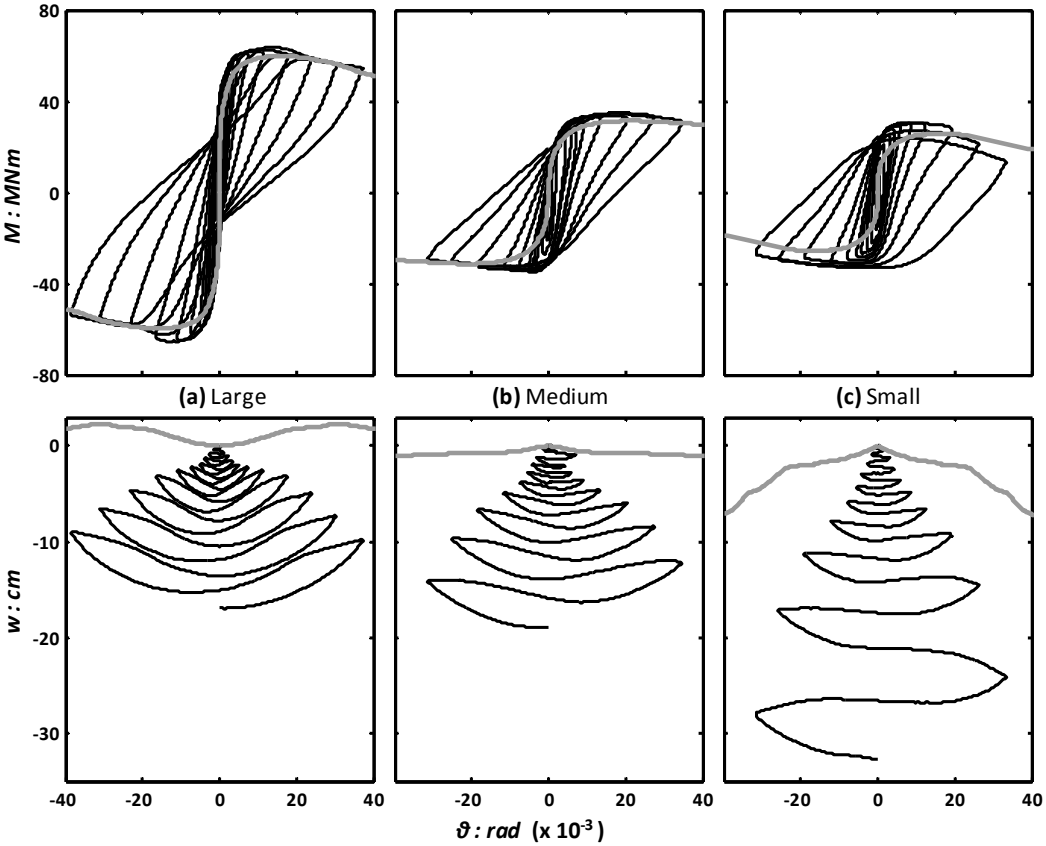


Figure 5. Monotonic (grey line) and slow-cyclic (black line) lateral pushover test results in terms of moment–rotation and settlement–rotation foundation response : (a) large foundation ($FS_v$ = 7.3) ; (b) medium foundation ($FS_v$ = 3.5) ; and (c) small foundation ($FS_v$ = 2.3).

Furthermore, $FS_V$ controls the interplay between uplifting and bearing capacity failure mechanisms. The gradient of the $w$–$\theta$ curves indicates whether the foundation midpoint loses contact with the supporting soil as the foundation rotates, giving evidence on the amount of uplift that takes place during the test. Evidently, the large foundation experiences significant uplifting, indicated by the ascending slope of $w$–$\theta$ in Figure 5a. Observe that in monotonic loading the large foundation midpoint moves upwards almost from the beginning of loading, revealing that more than half of the foundation detaches from the supporting soil.

As $FS_V$ reduces, soil nonlinearity becomes prevalent, resulting in greater rates of settlement per cycle, and reducing the extent of foundation uplift. Figures 5b and 5c clearly show downwards movement of the foundation midpoint with rotation, for both the medium-size and the small foundation respectively. Yet, the significant difference in the inclination of the respective cyclic curves indicates some limited uplifting of the medium-size foundation in contrast to the pure sinking response of the small foundation. The increased structural weight relative to the foundation capacity makes uplifting much more energy-consuming than soil yielding, which thus takes place for smaller foundation rotation. The supporting soil complies as the foundation rotates, and the foundation midpoint settles in every half-cycle of loading increasing dramatically the amount of settlement per cycle.

### 3.3 *Earthquake Loading*

Figure 6 presents the set of seismic motions used as excitations in the shaking table tests. Being selected so as to represent motions of various characteristics and intensities, this ensemble of acceleration histories involves both real earthquake records and artificial pulses of varying intensities and dominant periods. For the sake of brevity and for the purpose of focusing on the potentially favorable role of foundation nonlinearity under strong earthquake motion, the herein

presented shaking table results will be limited to one only excitation case — that in which the model was excited by a 2 Hz 12-cycle sine pulse with acceleration amplitude $A_E$ = 0.5 g.

Under such excitation all three foundations respond well within the nonlinear regime as indicated by the respective $M$–$\theta$ and $w$–$\theta$ loops of Figure 7. It is important to observe that the large foundation experiences a rotational motion of similar or larger amplitude than the two smaller foundations, possibly because its advantage of having larger moment resistance and rocking stiffness is counterbalanced by the two times greater inertial loading that it suffers. Hence, its design conservatism succeeds only in the limitation of the resulting settlement, which is indeed significantly reduced for the large foundation in comparison to the two smaller ones. On the other hand, being the product of foundation rotation, lateral pier displacements may not be directly correlated to foundation design safety factors.

Furthermore, it is worth noting that the acceleration time histories recorded at the deck of the pier (shown in Figure 8) are strictly cut-off at a particular critical value ($\alpha_c$) for each one of the three systems, this value being controlled by the foundation capacity in such way that the maximum transmitted inertial load may not exceed the lateral capacity at any instance. With reference to the ultimate moment capacity determined by pushover tests (Figure 5), the large foundation system may sustain $\alpha_c \approx 0.36$ g. Having about half the moment capacity of the large foundation, the two smaller foundations bound the seismic motion transmitted to the superstructure to a much lower level : $\alpha_c \approx 0.18$ g and 0.16 g, for the medium and the small foundation, respectively.

Acceleration time histories of Figure 8 confirm that the dynamic motion developed at the pier deck mass is bounded by the above calculated limiting values and verify this "rocking isolation" mechanism, which is presumably associated with full mobilization of foundation–soil moment capacity (expressed as uplifting and soil yielding) and hence forms the cornerstone of the new idea for allowing, and taking advantage of, nonlinear foundation response. The two under-designed foundation systems provide a drastic reduction of the seismic acceleration transmitted to the pier to only one third of the input peak acceleration $A_E$. Some limited isolation effect is observed even in the case of the large foundation system ($\alpha_{max}/A_E$ = 0.72). Yet, having a significantly larger capacity $M_u$ compared to the other two systems, the conservatively designed pier suffers much more intense shaking.

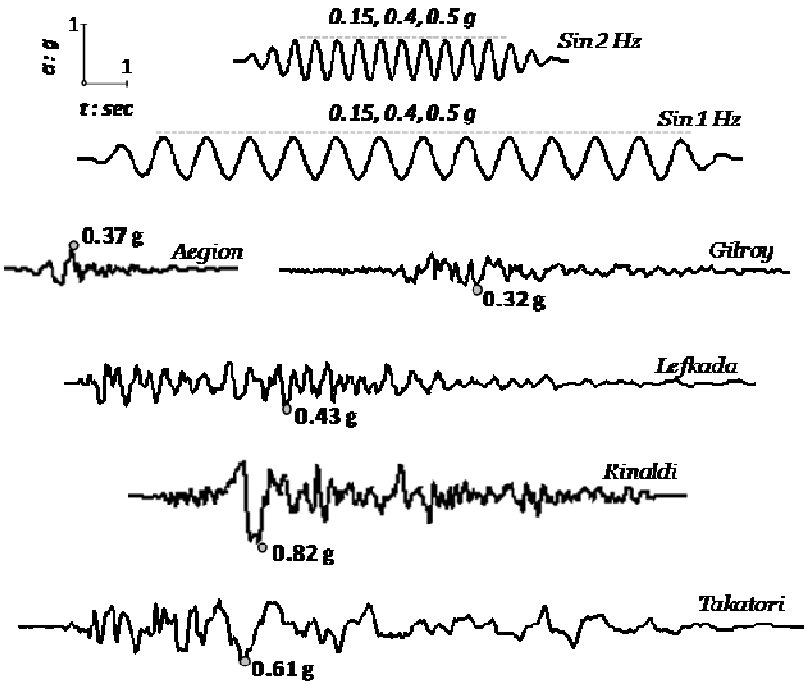


Figure 6. Real records and artificial accelerograms used as excitation in the shaking table tests.

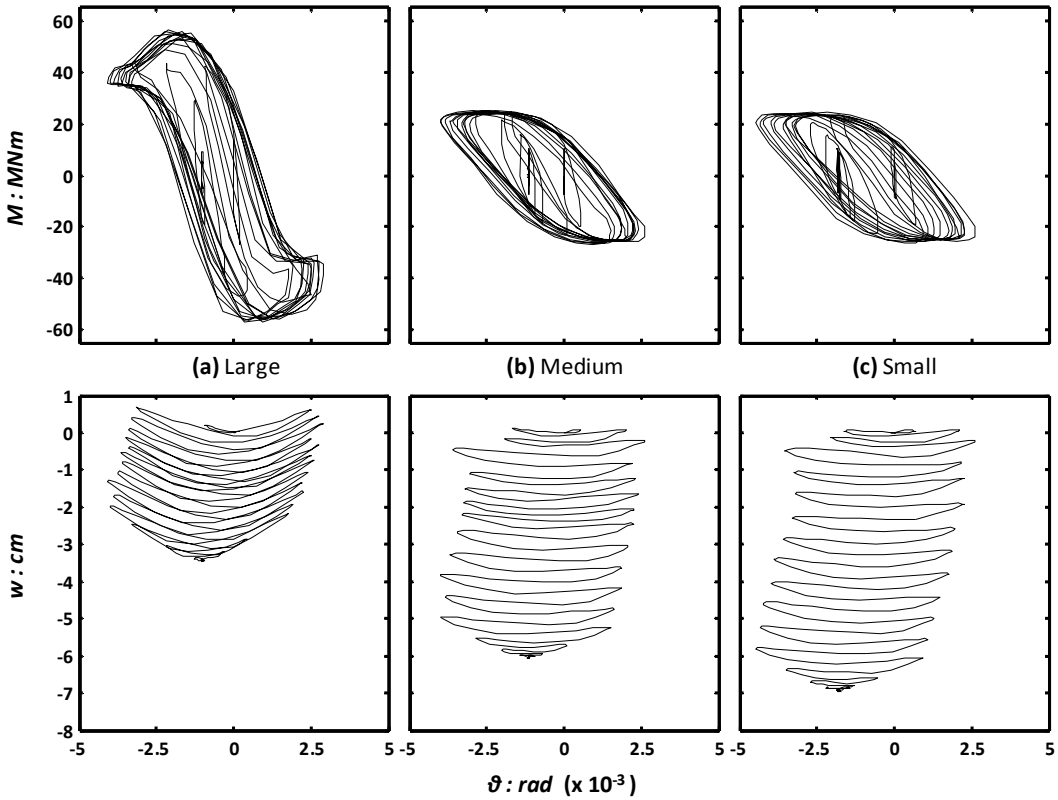


Figure 7. Foundation response to base excitation of a 12-cycle 2 Hz sine pulse with 0.50 g acceleration amplitude (Sin2-0.50 g). Moment−rotation and settlement−rotation response for : (a) the large foundation (FSv = 7.3) ; (b) the medium foundation (FSv = 3.5) ; and (c) the small foundation (FSv = 2.3).

## 4 CONCLUSIONS

The most significant outcome of this study is the experimental verification – "proof of concept" – of the potential effectiveness of rocking isolation as a means of seismic protection of a bridge pier. Acting as a safety "fuse", full mobilization of foundation capacity (in the form of uplifting and soil yielding) constrains the acceleration transmitted onto the superstructure to a value below a critical acceleration $\alpha_c$, which is directly associated with foundation capacity $M_{ult}$ and, hence, decreases with reducing foundation size. The effectiveness of rocking isolation in terms of inertial loading for the entire set of studied earthquake excitations is summarized in Figure 9. Evidently, the two under-designed foundations (medium and small) drastically reduce the maximum acceleration $\alpha_{max}$ transmitted to the deck for all studied seismic excitations.

Despite having quite different FS values, the medium and small foundations sustain practically the same moment loading and consequently permit similar levels of inertial loading to be transmitted onto the superstructure. This similarity in their capacity can be attributed to two observations : (i) lateral load capacity is principally controlled by the slenderness ratio *h/L*, and is much less sensitive to changes in the foundation out-of-plane dimension; and (ii) during cyclic loading, an overstrength mechanism was observed to take place and affect mainly the capacity of small foundations.

$FS_V$ affects the development and accumulation of permanent displacements. In the case of symmetric seismic motions such as the sine pulse presented herein, the increase of settlement appears to be the only significant argument against the rocking isolation concept (i.e. underdesigning the foundation for the sake of structural safety). Real – asymmetric excitations may also bring about in some considerable permanent foundation rotation, which will unavoidably result permanent deck drift. Yet, the problem reduces to defining the acceptable displacements of the superstructure in relation to performance requirements.

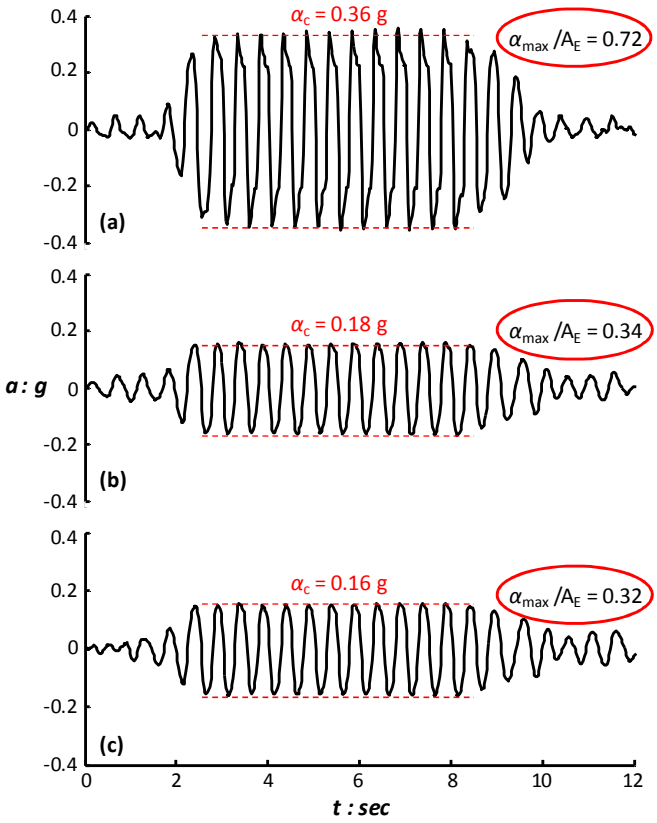


Figure 8. Acceleration time histories recorded at the level of the deck (center of mass) for base excitation with a 12-cycle 2 Hz sine of 0.15 g acceleration amplitude (Sin2-0.15 g) for : (a) the large foundation (FSv = 7.3) ; (b) the medium foundation (FSv = 3.5) ; and (c) the small foundation (FSv = 2.3).

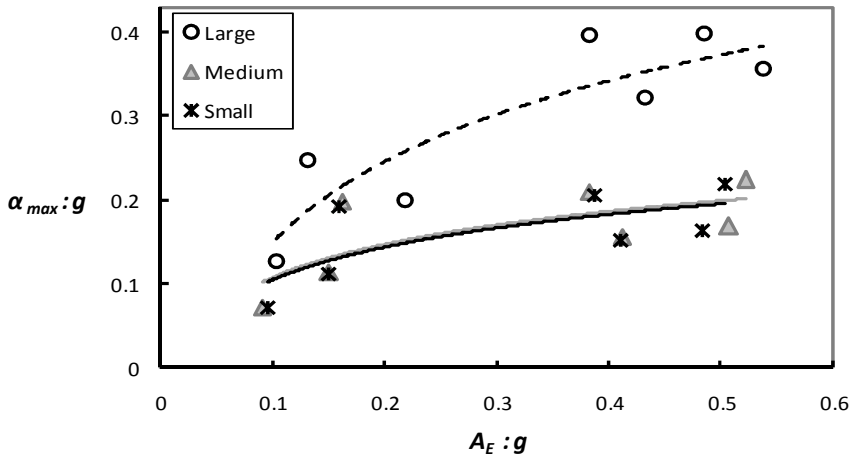


Figure 9. Rocking isolation effectiveness for the three pier–foundation systems : maximum deck acceleration αmax with versus the acceleration amplitude AE of the base excitation.

## 5 ACKNOWLEDGEMENT

The research presented in this paper was funded by the European Research Council (ERC) Program "IDEAS, Support for Frontier Research – Advanced Grant", under Contract number ERC–2008–AdG 228254–DARE.

## 6 REFERENCES

Anastasopoulos , I., Gazetas, G., Loli, M., Apostolou, M., Gerolymos, N. (2010a), "Soil failure can be used for seismic protection of structures", *Bulletin of Earthquake Engineering*, 8(2), pp. 309–326.

Beck, J. L. & Skinner, R. I. (1974), "The seismic response of a reinforced concrete bridge pier designed to step", *Earthquake Engineering & Structural Dynamics*, 2, pp. 343–358.

Butterfield, R. & Gottardi, G. (1994), "A complete three dimensional failure envelope for shallow footings on sand", *Geotechnique*, 44(1), pp. 181–184.

Chen, Y.H., Liao, W.H., Lee, C.L., Wang, Y.P. (2006), "Seismic isolation of viaduct piers by means of a rocking mechanism", *Earthquake Engineering and Structural Dynamics*, 35(6), pp. 713-736.

Chopra, A. & Yim, S. (1985), "Simplified Earthquake Analysis of Structures with Foundation Uplift", *Journal of Structural Engineering* (ASCE), 111, pp. 906–930.

Faccioli, E., Paolucci, R., Vivero, G. (2001), "Investigation of seismic soil-footing interaction by large scale cyclic tests and analytical models", *Proc. of 4th int. conf. recent advances in geotechnical earthquake engineering and soil dynamics*, San Diego, pp. 26–31.

Gajan, S., Kutter, B.L., Phalen, J.D., Hutchinson, T.C., Martin, G. (2005), "Centrifuge modeling of load-deformation behavior of rocking shallow foundations", *Soil Dynamics an Earthquake Engineering*, 25(7–10), pp. 773–783.

Gazetas, G., Anastasopoulos, I. and Apostolou M. (2007). "Shallow and deep foundations under fault rupture or strong seismic shaking." *Earthquake Geotechnical Engineering*, K. Pitilakis (ed), Springer Publ., Chapter 9, 185-215.

Harden, C., Hutchinson, T., and Moore, M. (2006), "Investigation into the effects of foundation uplift on simplified seismic design procedures", *Earthquake Spectra*, 22(3), pp. 663–692.

Housner, G.W. (1963), "The behavior of inverted pendulum structures during earthquakes" *Bulletin of the Seismological Society of America*, 53(2), pp. 404–417.

Huckelbridge, A. A. & Ferencz, R. M. (1981), "Overturning effects on stiffened building frames", *Earthquake Engineering & Structural Dynamics*, 9, pp. 69–83.

Martin, G. R. & Lam, I. P. (2000), "Earthquake Resistant Design of Foundations : Retrofit of Existing Foundations", *Proceedings of GeoEng 2000 Conference*, Melbourne, pp. 19–24.

Meek, J. W. (1978), "Dynamic response of tipping core buildings", *Earthquake Engineering & Structural Dynamics*, 6, pp. 437–454.

Mergos, P.E & Kawashima, K. (2005), "Rocking isolation of a typical bridge pier on spread foundation", *Journal of Earthquake Engineering*, 9(2), pp. 395–414.

Meyerhof, G.G. (1951), "The ultimate bearing capacity of foundations", *Géotechnique*, 2(4), pp. 301–332.

Muir Wood, D. (2004), *Geotechnical modelling*, Spon Press, London.

Paolucci, R., Shirato, M.,Yilmaz, M.T. (2007), "Seismic behavior of shallow foundations: shaking table experiments vs numerical modeling", *Earthquake Engineering and Structural Dynamics*, 37(4), pp. 577–595.

Pecker, A. & Pender, M. (2000), "Earthquake resistant design of foundations: new construction", *Proceedings of the GeoEng 2000 Conference*, Melbourne, Australia 2000, pp. 313–334.

Pecker, A. (2005), "Design and Construction of the Foundations of the Rion Antirion Bridge", *Proceedigs of the 1st Greece–Japan Workshop on Seismic Design, Observation, Retrofit of Foundations*, Athens, pp.119–130.

Priestley, M.J.N., Seible, F., and Calvi, G.M. (1996), *Seismic design and retrofit of bridges*, John Wiley & Sons.

Psycharis, I.N. & Jennings, P.C. (1983), "Rocking of slender rigid bodies allowed to uplift", *Earthquake Engineering and Structural Dynamics*, 11, pp. 57–76.

Sakellaraki, D. & Kawashima, K. (2006), "Effectiveness of seismic rocking isolation of bridges based on shake table tests", *Proceedings of the 1st European Conference on Earthquake Engineering and Seismology*, Geneva, Switzerland, pp. 1–10.

# INSTED: Innovative Stiffness and Energy Dissipation System, Final Report

Ph. S. Karydakis, I. Vagias, & G. Ioannidiss
*Steel Structures Laboratory, National Technical University, Athens, Greece*

ABSTRACT: The objective of this paper is the innovative stiffness and energy dissipation system (for short "INSTED"), for multi-storey steel buildings in seismic areas, initially presented in Eurosteel 2008 [6]. This system is further developed through the European project FUSEIS.
In this system, the usual moment resisting frames or anti-diagonal bracings with or without eccentricity are replaced by a vertical composite beam, made up from two strong columns of square hollow section, closely positioned, and joined together with horizontal beams in a relatively tight arrangement, a vertical vierendeel beam. This system resembles a shear resistance wall, but with the added advantage of the capability of large amount of energy dissipation through plastic deformation of the beams, and if needed, ease of replacement.The proposed system has been tested in full scale, in the Steel Structures Laboratory of the NTUA and analyzed theoretically with non linear analytical methods, static and dynamic.

## 1 INTRODUCTION

In Eurosteel 2008 [6], the principles of the INSTED system were initially presented, a new stiffness and energy dissipation system for multi-storey steel buildings in seismic areas. This system is further developed through the European project FUSEIS.

In this system, the usual moment resisting frames (Fig. 1a) or anti-diagonal bracings with or without eccentricity (Fig1. b-c) were replaced by a vertical composite beam, made up from two strong columns of square hollow section, closely positioned, and joined together with horizontal beams in a relatively tight arrangement, a vertical vierendeel beam (Fig. 1d).

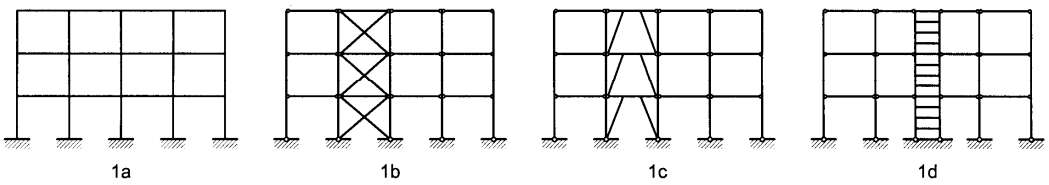


Figure 1. Usual types of horizontal resistance systems and the proposed "INSTED" system.

This **in**novative **s**tiffness and **e**nergy **d**issipation system (for short "INSTED") resembles a shear resistance wall, but with the added advantage of the capability of large amount of energy dissipation through plastic deformation of the beams, and if needed, ease of replacement. The pro-

posed system has been tested in full scale, in the Steel Structures Laboratory of the NTUA and analyzed theoretically with non linear analytical methods, static and dynamic.

## 2 THE SYSTEM

The INSTED system is formed by the two vertical strong columns, that remain elastic and the expandable horizontal connections, where plastic hinges are formed and energy dissipation takes place. The horizontal connections can be beams of any section, I-beams or hollow sections (Fig. 2,3,4,5), or solid rods or bars (Fig. 6,7,8,9). In both cases the expandable section is located at the middle of the span, with the use of receptacle beams welded to the columns, considerably stronger than the connecting elements. The receptable beams remain elastic, restraining the plastic hinges in the expandable middle section.

Figure 2. Bending moment diagram along the connecting elements.

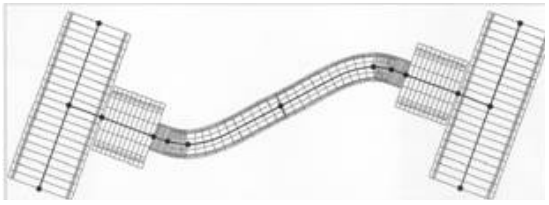

Figure 3. Beams as the connecting elements

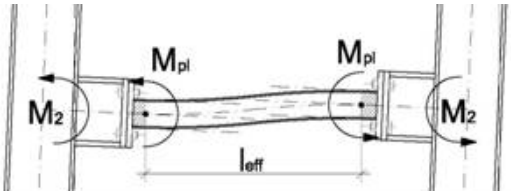


Figure 4. Bending moments along the connecting beam

Figure 5. Testing of an IPE 100 as the connecting beam.

Figure 6. Bending moment diagram along the connecting rod element.

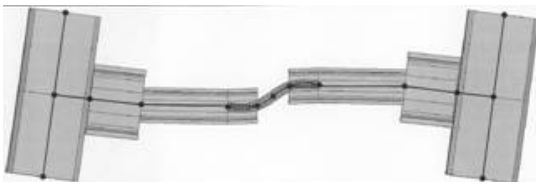

Figure 7. Central bars or rods as the connecting elements.

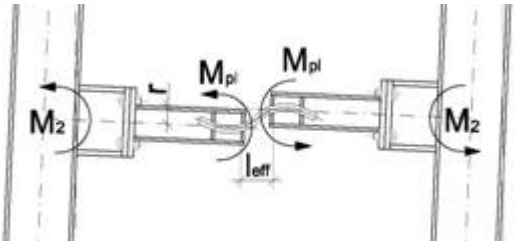


Figure 8. Bending moment along the connecting rod elements.

Figure 9. Testing of central bars (2*12/30) as the connecting elements.

The above set of sketches, diagrams and pictures, demonstrate the basic principle, that the more the expandable connecting element is moved away from the columns, by increasing the length of the receptable beams that remains elastic, the bending moment developed is smaller and so is the crossection needed. On the other hand, because of the bigger relative vertical displacement more plasticity is required. Additionally considerable axial force develops increasing the stiffness and strength of the insted system.

## 3 THE TESTS

During the first set of 15 tests performed in the Steel Structures Laboratory of NTUA, three groups of connecting elements were used:
Beams of similar section, 5 I-100, 5-SHS 80/5, 5 HE-A100.
Bars and rods of similar section 5 bars 2*12/30, 5 rods Φ33
Beams of variable crossections 5 IPE 80-160, 5 SHS 80/5 with var. holes, 5 HE-A 100 with var. dog bones, 5 rods Φ33, with var. ring slots.

The introduction of variable sections aims to the progressive failure of the system, introducing plastic hinges earlier in the structure to dissipate energy, but maintaining structural rigidity until total failure.

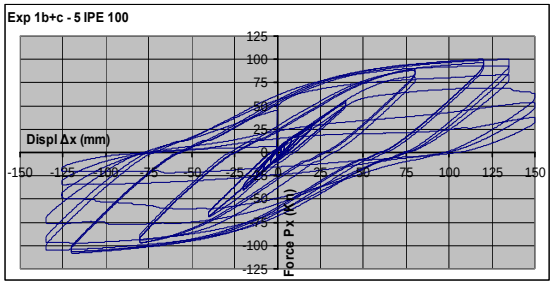


Figure 10. Hysteresis loops for the 5 IPE 100

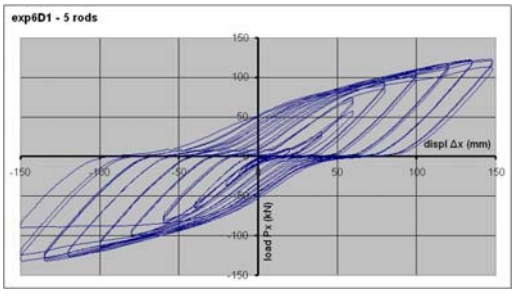


Figure 11. Hysteresis loops for the 5 bars 2*12/30

In the above diagrams (Fig. 10, 11) the energy dissipation of the system is clearly demonstrated. In the case of the centrally positioned solid bars, the increase in stiffness and strength is apparent.

## 4 THE MATERIAL

It is important for the insted system, to localize potential failure only in the expandable connection elements, so mild steel is preferred. The problem with today's steel production is that the mild steel in the market is of considerable higher quality than expected. In our case the prescribed S235, after testing (Fig. 12), had a yield point $f_y$=335 kN/cm$^2$ and ultimate strength $f_u$=420 kN/cm$^2$.

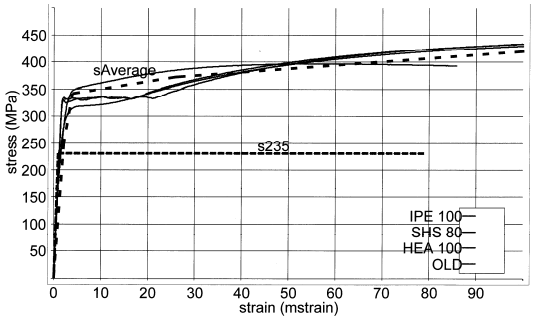


Figure 12. Steel elastic properties.

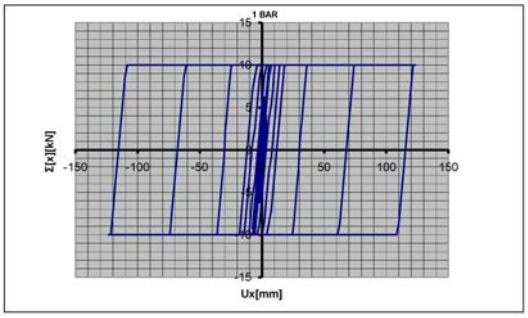


Figure 13. Analytical hysteresis loops for 5 bars.

## 5 ANALYTICAL INVESTIGATION

By applying simple equilibrium equations, the horizontal resistance of the INSTED system can be derived from the formula (eq 1):

$$P_1 = \sum_{n=1}^{N} M_{pl} \frac{2 \times b}{h \times l_{eff}}$$

Parallel to this simple method, additional non linear analysis was carried out by models of varying complexity, using the SOFISTIK software (Fig. 13). For the material properties, the standard bi-linear stress-strain diaphragm was used. The analytical results compared very well to simple equilibrium analysis results.

The software used, with linear or surface finite element models, gave simple bi-linear results without post yielding behavior of steel, final fracture or fatigue. It also did not include second order analysis to take into account the axial force effects on the stiffness and strength of the system.

## 6 CONCLUSIONS

The following table shows the simple numerical results based on basic equilibrium equations, converted by the yield value factor and the ultimate to yield factor, from the tested material properties, the experimental results and analytical numerical results from finite element analysis.

the index ($y^{S235}$) refers to the analysis based on the yield value of mild steel: $f_y$=23.5 kN/cm$^2$
the index ($y^{Stest}$) refers to the analysis based on the yield value of the tests: $f_y$=33.5 kN/cm$^2$
the index ($u^{Stest}$) refers to the analysis based on the ultimate value of the tests $f_u$=42.0 kN/cm$^2$
the index ($y^{exp}$) refers to the experimental results for yielding
the index ($u^{Stest}$) refers to the experimental results for yielding
the index ($y^{cal}$) refers to the results with F.E. based on the yield value of steel: $f_y$=23.5 kN/cm$^2$

Table 1. Mathematical and Experimental results

INNOVATIVE STIFFNESS AND ENERGY DISSIPATION SYSTEM
**(INSTED)**

Vetical Vierendeel height: h= 3.40 m
Distance bettween columns: b= 1.50 m

Material properties
$f_{ya(S235)}$= 23,5 kN/cm$^2$
$f_{ya(Stest)}$= 33,5 kN/cm$^2$
$f_{u(Stest)}$= 42 kN/cm$^2$

| | Connecting element | | effective length | Wpl | $Mpl_{(S235)}$ | $Mpl_{(Stest)}$ | $Mu_{(Stest)}$ | $P1y^{S235}$ | $P1y^{Stest}$ | $P1u^{Stest}$ | $P1y^{exp}$ | $P1u^{exp}$ | $P1y^{cal}$ |
|---|---|---|---|---|---|---|---|---|---|---|---|---|---|
| | | | cm | cm$^3$ | kNcm | kNcm | kNcm | kN | kN | kN | kN | kN | kN |
| 1 | IPE100 | 1 | 76,0 | 39,4 | 925,9 | 1319,9 | 1654,8 | 10,7 | 15,3 | 19,2 | 14,2 | 20,5 | 10,0 |
| 2 | IPE100 | 5 | 76,0 | 39,4 | 925,9 | 1319,9 | 1654,8 | 53,7 | 76,6 | 96,1 | 75,0 | 100,0 | 47,0 |
| 3 | SHS 80/5 | 5 | 76,0 | 41,7 | 980,0 | 1397,0 | 1751,4 | 56,9 | 81,1 | 101,7 | 78,0 | 108,0 | 52,0 |
| 4 | bar 2*12/30 | 1 | 11,0 | 5,4 | 126,9 | 180,9 | 226,8 | 10,2 | 14,5 | 18,2 | 20,0 | 24,0 | 10,0 |
| 5 | bar 2*12/30 | 5 | 11,0 | 5,4 | 126,9 | 180,9 | 226,8 | 50,9 | 72,6 | 91,0 | 75,0 | 126,0 | 51,0 |
| 6 | HE-A 100 | 5 | 76,0 | 83,0 | 1950,7 | 2780,8 | 3486,4 | 113,2 | 161,4 | 202,4 | 150,0 | 150,0 | 86,0 |
| 7 | HE-A 100 | 1 | 76,0 | 83,0 | 1950,7 | 2780,8 | 3486,4 | 22,6 | 32,3 | 40,5 | 30,0 | 38,0 | 17,0 |
| 8 | IPE80-160 | 5 | 76,0 | | | | | 91,6 | 130,5 | 163,6 | 150,0 | 150,0 | 86,0 |
| 9 | SHS 80/5 H | 5 | 76,0 | | | | | 40,5 | 57,8 | 72,4 | 60,0 | 76,0 | 42,0 |
| 10 | HE-A 100 DB | 5 | 76,0 | | | | | 84,5 | 120,4 | 151,0 | 120,0 | 150,0 | 65,0 |
| 11 | rod Φ33 1s | 1 | 12,5 | 6,0 | 140,8 | 200,7 | 251,6 | 9,9 | 14,2 | 17,8 | 15,0 | 23,0 | 9,8 |
| 12 | rod Φ33 2s | 1 | 12,5 | 6,0 | 140,8 | 200,7 | 251,6 | 9,9 | 14,2 | 17,8 | 15,0 | 23,0 | 9,8 |
| 13 | rod Φ33 2s | 1 | 12,5 | 6,0 | 140,8 | 200,7 | 251,6 | 9,9 | 14,2 | 17,8 | 15,0 | 30,0 | 9,8 |
| 14 | rod Φ33 1s | 5 | 12,5 | 6,0 | 140,8 | 200,7 | 251,6 | 49,7 | 70,8 | 88,8 | 78,0 | 120,0 | 48,0 |
| 15 | rod Φ33 1s | 5 | 9,0 | | | | | 27,6 | 39,3 | 49,3 | 40,0 | 63,0 | |

Table 2. Comparison of Mathematical and Experimental results

| | Connecting element | | effective length | $P1y^{S235}$ | $P1y^{Stest}$ | $P1u^{Stest}$ | $P1y^{exp}$ | $P1u^{exp}$ | $P1y^{cal}$ | $\Delta P_{1y}/P_{1y}$ | $\Delta P_{1u}/P_{1u}$ |
|---|---|---|---|---|---|---|---|---|---|---|---|
| | | | cm | kN | kN | kN | kN | kN | kN | | |
| 1 | IPE100 | 1 | 76,0 | 10,7 | 15,3 | 19,2 | 14,2 | 20,5 | 10,0 | 8% | -6% |
| 2 | IPE100 | 5 | 76,0 | 53,7 | 76,6 | 96,1 | 75,0 | 100,0 | 47,0 | 2% | -4% |
| 3 | SHS 80/5 | 5 | 76,0 | 56,9 | 81,1 | 101,7 | 78,0 | 108,0 | 52,0 | 4% | -6% |
| 4 | bar 2*12/30 | 1 | 11,0 | 10,2 | 14,5 | 18,2 | 14,0 | 24,0 | 10,0 | 4% | -24% |
| 5 | bar 2*12/30 | 5 | 11,0 | 50,9 | 72,6 | 91,0 | 75,0 | 126,0 | 51,0 | -3% | -28% |
| 6 | HE-A 100 | 5 | 76,0 | 113,2 | 161,4 | 202,4 | 150,0 | 150,0 | 86,0 | | |
| 7 | HE-A 100 | 1 | 76,0 | 22,6 | 32,3 | 40,5 | 30,0 | 38,0 | 17,0 | 8% | 7% |
| 8 | IPE80-160 | 5 | 76,0 | 91,6 | 130,5 | 163,6 | 150,0 | 150,0 | 86,0 | | |
| 9 | SHS 80/5 H | 5 | 76,0 | 40,5 | 57,8 | 72,4 | 60,0 | 76,0 | 42,0 | -4% | -5% |
| 10 | HE-A 100 DB | 5 | 76,0 | 84,5 | 120,4 | 151,0 | 120,0 | 150,0 | 65,0 | 0% | 1% |
| 11 | rod Φ33 1s | 1 | 12,5 | 9,9 | 14,2 | 17,8 | 15,0 | 23,0 | 9,8 | -6% | -23% |
| 12 | rod Φ33 2s | 1 | 12,5 | 9,9 | 14,2 | 17,8 | 15,0 | 23,0 | 9,8 | -6% | -23% |
| 13 | rod Φ33 2s | 1 | 12,5 | 9,9 | 14,2 | 17,8 | 15,0 | 30,0 | 9,8 | -6% | -41% |
| 14 | rod Φ33 1s | 5 | 12,5 | 49,7 | 70,8 | 88,8 | 78,0 | 120,0 | 48,0 | -9% | -26% |
| 15 | rod Φ33 1s | 5 | 9,0 | 27,6 | 39,3 | 49,3 | 40,0 | 63,0 | | -2% | -22% |

From the above results it is apparent, that the experimental results are very close to the analytical investigation, within a margin 3-8%. Only on the cases of the central bars or rods, the experimental results are 23-28% higher for ultimate strength and for a inter storey drift in the order of 4%. For these large displacements, combined with the small length of the connecting elements, the axial forces involved cause the increase in stiffness and strength.

It should be noted that the target inter storey drift of 4%, was reached in all experiments, while yielding and entrance in the plastic zone occurred at about 1.2%.

## 7 DESIGN PROCEDURE

By estimating the earthquake shear force at the base of the building, derived from the mass and code acceleration and the number of vertical Vierendeels possible, using the simple formula given Eq. (1), the number and the plastic moment of the necessary horizontal connections is easily calculated. Then the whole building, including the preselected type and number of the insted system composite beams can be analyzed by any space frame software.

## 8 FINAL DESIGN PROPOSAL

The use of expandable and of course replaceable elements, calls for ease of replacement after a major earthquake. Taking into account that the parts to be replaced are damaged, length adjustment is crucial. By using centrally positioned rods or bars, with or without screws at the ends, you have this obvious advantage.

The rods are easier to machine than rectangular bars, as are the supporting edges of the recepting beams, rounded to prevent local damage.

In the case of rods, ring slots resembling dog bones are easily constructed, leading to the formation of plastic hinges away from the supports and allowing for a long plastic zone with high plasticity, and progressive section plastification.

The proposed connecting element (Fig. 14) is a rod, between strengthened vertical columns that remain elastic, length adjusting screws at both ends and weakened crossection away from the supports.

Finally, with this type of connecting element, is easy to use different diameters in the weakened middle section, to achieve progressive plastification along the elements of one storey.

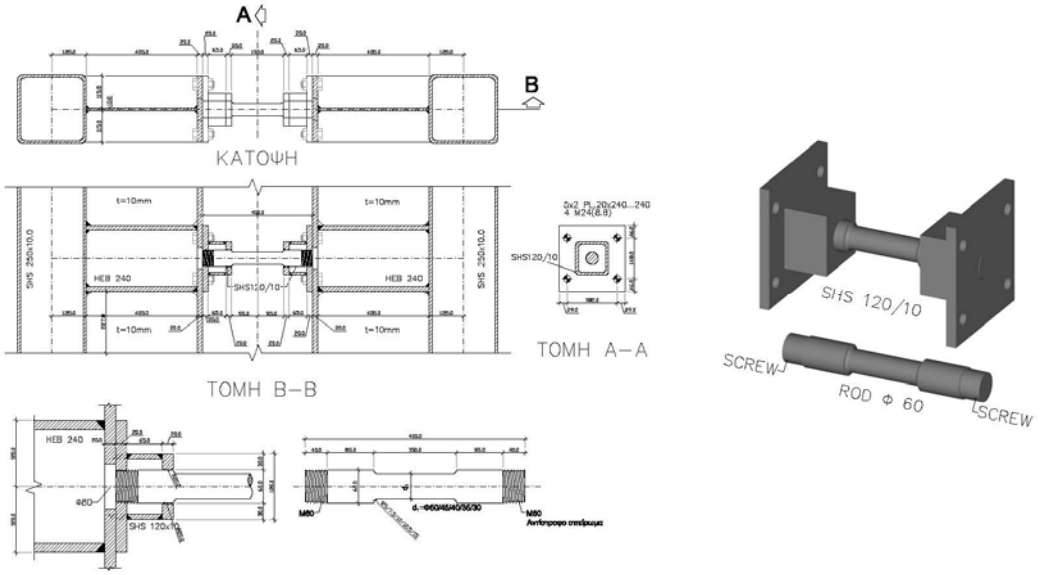


Figure 14. The proposed connecting element.

The research presented in this paper, is the basis of one part of the European project FUSEIS.

## 9 REFERENCES

[1] EN1993-1-1, Eurocode 3: “Design of steel structures - Part 1-1: General rules and rules for buildings”, CEN, 2003

[2] EN1998-1-1, Eurocode 8: “Design of structures for earthquake resistance – Part 1-1: General rules, seismic actions and rules for buildings”, CEN, 2003

[3] ATC – 40: “Seismic Evaluation and Retrofit of Concrete Buildings”, Applied Technology Council, 1997

[4] FEMA – 356: “Prestandard and Commentary for the seismic rehabilitation of Buildings”, 2000

[5] ECCS document: “Recommended testing procedure for assessing the behaviour of structural steel elements under cyclic loads”, Technical committee 1: structural safety and loadings, Technical working group 1.3: seismic design, 1986

[6] Karydakis Ph., Ioannides G., Vayas I.: "Innovative stiffness and energy dissipation system, for multi-storey steel buildings of aseismic design", *Proceedings of the 5th European conference on steel and composite structures,*. 3-5 September 2008, Gratz, Austria, R. Ofner, D. Beg, J. Fink, R. Greiner, H. Unterweger, volume B, p. 1383-1388, published by ECCS 2008

[7] Karydakis Ph., Ioannides G., Vayas I.: "Innovative stiffness and energy dissipation system, for multi-storey steel buildings of aseismic design", *Proceedings of the 6th National conference on steel and composite structures*, , 2-4 October 2008, Ioannina, Greece, volume II, p. 395-402, published by EEME 2008

[8] O. Palkopoulou, P. Karydakis & I. Vayas: Innovative bracing system for seismic resistant steel structures. *Stessa 2009: Behaviour of Steel Structures in Seismic Areas*. page 73, Mazzolani, Ricles & Sauce (eds), 2009 Taylor & Francis Group, London, ISBN 978-0-415-56326-0

# EARTHQUAKE DAMAGE ESTIMATING SYSTEM IN HANSHIN EXPRESSWAY NETWORK

Akito Higatani , Kazunori Sasaki & Nobuhiko Hamada
*HANSHIN EXPRESSWAY COMPANY LIMITED, Engineering Department, Japan*

ABSTRACT: Preparing for future disasters, Hanshin Expressway Company Limited founded Disaster Information Management Center in 1999. The center will be a functional hub to work at the time of disaster. The earthquake damage estimating system has been developed for a subsystem of Disaster Information Management System in order to estimate the level of earthquake damage in our highway network in real time. In this paper, we introduce the earthquake damage estimating system configurations and the trial calculation.

## 1 INTRODUCTION

### 1.1 *The South Hyogo prefecture Earthquake in 1995*

The South Hyogo Earthquake occurred on January 17th, 1995. The Hanshin Expressway suffered serious damage from the Earthquake. Then we made efforts to collect damage information immediately, but that was much trouble due to the unexpected serious damage to information and communication facilities. We learned many lessons from this earthquake and founded Disaster Information Management Center in 1999.

### 1.2 *Disaster Information Management System*

Disaster Information Management Center will be a functional hub to work at the time of disaster. Disaster Information Management System consists of disaster information-processing devices located some departments including Disaster Information Management Center. This system has various functions, displaying weather information, deployment of us, and so on.

The earthquake damage estimating system has been developed for a subsystem of Disaster Information Management System in order to estimate the level of earthquake damage in our highway network in real time. This system can display the estimated results right after the earthquake. This will be of some assistance to make the preliminary investigation more efficient. In this paper, we introduce the system configurations and the trial calculation.

## 2 EARTHQUAKE DAMAGE ESTIMATING SYSTEM

### 2.1 *System configurations*

The system configurations are shown in Figure 1. Two kinds of information are utilized in the system. One is the seismic wave data that is obtained on-line from the seismometers located on the Hanshin Expressway network. The seismic wave data is converted to SI. SI is calculated by Equation 1. The ordinary integral range for the spectral intensity is 0.1 s - 2.4 s. But we set the integral

range 0.2 s – 1.2 (s) in this system, because the natural periods of our bridge structures are placed emphasis on.

$$SI = \frac{1}{1.0}\int_{0.2}^{1.2} S_V(h,T)dT \tag{1}$$

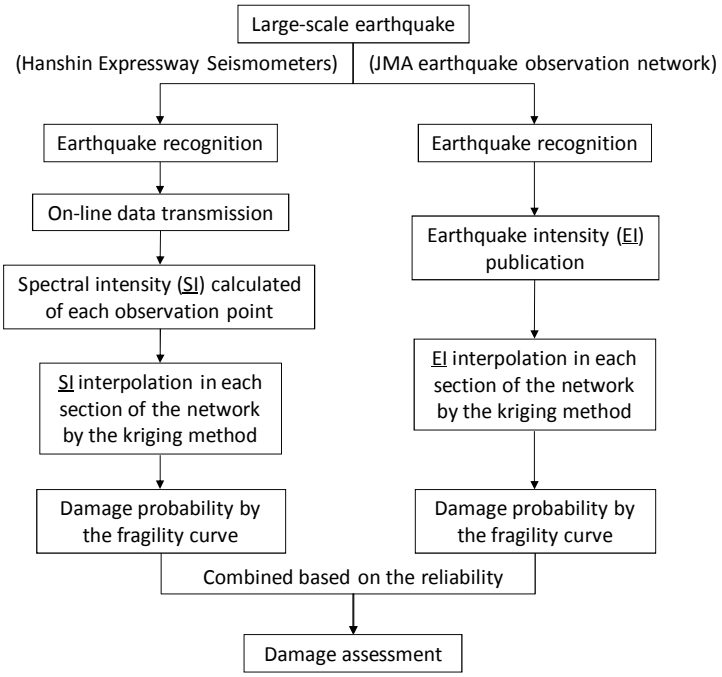


Figure 1. The configuration of the earthquake damage estimating system

Where SI= spectral intensity (cm/s), SV= velocity response spectra (cm/s), h= damping ratio (=20%), T= natural period (s)

The SI values in each Hanshin Expressway seismometer's point are converted into the SI values in each section of the network by the kriging method. The damage probability is estimated in each section of the network by the fragility curve.

On the other hand, JMA (Japan Meteorological Agency) publishes the EI data soon after the earthquake. The EI data can be obtained on-line by JMA. The EI values in each JMA observation point are also converted into the EI values in each section of the network by the kriging method. The damage probability is also estimated in each section of the network by the fragility curve.

The two kinds of damage probabilities are combined based on the reliability. The damage estimation is conducted by the combined damage probabilities.

### 2.2 *Locations of the seismometers*

The locations of the Hanshin Expressway seismometers are shown in Figure 2. There are the 19 seismometers allocated on the network. The locations of the JMA seismometers are shown in Figure 3. There are the 72 JMA seismometers near the Hanshin Expressway routes.

### 2.3 *Conversion of SI*

The conversion of SI is shown in Figure 4.The SI of the seismometers on the ground surface are converted to that on the base layer in order to improve the accuracy of interpolation. The conversion function is estimated by the dynamic response analysis of the surface layer on each site. The kriging method is adopted for the interpolation.

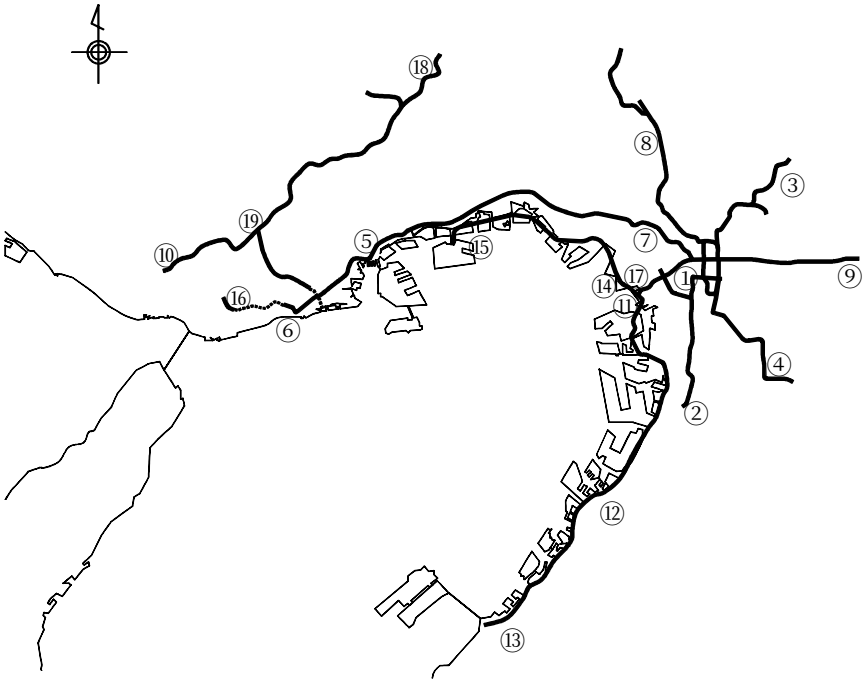


Figure 2. The locations of the Hanshin Expressway seismometers

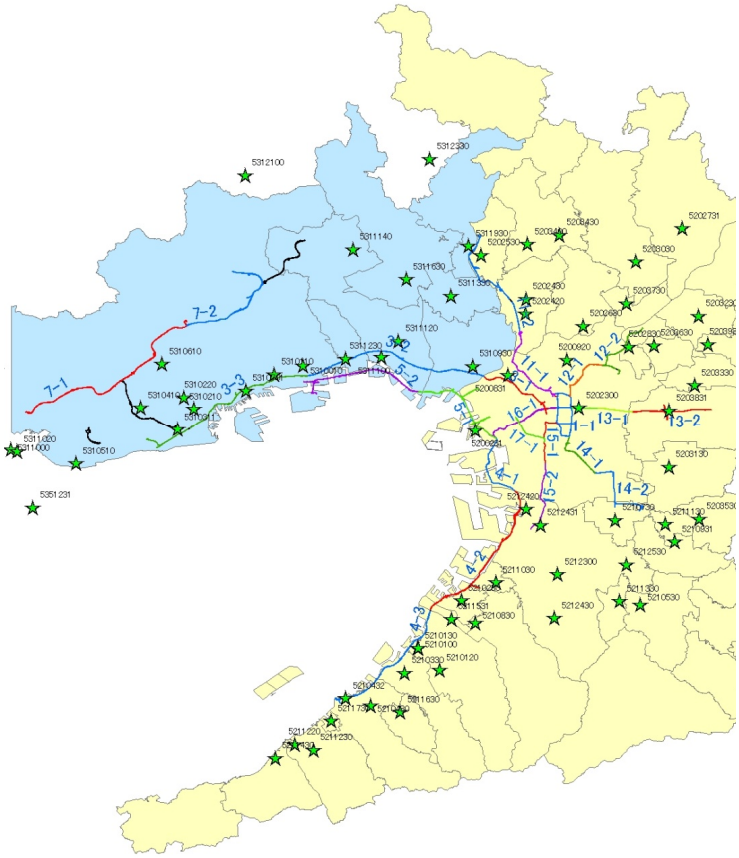


Figure 3. The locations of the JMA seismometers

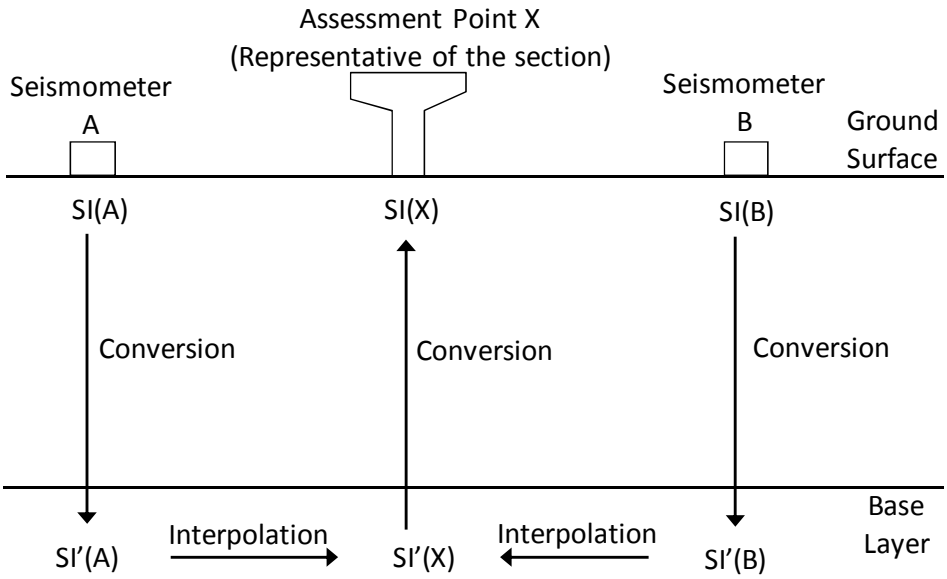


Figure 4. The conversion of SI between surface and base layer

### 2.4 *Fragility curve*

The fragility curves are shown in Figure 5 and Figure 6. The x-axis is EI in Figure 5 and SI in Figure 6, respectively. The data are plotted by the dynamic analysis of the reinforced concrete columns of the bridge structures. The damage probability is calculated by the number of the reinforced concrete columns that have the plastic response beyond the elastic response. The total number of the reinforced columns is 1425. The normal distribution function is applied to the fragility curve in case of EI. The log-normal distribution function is applied to the fragility curve in case of SI. In Figure 5 and Figure 6, the solid lines are average and the broken lines are the standard deviation $+\sigma$, $-\sigma$.

### 2.5 *Combination of the two damage probabilities*

Both EI and SI have the average value and standard deviation value in each section of the network, because the kriging method is used for the interpolation. The fragility curves have also the average and standard deviation. The damage probabilities are calculated by the superposition of the damage probability distributions corresponding to each EI or SI, shown in Figure 7. The normal distribution is assumed for the superposition of the damage probability distributions. Figure 8 shows the two damage probability distributions in case of both EI and SI. The combined damage probability is calculated by Equation 2.

$$\mu = \frac{\sigma_1 \mu_2 + \sigma_2 \mu_1}{\sigma_1 + \sigma_2} \tag{2}$$

Where $\mu$= the weighted average of damage probabilities, $\mu_1$= the average of damage probabilities of EI, $\mu_2$= the average of damage probabilities of SI, $\sigma_1$=the standard deviation of damage probabilities of EI, $\sigma_2$=the standard deviation of damage probabilities of SI.

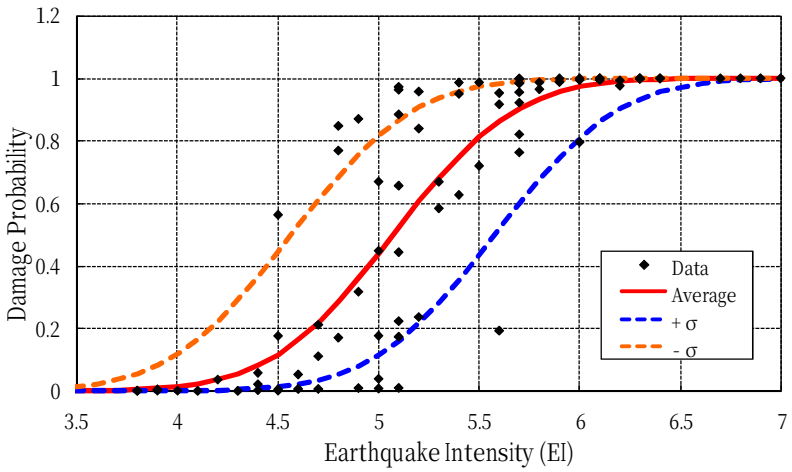


Figure 5. The fragility curve in case of EI

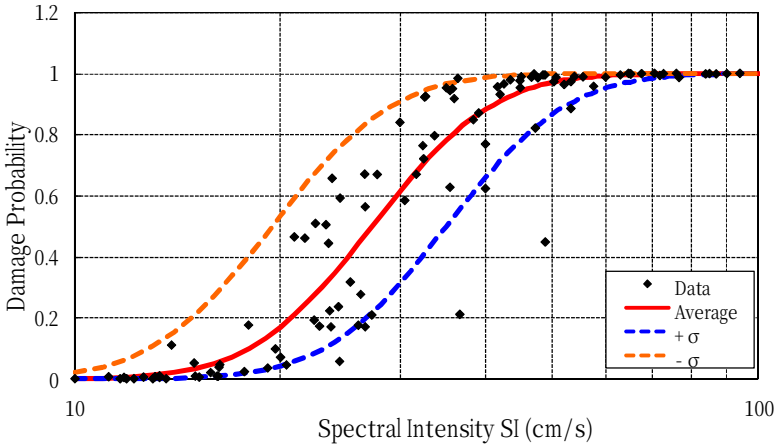


Figure 6. The fragility curve in case of SI

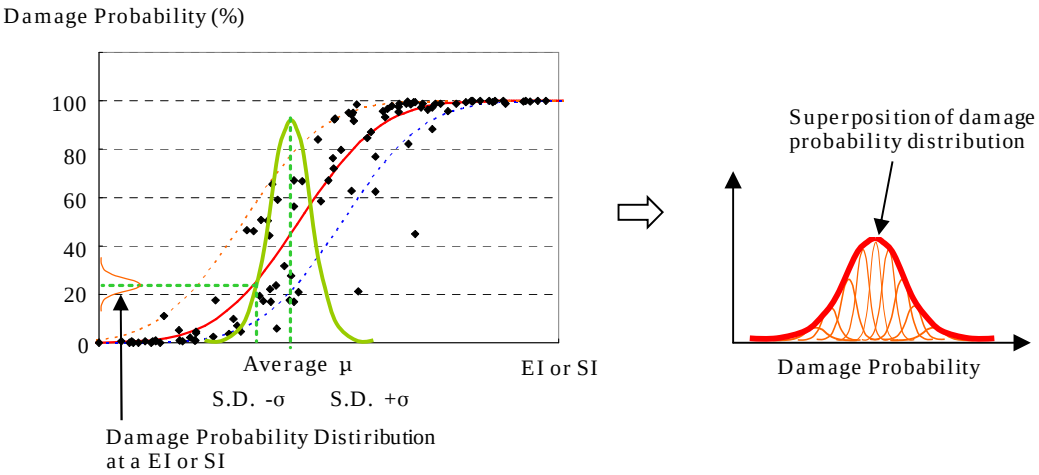


Figure 7. The calculation procedure of the damage probabilities from EI or SI

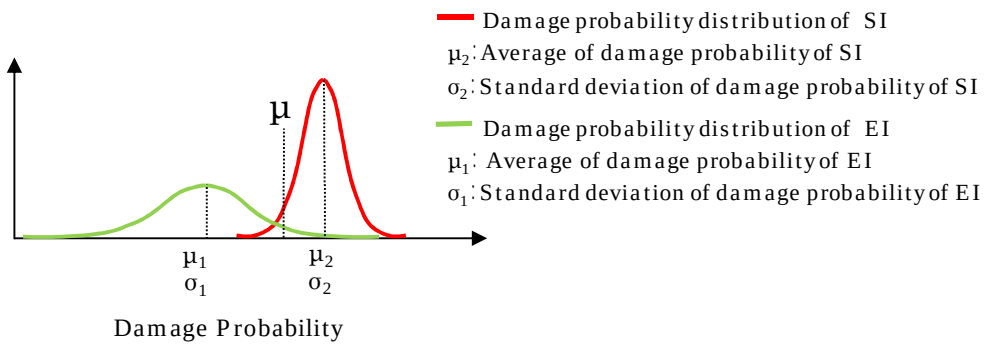


Figure 8. The damage probability distributions by EI and SI

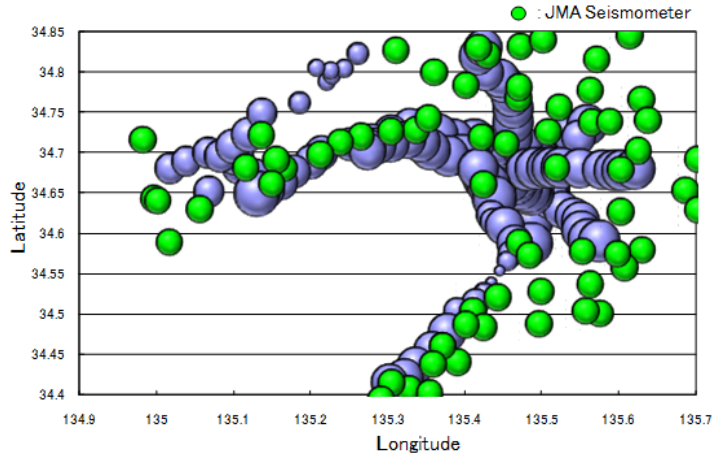


Figure 9. The average of EI by the kriging method

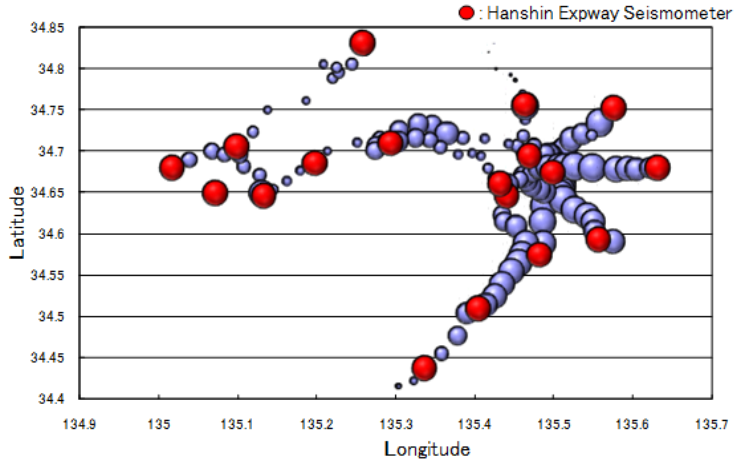


Figure 10. The average of SI by the kriging method

## 3 TRIAL CALCULATION

### 3.1 *Assumed earthquake*

The assumed earthquake for the trail calculation is brought about by Uemachi fault which runs north-south in the Osaka city area. The JMA magnitude is assumed to be 7.6.

### 3.2 *Average of EI and SI by the kriging method*

The averages of EI and SI by applying to the kriging method are shown in Figure 9 and 10, respectively. The locations of the JMA and Hanshin Expressway seismometers are also indicated in Figure 9 and 10. The bubble size stands for the average value.

### 3.3 *Average of the damage probability*

The average of the damage probabilities in case of both EI and SI are shown in Figure 11 and 12, respectively. Figure 13 shows the combined damage probabilities. The combined damage probabilities are thought to be more reliable than those of only EI or SI.

## 4 CONCLUSIONS

The earthquake damage estimating system of Hanshin Expressway has been developed. The system incorporates the spectral intensity (SI) from the Hanshin Expressway seismometers as well as the earthquake intensity (EI) from the JMA seismometers. The damage probabilities are estimated by the fragility curves for both SI and EI, respectively. The two damage probabilities are combined based on the reliability. The damage estimation is conducted by the combined damage probabilities. The trial calculation is conducted for the developed system.

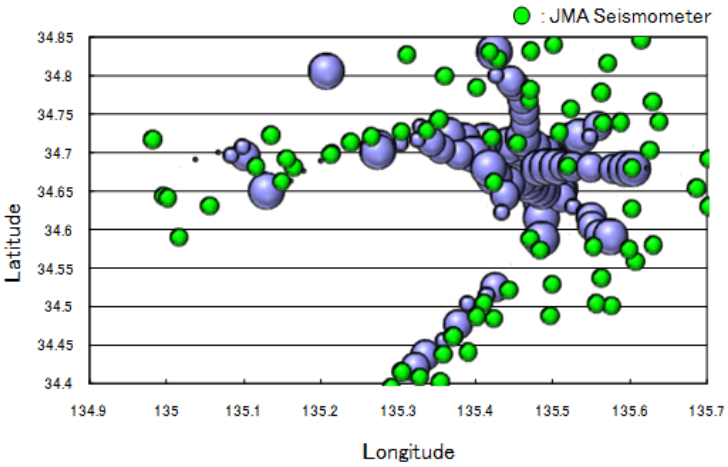


Figure 11. The average of the damage probabilities in case of EI

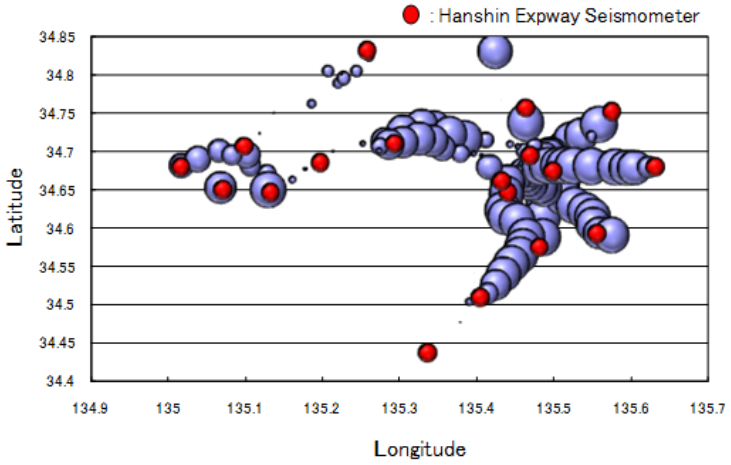


Figure 12. The average of the damage probabilities in case of SI

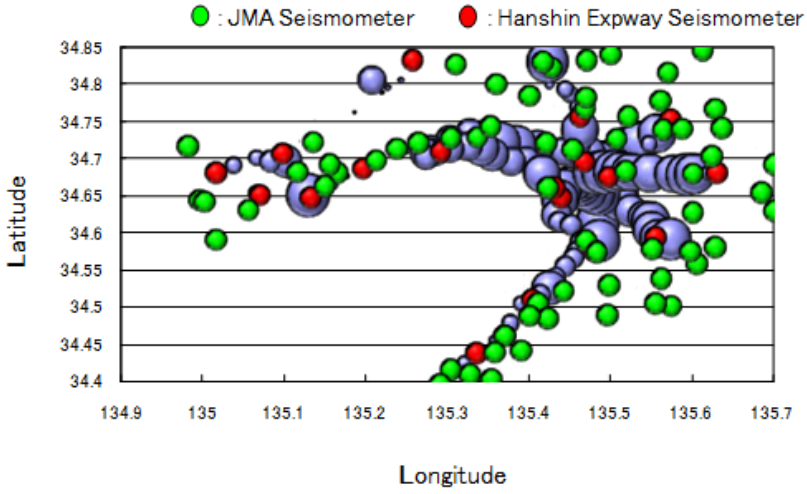


Figure 13. The combined damage probabilities of both EI and SI

# Historic Liquefaction Sites in Japan, 745–2008

K. Wakamatsu
*Kanto Gakuin University, Yokohama, Japan*

ABSTRACT: The locations of past liquefaction may be considered potential areas of liquefaction in future earthquakes. The author collected approximately 16,700 cases of liquefaction occurrence triggered by 150 Japanese earthquakes from 745 to 2008 and compiled into a book entitled "Map for historic liquefaction sites in Japan, 745–2008". In this book and its accompanying DVD-ROM, sites of liquefaction triggered by 150 earthquakes from 745 to 2008 are presented: the approximately 16,700 liquefied sites were listed and plotted onto 1:50000 scale topographic maps, and digitized into a GIS database. This paper presented the features of historic liquefaction occurrences in Japan based on the GIS database. They include: distribution of liquefied sites; recurrence of liquefaction at the same site; seismic intensity at liquefied sites; epicentral distance to the farthest liquefied sites; and geomorphologic conditions of liquefied sites. In addition liquefaction during the Tohoku earthquake of March, 11th 2011 is reported.

## 1 INTRODCTION

Liquefaction is known to occur repeatedly at the same site during more than one earthquake, as shown by examples from Japan, United States, and the Aegean region in Europe (e.g. Kuribayashi and Tatsuoka, 1975; Youd, 1984; Yasuda and Tohno, 1988; Wakamatsu, 1991; Papathanssiou et al., 2005). Thus, the locations of past liquefaction may be considered potential areas of liquefaction in future earthquakes. The author collected approximately 4000 cases of liquefaction occurrence triggered by 123 Japanese earthquakes from 863 to 1987 and in 1991 compiled a catalog and maps for liquefied sites (Wakamatsu, 1991). Since then, extensive liquefaction has been observed during more than a dozen earthquakes, including the 1995 Hyogoken-nambu (Kobe) earthquake. In addition, new data have been found on historical earthquakes that occurred before 1987. The author supplements the previous work by Wakamatsu (1991) with new data for the earthquakes since 1987 as well as for the earthquakes before 1987 and compiled a database and published as a book come with a DVD-ROM (Wakamatsu, 2011). In this book and its accompanying DVD-ROM, sites of liquefaction triggered by 150 earthquakes from 745 to 2008 are presented: the liquefied sites were listed and plotted onto 1:50000 scale topographic maps, and digitized into a GIS database.

## 2 HISTORIC LIQUEFACTION SITES

### 2.1 *Identification o liquefaction occurrences*

To search for records of liquefaction effects, various kinds of materials on earthquake damage, including reports, papers, web site contents, and ancient documents for all of Japan, were collected. Descriptions of liquefaction effects were picked up from these documents, and the sites where liquefaction took place were identified based on these descriptions. In addition, in several earth-

quakes the author conducted post-earthquake reconnaissance investigations, aerial photo interpretation, and interviews with local residents.

In the investigations, occurrences of liquefaction were identified by observed sand and water boiling and/or floating up of buried structures; fissures, lateral spreading, ground subsidence, and settlement of structures without sand and/or water boiling were excluded from the evidence of liquefaction effect. Figure 1 shows the oldest visual evidence of liquefaction which is appeared in the earthquake damage report on the earthquake of December 23, 1855. The caption says "A large earthquake attacked Suruga (present-day Shizuoka Prefecture) and sand and water were boiling"

Figure 1 Old print showing liquefaction during the Tokai earthquake of December 23, 1855

### 2.2 *Earthquakes that caused liquefaction*

Up to the present, approximately 1000 destructive earthquakes have been documented in various kinds of historical materials and seismic data in Japan (Usami, 2003). The oldest is the earthquake of August 23, 416, which was documented in the “Nihon Shoki”, an authorized historical document of Japan. The 1000 earthquakes that took place between 416 and 2008 in Japan were investigated in this study.

The investigation revealed that a total of 150 events have induced liquefaction at 16,688 sites between 416 and 2008, including the original 123 earthquakes previously presented by Wakamatsu (1991). The JMA (Japan Meteorological Agency) magnitude, *M*, of the earthquakes that induced liquefaction ranges from 5.2 to 8.6. The oldest event that was identified to have induce liquefaction is the earthquake in 745 that occurred in Gifu Prefecture, located in the central part of the main island of Japan; the most recent one is the Iwate-Miyagi Nairiku earthquake of June 14, 2008, which attacked southwestern Iwate Prefecture and northwestern Miyagi Prefecture in the northern part of the main island of Japan. Since 1885, when systematic earthquake observation began in Japan, 90 earthquakes have generated liquefaction. Thus liquefaction has occurred approximately 7 times in every decade somewhere in Japan during the last 125 years.

### 2.3 *Distribution of liquefied sites*

Information on a total of 16,688 liquefaction sites is listed as in order of the date of occurrence in the catalog of liquefied sites. It includes 32 items such as geographic name, the coordinates where liquefaction occurred, references to the liquefaction occurrence, earthquake source parameters, etc. In Figure 2, distribution of the liquefied sites during the 150 earthquakes is shown. Liquefaction phenomena are observed in most parts of Japan. Except in a few cases, the liquefied sites are located in low-lying areas whose subsurface ground consists of Holocene deposits or artificial fills.

Regional liquefaction distribution maps are prepared for the following 17 areas where liquefied sits are densely distributed: southeastern Hokkaido, southwestern Hokkaido, eastern Aomori

prefecture, western Aomori and Akita prefectures, southern Akita and western Yamagata prefectures, Sendai area, Niigata area, Toyama area and Noto peninsula, Nagano area, Fukui and Kanazawa areas, Kanto area, Nobi and Tokai areas, Kobe and Osaka areas, Okayama area, Hiroshima area, Tottori and Shimane areas, and Fukuoka area. In these maps, liquefied sites are plotted on 1:200,000 scale topographic maps. An example of the regional distribution maps for Kanto area is shown in Figure 3.

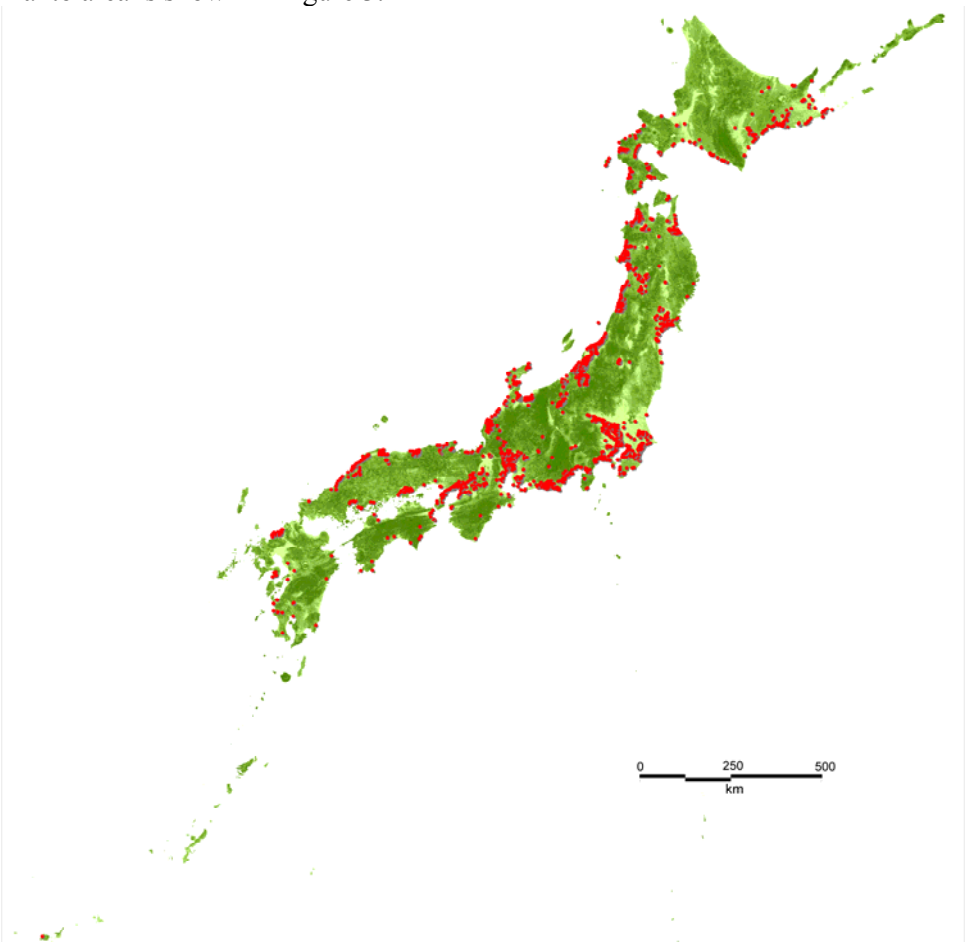


Figure 2 Distribution of liquefied sites during the earthquakes from 745 to 2008 (Wakamatsu, 2011)

All of the liquefied sites which could be identified by the locations where liquefaction occurred are plotted on 371 sheets of 1:50,000 scale topographic maps. Figure 4 shows an example of detailed distribution map of the liquefied sites. In the detailed liquefaction map, the liquefied sites are plotted by different symbols and colors for every earthquake, as shown in Figure 4. The sizes of the symbols such as hollow triangles and squares indicate the degree of certainty of locations of the liquefied sites: the large symbols correspond to sites which were identified by the name of a town or village -- i.e., the description was not precise enough to locate the exact liquefied site; the medium-sized symbols correspond to sites which are specified by the name of a section or a small village; and the small symbols correspond to sites which are specified by the name of a block. In contrast, the polygons represent the exact area of liquefaction specified on the basis of detailed surveys by site reconnaissance and/or the interpretation of aerial photographs taken immediately after the earthquake. The dots indicate the sites which were pinpointed as the exact locations of liquefaction.

All the liquefaction data were digitized into a GIS database. The data files are included on the DVD-ROM together with pdf files for 371 sheets of detailed liquefaction maps, and 17 sheets of regional maps, and catalog of 16,688 liquefied sites.

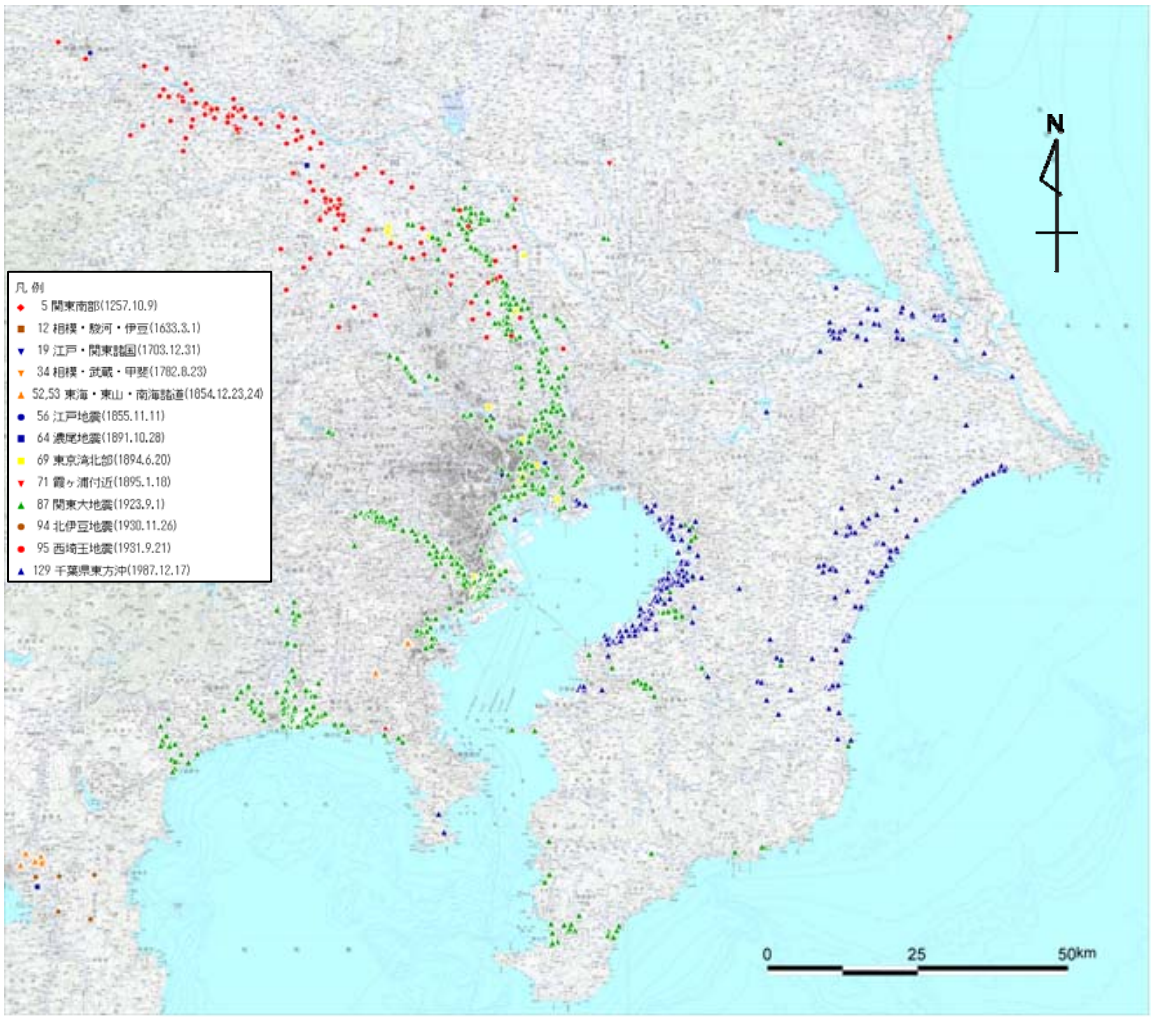

Figure 3 Distribution of liquefied sites in Kanto area (Wakamatsu, 2011)

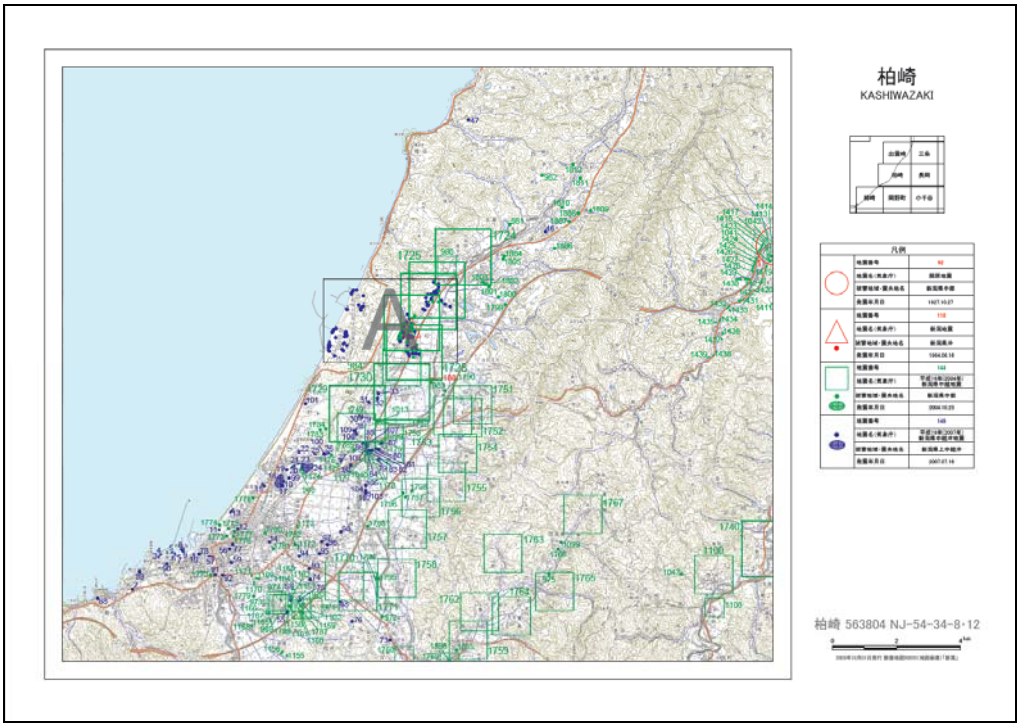

Figure 4 Detailed distribution map of the liquefied sites (Wakamatsu, 2011)

## 3 RECURRENCE OF LIQUEFACTION AT THE SAME SITE

Recurrence of liquefaction at the same site is indentified at 150 sites throughout Japan. The distribution of the re-liquefied sites is shown in Figure 5. Most of the sites are located in the north-eastern half of Japan. This may be explained by the fact that destructive earthquakes occurred repeatedly in recent years in these areas.

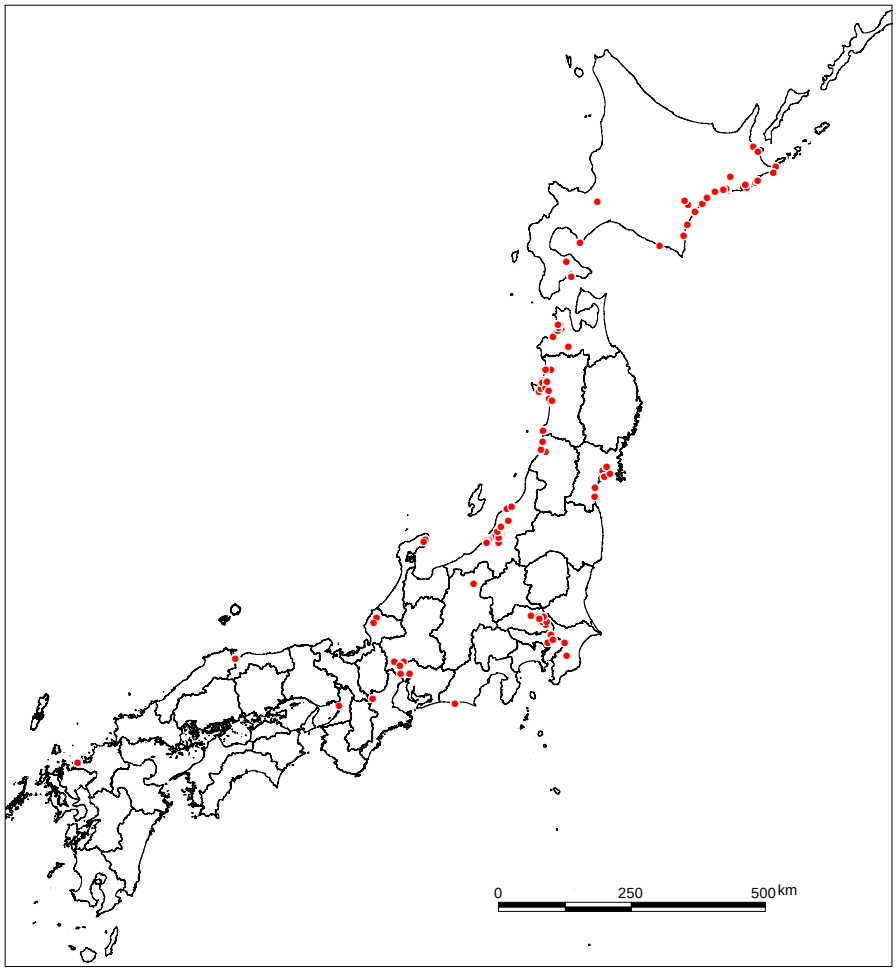


Figure 5 Distribution of re-liquefaction sites during successive earthquakes (Wakamatsu, 2011)

## 4 SEISMIC INTENSITY AT LIQUEFIED SITES

The extent of liquefaction in a susceptible area can be easily estimated for an earthquake based on seismic intensity if a correlation is established between past liquefaction occurrences and seismic intensity (TC4 ISSMGE, 1999). Figure 6 shows an example of the distributions of liquefied sites and JMA instrumental seismic intensities compiled by JMA. The instrumental intensity is calculated from acceleration time histories in three directions, which began to be used after October 1996 in Japan. The relationships between past liquefaction occurrences and seismic intensity were investigated for the earthquake occurred after 1996. The result show that most of the liquefied sites in each earthquake are located within the zones of JMA intensity 5 (upper) and greater; however, minor sites of liquefaction occurred at intensities of 5 (lower) or 4. All of the sites where liquefaction occurred at less than intensity 5 (upper) are artificial ground such as landfill, fill on paddy field, or backfill of excavated ground.

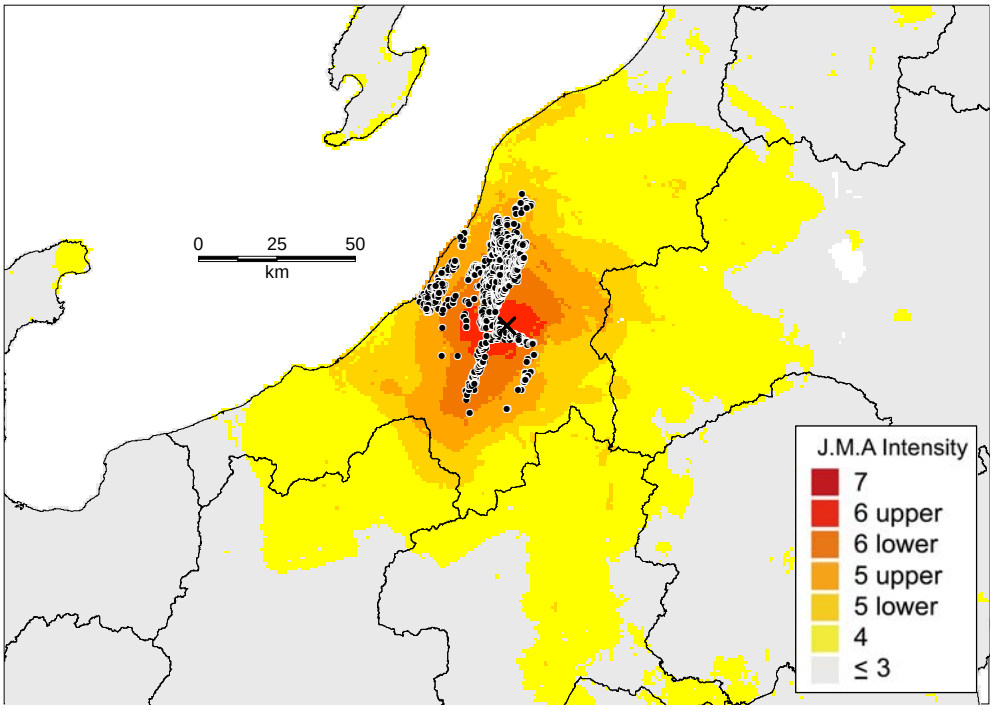

Figure 6 Example of distributions of liquefied sites and estimated JMA seismic intensity (courtesy of JMA) during the 2004 Niigata-ken Chuetsu earthquake (Wakamatsu, 2011)

## 5 EPICENTRAL DISTANCE TO THE FARTHEST LIQUEFIED SITES

If earthquake activity in an area is known from historic seismic data, the maximum extent of the area susceptible to liquefaction can be estimated directly from the magnitude of the predicted earthquake (TC4 ISSMGE, 1999). Several investigators have analyzed the distribution of liquefaction during past earthquakes and have compared the distance from the epicenter to the farthest liquefied site, $R$, with the earthquake magnitude, $M$. For example, Kuribayashi and Tatsuoka (1975) have shown, for 32 historic Japanese earthquakes, that the farthest epicentral distance to a liquefied site, $R$ in km, is bounded by a straight line on a magnitude-versus-logarithm-of-distance plot, which can be expressed as follows:

$$\text{Log } R = 0.77M - 3.6 \quad (M \geq 6) \quad \cdots\cdots\cdots\cdots\cdots\cdots\cdots\cdots (1)$$

where $M$ is the earthquake magnitude as defined using the Japan Meteorological Agency (J.M.A.) scale.

The work of Kuribayashi and Tatsuoka (1975) was supplemented by Wakamatsu (1991) with new data from 67 Japanese earthquakes over the past 106 years, including the original 32 earthquakes studied by Kuribayashi and Tatsuoka (1975). As a result of this study, Wakamatsu proposed an upper bound relationship between $M$ and $R$ as follows:

$$\text{Log } R = 2.22 \log (4.22M - 19.0) \quad (5 \leq M \leq 8.2) \quad \cdots\cdots\cdots\cdots (2)$$

Figure 7 shows the relationship between JMA earthquake Magnitude and the liquefaction sites farthest from the epicenter during 88 earthquakes whose focal parameters are reliable, together with the upper bound which is given by Eq. (2). The data of Surugawan earthquake of August 11, 2009 with a JMA magnitude of 6.5 and Tohoku Pacific earthquake of March 11 with a moment magnitude of 9.0 are added. The updated data are almost within the upper bound denoted by a solid line given by Eq. (2). This relationship can be used to predict the maximum range of liquefaction for a particular magnitude of earthquake in areas underlain by liquefiable Holocene sediments.

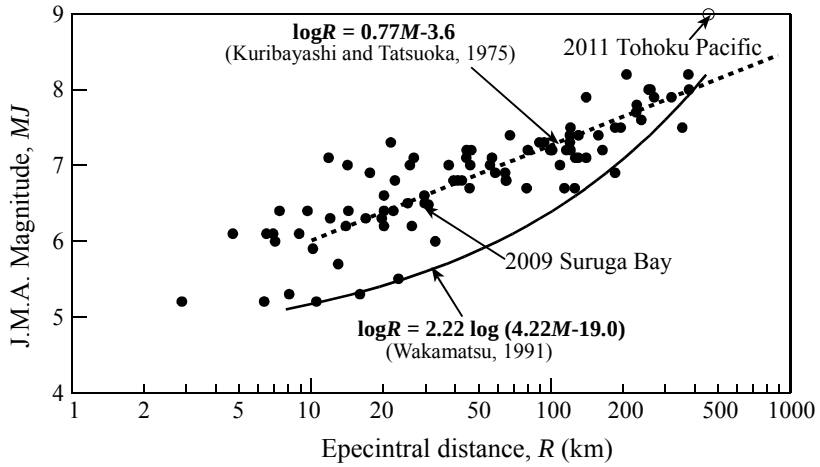


Figure 7 Epicentral distance to the farthest liquefied sites, *R*, in km for JMA magnitude *M* (modified from Wakamatsu, 2011)

## 6 GEORMORPHOLOGIC CONDITIONS OF LIQUEFIED SITES

Figures 8 and shows distributions of liquefied sites and geomorphologic land classification in the Kanto area including Tokyo metropolitan, which is the largest plain in Japan. Liquefied sites are located in reclaimed land areas and Holocene low-lying areas such as deltas, natural levees, back marshes, alluvial fans and coastal sand dunes.

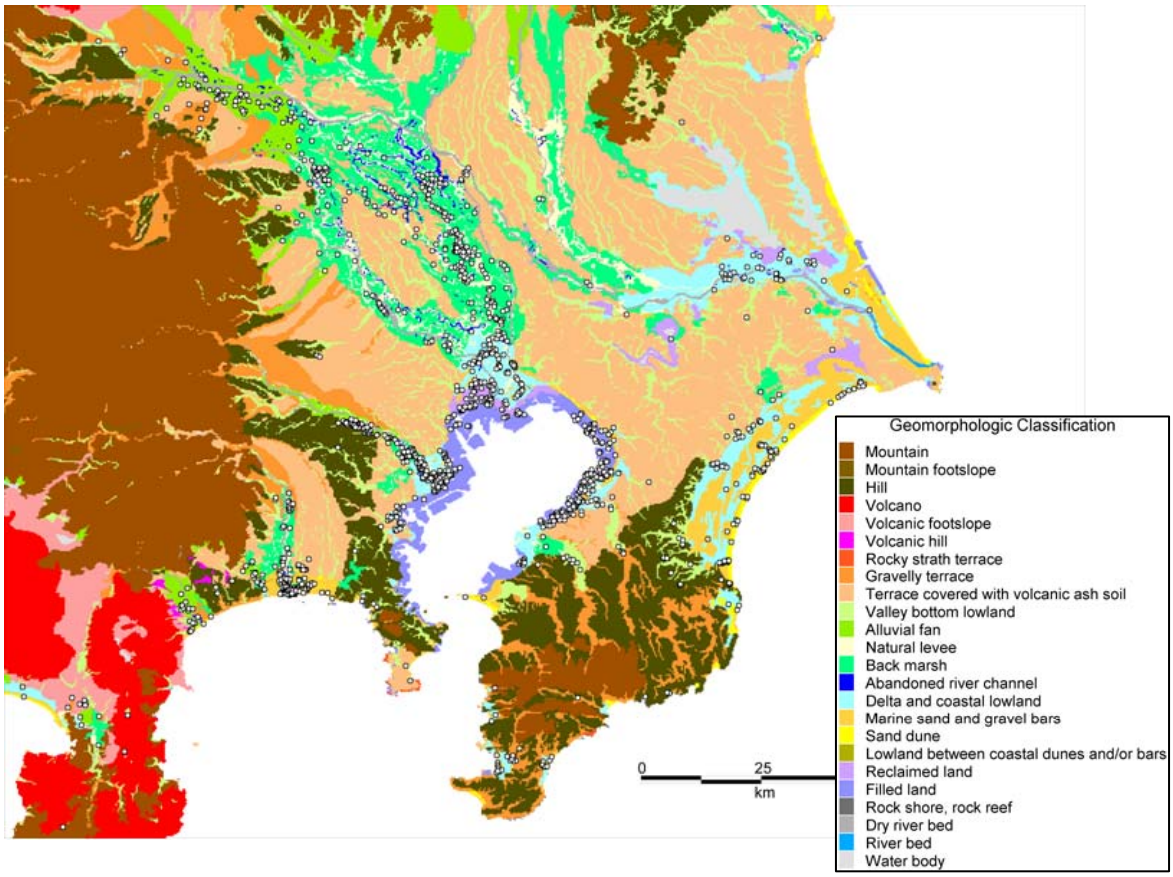


Figure 8 Distributions of liquefied sites and geomorphologic land classification in Kanto area. Hollow circles show liquefied sites. (Wakamatsu, 2011)

Based on the approximately 16,700 case histories presented in Wakamatsu (2011), the sites with the following conditions are the most easily liquefiable under smaller ground shaking:

1) Recently filled or reclaimed land
2) Former river channels
3) Flood-prone areas along large rivers
4) Skirts of coastal sand dunes and lowlands between dunes
5) Backfilled land after digging
6) Filled areas across streams in hilly areas
7) Land where liquefaction occurred during a past earthquake

## 7 LIQUEFACTION DURING THE 2009 AND 2011 EARTHQUAKES

After the completion of the liquefaction distribution maps and GIS database for earthquakes until 2008, liquefaction was triggered by the Suruga Bay earthquake of August 11, 2009, with a JMA magnitude of 6.5 and the Tohoku Pacific earthquake of March 11, 2011 with a moment magnitude of 9.0. Epicentral distance to the farthest liquefied sites is 32.6 km for the 2009 earthquake and approximately 442 km for the 2011 earthquake, respectively. These distances are plotted on Figure 7.

Liquefaction caused by the 2009 earthquake is local in a minority, but that by the 2011 earthquake is widespread; 500 km from north to south in vast numbers. Figure 9 shows locations of the municipalities (cities, special wards, towns, and villages) where liquefaction was observed. The liquefaction occurred at many sites in Kanto area including Tokyo Bay area which largely composed of low-lying area and fill-up land.

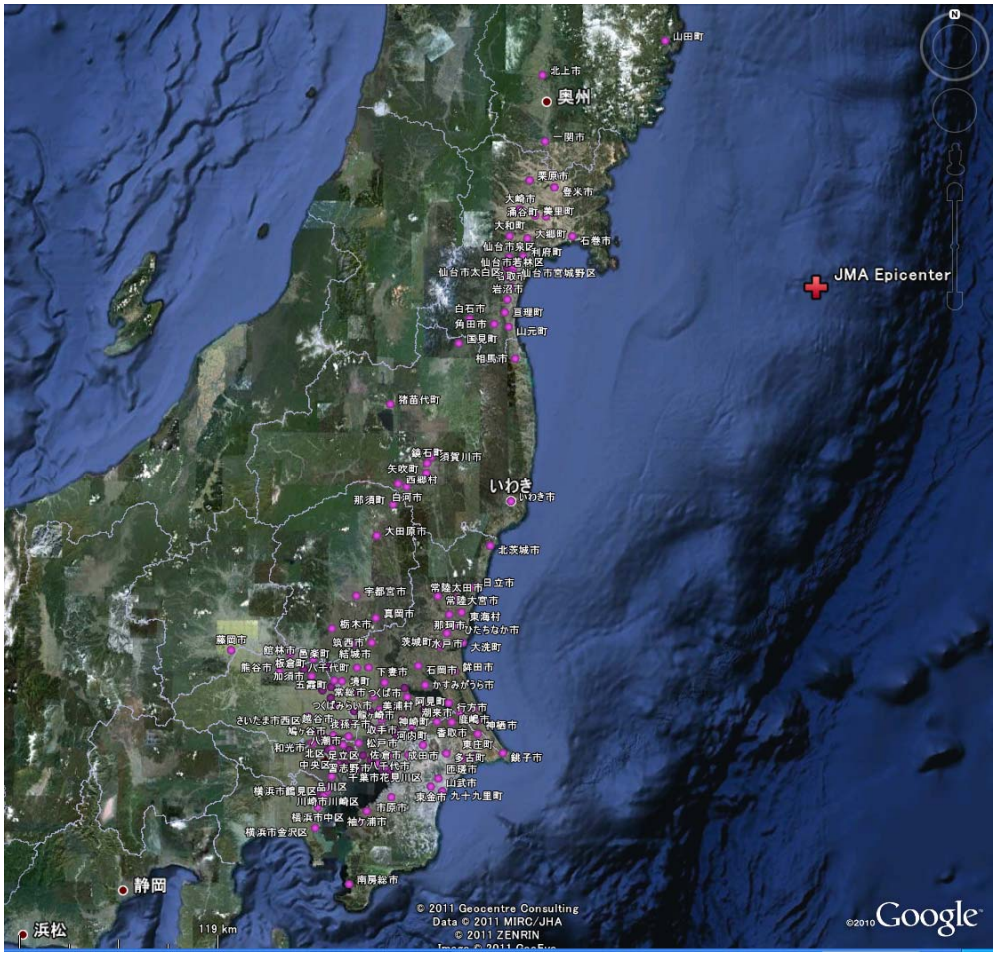

Figure 9 locations of the municipalities where liquefaction was observed

Re-liquefaction is identified at approximately 80 sites in Kanto and Tohoku areas during the 2011 Tohoku Pacific earthquake. Figure 10 is an example of re-liquefaction.

(a) 1987 Chiba-ken toho-oki earthquake (b) 2011 Tohoku Pacific earthquake

Figure 10 Liquefaction at same sites during the 1987 and 2011 earthquakes (Inashiki city, Ibaraki Prefecture)

## 8 CONCLUDING REMARKS

Historic liquefied sites induced by the past earthquakes since the year 416, when earthquake damage has been documented in Japan, were investigated for all of Japan and mapped and digitized into a GIS database. The investigation revealed that: a total of 150 events with magnitudes ranging from 5.2 to 8.6 have induced liquefaction from 745 to 2008; approximately 16700 sites of liquefaction appeared in most parts of Japan due to the earthquakes; most of them are located on low-lying areas underlain by liquefiable Holocene sediments and artificial fills; and the liquefaction was induced by seismic shaking with an intensity of 5 (upper) and greater on the JMA scale. The relationship between JMA earthquake Magnitude and the liquefaction sites farthest from the epicenter during 88 earthquakes and additional 2 earthquakes occurred after 2009 whose focal parameters are reliable was investigated. The updated data by this study are almost within the upper bound relationship between $M$ and $R$ proposed by Wakamatsu (1991).

## REFERENCES


Kuribayashi, E. and Tatsuoka, F. 1975. Brief Review of Soil Liquefaction during Earthquakes in Japan, Soils and Foundations, 15, 4, pp. 81-92.

Papathanssiou, G., Pavides, S., Christras, B. and Pitilakis K. 2005. Liquefaction Case Histories and Empirical Relations of Earthquake Magnituide versus Distance from the Broader Aegean Region, Geodynamics, 40, pp. 257-278.

The Technical Committee for Earthquake Geotechnical Engineering, TC4, of the International Society for Soil Mechanics and Geotechnical Engineering 1999. Manual for Zonation on Seismic Geotechnical Hazards Revised Version., The Japanese Geotechnical Society, 209 pp.

Usami, T. 2003. Materials for Comprehensive List of Destructive Earthquakes in Japan, 416-2001, Univ. of Tokyo Press. 605 pp. (in Japanese).

Wakamatsu, K. 1991. Maps for Historic Liquefaction Sites in Japan, Tokai University Press, Tokyo, 341 pp. (in Japanese with English abstract).

Wakamatsu, K. 2011. Historic Liquefaction Sites in Japan, 745–2008, with DVD-ROM University of Tokyo Press, 88pp. (in Japanese with English abstract and manual).

Yasuda, S. and Tohno, I. 1988. Sites of Reliquefaction Caused by the Nihonkai-Chubu Earthquake, Soils and Foundations, Vol. 28, No.2, pp. 61-72.

Youd, T.L. 1984. Recurrences of Liquefaction at Same Site, Proc., 8th World Conf. on Earthquake Engineering, San Francisco, 3, pp. 231-238.

# Physical Meaning of Phase in Earthquake Motions

T. Sato
*Kobegakuin University, Japan and South East University, China*

ABSTRACT: The purpose of this research is to make clear the phase spectrum characteristic of earthquake motion. After the introduction of past researches we introduce the concept of fractional Brownian process (FBP). A simple method is proposed to determine the Hurst index and the variance of a given process characterized by the FBP. We find that the phase characteristic of earthquake motion can be expressed by this process expressing as a function of the circular frequency. Using several observed earthquake motion we demonstrate this fact and show the efficiency of newly founded result by simulating realistic earthquake motion phase and also compare simulated earthquake motions with those of observed ones. We also simulate design response spectrum compatible earthquake motions

## 1 INTRODUCTION

### 1.1 *Demonstration of importance of phase spectrum to simulate earthquake motions*

To simulate time histories of signals such as earthquake motions we need information on Fourier amplitude and phase spectra. There have been many researches to simulate non stationary time histories based on Fourier analysis [1], Wavelet analysis [2] and time-frequency analysis [3]. But almost all researches have paid attention only to the non-stationary characteristics of amplitude spectrum and less interest in the phase spectrum. Fig.1 shows an example to demonstrate importance of phase spectrum. The upper and bottom figures are the velocity time histories of observed earthquake motions at the Meteorological observatories of Kobe during the 1995 Kobe earthquake and that of Kushiro during the 1994 Off Kushiro earthquake, respectively. The middle figure is a recomposed velocity time history using Kushiro Fourier amplitude spectrum and Kobe Fourier phase spectrum. Because Kushiro earthquake motion contains high frequency components its time history fluctuates with high frequency but arrival times of its peak and trough almost same as the Kobe record. From this figure it is easily recognize the importance of phase

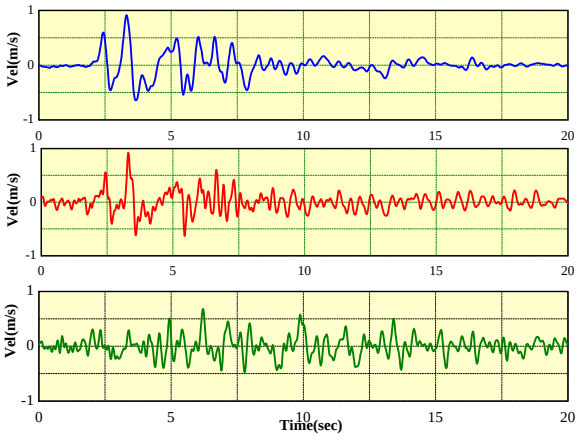


Figure 1. Velocity time histories of earthquake motions. **Upper** Kobe record; **Bottom** Kushiro record; **Center** Amplitude from Kushiro and phase from Kobe

spectrum to simulate an earthquake motion.

### 1.2 *Importance of earthquake motion phase for design purpose*

The response spectrum defined in a code plays essential roles in the seismic design of structural systems. To use the response spectrum we have to simplify the target structural system, it is usually necessary to check seismic performance of the designed structural system by a dynamic response analysis. Because the response spectrum gives us a sort of amplitude characteristic we have to set the phase spectrum to simulate a response spectrum compatible earthquake motion. There are no reasonable simulation models of the phase spectrum it is recommended to use typical observed earthquake motion phase spectra in usual seismic design codes. Fig.2 shows examples of response spectrum compatible earthquake motions. The response spectrum used here is defined in the seismic design code of railway facilities in Japan, the spectrum I [4] which is defined for the inter plate earthquake motions. The upper and lower charts are simulated acceleration time histories using Kobe and Kushiro record phase spectra, respectively. Although the response spectrum is the same the simulated time history characteristics are totally different.

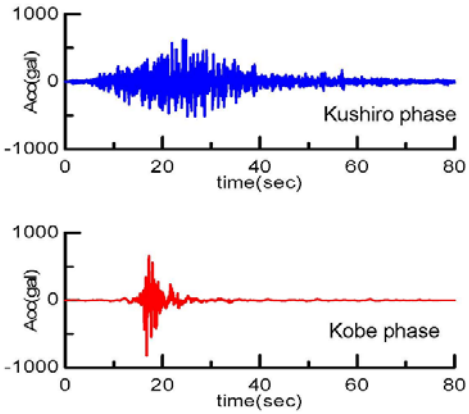


Figure 2. Response spectrum compatible earthquake motions. **Upper:** Using Kushiro phase; **Bottom:** Using Kobe phase

Those differences are especially important to evaluate nonlinear dynamic performance of a structure. Fig.3 compares the yield acceleration demand nonlinear response spectrum (YADRS) calculated by using both time histories for the case of structural ductility factor being fixed as 4. The abscissa is the natural period of the structure calculated by the initial stiffness of the force-deformation relation. The ordinate is the yield acceleration which is defined by the yield strength of the structure divided by structural mass. We assume the Clough type of force-deformation characteristic in dynamic analysis. From this figure it is clearly seen that YADRS is strongly affected by the phase spectrum of earthquake motion. The value of YADRS at the natural period of 0.8 sec for the case of Kobe phase spectrum is 350 gal but 250gal for the case of Kushiro phase spectrum. From these examples it can be seen that the modeling of the phase spectrum of earthquake motion is essential for seismic design of structures taking into account the nonlinear behavior of structures.

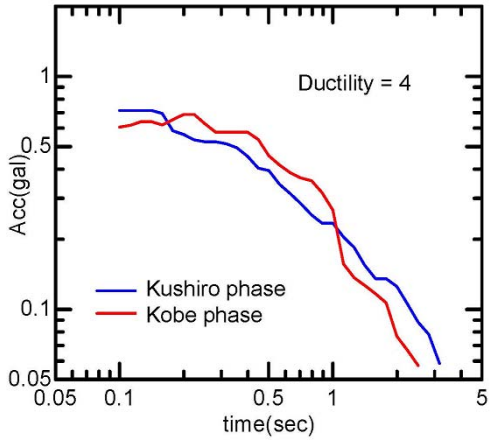


Figure 3. Yield acceleration demand nonlinear response spectra for a structure by keeping the ductility being equal to 4

### 1.3 *Past researches on phase modeling of earthquake motions*

After the pioneering work done by Osaki to investigate the phase characteristic by using phase difference concept [5] several efforts to model the Fourier phase spectrum have been conducted by mainly Japanese researchers [6,7,8]. The modeling of the phase spectrum using the group delay time (GDT; the first order derivative of the phase spectrum with respect to circular frequency) concept has attracted researchers interest, such as defining the probabilistic distribution

characteristic of GDT [8] and an attempt to seek a possibility for simulating GDT by using the stochastic differential equation [9] as well as an effort to identify the coefficients of the stochastic deferential equation as functions of the earthquake magnitude, epicenter distance and local soil conditions [10]. The mean value of GDT represents the arrival time of the main energy of earthquake motion and the standard deviation of GDT gives us the information on the duration of earthquake motion. Those values are modeled as functions of the earthquake magnitude, epicenter distance and local soil conditions [11], even the effect of the rupture directivity being included [12]. In those analyses we used the Meyer's band pass filters which satisfy the orthogonal condition among filters [2]. We also assumed that the mean and standard deviation values of GDT have constant values with in each frequency band, therefore these values are also defined as functions of the center circular frequency of each band pass filter. To simulate GDT we need not only the mean and standard deviation but also the stochastic characteristic of GDT. The main purpose of this research is therefore to make clear the stochastic characteristic of GDT and its physical background.

## 2 RESEARCH BACKGROUND

### 2.1 *Questions raised so far to model phase spectrum of earthquake motion*

Fourier transformation of real time function $f(t)$ is defined by

$$F(\omega) = R(\omega) + iI(\omega) = \int_{-\infty}^{\infty} f(t)\exp(-i\omega t)dt \tag{1}$$

in which $\omega$ is the circular frequency, $R(\omega)$ and $I(\omega)$ are real and imaginary parts of Fourier transform of $f(t)$. The Fourier amplitude and phase as well as the GDT are defined by

$$A(\omega) = \sqrt{R(\omega)^2 + I(\omega)^2} \quad \phi(\omega) = \tan^{-1}\left(\frac{I(\omega)}{R(\omega)}\right) \quad \xi(\omega) = \frac{d\phi(\omega)}{d\omega} = \frac{I'R - R'I}{R^2 + I^2} \tag{2}$$

in which $A(\omega)$ is the Fourier amplitude, $\phi(\omega)$ the Fourier phase and $\xi(\omega)$ the GDT, $(\ )' = d(\ )/d\omega$.

In our former research the distribution of GDT in each frequency band was assumed to be expressed by the Gaussian distribution. Fig.4 is an example verifying this hypothesis by using GDT calculated from an observed earthquake motion. The first question raised is that the independently generated Gaussian samples between discrete circular frequencies are acceptable or not for simulating GDT. Because the sampled GDT should not be influenced by the discretized interval of circular frequency a simple correlation function of GDT in the circular frequency region was proposed as shown in Fig.5. This modeling of GDT is simply summarized as follows:

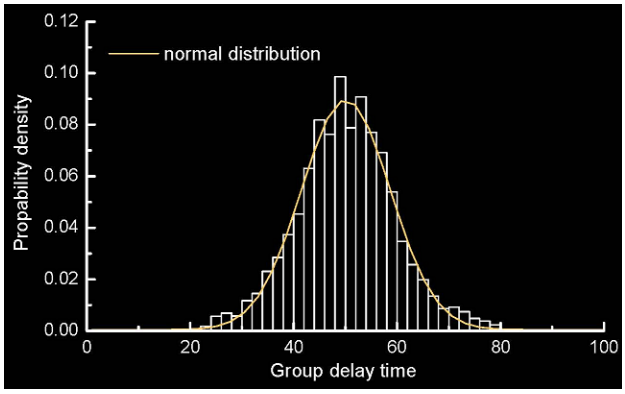


Figure 4. An example of group delay time distribution in a certain frequency range of Meyer wavelet sets.

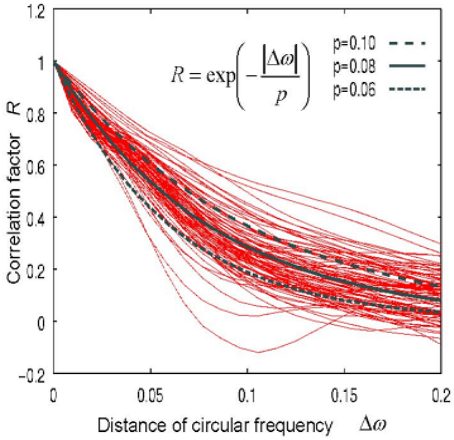


Figure 5 Frequency correlation of group delay time

If the number of discrete points is *n* in the circular frequency domain the probability density function of the discrete group delay time vector $\mathbf{y}$ composed of *n* components is expressed by the following equation

$$p(\mathbf{y}) = \frac{1}{\sqrt{(2\pi)^n |\mathbf{R}|}} \exp\left\{ -\frac{1}{2} (\mathbf{y} - \bar{\mathbf{y}})^T \mathbf{R}^{-1} (\mathbf{y} - \bar{\mathbf{y}}) \right\} \tag{3}$$

in which $\mathbf{y} = (\xi_1, \xi_2, ..., \xi_n)^T$, $\xi_i$ is the group delay time at the discrete point $i$, $\bar{\mathbf{y}} = (\bar{\xi}_1, \bar{\xi}_2, ..., \bar{\xi}_n)$ which defines the mean vector of $\mathbf{y}$, $\bar{\xi}_i$ the mean GDT at the discrete point $i$, $\mathbf{R}$ is the covariance matrix of the discrete GDT. This formula is simple for simulating the GDT but to investigate its stochastic characteristics on dynamic behavior of structural systems the formula expressed by state system transfer equation is much easer to treat. We therefore proposed the following formula expressed by a stochastic differential equation [10]

$$d\xi(\omega) = c_1(\omega)\xi(\omega) + c_2(\omega) + \{\sigma_1 \xi(\omega) + \sigma_2(\omega)\} dW_\omega \tag{4}$$

in which $c_1(\omega)$ and $c_2(\omega)$ are parameters controlling deterministic part of GDT, $\sigma_1(\omega)$ and $\sigma_2(\omega)$ parameters controlling stochastic part of the GDT, $W_\omega$ the Wiener process.

The final target of present research is to make clear the physical meaning of GDT for simulating phase. So far we have not found any cues on the relationship between two GDT models but we could propose here a new idea possible to detect physical meaning of the Fourier phase characteristic of earthquake motion.

## 2.2 *Self Affine Fractal*

Before defining the self affine fractal we need the Wiener process $W(t)$ which is characterized by the following three properties

1. The initial value is equal to zero, $W(0) = 0$.
2. Almost surely (with probability =1) continuous function with respect to $t$.
3. $W(t)$ has independent increment, and the stochastic characteristic of $W(t) - W(s)$ is expressed by the Normal distribution of $N(0, t-s)$ for independent $s$ and $t$ satisfying $0 \le s < t$.

If we put $T = t - s$ and $\Delta W = W(t) - W(s)$ then the probability density function of $\Delta W$ is given by

$$p(\Delta W) = \frac{1}{\sqrt{2\pi T}\sigma} \exp\left( -\frac{\Delta W^2}{2T\sigma^2} \right) \tag{5}$$

in which $\sigma^2$ is the parameter controlling the variance of $\Delta W$. Form this formula it can be seen that if $T$ is scaled to $cT$ then the scale factor of $\Delta W$ becomes $c^{\frac{1}{2}}$. The phenomenon possessing this kind of similarity, scaling factors are different in different direction, is called as the affine fractal. The Weiner process is a special case of the affine fractal. We have to introduce the Hurst index [13] defined by $H$ to define the general affine fractal. This index is defined within the range of $0 \le H \le 1$. Using this value we can introduce the generalized Weiner process [14] as follows

$$W_H(t) - W_H(0) = \frac{1}{\Gamma\left(H + \frac{1}{2}\right)} \int_{-\infty}^{t} K(t-\tau) dW(\tau) \tag{6}$$

in which $W(\tau)$ is the Weiner process defined by Eq.(5), $W_H(0)$ a given initial condition, $\Gamma(t)$ Gamma function defined by $\Gamma(t) = \int_0^\infty \exp(\tau)\tau^{t-1} d\tau$, the integral kernel $K(t\text{-}\tau)$ is given by

$$K(t-\tau) = \begin{cases} (t-\tau)^{H-1/2} & (0 \le \tau \le t) \\ (t-\tau)^{H-1/2} - (-\tau)^{H-1/2} & (\tau < t) \end{cases} \tag{7}$$

Based on this definition the stochastic variable $W_H(t)$ depends on all the past Weiner process increment $dW(\tau)$. This process called a by name of the fractional Brownian process

(FBP). The mean of this process is zero but the variance and the correlation function $R(t)$ of this process are defined by [15]

$$E\left[\left(W_H(t)-W_H(s)\right)^2\right]\cong|t-s|^{2H} \tag{8}$$

$$R(t)=2^{2H-1}-1 \tag{9}$$

For the case of $H=\frac{1}{2}$, the special case of the Weiner process, the correlation function becomes zero which satisfies the condition 3 to compose the Weiner process. But for the case of $H\neq\frac{1}{2}$ the correlation function has a constant value which means the all process form the past to the future correlated no fading effect based on the distance.

It is not convenient for simulating the fractional Brownian process by directly using Eq.(6). A simple and more efficient algorithm was proposed to simulate a discrete sample process by Voss [15]. Fig.6 shows simulated fractional Brownian process with different Hurst indexes. As the Hurst index becomes large the fluctuation of the process reduces.

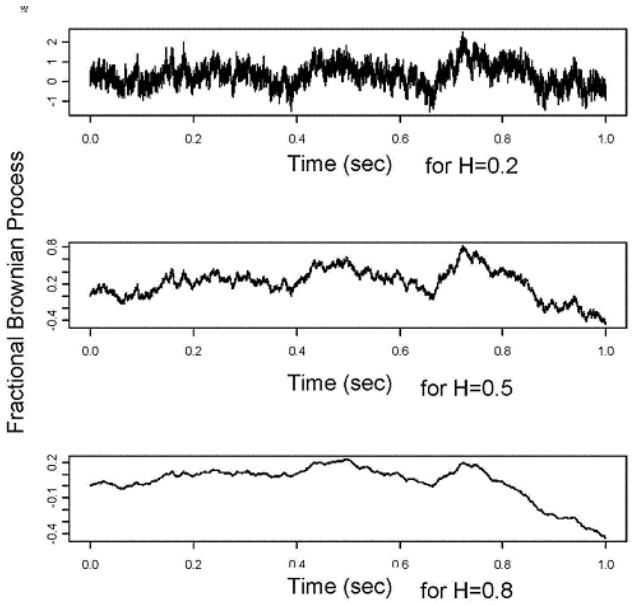


Figure 6. Examples of fractional Brownian processes for the cases of H=0.2, H=0.5 and H=0.8. The case of H=0.5 becomes the Wiener process

## 2.3 *Method to detect the Hurst index from a given signal*

The simple way to detect the value $H$ is to collect many signals and calculate the ensemble average of $\left(W_H(t_i)-W_H(0)\right)^2$ for different $t_i$ then using an appropriate method, such as the least square method, to determine the value of $H$. For the case that we can not get no more than one process of signal we can determine the value of $H$ from the data set of keeping the difference $t_i=t-s$ being a constant and shifting $t$ and $s$ in the signal range and calculating the ergodic average of $\left(W_H(t)-W_H(s)\right)^2$ for many $t_i$. Figs.6 and 7 are comparison of both methods for the case of $H=0.8$. In the both figures the circles are data obtained from samples and the full line is the leas square fitting. Fig.6 was obtained by the ensemble averaging method using 200 signals with identified vale of $H=0.805$ and Fig.7 was by the ergodic averaging method with identified vale o $H=0.760$ by selecting an arbitral signal in the 200 signals. Based on this result it is clear that we can identify the Hurst index by using the ergodic averaging method not the ensemble averaging method.

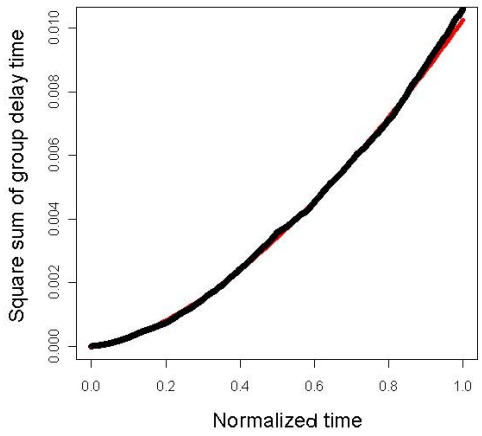


Figure 7. Determined Hurst index by ensemble averaging method for the case of 200 samples with H=0.8
**Full line**: Lest squire line with H=0.805
**Circles**: From ensemble averaging

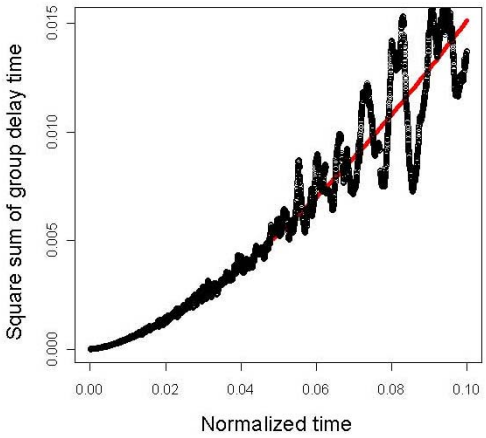


Figure 8. Determined Hurst index by using ergodic averaging method from one sample with H=0.8
**Full line**: Least squire line with H=0.760
**Circles**: From ergodic averaging

## 3 FRACTAL CHARACTERISTIC OF EARTHQUAKE MOTION PHASE

To analyze phase spectrum of earthquake motion we should be provided as many as possible discrete data points we therefore add zero to the digitized time history of earthquake motion as the total number of data points being 131072. First taking Fourier transform of earthquake time history and obtain the GDT $\xi(\omega)$by using the last form of Eq.(2). Integrating GDT with respect to the circular frequency the earthquake motion phase spectrum is obtained. Because the mean value of the GDT represents the arrival time of main energy of earthquake motion the GDT usually can be expressed by

$$\xi(\omega) = -T_0 + \eta(\omega) \tag{10}$$

in which $T_0$ is a constant and $\eta(\omega)$ is a function expressing the fluctuation of the GDT. both characterize the phase spectrum of an earthquake motion. The phase spectrum can be obtained by integrating GDT

$$\phi(\omega) = -T_0\omega + \phi_0(\omega) \quad \text{where} \quad \phi_0(\omega) = \int_0^{\omega} \eta(x)dx \tag{11}$$

From this equation it is easily understand that the basic characteristic of phase spectrum is controlled by $\eta(\omega)$, i.e. $\phi_0(\omega)$ integration of GDT with respect to the circular frequency, and $T_0$ which is a time delay parameter just shifting the earthquake motion.

Fig 9 is the case using acceleration time history of earthquake motion observed at Kobe Meteorological observatory during the 1995 Kobe earthquake in Japan. Upper and middle figures are $\eta(\omega)$ and $\phi(\omega)$. From the middle chart the phase change with respect to the circular frequency seems like a straight line with negative gradient. This is because of $-T_0\omega$ term appearing in Eq.(11) but important part of phase is $\phi_0(\omega)$. We therefore show only this part in Figs.11 and 12. The bottom figure shows the process to identify the Hurst index and the variance of the Weiner process which is necessary to generate the fractional Brownian process. First we subtract the effect of $-T_0\omega$ from calculated phase $\phi(\omega)$ and obtain $\phi_0(\omega)$ then

calculate the ergodic average of $(\Delta\phi_{0k})^2 = (\phi_0(\omega_i) - \phi_0(\omega_j))^2$, which is expressed by $E_e(\Delta\phi_{0k}^2)$, under the constraint of $\Delta\omega_k = \omega_i - \omega_j$ keeping constant.

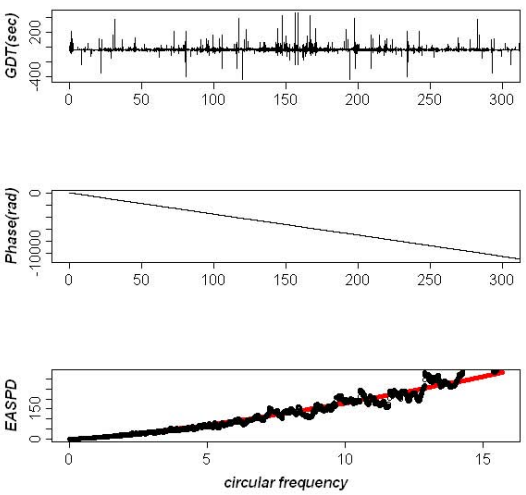


Fig.9 The case of using Kobe record.
**Upper**: group delay time, **Middle:** phase, **Bottom:** ensemble average of squared phase difference (EASPD), dots are calculated from the record, curve is the least squire fitting

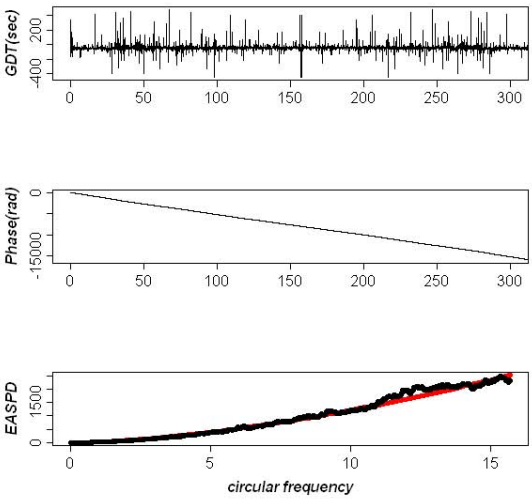


Fig.10 The case of using KUSHIRO record.
**Upper**: group delay time, **Middle:** phase, **Bottom:** ensemble average of squared phase difference (EASPD), dots are calculated from the record, curve is the least squire fitting

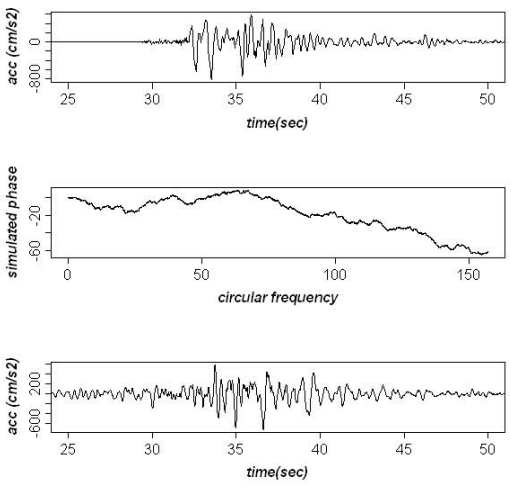


Figure 11. Comparison of Kobe record (Upper) and resimulated Kobe acceleration time history (Bottom). Middle is the phase spectrum simulated by a fractional Brownian

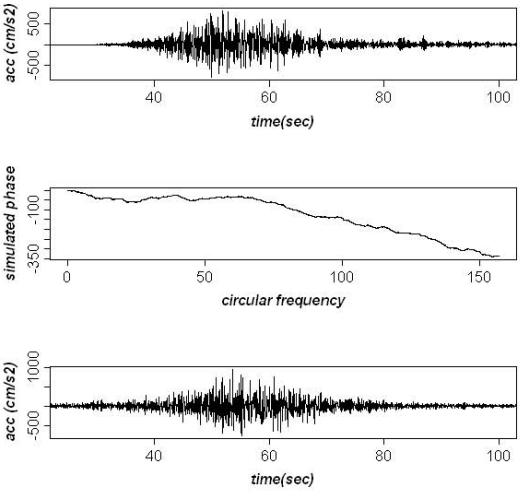


Figure 12. Comparison of Kushiro record (Upper) and resimulated Kushiro acceleration time history (Bottom). Middle is the phase spectrum simulated by a fractional Brownian process.

Each open circle is the relation between $\Delta\omega_k$ and $E_e(\Delta\phi_{0k}^2)$. The full line is the least square curve fitted to the ergodic average points. The intercept with vertical axis is the value of variance $\sigma^2$ defined in Eq.(5). The identified $H$ and $\sigma^2$ are 0.679133 and $10^{0.896434}$,

respectively. Fig.10 is for the case of the off Kushiro earthquake motion observed in 1994 at Kushiro Observatory. For this case we obtained $H = 0.812290$ and $\sigma^2 = 10^{1.458894}$.

Using these identified data we can simulate a sample of $\phi_0(\omega_i)$ at each discrete point $\omega_i \ (i = 1,2,...,N)$ with an equal increment of circular frequency $\Delta\omega$. Fig. 11 is the case to resimulate Kobe record by using the identified $H$ and $\sigma^2$. Upper figure is the original Kobe earthquake acceleration time history. Middle part is a simulated $\phi_0(\omega)$. Bottom is a resimulated acceleration time history using this $\phi_0(\omega)$ and assigning the same $T_0$ and Fourier amplitude of Kobe earthquake motion. Comparing the upper and bottom figures it is concluded that our proposed method to simulate an earthquake phase spectrum works well. Fig.12 is a resimulated Kushiro time history of acceleration. The values of $T_0$, $H$ and $\sigma^2$ as well as the Fourier amplitude spectrum are from Kushiro record.

Fig 13 shows examples of design response spectrum compatible earthquake motions. We selected the SPECTRUM II (absolute acceleration spectrum) defined in the seismic design code of railway facilities [4]. Upper figure of $\phi_0(\omega)$ is simulated by using $H$ and $\sigma^2$ obtained in Fig.9 (Kobe data) and as well in the Bottom figure we use those data obtained in Fig.10 (Kushiro data). Even the response spectrum is same the simulated earthquake motion time histories completely different.

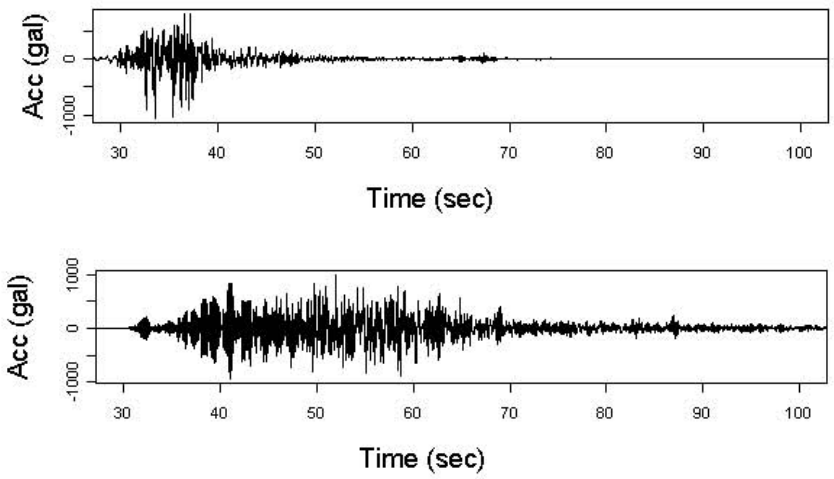


Figure 13. Response spectrum compatible earthquake motions
Upper: using simulated Kobe phase
Bottom: using simulated Kushiro phase

## 4 CONCLUDING REMARKS

In this paper we tried to make cleat the physical meaning of the phase spectrum of earthquake motions. The new finding was that the fluctuated part of the phase spectrum above the constant delay of phase was expressed by a fractional Brownian process (FBP). This finding is compatible with the recent research of wave propagation in random media assuming the FBP on reflection and reflection of wave motions [16]. It is also commonly known and accepted results that the surface of shear fractured rock shows a fractal surface configuration [17]. Because the fault rapture process is a shear rupture process the fractal characteristics should be included in the earthquake motions. This is the motivation to start this research and it was hided in the phase characteristic of earthquake motion. We also developed a method to identify the parameters

specifying the FBP such as the Hurst index and the variance of the Wiener process which was used to define the FBP. Using this method we can identify the fractal characteristics of earthquake motion phase. Based on these information there is a possibility to determine the fracture behavior of an earthquake fault. This is a future research topic. Here we only demonstrated the efficiency of our finding to simulate the phase spectrum of earthquake motions through several numerical examples.

## 5 AKNOWLEGEMENTS

The author would like to acknowledge Dr.Yoshitaka Murono at the Railway Technical Research Institute for his comments and preparation of figures used in the introduction. Partial support for this research efforts presented in this paper was provided by the Japan Society for Promotion Science through Grant No.23560531.

## 6 PREFERENCES

1) Papolis, A. (1962) "The Fourier integration and it application", McGraw Hill.
2) Meyer, Y. (1992), "Wavelets and operator", Cambridge University Press.
3) Cohen, L. (1995), "Time –Frequency Analysis", Prentice-Hall, Inc.
4) Ministry of Transportation and Railway Research Institute, "Seismic Design Standards for Railway Facilities, Maruzen, 1999 (in Japanese).
5) Ohsaki, Y. (1979). "On the significance of phase content in earthquake ground motions, "*Earthquake Engineering and Structural Dynamics*, 7, 427-439.
6) Katsukura, K. and Izumi, M. (1983). "A foundamental study on the phase properties of seismic waves," *Journal of Structural and Construction Engineering, Transactions of AIJ*, 327, 20-27. (In Japanese).
7) Sato,T., Uetake、T. and Sugawara、Y. (1997), :"A Study on Empirical Envelope Model of Long Period Strong Motions by Using Group Delay Time", *Journal of. Structural and. Construction. Engineering, Transaction of AIJ,* No.493, 31-39 (in Japanese).
8) Nigam, N.C. (1982). "Phase properties of a class of random process," *Earthquake Engineering and Structural Dynamics* 10, 711-717.
9) Boore, D. M. (2003). "Phase derivatives and simulation of strong ground motions," *Bulletin of the Seismological Society of America* 93(3), 1132-1143.
10) Zhang, C., Sato, T. and Lu, L.Y. (2011). "A phase model of earthquake motions based on stochastic differential equation," *KSCE Journal of Civil Engineering* 15(1), 161-166.
11) Sato, T., Murono, Y. and Nishimura, A. (2002). "Phase spectrum modeling to simulate design earthquake motion," *Journal of Natural Disaster Science*, 24(2), 91-100.
12) Sato, T. Murono, Y and M. Murakami (2002), "Modeling of Phase Spectra for Near-Fault Earthquake Motions", *Proceedings of 12th European Conference on Earthquake Engineering* CD-ROM paper No.279
13) Matsushita, M. (2002) "Physics of Fractal", Shokabo Co. Ltd. (in Japanese).
14) Biagini, F., Hu, Y., Oksendal, B. and Zhang, T. (2008), "Stochastic Calculus for Fractional Brownian Motion and Applications", Springer-Verlag London Lit.
15) Honda, K. (2008), "Fractal" Asakura book Co. Ltd. (in Japanese).
16) Browaeys T. J. and Fomel, S. (2009), "Fractal heterogeneities in sonic logs and low-frequency scattering attenuation" *Geophysics*, Vol.72, No.2, WA77-WA92.
17) Kruhl, J. H (ed) (1994), "Fractal and Dynamic Systems in Geosciences", Springer-Verlag, New York.

# New soil classification system and amplification factors for seismic code provisions

K. Pitilakis, A. Anastasiadis and E. Riga
*Department of Civil Engineering, Aristotle University of Thessaloniki, Greece*

ABSTRACT:

According to the latest views, local site conditions strongly affect the high frequency content of strong motion records. Contemporary seismic codes have largely accepted the significant role of site effects and attempt to incorporate their influence either by means of a constant amplification factor exclusively dependent on the soil class or including additional parameters like the shaking intensity, near field conditions, etc. Even though different approaches concerning site classification exist, the average shear wave velocity over the upper 30m of soil profile ($V_{s,30}$) is considered to be a sound parameter for site classification. However, several recent works, both numerical and experimental, prove that the unique use of this descriptive parameter may lead in several cases to serious errors and underestimations of the ground motion. Moreover, the soil classification in only a few classes (e.g. A, B, C, D and E for Eurocode 8), with a broad range of descriptive values, is not capable of accurately describing the soil amplification in a broad spectrum of frequencies.

Based on these fundamental observations, a new improved soil and site classification system, which includes extra parameters, such as the thickness of soil deposits, the average shear wave velocity to the 'seismic' bedrock and the fundamental period of the site, is presented. The present constitutes the next step to previous work (Pitilakis et al., 2004, 2006), in which site classification and associated amplification factors were assessed based exclusively on 1D theoretical analyses of various representative models of realistic site conditions. This past work has been further extended and enriched with the analysis of records from real sites, which dispose a well documented soil profile concerning dynamic properties and depth up to the 'seismic' bedrock ($V_s$>800 m/s). The records originated from the new worldwide database of strong ground motion records, compiled in the framework of SHARE FP7 Collaborative Project of the European Union. More than 3000 strong motion records from more than 500 sites from Greece, Italy, Turkey, USA and Japan are selected, processed and uniformly analysed. Site amplification factors are derived for the soil classes of the new classification system and for the existing soil classes of EC8 using different state-of-the-art methods. Normalized response spectra are also proposed for the new soil classification scheme.

## 1 INTRODUCTION

Modern seismic codes have acknowledged the significant role of local site conditions and have incorporated their influence in their provisions. The most common way for codes to account for site effects is the suggestion of appropriate elastic response spectra based on different soil categories and level of seismic actions. Site amplification is usually expressed by a constant ampli-

fication factor, which is dependent on soil class or on additional criteria, such as level of seismic intensity, near field conditions, etc.

The main parameter used in modern code provisions concerning site classification is $V_{s,30}$, i.e. the average value of shear wave velocity in the upper 30m of the soil profile, which is computed by dividing 30m by the travel time from the surface to depth of 30m. This parameter was first proposed by Borcherdt and Glassmoyer (1992) and Borcherdt (1994). The depth of 30m was selected since it is a typical depth of geotechnical borings and, thus, of site characterization. Eurocode 8 uses $V_{s,30}$ as the main soil categorization parameter, along with $N_{SPT}$ blow count and undrained strength $C_u$ to define five soil types (A to E), while two extra special ground types are also defined (CEN, 2004). The elastic design response spectrum depends on the ground type, the reference peak ground acceleration for the specific zone (defined by each country's national annex) and the level of seismicity (surface-wave magnitude $M_s \leq 5.5$ or $M_s > 5.5$).

However, several recent works, both numerical and experimental, prove that the unique use of this descriptive parameter may lead in several cases to serious errors and underestimates of the ground motion. Moreover, the soil classification system proposed in Eurocode 8, which includes only five classes (A, B, C, D and E) with a broad range of descriptive values (geometrical, physical and mechanical) is not capable of accurately describing the soil amplification in a broad spectrum of frequencies. In particular, it is widely accepted that there are several more factors that may affect the seismic ground motion and site response, such as the impedance contrast between surface and underlying stiff deposits or rock basement, the soil type and stratigraphy, the material non linearity and damping and its potential variation with the intensity of the ground motion; all these should ideally be taken into account in an improved site classification system.

Based on these fundamental observations we present a new improved soil and site classification system, suitable for seismic code provisions, based on a new worldwide database of strong ground motion records. The present work constitutes a further step to previous work performed in the Laboratory of Soil Mechanics, Foundations & Geotechnical Earthquake Engineering of Aristotle University (Pitilakis et al. 2004, 2006), in which a new soil classification system that includes soil type, stratigraphy, depth and soil stiffness as key parameters was presented, and amplification factors were assessed, based exclusively on 1D theoretical analyses of various representative models of realistic site conditions. At this stage, only ground motions recorded at real sites, which are characterized by a well documented soil profile concerning dynamic properties and depth up to the 'seismic' bedrock ($V_s > 800$ m/s) are used. The selected recordings are mainly provided from the database, which has been compiled in the framework of the EU FP7 Collaborative Project 'Seismic Harmonization in Europe' (SHARE). The database includes the 5% spectral acceleration values for all records, at different frequencies and a very rich and complete metadata base with seismological, source and geotechnical information (Yenier et al., 2010). Further compilation and improvement of the metadata base have been made in the framework of the present research using different sources (Akkar et al., 2010, Sandikkaya et al., 2010, ITACA website, Kik-Net website, K-Net website, D.M. Boore's homepage, ROSRINE website).

The objective of this work is to propose an improved soil classification system, along with the corresponding elastic acceleration response spectra and soil amplification factors, suitable for incorporation in seismic code provisions. Soil amplification factors are also assessed for the existing soil classes of EC8.

## 2 STRONG MOTION DATABASE

In the framework of SHARE, an extended strong motion database has been compiled, which consists of accelerograms gathered from the European strong motion database, the Turkish national strong-motion database, the Next Generation Attenuation database, the KIK-Net database and the global worldwide database compiled by Cauzzi and Faccioli (Yenier et al., 2010). The database (v1.0) covers earthquakes back to 1930s and contains a total of 14193 records from

2448 events. Considering the goal of the present work and wishing to reduce to minimum the uncertainties associated with the soil and site description, only the strong motions which have been recorded at sites (stations) which dispose a well documented soil profile concerning dynamic properties and depth up to the 'seismic' bedrock ($V_s$ >800 m/s) have been used for this work. As a result, a new database was created, which contains a subset of the records of the original database (3678 strong motion records from 540 stations). The geographic distribution of the selected stations and records is presented in Figures 1 and 2. Moment magnitude $M_w$ and peak ground acceleration *PGA* distributions with the epicentral distance *R* of the selected records are given in Figures 3 and 4. It is observed that there are significantly less records with large *PGA* values exceeding 200 cm/sec$^2$ and very few records with *R*<5 km.

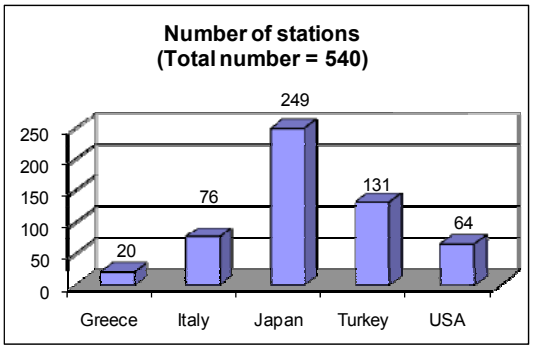

Fig. 1: Geographic distribution of selected stations

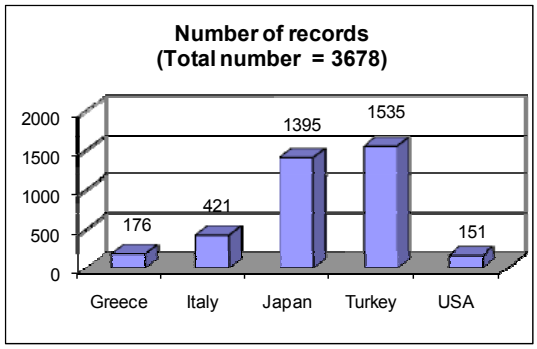

Fig. 2: Geographic distribution of selected records

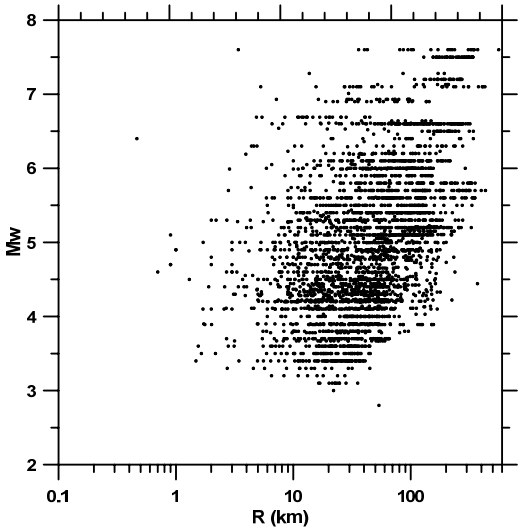

Fig. 3: *Mw-R* distribution of the selected records.

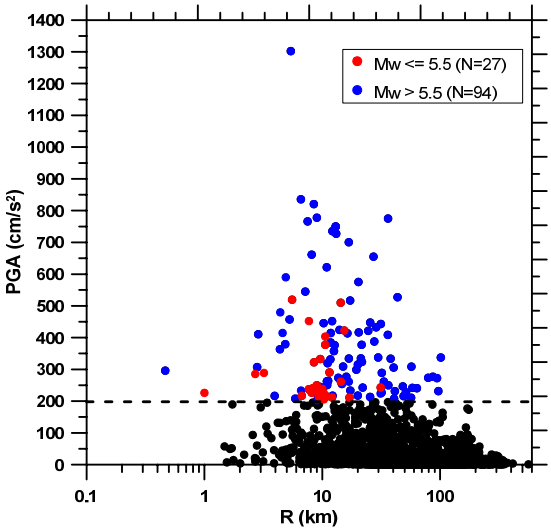

Fig. 4: *PGA-R* distribution of the selected records.

For all 540 stations, new parameters, not included in the original database were determined. These include the thickness of the soil deposits (i.e. depth to "seismic" bedrock - $V_s$>800 m/s), the depth until which the $V_s$ profile, based on measured data in each station site, is known, the average shear wave velocity $V_{s,av}$ of the entire soil deposit and the fundamental period $T_0$ of the soil deposit. In most cases the depth of bedrock and $V_s$ profile until bedrock were well known from detailed geotechnical surveying including in most cases cross-hole or down-hole measurements; in some cases, however, they were estimated using H/V technique on the available records and statistical analysis.

## 3 AMPLIFICATION FACTORS FOR EXISTING SOIL CLASSES OF EC8

The classification of the 540 stations of the database according to EC8 classification scheme is presented in Figure 5.

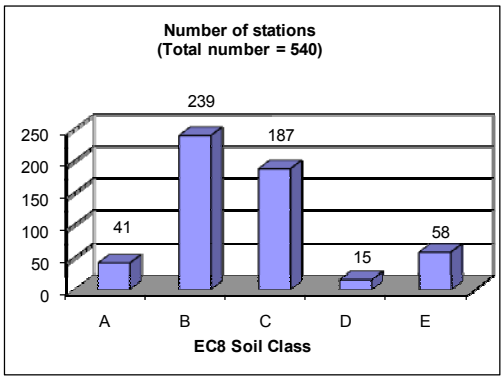


Fig. 5. Classification of selected sites according to EC8.

Two different methodologies were used to estimate amplification factors for the EC8 soil classes. The first calculates a constant period-independent amplification factor for the whole spectrum (similar to the Soil Factor, *S,* suggested by EC8), with respect to the rock sites of the database, while the second uses Ground Motion Prediction Equations (GMPEs) for the estimation of reference acceleration spectral values (i.e. for soil class A).

### 3.1 Period-independent amplification factor approach (Approach 1)

In this approach, proposed by Rey et al. (2002), the soil amplification factor for each soil class was calculated with respect to the rock sites (soil class A) of the database. 5% spectral ordinates $S_a(T)$ for all vibration periods were first distance-normalized (i.e. multiplied by the epicentral distance $R$) and grouped within magnitude intervals of $M_s$ = 0.5, ranging from $M_s$ =3 to $M_s$ =7.5. According to Rey et al. (2002), such normalization is supported by attenuation relationships, which show that shapes of response spectra do not change significantly with distance. The log average of normalized spectral ordinates $RS_a(T)$ was then calculated and plotted for each soil type and interval of magnitude. Figure 6 illustrates the log average of distance-normalized response spectra for EC8 soil class B, with respect to soil class A, for 3 different magnitude intervals. The log average curves for soil type B lie consistently above the corresponding curves for soil A, so it makes sense to estimate the average amplification through a single period-independent factor (Rey et al., 2002).

The amplification factors $S$ for each soil class and magnitude interval were calculated using the following equation:

$$S = (I_{soil} / I_{rock}) \cdot (1 / SR) = (I_{soil} / I_A) \cdot (1 / SR) \quad (1)$$

In Equation (1) $I_{soil}$ and $I_{rock}$ are the spectrum intensities for soil and rock respectively, originally defined by Housner (1952) for spectral velocities and here adapted for spectral accelerations, given by the following equation:

$$I = \int_{0.05}^{2.5} \overline{RS_A(T)} dt \quad (2)$$

$SR$ is the spectral shape ratio, which represents the amplification due to the change in shape of $PGA$-normalized response spectra. Since average spectra of softer soils tend to have a larger and shifted towards longer periods plateau compared to rock spectra, the introduction of $SR$ in equation (2) assures that amplification factor $S$ represents only the amplification related to the in-

crease of ordinates of soil spectra with respect to rock spectra (Rey et al., 2002). Spectral shape ratios *SR* for EC8 classification scheme are given in Table 1.

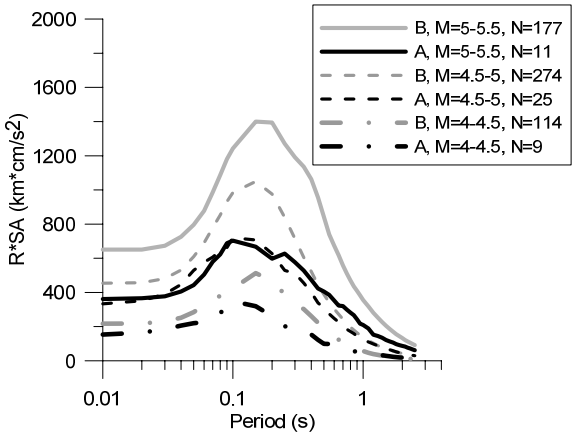


Fig. 6. Log-average, distance-normalized acceleration response spectra for earthquakes with $4<M\leq4.5$, $4.5<M\leq5$, and $5<M\leq5.5$ for sites of soil class B (grey lines) and rock sites (black lines).

Table 1. Spectral shape ratios *SR* for EC8 classification scheme.

| Soil Class | $M_s\leq5.5$ | $M_s>5.5$ |
|---|---|---|
| B | 1.00 | 1.16 |
| C | 0.99 | 1.29 |
| D | 1.13 | 1.53 |
| E | 1.00 | 1.16 |

$I_{soil}/I_A$ ratios were calculated for soil classes B, C and E, for all magnitude intervals (M.I.). The available data for soil class D were very few, so we were not able to calculate reliable amplification factors for this soil class. Table 2 presents the results for soil class B. The table also contains the number of available strong motion records (third column) and the associated range of PGA (fourth column, with the number in the parenthesis representing the average *PGA*) for each magnitude interval. It is obvious that there were not adequate data for all magnitude intervals, so the corresponding $I_{soil}/I_A$ ratios could not be considered reliable. The magnitude intervals with a satisfactory number of available strong motions for both soft soil and rock are depicted in bold. Only the ratios corresponding to these intervals were later on used for the estimation of amplification factors *S*. Similar tables were created for classes C and E.

Table 3 gives the $I_{soil}/I_A$ ratios for soil classes B, C and E and for the two seismicity contexts of EC8. $I_{soil}/I_A$ coefficients of Table 3 were calculated as the mean values of the coefficients from the magnitude intervals considered to be as most reliable (see also previous paragraph). The actual amplification factors *S*, as derived by equation (1), are given in Table 4, along with the corresponding soil factors proposed by EC8.

Table 2. $I_{soil}/I_A$ ratio for EC8 soil class B and all magnitude intervals. The magnitude intervals and corresponding ratios used for calculation of amplification factors are depicted in Bold.

| M.I. | $I_B/I_A$ | $n(B)/n(A)$ | $PGA$ (cm/s2) |
|---|---|---|---|
| **3-3.5** | **1.54** | 180/15 | <=186 (15) |
| 3.5-4 | 1.19 | 205/8 | <=285 (17) |
| 4-4.5 | 1.43 | 114/9 | <=133 (15) |
| **4.5-5** | **1.28** | 274/25 | <=261 (23) |
| 5-5.5 | 1.88 | 177/11 | <=777 (40) |
| 5.5-6 | 1.44 | 84/1 | <=410 (36) |
| **6-6.5** | **1.38** | 85/9 | <=590 (76) |
| **6.5-7** | **1.12** | 78/19 | <=820 (148) |
| 7-7.5 | 2.97 | 32/2 | <=654 (51) |

Table 3. $I_{soil}/I_A$ ratios for EC8 soil classes B, C and E and both seismicity contexts.

| | $M_s$≤5.5 | | $M_s$>5.5 | |
|---|---|---|---|---|
| Soil Class | Selected M.I. | $I_{soil}/I_A$ | Selected M.I. | $I_{soil}/I_A$ |
| B | 3-3.5, 4.5-5 | 1.41 | 6-6.5, 6.5-7 | 1.25 |
| C | 3-3.5, 4.5-5 | 1.85 | 6-6.5, 6.5-7 | 2.09 |
| E | 3-3.5, 4.5-5 | 1.85 | 6-6.5, 6.5-7 | 0.81 |

Table 4. Amplification factors determined from Approach 1 compared to EC8.

| | $M_s$≤5.5 | | $M_s$>5.5 | |
|---|---|---|---|---|
| Soil Class | Approach 1 | EC8 | Approach 1 | EC8 |
| B | 1.41 | 1.35 | 1.08 | 1.20 |
| C | 1.87 | 1.50 | 1.62 | 1.15 |
| E | 1.85 | 1.60 | 0.70 | 1.40 |

3.2 Approach with GMPEs (Approach 2)

In this approach the amplification factor for ground motion $j$, $F_{ij}$, is evaluated from the geometric mean of 5% damped acceleration response spectra for the two horizontal components of shaking, $S_{ij}$ , and the reference ground motion for the site, $(S_r)_{ij}$, as follows (Choi and Stewart, 2005):

$$F_{ij}(T) = S_{ij} / (S_r)_{ij} \tag{3}$$

$T$ is the spectral period. In Equation (3) $S_{ij}$ and $(S_r)_{ij}$ are computed at the same spectral period, which is varied from 0 to 2.5s. Reference motion parameter $(S_r)_{ij}$ is taken as the average spectral acceleration calculated from a Ground Motion Prediction Equation for rock sites. The following GMPEs were used: Cauzzi and Faccioli (2008) and Akkar and Bommer (2010).

The Cauzzi and Faccioli (2008) GMPE for rock sites, herein called C&F, considers moment magnitude $M_w$, hypocentral distance $r_{hyp}$ and faulting style. Reference peak ground acceleration $PGA$ and spectral displacements $S_d$ were estimated for all ground motions with available $M_w$, $r_{hyp}$ and faulting style, with the assumption of a rock site. Spectral displacement values were then transformed into spectral acceleration values $S_a$ using the following equation:

$$S_a(T) = S_d(T) \cdot 4\pi^2 / T^2 \tag{4}$$

The Akkar and Bommer (2010) GMPE for rock sites, herein called A&B, considers moment magnitude $M_w$, Joyner-Boore distance $r_{jb}$ and faulting style. As previously, reference spectral accelerations were estimated for all ground motions with available $M_w$, $r_{jb}$ and faulting style, with the assumption of a rock site.

As a result, 2 different amplification factors were estimated for each ground motion and each spectral period. The results were grouped based on the soil class of the site and the magnitude of the event ($M_s$≤5.5 or $M_s$>5.5). For each soil class, level of magnitude and GMPE, the median values of the amplification factors were calculated for each spectral period, along with the 16$^{th}$ and 84$^{th}$ percentiles. The specific percentiles were selected since, in the case of normal distribution of data, they represent the values of average minus one standard deviation and average plus one standard deviation respectively. Figures 7 and 8 show the amplification factors estimated for soil class B, using both GMPEs, for $M_s$≤5.5 and $M_s$>5.5 respectively. Similar graphs have been plotted for soil classes C, D and E.

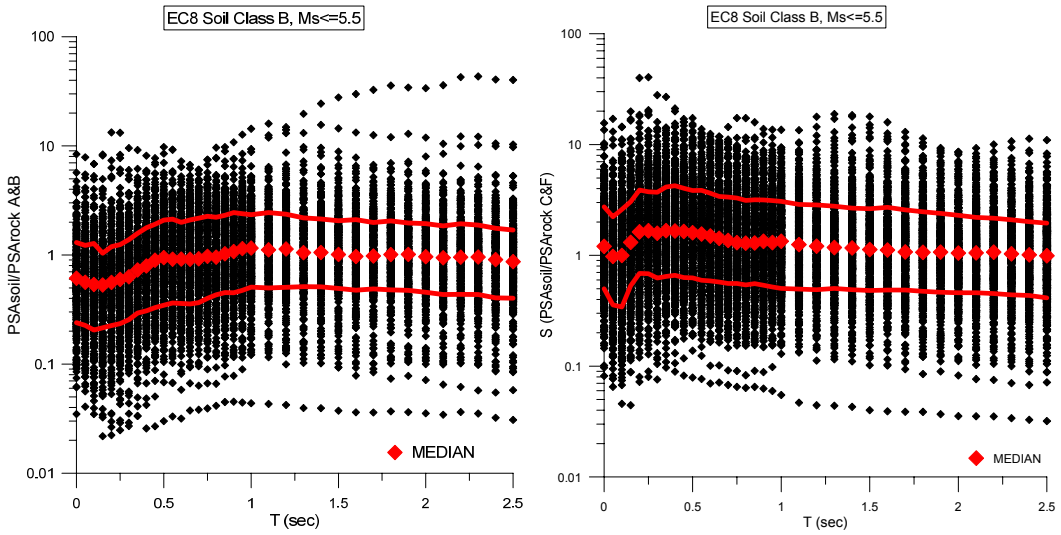


(a) (b)

Fig. 7. Amplification factors for soil class B, $M_s$≤5.5 and $PSA_{rock}$ estimated with (a) A&B GMPE and (b) C&F GMPE. The red lines represent the 16$^{th}$ and 84$^{th}$ percentiles.

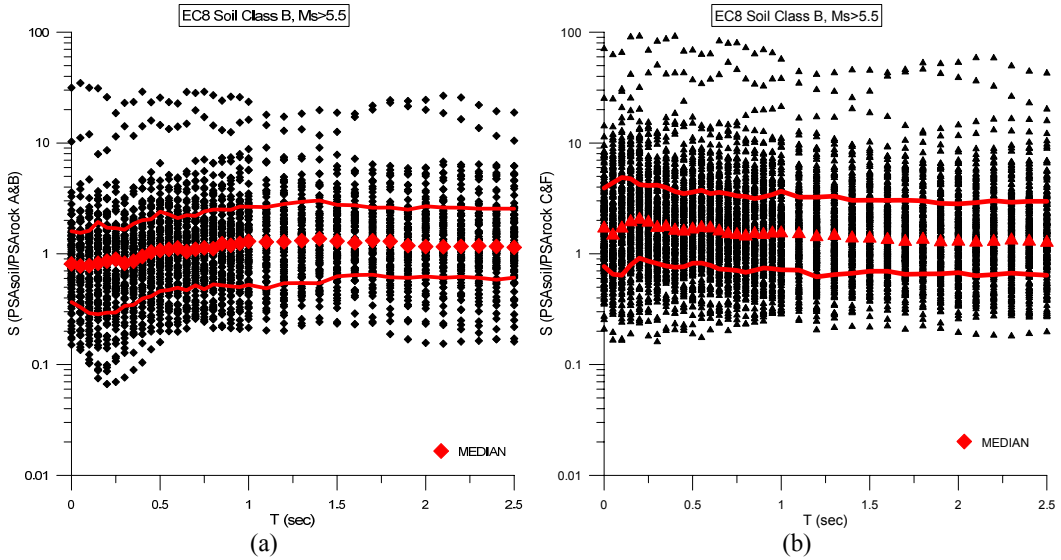


(a) (b)

Fig. 8. Amplification factors for soil class B, $M_s$>5.5 and $PSA_{rock}$ estimated with (a) A&B GMPE and (b) C&F GMPE. The red lines represent the 16$^{th}$ and 84$^{th}$ percentiles.

Figures 9-12 illustrate the medians of the amplification factors estimated using each GMPE for the estimation of reference ground motion. The mean values of the two median amplification factors for each period, as well as the corresponding EC8 acceleration response spectra divided

by the spectral values for soil class A are also shown. It is observed that in most cases and in particular for $M_s$>5.5 the use of the C&F GMPE leads to higher amplification factors.

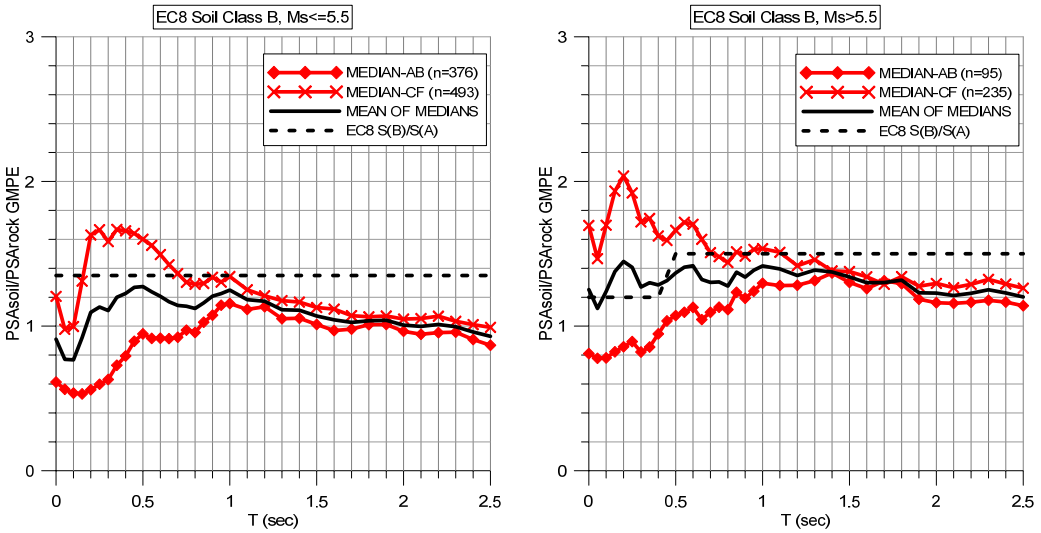


Fig. 9. Median amplification factors for soil class B and $PSA_{rock}$ estimated with both GMPEs for (a) $M_s$≤5.5 and (b) $M_s$>5.5, along with the mean of medians and the corresponding EC8 spectra.

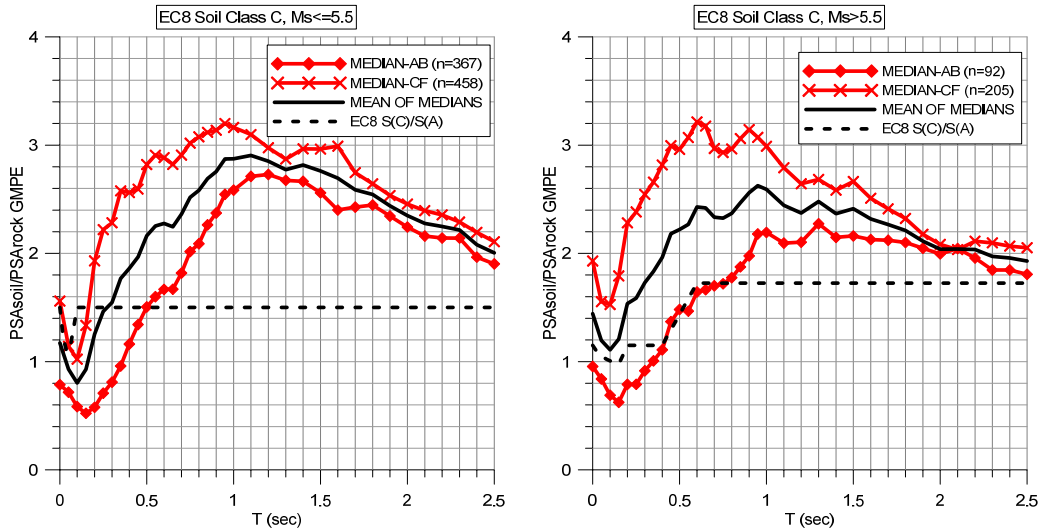


Fig. 10. Median amplification factors for soil class C and $PSA_{rock}$ estimated with both GMPEs for (a) $M_s$≤5.5 and (b) $M_s$>5.5, along with the mean of medians and the corresponding EC8 spectra.

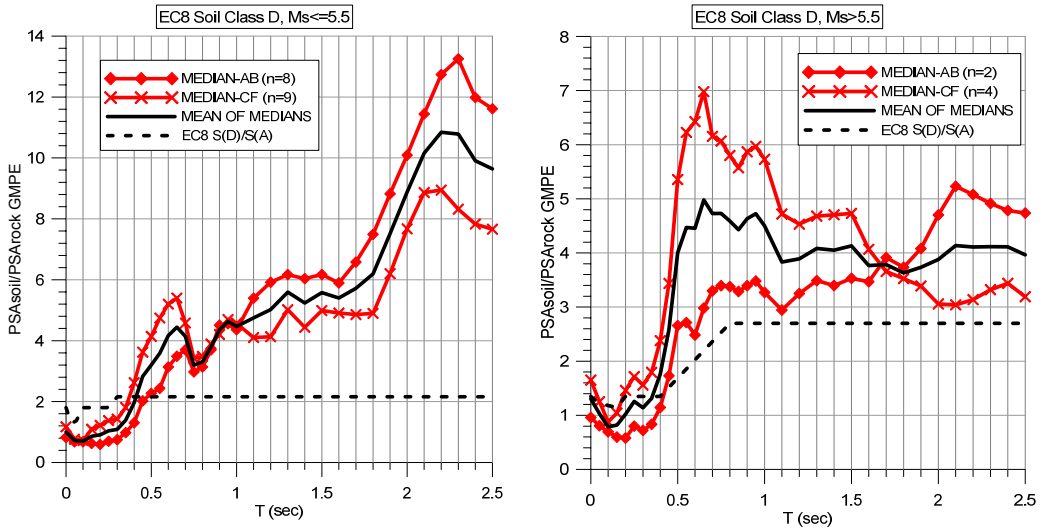


(a) (b)

Fig. 11. Median amplification factors for soil class D and $PSA_{rock}$ estimated with both GMPEs for (a) $M_s$≤5.5 and (b) $M_s$>5.5, along with the mean of medians and the corresponding EC8 spectra.

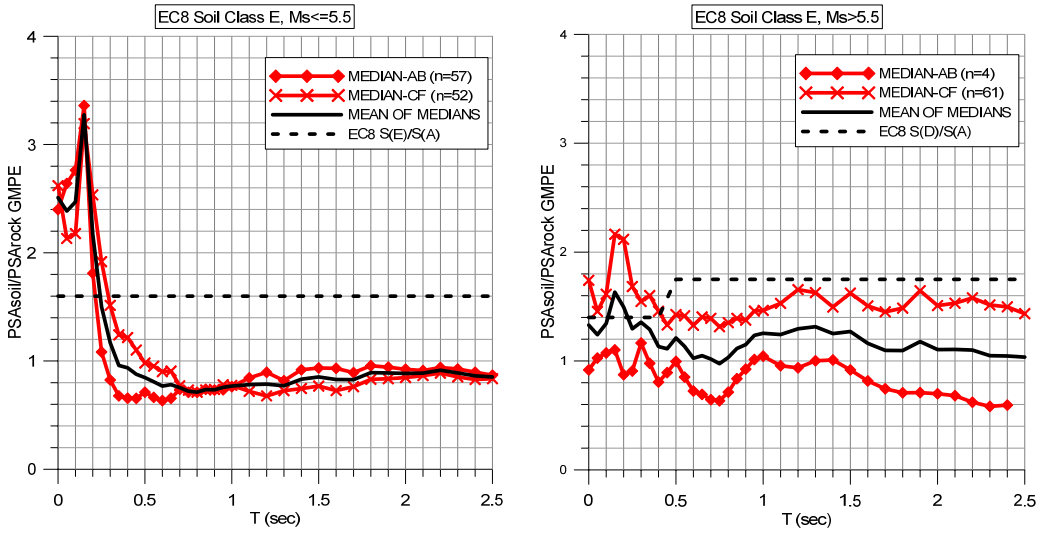


(a) (b)

Fig. 12. Median amplification factors for soil class E and $PSA_{rock}$ estimated with both GMPEs for (a) $M_s$≤5.5 and (b) $M_s$>5.5, along with the mean of medians and the corresponding EC8 spectra.

Since EC8 provides a single period-independent amplification factor, the amplification spectra were averaged over a range of periods from $T$=0s to $T$=2.5s, so that the results can be directly compared to the $S$ factors proposed by EC8. The resulting amplification factors, along with the corresponding EC8 $S$ factors are presented in Table 5.

Table 5. Amplification factors determined from Approach 2 compared to EC8.

| Soil Class | $Ms$≤5.5 | | $Ms$>5.5 | |
|---|---|---|---|---|
| | Approach 2 | EC8 | Approach 2 | EC8 |
| B | 1.10 | 1.35 | 1.30 | 1.20 |
| C | 2.30 | 1.50 | 2.10 | 1.15 |
| D | 5.40 | 1.80 | 3.50 | 1.35 |
| E | 1.00 | 1.60 | 1.20 | 1.40 |

3.3 Comparison of the two approaches and proposed S factors

The values for soil factors *S* for the soil classes of EC8 obtained with the two different approaches described in 3.1 and 3.2 are summarized in Tables 6 and 7. It is noted that for soil class C, the *S* values in both approaches are significantly higher than the ones suggested by Eurocode 8 for both Type 1 and Type 2 spectra. For soil class B, the values from this study are closer to the values of EC8, but do not exhibit a constant behavior. For Type 2 earthquakes, Approach 2 gives a lower value than EC8, while Approach 1 gives a higher value. For Type 1, Approach 2 gives a higher value than EC8, while Approach 1 gives a lower one. Tables 6 and 7 also include the proposed values for EC8 soil classes derived by this study. For soil classes B and C, they are the mean of the values obtained with the two approaches considered. For soil classes D and E, the amount of available data was not considered adequate for statistical analysis. As a result, no amplification factors are suggested for soil class D. For soil class E amplification factors were finally estimated using exclusively selected Kik-Net stations, where there are available strong-motion records both at surface and on the bedrock. These amplification factors were finally considered as more reliable and are the ones given in Tables 6 and 7 as proposed factors for soil class E.

Table 6. Amplification factors obtained with Approaches 1 and 2, proposed values and corresponding EC8 factors for $M_s \leq 5.5$.

| | $M_s \leq 5.5$ | | | |
|---|---|---|---|---|
| Soil Class | Ap. 1 | Ap.2 | Proposed | EC8 |
| B | 1.41 | 1.10 | 1.30 | 1.35 |
| C | 1.87 | 2.30 | 2.00 | 1.50 |
| D | | 5.40 | - | 1.80 |
| E | 1.85 | 1.00 | 2.00 | 1.60 |

Table 7. Amplification factors obtained with Approaches 1 and 2, proposed values and corresponding EC8 factors for $M_s > 5$.

| | $M_s > 5.5$ | | | |
|---|---|---|---|---|
| Soil Class | Ap. 1 | Ap.2 | Proposed | EC8 |
| B | 1.08 | 1.30 | 1.20 | 1.20 |
| C | 1.62 | 2.10 | 1.90 | 1.15 |
| D | - | 3.50 | - | 1.35 |
| E | 0.70 | 1.20 | 1.40 | 1.40 |

## 4 PROPOSED SOIL AND SITE CLASSIFICATION SCHEME

The classification scheme and the corresponding response spectra, proposed by Pitilakis et al. (2004, 2006) based exclusively on theoretical analyses, were improved with the empirical data. The main soil classes remained unchanged, with some modifications in the limits of the parameters describing each class. The proposed classification system is presented in Table 8.

Table 8: Soil and Site Characterization and parameters defining proposed elastic acceleration response spectra.

| Soil Class | Description | $T_0$(s) | Remarks |
|---|---|---|---|
| **A1** | Rock formations | | $Vs$≥1500 m/s |
| **A2** | Slightly weathered / segmented rock formations (thickness of weathered layer <5.0m) | ≤0.2 | Surface weathered layer: $Vs$≥200 m/s<br>Rock Formations: $Vs$≥800 m/s |
| | Geologic formations resembling rock formations in their mechanical properties and their composition (e.g. conglomerates) | | $Vs$ ≥ 800 m/s |
| **B1** | Highly weathered rock formations whose weathered layer has a considerable thickness (5.0m - 30.0m) | ≤0.5 | Weathered layer: $Vs$ ≥ 300 m/s |
| | Soft rock formations of great thickness or formations which resemble these in their mechanical properties (e.g. stiff marls) | | $Vs$: 400-800 m/sec<br>$N$-SPT > 50, $Su$> 200 KPa |
| | Soil formations of very dense sand – sand gravel and/or very stiff/ to hard clay, of homogenous nature and small thickness (up to 30.0m) | | $Vs$: 400-800 m/s<br>$N$-SPT > 50, $Su$> 200 KPa |
| **B2** | Soil formations of very dense sand – sand gravel and/or very stiff/ to hard clay, of homogenous nature and medium thickness (30.0 - 60.0m), whose mechanical properties increase with depth | ≤0.8 | $Vs$: 400-800 m/s<br>$N$-SPT > 50, $Su$ > 200 KPa |
| **C1** | Soil formations of dense to very dense sand – sand gravel and/or stiff to very stiff clay, of great thickness (> 60.0m), whose mechanical properties and strength are constant and/or increase with depth | ≤1.5 | $Vs$: 400-800 m/s<br>$N$-SPT> 50, $Su$ > 200 KPa |
| **C2** | Soil formations of medium dense sand – sand gravel and/or medium stiffness clay ($PI$ > 15, fines percentage > 30%) of medium thickness (20.0 – 60.0m) | ≤1.5 | $Vs$: 200-450 m/s<br>$N$-SPT> 20, $Su$ > 70 KPa |
| **C3** | Category C2 soil formations of great thickness (>60.0m), homogenous or stratified that are not interrupted by any other soil formation with a thickness of more than 5.0m and of lower strength and $Vs$ velocity | ≤1.8 | $Vs$:200-450 m/s<br>$N$-SPT > 20, $Su$ > 70 KPa |
| **D1** | Recent soil deposits of substantial thickness (up to 60.0m), with the prevailing formations being soft clays of high plasticity index ($PI$>40), high water content and low values of strength parameters | ≤2.0 | $Vs$ ≤ 300 m/s<br>$N$-SPT < 25, $Su$ < 70KPa |
| **D2** | Recent soil deposits of substantial thickness (up to 60.0m), with prevailing fairly loose sandy to sandy-silty formations with a substantial fines percentage (not to be considered susceptible to liquefaction) | ≤2.0 | $Vs$ ≤ 300 m/s<br>$N$-SPT < 25 |
| **D3** | Soil formations of great overall thickness (> 60.0m), interrupted by layers of category D1 or D2 soils of a small thickness (5.0 – 15.0m), up to the depth of ~40m, within soils (sandy and/or clayey, category C) of evidently greater strength, with $Vs$≥ 300 m/sec | ≤3.0 | $Vs$: 150-600 m/s |
| **E** | Surface soil formations of small thickness (5.0 – 20.0m), small strength and stiffness, likely to be classified as category C and D according to its geotechnical properties, which overlie category A formations ($Vs$ ≥ 800 m/sec) | ≤0.7 | Surface soil layers:<br>$Vs$ ≤ 400 m/s |
| **X** | Loose fine sandy-silty soils beneath the water table, susceptible to liquefaction (unless a special study proves no such danger, or if the soil's mechanical properties are improved), Soils near obvious tectonic faults, Steep slopes covered with loose lateral deposits, Loose granular or soft silty-clayey soils, provided they have been proven to be hazardous in terms of dynamic compaction or loss of strength. Recent loose landfills, Soils with a very high percentage in organic material | | |

| | **Type 2 - $Ms$≤5.5** | | | | | **Type 1 - $Ms$>5.5** | | | | |
|---|---|---|---|---|---|---|---|---|---|---|
| | $T_B$ | $T_C$ | $T_D$ | $\beta$ | $S$ | $T_B$ | $T_C$ | $T_D$ | $\beta$ | $S$ |
| **A** | 0.05 | 0.3 | 1.2 | 2.75 | 1.00 | 0.1 | 0.4 | 2 | 2.75 | 1.00 |
| **B1** | 0.05 | 0.25 | 1.2 | 2.75 | 1.50 | 0.1 | 0.5 | 2 | 2.75 | 1.10 |
| **B2** | 0.05 | 0.3 | 1.2 | 2.75 | 1.70 | 0.15 | 0.6 | 2 | 2.75 | 1.50 |
| **C1** | 0.1 | 0.25 | 1.2 | 2.75 | 2.40 | 0.15 | 0.7 | 2 | 2.5 | 1.50 |
| **C2** | 0.1 | 0.4 | 1.2 | 2.5 | 2.20 | 0.1 | 0.8 | 2 | 2.5 | 1.10 |
| **C3** | 0.1 | 0.8 | 1.2 | 2.5 | 1.60 | 0.1 | 0.9 | 2 | 2.5 | 1.30 |
| **D** | 0.1 | 0.7 | 1.2 | 2.5 | 2.30 | 0.1 | 0.8 | 2 | 2.5 | 1.60 |
| **E** | 0.05 | 0.2 | 0.5 | 3 | 2.00 | 0.1 | 0.3 | 2 | 3 | 1.40 |

The classification of the stations according to the new system is illustrated in Figure 13. Due to lack of all necessary data for the classification of D sites to subclasses D1, D2 and D3, the three subclasses were unified to one single class (D).

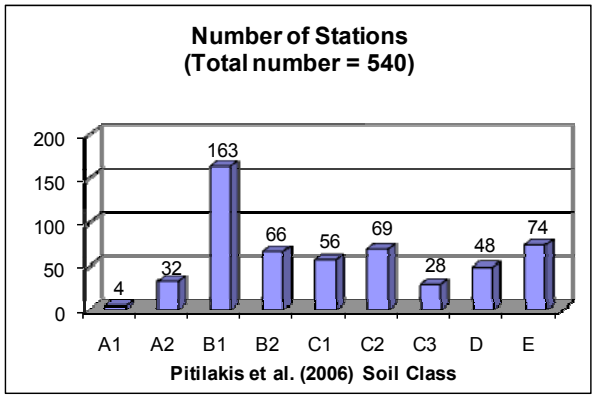


Fig. 13. Classification of selected sites according to the new soil classification scheme.

4.1 Normalized response spectra

For each soil category, normalized acceleration response spectra were specified for two levels of earthquake intensity, the same as the ones proposed by EC8 (Type 1 for $M_s$>5.5 and Type 2 for $M_s$≤5). The normalized acceleration spectra from the strong-motion records were plotted, for each soil class, with spectral periods ranging from 0 to 2.5sec. The median normalized acceleration spectra, as well as the 16$^{th}$ and 84$^{th}$ percentiles were calculated. The proposed normalized acceleration spectra resulted by trying to fit the general spectral equations of Pitilakis et al. (2004, 2006) to the 84$^{th}$ percentile, by adjusting $T_B$, $T_C$, $T_D$ and $\beta$ parameters:

$$0 \le T \le T_B: \ \frac{S_a(T)}{PHGA_s} = 1 + \frac{T}{T_B} \cdot (\beta - 1) \tag{5}$$

$$T_B \le T \le T_C: \ \frac{S_a(T)}{PHGA_s} = \beta \tag{6}$$

$$T_C \le T \le T_D: \ \frac{S_a(T)}{PHGA_s} = \beta \cdot \frac{T_C}{T} \tag{7}$$

$$T_D \le T: \ \frac{S_a(T)}{PHGA_s} = \beta \cdot T_C \cdot \left( \frac{T_D}{T^2} \right) \tag{8}$$

$PHGA_s$ is the peak surface horizontal ground acceleration, $T_B$ and $T_C$ are the limits of the constant spectral acceleration branch, $T_D$ is the value defining the beginning of the change of the slope branch and $\beta$ is the spectral amplification parameter. The proposed parameters for the normalized acceleration response spectra described by Equations (5) – (8) are included in Table 8, while the spectral ratios *SR* of the normalized response spectra are presented in Table 9.

Table 9. Spectral shape ratios *SR* for the new normalized elastic acceleration response spectra.

| Soil Class | $M_s$≤5.5 | $M_s$>5.5 |
|---|---|---|
| B1 | 0.88 | 1.16 |
| B2 | 1.00 | 1.29 |
| C1 | 0.87 | 1.28 |
| C2 | 1.09 | 1.39 |
| C3 | 1.64 | 1.49 |
| D | 1.53 | 1.39 |
| E | 0.65 | 0.89 |

Figure 14 is an example of the way that the proposed normalized spectra were specified for the case of soil class C3 and for both spectrum types. The corresponding EC8 spectra for soil class C of EC8 are also shown. It is obvious that the EC8 spectra are rather inadequate and more importantly, they are non-conservative for long periods.

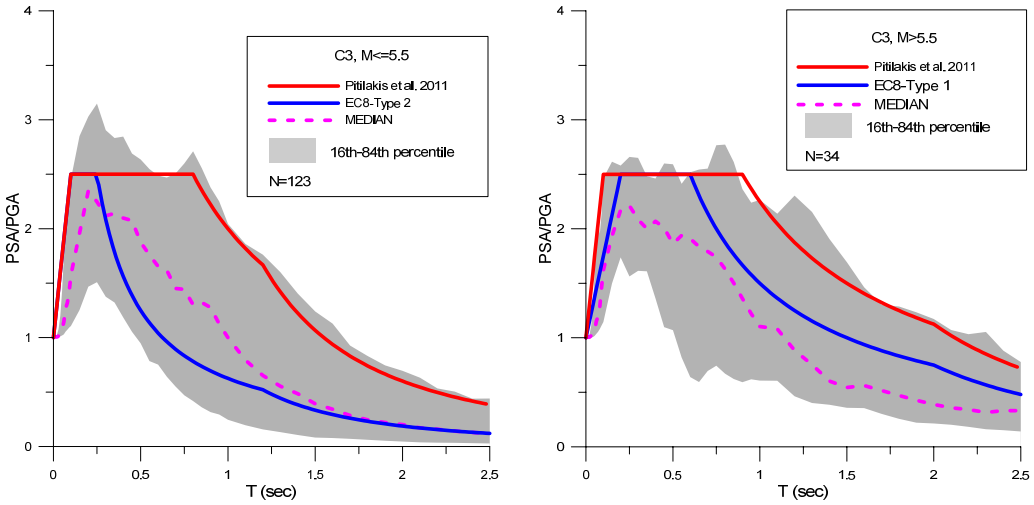


(a) (b)

Fig. 14. Normalized elastic acceleration response spectra for soil class C3 and for (a) Type 2 - $M_s$≤5.5 and (b) Type 1 - $M_s$>5.5.

## 4.2 Amplification factors

Using Approach 1, described in detail in paragraph 3.1, amplification factors were estimated for soil classes B1, B2, C1, C2, C3, D and E. Mean $I_{soil}/I_A$ ratios for the two seismicity contexts, calculated only from magnitude intervals with adequate data, are presented in Table 10. The actual amplification factors $S$, as derived from equation (1), along with the proposed factors are given in Table 11. For soil class E, the proposed factors are again the ones estimated from Kik-Net surface and borehole records. For reasons of completeness, amplification factors are also included in Table 8.

Table 10. $I_{soil}/I_A$ ratios for the new soil classes.

| | $M_s$≤5.5 | | $M_s$>5.5 | |
|---|---|---|---|---|
| Soil Class | Selected M.I. | $I_{soil}/I_A$ | Selected M.I. | $I_{soil}/I_A$ |
| B1 | 4.5-5, 5-5.5 | 1.36 | 6-6.5, 6.5-7 | 1.31 |
| B2 | 4.5-5, 5-5.5 | 1.69 | 6-6.5, 6.5-7 | 1.94 |
| C1 | 4.5-5, 5-5.5 | 2.09 | 6-6.5, 6.5-7 | 1.89 |
| C2 | 4.5-5, 5-5.5 | 2.37 | 6-6.5, 6.5-7 | 1.57 |
| C3 | 4.5-5, 5-5.5 | 2.58 | 6-6.5 | 1.96 |
| D | 4.5-5, 5-5.5 | 3.53 | 6-6.5 | 2.26 |
| E | 4.5-5, 5-5.5 | 1.48 | 6-6.5, 6.5-7 | 0.88 |

Table 11. Amplification factors for the new soil classes.

| | $M_s$≤5.5 | | $M_s$>5.5 | |
|---|---|---|---|---|
| Soil Class | Calculated | Proposed | Calculated | Proposed |
| B1 | 1.55 | 1.50 | 1.13 | 1.10 |
| B2 | 1.69 | 1.70 | 1.50 | 1.50 |
| C1 | 2.40 | 2.40 | 1.48 | 1.50 |
| C2 | 2.17 | 2.20 | 1.13 | 1.10 |
| C3 | 1.57 | 1.60 | 1.32 | 1.30 |
| D | 2.31 | 2.30 | 1.63 | 1.60 |
| E | 2.28 | 2.00 | 0.99 | 1.40 |

The proposed acceleration response spectra for each site category of Table 8, normalized to the design ground acceleration at rock-site conditions $a_g$, are illustrated in Figures 15 and 16 for $M_s$≤5.5 and $M_s$>5.5 respectively.

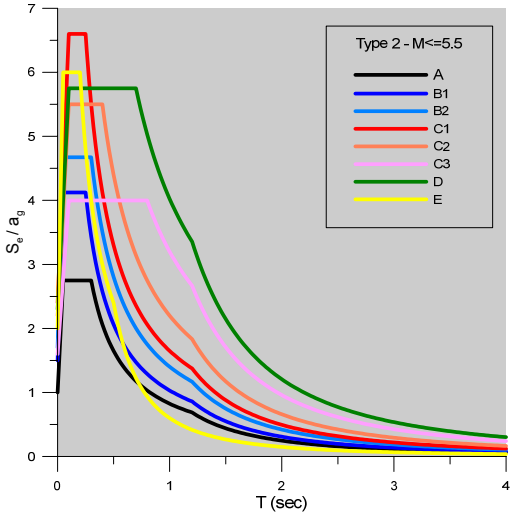


Fig.15. Proposed elastic acceleration response spectra for $M_s$≤5.5.

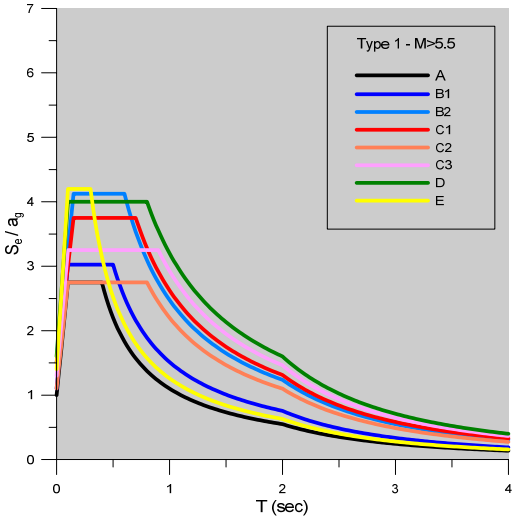


Fig. 16. Proposed elastic acceleration response spectra for $M_s$>5.5.

## 5 CONCLUSIONS

A new soil and site classification system, which uses new parameters, such as the thickness of soil deposits, the average shear wave velocity to the 'seismic' bedrock and the fundamental period of the site, was presented. The new system was based on a worldwide database of strong ground motion records from sites with a well documented soil profile up to the 'seismic' bedrock ($V_s$>800 m/s), and on previously conducted theoretical analyses. Site amplification factors, as well as normalized acceleration spectra were proposed for each soil class and for two seismicity contexts ($M_s$≤5.5 and $M_s$>5.5). The proposed classification system, which aims at eliminating the drawbacks of using $V_{s,30}$ as a key parameter for the definition of different soil classes and description of amplification potential for different soil conditions, is suitable for incorporation in seismic code provisions such as Eurocode 8. New soil amplification factors were also estimated for the existing EC8 site classes, using two different state-of-the art methods. The comparison between the estimated values and the ones proposed by EC8 shows that, for soil classes C (both spectrum types) and E (Type 2), the proposed values are much lower than the ones estimated in the present work, which shows that EC8 underestimates the design ground motion for these cases.

ACKNOWLEDGEMENT
The present work has been performed in the framework of the EU collaborative project SHARE (FP7, Reference code 226967, http://www.share-eu.org/).

## REFERENCES

Akkar, R S. and Bommer, J.J. (2010). Empirical equations for the prediction of PGA, PGV and spectral accelerations in Europe, the Mediterranean region and the Middle East, Seismological Research Letters 81, pp. 195-206.

Akkar, S., Çağnan, Z., Yenier E., Erdoğan O. and Sandıkkaya, M.A. (2010). The recently compiled Turkish strong motion database: preliminary investigation for seismological parameters, Journal of Seismology 14, pp. 457–479.

Boore D.M., personal homepage, http://www.daveboore.com/, Accessed February-May 2011.

Borcherdt, R.D. (1994). Estimates of site-dependent response spectra for design (methodology and justification), Earthquake Spectra 10, pp. 617-653.

Borcherdt, R.D. and Glassmoyer, G. (1992). On the characteristics of local geology and their influence on ground motions generated by the Loma Prieta earthquake in the San Francisco Bay region, California, Bull. Seismol. Soc. Am. 82, pp. 603-641.

Cauzzi, C. and Faccioli, E. (2008). Broadband (0.05 to 20 s) prediction of displacement response spectra based on worldwide digital records. Journal of Seismology 12, pp. 453–475.

CEN (European Committee for Standardisation) (2004). Eurocode 8: Design of structures for earthquake resistance - Part 1: General rules, seismic actions and rules for buildings, EN 1998-1:2004, Brussels, Belgium.

Choi, Y. and Stewart, J.P. (2005). Nonlinear site amplification as function of 30 m shear wave velocity, Earthquake Spectra 21, pp. 1-30.

Housner, G.W. (1952). Spectrum intensities of strong-motion earthquakes, Proceedings of the Symposium on Earthquakes and Blast Effects on Structures, Earthquake Engineering Research Institute.

ITACA Working Group (2010). Data Base of the Italian strong motion records, http://itaca.mi.ingv.it, Accessed January-March 2011.

Kik-net Digital Strong Motion Seismograph Network, National Research Institute for Earth Science and Disaster Prevention, http://www.kik.bosai.go.jp/, Accessed June-August 2010.

Kyoshin Network K-Net, National Research Institute for Earth Science and Disaster Prevention, http://www.k-net.bosai.go.jp/, Accessed April-May 2011.

Pitilakis, K., Gazepis, C. and Anastasiadis, A. (2004). Design response spectra and soil classification for seismic code provisions, 13th World Conference on Earthquake Engineering, Vancouver B.C., Canada, Paper No. 2904.

Pitilakis, K., Gazepis, C. and Anastasiadis, A. (2006). Design response spectra and soil classification for seismic code provisions, Proceedings of geotechnical evaluation and application of the seismic Eurocode EC8 2003-2006, ETC-12 Workshop, NTUA Athens.

Resolution of Site Response Issues from the Northridge Earthquake (ROSRINE), http://gees.usc.edu/ROSRINE/, Accessed September - December 2010.

Rey, J., Faccioli, E. and Bommer, J.J. (2002). Derivation of design soil coefficients (S) and response spectral shapes for Eurocode 8 using the European Strong-Motion Database, Journal of Seismology 6, pp. 547-555.

Sandıkkaya, M.A., Yilmaz, M.T., Bakir, B.S. and Yilmaz, O. (2010). Site classification of Turkish national strong-motion stations, Journal of Seismology 14, pp. 543–563.

Yenier, E., Sandikkaya, M.A. and Akkar, S. (2010). Report on the fundamental features of the extended strong motion databank prepared for the SHARE project (v1.0).

# Seismic risk assessment and management of lifelines, utilities and infrastructures

K. Pitilakis, K. Kakderi
*Department of Civil Engineering, Aristotle University of Thessaloniki, Greece*

ABSTRACT:

Vulnerability assessment and seismic risk management using advanced methodologies are of major importance for the reduction of seismic risk in urban areas. The development of an advanced and integrated methodological tool for the efficient seismic risk management of complex lifeline and utility systems is necessary for the establishment of efficient and effective mitigation schemes. To this end, a modular methodology has been recently developed in Greece in the framework of national and EU research projects for the vulnerability assessment and seismic risk management of lifelines, utilities and infrastructures. The general description of the methodology is provided, along with several representative example applications. Key factors of the methodology are the inventory, the typology, the fragility, the specific characteristics and the importance (global value) of the elements at risk, the development of seismic scenarios (seismic hazard) and the geotechnical characterization, with the detailed site response analysis. Based on estimated losses and assigned priorities, restoration policies and mitigation strategies could be defined. Furthermore, new developments and important aspects of the risk mitigation procedure are further analyzed and commented on, while the ongoing research efforts in Europe are shortly summarized. These new developments include mainly the systemic physical and socio-economic vulnerability and risk analysis, the incorporation of decision-making processes in the seismic rehabilitation studies and the use of real-time damage estimation for the reduction of potential impact on urban societies on the basis of timely and correct actions after a disastrous earthquake. Finally, specific guidelines are provided for the management and reduction of seismic risk of lifelines and infrastructures in urban environments

## 1 INTRODUCTION

Large destructive earthquakes occurred worldwide in highly urbanized areas in the last twenty years or so, (Loma Prieta, CA, 1989; Northridge, CA, 1994; Kobe, Japan 1995; Izmit, Turkey and Chi-Chi, Taiwan, 1999) have prompted researchers to undertake large-scale studies on the expected losses due to a major earthquake. Studies of this type serve the main purposes of designing mitigation strategies and of planning emergency and recovery measures.

Existing methodological frameworks have been developed mainly in the United States. HAZUS (NIBS, 2004) is a risk assessment methodology for analyzing potential losses from floods, hurricane and earthquakes and distributed by FEMA. HAZUS couples scientific and engineering knowledge with geographic information systems (GIS) technology to produce estimates of hazard-related damage before, or after, a disaster occurs. Recently the Impact of Earthquakes on the Central USA has been the object of the "New Madrid Seismic Zone Catastrophic Earthquake Response Planning Project" funded by FEMA and carried out by the Mid-America Earthquake Center (MAEC, 2009). This project comprises a multi-phase investigation of possible earthquake scenarios, analytical earthquake impact assessments, and social impact estimates

that will assist federal, state, and local governments to develop coordinated response plans for a catastrophic earthquake in Central USA. In Latin America there is a very interesting tool of similar possibilities (Central American Probabilistic Risk Assessment - CAPRA; Anderson, 2008). In Europe, among other efforts we state a software developed by the Earthquake Engineering Department of Bogazici University, Kandilli Observatory and Earthquake Research Institute (KOERI) (KOERILoss, Erdik and Aydinoglu, 2002; Erdik et al., 2003; Erdik and Fahjan, 2006), which applies a loss estimation methodology to perform analyses for estimating potential losses from earthquakes (building damage estimation analysis and estimation of the direct economic losses and casualties related to building damages). Another example is the LNECLOSS software package developed by the Laboratorio Nacional de Engenharia Civil (LNEC) in Lisbon, Portugal (Sousa et al., 2004). However, the direct application of these approaches to areas different than the ones they have been developed is not straightforward and requires serious readjustments. Moreover, a systemic treatment of the complex network of lifelines and infrastructures is still missing, while socio-economic issues are only addressed in a very simplified way.

A general modular methodology for the vulnerability assessment and seismic risk management of lifelines and infrastructures (potable water, waste-water, gas, electric power, telecommunication, fire-fighting, roadway, railway, airport, port and critical facilities) has been recently developed in Greece, in the framework of national and EU research projects (SRMLIFE, 2003-2007; RISK-UE, 2001-2004; LESSLOSS, 2004-2007). The general description of the methodology is provided below along with some representative example applications, while some important aspects of the risk mitigation procedure are further discussed, providing specific guidelines for the management and reduction of seismic risk of lifelines, utilities and infrastructures in urban environments.

## 2 METHODOLOGICAL FRAMEWORK

The general framework of the methodology is illustrated in Figure 1. The vulnerability of buildings and lifeline systems in the city are assessed for different seismic scenarios (Pitilakis et al., 2006a,b; Pitilakis et al., 2007a,b; Argyroudis et al., 2005). Loss estimates including direct and indirect losses, depend on the inventory and typology classification of the elements at risk, the vulnerability models and the existing interactions between lifeline components. Inventory is an essential step to identify, characterize and classify all types of lifeline elements, according to their specific typology and their distinctive geometric, structural and functional features. Geographical information systems (GIS) offer the perfect platform to implement any inventory inquires. Within this context, earthquake damage is directly related to structural properties of lifeline elements. Typology is a fundamental descriptor of a system, derived from the inventory of each element at risk. The level of seismic input motion is defined on the basis of site specific ground response analysis for several probabilities of exceedance. The hazard analysis is thus based on seismic scenarios, and a detailed ground response mapping (Anastasiadis et al., 2001; Pitilakis et al., 2007a). The vulnerability assessment deals mainly with the quantification of damage of each element at risk, using appropriate fragility functions. Given the spatial distribution of the characteristics of earthquake motion, loss scenarios for buildings, utility and transportation systems, critical facilities and strategic buildings are produced, using inventory data and adequate fragility relationships. Furthermore, a hierarchy model has been proposed to evaluate and quantify the relative importance of various elements at risk and systems as well as city regions and districts, taking into account different criteria, such as their functional relations and the urban activities and relations of lifelines with the surrounding urban or rural environment (see Global Value approach in RISK-UE, 2001-2004). The assessment of the "global value" (physical and non-physical) is performed, in order to classify the importance of each lifeline element in different periods (normal, crisis and recovery) and prioritize in a more efficient way the pre-earthquake retrofitting actions and the post earthquake restoration efforts. Based on the hierarchy of importance of lifeline components, as well as available techniques, man-power, material and equipment, estimates of the restoration process are performed. An important step for the implementation of an "efficient mitigation strategy" includes a simplified or a more advanced reliability analysis of the damaged and the undamaged system, in order to estimate the level of the remaining serviceability of the system, which is closely connected with the func-

tionality of the community. Thus, a rigorous disaster management process including mitigation, preparedness, response and recovery actions could be assigned.

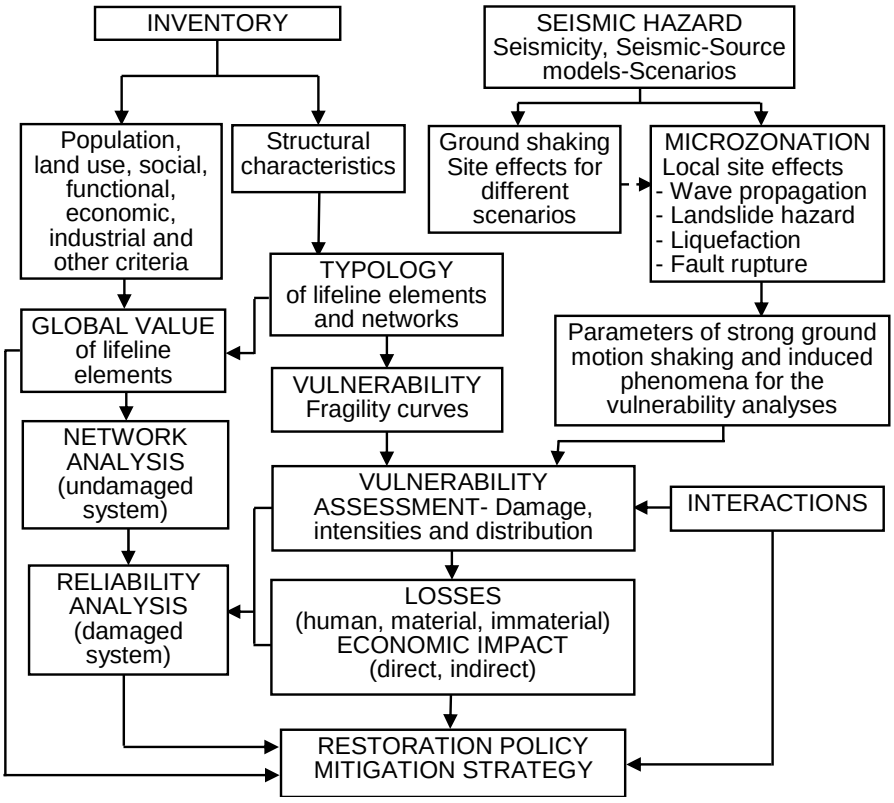


Figure 1. Seismic risk mitigation approach for lifelines and infrastructures.

## 3 SEISMIC SCENARIOS – SITE SPECIFIC GROUND RESPONSE ANALYSIS

Seismic hazard for the vulnerability analysis and risk assessment of lifelines, utilities and infrastructures, should be specified according to the precise needs for the particular lifeline components and networks, as well as the most adequate models used to describe vulnerability and fragility relationships. Moreover due to the spatial extent of lifeline systems, spatial variability of ground motion, considering local soil conditions, is of great importance (Pitilakis et al., 2005a). Site effects play a crucial role and with respect to the spatial variability and typology of various assets, their spatial variability may change completely the intensity and spatial variability of damages and losses. The simple use of seismic code soil classification schemes, and associated design acceleration values, is completely inadequate for a "high technology" vulnerability analysis and risk assessment.

Thus, specific geotechnical-surface geology information is required, and adequate studies should be performed to estimate the necessary ground shaking parameters, in terms of seismic scenarios with different mean return periods. These studies are conventionally referred as "microzonation studies". Moreover, advanced seismic risk analysis studies require maps with the spatial distribution of strong ground motion parameters (e.g. PGA, PGV, PGD) in the study area.

In the following, two examples are given of the detailed microzonation and ground response analyses that have been performed in the cities of Thessaloniki (Greece) and Düzce (Turkey) in the framework of national and European research projects (RISKUE, 2001-2004; SRMLIFE, 2003-2007; MERP, 2002-2005; SRM-DGC, 2006-2008), aiming to the definition of ground motion input parameters for the vulnerability assessment of lifelines and infrastructures in the two cities.

### 3.1 Thessaloniki microzonation study

In Thessaloniki, a detailed microzonation study has been conducted for three different mean return periods of Tm=100, 475 and 1000 years. The study is based on the results of a probabilistic seismic hazard analysis using recent data regarding the seismicity, the corresponding seismic zones and the seismic faults in the greater area (RISK-UE, 2001-2004; SRMLIFE, 2003-2007). A detailed model of the surface geology and geotechnical characteristics, for site effect studies, was generated for the city area. The initial geotechnical map is based on numerous data provided by geotechnical investigations, geophysical surveys, microtremors measurements, classical geotechnical and special soil dynamic tests (Pitilakis et al., 1992; Pitilakis and Anastasiadis, 1998; Raptakis et al., 1994a,b; Raptakis, 1995; Anastasiadis et al., 2001; Apostolidis et al., 2004). The dynamic properties of the main soil formations have been defined from an extended laboratory testing including resonant column and cyclic triaxial tests (Pitilakis et al., 1992; Pitilakis and Anastasiadis, 1998; Anastasiadis, 1994).

Site effects are based mainly on 1D linear equivalent response analyses, and few 2D analyses in selected cross sections, in order to take into account the influence of local geotechnical characteristics and dynamic properties of the main soil formations, on expected seismic ground motion. The analysis is conducted for five different scaled real accelerograms (for bed rock motions), appropriately selected according to the seismic hazard study, for the three scenarios (Papaioannou, 2004).

As an example, the characteristics of the calculated mean seismic ground motions at the free surface, in terms of peak acceleration (PGA) and velocity (PGV) are presented in Figure 2 for the earthquake scenario with 10% probability of exceedance in 50 years (mean return period of 475 years). It is mentioned here that PGA values are varying from 0.15g to 0.55g while, if the whole analysis was based on the Hellenic seismic code, the design PGA should be equal only to 0.16g. Similar maps have been generated for all seismic scenarios, and for several other ground motion parameters (i.e. ground strains, response spectra at different periods, etc).

Finally, in order to account for the liquefaction-induced phenomena, the evaluation of permanent ground horizontal and vertical displacements, (lateral spreading and settlements), has been performed for the three scenarios, using empirical and analytical procedures (Seed et al., 2003; Youd et al., 2001; EC8; Ishihara and Yoshimine, 1992; Elgamal et al., 2001). Figure 3 illustrates the spatial distribution of permanent ground settlements for the 475 years scenario.

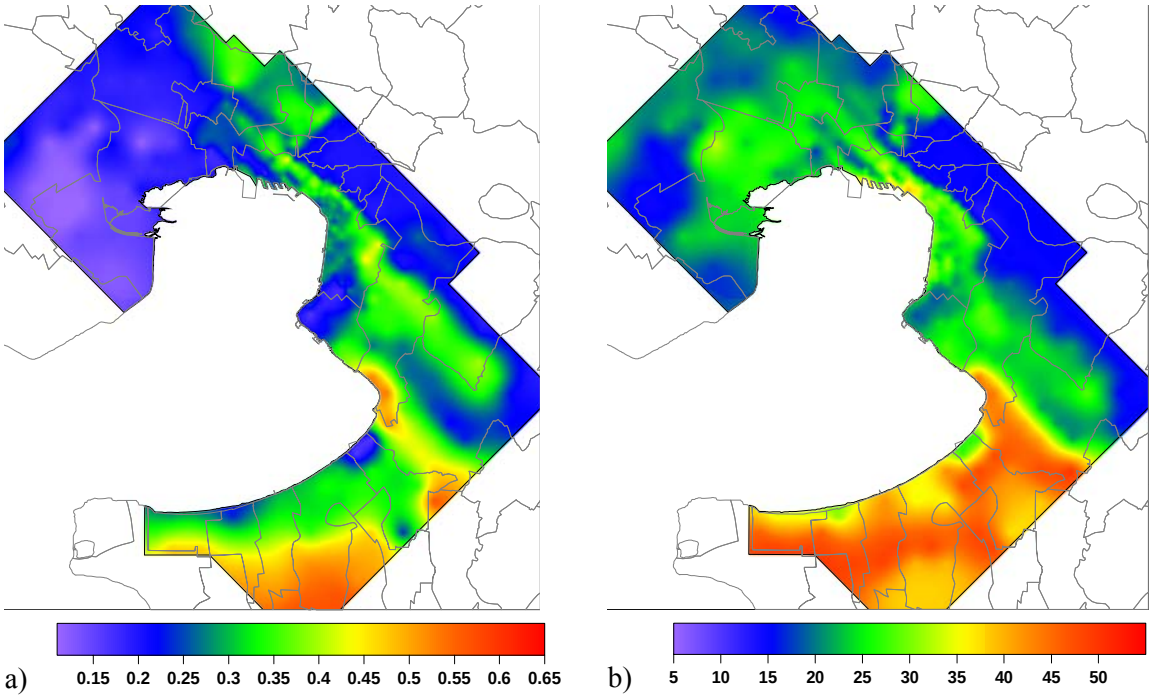


Figure 2. (a) Distribution of mean peak ground acceleration (PGA in g) and (b) mean peak ground velocity (PGV in cm/s) for the 475 years seismic scenario.

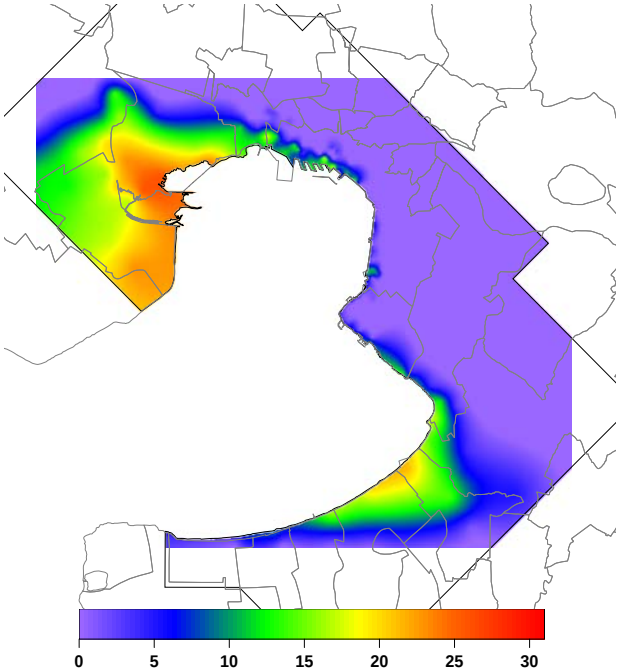

Figure 3. Distribution of the mean values of peak permanent ground settlements due to liquefaction - Δv(cm) for the 475 years seismic scenario.

### 3.2 Düzce microzonation study

The region of Düzce is one of the more active seismic areas worldwide, as is located very close to the North Anatolian Fault (NAF). Both Kocaeli (August 17, 1999, M=7.8) and Düzce (November 12, 1999, M=7.2) earthquakes occurred in a region dominated by the North Anatolian Fault. Site-specific ground response analysis has been performed for the city of Düzce, for different earthquake scenarios, based on one hand on the available geological, seismological and geotechnical data, and on the other hand on specific geotechnical and geophysical surveys performed for the purposes of this study (Manou et al., 2007, 2010; Pitilakis et al., 2010a). The study has been conducted in the framework of several research projects (MERP, 2002-2005; SRM-DGC, 2006-2008).

A simplified soil classification provided by EC8 was followed taking into consideration the geological zonation of the Düzce region, for the case of the Düzce 1999 earthquake event based to the deconvoluted acceleration time history of Düzce 12-11-1999 record. The estimation of the peak ground acceleration was based on the results of the seismic hazard study for the Düzce case. Then a series of 1D analysis was performed in several well-selected and representative sites along the city of Düzce, for several seismic scenarios proposed by the seismic hazard analysis (Alexoudi et al., 2008a) and for six input motions scaled to the estimated in each scenario, PGA for outcrop conditions. The dynamic properties of the soil configurations for the synthesis of the soil profiles were derived from the results of all available geotechnical data and geophysical surveys (HVSR technique and microtremor measurements), that are performed in Düzce. This correlation led to the synthesis of 2D geotechnical cross-sections; then, based on these detailed cross sections, we derived thirty representative 1D dynamic soil profiles for the 1D EQL site response analysis.

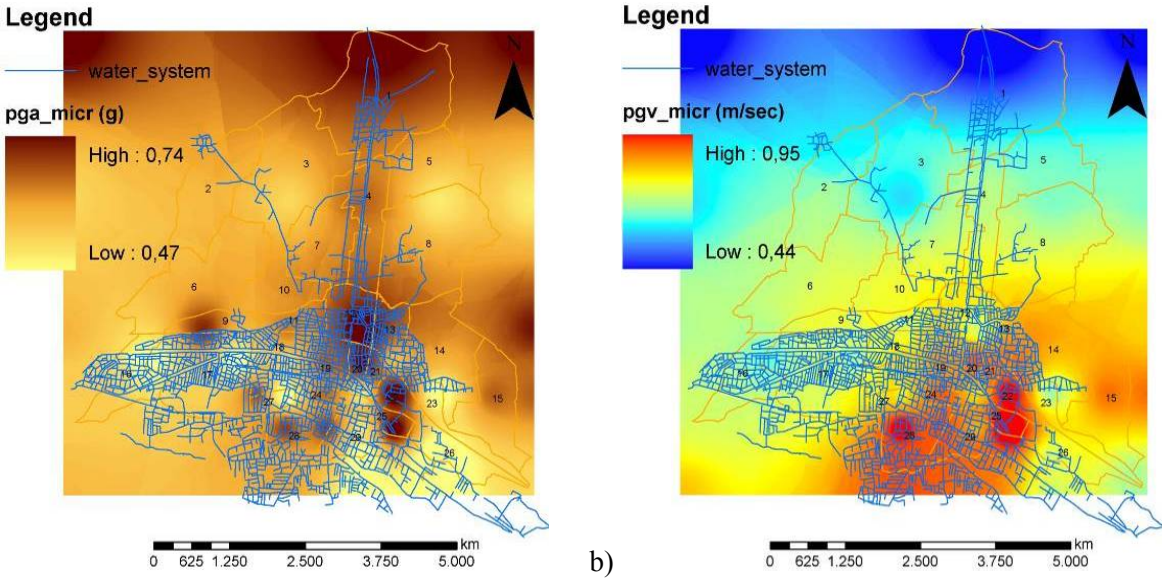


a) b)

Figure 4. Spatial distribution of (a) average PGA (g) and (b) average PGV (cm/sec) values in Düzce.

The results derived from the 1D seismic response study were further analyzed in order to estimate average acceleration response spectra, peak ground acceleration and displacement values at the ground surface, peak ground velocity values at the pipelines' depth and peak spectral acceleration values for specific period values. Based on the geophysical, geotechnical and geological investigations, a correlation of the results in adjacent sites was carried out in order to accomplish the zonation of the city in uniform seismic response zones. The results are presented in terms of tables, diagrams and maps in GIS format that present the spatial distribution of the strong ground motion. Figure 4 illustrates the spatial distribution of the average Peak Ground Acceleration (PGA) and Velocity (PGV) values in Düzce.

## 4 VULNERABILITY ASSESSMENT AND LOSS SCENARIOS

A fundamental requirement for assessing the seismic performance of a system is the ability to quantify correctly the damages related to the level of seismic hazard intensity, and of course the typology of each component and system. In general, vulnerability functions are deterministic, statistical or probabilistic relationships relating the component's damage state, functionality, economic losses etc, with an appropriate measure of the intensity of the earthquake hazard. The characterization of the components is based on the specification for each component type generic fragility functions (see e.g. HAZUS, NIBS, 2004; RISK-UE, 2001-2004; LESSLOSS, 2004-2007). Besides the great inherent uncertainties, the key assumption in the vulnerability assessment of lifeline systems and infrastructures is that structures having similar structural characteristics, being in similar geotechnical conditions are expected to perform in the same way for a given seismic loading. The spatial variability of the ground motion, which is one of the major causes of lifeline damages, is due mainly on the differential site amplification characteristics inherent to the local site conditions. Basin edge and azimuth effects may be also considered through appropriate 2D or/and 3D modeling of ground motion, which may modify the final ground motion for the vulnerability assessment (Pitilakis et al., 2010b; Pitilakis et al., 2001; Paolucci and Pitilakis, 2007). Thus, the respective fragility functions should be defined on the basis of the typological characteristics of the elements at risk, taking also into consideration specific construction practices and distinctive features affecting their seismic behaviour.

Several representative examples are given below of the vulnerability assessment of lifelines and infrastructure systems in the cities of Thessaloniki and Düzce. Seismic loss scenarios have been estimated in the framework of national and European research projects (RISK-UE, 2001-2004; SRMLIFE, 2003-2007; LESSLOSS, 2004-2007; SRM-DGC, 2006-2008), based on the results of the microzonation studies performed for the two cities. To this end appropriate inventory has been performed and appropriate fragility curves have been selected.

4.1 Roadway system of Thessaloniki

The inventory for the roadway network in the metropolitan area of Thessaloniki includes about 600 km of road-lines and 80 bridges. The roadway system is rather insufficient, especially in the centre, where the densely built up area creates a complex network, with narrow streets and inadequate parking areas. Roads are classified in freeways, major and secondary arterials, primary and secondary collectives, based on their geometry and functional role in the network. The majority of bridges are in the ring road and the main exits of the city. Their classification is based on the number of spans (single or multiple), the design seismic code level (low or upgraded), the pier type (single or multiple columns) and the span continuity (continuous or simple support). The vulnerability analysis of the network includes the estimation of direct losses such as bridge and road damage due to ground shaking or ground failure, and indirect such as street blockades, due to debris of collapsed buildings.

The expected level of damages for bridges is assessed based on the fragility curves that are provided in HAZUS (NIBS, 2004), for the input earthquake hazard scenario and the estimated mean spectral acceleration at T=1.0sec considering the site specific analysis of ground motion (Argyroudis, 2010). The estimated damage state for each bridge for the 475 years seismic scenario is presented in Figure 5 (Pitilakis et al., 2010c). The majority of bridges will respond in a satisfactory way, but there are still few bridges, which are expected to sustain serious damage for the specific seismic hazard scenario. This is due to the higher vulnerability of these bridges (single column, simple support bridges and inadequate seismic design), and the higher values of the expected surface spectral acceleration. The latter is attributed to the local soil conditions and the proximity of the seismic source (ex. southeast part). For instance, in the west part of the city, deep soft alluvium deposits of sandy-silty clays to clayey sands-silts, with low strength and high compressibility, (category C and D in EC8), present stronger amplification at longer periods.

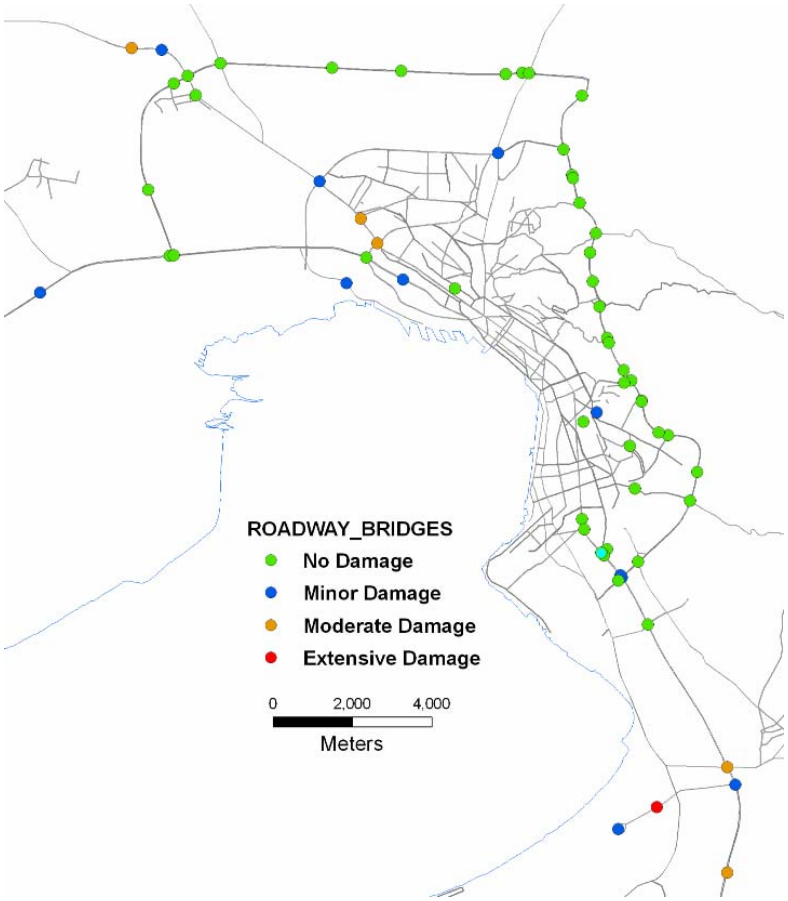


Figure 5. Distribution of expected damages to roadway bridges of Thessaloniki for the 475 years seismic scenario.

For the functionality of roads just after the earthquake a correlation between the building's height (i.e. number of storey) and the width of the induced debris is used, in order to estimate the impact of collapsed buildings (Anastassiadis and Argyroudis, 2007; Argyroudis, 2010). The spatial distribution of the collapsed or heavily damaged buildings is again depending on their typology and the site conditions. A Gaussian distribution describes the variation of the debris width, which is a function of the building collapse angle (φ) and the building volume reduction (kv). This model is used in order to estimate the exceedance probability of certain road function levels (100% open, 50% open, 0% closed or one lane open). The collapse probability of buildings is estimated based on appropriate fragility models which have been developed for the building types commonly presented in Thessaloniki, as a function of the peak ground acceleration (Kappos et al., 2006; Penelis et al., 2002).

Past experience in Greece reveals that a percentage of collapses ranging between 10 and 20% can have such form and amount of debris, which can result to road closure. The probability of closure due to building collapse is calculated based on the combination of the aforementioned probabilities for each road segment (node to node). Figure 6 illustrates the probability of closure for the main roads in the central city due to building collapses for the scenario with a mean return period 1000 years. The reduction of the road width depends on the distance from the buildings, the width of the road and the induced debris width, while the closure probabilities depends on the concentration of the most vulnerable building type, the length of the road segment and the discrete collapse probabilities related to the local site conditions.

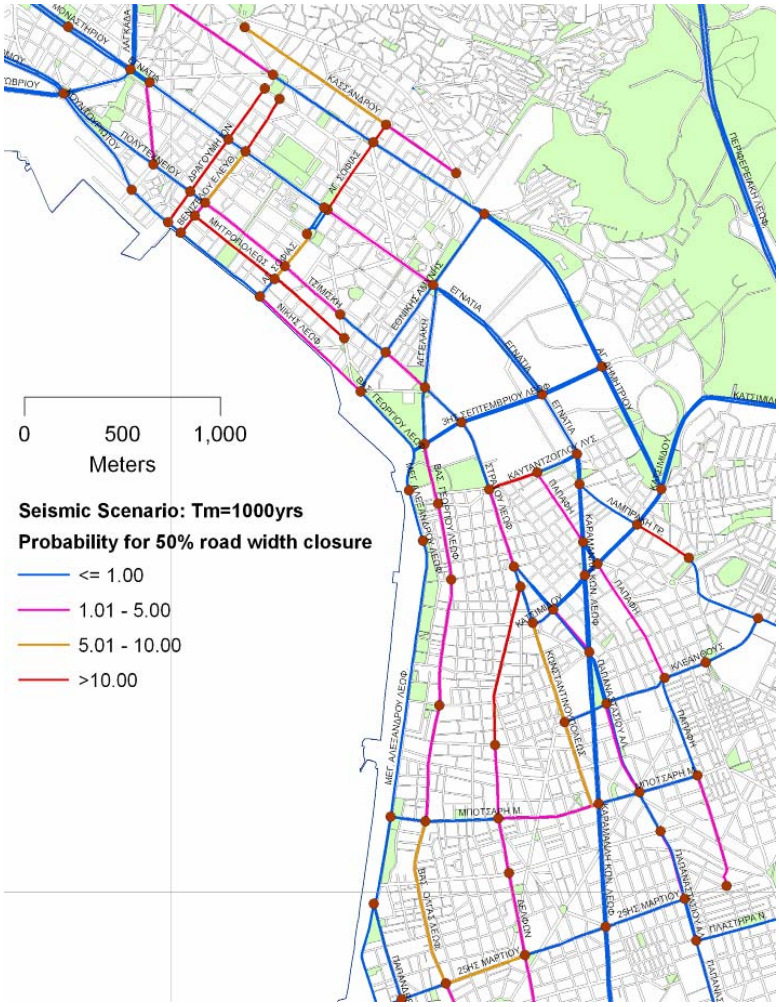


Figure 6. Sample map with probabilities for 50% road width closure of the main road network due to building collapses for the 1000 years seismic scenario.

4.2 Port system of Thessaloniki

The Port of Thessaloniki covers an area of 1,500,000 m2 and trades approximately 15,000,000 tons of cargo annually, having a capacity of 200,000 containers and 6 piers with 6,500m length. In collaboration with the port authority (Thessaloniki Port Authority, THPA), various data was collected and implemented in GIS format for the construction, typological and functional characteristics of the considered elements at risk, including cargo and handling equipment, waterfront structures, electric power, potable and waste water, telecommunication, railway and roadway systems as well as buildings and critical facilities.

Loss estimations are performed for the port facilities, utility networks, transportation systems and buildings based on the results of the site specific (microzonation) study presented earlier and for the three seismic scenarios ($T_m$= 100, 475 and 1000 years). The soil conditions are quite poor dominated by soft – loose alluvial deposits at great depth. In each particular system, adequate fragility curves and/or vulnerability relationships were used, based on the specific features and typology of the considered elements at risk. The type, extent and spatial distribution of induced earthquake damage were specified and illustrated in GIS thematic maps (Kakderi and Pitilakis, 2011). In the following, an example of the vulnerability assessment and estimated direct damages is provided for the building structures of Thessaloniki's port.

Buildings in a port system include administration and control buildings, traffic control buildings, passenger terminals, offices, security and maintenance buildings, sheds and warehouses and other critical facilities. Furthermore, buildings within lifelines systems and infrastructures are also considered (e.g. pumping stations, engine-houses, electric power substations, etc). Thessaloniki's port includes 88 elements of this type. Their typology was defined based on the construction material, structural type, height and seismic design code level.

The vulnerability analysis of R/C buildings is performed based on fragility curves (in terms of PGA) that have been developed using a hybrid technique combining analytical results and statistical data (Kappos et al., 2006). Moreover, fragility curves (in terms of both PGA and $S_d$) for masonry structures that were developed for all typologies common in Greece were used in the present application (Penelis et al., 2002). Vulnerability assessment for the three seismic scenarios has been performed, using a reduction factor of 0.7 for the conversion of peak to effective values of ground acceleration. The distribution of estimated damages for the port building for the 475 years scenario is illustrated in Figure 7. 27%, 64% and 9% are estimated to sustain minor, slight and complete damages respectively.

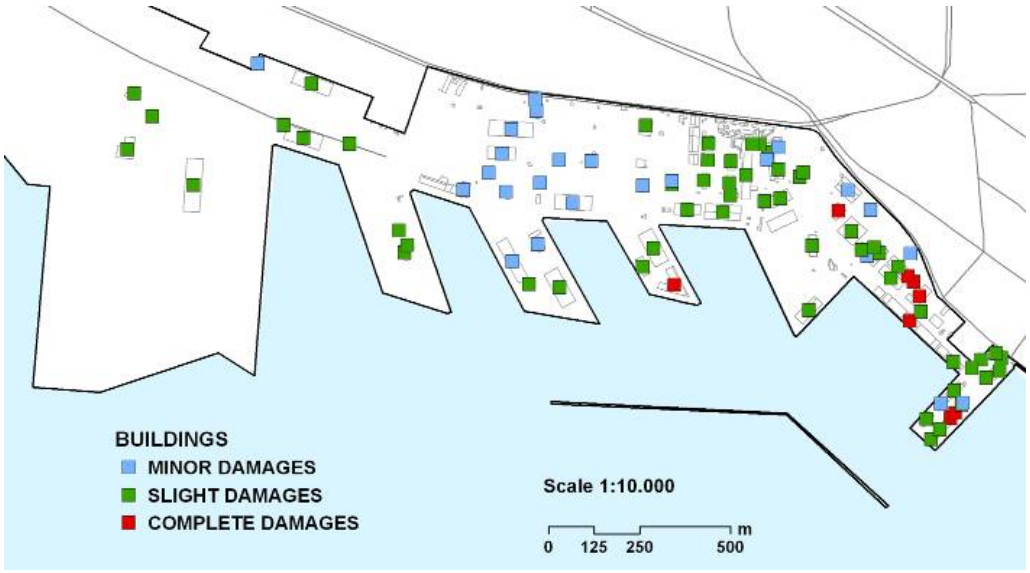


Figure 7. Distribution of damages to building structures of Thessaloniki's port ($T_m$=475 years).

4.3 Water system of Düzce

The water system in Düzce is about 500 km long and the great percentage dates back to 1940s (Tadday and Sahin, 2001). The network consists mainly of cast iron (CI) and asbestos cement (AC) pipes, which could be classified as brittle pipes. A 600mm diameter AC pipe conveys raw water from the main source, the River Ugur, to the water treatment plant at the south of the town. A 100 cm diameter steel pipe then carries the treated water to the distribution network, joining the town in the Azmimilli District. Twin CI pipes, of diameter 125 mm, transport water from a well field and reservoir to supplement the main river water supply; these pipes join the town in the north east district. The digitized pipeline network, with a total length of 298km, is a mixed system, comprising both old and recently constructed parts.

The vulnerability assessment of the water supply network of Düzce (in terms of the expected Repair Rate per pipe km - RR/km) is performed combining the results from the microzonation study of Düzce, with a mean return period of 475 years, and from two specific earthquakes using as input the deconvoluted time histories of Kocaeli and Düzce earthquakes recorded at the Meteorological Station in Düzce. Expected damages (leaks and/or breaks) caused by wave propagation are estimated using O' Rourke and Ayala (1993) fragility relation proposed by HAZUS (NIBS, 2004) according to the type of ground failure (for wave propagation: 20% of failures is assumed as breaks and 80% as leaks); the seismic loading is described in terms of peak ground velocity (PGV). Prior to their application, these empirical vulnerability functions have been validated with recorded damages in Düzce 1999 earthquake and in Lefkas- Greece 2003 earthquake (Alexoudi, 2005; Pitilakis et al., 2005b). Tromans' (2004) and Alexoudi (2005) database for water pipelines in Düzce was used for the validation. The percentage of the pipelines of the network that are expected to have some type of damage for the Kocaeli and Düzce earthquakes, and for the average values given by the microzonation study, is 7%, 9% and 13% respectively (Alexoudi et al., 2010).

Figure 8 illustrates the spatial distribution of the estimated water pipe damages per district in Düzce for the microzonation study. The majority of damages are expected at the southern and eastern part of the city, which is well compared with the recorded damage distribution during the sequence of Kocaeli and Düzce earthquakes (Manou et al., 2007).

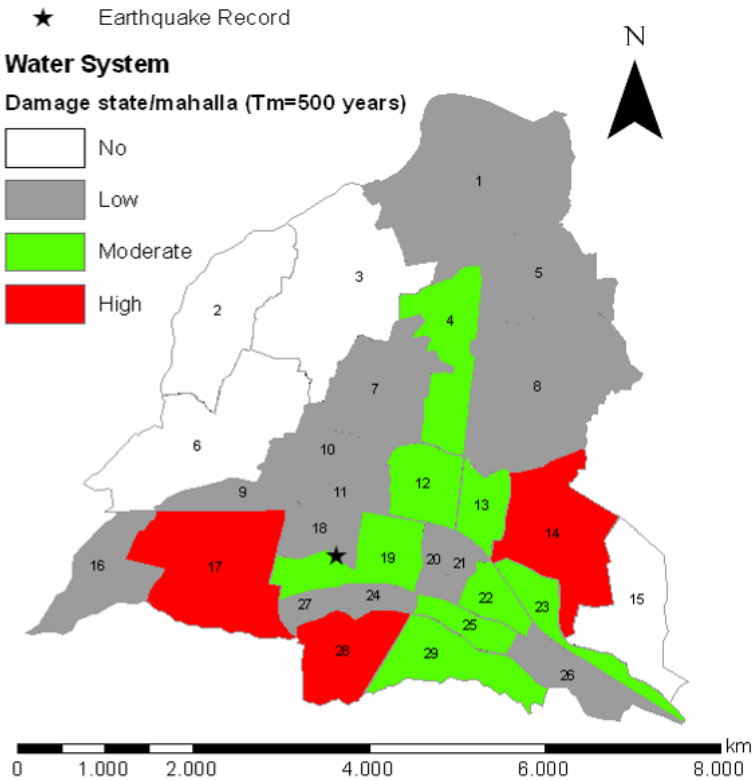


Figure 8. Estimated water pipe damages per district (machala) in Düzce for the microzonation study.

## 5 SYSTEMIC SEISMIC PHYSICAL AND SOCIO-ECONOMIC VULNERABILITY AND RISK ANALYSIS

The impact of the disaster caused by a natural hazard (like an earthquake event) on a system evolves with time elapsed from the event and in space. In the aftermath of the event, the damaged infrastructure operates in a state of emergency, and only progressively returns to the previous or a different state of normal functionality. Correspondingly, the spatial extent of interest to the study of the infrastructure response increases, involving adjacent regions in the economic recovery phase and multiple interactions between systems and with the built environment. A representative case of interactions among different lifeline systems during the restoration period is reported after the 1995 Kobe earthquake by Hada and Meguro (2000). They outlined the problems in the restoration activities of water and gas network in Kobe area due to traffic congestion, street blockades, damaged buildings and water flowed into gas pipelines; they also analyzed their effects based on real data. In the framework of a comprehensive risk analysis and management of interacting lifeline and infrastructure systems, their seismic performance should be considered in a rigorous and unified way. This could only be achieved through the assessment of the systems functionality, considering the complexity of structures and the interdependencies among systems and their components.

The relation/ interactions between the components can be distinguished into intra-relations between the components of each system, and inter-relations between the systems making up the infrastructure (Figure 9). The formulation of a system function allows for the evaluation of the state of the system as a function of the states of its components. The availability of such a function is a prerequisite for the evaluation of the system performance. It is noted here that the spatial characterization of the components (sub-systems) of an infrastructure has a direct relation with the approaches to be used for the definition of both their hazard and vulnerability.

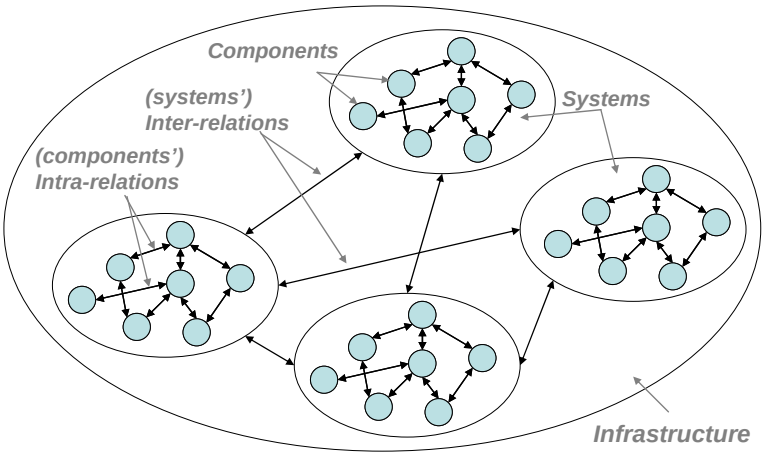


Figure 9. Graphical representation of an infrastructure comprising a number of systems with their interactions.

Several approaches are available in the literature to help describe the relations existing between a system's components. Some of these are: Graph theory; Fault-tree analysis (FTA); Event-tree analysis (ETA); Series system in parallel (SSP); Agent-based models and Complex Adaptive Systems (Amin, 2001; Little, 2002; Brown et al. 2004; Bernhardt and McNeil, 2004; Tolone et al., 2004).

The probabilistic evaluation of the performance of the system (PNET) can be carried out employing the methods of System Reliability Analysis. These include expansion methods, such as FORM/SORM or the response surface technique (Ditlevsen and Madsen, 1996), as well as the Monte Carlo simulation methods (Rubinstein, 1981). Depending on the nature of uncertainty and the aptitude to determine them, the probabilistic approach may be replaced or enhanced by possibilistic approaches based on Fuzzy Logics, so-called Fuzzy Networks.

Despite the fact that non-simulation methods have recently seen interesting advances, e.g. in the form of Matrix System Reliability Analysis (Song and Der Kiureghian, 2003; Der Ki-

ureghian and Song, 2008), the complexity of civil infrastructural systems, (especially the analysis of capacitive networks such as transportation, power transmission and water-supply networks), and the increasingly quantitative approach to the evaluation/ prediction of the behavior of other complex systems, of economic or social nature, the simulation approaches have recently undergone most significant progresses. These new developments, collectively denoted as "Modern simulation methods", consist of smart techniques dealing with sensitivity analysis and stochastic optimization of computer simulation models (Rubinstein and Melamed, 1998) or Neural networks (NN).

Several researchers have tried to go beyond the simple summation of direct loss and include consideration of the interactions between system components in determining the deterioration of the system function due to an earthquake. As an example, one can mention the studies undertaken by Franchin et al. (2006), Nuti and Vanzi (1998), Basoz and Kiremidjian (1996), Werner et al. (1999), Shinozuka et al. (2003), Douglas et al. (2007), Karaca (2005), and Veneziano et al. (2002) for transportation networks, by Pachakis and Kiremidjian (2003, 2004) for harbor facilities and by Shinozuka et al. (1999), Liu et al. (2004), Ostrom (2003), Giannini et al. (1999), Vanzi (1996, 2000), Nuti et al. (2007) for electric supply networks. The studies for the seismic risk analysis of roadway networks in terms of road closures due to collapsed buildings and/or adjacent are limited (Goretti, 2005; Anastassiadis and Argyroudis, 2007; Argyroudis, 2010).

Furthermore, the probabilistic assessment of the seismic performance of any system must yield as outcome a quantity that is meaningful to the decision-makers and the stake-holders (JCSS, 2008). The definition of the most appropriate quantity for each system, denoted as "performance measure", is itself a challenging task. For example, measures have been proposed to quantify the reduced performance of a damaged/ congested transportation network in the form of a "Driver's Delay" (Shinozuka et al., 2003) or, to quantify the performance of a health-care facility, in the form of the "Hospital Treatment Capacity" (HTC) i.e. the number of patients that can be given surgical treatment per hour (Lupoi et al., 2008). For electric power transmission or water supply networks performance measures have been proposed in the form of the "Service Flow Reduction", i.e. the amount of flow that can be delivered to users compared to the amount prior to the damage/ disturbance (Dueñas-Osorio et al., 2007).

Moving to a higher level, interactions between different critical infrastructures which may seriously affect the seismic risk management (response, recovery and mitigation) is an emerging research area where special interest has been recently given into. Several researchers have proposed different types of interdependency simulation models (Wong and Isenberg, 1995; Kameda, 2000; Giannini and Vanzi, 2000; Rinaldi et al., 2001; Peerenboom et al., 2001; Amin, 2001; Haimes and Jiang, 2001; Little, 2002; Li and He, 2002; Tang et al., 2004; Yao et al., 2004; Brown et al., 2004; Bernhardt and McNeil, 2004; Santos and Haimes, 2004). Only few methodologies have incorporated interdependencies in the seismic risk analysis of lifelines (Hoshiya and Ohno, 1985; Nojima and Kameda, 1991; Scawthorn, 1992; Eidinger, 1993; Shinozuka et al., 1993; Shinozuka and Tanaka, 1996; Menoni, 2001; Dueňas-Osorio, 2007; Tang and Wen, 2009) in a quite simplified way and lacking an integrated view of the response of complex infrastructure networks during the different periods in respect to the occurrence of an earthquake event.

Furthermore, very few studies can be found in the literature dealing with the highest level problem of multiple systems interaction in the case of seismic vulnerability and loss estimates (Dueňas-Osorio et al. 2007, Kim et al. 2007). They have still an exploratory character and are based on rather extreme simplifications, being limited to the analysis of at most two systems. Infrastructures' interdependencies are usually addressed through network analysis. Graph theory is adopted by several researchers. The Bayesian approach is often used for network analysis. The function states of the systems are also analyzed using flow analysis and connectivity analysis. One of the most comprehensive studies available, albeit including only a part of the vulnerable systems, is the one in Karaca (2005), which explores the consequences of a major earthquake in the Central-Eastern US by modelling the economic activity in the whole US and its disruption due to the event. Finally some recent studies have been focused on the proposal of a methodology to evaluate the associated losses of interacting lifeline elements for various strong motion intensities and the estimation of complex fragility curves of interdependent components (Kakderi et al., 2007, 2008; Alexoudi et al., 2008b,c).

In the most recent study developed in Aristotle University of Thessaloniki (AUTH) by Selva et al. (2010) a generic procedure is developed for the assessment of the serviceability of a system, if one or more interacting components of the system are damaged by an earthquake, assessing and merging the different levels of both "physical damage" and "non-functionality". Either a single system composed by many interacting components (e.g., one lifeline) or a system of systems (e.g., a set of lifelines and infrastructures) are addressed, where interaction among components and systems are accounted for. The various types of uncertainties (aleatory and epistemic) are treated with the use a Bayesian inference. The proposed methodology is quite general and it is applicable, eventually with several further improvements, assumptions and/or simplifications, to real systems with diverse degrees of complexity and knowledge of system and components details.

What is also of major importance is to transfer the interdependencies and consequences of losses in physical systems (buildings, utility and transportation network components, critical facilities) to their direct and indirect consequences on society and economy (city and regional scale), as measurable indicators and values of socio-economic losses upon which policy and decision-making can take place. The quantification of the socio-economic consequences of a major earthquake is currently carried out at different levels of complexity. The vast majority of available studies are limited only to a first estimation of direct economic losses. The simple summation of the monetary losses separately incurred by the various systems does not represent, however, the actual total loss suffered by a society hit by an earthquake. Loss can be subdivided into direct and indirect. The former correspond to direct damage to the physical components of the system, while the latter stem from loss of function resulting from the physical damage, associated for example with economic losses due to business interruption, loss of productivity due to increased travel times on damaged transportation networks, the interruption of harbour activities, etc. Even if indirect loss can likely be the dominant contributor to total loss, it is usually estimated in approximate ways, since an accurate estimation of the economic consequences of the loss of function of one system requires the evaluation of its impact on the other systems of the infrastructure.

Regarding merely social costs losses (i.e. fatalities, injuries, homeless, shelter needs, etc.), one of the most referenced social loss methodologies is the one proposed by Coburn and Spence (2002), which however has not been proved reliable for developed countries. Other available in the literature global social and economic consequence functions include the methods proposed by Spence (2007), ATC-13, Badal and Samardzhieva (2003), KOERILoss (Erdik et al., 2003) Bal et al. (2008 a, b), MAEViz (MAEC, 2009), Porter et al. (2008 a, b). The current state of the art in earthquake loss estimation software provides several parameters of direct socio-economic consequences which are needed to support effective decision making. These include parameters such as casualties, homeless, and business failures by industry, for example. However, poor linkages between damage estimates at a system's and system of systems level and the social and economic vulnerability conditions contribute to significant limits within existing earthquake loss estimation. Including social vulnerability allows for a greater level of information to be obtained from the vulnerability modeling results for use in disaster response (e.g. homeless shelter needs and required supply). The definition and characterization of human, institutional and functional vulnerability (and resilience) of a city or region to earthquake damage of complex infrastructures should be accounted for in terms of recovering from the impacts of an earthquake.

Currently, there is an ongoing research effort to increase the understanding of the vulnerability of various societal elements at risk belonging to a system (city, region, lifeline network, etc) and to develop appropriate methods and tools to consider inter-element and intra-systems interdependencies, including socio-economic features under the European project SYNER-G (2009-2011) coordinated by the first of the authors of this paper (www.syner-g.eu). Figure 10 illustrates graphically the main concepts and goals of SYNER-G. Apart from the selection of the most advanced fragility functions and methods to assess the physical and societal-economic vulnerability of assets (buildings, utility systems and transportation infrastructures, society, economy), improving and further developing new ones where necessary, considering European distinctive features and the proposal of the most appropriate means of selecting seismic scenarios at system level, the ongoing research efforts are focused on the development of a unified methodology to assess vulnerability at a system level considering interdependencies between elements at risk (physical and non-physical), belonging to different systems and between differ-

ent systems as a whole at city and regional scale. An appropriate open-source software and tool will be built to deal with systemic vulnerability in order to improve the seismic risk assessment and management, while the effectiveness of the methodology and the tools will be validated to specific and well selected case studies at city and regional scale.

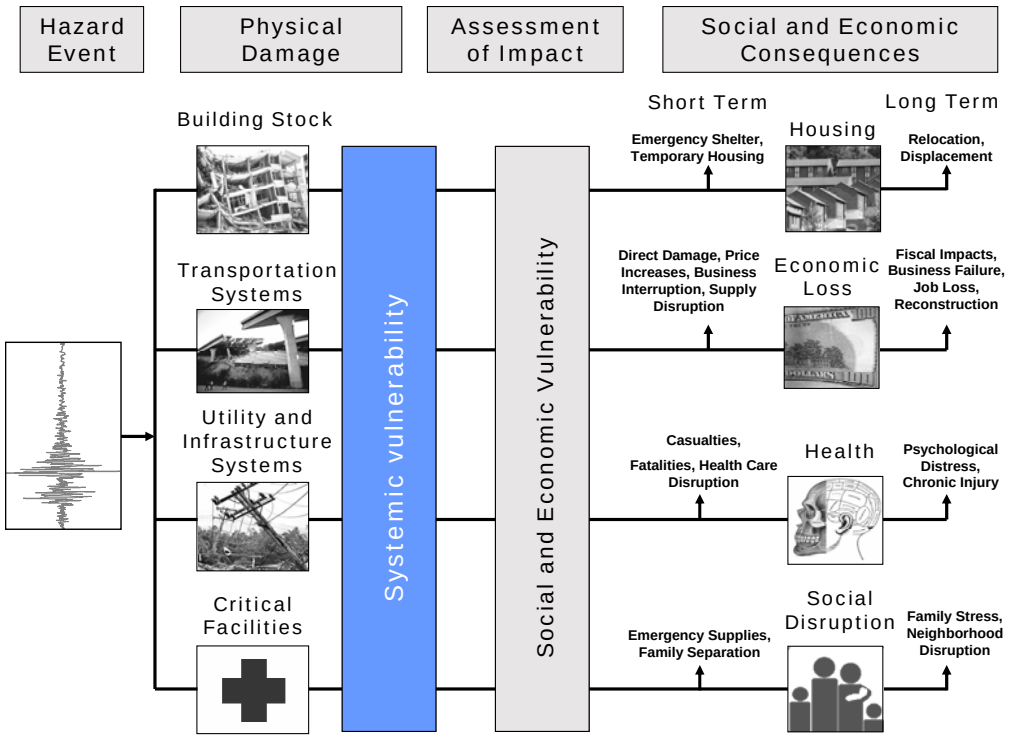


Figure 10. General graphical layout of the concept and goals of SYNER-G (2009-2011) (www.syner-g.eu)

## 6 MANAGEMENT AND MITIGATION OF SEISMIC RISK

### 6.1 Global value analysis

A conventional seismic risk analysis is limited to the evaluation of the direct impact (usually in economic terms and fatalities), of isolated components, based on the seismic hazard and the physical vulnerability of the elements. An advanced seismic risk study of lifelines, utilities and infrastructures should include the functional and social vulnerability, taking into account the functional relations between the different elements, urban activities (production, consumption, exchanges) and relations of the network with its surrounding urban or rural environment. In that way each system will be analyzed as an integrated part of the seismic risk scenario and as a part of the urban system, while the main issues of the lifeline system will be identified. This is performed through a "global value" analysis of the elements at risk; a methodology originally developed within the RISK-UE (2001-2004) project.

The aim of the global value analysis is to identify the main issues and relative importance of each lifeline network, through appropriate ranking of the value of the exposed elements, based on various factors that describe the role of each element in the urban system. In that way, the global value of each element at risk, depends not only on its direct specific value or content (physical and human), but also upon its indirect/immaterial value, that is represented by the usefulness and relative role in the whole urban system, at a specific time. Three periods are identified in respect to the occurrence of an earthquake event: normal, crisis and recovery. "Global value" evaluation in different periods could be a powerful tool for the prioritization of pre-earthquake actions and quantification of the overall importance of different complex and coupled lifeline systems (Pitilakis et al., 2006a). Several criteria for this are used, such as operational attributes, land use, population influenced, human losses, economic and social weight un-

der normal, crisis and recovery circumstances, identity/ radiance, environmental impact and other. Appropriate qualitative or quantitative indicators can then be defined for each period, while relevant measuring units are used for their evaluation and the identification of "main", "important" and "secondary" elements and system's weak points.

Table 1. Indicators used for the global value analysis and classification of importance of waterfront structures of Thessaloniki's port.

| WATERFRONT STRUCTURES | | | PERIOD | | |
|---|---|---|---|---|---|
| Components | Indicators | Description | Normal | Crisis | Recovery |
| Operation | 1. Operational depth | Maximum draught of the ships able to harbor. | • | • | • |
| Operation | 2. Alternative use (redundancy) | Alternative equipment to cover the activity. | - | • | • |
| Urban activities and interactions | 3. Impact radius | Impact radius. Type of cargo/ movements served. | • | • | • |

The methodology has been applied for the global value analysis of lifelines and infrastructures systems in Thessaloniki (Greece), in the framework of the national project SRM-LIFE (2003-2007) (Pitilakis et al., 2007b; Pitilakis et al., 2010c). An example of the indicators used for the classification of the importance of Thessaloniki's port cargo handling equipment is provided in Table 1. Cargo handling operation during and after the crisis is crucial for the successful recovery reaction and resilience following a major earthquake event. Other elements at risk have different indicators depending on their relative importance in the crisis management process. Representative GIS maps illustrating the definition of main, important and secondary elements at risk can also be constructed. As a representative example, Figure 11 illustrates the classification of the importance of waterfront structures of Thessaloniki's port during the crisis period.

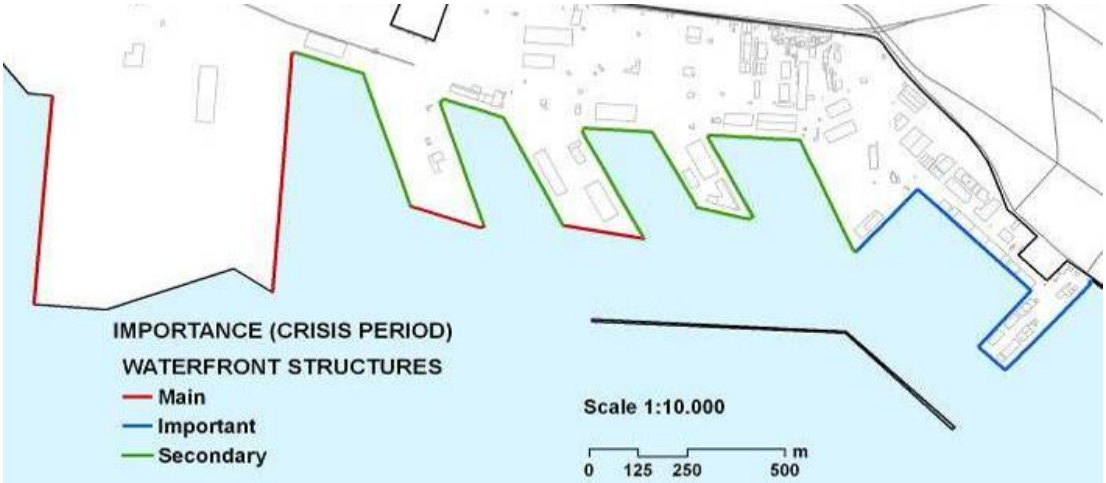


Figure 11. Classification of the importance of waterfront structures of Thessaloniki's port during the crisis period.

## 6.2 Restoration policies and mitigation strategies

The pre-earthquake mitigation plans must be based on appropriate prioritization criteria that combine engineering techniques, economic analysis tools and decision-making or political aspects. The identification of "main", "important" and "secondary" element at risk in "normal" period provides a prioritization according to the importance of the activities, the social and economical values and the daily demand for serviceability.

A disaster management plan can enhance the pre-earthquake activities for retrofitting (or strengthening), important and critical components in the urban environment and prepare an efficient organization of public services and local authorities for "crisis" period. For the "recovery"

period an efficient management plan must minimize the restoration time, the efforts and the cost. In order to achieve reliable estimates of the required time for recovery, lifeline owning and operating companies, local actors in collaboration should define restoration curves for every component in each lifeline system, with lifelines experts using basically qualitative evaluations.

A method was developed applying the "global value" approach which uses the classification of lifeline system components into main, important and secondary, according to their global value (SRM-LIFE, 2007-2007). Combining "global value" evaluation and vulnerability assessment, it is possible, using, if necessary, an "expert opinion" as well, to estimate priorities and to account for the economic and social losses, for a specific utility system and a given seismic scenario. Recovery activities could also follow these priorities aiming at efficient seismic risk management procedures.

This method was applied to the city of Thessaloniki (Pitilakis et al., 2007b; Pitilakis et al., 2010c). Table 2 provides an example of the pipelines retrofitting priorities. Restoration curves have also been defined in collaboration with the local authorities, based on available man power, and capabilities, local experience and expertise. Figure 12 illustrates the functionality level of water pipelines 7 days after the seismic event for the 475 years scenario, assuming that the restoration process starts immediately after the earthquake.

Table 2. Risk analysis matrix showing pipelines seismic retrofit priorities.

| URBAN RISK/ SEISMIC HAZARD | PRIORITIES | | |
|---|---|---|---|
| | Main | Important | Secondary |
| Break | 1st priority | 1st priority | 2nd priority |
| Leak | 2nd priority | 3rd priority | 4th priority |

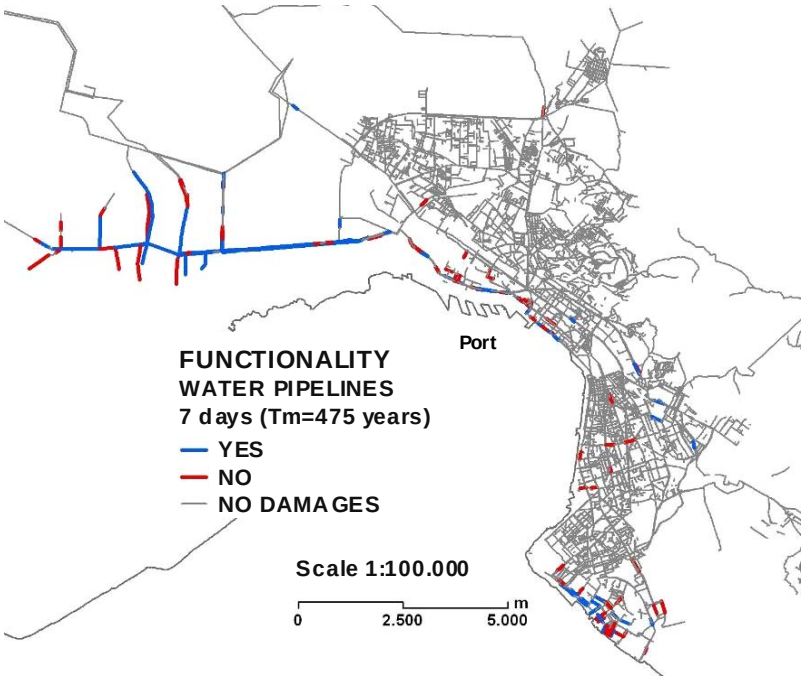


Figure 12. Functionality of pipelines of Thessaloniki's water system 7 days after the seismic event ($T_m$=475 years).

## 6.3 Retrofitting actions – Decision analysis

Seismic rehabilitation of structures is certainly the best way to reduce seismic losses. Multiple conflicting criteria and various uncertainties inherent in the seismic hazard and the systems' response, are systematically incorporated in any decision of intervention schemes to be applied for the reduction of earthquake risk (Park, 2004). Several factors like structural performance and/or direct structural cost, life losses and secondary economic losses, should be taken into consideration.

On the basis of a decision analysis for identification of the optimal target reliability level for rehabilitation of a given structure against seismic hazard as well as the best solution among several alternative rehabilitation schemes, different mitigation actions could be identified and implemented. The final decision on mitigation action(s) and level of intervention should be based on estimated results in relation to the reduction of potential losses, direct and indirect costs estimates for different mitigation actions and expected economic losses. Cost–benefit models have been proposed for the evaluation of the profitability of public or private investment in seismic retrofitting. Cost-benefit analysis (CBA) is a systematic procedure for evaluating decisions that have an impact on society. There are different ways to conduct a CBA, depending on the information one has and the nature of the problem at hand. In the case of seismic mitigation strategies, a comparison between the upfront investment costs of mitigation to the benefits of mitigation (e.g., reduction in loss, reduction in casualties, and reduction in lifeline system downtime) is completed. Studies performed mainly for buildings are for example the ones given in FEMA(1992), Chang and Shinozouka (1996) and Kanda and Shah (1997). These models permit comparison among alternatives by assigning monetary values to costs and benefits happening in the future and discounting them at the present time accounting for inflation and interest rate. In the case of Thessaloniki, the effects of three mitigation schemes that could be proposed for the reduction of potential losses of the building stock are investigated (Pitilakis et al., 2007a). Some of the most advanced models also account for the system behaviour of the networks (e.g. Augusti and Ciampoli, 1997; 1998; Kunreuther et al., 2001; Chang, 2003; Seligson et al., 2003). However, whether particular mitigation measures will be viewed as worth adopting is not a foregone conclusion but requires a detailed assessment of the costs and benefits under various hazard scenarios. The final decision is conditional to the available budget and the desirable level of the intervention and of course the anticipated level of physical damage for the specific seismic scenario. Finally, it is pointed out that a rigorous and effective risk management plan should be based on the comparative consideration of estimated losses through the assessment of the relative effects of different mitigation actions.

### 6.4 Real-time mitigation of seismic risk

Finally, an important progress is expected to the risk management of lifelines by applying real-time damage estimation data under GIS platforms. More accurate, and thus much more reliable data could be the basis for emergency services, predictions of damages intensity and spatial distribution for future events, loss estimations for each material and immaterial element at risk and mitigation strategies. Earthquake Early Warning (EEW) systems are mainly involved in the co-seismic phase. These involve the generation of real time ground motion estimation maps as products of real-time seismology and/or generation of alarm signals directly from on-line instrumental data. The Rapid Response Systems take part immediately after the earthquake and provide assessment of the distribution of ground shaking intensity (Shake Maps) or physical damage and casualties (Loss Maps). These maps can serve to direct the search and rescue teams to the areas most needed and assist civil protection authorities in the emergency action.

Few efforts made so far (i.e. Eguchi et al., 1997; Shimizu and Yamazaki, 1998; Nakayama et al., 2004), proved that these systems are probably the most powerful and efficient way to mitigate seismic risk reducing the uncertainties involved in all other methodologies. A summary of the work done over last decades regarding the development of new approaches and setting up of new applications for earthquake rapid response systems that function to estimate earthquake losses in quasi real time after an earthquake is provided by Erdik et al. (2010). Currently operating near real time loss estimation tools can be classified under two main categories depending on the size of area they cover: Global and Local Systems. Global or regional near real time loss estimation systems include the Global Disaster Alert and Coordination System (GDACS, http://www.gdacs.org), World Agency of Planetary Monitoring Earthquake Risk Reduction (WAPMERR, http://www.wapmerr.org), Prompt Assessment of Global Earthquakes for Response (PAGER, http://earthquake.usgs.gov/eqcenter/pager/) system of USGS and NERIES-ELER (http://www.neries-eu.org) methodologies. Several local systems (country-, city- or, facility-specific) capable of computing damage and casualties in near real time already exist in several regions of the world. For example the Taiwan Earthquake Rapid Reporting System, the Real-time Earthquake Assessment Disaster System in Yokohama (READY), The Real Time

Earthquake Disaster Mitigation System of the Tokyo Gas Co. (SUPREME) and the Istanbul Earthquake Rapid Response System (IERRS) provide near-real time damage estimation after major earthquakes (Erdik and Fahjan, 2006). Almost all of these systems are based on the assessment of demand in real time from dense strong motion instrument arrays and the estimation of damage on the basis of known inventory of elements exposed to hazard and the related vulnerability relationships. After an earthquake the shaking and damage distribution maps are automatically generated on the basis of the ground motion intensity measure data received from the field stations, building inventory and the vulnerability relationships. The latter is probably one of the weak points, as they are not actually time dependent, while both structures' quality and strength, and hazard are time dependent. Thus, the development of reliable inventory data and system time dependent vulnerability and loss assessment methodologies is a pre-requisite.

## 7 CONCLUSIONS

A rigorous disaster management process includes mitigation, preparedness, response and recovery actions in three periods: normal, crisis and recovery. A breakdown between the different processes and periods can help to evaluate the contribution of each phase to the overall safety management. A reliability earthquake risk reduction policy needs a multidisciplinary approach to estimate the likely emergency response resource needs and socioeconomic impacts of large earthquakes in urban areas. The expected economical (direct, indirect) and social consequences of an earthquake should be compromised with the level of tolerable risk.

Seismic vulnerability assessment is used to quantify potential losses in a given region or to a particular portfolio of lifelines, utilities and infrastructures, due to future earthquakes. The existence of preparedness plans based on the assessment of the impact of earthquakes and the minimization of their consequences are the most important tasks of civil protection. To fulfill these tasks, comprehensive earthquake loss scenarios have to be developed, in order to reduce the expected losses and improve the recovery actions.

Seismic risk scenarios take into consideration the inventory, the typology and vulnerability characteristics of different elements at risk, as well as the seismic hazard, geotechnical characterization and site response of the main soil formations for different seismic scenarios. Thus, vulnerability and loss estimates for lifelines and infrastructures are evaluated on the basis of site specific seismic hazard analysis using available inventory data and adequate fragility curves. Local site conditions and specific seismic ground response, conventionally referred as "zoning study", plays the key role in the vulnerability analysis and loss assessment.

Analyzing physical infrastructure systems in terms of the dimensions of systems interdependencies, namely infrastructure system characteristics, inter-system and intra-system causal relationships, environmental impact such as climate change, response behavior, failure types, state of operation and interdependency risks, yields new insights into infrastructure systems behavior and a consequent expanded thinking on risk informed decision making of critical infrastructure. Interdependent analysis can enhance loss estimation methodologies and indicate strategies for robust design and growth of infrastructures.

The identification of "main", "important" and "secondary" element at risk in "normal" period provides a prioritization according to the importance of the activities, the social and economical values and the daily demand for serviceability. A disaster management plan can enhance the pre-earthquake activities for retrofitting important and critical components in the urban environment and prepare an efficient organization of public services and local authorities for "crisis" period. For the "recovery" period an efficient management plan must minimize the restoration time, the efforts and the cost.

Earthquake hazard has in general low probability but high social and economic impact. The aim of a risk management strategy, especially for lifelines, is to maintain community safety and also to reduce physical damage and social and economic disruption. All decisions are based on the selection of the acceptable risk for the estimated seismic scenario. The selection of the acceptable risk and the appropriate seismic scenario or scenarios should combine the level of detail of the seismic hazard (microzonation study), the will of central and local actors, the available funds, the financial capability of the community and the country without neglecting the epistemic and physical uncertainties involved in every path of the any earthquake risk reduction policy.

The actual vulnerability and the associated risk of any element at risk may be reduced with appropriate mitigation countermeasures. The decision for mitigation of lifelines against seismic hazard is a quite complex issue as different parts such as government, local authorities, lifeline companies or insurance industry are involved. Moreover the decision by its self is very difficult because it should be made based on the results of the seismic risk assessment of lifelines which includes various uncertainties, owing to seismic hazard, vulnerability, performance and loss estimation procedures. The loss results can be used in order to prioritize the pre-earthquake mitigation measures, such as the retrofitting or redundancy of the elements with greater risk. Moreover, the loss results are considered to be the guide for an effective restoration policy.

Finally, potential impact of large earthquakes on urban societies can be reduced by timely and correct action after a disastrous earthquake. Modern technology permits measurements of strong ground shaking in near real-time for urban areas exposed to earthquake risk and should be further developed.

## REFERENCES


Alexoudi, M. (2005). Contribution to seismic assessment of lifelines in urban areas. Development of a holistic methodology for seismic risk. PhD Thesis, Civil Engineering Department, Aristotle University of Thessaloniki (in Greek).

Alexoudi, M., Manou, D. and Pitilakis, K. (2008a). Seismic vulnerability analysis of wastewater system. Methodology and application for Düzce and Kocaeli earthquakes. Proc. 14th World Conference on Earthquake Engineering (14WCEE), Beijing, China.

Alexoudi, M.N., Kakderi, K.G. and Pitilakis, K.D. (2008b). Advanced Fragility Curves of Interdependent Lifelines Using Decision Making Process. Proc. 1st International Symposium on Life-Cycle Civil Engineering (IALCCE'08).

Alexoudi M.N., Kakderi, K. and Pitilakis, K.D. (2008c). Seismic Risk of Interdependent Lifeline System Using Fuzzy Reasoning. Proc. 14th World Conference on Earthquake Engineering (14WCEE).

Alexoudi, M., Manou, D., Chatzigogos, Th. and Pitilakis, K. (2010). Influence Of Local Site Conditions In The Seismic Risk Assessment of The Water System in Düzce (Turkey). Proc. 6th National Conference of Geotechnical and Environmental Engineering, Volos, Greece (in Greek).

Amin, M. (2001). Toward Self-Healing Energy Infrastructure Systems. IEEE Computer Applications in Power, Vol. 14, No. 1, pp. 20-28.

Anastasiadis, A. (1994). Contribution to the determination of the dynamic properties of natural Greek soils. Ph.D. Thesis, Department of Civil Engineering, Aristotle University of Thessaloniki (in Greek).

Anastasiadis, A., Raptakis, D. and Pitilakis, K. (2001). Thessaloniki's Detailed Microzoning: Subsurface Structure as basis for Site Response Analysis. Pure and Applied Geophysics – PAGEOPH, Vol. 158 No. 12, pp. 2597-2633.

Anastassiadis, A.J. and Argyroudis, S.A. (2007). Seismic Vulnerability Analysis in Urban Systems and Road Networks. Application to the City of Thessaloniki, Greece. Sustainable Development and Planning, Vol. 2, No. 3, pp. 287-301.

Anderson, E. (2008). Central American Probabilistic Risk Assessment (CAPRA): objectives, applications and potential benefits of an open access architecture. Global Risk Forum, GRF Davos, Switzerland.

Apostolidis, P., Raptakis, D., Roumelioti, Z. and Pitilakis, K. (2004). Determination of S-wave velocity structure using microtremor and SPAC method applied in Thessaloniki (Greece). Journal of Soil Dynamics and Earthquake Engineering, Vol. 24, pp. 49-67.

Applied Technology Council (1985). Earthquake Damage Evaluation Data for California. Report ATC-13, Applied Technology Council, Redwood City, California, U.S.A.

Argyroudis, S., Pitilakis, K. and Anastasiadis, A. (2005). Roadway Network Seismic Risk Analysis in Urban Areas: The case of Thessaloniki - Greece. Proc. International Symposium of GEOLINE, Lyon.

Argyroudis, S. (2010). Contribution to seismic vulnerability and risk of transportation networks in urban environment. PhD Thesis, Department of Civil Engineering, Aristotle University of Thessaloniki, Greece (in Greek).

Augusti, G. and Ciampoli, M. (1997). Optimal distribution of seismic upgrading interventions to maximize the expected flow in a road network. VII IFIP WG 7.5. Boulder, CO: VII IFIP WG 7.5.

Augusti, G. and Ciampoli, M. (1998). Multi objective optimal allocation of resources to increase the seismic reliability of highways. Mathematical Methods of Operations Research, Vol. 47, No. 1, pp. 33–49.

Badal, J. and Samardzhieva, E. (2003). Prognostic estimations of casualties caused by strong seismic impacts. EGS-AGU-EUG Joint Assembly, Nice, France.

Bal, I.E., Crowley, H. and Pinho, R. (2008a). Displacement-Based Earthquake Loss Assessment for an Earthquake Scenario in Istanbul. Journal of Earthquake Engineering, Vol. 11 No. 2, pp. 12-22.

Bal, I.E., Crowley, H., Pinho, R. and Gülten Gülay, F. (2008b). Detailed assessment of structural characteristics of Turkish RC building stock for loss assessment models. Soil Dynamics and Earthquake Engineering, Vol. 28, No. 10-11, pp. 914-932.

Basoz, N., and Kiremidjian, A. (1996). Risk Assessment for Highway Transportation Systems. Stanford, Calif.: J.A. Blume Earthquake Engineering Center, Department of Civil Engineering, Stanford University, Report No. 118.

Bernhardt, K.L.S. and McNeil, S. (2004). An Agent Based Approach to Modeling the Behavior of Civil Infrastructure Systems. Engineering Systems Symposium, Tang Center, MIT.

Brown, Th., Beyeler, W. and Barton, D. (2004). Assessing Infrastructure Interdependencies: the Challenge of Risk Analysis for Complex Adaptive Systems. International Journal of Critical Infrastructures, Vol. 1, No. 1, pp. 108-117.

Chang, S.E. and Shinozouka, M. (1996). Life-cycle cost analysis with natural hazard risk. Journal of Infrastructure Systems, ASCE, Vol. 2, No. 3, pp. 62–78.

Chang, S.E. (2003). Evaluating disaster mitigations: Methodology for urban infrastructure systems. Natural Hazards Review, Vol. 4, No. 4, pp. 186–196.

Coburn, A. and Spence, R. (2002). Earthquake protection, Second edition, John Wiley & Sons Ltd, ISBN: 0-471-49614-6.

Der Kiureghian, A. and Song, J. (2008). Multi-scale Reliability Analysis and Updating of Complex Systems by use of Linear Programming. Reliability Engineering and System Safety, Vol. 93, No. 2, pp. 288-297.

Ditlevsen, O. and Madsen, H.O (1996). Structural Reliability Methods. John Wiley & Sons Ltd, Chichester.

Douglas, J., Serrano, J.J., Comte, J., Bouc, O., Arnal, C., Robida, F., Modaressi, H., Logtmeijer, C., Vowles, G. and Holt, I. (2007). Risk Assessment for the Road Network in the French-Iralian Border Region using web Services. Seventh IIASA-DPRI Forum on Integrated Disaster Risk Management - Stresa - Italie.

Dueñas-Osorio, L., Craig, J.I. and Goodno, B.J. (2007). Seismic Response of Critical Interdependent Networks. Earthquake Engineering and Structural Dynamics, Special Issue on Earthquake Engineering for Electric Power Equipment and Lifeline Systems, Vol. 36, No. 2, pp. 285-306.

EC8 (1998). Eurocode 8 - Design of structures for earthquake resistance -Part 5: Foundations, retaining structures and geotechnical aspects.

Eguchi, R.T., Goltz, J.D., Seligson, H.A., Flores, P.J., Blais, N.C., Heaton, T.H. and Bortugno, E. (1997). Real Time Loss Estimation as an Emergency Response Decision Support System: The Early Post-Earthquake Damage Assessment Tool (EPEDAT). Earthquake Spectra, Vol. 13, No. 4, pp. 815-832.

Eidinger, J. (1993). Fire Conflagration and Post-Earthquake Response of Power and Water Lifelines. Proc. 4th DOE of Energy Natural Phenomena Hazards Mitigation Conference, Atlanta, GA.

Elgamal, A., Yang, Z., Parra, E. and Ragheb, A. (2001). CYCLIC 1D. UCSD.

Erdik, M. and Aydinoglu, N. (2002). Earthquake performance and vulnerability of buildings in Turkey. Report prepared for World Bank Disaster Management Facility, Washington, DC.

Erdik, M., Aydinoglu, N., Fahjan, Y., Sesetyan, K., Demircioglu, M., Siyahi, B., Durukal, E., Ozbey, C., Biro, Y., Akman, H. and Yuzugullu, O. (2003). Earthquake risk assessment for Istanbul metropolitan area. Earthquake Engineering and Engineering Vibration, Vol. 2, No. 1, pp. 1–25.

Erdik, M. and Fahjan, Y. (2006). Damage scenarios and damage evaluation in 'assessing and managing earthquake risk.' In: Oliveira CS, Roca A, Goula X (eds), Assessing and managing earthquake risk. Springer, Netherlands, pp. 213–237.
Erdik, M., Sesetyan, K., Demircioglu, M.B., Hancilar, U. and Zulfikar C. (2010). Rapid Earthquake Loss Assessment After Damaging Earthquakes. Chapter 21, in Earthquake Engineering in Europe, Garevski, M. and Ansal, A. (Eds), Geotechnical, Geological, and Earthquake Engineering, Vol. 17, Part 6, pp. 523-547, DOI: 10.1007/978-90-481-9544-2_21.
FEMA (1992). A benefit–cost model for the seismic rehabilitation of buildings, FEMA-227Vols. 1 and 2. Sacramento, CA: Federal Emergency Management Report, 1992.
Franchin, P., Lupoi, A. and Pinto, P.E. (2006). On the Role of Road Networks in Reducing Human Losses after Earthquakes. Journal of Earthquake Engineering, Vol. 10, No. 2, pp.195-206.
Giannini, R., Pinto, P.E. and Vanzi, I. (1999). Earthquake Hazard Analysis Software: ASKx-ELP. Assessment of Seismic Risk for Electric Power Networks and Interaction with other Indicators of Seismic Damage. National Information Service for Earthquake Engineering, University of California, Berkeley, U.S.A.
Giannini, R. and Vanzi, A. (2000). Seismic Reliability of Electric Networks and Interaction with other Damage Indicators. Proc. 12th World Conference on Earthquake Engineering.
Goretti, A. (2005). A Probabilistic Model Able to Handle Interaction Among Road Network, Buildings and Emergency Services in Urban Areas. Proc. IX International Conference on Structural Safety and Reliability, ICOSSAR'05, Rome.
Hada, Y., and Meguro, K. (2000). Optimum Restoration Model Considering Interactions among Lifeline Systems-Interactions Among Restoration Activities of Lifeline Utilities. Proc. 12th World Conference on Earthquake Engineering.
Haimes, Y.Y., and Jiang, P. (2001). Leontief-based model of risk in complex interconnected infrastructures. Journal of Infrastructure Systems, Vol. 7, No. 1, pp. 1-12.
Hoshiya, M. and Ohno, H. (1985). A System Dynamic Model in Seismic Performance Assessment of Electric Power and Water Supply Networks. Proc. Trilateral Seminar – Workshop on Lifeline Earthquake Engineering, Taipei, Taiwan, pp. 181-189.
Ishihara, K. and Yoshimine, M. (1992). Evaluation of settlements in sand deposits following liquefaction during earthquakes, Soils and Foundations, Vol. 32, No. 1, pp. 173-188.
JCSS, (2008). Risk Assessment in Engineering Principles, System Representation & Risk Criteria. Joint Committee for Structural Safety, http://www.jcss.ethz.ch/.
Kakderi, K., Alexoudi, M. and Pitilakis, K. (2007). Seismic Risk Analysis of Interdependent Lifeline systems. Proc. 4th International Conference on Geotechnical Earthquake Engineering.
Kakderi, K., Alexoudi, M. and Pitilakis, K. (2008). Seismic Risk Analysis of Interdependent Lifeline Systems. Proc. 3rd Greek Conference on Earthquake Engineering and Engineering Seismology (in Greek).
Kakderi, K. and Pitilakis, K. (2011). Seismic performance and reliability of port facilities – The case of Thessaloniki (Greece). Proc. 5th International Conference on Earthquake Geotechnical Engineering, Santiago, Chile.
Kameda, H. (2000). Engineering Management of Lifeline Systems Under Earthquake Risk. Proc. 12th World Conference on Earthquake Engineering.
Kanda, J. and Shah, H. (1997). Engineering role in failure cost evaluation for 790 buildings. Structural Safety, Vol. 19, No. 1, pp. 79–90.
Kappos, A., Panagopoulos, G., Panagiotopoulos, Ch. and Penelis, Gr. (2006). A hybrid method for the vulnerability assessment of R/C and URM buildings. Bulletin of Earthquake Engineering, Vol. 4, No. 4, pp. 391-413.
Karaca, E. (2005). Regional Earthquake Loss Estimation: Role of Transportation Network, Sensitivity and Uncertainty, and Risk Mitigation. PhD thesis, MIT, Cambridge, MA.
Kim, Y.S., Spencer, B.F., Song, J., Elnashai, A.S. and Stokes, T. (2007). Seismic Performance Assessment of Interdependent Lifeline Systems. MAEC Report, Mid America Earthquake Research Center, University of Illinois, Urbana-Champaign, CD Release 07-16.
Kunreuther, H., Cyr, C., Grossi, P. and Tao, W. (2001). Using cost-benefit analysis to evaluate mitigation for lifeline systems. MCEER research projects and accomplishments:2000–2001.

LESSLOSS, (2004-2007). Risk Mitigation for Earthquakes and Landslides. Research Project, European Commission, Sixth Framework Programme, Priority 1.1.6.3, Global Change and Ecosystems, Contract Number: GOCE-CT-2003-505448.

Li, J., and He. J. (2002). A recursive decomposition algorithm for network seismic reliability evaluation. Journal of Earthquake Engineering and Structural Dynamics, Vol. 31, No. 8, pp. 1525-1539.

Little, R.G. (2002). Controlling Cascading Failure: Understanding the Vulnerabilities of Interconnected Infrastructures. Journal of Urban Technology, Vol. 9, No. 1, pp. 109–123.

Liu, G.-Y., Liu, C.-W., Wang, Y.-J. and Jean, W.-Y. (2004). Seismic Risk Analysis of Power Transmission System. Proc. 3rd Taiwan-Japan Workshop on Lifeline Performance and Disaster Mitigation.

Lupoi, G., Franchin, P., Lupoi, A., Pinto, P.E. and Calvi, G.M. (2008). Probabilistic Seismic Assessment for Hospitals and Complex-Social Systems. IUSS Press, Pavia, Italy.

Manou, D., Alexoudi, M., Raptakis, D. and Pitilakis, K. (2007). Düzce (M7.2, 1999) earthquake: Damage Correlation with the microzonation study and vulnerability assessment of the water system in Düzce, Turkey. Proc. 4th International Conference on Earthquake Geotechnical Engineering (4ICEGE), Thessaloniki, Greece Paper No. 1621.

Manou, D., Manakou, M., Alexoudi, M., Anastasiadis, A. and Pitilakis, K. (2010). Microzonation study of Düzce, Turkey. Proc. 5th International conference on recent advances in Geotechnical Earthquake engineering and Soil Dynamics and Symposium in honour of professor I. M. Idriss, San Diego, CA, Paper No. 7.12b.

Menoni, S. (2001). Chains of damages and failures in a metropolitan environment: some observations on the Kobe earthquake in 1995. Journal of Hazardous Materials, Vol. 86, No. 1, pp. 101–119.

MERP, (2002-2005). Marmara Earthquake Rehabilitation Programme - An Integrated intervention for the Rehabilitation of Düzce, Research Project, European Commission, Republic of Turkey, Prime Minister Project, Implementation Project, PIU-ID-MERP-2002-2004, 2002-2005.

Mid-America Earthquake Center (MAEC) (2009). MAEviz Software. <http://mae.cee.uiuc.edu/software_and_tools/maeviz.html>.

Nakayama, W., Shimizu, Y. and Koganemaru K. (2004). Development of super dense realtime disaster mitigation system for urban gas supply network. Journal of Japan Association for Earthquake Engineering, Special Issue.

NIBS (2004). HAZUS: Hazard US: Earthquake Loss Estimation Methodology. National Institute of Building Sciences, NIBS document 5200-03, Washington, DC.

Nojima, N. and Kameda, H. (1991). Cross Impact Analysis for Lifeline Interactions. Proc. 3rd US Conference on Lifeline Earthquake Engineering, Los Angeles, California, TCLEE/ASCE, Monograph No. 4, edited by M. A. Cassaro, pp. 629- 638.

Nuti, C. and Vanzi, I. (1998). Assessment of Post-Earthquake Availability of Hospital System and Upgrading Strategies. Earthquake Engineering and Structural Dynamics, Vol. 27, No. 12, pp. 1403-1423.

Nuti, C., Rasulo, A. And Vanzi, I. (2007). Structural Safety Evaluation of Electric Power Supply at Urban Level. Earthquake Engineering and Structural Dynamics, Special Issue on Earthquake Engineering for Electric Power Equipment and Lifeline Systems, Vol. 36, No. 2, pp. 245-263.

O'Rourke, M.J. and Ayala, G. (1993). Pipeline damage due to wave propagation. Journal of Geotechnical Engineering, ASCE, Vol. 119, No. 9, pp. 1490-1498.

Ostrom, D.K. (2003). SERA II. Proc. 6th U.S. Conference and Workshop on Lifeline Earthquake Engineering, TCLEE, Monograph No. 25, pp. 587-596.

Pachakis, D. and Kiremidjian, A. (2003). The use of Simulation in Disaster Response Planning and Risk Management of Ports and Harbors. Proc. 6th U.S. Conference and Workshop on Lifeline Earthquake Engineering, TCLEE, Monograph No. 25.

Pachakis, D. and Kiremidjian, A. (2004). Estimation of Downtime-Related Revenue Losses in Seaports Following Scenario Earthquakes. Earthquake Spectra, Vol. 20, No. 2, pp. 427–449.

Paolucci, R. and Pitilakis, K., (2007). Seismic Risk Assessment of Underground Structures under Transient Ground Deformations. in Pitilakis K. (Ed.). Earthquake Geotechnical Engineering, Chap. 18, pp. 433-459, Springer.

Papaioannou, Ch. (2004). Technical Report Research Program SRM-LIFE, Seismic Hazard Scenarios: Probabilistic Analysis of Seismic Hazard. Coord. K.Pitilakis, Thessaloniki.

Park, J. (2004). Development and application of probabilistic decision support framework for seismic rehabilitation of structural systems. Thesis, Georgia Institute of Technology.

Peerenboom, J., Fisher, R. and Whitfield, R. (2001). Recovering from disruptions of interdependent critical infrastructures. Proc. Workshop on Mitigating the Vulnerability of Critical Infrastructures to Catastrophic Failures, Lyceum, Alexandria, Virginia.

Penelis, Gr.G., Kappos, A.J., Stylianidis, K.C. and Panagiotopoulos, C. (2002). 2nd level analysis and vulnerability assessment of URM buildings. Proc. International Conference on Earthquake Loss Estimation and Risk Reduction, Bucharest, Romania.

Pitilakis, K., Anastasiadis, A. and Raptakis, D. (1992). Field and Laboratory Determination of Dynamic Properties of Natural Soil Deposits. Proc. 10th World Conference on Earthquake Engineering, Madrid, Vol. 5, pp.1275-1280.

Pitilakis, K. and Anastasiadis, A. (1998). Soil and site characterization for seismic response analysis. Proc. XI ECEE, Paris, Invited Lecture, pp.65-90.

Pitilakis, K., Makra, K. and Raptakis, D. (2001). 2D vs 1D site effects with potential applications to seismic norms: The cases of EURO-SEISTEST and Thessaloniki. Invited lecture in XVth International Conference on Soil Mechanics & Geotechnical Engineering, pp. 123-133, Istanbul – Turkey.

Pitilakis, K., Alexoudi, A., Argyroudis, S., Monge O. and Martin, C. (2005a). Chapter 9: Vulnerability assessment of lifelines. C.S. Oliveira, A. Roca and X. Goula ed. Assessing and Managing Earthquake Risk. Geo-Scientific and Engineering Knowledge for Earthquake Risk mitigation: Developments, Tools and Techniques. Springer Publ.

Pitilakis, K., Alexoudi, M., Kakderi, K., Manou, D., Batum, E. and Raptakis, D. (2005b). Vulnerability analysis of water systems in strong earthquakes. The case of Lefkas (Greece) and Düzce (Turkey). Proc. International Symposium on the Geodynamics of Eastern Mediterranean: Active Tectonics of the Aegean, Istanbul.

Pitilakis, K., Alexoudi, A., Argyroudis, S., Monge, O. and Martin, C. (2006a). Earthquake Risk Assessment of Lifelines. Bulletin of Earthquake Engineering, Vol. 4 No.4, Special Issue: The Risk-Ue Project (Ed. Atilla Ansal), pp. 365-390.

Pitilakis, K., Alexoudi, M., Argyroudis, S. and Anastasiadis, A. (2006b). Seismic Risk Scenarios for an Efficient Risk Management: The Case of Thessaloniki (Greece). In Advances in Earthquake Engineering for Urban Risk Reduction, Eds. S.T. Wasti and G. Ozcebe, Springer, pp.229-244.

Pitilakis, K., Anastasiadis, A., Kakderi, K., Argyroudis, S. and Alexoudi M. (2007a). Seismic Zonation, Vulnerability Assessment and Loss Scenarios in Thessaloniki. Proc. 2nd Japan-Greece Workshop on Seismic Design, Observation, and Retrofit of Foundations, Tokyo, Japan.

Pitilakis, K., Anastasiadis, A., Kakderi, K., Argyroudis, S. and Alexoudi M. (2007b). Vulnerability Assessment and Risk Management of Lifelines, Infrastructures and Critical Facilities. The case of Thessaloniki's Metropolitan area. Proc. 4th International Conference on Geotechnical Earthquake Engineering, June 25-28, Thessaloniki, Greece, paper ID: 1774.

Pitilakis, K.D., Anastasiadis, A.I., Kakderi, K.G., Manakou, M.V., Manou, D.K., Alexoudi, M.N., Fotopoulou, S.D., Argyroudis, S.A. and Senetakis, K.G. (2010a). Development of comprehensive earthquake loss scenarios for a Greek and a Turkish city: Seismic hazard, Geotechnical and Lifeline Aspects. Earthquakes and Structures, (submitted).

Pitilakis, K., Raptakis, D., Makra, K., Manakou, M. and Chávez-García, F.J. (2010b). EURO-SEISTEST 3D Array for the Study of Complex Site Effects. Akkar, D. Sinan; Gülkan, Polat; Eck, Torild van (Eds.), Earthquake Data in Engineering Seismology, Predictive Models, Data Management and Networks. Series: Geotechnical, Geological, and Earthquake Engineering, Vol. 14.

Pitilakis, K., Anastasiadis, A., Kakderi, K., Alexoudi, M. and Argyroudis, S. (2010c). The role of soil and site conditions in the vulnerability and risk assessment of lifelines and infrastructures. The case of Thessaloniki (Greece). Proc. 5th International conference on recent advances in Geotechnical Earthquake engineering and Soil Dynamics and Symposium in honour of professor I. M. Idriss, San Diego, CA.

Porter, K., Jaiswal, K., Wald, D., Earle, P. and Hearne, M. (2008a). Fatality models for the U.S. Geological Survey's Prompt Assesment of Global Earthquake for Response (PAGER) system. Proc. 14th World Conference on Earthquake Engineering, Beijing, China, 8 pp.

Porter, K.A., Jaiswal, K.S., Wald, D.J., Greene, M. and Comartin, C. (2008b). WHE-PAGER Project: a new initiative in estimating global building inventory and its seismic vulnerability. Proc. 14th World Conference on Earthquake Engineering, Beijing, China 8 pp.Porter et al. (2008).

Raptakis, D.G., Anastasiadis, A.J., Pitilakis, K.D. and Lontzetidis, K.S. (1994a). Shear wave velocities and damping of Greek natural soils. Proc. 10th European Conference on Earthquake Engineering, Vienna, Austria, Vol. 1, pp. 477-482.

Raptakis, D.G., Karaolani, E., Pitilakis, K. and Theodulidis, N. (1994b). Horizontal to vertical spectral ratio and site effects: The case of a down-hole array in Thessaloniki (Greece). Proc. XXIV General Assembly, ESC, Athens, Vol. 3, pp.1570-1578.

Raptakis, D. (1995). Contribution to the determination of the geometry and the dynamic characteristics of soil formations and their seismic response. Ph.D. Thesis, Department of Civil Engineering, Aristotle University of Thessaloniki (in Greek).

Rinaldi, S.M., Peerendoom, P. and Kelly, T.K. (2001). Identifying, Understanding, and Analyzing Critical infrastructure interdependencies. IEEE Control Systems Magazine, Vol. 21, No. 6, pp. 11-25.

RISK-UE, (2001-2004). An Advanced Approach to Earthquake Risk Scenarios with Applications to Different European Towns. Research Project, European Commission, DG XII2001-2004, CEC Contract Number: EVK4-CT-2000-00014.

Rubinstein, R.Y. (1981). Simulation and Monte Carlo Method. Wiley, New York.

Rubinstein, R.Y. and Melamed, B. (1998). Modern Simulation and Modeling. Wiley, New York (ISBN 0-471-17077-1).

Santos, J.R., and Haimes, Y.Y. (2004). Modeling the Demand Reduction Input-Output (I-O) Inoperability Due to Terrorism of Interconnected Infrastructures. Risk Analysis, Vol. 24, No. 6, pp. 1437-1451.

Scawthorn, C. (1992). Lifeline Interaction and Post- Earthquake Functionality. Proc, 5th U.S-Japan Workshop on Earthquake Disaster Prevention for Lifeline Systems, pp. 441- 450.

Seed, R.B., Cetin, K.O., Moss, R.E.S., Kammerer, A.M., Wu, J. and Pestana, J.M. (2003). Recent Advances in Soil Liquefaction Engineering: A Unified and Consistent Frame work. Proc. 26th Annual ASCE Los Angeles Geotechnical Spring Seminar, Keynote Presentation, H.M.S. Queen Mary, Long Beach, California.

Seligson, H.A., Ballantyne, D.B., Huyck, C.K., Eguchi, R.T., Bucknam, S. and Bortugno, E. (2003). URAMP (utilities regional assessment of mitigation priorities) – a benefit-cost analysis tool for water, wastewater and drainage utilities: Methodology development. Proc. 6th U.S. Conference on Lifeline Earthquake Engineering, ASCE, TCLEE, Long Beach, California.

Selva, J., Kakderi, K., Alexoudi, M. and Pitilakis, K. (2010). Serviceability of a system of interdependent components, (submitted).

Shimizu, Y. and Yamazaki, F. (1998). Real-Time City Gas Network Damage Estimation System-SIGNAL. Proc. 11th European Conference on Earthquake Engineering, Balkema, Rotterdam.

Shinozuka, M., Hwang, H. and Tanaka, S. (1993). GIS - Based Assessment of the Seismic Performance of Water Delivery System. Proc. 5th US-Japan Workshop on Earthquake Disaster Prevention for Lifeline Systems, edited by K. Kawashima, H. Sugita and T. Nakajima, PWRI 3198, Public Works Research Institute, Tsukuba, Japan, pp. 233-249.

Shinozuka, M. and Tanaka, S. (1996). Effects of Lifeline Interaction Under Seismic Conditions. Proc. 11th World Conference on Earthquake Engineering.

Shinozuka, M., Cheng, T.C., Feng, M. and Mau, S.T. (1999). Seismic performance analysis of electric power systems. Research Progress and Accomplishments 1997–1999, MCEER, pp. 61–69.

Shinozuka, M., Murachi, Y., Dong, X., Zhu, Y. And Orlikowski, M.J. (2003). Seismic performance of highway transportation networks. Proc. China-US Workshop on protection of urban infrastructure and public buildings against earthquakes and man-made disasters, Beijing, China.

Song, J. and Der Kiureghian, A. (2003). Bounds on system reliability by linear programming. Journal of Engineering Mechanics, ASCE, Vol. 129, No. 6, pp. 627-636.
Sousa, M.L., Campos Costa, A., Carvalho, A. and Coelho, E. (2004). An automatic seismic scenario loss methodology integrated on a geographic information system. Proc. 13th World Conference on Earthquake Engineering, Vancouver, BC, Canada.
Spence, R. Ed (2007). Earthquake disaster scenario predictions and loss modelling for urban areas. LESSLOSS Report 7, IUSS Press, Pavia, Italy.
SRM-DGC, (2006-2008). Development and proposition for implementation of an efficient methodology and appropriate local instruments for the management, prevention and reduction of seismic risk in Düzce -Turkey, Grevena - Greece and Catania – Italy. Research project, Interreg III B Archimed, Code Number. A.1.010.
SRMLIFE, (2003-2007). Development of a global methodology for the vulnerability assessment and risk management of lifelines, infrastructures and critical facilities. Application to the metropolitan area of Thessaloniki. Research Project, General Secretariat for Research and Technology, Greece.
SYNER-G, (2009-2011). Systemic Seismic Vulnerability and Risk Analysis for Buildings, Lifeline Networks and Infrastructures Safety Gain. Research Project, European Commission, 7th Framework Programme, Contract Number: 244061.
Tadday, K. and Sahin, M. (2001). Situation analysis and recommendations related to improvement measures for drinking water supply system in Düzce. Proc. Symposium on Water Supply Situation in Earthquake Affected Region, Düzce.
Tang, A.P., Ou, J.W.A. and Tao, X. (2004). Lifeline Systems Interaction and their Seismic Performance Assessment. Proc. 13th World Conference on Earthquake Engineering, Vancouver, B.C., Canada.
Tang, A., and Wen, A. (2009). An intelligent simulation system for earthquake disaster assessment. Computers and Geosciences, Vol. 35, No. 5, pp. 871-879.
Tolone, W.J., Wilson, D., Raja, A., Xiang, W.-N., Hao, H., Phelps, S. and Johnson, E.W. (2004). Critical Infrastructure Integration Modeling and Simulation. Proc. 2nd Symposium in Intelligence and Security Informatics, Tucson, Arizona.
Tromans, J. (2004). Behaviour of buried water supply pipelines in earthquake zones. PhD Thesis, Imperial College of Science, Department of Civil and Environmental Engineering, University of London.
Vanzi, I. (1996). Seismic Reliability of Electric Power Networks: Methodology and Application. Structural Safety, Vol. 18, No. 4, pp. 311–327.
Vanzi, I. (2000). Structural upgrading strategy for Electric Power Networks under Seismic Action. International Journal of Earthquake Engineering and Structural Dynamics, Vol. 29, No. 7, pp. 1053–1073.
Veneziano, D., Sussman, J., Gupta, U. and Kunnumkal, S.M. (2002). Earthquake Loss under Limited Trasnsportation Capacity: Assessment, Sensitivity and Remediation. Proc. 7th US-NCEE, Boston, MA, USA.
Werner, S.D., Taylor, C E. and Ferritto, J.M. (1999). Seismic Risk Reduction Planning for Ports Lifelines. Proc. 5th U.S. Conference on Lifeline Earthquake Engineering, TCLEE, Monograph No. 16.
Wong, F.S. and Isenberg, J. (1995). Effects of Lifeline Interaction on Seismic Performance of Communications Networks. Proc. 4th U.S. Conference on Lifeline Earthquake Engineering, TCLEE/ASCE, Monograph No.6, edited by J. O' Rourke, pp. 557-564.
Yao, B., Xie, L. and Huo, E. (2004). Study Effect on Lifeline Interaction under Seismic Conditions. Proc. 13th World Conference on Earthquake Engineering, Vancouver, B.C., Canada.
Youd, T.L., Idriss, I.M., Andrus, R.D., Arango, I., Castro, G., Christian, J.T., Dobry, R., Liam Finn, W.D., Harder Jr., L.F., Hynes, M.E., Ishihara, K., Koester, J.P., Liao, S.S.C., Marcuson, W.F., Martin, G.R., Mitchell, J.K., Moriwaki, Y., Power, M.S., Robertson, P.K., Seed, R.B. and Stokoe, K.H. (2001). Liquefaction Resistance of Soils: Summary Report from the 1996 NCEER and 1998 NCEER/NSF Workshops on Evaluation of Liquefaction Resistance of Soils. Journal of Geotechnical and Geoenvironmental Engineering, Vol. 127, No.10, pp. 817-833.

# The Christchurch 2011 Earthquake: Elastic and Perfectly-Plastic Response Potential of Selected Ground Motions

Ev. Garini & G. Gazetas
*Soil Mechanics Laboratory, National Technical University, Athens, Greece*

ABSTRACT: The 22 February 2011 $M_w$ 6.3 Earthquake produced a number of unique accelerograms in the city of Christchurch and the port of Lyttelton. Four of these records are analyzed in this paper. Their elastic response spectra are discussed and associated with some salient characteristics of the motions. Also, symmetric and asymmetric sliding of a block resting through Coulomb friction on horizontal or inclined planes, when excited at their base by these records, offer a strong indication of their "destructiveness potential" in terms of perfectly-plastic response.

## 1 INTRODUCTION: THE CHRISTCHURCH EARTHQUAKE

Three earthquakes (Darfield, 4 September 2010, Christchurch, 22 February 2011, and 10 km east of Christchurch, 13 June 2011) with $M_w$ 7.1, $M_w$ 6.3 and $M_w$ 6.0, respectively, shook the area of Canterbury in New Zealand. Several accelerograph stations, well-distributed in the city and the surrounding communities, recorded the events, offering invaluable ground motions. Only records from the second event, the Christchurch $M_w$ = 6.3 earthquake, are examined in this paper. Table 1 lists all those records along with their peak values of acceleration and their Arias Intensity in all three directions. Figure 1 depicts the locations of the stations on the map. Two city stations, CHHC near the city hospital and CCCC on the grounds of the Catholic Community College, are discussed. The third record, LPCC, is from a station in the port of Lyttelton, placed directly on volcanic rock outcrop. The fourth record, HVSC, is a motion on very-stiff-and-shallow soil at the edge of what appears to be a triangular valley, in the mountainous southernmost end of the city.

Table 1. The selected records of the 24 February 2011, $M_W$ = 6.3 Christchurch EQ studied in the paper.

| Record Name | $PGA_{H1}$ [g] | $PGA_{H2}$ [g] | $PGA_V$ [g] | Soil Site |
|---|---|---|---|---|
| Christchurch Catholic Cathedral College [CCCC] | 0.47 | 0.36 | 0.68 | Estuarine Deposits |
| Christchurch Hospital [CHHC] | 0.33 | 0.35 | 0.50 | Estuarine Deposits |
| Heathcote Valley Primary School [HVSC] | 1.43 | 1.16 | 1.44 | Very Stiff Deposit |
| Lyttelton Port Company [LPCC] | 0.77 | 0.86 | 0.41 | Volcanic Rock |

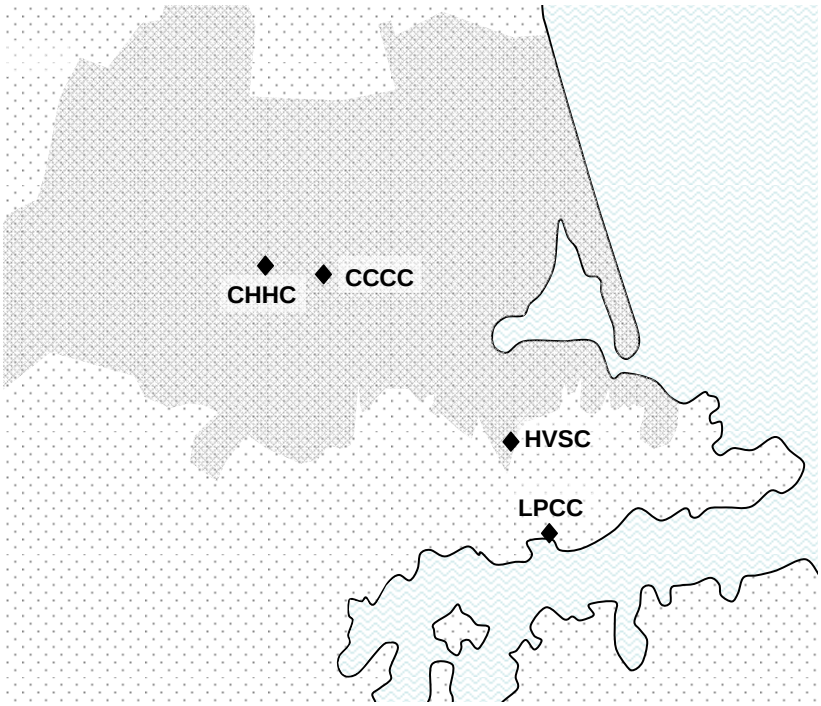

Figure 1. Map of Christchurch area with the location of the four seismograph stations whose records are studied here.

## 2 GROUND MOTIONS

### 2.1 *Characteristics of the selected motions*

The four records offer a representative sample of the intensity and nature of shaking in the broader Christchurch area. In particular, the two records in the city center, CHHC and CCCC, bear the effects of soft soil conditions, including long-period amplification, as well as the acceleration deamplification and period lengthening upon the occurrence of liquefaction. The other two motions, LPCC and HVSC, are unique among the records: they have the highest amplitudes in almost all their three components and the highest dominant frequencies of all the records — as expected from motions on rock or very-stiff soil deposit. The three components of each of the four recorded acceleration time-histories are plotted in Figure 2; the corresponding velocity time-histories in Figure 3.

The scope of this paper is to study what is the potential of these motions to inflict damage to engineering systems.

### 2.2 *Elastic response*

The damped elastic response spectra, in terms of acceleration, $S_A$, velocity $S_V$, and displacement, $S_D$, offer a complete visual assessment of the potential of a ground motion to cause large response to viscous–elastic spring–mass systems. Figure 4 compares the 5%-damped response spectra (hereafter called simply 'elastic response spectra') of the horizontal components of the four studied motions: the left column of the two soil records, CCCC and CHHC, and the right column of the two rock/stiff-soil records, LPCC and HVSC.

The two soil motions, CCCC and CHHC, produce response spectra with two broad peaks which hint at probable effects of soil amplification: (i) in the period range $1 < T(s) < 1.7$ ; and (ii) in the range $2.8 < T(s) < 3.5$, approximately. The latter is most likely the result of the oscillatory ground motion after liquefaction has occurred at depth. Such motion is clearly seen in all four acceleration time histories (as well as in their respective velocity histories) after about 6 seconds of motion.

The very–stiff–soil motion, HVSC, with its huge values of PGA (both components exceeding 1 g) and low-period max $S_A \approx 4$g, is richer in higher periods. A distinctive $S_A \approx 2$ g plateau in

the period range $0.5 < T\ (s) < 0.85$, approximately, with associated peaks of $S_V \approx 220$ cm/s and $S_D \approx 30$ cm, indicates plausible 2D valley–amplification soil effects on the S26W component of motion. A plausible cause of this high-amplitude plateau at $T \approx 0.50$–$0.85$ is forward-rupture directivity. The fact that HVSC is located at the edge of the seismogenic steeply-dipping rupture plane lends credence to this hypothesis.

Rock motion LPCC produces high spectral accelerations at very low periods (average max $S_A \approx 3g$ at $T \approx 0.18$ s), but their "elastic potential" drops very rapidly with increasing period. This is not a surprising behavior for rock motion having PGA ≈ 0.80 g and many high–frequency cycles in excess of 0.60 g.

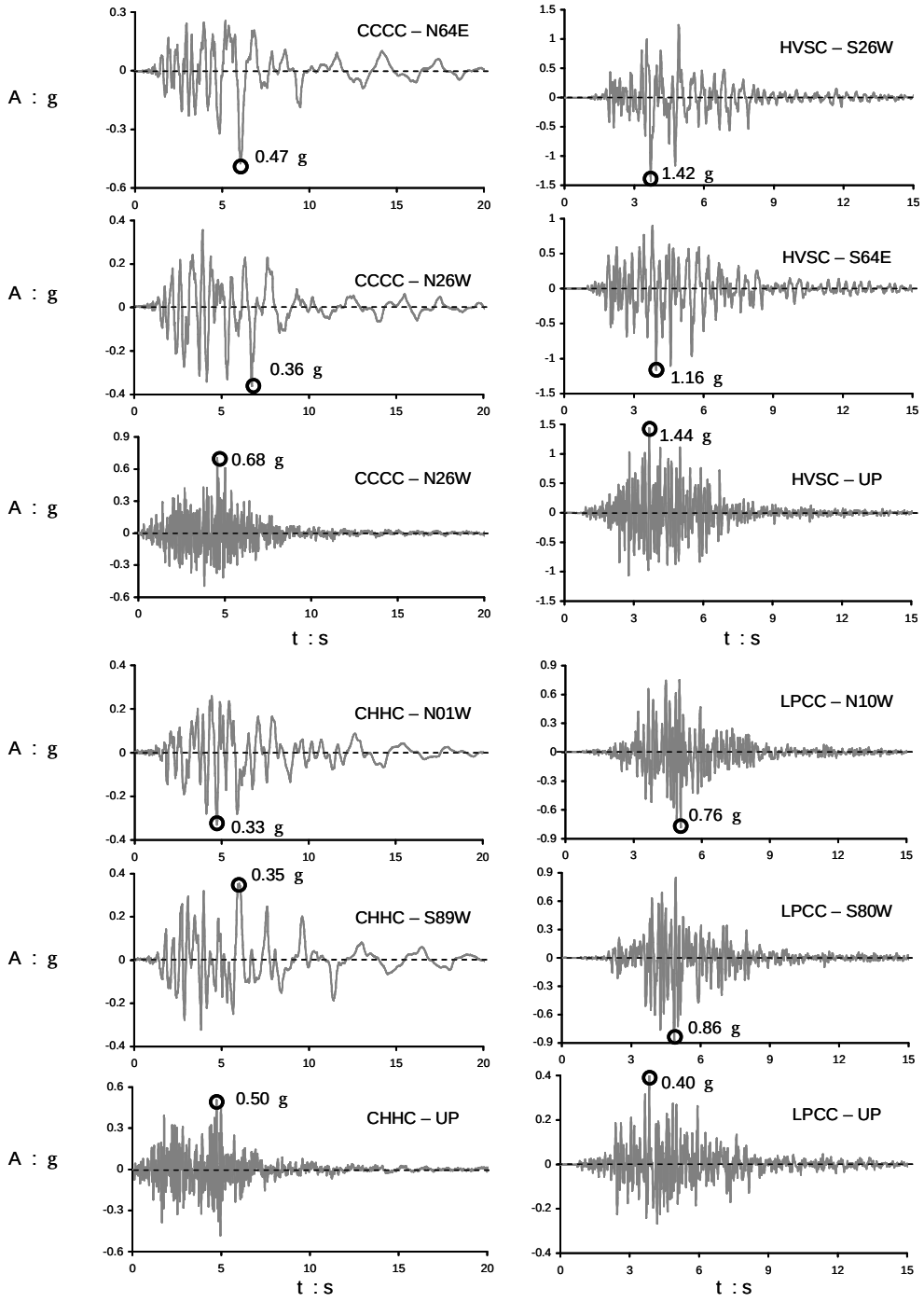


Figure 2. Acceleration time histories of the four records that we obtain from the NGS strong motion database.

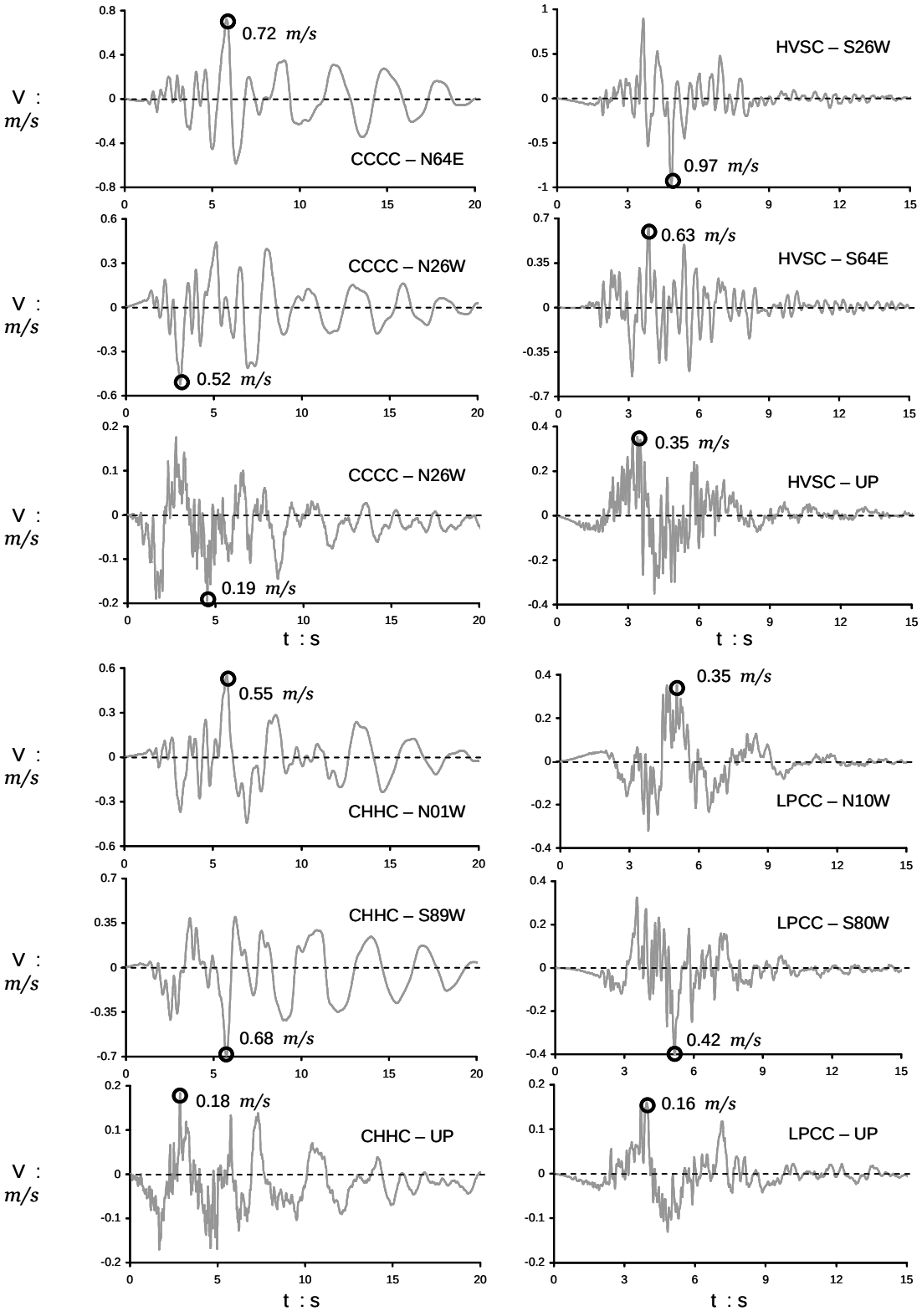


Figure 3. Velocity time histories of the four records that we obtain from the NGS strong motion database.

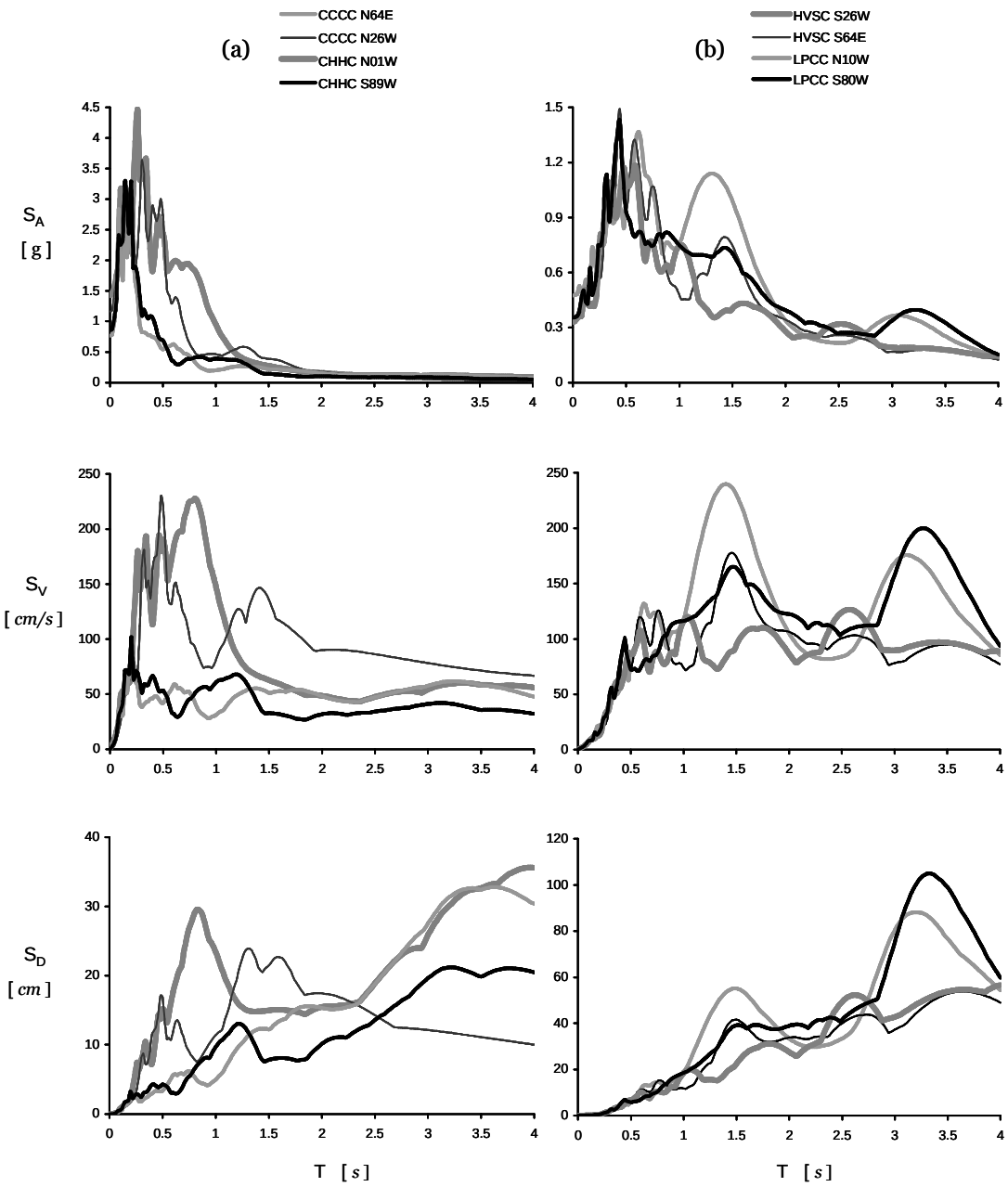


Figure 4. Elastic acceleration, velocity and displacement spectra of horizontal components of the recorded shaking motions (5% damping).

## 2.3 *Symmetric and asymmetric sliding response*

For systems whose deformation involves restoring mechanisms with a dominant linear component, the viscous-elastic response spectra provide an effective indication of its potential to cause unacceptable amplitudes of deformation. However, for systems with strongly nonlinear and/or inelastic restoring mechanisms, elastic response spectra are often inadequate descriptors of the damage potential.

To assess the potential of an accelerogram to inflict large irrecoverable deformation on highly inelastic systems, the seismic behavior of two idealized systems is examined: the sliding of a rigid block on a horizontal base, and the sliding on an inclined plane. These sliding systems are characterized by a rigid-plastic symmetric or asymmetric restoring force versus displacement relationship obeying Coulomb's friction law, as illustrated in Figure 5. The maximum resistance of sliding systems is controlled by the coefficient of friction. By letting the "yield ac-

celeration" (defined as the maximum resistance divided by the mass of the block) to vary parametrically for a given ground motion, we obtain "sliding" spectra.

Response of a block on horizontal or inclined base which is subjected to motion A(t) parallel to the plane is obtained from elementary rigid body kinematics along with Newton's second law of motion. The critical acceleration(s) which must be exceeded for slippage to be initiated are simply:

$$A_C = \mu g \quad (1)$$

$$A_{C1} = (\mu \cos\beta - \sin\beta)\, g \quad (2a)$$

$$A_{C2} = (\mu \cos\beta + \sin\beta)\, g \quad (2b)$$

in which $A_C$ = the critical acceleration for sliding in either direction of the symmetric system; $\mu$ = the (constant) coefficient of friction; $A_{C1}$ and $A_{C2}$ = the critical accelerations for downhill and uphill sliding for the asymmetric system of a plane inclined at an angle $\beta$. Usually $A_{C1} << A_{C2}$ and as a result sliding takes place only downhill. Whenever the base acceleration exceeds $A_C$ or $A_{C1}$ (or, rarely, $A_{C2}$) slippage of the block takes place with respect to the base.

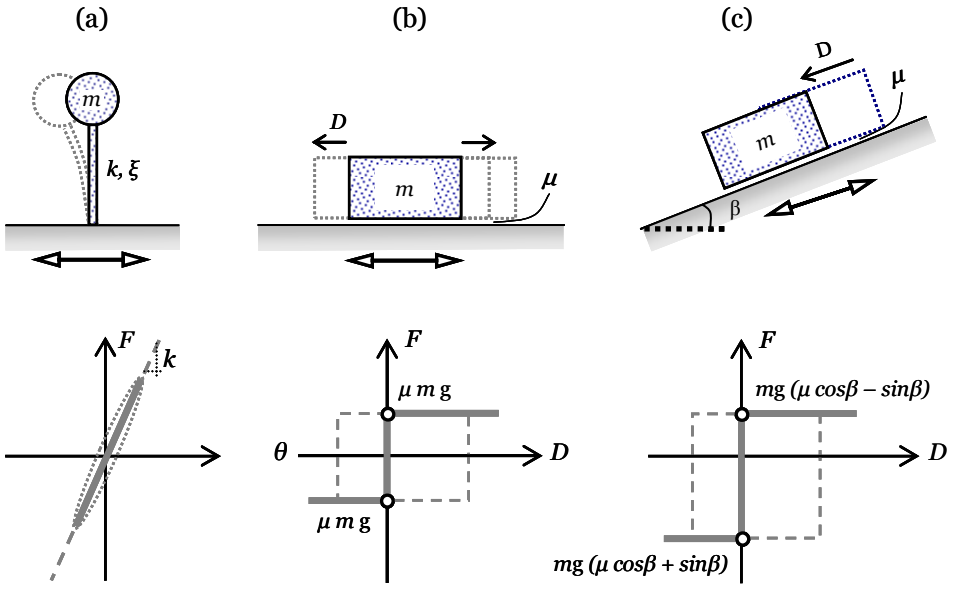


Figure 5. The fundamental systems ("analogues") studied in the paper with their restoring force-displacement relations: (a) visco-elastic oscillation of a single-degree-of-freedom system, (b) ideally rigid-plastic sliding on a horizontal plane, and (c) ideally rigid-plastic sliding on an inclined plane.

A graphical presentation of the solution procedure is given in Figures 6 and 7, for the strongest components of the CCCC and the HVSC motions. Having selected a critical acceleration $A_C$ = 0.10 g for both the horizontal and inclined base problems, these figures illustrate the acceleration and velocity time-histories of the block and the base, and the resulting relative displacement of the block with respect to the base.

By varying the critical acceleration from $A_C$ = 0.05 g to $A_C$ = 0.30 g the spectra of the symmetric and asymmetric sliding displacements are obtained for each component of all four studied motions. Figures 8 and 9 compare these sliding spectra, for the horizontal and inclined base, respectively. The symmetric sliding potential of the two motions recorded on top of soil (CCCC and CHHC) is in general the highest, while that of the rock motion (LPCC) is the lowest — in spite of the far larger PGA values of this record (see Table 1). The potential of the

HVSC motion is only about twice as large as the LPCC motion — but overall much smaller than the potential of the soil motions.

The above general picture is valid only for small values of the yield acceleration, say $A_C$ < 0.20 g – 0.25 g, depending on the record. For larger $A_C$ values, i.e. for less inelastic response, whereas the sliding spectra of the soil motions (CCCC, CHHC) decrease rapidly with $A_C$ , the spectra of HVSC and LPCC barely experience any drop and, in fact, may even increase with increasing $A_C$. The explanation of the former behavior is straightforward: as the $A_C$ values approach 0.30 g, the PGA values of three of the soil motions (0.36 g, 0.30 g, 0.33 g) marginally exceed $A_C$ — hence sliding is negligibly small; the fourth soil motion, with PGA = 0.47 g, gives a somewhat larger slippage of 7 cm compared with the HVSC's 9 cm (maximum). As for the paradoxical increase of slippage with increasing critical acceleration $A_C$ (i.e. increasing resistance to sliding), the reader is referred to Gazetas et al (2009) for a detailed convincing explanation of what was named the "Safe Gulf Paradox".

With asymmetric (downhill) sliding, the damage potential of the motions is not vastly different: HVSC and CCCC have in general the highest and similar potential; the LPCC has about 40% and CHHC about 70% of their potential.

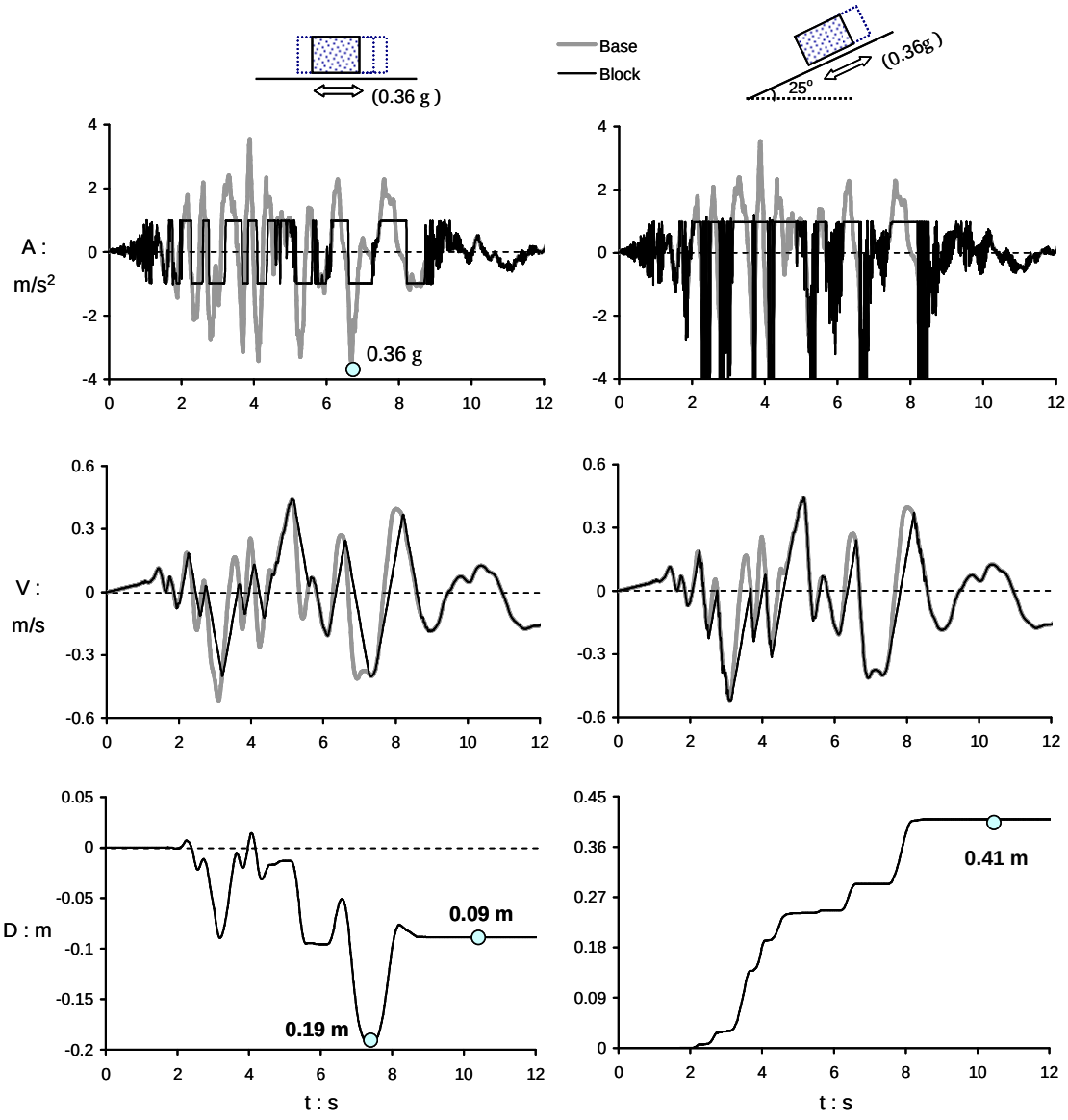


Figure 6. Influence of the symmetric (left) or asymmetric (right) nature of sliding to the response induced by the CCCC-N26W ground motion for $A_C$ = 0.1 g.

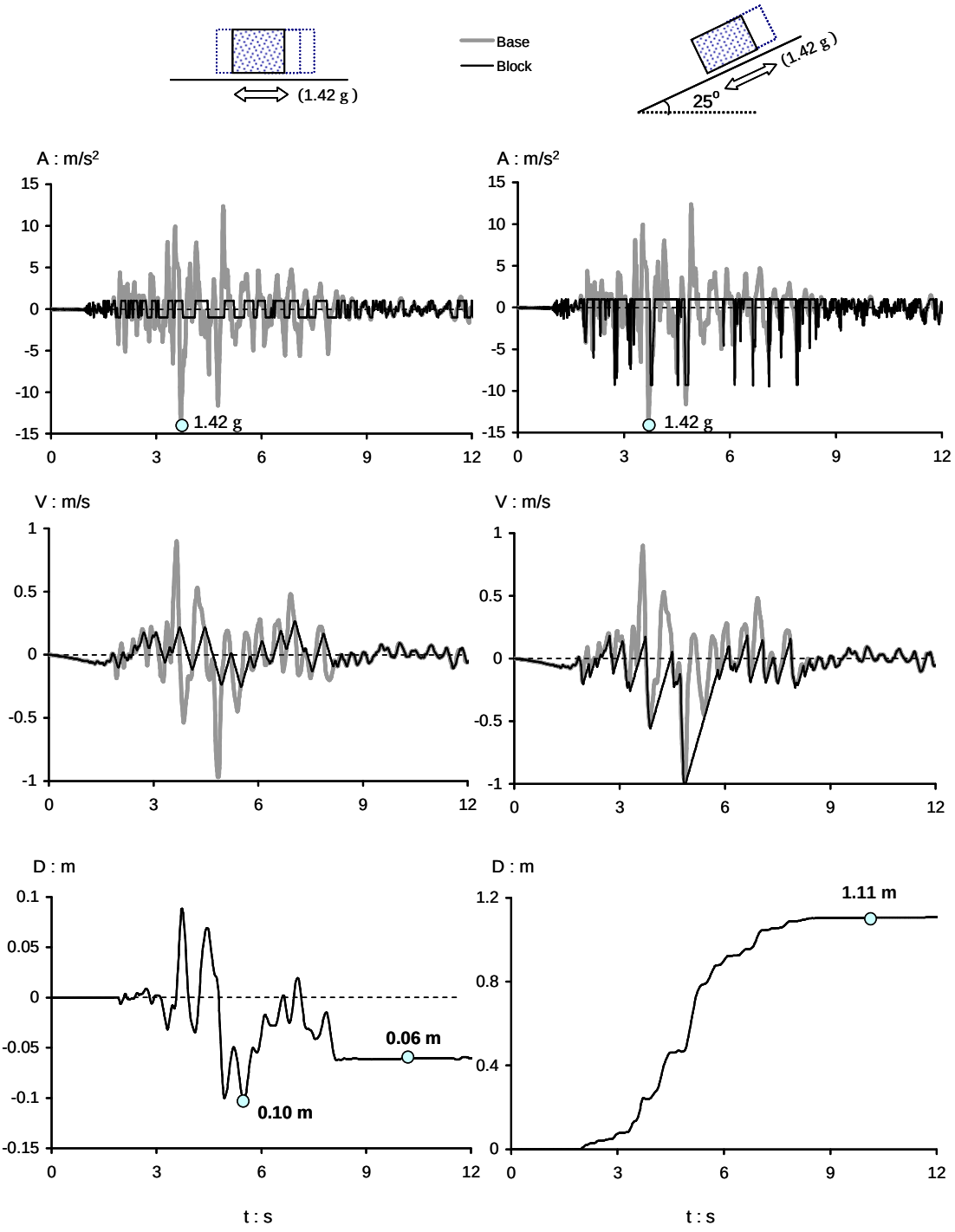


Figure 7. Influence of the symmetric (left) or asymmetric (right) nature of sliding to the response induced by the HVSC-S26W ground motion for $A_C$ = 0.1 g.

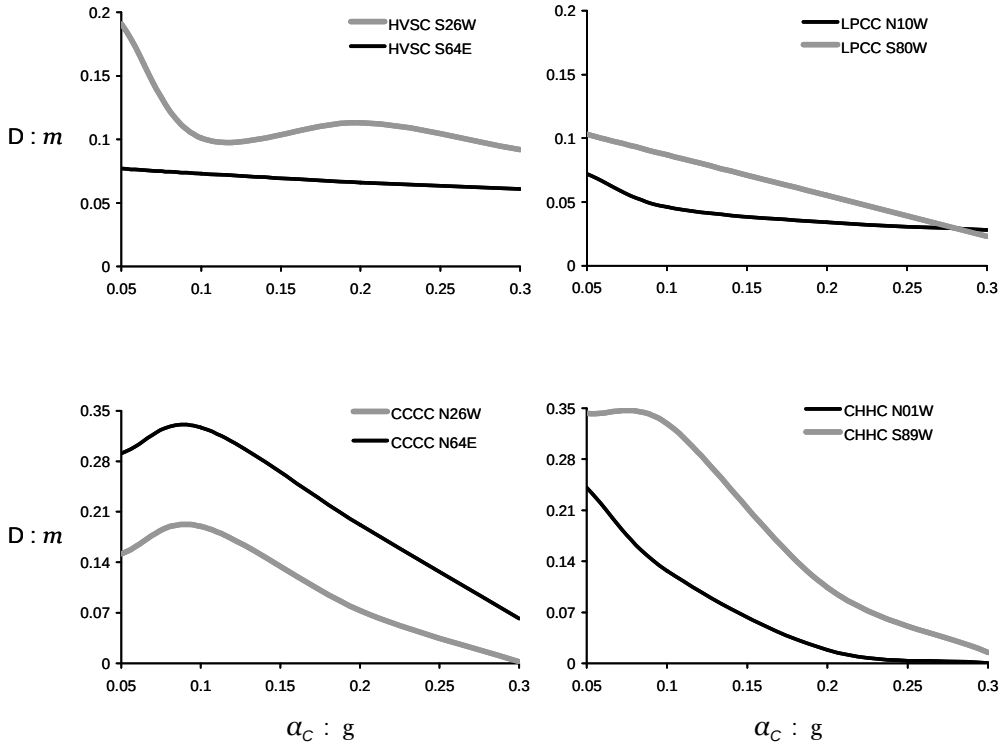


Figure 8. Sliding response of a block resting on a horizontal plane, also subjected to horizontal motion. The excitations are the four selected accelerograms. Results are presented in terms of slippage, D, versus yielding acceleration, $A_C = \mu g$.

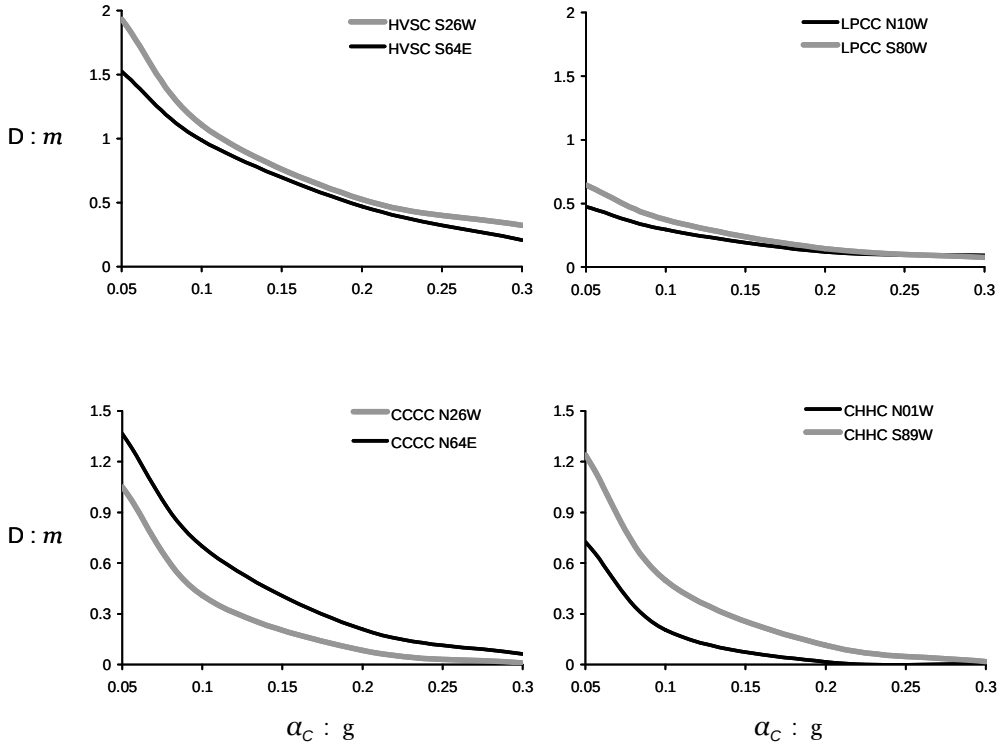


Figure 9. Asymmetric slippage of a block on top of an inclined plane subjected to horizontal motion. The excitations are the four selected accelerograms. Results are presented in terms of slippage, D, versus the downhill yielding acceleration, $A_{C1} = (\mu \cos \beta - \sin \beta)\, g$.

## 3 CONCLUSIONS

For strongly inelastic systems the paper introduced two new spectra to serve as indices of the "destructiveness" potential of a motion: the sliding spectra $D = D(A_C)$ and $D = D(A_C, \beta)$ for symmetric and asymmetric slippage of a rigid block, respectively. It was shown that the Christchurch motions were of sufficient damaging potential to explain the overall damage in the city.

## 4 ACKNOWLEDGEMENTS

The financial support for the expedition to the earthquake–stricken area and the work outlined in this paper has been provided under the research project "DARE", funded through the "IDEAS" Programme of the European Research Council (ERC), under contract number ERC-2-9-AdG228254-DARE. The authors would like to thank Professor John Berrill for providing data for the Christchurch 2011 event.

## 5 REFERENCES

Aki, K. 1988. Local site effects on strong ground motion. In J.L. Von Thum (ed.), *Earth-quake Engineering and Soil Dynamics II–Recent advances in ground motion evaluation, Geo-technical Special Publication No.20*, ASCE, New York, 103–155.

Bertero, V. V. 1976. Establishment of design earthquakes: evaluation of present methods. *Proceedings of the international symposium of earthquake structural engineering*, University of Missouri–Rolla, St Louis, Vol.1, 551–580.

Bertero, V. V., Mahin, S. A. & Herrera, R. A. 1978. Aseismic design implications of near–fault San Fernando earthquake records. *Earthquake Engng Strut. Dynamics* 6(1), 31-42.

Berrill, J. B., Davis, R. O. & McCahon J. F. 1993. Christchurch seismic hazard pilot study, *Bull. New Zealand Nat. Soc. Earthquake Eng.* 26, 14–27.

Bradley, B. A., Cubrinovski, M., Dhakal, R. P., & MacRae, G. A. 2009. Probabilistic seismic performance assessment of a bridge-foundation-soil system. *Proceedings of the NZSEE Conference, Christchurch, N. Zealand, 3-5 April.*

Brown, L. J., & Weeber, J.H. 1992. Geology of the Christchurch urban area: Scale 1:25,000. Institute of Geological & Nuclear Sciences (ed.), Geological Map 1, New Zealand.

Cubrinovski, M., Green, R., Allen, J., Ashford, S., Bowman, E., Bradley, B., Cox, B., Hutchinson, T., Kavazanjian, E., Orense, R., Pender, M., Quigley, M., Wilson, T. & Wotherspoon, L. 2010. Geotechnical reconnaissance of the 2010 Darfield (New Zealand) earthquake, *Bulletin of the New Zealand Society for Earthquake Engineering*, 43 243-320.

Gazetas, G., Garini, E., Anastasopoulos, I. & Georgarakos, T. 2009. Effects of near–fault ground shaking on sliding systems. *J. Geotech. Geoenviron. Engng*, ASCE 135(12), 1906-1921.

Garini, E., Gazetas, G. & Anastasopoulos, I. 2010. Asymmetric 'Newmark' sliding caused by motions containing severe 'directivity' and 'fling' pulses. *Géotechnique*, Vol.60, doi: 10.1680/geot.2010.60.00.1

Makris, N. & Roussos, Y. S. 2000. Rocking response of rigid blocks under near–source ground motions. *Geotechnique*, 50(3), 243-262.

Newmark, N. M. 1965. Effects of earthquakes on dams and embankments, *Geotechnique* 15(2), 139-160.

Sasani, M. & Bertero, V. V. 2000. Importance of severe pulse-type ground motions in performance-based engineering: historical and critical view. *Proc. 12th World Conf. Earthquake Engng*, Auckland, New Zealand, paper no. 1302.

Tasiopoulou, P., Smyrou, E., Bal, İ. E., Gazetas, G. & Vintzileou, E. 2011. Geotechnical and Structural Field Observations from Canterbury, New Zealand Earthquakes. *Research Report*, National Technical University of Athens, Greece.

Youd, T. L. & Carter, B.,L. 2005. Influence on soil softening and liquefaction on spectral acceleration, *Journal of Geotechnical and Geoenvironmental Engineering*, ASCE, 131(7) 811–825.

# Seismic vulnerability of ancient churches: damage observation after L'Aquila earthquake (2009)

S. Lagomarsino
*Dept. of Civil, Environmental and Architectural Engineering, University of Genoa, Italy*

ABSTRACT: L'Aquila earthquake, which occurred on April 6, 2009, proved the high vulnerability of cultural heritage, with particular reference to churches. Damage assessment in the emergency was carried out on more than 700 churches with a methodology aimed at recognizing the collapse mechanisms in the different architectonic elements of the church. The method was developed after the earthquake in Umbria and the Marches (1997) and has been widely used in the last decade; this approach is also very useful for seismic prevention, as it allows one to single out the most vulnerable structures. Some examples are presented in this paper, representative of recurrent damage in the main elements of the church: the façade, the roof, the apse and the belfry. It emerges that, for a correct interpretation of damage and vulnerability, it is necessary a deep knowledge of local construction techniques and of the historic transformation sequence. Moreover, the bad behaviour of churches strengthened by modern techniques, such as the substitution of original timber roofs with stiff and heavy r.c. slabs, was observed. Starting from the observation of some case studies, the paper achieves some worth results, which may be useful for correctly driving future strengthening interventions.

## 1 INTRODUCTION

The earthquake which struck L'Aquila and the Aterno Valley on 6 April 2009 caused severe damage to churches, in many cases with extensive collapse. This attests to the fact that this type of structure is perhaps the most vulnerable among historical buildings. In fact, history has shown that churches have often registered numerous victims. Therefore, there is a problem of safety for people and the seismic capacity of structures should be improved. However, there is also a problem of preservation of the cultural value, both in restoring damaged heritage and in strengthening historical buildings in other areas prone to earthquakes.

The high level of damage in many churches, after L'Aquila earthquake, obliges rebuilding wide parts of the original structures and it is necessary to understand if it is possible to guarantee the required safety with traditional masonry elements. Moreover, the quality of masonry in L'Aquila region is also under investigation, as compatible strengthening techniques may not be sufficient in such a highly seismic area.

The answers to these questions has to be complex and detailed because of the many factors which influenced the seismic behaviour in the historical Aquilan buildings.

First of all, it is important to consider the characteristics of the seismic event. The fault broke very close to the surface (the epicentre was at a depth of only 10 km) therefore the effects were very intense but included a relatively limited area. Such a superficial earthquake produced a very intense and energetic vertical component compared to the horizontal one, which is usually more severe and considered more dangerous to constructions. In other words, the earthquake produced not only horizontal forces creating out-of-plane and in-plane damage mechanisms, but

also a strong increase and annulment of vertical action with the result of crushing masonry piers or the loss of stability to domes. Besides that, in this earthquake perhaps more than others, local seismic amplification played an important role: if one analyses the macro seismic effects in many of the historical centres in the Aterno Valley (south-east of L'Aquila), it is immediately apparent that the villages heavily damaged by the earthquake were next to others which sustained little damage. Even within the same historical centre, there are zones where the damage is clearly concentrated.

This paper will be limited to an interpretation of damage to certain building types considering the most vulnerable elements of churches; the collapse mechanisms are in fact different and often easier to identify compared to those commonly found in other buildings in historical centres (Carocci and Lagomarsino, 2009; D'Ayala and Paganoni, 2011). Following this earthquake, bad behaviour was also caused by the modern reinforcement techniques used, and particularly those which utilized concrete slabs to substitute wooden roofs and diaphragms, which resulted in increased mass and excessive structural rigidity. From the seismic vulnerability observed, it is possible to obtain indications for choosing truly effective seismic improvement interventions. The time has come for a decisive change of direction in seismic consolidation, based on in-depth knowledge of structures, diagnostic interpretation, as well as the use of proven evaluation models of structural safety.

## 2 SEISMIC VULNERABILITY AND RISK PREVENTION OF CULTURAL HERITAGE

The meaning of the word vulnerability indicates the predisposition to damage of a building. In the field of seismic risk, vulnerability is one of the steps of the analysis, that establishes the correlation between the seismic input (hazard) and the physical damage for classes of homogeneous buildings. The aim of risk analysis is to evaluate the expected losses in a wide area due to a well defined strong earthquake (scenario analysis) or considering all possible earthquakes (probabilistic risk analysis). In either case, it is necessary to:

1. identify the elements at risk (residential buildings, public and/or strategic buildings, infrastructure, water and gas lines, etc.);
2. define an appropriate measurement of direct damage (cracking, usability) or indirect damage (victims, homeless, economic losses);
3. evaluate the hazard through seismological studies (or the characteristics of the expected earthquake at the site);
4. estimate vulnerability, or the functional relationship between hazard and damage.

Seismic risk is therefore a combination of three different factors: exposure, hazard and vulnerability. It is higher in urban areas (because of the exposure), and it increases in relation to the seismic hazard of the zone (in Italy, the L'Aquila zone is certainly one of the highest risk areas), but it also depends on the construction characteristics and their vulnerability.

Until the 1990's, cultural heritage was not considered in risk analyses. Due to the unique architectural characteristics of each building, a global evaluation by a simplified model was not thought to be reliable, due to the impossibility of considering the history and construction characteristics of each. But seismic risk to cultural heritage is a real problem in Italy, due to both the high number of protected heritage buildings as well as their high level of vulnerability (as proven by each earthquake).

Studies done on churches, starting from the observation of damage after the Friuli earthquake in 1976 (Doglioni et al., 1994) and more systematically after the earthquakes in Umbria and the Marches in 1997 (Lagomarsino and Podestà, 2004a) and Molise in 2002 (Lagomarsino and Podestà, 2004c), have demonstrated that damage mechanisms in churches have certain recurring characteristics, notwithstanding the uniqueness of each site. In particular, the interpretation using macro elements has proven very useful, i.e. observation of damage in various parts of churches (façade, nave, triumphal arch, dome, apse, bell tower, etc.), due to the fact that collapse usually occurs locally and in function of the type of macro element (geometrical configuration or construction details).

From the systematic observation of a vast number of churches, in different regions and characterized by different materials and construction techniques, a certain number of possible mechanisms have been identified for each macro element, depicted by easily understood graphic drawings.

The classification into macro elements and collapse mechanisms has allowed the definition of methods to assess damage and to quickly acquire useful information for handling emergencies (first aid interventions, fitness for habitation, economic damage estimates, planning support and project management). The schemes developed after the earthquakes in Umbria and the Marches were later published (G.U. no. 55, 2006) and officially adopted by the system for seismic emergency management as detailed by the Civil Protection Department which presides over cultural heritage in collaboration with the Ministry for Cultural Heritage and Activities.

The statistical analysis of damage observed led to the formulation of vulnerability models (Lagomarsino and Podestà, 2004b), which allowed us to assign a vulnerability index to each church, taking into consideration both its weakest elements and the preventive constructive details, as well as to estimate damage according to expected earthquake intensity. This model was adopted in the Guidelines (G.U. no. 24, 2008) issued by the Ministry for Cultural Heritage and Activities as a tool for the evaluation and mitigation of seismic risk to cultural heritage as well as to give direction and control to seismic strengthening interventions.

This interpretation of vulnerability and seismic damage in terms of macro elements and collapse mechanisms has also allowed the definition of new mechanical models for the evaluation of seismic response, based on the statics of rigid bodies and the traditional methods of equilibrium limit analysis (Lagomarsino and Resemini, 2009). The recent Italian seismic code for constructions adopted this approach (G.U. no. 47, 2009), and has proven very useful in the planning of seismic strengthening interventions.

## 3 THE DAMAGE ASSESSMENT OF CHURCHES AND EMERGENCY MANAGEMENT

Damage assessment and emergency management of cultural heritage has been coordinated by the Vice Commissioner Luciano Marchetti, on behalf of the Civil Protection Department, also involving the Ministry of Cultural Heritage and ReLUIS, the Italian University Laboratories Network of seismic engineering; moreover, the support of the Institute for the building technologies in L'Aquila, which operates inside the National Research Council (CNR), has been helpful. Damage assessment has been carried out by teams of technicians with different expertise: architects of the Monuments and Fine Arts Office, structural experts (engineers or architects) from the University, historians for the assessment of artistic assets, engineers from the Fire Brigade (aimed at ensuring safety during the survey and to arrange for the necessary provisional interventions). This assessment was devoted not only to churches and palaces, but also to towers, castles, urban walls, fortified doors, etc.

However, only for churches and palaces are there well defined forms, already mentioned (G.U. no. 55, 2006), that allow one to collect data in an effective way, with the aim of: a) deciding if the building is suitable for immediate occupancy; b) advising about the need for provisional interventions, in order to prevent further damage due to replica shocks; c) estimating the restoration costs, in order to find necessary funds and plan the priorities of intervention.

In particular, the church form considers 28 damage and collapse mechanisms that can frequently occur in the different architectonic elements (named macroelements) which compose churches (Lagomarsino and Podestà, 2004c). Table 1 shows the mechanisms considered and the related macroelement. Figure 1 shows some typical collapse mechanisms; these schematic sketches are very useful during the survey, to recognize and interpret damage. For each mechanism, the assessment consists of assigning a damage grade (from 0, no damage, to 5, complete).

The collection of damage data in each single architectonic element of the church allows one to single out the need for provisional interventions. Moreover, an automatic procedure was established which estimates the total restoration cost, considering the level of damage in each macroelement and the dimensions.

Damage assessment, by singling out the activated collapse mechanisms and evaluating the damage level for each one, allows one to evaluate a synthetic score, the damage index, which is representative of the average damage in the church (Lagomarsino and Podestà, 2004a). The damage index, which ranges between 0 (no damage) and 1 (total collapse), is a weighted average of all possible collapse mechanisms, also considering the ones that were not activated by the earthquake; it is a useful parameter for the preparation of a damage list, in order to compare the severity of damage in churches of different size and typology.

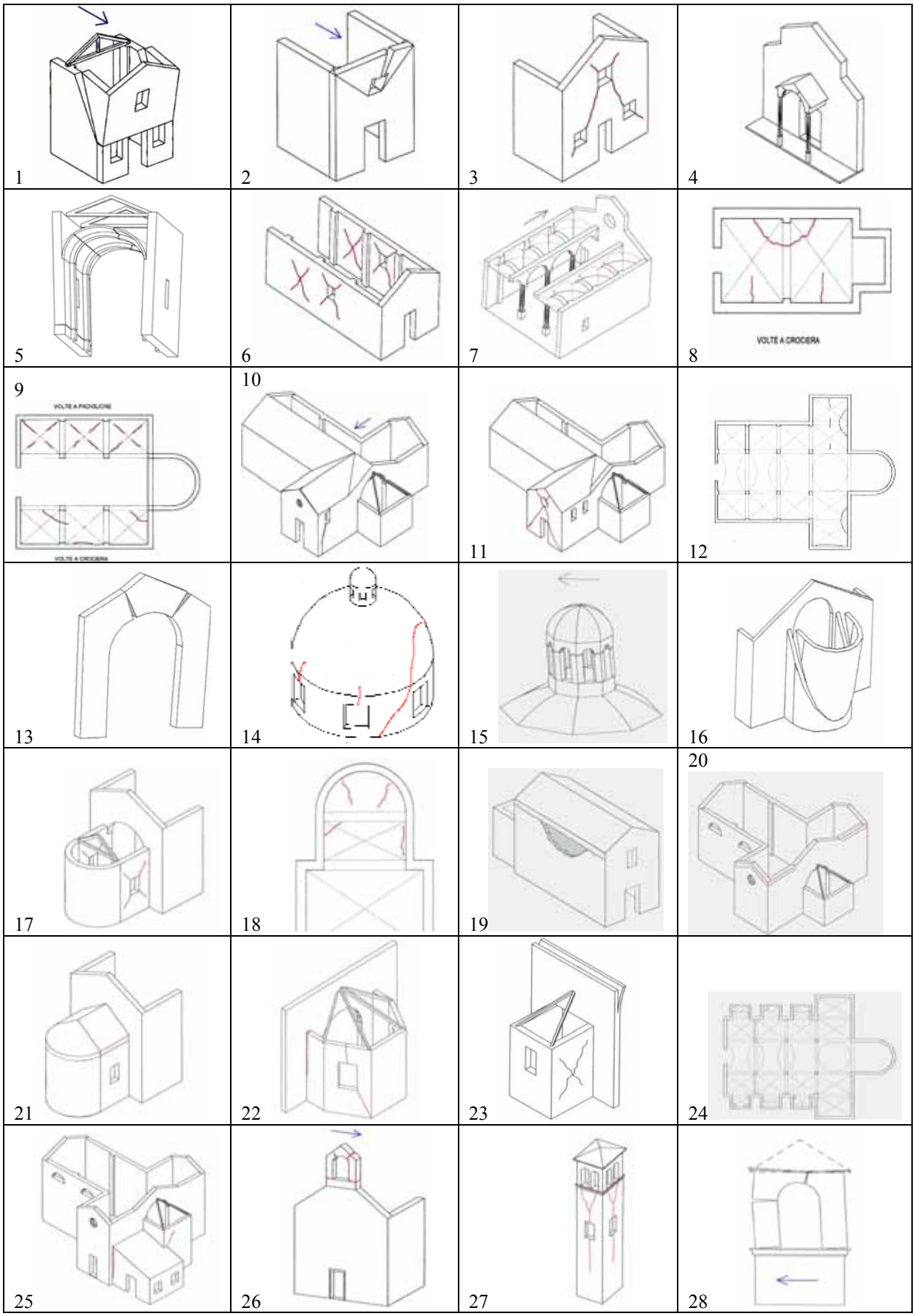


Figure 1. Damage mechanisms considered in the vulnerability method

All data was collected in a database, which allows one to manage the emergency actions (plan of multiple surveys, due to replica shocks; news about the safety of the building for the immediate occupancy; need for provisional interventions) and to plan the following phase of restoration interventions.

Thanks to the high number of churches surveyed, the statistical analysis of damage data gives useful information for the validation and tuning of the church vulnerability model, which was developed after the Umbria-Marche earthquake (Lagomarsino and Podestà, 2004 b). This analysis (Podestà et al., 2010) was performed after an accurate quality control of the completed forms that were filled in by different teams, not all provided with the same expertise, and in some cases without the possibility of a complete survey (for example, some churches were assessed only from outside, for safety reasons). Among the 723 forms of churches surveyed, inaccuracy in compilation has been found in 9% of cases, which were not considered in the statistical analysis.

The outcome of the safety evaluation for the immediate occupancy is described by Figure 2, which shows, as a function of the macroseismic intensity, the percentage in the different possible outcomes, according to the classification used by the Italian Civil Protection Department: A) safe for immediate occupancy; B) fit for use after provisional interventions; C) partially unfit for use; D) temporarily unfit for use (to be examined again); E) unfit for use; F) unfit for use due to external reasons. It is worth noting that for I≥8 MCS all churches are unfit for use (only 15% may be usable after a proper provisional intervention). Moreover, also in the areas which are far from the epicentre (I=5 MCS), only for less than 50% of churches is an immediate occupancy possible; this confirms the high vulnerability of churches, even for low intensity earthquakes.

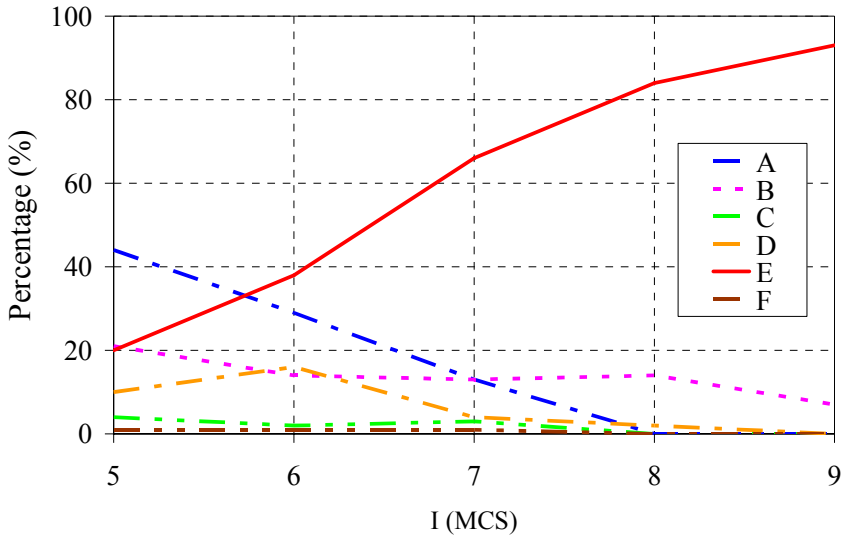


Figure 2. Results of safety evaluations for the immediate occupancy of churches for different values of the macroseismic intensity (the macroseismic survey in Italy was made by MCS scale).

Even if it is not possible, for safety and responsibility reasons, to establish a direct correlation between usability and damage index, it emerges that usually when the damage index is greater than 0.3 the church is unfit for use. The same result was obtained after the Umbria-Marches (1997) and Molise (2002) earthquakes, thus supporting the reliability of the survey procedure. However, a low value of the damage index results in a church with a local collapse in one macro element and with slight damage in the other elements, but it should be classified as unfit for use.

The statistical analysis of damage data to churches after the various earthquakes that have occurred in Italy in the last 30 years allowed us to proposed a methodology for preventive vulnerability evaluation, to be used in seismic risk analyses. The survey of construction details in each macroelement, some of them positive while others are negative for the seismic behaviour, allows one to assign a vulnerability index IV (which ranges between 0 to 1) to each church and, consequently, a vulnerability curve (correlation between the macroseismic intensity and the mean damage grade, related to the damage index). Since the observed damage histograms, for different macroseismic intensity, are well fitted by a binomial distribution, through the vulnera-

bility curve it is possible to obtain the Damage Probability Matrix for a given church. Podestà et al. (2010) shows the damage histograms obtained for the set of 654 churches, damaged by the L'Aquila earthquake, even in areas quite far from the epicentre.

Table 2 allows one to compare the mean observed damage grade, due to different Italian earthquakes, as a function of the macroseismic intensity. The robustness of the damage assessment methodology and the reliability of the vulnerability model are evident, for there use in risk analysis. In Figure 3 the observed damage data is compared with the analytical vulnerability curves, for usual values of the vulnerability index IV, from 0.2 to 0.6 (Lagomarsino and Podestà, 2004b).

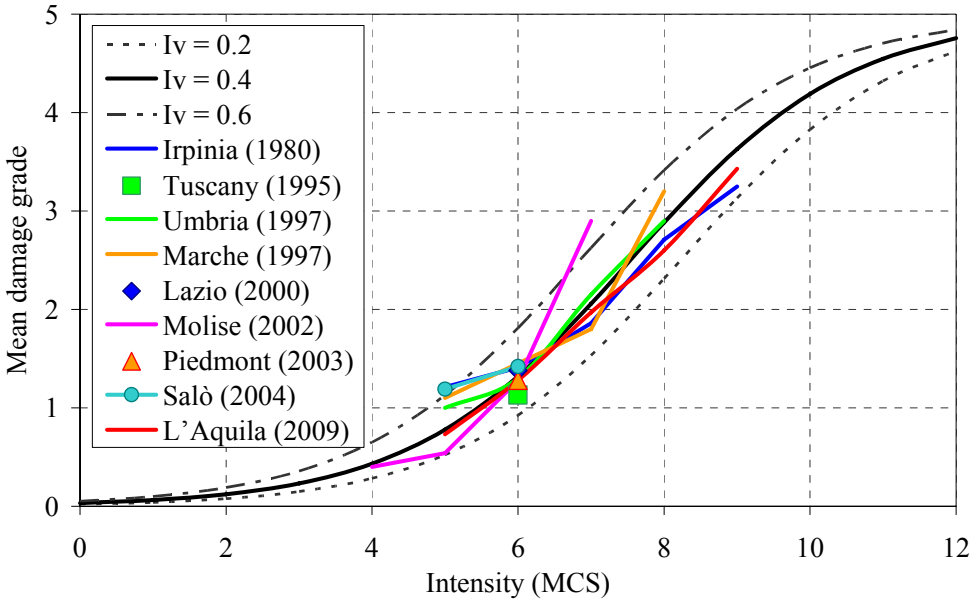


Figure 3. Comparison among the vulnerability curves for most of the churches (IV between 0.2 and 0.6) and the damage observed data, after Italian earthquakes of the last 30 years.

This vulnerability model, as already mentioned, is at the base of the model proposed in the Guidelines (G.U. no. 24, 2008) issued by the Ministry for Cultural Heritage and Activities as a tool for the evaluation and mitigation of seismic risk to cultural heritage; in this case a correlation between intensity and peak ground acceleration was adopted.

The statistical analysis may be done not only on the average damage but also considering the typology of macroelements and the related damage level. Podestà et al. (2010) show some interesting peculiarities of churches in L'Aquila. Most churches have only one nave, without a transept or lateral chapels; structural vaults are present only in 40% of cases, while the bell tower is present only in 35% of churches. Perhaps the awareness of ancient builders of the high seismic hazard in L'Aquila area suggested the adoption of simplicity and regularity. It is worth noting that the macroelements which are present in a few cases are the most vulnerable ones: the dome (seriously damaged in 80% of cases); the vaults in the central nave and, in particular, in the lateral aisles (damaged in more than 70% of cases).

In this paper, instead of considering the vulnerability from a statistical point of view, some specific cases are considered, which however can be considered representative of typical recurrent mechanisms, according to the methodology described above.

## 4 THE EARTHQUAKE IN L'AQUILA ON APRIL 6, 2009

On April 6, 2009 at 3:32 a.m. a Mw=6.3 earthquake with shallow focal depth (10 kilometres) struck central Italy in the vicinity of L'Aquila, a town of about 73,000 people, capital of the Abruzzo region. The earthquake killed 305 people, injured 1,500, destroyed or damaged more or less 10,000-15,000 buildings, prompted the temporary evacuation of 70,000-80,000 residents and left more than 24,000 homeless. This event was the strongest of a sequence that started a

few months earlier and numbered 23 earthquakes of Mw>4 between September 2009 and April 2010, including a Mw=5.6 on April 4 and a Mw=5.4 on April 9 (Bazzurro et al., 2009).

A total of 81 municipalities were affected by the earthquake and 49 of them were in the list of highest hazard areas in Italy. The population of L'Aquila includes 14 surrounding boroughs such as Onna, Paganica, and Tempera. The total population of the other 48 high hazard towns is 60,352; most range in size from 1,000 to 3,000 people, with two larger towns of 5,000 and 8,500 inhabitants.

The historical centres of villages in the Aterno River valley, southwest of L'Aquila (such as Onna, Paganica, Castelnuovo and Villa Sant'Angelo), were essentially obliterated, with shaking intensities of up to X MCS. Conversely, damage did not exceed MCS intensity VI nearly anywhere to the northwest of L'Aquila. This south-eastward elongation of the damage pattern probably reflects a combination of rupture directivity and seismic lithostratigraphic amplification effects.

Figure 4 shows the earthquakes that have struck the city of L'Aquila and the villages around it since 1300 (Stucchi et al. 2007, Rovida et al. 2009). L'Aquila has been severely damaged at least five times in the last 700 years, specifically in 1315 (Mw≈6.7), 1349 (Mw≈6.5), 1461 (Mw≈6.5), 1703 (Mw≈6.7), and 1915 (Mw≈7.0). The 1461 event shows a damage distribution similar to that of the April 6, 2009 earthquake, although it has shifted to the east by a few km.

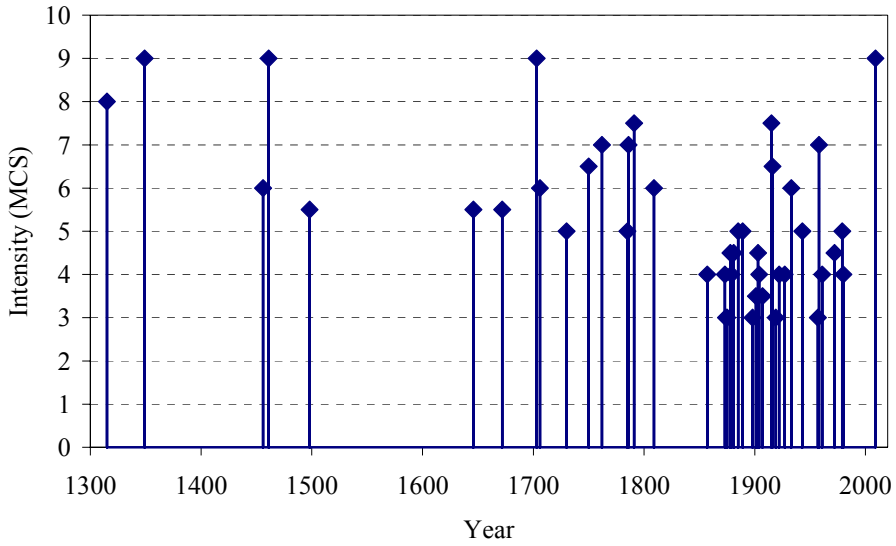


Figure 4. Historical MCS macroseismic intensity of the major events in L'Aquila (source: INGV Database Macrosismico Italiano-2008, http://emidius.mi.ingv.it/DBMI08/).

Among approximately 300 digital strong-motion stations operated by the Italian Strong Motion Network (RAN), managed by the Italian Civil Protection Department, 56 of them recorded the main shock; in addition, 142 broad-band stations recorded it (14 stations are in the Abruzzo region, while the remaining ones are scattered in the Apennines, mostly NW and SE of L'Aquila). This makes the Abruzzo Mw 6.3 event one of the best recorded earthquakes caused by a normal fault mechanism.

Four stations, all on the hanging wall of the rupture, were located within 10 km of the epicentres, and all recorded a horizontal peak ground acceleration exceeding 0.35g. The stations AQG and AQK are on rock or stiff material, while AQA and AQV are on recent alluvium.

The 5% damped spectra of the two horizontal directions are shown in Figure 5, compared with the one proposed for L'Aquila by the new Italian seismic code for ground type B (very dense sand, gravel, or very stiff clay, characterised by a gradual increase of mechanical properties with depth), for a return period TR=475 years; the frequency content is very wide and in particular AQK has significant values also for periods greater than 1 s. The ground motion had relatively short duration: 95% of the energy was released in 10 seconds or less. Finally, unprocessed data obtained from many stations show permanent displacements of up to 15 cm.

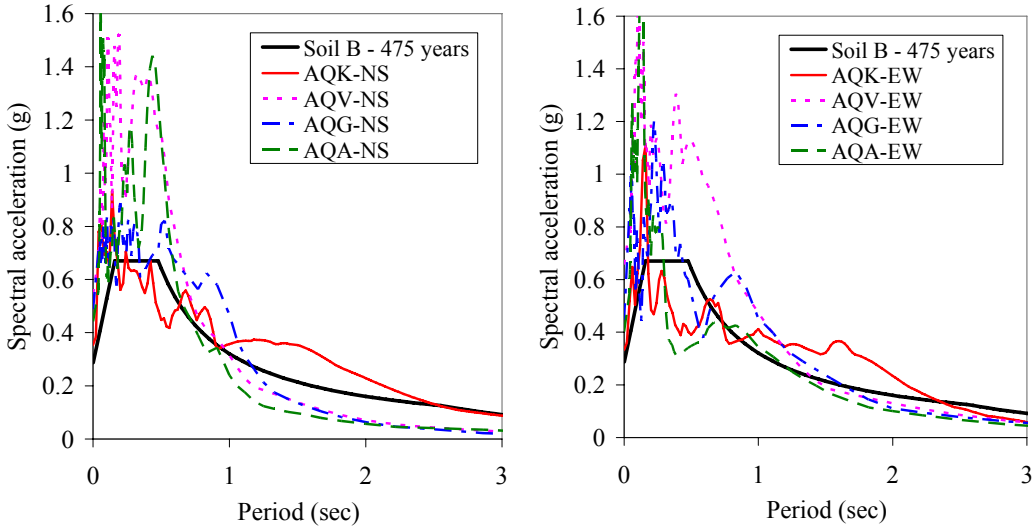

Figure 5. Response spectra for 5% damping of the 4 recorded accelerograms, compared with the elastic spectrum proposed by the Italian seismic code for ground type B (TR=475 years).

## 5 VULNERABILITY OF THE CHURCHES IN L'AQUILA AREA

Certain specific characteristics of Aquilan constructions proved to be decisive in analysing and interpreting the damage. Many churches dated back to the Middle Ages and from a typology point of view were simple naves with the typical Aquilan rectangular façade. An essential element to understand the vulnerability of churches and more generally all of the Aquilan buildings as a whole, was the devastating earthquake which hit L'Aquila in 1703 with an estimated intensity in historical documents of I=9-10. Nearly all of the churches were severely damaged. In some cases, simple repairs and reinforcements were performed, while in others, partial reconstruction (along with important enlargements and modifications to the original structure also linked to the architectural style of the period), and some churches were entirely rebuilt.

These factors contributed greatly to vulnerability, due to discontinuity in the masonry wall (in presence of enlargements), added height (with the possibility of vertical shifting in the wall), and the reconstruction of collapsed wall portions (rarely efficiently connected).

On the other hand, newer buildings benefited from knowledge of anti-seismic construction techniques always found in territories subject to strong earthquakes and usually handed down to builders over generations. In particular, L'Aquila systematically utilized the technique of "wooden ties" (Figure 6), which consists in the insertion of horizontal wooden elements built into the masonry during construction and joined at the extremities by small metal plates (fixed to the wood by two nails) and connected to the external wall by means of a small key. This solution was certainly derived from the realization after the earthquake in 1703 that the first collapse mechanisms were caused by out-of-plane overturning, and for this reason called first-mode mechanisms (Giuffrè 1993).

Therefore, it is necessary to connect each wall to the orthogonally adjoining one well in order to activate in-plane shear resistance (second-mode mechanism, typically characterized by diagonal cracking). An efficient connection between walls at the corners is not usually sufficient, also due to the fact that Aquilan masonry is not necessarily of poor quality but is characterized by small or medium sized, irregular stones. Metallic tie rods are present in L'Aquila only for repair or reinforcement interventions, while the connection between walls is made using "wooden ties", where anchoring is not limited to the extremities but is diffused thanks to friction that develops over the entire wooden element inserted in the masonry. For this reason, the external metal keys are always quite small (nevertheless the weak point is always found at the connection of the two nails between the metal plate and the wooden beam).

Figure 6. Some examples of “wooden ties” and connections: a) “wooden ties” at different levels of the dome of Santa Maria del Suffragio church in L’Aquila; b) the terminal connection elements, taken from the debris: the key and the steel plate (with two nails); c) the external key; d) and external wooden key for the connection of the trusses in Santa Maria del Carmine church in L’Aquila.

There was probably another reason the builders of the time used “wooden ties”; to protect against flexional out-of-plane mechanisms, which are activated in central portions of the façade when the internal walls are too thin and the frontal wall is weakened by the presence of openings.

Roofs also contain elements that clearly necessitate the addition of anti-seismic construction details. The extremities of trusses or roof rafters are not simply placed upon walls, but connected by means of wooden planks that protrude externally and are fixed into the walls by means of a wooden key (Figure 6d).

Another important factor of vulnerability is certainly caused by decay, which can be avoided altogether with proper maintenance. Water infiltration through cracks or due to lack of roof maintenance in many cases hastened the decay of wooden elements especially at the extremities near the connection with the metal plates.

Finally, also the Aquilan churches were found vulnerable due to the bad behaviour of modern interventions of structural strengthening. The term “modern” meaning building techniques used during the last century and particularly reinforced concrete and steel. Wooden roofs which are relatively light and flexible were often substituted with heavy and rigid reinforced concrete slabs, which almost always resulted in having a negative effect on the structure as well as its preservation (Figure 7).

Figure 7. The modern roof made by r.c. precast elements and unreinforced concrete slab in Santa Maria Paganica church in L'Aquila: a) the small portion over the dome which did not collapse; b) trusses with pre-cast r.c. joists.

## 6 INTERPRETATION OF DAMAGE AND COLLAPSE MECHANISMS

This paragraph will comment on a few cases of damage to churches in the Aquilan area referring to certain macroelements and the most significant damage mechanisms. The churches chosen were not necessarily the most relevant to the territory, nor noteworthy of media attention. Damage is interpreted directly, following the prompt approach commonly used during a seismic emergency to determine collapse mechanisms in order to highlight its value as an initial structural evaluation notwithstanding its limits.

### 6.1 *Overturning mechanisms of the façade*

Façade walls are almost always among the most vulnerable elements of churches. They are often subject to out-of-plane overturning mechanisms at any height or limited to the tops of the walls (gable).

The typical L'Aquila church façade has a rectangular shape. A summit mechanism that was observed in many cases was overturning of the raised triangle over the line of the roof. The façade is nearly always connected to lateral walls with "wooden ties" and the roof constitutes another connection through the ridgepole and the purlins. The demand for displacement due to the earthquake was therefore concentrated in the only unbound portion, with frequent cases of collapse or disarticulation from the stone ashlars (the façade is in fact often a wall made of poorly mortared, squared off ashlars; the top portions of the wall cannot benefit from the important contribution of friction due to low compression stresses).

One of the emblematic examples is S. Maria degli Angeli, located in Civita di Bagno (Figure 8), which shows out-of-plane overturning in the upper part of the left side and marked cracking proving an analogous mechanism on the right side, which did not evolve to the point of complete collapse.

The case is interesting because it highlights certain types of construction solutions. The corners were made of squared stones while the façade walls and lateral walls were made of irregular stones. This solution dictated by aesthetic reason but perhaps also by the desire for better connection, represents instead a point of weakness because the connection between the two types of masonry created discontinuity. In this case, an overturning mechanism was definitely activated with a fracture line throughout the plane of the façade rather than in correspondence with the connection to the lateral walls (as usually occurs). One can note the presence of anchoring stakes of "wooden ties" which however did not hold in the façade probably due to decay at the extremities of the wooden beam.

An interesting case is the façade of the Cathedral of S. Bernardino in L'Aquila (Figure 9), which did not overturn despite the large and slender raised portion. Rocking of slender masonry elements is a very complex problem, which depends on various factors: characteristics of seis-

mic motion; monolithic nature of the masonry structures; slenderness; size of the element (particularly its thickness). The seismic activation of the oscillation depends on wall slenderness but overturning is strongly related to the thickness. Moreover, in the presence of irregular masonry, a wall cannot oscillate on sharp edges, but localized crushing occurs, with a lesser capacity to withstand repetitive cycles (due to progressive decay). The façade of S. Bernardino was made of excellently hewn marble ashlars and had been reinforced in the 1960's with a reinforced concrete covering to the rear face of the wall. This intervention certainly increased resistance and stability to horizontal actions, but also increased its stiffness; as a consequence, the horizontal equivalent seismic actions were increased, compared with the one that would have occurred in the case of unreinforced walls, with notable compressive stresses at the edges. This was demonstrated by widespread localized crushing at the base of the semi-columns and capitals (Figure 9). In the absence of r.c. reinforcement, the wall would surely be subjected to wider oscillation but fewer compressive stresses in the edges (and therefore less localized damage).

Figure 8. Santa Maria degli Angeli church, in Civita di Bagno, L'Aquila.

Figure 9. S. Bernardino basilica in L'Aquila: a) the façade; b-c) details of some local crushing of marble elements due to out-of-plane overturning mechanism.

Another interesting case is the church of the Madonna dei Raccomandati in San Demetrio ne' Vestini (Figure 10). Here, the façade was erected in Baroque style after the earthquake of 1703 and the gable collapsed in the recent earthquake. It can be observed how the new roof, recently rebuilt with a wooden trussed structure, did not lean on the tympanum, and therefore resulted in a total lack of connection. Within the masonry, a "wooden tie" element was present, made of irregular trunks which were too short (in other words, the builder believed that the length of overlapping was sufficient for adherence, which instead proved to be insufficient).

Figure 10. Madonna dei Raccomandati church in San Demetrio né Vestini.

### 6.2 *Roof coverings: direct or induced damage*

The topic of induced vulnerability by the substitution of original wooden roofs with new rigid and heavy r.c. slabs has been the subject of intense arguments over the last few years (in particular since the earthquakes in Umbria and the Marches in 1997) both in scientific and professional fields. The recent Italian technical regulations (instruction document of the NTC 2008 – G.U. no. 47, 2009) states clearly that this kind of interventions should be avoided. Even though there are many cases of severe damage to churches and buildings where the roof was substituted by a r.c. slab, there are still those who argue that a certain amount of stiffness at the roof level may be useful and the mass increase is often narrow (compared to the total weight of the structure). However, the systematic and often in-depth observation of many cases gave rise to some important beliefs.

One must distinguish between the case of the simple construction of a r.c. stringcourse on top of the masonry from the much more invasive construction of a rigid roof with a thick r.c. slab, which can slide and crumble the masonry due to the low compressive stresses. The realization of a stringcourse at the top can certainly improve the overall behaviour as long as it is not too rigid nor heavy, especially in the presence of flexible walls as is the case in the lateral sides of churches. Efficient stringcourses can be made without using r.c. (reinforced brick masonry stringcourses; horizontal truss of steel plate over the top of the wall; stringcourses with external steel plates well-connected through masonry by bolts), but small reinforced concrete ones can also be a good solution.

Instead, the realization of a continuous, rigid and heavy diaphragm is always negative for various reasons:

1) when the slab is very thick, the increase in mass is significant and the fact that dynamic amplification increases with height should not be overlooked, so adding weight at the top of the construction is certainly a mistake;
2) adding stiffness to the roof further increases the in-plane action of the façade and in the triumphal arch due to the limitation to transverse displacement in intermediate arch spans (it is better to improve the capacity of the latter rather than expect the façade and the triumphal arch to sustain the seismic actions of the whole nave);
3) in the case of collapse, the presence of a monolithic element impedes localized damage to the

areas concerned, but produces a snowball effect, contrary to modern criteria of the structural robustness (take the example of Noto cathedral, which collapsed in 1996: in absence of the r.c. roof slab, the collapse would probably have been limited to the arch near the piers that collapsed due to crushing).

Another negative effect of stiff r.c. roofs is what they do to the gable of the façade. An example is the church of S. Domenico in L'Aquila (Figure 11), which can be considered representative of many analogous situations. At first glance, the collapse of the gable seems to be caused by an overturning mechanism, but the stringcourse did not allow that mechanism by creating a connection at the summit. In the presence of a flexible wooden roof, the overturning mechanism is associated with a rise in the gable due to the opening of the hinge at its base; the ridgepole and the purlins lean on the gable, if they are well-connected, and can contrast overturning. Instead in a roof with a r.c. slab, the flexural stiffness opposes the uplift of the gable with a subsequent increase in vertical compression stresses; this compression provokes collapse due to wall crushing. In fact, this was found and caused the masonry wall to crumble rather than overturn as a rigid block. Figure 11d shows that also king trusses are made from r.c.; this is an emblematic case of the faith in this material during the last century for the static restoration of historic constructions (it is important to consider the difficulty of utilizing a material which must be cast on site, necessitates lengthy drying and hardening times, and is subject to "fluage" phenomena; wood or steel are for sure the proper materials for a king truss).

Figure 11. San Domenico church in L'Aquila: a) the facade; b) the collapsed gable of the facade; c-d) collapse of the transept vault due to substitution of the roof, made by r.c. trusses.

### 6.3 *Apses*

The apse is another part of a church frequently subject to damage, which occurs through clearly identifiable collapse mechanisms. The understanding of behaviour and knowledge of construction history of a building is fundamental; the apse is often the oldest part of the church so it is often made of very large, squared stones. Given its vulnerability, however, one may often find frequent repairs or reconstruction following damage after past earthquakes.

An interesting example of damage in the apse was found in the church of S. Eusanio Martire in Sant'Eusanio Forconese (Figure 12). There is a very tall semi-circular apse with well-hewn stone masonry walls divided into three parts by two small pilasters. The earthquake provoked the collapse in the external leaf of the masonry in the central portion, which occurred for various reasons:

1) the external leaf, though apparently in good condition, was very thin and bad connected to the internal masonry nucleus (this is typical in many hewn ashlar walls);
2) the pilasters did not have a static function (due to their reduced thickness) and created discontinuity in the external masonry leaf, favouring its detachment in the central portion (note the detachment of the pilaster in the first photograph even when the external leaf did not collapse; certainly, in the absence of the pilasters, the wall would have behaved better);
3) the roof of the church had recently been replaced (note the stringcourses and concrete elements) and this certainly could have increased the local stresses at the interface between masonry and r.c. elements.

Figure 12. The apse of S. Eusanio Martyr church in Sant'Eusanio Forconese.

### 6.4 *Belfries*

Plane belfries and bell cells in towers are among the most vulnerable elements of a church, according to the statistics of damage assessment. These elements are made of flat or three-dimensional, arch-pier systems, which manifest mechanisms with the formation of hinges at the base and top of the piers or in the arch, even for low value of horizontal components of the seismic action. Moreover, it must be considered that these elements are subjected to a motion at their base which is significantly amplified by the building with respect to the seismic ground motion (actually, the bell cells are at the top of a tower, while plane belfries are at the summit of the façade).

It is therefore almost inevitable that these elements suffer great damage in the case of an earthquake, because of the high displacements imposed at their base. The solution to avoid collapse is to allow displacement, guaranteeing ductility; in other words, allows oscillation without loss of equilibrium or local wall collapse. Regarding the latter, the use of tie-rods with flexible devices may be very useful.

Here are two examples of this concept: the bell tower of the ex-convent of S. Domenico in L'Aquila (Figure 13a); the church of S. Felice Martire in Poggio Picenze (Figure 13b).

Figure 13. a) Bell cell in the ex-convent of S. Domenico in L'Aquila; b) bell cell of S. Felice Martire church in Poggio Picenze.

In the first case, there are "wooden ties" at the base and at the top of the cell; the piers developed an overturning mechanism, which in the upper portions involved the arches; in the absence of tie rods, there were openings of the hinges and sliding in the central ashlar, though limited by the upper wooden tie rod. The possibility of developing this overturning mechanism limited shearing damage to the piers.

On the contrary, in the case of the church in Poggio Picenze, an intervention, debatable even on a formal level, had been carried out, which was aimed at creating better connection but added exaggerated rigidity to the structure. Instead of classic tie rods, small metallic bars connected in pairs had been inserted at the base of the piers and at the base of the arches. The result was that the possibility of deformation was localized only in the piers (due to the fact that the upper section was completely rigid), with subsequent serious damage due to shearing. The photograph clearly demonstrates how complete collapse did not occur only by luck, and nevertheless, the problem of restoring the tower must be dealt with considering the extent of the damage.

It can be concluded that allowing displacement is better, with the subsequent reduction of solicitation induced in the walls, rather than adding rigidity, increasing seismic action and concentrating deformation to limited areas.

Plane belfries are characterized by different behaviour. Being flat structures, they suffer damage to the arch-pier system (in this case, the consideration above for bell cells should be applied), but they are also subject to out-of-plane overturning. Almost always, their thinness induces excessive worries regarding stability; the structure they are built upon is decidedly more rigid and therefore no amplification of the seismic action occurs in their frequency range. In this case as well, the addition of elements which add rigidity to the structure is not positive for seismic strength.

The Case of the church of S. Michele Arcangelo in Villa Sant'Angelo is interesting (Figure 14). The first image shows severe in-plane damage to the three piers and two arches. The belfry was equipped with three external vertical tie rods, and axial to the piers and connected to the wall at the extremities and in the centre (please do not confuse them with the horizontal bars put in place after the earthquake for safety measures).

The vertical bars limited the formation of hinges at the base of the piers, but shifted the damage under the anchoring point of the bars themselves. In the upper portion the mechanism formed along the arches with a strong concentration of damage near the connections between the bars and the walls. One can also note the troubling diagonal cracking with displacement under the external pier which was a consequence of the strong shearing action at the base due to the bars which increased stiffness.

Figure 14b is also interesting and shows an out-of-plane oscillation mechanism with horizontal cracking on the side of the façade (directly below the connection of the vertical tie rods) and vertical cracking of detachment to the lateral walls of the church.


Figure 14. Plane belfry of S. Michele Arcangelo church in Villa Sant'Angelo.

## 7 CONCLUSIONS

The damage case studies illustrated herein are by no means exhaustive. With reference to the macroelements considered, the types of damage are in fact numerous and determined by a complex series of factors: geometrical configuration, construction characteristics, the history of transformations and past damage and ineffective strengthening interventions. Moreover, many other elements in churches turned out to be vulnerable after this earthquake: triumphal arches, domes and vaults.

The approach to identify macroelements has also proven to be effective following the earthquake in L'Aquila, because it allows rapid and objective interpretation of seismic behaviour, which is useful in determining fitness for use and the necessary emergency safety measures to be taken. Thanks to this approach, heavy and often useless propping could be avoided since the request for provisional measures must respond to the actual damage mechanisms found with a certain level of severity.

The planning of restoration interventions, the rebuilding of collapsed portions and the design of seismic strengthening should start from the interpretation of the behaviours made after the earthquake on 6 April 2009 by this assessment methodology.

This paper showed the bad behaviour of churches which were strengthened by r.c. elements. In particular the increase of mass and stiffness due to the substitution of timber roofs by r.c. slabs produced a negative effect; these interventions should be avoided in the future.

A topic that should be further investigated is the evaluation of L'Aquila masonry quality. On this point, one must not be limited to a qualitative interpretation, but on-site experimentations are needed to measure mechanical properties. This data is indispensable for verifying safety, by means of proper mechanical models. In particular for churches safety evaluation with regards to a severe seismic action is possible through mechanical and intuitive models, based on equilibrium limit analysis applied to masonry walls, considered as rigid bodies, non-resistant to tensile stresses and equipped with friction. Mechanical models for the displacement based assessment of cultural heritage structures are going to be developed in PERPETUATE project (Lagomarsino et al., 2010).

REFERENCES


Bazzurro P. et al. (2009) The MW 6.3 Abruzzo, Italy, Earthquake of April 6, 2009. EERI Special Earthquake Report (http://www.eeri.org/site/reconnaissance-activities/69-italy/544-m-63-laquila-italy).

Carocci C., Lagomarsino S. (2010) Masonry buildings in the historic centres of the L'Aquila area. in Il Terremoto del 6 aprile 2009 in Abruzzo, Progettazione Sismica, Vol. 3, IUSS Press.

D'Ayala D.F., Paganoni S. (2011) Assessment and analysis of damage in L'Aquila historic city centre after 6th April 2009. Bullettin of Earthquake Engineering, vol. 9, pp.81-104

Doglioni F., Moretti A., Petrini V. (1194) Churches and the earthquake. Ed. LINT, Trieste (in Italian).

G.U. no. 47, 26/02/2011 (suppl. ord. no. 54). Directive of the Prime Minister dated on 9/02/2011, Assessment and mitigation of seismic risk of cultural heritage with reference to the Technical Code for the design of constructions, issued by D.M. 14/1/2008 (in Italian).

G.U. no. 55, 7/03/2006. Decree of the Prime Minister dated on 23/02/2006, Approval of forms for the seismic damage assessment of cultural heritage buildings. (in Italian)

G.U. no. 47, 26/02/2009 (suppl. ord. no. 27), Circular 2/02/2009, no. 617. Instructions for the application of the new Technical Code for the design of constructions, issued by D.M. 14/01/2008. (in Italian)

Giuffrè A. (1993) Safety and conservation of historical centres. The case study of Ortigia, Editori Laterza, Bari (in Italian).

Lagomarsino S., Podestà S. (2004a) Seismic vulnerability of ancient churches. Part 1: damage assessment and emergency planning. Earthquake Spectra. Vol. 20, pp. 377-394, ISSN: 8755-2930

Lagomarsino S., Podestà S. (2004b) Seismic vulnerability of ancient churches. Part 2: statistical analysis of surveyed data and methods for risk analysis. Earthquake Spectra. Vol. 20, pp. 395-412, ISSN: 8755-2930

Lagomarsino S., Podestà S. (2004c) Damage and vulnerability assessment of churches after the Molise earthquake (2002). Earthquake Spectra, Vol. 20 (S1), pp. S271-S283, ISSN 8755-2930.

Lagomarsino S., Resemini S. (2009) The assessment of damage limitation state in the seismic analysis of monumental buildings. Earthquake Spectra, Vol. 25, No 2, pp. 323-346.

Lagomarsino S., Calderini C., Cattari S., Modaressi H., Pitilakis K., Bosiljkov V., D'Ayala D., Benouar D., Gazetas G., Gostic S., Ginanni Corradini R. (2011) PERPETUATE Project: the proposal of a performance-based approach to earthquake protection of cultural heritage. 4th Japan-Greece Workshop: *Seismic Design of Foundations, Innovations in Seismic Design, and Protection of Cultural Heritage*, October 6-7, 2011, Kobe, Japan.

Podestà S., Brignola A., Curti E., Parodi S., Lemme A. (2010) Damage assessment and seismic vulnerability of churches: the Abruzzo earthquake. Ingegneria Sismica, XXVII, N. 1, pp. 21-35 (in Italian, with an extended abstract in English).

Rovida A., Castelli V., Camassi R., Stucchi M. (2009) Historical seismicity in the area of the seismic sequence of April 2009. INGV Report, Istituto Nazionale di Geofisica e Vulcanologia (in Italian) (http://www.mi.ingv.it/eq/090406/storia.html).

Stucchi et al. (2007) DBMI04, the database of macroseismic survey of Italian earthquakes used for the seismic parametric catalogue CPTI04. Quaderni di Geofisica, 49, pp. 38 (in Italian) (http://emidius.mi.ingv.it/DBMI04/)

# Structural Stability and Bearing Capacity Analysis of the Tunnel-Entrance to the Stadium of Ancient Nemea

H. Alexakis & N. Makris
*Dept. of Civil Engineering, Univ. of Patras, Patras, Greece*

ABSTRACT: In the archaeological site of Ancient Nemea, Greece, southeast of the Temple of Zeus, there is an ancient stadium in which the athletes of the past entered through a 36 m-long tunnel − a cut-and-cover vaulted structure − constructed of limestone. The tunnel was buried with earth until it was discovered in 1978. At present, some limestone blocks of the tunnel show appreciable damage mainly due the humidity fluctuation within the tunnel. In this paper we present a comprehensive structural analysis of the tunnel which ranges from the thrust line limit analysis and the discrete element method, to a comprehensive finite-element analysis of the tunnel and its surrounding soil. The study concludes that the tunnel with its overburden soil is structurally stable and has ample bearing capacity. However, selective stones of the structure need to be retrofitted in order to avoid further local failures, while the humidity fluctuation inside the tunnel needs to be minimized.

## 1 INTRODUCTION

The entrance from the west to the ancient stadium at Nemea, Greece (see Fig. 1), is a 36.35 m long vaulted tunnel with inner width that is approximately 2.10 m and with inner height that is approximately 2.45 m.

The tunnel was constructed during the 4th century B.C. as a cut-and-cover structure and subsequently was covered with earth. Both ends of the tunnel were discovered in 1978 (Miller 2001). They were completely filled with and covered over by silt soil. The interior however, had not completely filled. According to Miller (2001), the earth above the tunnel has stabilized over the past 2300 years. Figure 2 shows a section of the tunnel along its longitudinal axis, together with the overburden earth, as was measured in 1978 (Miller 2001). No excavation over it has been attempted until now, because there was the fear that this could affect the stability of the structure with destructive consequences. Part of the motivation of this work is to analyze the structural behavior and offer a dependable load bearing capacity estimate of the tunnel in order to reach conclusions on the stability of the tunnel based on technical arguments.

The fact that the ends of the tunnel were completely filled and prevented the circulation of air had a most beneficiary role on the structural integrity of the tunnel since it minimized the fluctuation of humidity. Although the tunnel was remarkably well preserved, a few of the blocks of the vault were missing, while the face of many of the voussoirs had split off (Miller 2001, see also Fig. 11 bottom). Figure 3 (top) shows the entrance of the tunnel (western end), while Figure 3 (bottom) shows the exit of the tunnel to the stadium (eastern end) as they appear today. Upon the removal of the earth that filled the entrance, the tunnel was subjected to a more intense fluctuation of humidity and further exfoliation of stones has been observed during the recent years.

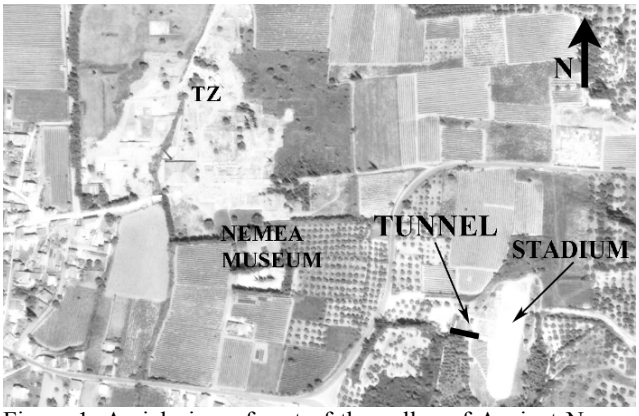

Figure 1. Aerial view of part of the valley of Ancient Nemea, showing the locations of the Sanctuary of the Temple of Zeus (TZ), the Stadium and its tunnel entrance from the west.

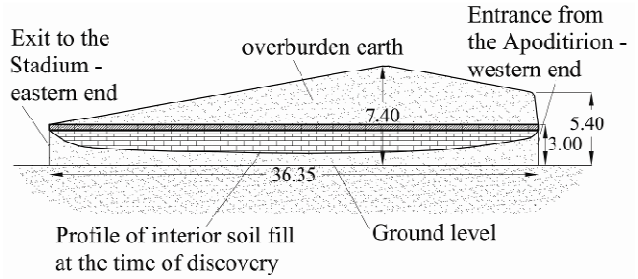

Figure 2. Schematic section of the tunnel along its longitudinal axis showing the levels of earth fill inside and above the tunnel.

## 2 DESCRIPTION OF THE TUNNEL STRUCTURE AND ITS INTERACTION WITH THE SURROUNDING SOIL

The tunnel was initially constructed in a straight trench that was excavated in a firm soil/soft rock. It consists of two vertical stone walls which support the cylindrical dome (see Fig. 3). The vertical wall and the cylindrical vault consists of limestones of about the same size, with dimension of the order of 40 cm, built in horizontal rows, as shown in Figure 11 (bottom). Figure 4 shows a drawing with the average dimensions of the stone blocks at a given cross section of the tunnel. At each side, the lower stone row is the foundation and the above four (4) rows form the walls of the tunnel, as shown in Figure 3. The cylindrical vault consists of a central row of key stone and four (4) rows of voussoirs on each side. The width of the voussoirs at the extrados exceeds 45 cm, while the width of the voussoirs at the intrados is of the order of 34 cm.

Between the vertical walls of the tunnel and the vertical surface of the excavated soft rock, there is a gap with variable width between 15 and 25 cm. Upon construction of the walls, this gap was filled with silt (probably from the excavated material from the trench), which appears to be well compacted. Accordingly, the backfill soil between the vertical walls and the soft rock initially was in a triaxial stress state. The good construction of the tunnel in association with the shape of the thrust line of the free standing tunnel before the backfill was placed (see Fig. 6) together with the relative high value of the coefficient of the friction along limestone surface $\mu_{LS}$>0.7 (Konstantinidis and Makris 2005) opposes any potential movement of the stones of the walls to the inside; therefore it is unlikely that the backfill soil deteriorated to an active state of stress (point 1 in Fig. 5).

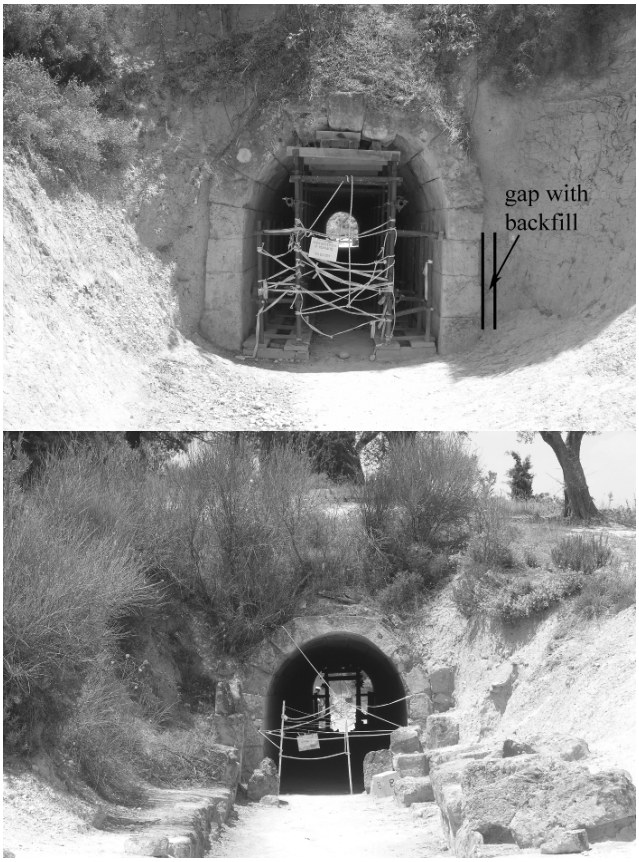

Figure 3. Current view of the entrance of the tunnel (western end - top) and the exit to the stadium (eastern end - bottom).

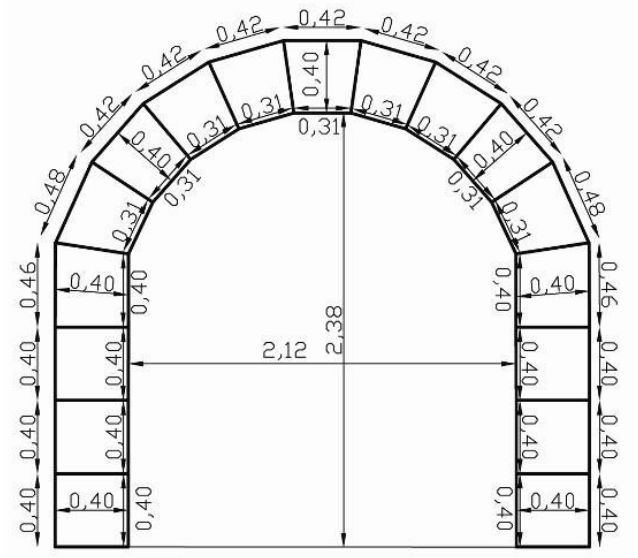

Figure 4. Schematic of a tunnel section showing the dimensions of the stone blocks used in the analysis.

Therefore in addition to the active limit case we examine the case where the horizontal soil stresses $\sigma_h \geq K_a \sigma_v$, where

$$K_a = \frac{1-\sin\phi}{1+\sin\phi} \tag{1}$$

is the coefficient of active stress. Accordingly, at rest we assume a horizontal stress $\sigma_h=0.5\sigma_v$ (point 2 in Fig. 5).

Within the context of the limit analysis for the tunnel-surrounding soil system that this work offers, we adopt for the soil the Morh-Coulomb failure law

$$\tau_y = c + \sigma_y \tan\phi \tag{2}$$

where $c$ is the cohesion intercept of the failure line with the shear-stress axis and $\varphi$ is the friction angle (angle of shearing resistance) of the soil. Given the lack of information regarding the exact behavior of the backfill soil at failure, we assume that the cohesion intercept $c$=0 and the failure law for the backfill soil simplifies to

$$\tau_y = \sigma_y \tan\phi \tag{3}$$

The simplified failure law given by Equation (3) and shown schematically in Figure 5 is attractive since the same expression (with a different value for the friction angle $\varphi$) is used for the shearing resistance along the interfaces of the limestones of the tunnel; while the reasoning regarding the state of horizontal stresses is not affected by the assumption $c$=0. With reference to Figure 5 the vertical $\sigma_v$ and horizontal $\sigma_h=0.5\sigma_v$ geostatic stresses of the backfill soil are shown respectively with point V and point 2 along the horizontal σ-axis. It is worth mentioning that an analysis with $\sigma_h=0.5\sigma_v$ and a given value of friction angle $\varphi$ corresponds to a case where $\sigma_h$ is now an active stress in association with a lower value of $\varphi$.

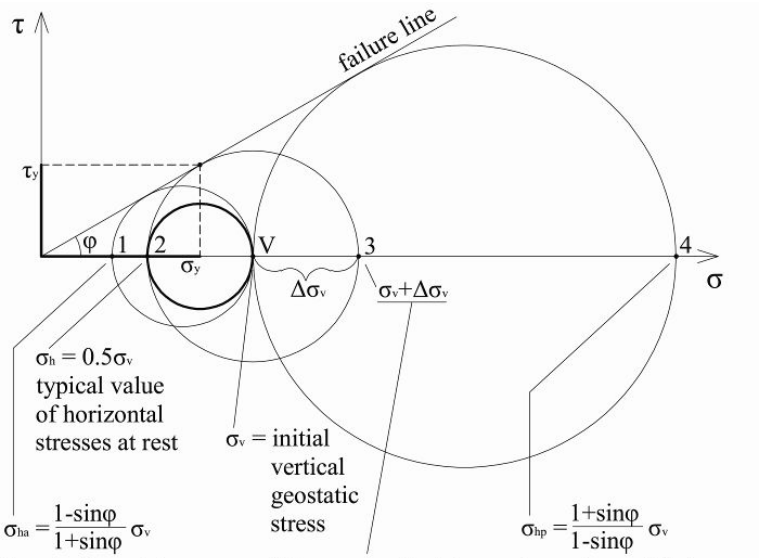

Figure 5. Admissible state of stresses under geostatic conditions.

Through the years, additional soil was transferred over the tunnel and the initial vertical stress at a point $\sigma_v$ (point V in Fig. 5) may have increased to $\sigma_v+\Delta\sigma_v$ (point 3 in Fig. 5). Such an increase in the vertical stress may create a sufficient difference between $\sigma_v+\Delta\sigma_v$ and $\sigma_h$ (segment 2-3) so that $\sigma_h$ at point 2 becomes an active stress due to the new stress state. It should be noted however that the narrow gap between the wall of the tunnel and the vertical surface does not allow for a linear increase of the vertical stress ($\sigma_v=\gamma z$) as $z$ increases, given that there is substantial friction of the soil with the stone wall of the tunnel and the neighboring excavated vertical wall of the soft rock. Based on the above discussion the structural analysis that follows, in addition to the active limit state $\sigma_h=\sigma_v(1-\sin\varphi)/(1+\sin\varphi)$, investigates the vertical load carrying capacity of the tunnel where the horizontal soil stress $\sigma_h=0.5\sigma_v$. In the analysis that follows the friction angle for the backfill is assumed $\varphi=30^o$. Consequently the results for the geostatic case $K_o=0.5$ ($\sigma_h$ is point 2 in Fig. 5) corresponds to a conservative active limit state ($K_a=(1-\sin\varphi)/(1+\sin\varphi)$) where $\varphi\approx20^o$ (Gazetas and Kavvadas 2009).

The evolution of the thrust line as the backfill height increases in association with the inclination of the limestone interfaces with the thrust line and the typical value of the coefficient of friction along the limestone interfaces indicate that it is unlike that the stones of the walls have move out by an appreciable amount due to hinging of the tunnel, therefore the possibility of encountering a passive failure is excluded (point 4 in Fig. 5). Interestingly, this paper shows that hinging of the tunnel may only happen under very large overburden loads which exceed by far the values of the overburden loads that generate compression failure of the stone blocks of the tunnel.

## 3 BACKGROUND ON THE STRUCTURAL ANALYSIS OF MASONRY ARCHES AND VAULTED STRUCTURES

The two main approaches for the structural analysis of arches and vaulted structures are: (a) the ultimate stability analysis - also reported as limit stability/equilibrium analysis, rigid-plastic analysis or thrust line method - (Heyman 1966, 1995, Smith et al. 1990, Harvey 1991, Huerta 2001, Boothby 2001, Block et al. 2006, Gilbert 2007, Roca et al. 2010, among others) and (b) a stress analysis of the structure.

For historic masonry structures in general and more specifically for those constructed from massive bearing stones, the thrust line method is the choice, since compressive stresses are an order of magnitude smaller than the failure stress of the masonry and the issue of stability prevails.

In this paper the loading resistance/capacity of the tunnel-entrance to the Stadium of Ancient Nemea is examined first via an ultimate stability analysis and subsequently via a finite element analysis (FEM). The ultimate stability analysis is first implemented through its classical formulation, using the simplifying assumptions of Heyman (1966, 1995) and subsequently via an advanced formulation, using linear programming method based on the kinematic approach, which by virtue of an optimization process finds the limit load of a rigid block structure to be stable. Livesley (1978) was the first who introduced this advanced formulation and his work was followed by several other investigators (Gilbert & Melbourne 1994, Baggio & Trovalusci 1998, Ferris & Tin-Loi 2001, Casapulla & D'Ayala 2001, Orduña & Lourenço 2003, 2005a,b, among others). Additionally, the distinct element method (DEM) adapted in the principles of the ultimate stability analysis and comparable with its classical and advanced form is also employed.

## 4 LIMIT EQUILIBRIUM ANALYSIS - THE THRUST LINE APPROACH

The thrust line (limit-state) approach has been widely used for the stability of masonry structures since the years of Hooke (1635-1709), who described the analogy between the tension in a hanging chain due to its own weight and the compression along the thrust line of a masonry arch. Heyman (1966) was probably the first who proposed that the limit equilibrium analysis, which derives from the plastic theory of metal structures, may also be applied for the analysis

of stone and masonry structures such as masonry arches and vaults provided that three (3) basic assumptions are introduced:
(a) the joints of the masonry blocks do not transmit tension (zero tensile tension)
(b) the masonry blocks are rigid and incompressible
(c) the masonry blocks do not slide at the joints.
In the case of the vaulted tunnel of Nemea, the assumptions (a) and (b) apply since the working stress along the tunnel (~1.0 MPa) are more than an order of magnitude less than the average strength of the limestone (~13 MPa) (Makris & Psychogios 2004). Moreover, given that there is no mortar at the stone block interfaces in association with the relative high value of the modulus of elasticity (~$E$=6.5 GPa) to the working stresses (~1.0 MPa), the stone blocks may considered as rigid.

The equilibrium-stability of a stone arch is established via the thrust line. This is a physicaly realizable line that represents the load path of the resultant of the compressive forces through the stone skeleton. For a structure in pure compression to be in equilibrium with the applied loads there must be a line of thrust that lies entirely within the section of the structure.

In this work the limit equilibrium analysis is performed with two validated computer codes known as ARCO v1.1 (Gelfi 2002) and RING v1.5 (Gilbert et al. 2005). Both codes idealize a vaulted structure as an assemblage of rigid blocks. Software ARCO assumes that no sliding occurs at the block interfaces and computes the optimum thrust line via an optimization process which converges to the thrust line that minimizes the normal stresses at the extrados and intrados of each block interface. Software RING analyses only the collapse state of the structure. In addition to basic equilibrium considerations, in the context of masonry gravity structures, the following conditions may then be used to test for ultimate collapse, assuming both hinging (initially assuming that the masonry possesses infinite compressive strength, so the line of thrust can be transmitted through a hinge point lying on an exterior face of the arch) and sliding (assuming that sliding failures obey an associative flow rule). Accordingly, the following failures are considered possible:
(i) The yield condition, which may be deemed to be satisfied providing the line of thrust both lies entirely within the masonry and does not cross any joint at a subtended angle less than the angle of the masonry material.
(ii) The mechanism condition, which may be deemed to be satisfied providing the line of thrust either touches exterior faces of the masonry blocks and/or crosses sufficient joints at an angle equal to the frictional angle of the masonry material.

## 5 LIMIT EQUILIBRIUM ANALYSIS OF THE IDEALIZED TUNNEL

The thrust line can be graphically described by the use of the force polygon. Figure 6 (top) shows the thrust line of the free-standing tunnel (no backfill - there is no vertical or lateral earth pressure) where the only load is the weight of each block (W1-W9). Figure 6 (top-right) shows graphically the vector summation of forces (force polygon) as we move from the keystone (No 9) to the above-the-foundation stone of the wall (No 1). With reference to Figure 6, note that the thrust line meets the interfaces of the stone blocks at various angles $\psi$. The force normal to the stone interface (potential failure plane) is $N=F_c\cos\psi$, while the force tangential to the stone interface is $T=F_c\sin\psi$. Assuming that the coefficient of friction at the stone interface is $\mu$, sliding along the interface will not happen as long as

$$T = F_c \sin\psi < \mu N = \mu F_c \cos\psi \quad \text{or} \quad \tan\psi < \mu \tag{4}$$

When the thrust line is inclined enough ($\tan\psi=\mu$), sliding=failure occurs and in this case

$$T = N \tan\psi \tag{5}$$

Equation (5) is the same expression (in terms of forces) as Equation (3) and indicates that upon dividing the forces with the contact surface of the adjacent stones, the Morh-Coulomb criterion introduced earlier as the failure law for the backfill soil is also valid for the limestone where the angle of shearing resistance $\varphi$ for the soil is replaced with the angle for shearing resistance $\psi$ for the limestone.

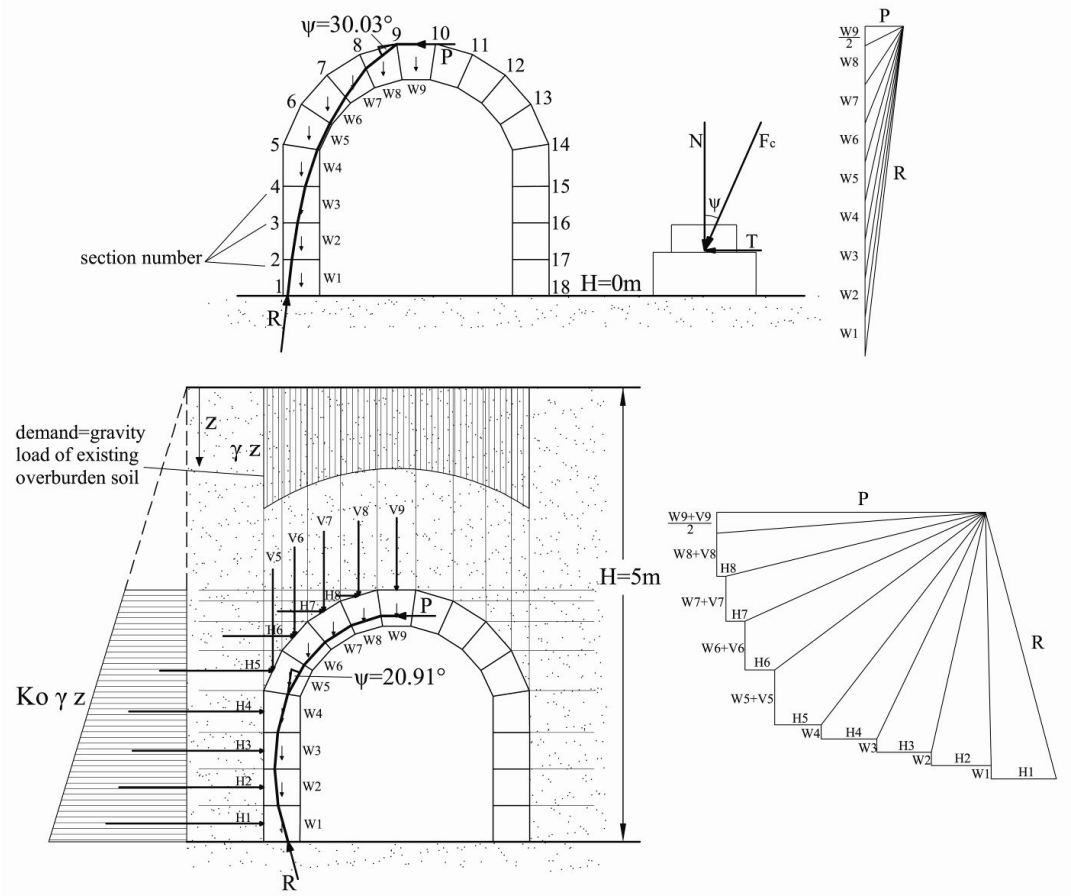


Figure 6. Thrust line and force polygon of the free-standing tunnel (no backfill - top) and with 5m of backfill (bottom).

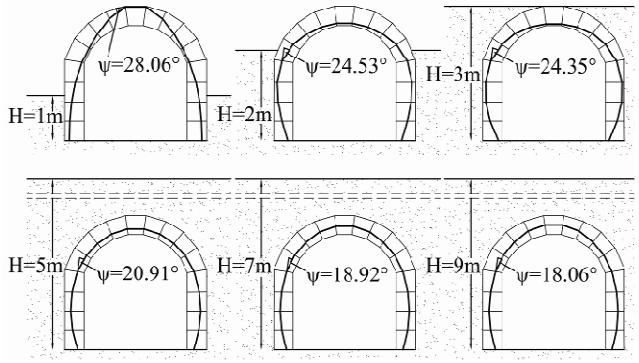


Figure 7. Evolution of the thrust line of the Nemea tunnel as the backfill height *H* increases. As *H* increases the longest deviation of the thrust line from the perpendicular to the stone interface decreases, leading to a more stable configuration.

For limestones, a conservative value for the coefficient of friction is $\mu_{LS}$=0.7, therefore sliding will occur for an angle $\psi > \tan^{-1}\mu_{LS} = 35^{o}$ (capacity). Figure 6 (top) shows that the larger angle of incidence of the thrust line (demand) is $\psi_{max}=30.03^{o}$, therefore assuming that all stones are in healthy condition ($\mu_{LS}$=0.7) the possibility of sliding is excluded given that $\psi_{max}=30.03^{o} < \tan^{-1}\mu_{LS} = 35^{o}$. Figure 6 (top) also shows that the geometry of the thrust line of the free-standing

tunnel (no backfill soil) is such that the tangential-to-the-stone interface forces along the walls of the tunnel are towards the outside. Accordingly, upon the tunnel was constructed and the backfill soil was placed the situation where the stones of the wall move to the inside leading to an active failure of the soil is excluded. Figure 6 (bottom) shows the thrust line of the tunnel when there is 5m high of backfill ($\rho$=1.8Mg/m3) and the horizontal soil stresses $\sigma_h$=0.5$\sigma_v$ (point 2 in Fig. 5, $\varphi$=30$^o$). As we move from the keystone to lower stones of the walls, in addition to the gravity loads, the stones are subjected to horizontal forces from the backfill soil. This coexisting lateral trust bends the thrust line to the inside as depicted schematically in the vector summation of forces shown at the bottom-right of Figure 6. Note that for this case the largest deviation of the thrust line from the perpendicular to the stone interface is at the first stone of the vault (springer), where $\psi_{max}$=20.91$^o$, a value that is appreciable lower than the 30$^o$ to 35$^o$ of available frictional resistance. This finding indicates that the tunnel is a well engineered "self-locking" structure which does not allow any movements of its constituents stones neither to the outside nor to the inside; therefore the outside backfill soil shall remain at rest ($K_o$=0.5).

Figure 7 shows the evolution of the thrust line of the tunnel as the backfill height increases from $H$=1 m to $H$=9 m. Note that as the backfill height increases the largest deviation of the thrust line from the perpendicular to the stone interface decreases, leading to a more stable configuration. Table 1 offers the maximum values of angle $\psi$ and the interfaces where they appear together with the corresponding values of coefficient of friction needed for no sliding and the maximum compressive stresses that develop at the stone interfaces. Note that even when the backfill soil reaches a height $H$=9 m the maximum compressive stress is below 1.0 MPa − that is an order of magnitude less than the compressive strength of the Nemea limestone ($\sigma_u$~13-15 MPa).

Table 1. Maximum compressive stresses at the extrados and the intrados together with the angle $\psi$ of thrust line with the normal to the contact surface of the stones.

| Buckfill height $H$ | Max $\sigma_{ex}$ | | Max $\sigma_{in}$ | | Min percentage of interface area under compression | | Max $\psi$ demand | | Min $\mu$ for no sliding |
|---|---|---|---|---|---|---|---|---|---|
| m | MPa | Sec. No* | MPa | Sec. No* | % | Sec. No* | degrees | Sec. No* | |
| 0 | 0.380 | 1, 18 | 0.380 | 5, 14 | 6.0 | 9, 10 | 30.03 | 9, 10 | 0.5780 |
| 1 | 0.205 | 9, 10 | 0.205 | 5, 14 | 11.7 | 9, 10 | 28.06 | 9, 10 | 0.5331 |
| 2 | 0.174 | 4, 15 | 0.174 | 1, 18 | 34.2 | 9, 10 | 24.53 | 5, 14 | 0.4564 |
| 3 | 0.304 | 3, 16 | 0.304 | 9, 10 | 24.9 | 9, 10 | 24.35 | 5, 14 | 0.4526 |
| 5 | 0.447 | 3, 16 | 0.447 | 1, 18 | 75.6 | 7, 12 | 20.91 | 5, 14 | 0.3821 |
| 7 | 0.683 | 3, 16 | 0.683 | 1, 18 | 90.2 | 6, 13 | 18.92 | 5, 14 | 0.3428 |
| 9 | 0.921 | 3, 16 | 0.921 | 1, 18 | 94.5 | 6, 13 | 18.06 | 5, 14 | 0.3261 |

* For section number see Figure 6 (top)

Our limit equilibrium analysis proceeds with the limit analysis of a slice of the tunnel that is 1m thick and with variable backfill height $H$, that is further loaded with a distributed load that ranges over the 3 m width of the tunnel. What is interesting, is to compute what additional distributed load will take to fail the tunnel. For instance, Figure 8 shows that when there is 5 m of backfill the gravity load of the existing overburden soil along 1 m of tunnel depth is 133 kN whereas it takes 773 kN distributed over the 3 m-width of the tunnel to fail the 1 m thick tunnel section. It is important to note that under this very high overburden load the tunnel fails because we exceed the compressive strength of the limestones (say $\sigma_u$=10 MPa) − not because we reached instability due to hinging of the tunnel. At the bottom stone and the springer where the compressive stresses reach 10 MPa, there is still room between the thrust line and the extrados and intrados respectively. Consequently, regardless of what is the exact value of the compressive strength ($\sigma_u$=10~13 MPa), the tunnel has ample bearing capacity. Again, as in Figure 6 (top), the larger angle of incidence of the thrust line is 29.62$^o$; therefore, assuming that all stones are in healthy condition, the possibility of sliding is excluded given that with $\mu_{LS}$=0.7, $\psi_{max}$=29.62o< $\tan^{-1}\mu_{LS}$ =35$^o$.

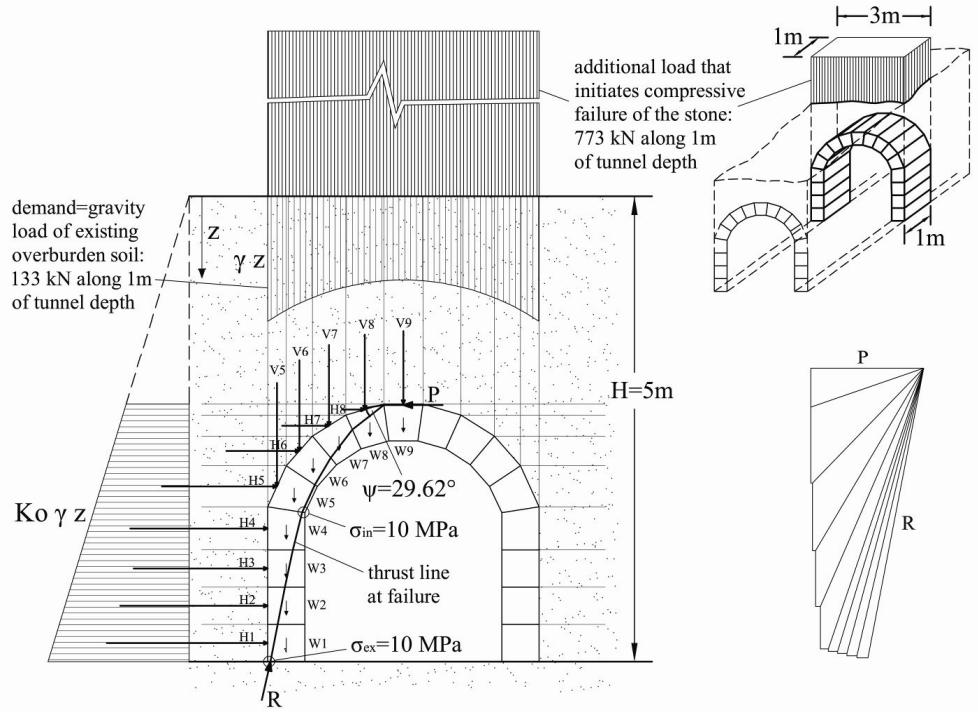


Figure 8. Thrust line of the Nemea tunnel when compressive failure of the stone blocks is reached, together with the loads needed to fail a 1.0m thick section of the tunnel.

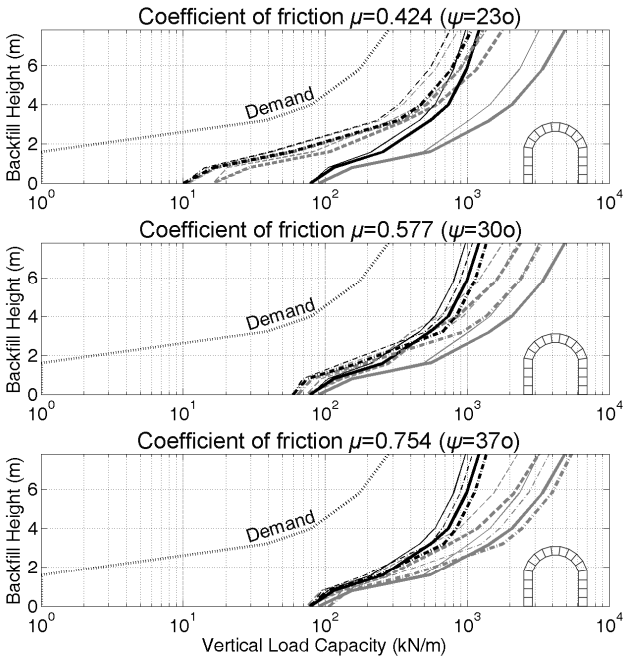


Estimated Capacity

| | Finite Compression strength: σu=10 MPa | | Unlimited Compression strength | |
|---|---|---|---|---|
| | *Ka* | *Ko* | *Ka* | *Ko* |
| ARCO | ——— | ——— | ——— | ——— |
| RING | – · – · – | – · – · – | – · – · – | – · – · – |
| UDEC | NA | NA | – – – | – – – |

Figure 9. Vertical load carrying capacity as a function of the backfill height next and above the tunnel.

Figure 9 shows that the additional load that is needed to fail the Nemea tunnel is an increasing function of the existing backfill height. All lines except the demand line in Figure 9 show the entire vertical load that a one-meter-thick slice of the tunnel can sustain (see Fig. 8). The continuous dark and gray lines are computed with software ARCO which assumes that no sliding occurs along the stone interfaces. The dark lines show the ultimate load which is controlled by the compressive failure of the limestone ($\sigma_u$=10 MPa), while the gray lines show a fictitious ultimate load which is controlled from the hinging of the tunnel assuming building blocks with unlimited compressive strength. The thick lines is when the lateral soil stress ratio $K$=$K_o$=0.5; whereas, the thin lines is when the lateral soil stress ratio $K$=$K_a$ ($\varphi$=30$^o$). The corresponding chain lines are computed with the software RING which also examines whether sliding occurs. The results presented in Figure 9 (bottom) are for a relative high value of the coefficient of friction $\mu$=0.754 ($\psi$=37$^o$). The results from both computer codes are in good agreement. Next to these lines are the results from the distinct element method (dashed lines) introduced in the following section. The dotted line plots the existing demand due to the current backfill.

Figure 9 (centre and top) plots the same results as those presented in Figure 9 (bottom), whereas now the coefficient of friction along the block interfaces is $\mu$=0.577 ($\psi$=30$^o$) and $\mu$=0.424 ($\psi$=23$^o$) respectively. Note now the results obtained with software RING which allows for sliding along the block interfaces predict a bearing capacity lower than the bearing capacity predicted with ARCO, since the lower value of friction coefficient assumed in this analysis ($\mu$=0.577 and $\mu$=0.424) may allow for some sliding along the stone interfaces. In any event, Figure 9 shows that regardless of what is the exact value of the horizontal soil stresses, the tunnel at Nemea has ample vertical load carrying capacity.

## 6 CORRELATION OF COMPUTED LOAD PATHS WITH OBSERVED/REPORTED DAMAGE

The vaulted tunnel next to the stadium of Ancient Nemea was discovered in 1978 by S.G. Miller (2001). In volume II of his work *Excavations at Nemea* entitled *The Early Hellenistic Stadium*, Miller (2001) offers a thorough description of the observed damage of the tunnel with emphasis on a keystone block and its adjacent voussoir stones which had fallen down about 25 m from the eastern end of the tunnel. Miller indicates that the fallen stones had disintegrated while structural problems in this part of the tunnel must have begun very early in its history given that large fragments of the one or more voussoirs were found in layers as low as only 20 cm above the floor of the tunnel.

The structural analysis presented in this paper may offer a plausible explanation of this failure. Figure 6 (top) shows that when the tunnel is without backfill, its thrust line at the keystone approaches the extrados and exerts a compressive force at the outer corner of voussoir stone, No 8, adjacent to the keystone, No 9. Given the local character of this trust in association with a possible poor quality of this specific stone, yielding or crashing of the corner of this voussoir No 9 at the extrados may have occurred. Figure 6 (top) also indicates that when the tunnel is free-standing (no backfill) the thrust line meets the interfaces of the voussoir stone No 8 and the keystone No 9 at the higher angle $\psi$=30.03$^o$. A value of $\psi$=30.03$^o$ corresponds to a demand friction coefficient $\mu$=tan$\psi$>0.578 for sliding not to happen. In the event that this specific voussoir stone is of poor quality it is possible that such a value of coefficient of friction ($\mu$=0.578) did not develop at this specific interface and in association with the possibility that its upper extrados corner has crashed, the result was that this voussoir stone to slide inwards. Figure 7 indicates that as the backfill height increases the thrust line at the key stone lowers towards the intrados. The presence of these compressive forces in association with the fluctuation of humidity may have further chipped the voussoir stone or the keystone at the intrados. It is this combined effect of a premature sliding of the voussoir to the inside due to the relative high value of the incident angle $\psi$ before the backfill was placed in association with the humidity fluctuation that may have caused the local failures reported by Miller (2001). The alternative explanation for the observed failure offered by Miller (2001) − that due to the settling weight of the earth above the vault forced the walls of the tunnel to bow out (therefore reaching a passive limit state of the soil in the vicinity of the springer), thus increasing the width of the tunnel and opening the vault enough so that the wedge shape block could fall in − is most unlikely since as the

value of the backfill increases the value of the maximum incident angle $\psi$ decreases (see Fig. 7); therefore the tunnel becomes even more stable and the possibility of the stone blocks to move out is further reduced. The failure mode conceived intuitively by Miller which requires the development of passive soil stresses in the neighborhood of the springer stone is a fictitious mode which cannot be reached given that the tunnel will have failed earlier (under lower overburden loads) due to compressive failure of the stone blocks as shown in Figure 8.

## 7 THE DISTINCT ELEMENT METHOD

The last years, an increasing number of researchers are using the distinct element method for modelling and analyzing masonry structures (Cundall & Hart 1971, Pagnoni 1994, Pagnoni & Vanzi 1995, Lemos 1995, 2007, Papantonopoulos et al. 2002, among others). The software UDEC v4.0 (Itasca 2004) simulates the response of discontinuous media (such as a jointed rock mass) subjected to either static or dynamic loading. In the distinct element method (DEM), a structural system is represented as an assembly of discrete blocks. The method works in terms of forces and displacements and each block is treated as a separate entity, allowed to undergo unlimited translation and rotation. Each block is treated as a separate entity and the calculations satisfy equilibrium at every time step. The method adopts an elastic behaviour which leads to the need to define the normal-to-the-contact surface, $K_n$, and the tangential-to-the contact surface, $K_s$, equivalent linear elastic constants. The discontinuities are treated as boundary conditions between blocks; whereas, large displacements along discontinuities and rotations of blocks are allowed.

In our parametric analysis the normal-to-the contact surface $K_n$ assumes values in the range 5 MPa/mm $\leq K_n \leq$ 150 MPa/mm and the tangential-to-the contact surface $K_s$ assumes values in the range 1 MPa/mm $\leq K_s \leq$ 50 MPa/mm (Bandis et al. 1983), while the angle of internal friction of the limestone $\psi$ covers the range $23^o \leq \psi \leq 37^o$. In all calculations the mass density of the limestone was assumed equal to 2.2 Mg/m3. Our parametric analysis concludes that the result remain indifferent to wide variations of $K_n$ and $K_s$, while the dependence on the angle of internal friction $\psi$ is shown in Figure 9. Note that since the software UDEC allows possible sliding along the block interfaces the results of UDEC shall be compared with the results of RING which also allows for the formation of the same mechanism.

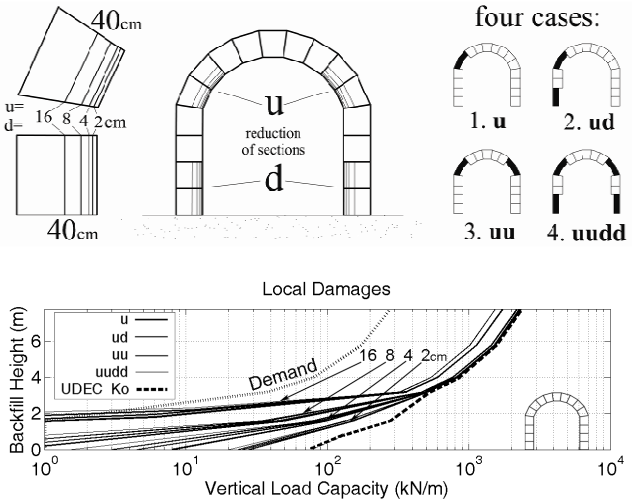


Figure 10. Variation of the vertical load carrying capacity of the tunnel due to the severity of reduction of the stone material (exfoliation) at four critical locations.

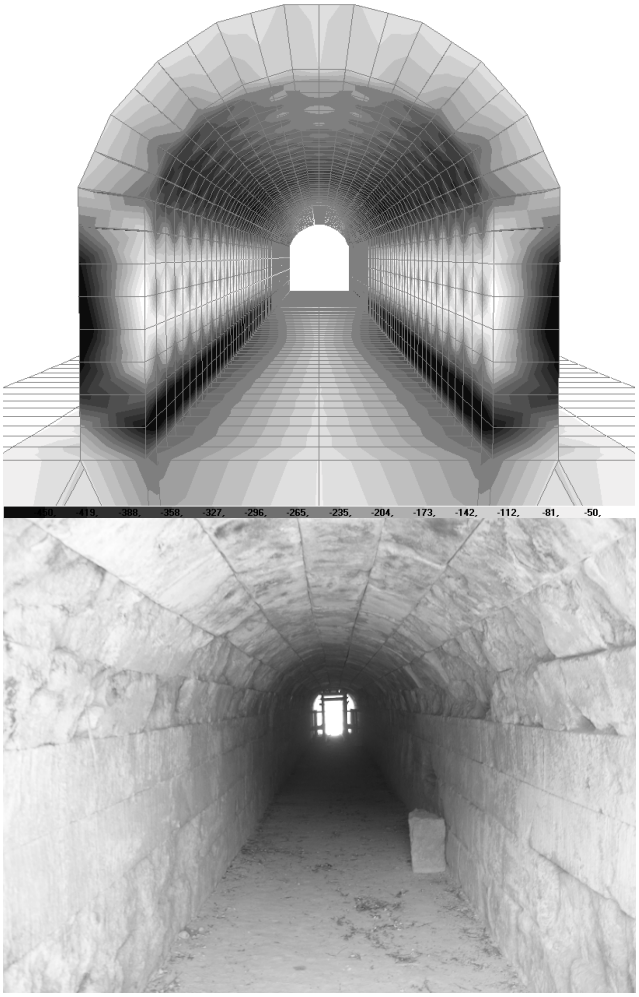

Figure 11. Contours of the stress field along the tunnel computed with finite element analysis (top) and correlation of the exfoliated stones (bottom) with the compression areas of the tunnel.

## 8 LIMIT EQUILIBRIUM ANALYSIS OF THE TUNNEL WITH LOCAL DAMAGE

Visual inspection of the tunnel from the inside indicates that the most appreciable exfoliation (chipping of the stones) has happened at the two bottom rows of stone as well as the rows of the springer stone and the voussoir stone above it (see Fig. 11 bottom). In order to estimate the influence of this absence of stone material (exfoliation) to the path of the thrust line and the overall stability of the tunnel, we conducted a parametric analysis of the limit equilibrium of the tunnel by reducing the width of the stone in the neighbourhood of the bottom stones and in the neighbourhood of the springer voussoir. Figure 10 top shows schematically section of the tunnel and the location of the reduced stone blocks. The reduction of the stone material ranges from 2 cm up to 16 cm at a stone block with width = 40 cm. Our parametric analysis examines four cases: (a) the stones in the neighbourhood of the springer at one side have been reduced - case u, (b) the stones in the neighbourhood of the springer and the base at one side have been reduced - case ud, (c) the stones in the neighbourhood of the springer at both sides have been

reduced - case uu and (d) the stones in all four critical locations have been reduced - case uudd. Figure 10 (bottom) shows that even when the width of the stones of the tunnel has been reduced at the critical location, the tunnel with its overburden soil exhibits appreciable stability. Nevertheless, when the reduction of the stone material is more than 8 cm the tunnel can no longer stand free and needs backfill soil to reach stability. Consequently, caution should be exercised before excavate above the tunnel given that the present overburden soil enhances appreciably the stability of the exfoliated tunnel.

## 9 FINITE ELEMENT STRESS ANALYSIS

Our study proceeds with a small-amplitude finite element analysis in an effort to better understand the stress distribution along the voussoir of the tunnel. A three-dimensional model of the tunnel is composed with 3d-solid, eight-node elements. Similarly with the same 3d-solid elements we discretize the foundation soil. The vertical and lateral earth pressures of the soil are simulated with static loads on the nodes for active and at-rest conditions. The analysis is conducted with software SAP2000 v14.1.0 (Computers and Structures, Inc. 2009). In the analysis the parameters of the limestone blocks are: Young's Modulus $E$=25 GPa, Poisson's Ratio $\nu$=0.25 and mass density $\rho$=2.2 Mg/m3.

Figure 11 (top) plots contour diagrams of the stress field that develops in the tunnel when is loaded with the overburden soil profile shown in Figure 2. Dark shades correspond to compression and light shades correspond to a stress free area. Note that the stress field of the tunnel as results from the finite element analysis is in good agreement with the results obtained with the thrust line analysis as presented in Figure 7. Figure 11 (bottom) is a photograph of the interior of the tunnel that shows clearly the loss of material at the bottom of the walls and in the vicinity of the springer stone. This exfoliation pattern is in direct correlation with the dark region (compression) of the intrados shown above. Figure 11 reveals that the surfaces of the stones which have suffered from exfoliation are those which are in compression. Clearly, the combined action of compressive stresses and the fluctuation of humidity in the inside of the tunnel resulted to the damages that appear in Figure 11 (bottom). This finding suggests that the fluctuation of humidity needs to be minimized by placing doors or curtains at both entrances of the tunnel in order to prevent the active circulation of air.

## 10 CONCLUSIONS

In this paper we present a comprehensive structural analysis of the tunnel-entrance to the stadium of the Ancient Nemea. The analysis ranges from the thrust line limit analysis and the discrete element method, to a comprehensive finite element of the tunnel and the surrounding soil.

The study concludes that for all levels of the overburden soil the thrust line meets the normal to the interfaces of the stone blocks at angles $\psi$ which are lower than the available frictional resistance. Consequently the tunnel is a well engineered "self-locking" structure which does not allow any movements of its constituent stones either to the outside or to the inside. This finding implies that the soil next and above the tunnel remained through the years at rest and that the possibility that it deteriorated to an active limit state is remote. The limit equilibrium analysis shows that even when an active limit state for the soil has been assumed (most conservative scenario) the tunnel at Nemea has ample vertical load carrying capacity.

Assuming that the overburden load above the tunnel increases, the tunnel will fail due to compression failure of its stone blocks − not due to hinging of the tunnel. This finding concludes that the development of passive soil stresses is not realizable.

The stress results from a finite element analysis reveal that the surfaces of the stones of the tunnel which have suffered from exfoliation are those which are in compression. Given that the exfoliation is the result from a combination of the fluctuation of humidity and compressive stresses, the study concludes that the fluctuation of humidity needs to be minimizes by preventing the active circulation of air through the tunnel.

Finally, the study concludes that the tunnel with its overburden soil mass has ample bearing capacity. Nevertheless, caution should be exercised before excavate above the tunnel given that the present overburden soil enhances appreciably the stability of the exfoliated tunnel.

## ACKNOWLEDGEMENTS

Partial financial support has been provided by the EU research project "DARE" ("Soil-Foundation-Structure Systems Beyond Conventional Seismic Failure Thresholds: Application to New or Existing Structure and Monuments"), which is funded through the European Research Council's (ERC) "Ideas" Programme, in Support of Frontier Research - Advanced Grand, under contract number ERC-2—9 −AdG228254-DARE to Prof. G. Gazetas.

## REFERENCES

Baggio, C. & Trovalusci, P. (1998). Limit Analysis for No-Tension and Frictional Three-Dimensional Discrete Systems. *Mech. Struct. Mach.,* 26(3):287-304.

Bandis, S. C., Lumsden, A. C. & Barton, N. R. (1983). Fundamentals of rock joint deformation. *Int. J. Rock Mech. & Mining Sci. & Geomech. Abs.,* 20(6), 249-268.

Block, P., Dejong, M. & Ochsendorf, J. (2006). As Hangs the Flexible Line: Equilibrium of Masonry Arches. *Nexus Network J.,* 8(2), 13-24.

Boothby, T. E. (2001). Analysis of masonry arches and vaults. *Prog. Struct. Engng Mater,* 3, 246-256.

Casapulla, C. & D'Ayala, D. (2001). Lower bound approach to the limit analysis of 3D vaulted block masonry structures. *Proc., 5th Int. Symp. on computer methods in structural masonry, STRUMAS V Rome,* 28–36.

Computers and Structures, Inc. (2009). SAP2000, Version 14.1.0, University of California, Berkeley.

Ferris, M. C. & Tin-Loi, F. (2001). Limit analysis of frictional block assemblies as a mathematical program with complementarity constraints. *Int. J. of Mech. Sci.,* 43, 209-224.

Gazetas, G. & Kavvadas, M. (2009). Soil-Structure Interaction, *Monograph, Published by the National Technical University of Athens, Greece (in Greek).*

Gelfi, P. (2002). Program ARCO: Assessment of masonry arches and vaults, Version 1.1 (free distribution), <http://dicata.ing.unibs.it/gelfi/arco.htm>, University of Brescia.

Gilbert, M. & Melbourne, C. (1994). Rigid-block analysis of masonry structures. *Struct. Eng.,* 72(21), 356-361.

Gilbert, M., Ahmed, H. M. & Sollis, A. J., (2005). RING: Analysis software for masonry arch bridges, Version 1.5 (free distribution), <http://www.ring.shef.ac.uk/index.html>, University of Sheffield.

Gilbert, M., Casapulla, C. & Ahmed, H.M. (2006). Limit analysis of masonry block structures with non-associative frictional joints using linear programming. *Comput Struct,* 84, 873–887.

Gilbert, M. (2007). Limit analysis applied to masonry arch bridges: state-of-the-art and recent developments. *Proc., 5th Int. Conf. on Arch Bridges, Funchal, Madeira,* 13-28.

Harvey, W. J. (1991). Stability, strength, elasticity and thrustlines in masonry structures. *Struct. Eng.,* 69(9), 181-184.

Heyman, J. (1966). The Stone Skeleton. *Int. J. Solids Struct.,* 2(2), 249-279.

Heyman, J. (1995). The Stone Skeleton. *Cambridge University Press, Cambridge.*

Hooke, R. (1675). A description of helioscopes, and some other instruments. *London.*

Huerta, S. (2001). Mechanics of masonry vaults: The equilibrium approach. *Historical Constructions. University of Minho, Guimaraes,* 47-69.

Itasca Consulting Group, Inc. (2004). UDEC: Universal Distinct Element Code. Version 4.0. Itasca, Minneapolis.

Jaky, J. (1944). The coefficient of earth pressure at rest. *J. Soc. Hungarian Archit. Eng.,* 78(22), 355-358.

Konstandinidis, D. & Makris, N. (2005). Seismic Response Analysis of Multidrum Classical Columns *Earthq Eng Struct Dyn,* 34, 1243-1270.

Lemos, J.V. (1995). Assessment of the ultimate load of a masonry arch using discrete elements. *Computer Methods in Structural Masonry, J. Middleton and G.N. Pande, eds., 3, Swansea: Books & Journals International,* 294-302.

Lemos, J.V. (2007). Discrete element modelling of masonry structures. *Int. J. Archit. Heritage,* 1(2), 190-213.

Livesley, R. K. (1978). Limit analysis of structures formed from rigid blocks. *Int. J. Numer. Methods Eng.,* 12(12), 1853-1871.

Makris, N. & Psychogios, T. (2004). Static and dynamic analysis of columns and part of the entablature of the NE corner of the temple of Zeus at Nemea. *Report to American School of Classical Studies, Athens.*

Miller, S. G. (2001). Excavations at Nemea II: The early Hellenistic Stadium. *Berkeley and Los Angeles, California: University of California Press.*

Orduña, A. & Lourenço, P. B. (2003). Cap Model for Limit Analysis and Strengthening of Masonry Structures. *J. Struct. Eng.,* 129(10), 1367-1375.

Orduña, A. & Lourenço, P. B. (2005). Three-dimensional limit analysis of rigid block assemblages. Part I: Torsion failure on frictional interfaces and limit analysis formulation. *Int J Solids Struct,* 42(18-19), 5140-5160.

Orduña, A. & Lourenço, P. B. (2005). Three-dimensional limit analysis of rigid blocks assemblages. Part II: Load-path following solution procedure and validation. *Int J Solids Struct,* 42(18-19), 5161-5180.

Pagnoni, T. (1994). Seismic analysis of masonry and block structures with the discrete element method. *Proc., 10th European Conf. on Earthquake Engineering, vol. 3,* 1669-1674.

Pagnoni, T. & Vanzi, I. (1995). Experimental and numerical study of the seismic response of block structures. *Computer Methods in Structural Masonry, J. Middleton and G.N. Pande, eds., Swansea: Books & Journals International,* 213-222.

Papantonopoulos, C., Psycharis, I.N., Papastamatiou, D.Y., Lemos, J.V. & Mouzakis, H.P. (2002). Numerical prediction of the earthquake response of classical columns using the distinct element method. *Earthq Eng Struct Dyn,* 31, 1699-1717.

Roca, P., Cervera, M., Gariup, G. & Pela', L. (2010). Structural Analysis of Masonry Historical Constructions. Classical and Advanced Approaches. *Arch Comput Methods Eng,* 17, 299–325.

Smith, F. W., Harvey, W. J. & Vardy, A.E. (1990). Three-hinge analysis of masonry arches. *Struct. Eng.,* 68(11), 203-214.

Taylor, N. & Mallinder, P.A. (1993). The brittle hinge in masonry arch mechanisms. *Struct. Eng.,* 71(20), 359-366.

# Seismic Damage Evaluation on Full-scale Reinforced Concrete Bridge Columns based on Ambient Vibration Monitoring

S. Nagata & K. Kanazawa
*Central Research Institute of Electric Power Industry, Chiba, Japan*

K. Kajiwara
*National Research Institute for Earth Science and Disaster Prevention, Hyogo, Japan*

ABSTRACT: This paper presents a damage detection of reinforced concrete structures based on natural frequency reduction. Ambient vibration monitoring was conducted on full-scale RC bridge column specimens that were constructed for a shake table project at E-Defense. Damage levels after the seismic excitations were classified into the safety, the yield, and the ultimate states from the response ductility. Reduction ratios of natural frequency caused by the seismic damage were obtained from the ambient vibration records. The relation between the damage levels and the reduction ratios of the natural frequency were clarified. The evaluation of the safety, the yield, and the ultimate states can be realized by the combination of the ambient vibration monitoring and the visual inspection.

## 1 INTRODUCTION

When civil infrastructures suffer extensive damage due to a strong earthquake, damage levels of the structures should be accurately evaluated for immediate restoration. The seismic damage is generally detected based on visible inspection, but damage is not always appeared clearly on the surface of the structural members. And also if damage is visually detected, its levels cannot be always identified adequately.

Vibration-based damage detection is considered to be one of the effective methods giving an objective evaluation for damage levels (Seki et al. 1996, Housner et al. 1997 & Rens et al. 1997). Application of this methods is expected especially to reinforced concrete structures, because it is well known that natural frequency changes depending on the damage level in the reinforced concrete members. Recent development of measuring and data acquisition tools make it possible to identify natural modes and natural frequencies of structures based on ambient vibration data, instead of forced vibration or free vibration data (Petters & De Reock 2001, Kanazawa et al. 2003), and such a measuring technique gives us easier way of damage evaluation (Uehan. & Megro 2003).

Even though the measuring tools and the system identification methods are significantly developed, practical use of the ambient vibration is still limited. This is because only few data are available about relation between damage level and reduction of natural frequency that needed to establish criteria for damage evaluation. Some experimental researches have been carried out, related to the criteria for reinforced concrete bridge columns (Seki et al. 2003, Kobayashi et al. 2005), using free vibration or earthquake response data instead of ambient vibration data. But amplitude of these data is much larger than that of the ambient vibration data, and natural frequency is generally sensitive to amplitude level of vibration data. In addition, the test cases as well as scale are not enough to adapt various types of structures or to use in more realistic situation.

In this research, ambient vibration monitoring was conducted on full-scale bridge column specimens constructed for a large-scale bridge experimental project at E-defense (Ukon et al. 2007, Kawashima et al. 2009 & Kawashima et al. 2010) to obtain the relation between seismic damage level and reduction of the natural frequency.

Table 1. Target specimens for the ambient vibration monitoring.

| Specimen | Seismic performance assumed for the specimens |
|---|---|
| C1-1 | Typical columns built in 1970s that fails in flexure |
| C1-5 | Typical columns designed based on current seismic design code |

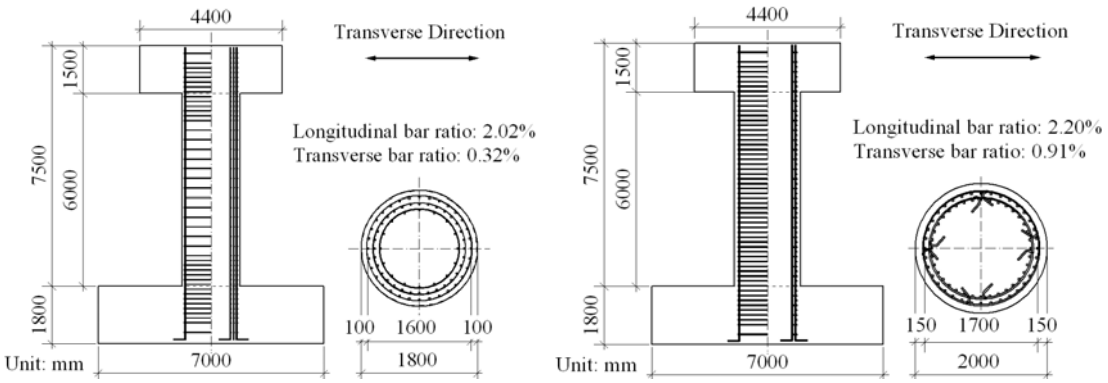


(a) Specimen C1-1 (b) Specimen C1-5

Figure 1. Full-scale bridge column specimens constructed for the E-Defense project.

## 2 EXPERIMENTAL CONDITIONS AND DAMAGE OF COLUMNS

### 2.1 *Specimens and experimental conditions*

Target structures of the ambient vibration monitoring are specimen C1-1 and C1-5 that constructed for a large-scale bridge experimental project at E-defense, as show in Table 1. The specimen C1-1 is a typical column that was built in 1970s that designed based on a combination of the static lateral force method and working stress design (Japan Road Association 1964). Collapse of this column was one of the major causes of the extensive damage during the 1995 Kobe, Japan earthquake.

The Specimens C1-5 is typical column that designed in accordance with current seismic design codes (Japan Road Association 2002). Both of the columns are 7.5m tall and have a circular cross-section as shown in Fig. 1. The diameters of the cross-section in the Specimen C1-1 and C1-5 are 1.8m and 2.0m respectively. They were anchored to E-Defense by 2.0m thick square footing. Longitudinal reinforcement ratios of the specimen C1-1 and C1-5 are 2.02% and 2.20%, and tie volumetric reinforcement ratios are 0.32% and 0.91%, respectively. Nominal yield strength of the reinforcements is 345MPa (SD345). Design strength of concrete is 27MPa in both of these specimens.

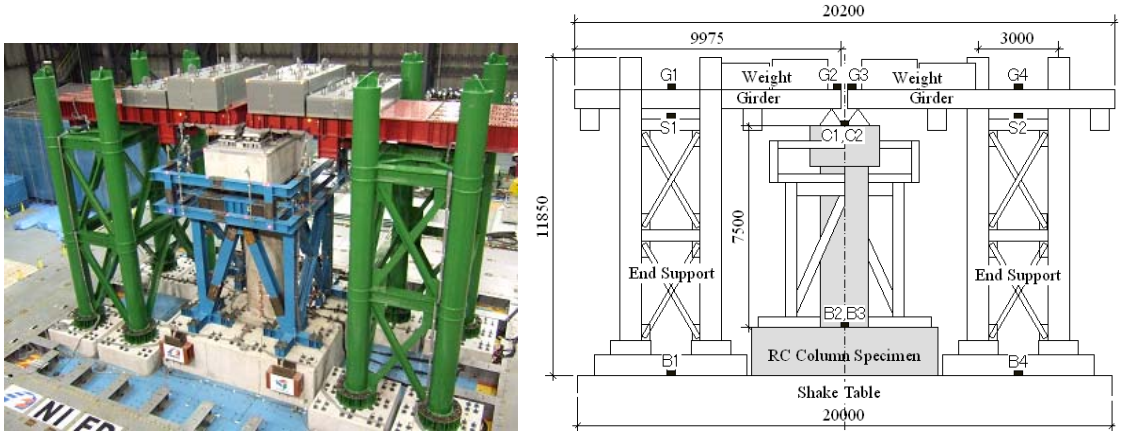


(a) Whole view of the specimen on the table (b) Side view of the specimen on the table

Figure 2. Setup of a column specimen for the shake table test.

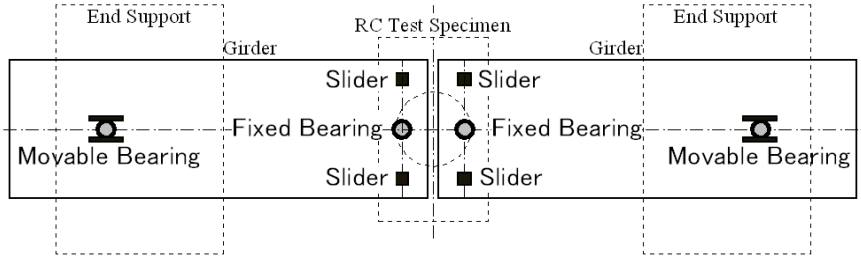


Figure 3. Supporting condition of two girders on the column specimen and two end supports.

The setup of the specimen on the shake table is shown in Fig.2. Two simply supported girders were set on the column specimen and on the two steel end supports. The girders were set to fix the mass blocks to the column however they were not designed with the stiffness and strength of real girders. Fig. 3 shows Supporting condition of two girders on the column specimen and two end supports. Each girder was supported on a fixed bearing on the column and a movable bearing (friction bearings) on the end support. Two side sliders (friction bearings) were set besides the fixed bearing to prevent rotation of the decks around their axis. Such a complex support condition was adopted so that column response displacement in the transverse direction is not restricted by two rigid end supports through the torsional rigidity of the girders. Total weight of the girder, mass and bearings on the column specimen is 3,083kN. But in collapse tests of the specimen C1-5, extra masses are added so that the total weight becomes 3,722kN.

Table 2 shows the evaluation of the seismic performance of the specimens based on the 2002 specification. Computed natural frequency based on the gross-section stiffness and the yield stiffness are also shown in this table. An example of the lateral force vs. lateral displacement hysteresis assumed in the seismic design is shown in Fig. 4 to describe the classification of damage level based on the displacement ductility. In this research, the damage levels after the seismic excitations were classified into the safety, the yield, and the ultimate states.

Table 2. Seismic performance estimated based on the current design codes.

| Specimen | C1-1 | | C1-5 | | C1-5 (mass added) | |
|---|---|---|---|---|---|---|
| | LG | TR | LG | TR | LG | TR |
| Yield displacement (mm) | 46 | 62 | 41 | 44 | 41 | 44 |
| Ultimate displacement. (mm) | 98 | 123 | 214 | 217 | 211 | 214 |
| Ultimate ductility | 2.1 | 2.0 | 5.2 | 4.9 | 5.1 | 4.9 |
| Natural frequency 1**(Hz) | 2.5 | 2.4 | 3.0 | 2.9 | 2.8 | 2.6 |
| Natural frequency 2**(Hz) | 1.6 | 1.6 | 2.0 | 1.9 | 1.8 | 1.8 |

* Computed natural frequency based on the gross-section stiffness.
** Computed natural frequency based on the yield stiffness.

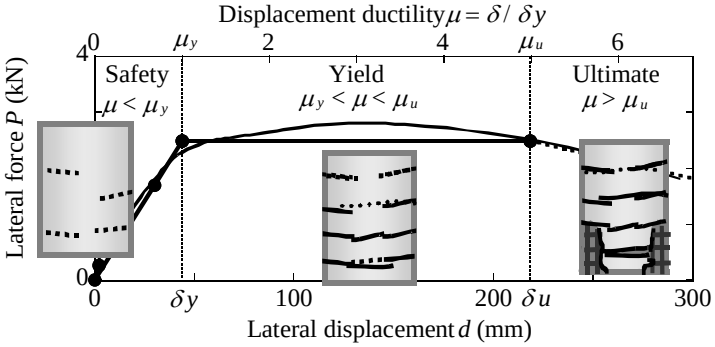


Figure 4. Classification of damage level based on the force vs. displacement hysteresis assumed in the seismic design.

The input ground motion of the shake table test is a near field ground motion recorded at the JR Takatori station during the 1995 Kobe, Japan earthquake. Taking into account of the soil structure interaction effect, a ground motion with 80% the original intensity o f JR Takatori record was imposed as a command to the table in the experiment. NS, EW and UD components of the modified ground motion were imposed in the longitudinal, transverse and vertical direction respectively. Both of the specimens were first subjected to 10%-30% of the modified Takatori ground motions to check the linear of the columns. Main excitation using 100% ground motion was then conducted twice. In the specimen C1-5, extra masses was added on the girder and again excitation using 100% ground motion was conducted once and twice 125% excitation tests were conducted. Free vibration tests using pulse excitations were conducted prior to and after each excitation test to obtain the natural frequency of the column.


(a) After the 1st 100% level excitation (b) After the 2nd 100% level excitation

Figure 5. Damage of the column C1-1 after the seismic excitations.

Table 3. Response ductility and damage level of the specimen C1-1 after the seismic excitation.

| Amplitude** | Displacement response (mm) | | Response ductility | | Damage level** | |
|---|---|---|---|---|---|---|
| | LG | TR | LG | TR | LG | TR |
| 30% | 14 | 16 | 0.3 | 0.3 | safety | safety |
| 100% | 173 | 134 | 3.8 | 2.2 | ultimate | ultimate |
| 100% | 277 | 174 | 6.0 | 2.8 | ultimate | ultimate |

* Magnification of input ground motion (JR Takatori ground motion).

** Damage level that classified into safety, yield, and ultimate based on design ductility capacity.

## 2.2 *Damage of columns after experiments*

a) Specimen C1-1

The specimen was first subjected to 10%-30% of the modified Takatori ground motions. No visible damage occurred on the column during these test. Fig. 5 shows the damage of the column C1-1 after 100% of the excitations. Typical Flexural failure was seen at the bottom of the column. Spalling of the covering and core concrete, as well as local buckling of the reinforcements, were initiated in the first excitation. This damage then became more significant in the second excitation.

Table 3 shows response ductility and damage levels, which defied in Fig. 4, of the specimen during the seismic excitation. In the test using 10%-30% level excitations, the maximum displacement response is 14mm, 16mm in the longitudinal and the transverse directions respectively. Both of them are smaller than the yield displacement of 46mm, 62mm, thus the damage level corresponds to safety state in the both direction. Since the response displacement (173mm, 134mm in the longitudinal and transverse directions respectively) exceeds the ultimate displacement in the both direction (2.1mm, 2.0mm respectively) during the first a100% level excitation, the damage level was assumed to be ultimate state.

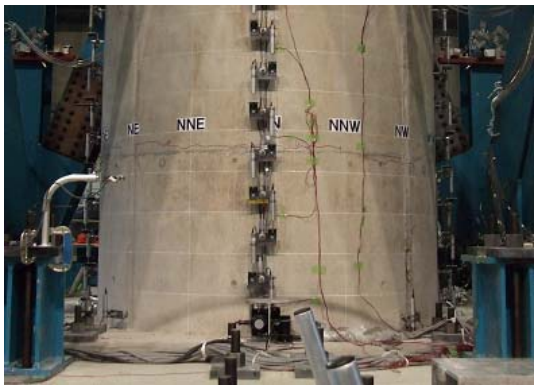


(a) After the 30% level excitations

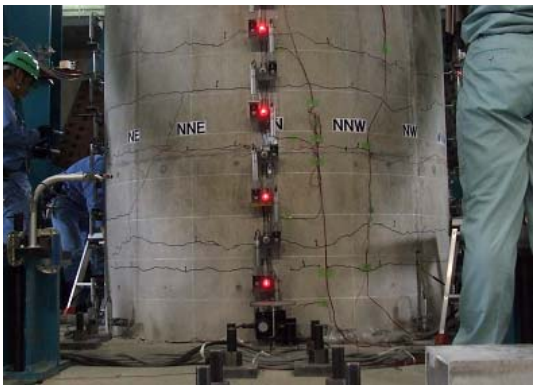


(b) After the 1st 100% level excitation


(c) After the 2nd 100% level excitation


(d) After the 3rd 100% level excitation (mass added)

Figure 6. Damage of the column C1-5 after the seismic excitations.

Table 4. Response ductility and damage level of the specimen C1-5 after the seismic excitation.

| Amplitude** | Displacement response (mm) | | Response ductility | | Damage level** | |
|---|---|---|---|---|---|---|
| | LG | TR | LG | TR | LG | TR |
| 30% | 12 | 14 | 0.3 | 0.3 | safety | safety |
| 100% | 83 | 69 | 2.0 | 1.6 | yield | yield |
| 100% | 122 | 105 | 3.0 | 2.4 | yield | yield |
| 100%(mass added) | 238 | 121 | 5.8 | 2.8 | ultimate | yield |
| 125%(mass added) | 457 | 257 | 11.1 | 5.8 | ultimate | ultimate |
| 125%(mass added) | 562 | 359 | 13.7 | 8.1 | ultimate | ultimate |

* Magnification of input ground motion (JR Takatori ground motion).
** Damage level that classified into safety, yield, and ultimate based on design ductility capacity.

b) Specimen C1-5

Fig. 6 shows the damage of the column C1-5 after a series of the excitations. The specimen was first subjected to 10%-30% of the modified Takatori ground motions and flexural cracks slightly developed on the column. The flexural cracks became more significant during twice of the 100% excitations, and spalling of the covering concrete occurred in a 100% excitation with added mass but buckling of the reinforcements did not occurred. The 125% level excitation was imposed to the specimen twice and more significant spalling of the covering concrete occurred at the bottom of column, but damage of the reinforcement was not appeared.

Table 4 shows response ductility and the damage levels 4, of the specimen C1-5 during the excitations. In test using 10%-30% level excitations, the maximum displacement is 12mm, 14mm in the longitudinal and the transverse directions, respectively, which are smaller than the yield displacement of 41mm, 44mm. therefore the damage level corresponds to safety state in

the both direction. The response displacements during the first a100% level excitation (83mm, 69mm in the longitudinal and transverse directions respectively) were over the yield displacement in the both direction (41mm, 44mm), but within ultimate displacements (214mm, 217mm). Therefore the damage level was assumed to be the yield state in the both direction. Again the damage was evaluated as the yield state after the second 100% excitation. From third 100% excitation with adding extra mass, the displacement response exceeded the ultimate displacement such that the column damage became the ultimate state.

Because in the ultimate state, more visible damage such as spalling of concrete develops, visual identification of damage between the yield and ultimate states seems to be easier than that between the safety and yield states. Therefore, it is important that the ambient vibration data can be used for the evaluation of the safety and yield states.

## 3 NATURAL FREQUENCY BASED ON AMBIENT VBIRATION MONITOERING

Twelve set of three-directional accelerometers of G1-4, C1-2, B1-4 and S1-2 were set on the girders, columns, tables, and end supports respectively, as shown in Fig. 3, in order to measure ambient vibration. In the monitoring, sampling frequency, measuring range of the accelerations, and resolutions are set to 200Hz, 2.5cm/s$^2$, and 24bit respectively. Because of such small measuring range, the acceleration cannot measure sometimes when the shake table works. Therefore quite small vibration absorbed when the shake table stop was used in identification of natural frequency. System identification scheme based on ARMA model (Kanazawa & Hirata, 2000) was used to obtain the natural frequency of the column specimens.

Natural frequencies of the specimen C1-1 after each test are shown in Table 5. The variations of the natural frequency are described in Fig. 7. Table 6 and Fig. 8 shoes the results of the specimen C1-5. The natural frequencies obtained from the free vibration test are also shown in the tables and the figures. Although natural frequencies based on the ambient vibration are larger in general trend than those based on the free vibration, the tendency of natural frequency reduction is similar in the both cases.

Table 5. Variation of the natural frequency of the specimen C1-1 after the tests.

| Test cases** | Longitudinal direction | | Transverse direction | |
|---|---|---|---|---|
| | Ambient vibration | Free vibration | Ambient vibration | Free vibration |
| Before tests | 2.31Hz | 2.16Hz | 1.98Hz | 1.82Hz |
| 30% | 2.20Hz | 2.06Hz | 1.86Hz | 1.74Hz |
| 100% | 1.67Hz | 1.31Hz | 1.28Hz | 1.14Hz |
| 100% | 1.48Hz | 1.12Hz | 1.12Hz | 0.98Hz |

* The cases identified as the magnification of input ground motion (JR Takatori records).
** Damage level that classified into safety, yield, and ultimate based on design ductility.

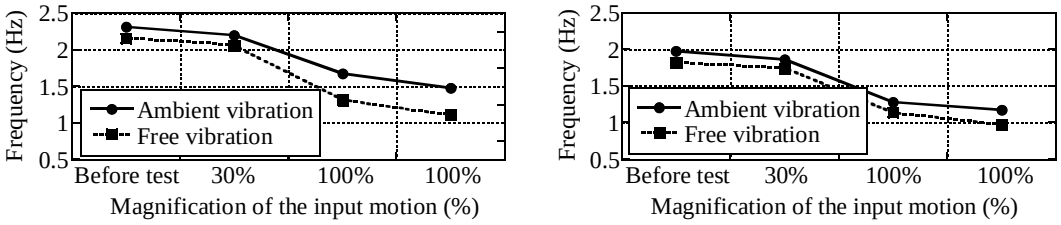


(a) Longitudinal direction (b) Transverse direction
Figure 7. Reduction of the natural frequency of C1-1 detected by the ambient vibration monitoring.

Table 6. Variation of the natural frequency of the specimen C1-5 after the tests.

| Test cases** | Longitudinal direction | | Transverse direction | |
|---|---|---|---|---|
| | Ambient vibration | Free vibration | Ambient vibration | Free vibration |
| Before tests | 2.62Hz | 2.46Hz | 2.27Hz | 2.05Hz |
| 30% | 2.53Hz | 2.28Hz | 2.07Hz | 1.85Hz |
| 100% | 1.92Hz | 1.67Hz | 1.63Hz | 1.48Hz |
| 100% | 1.70Hz | 1.48Hz | 1.50Hz | 1.35Hz |
| 100%( mass added) | 1.65Hz | 1.40Hz | 1.37Hz | 1.24Hz |
| 100%( mass added) | 1.56Hz | 1.27Hz | 1.30Hz | 1.15Hz |
| 125%( mass added) | 1.40Hz | 1.15Hz | 1.19Hz | 1.04Hz |
| 125%( mass added) | 1.48Hz | 1.09Hz | 1.20Hz | 1.03Hz |

* The cases identified as the magnification of input ground motion (JR Takatori records).
** Damage level that classified into safety, yield, and ultimate based on design ductility.

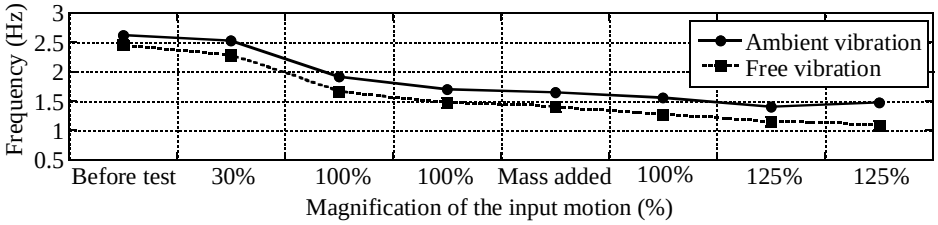


(a) Longitudinal direction

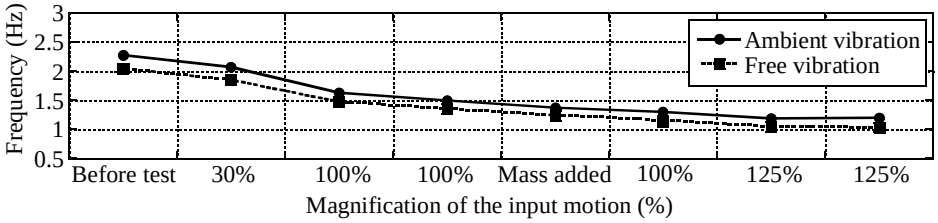


(b) Transverse direction

Figure 8. Reduction of the natural frequency of C1-5 detected by the ambient vibration monitoring.

## 4 RELATION BETWEEN DAMAGE LEVEL AND NATURAL FRECENCY REDUCTION

Fig. 9 shows relationships between the damage levels and the reduction ratios of the natural frequencies. The damage levels were classified into the safety, the yield and the ultimate states evaluated from comparison between the response ductility in the shake table tests and the ductility performance computed based on the current seismic design codes. The ratio of the natural frequency is obtained here normalizing the natural frequency obtained from the ambient vibration data or the free vibration data by the design frequency computed by the gross-sectional stiffness of the columns.

According to Fig. 9(a), when the ratio of the natural frequency based on the ambient vibration is less than 0.7, the column specimens suffer damage corresponding to the yield state or the ultimate state, while Fig. 9(b) shows that this boundary of the safety and yield states is about 0.6. This boundary is slightly higher in the case of the ambient vibration than that of the free vibration, because the natural frequency is estimated relatively higher in the ambient vibration due to its small vibration amplitude.

Since visual identification of damage between the safety and yield states is more difficult than that between the yield and ultimate states, it is important that the ambient vibration data can be used for the evaluation of the safety and yield states. This indicates a possibility that the evaluation of the safety, the yield, and the ultimate states could be realized by the combination of the ambient vibration monitoring and visual inspection.

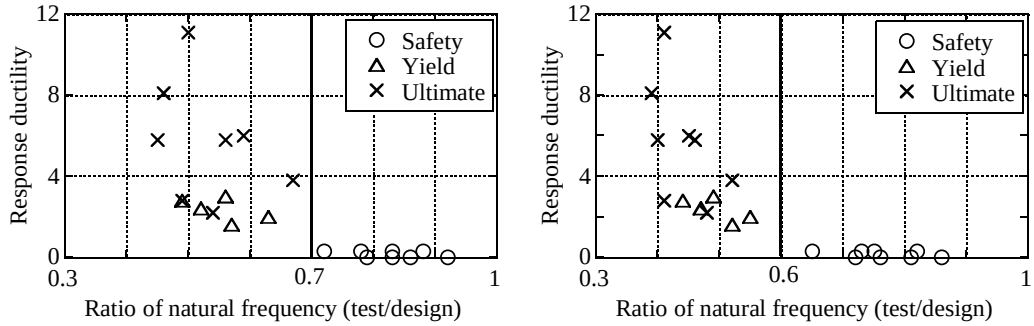


(a) Based on the ambient vibration data (b) Based on the free vibration data

Figure 9. Relationships between the damage levels and the reduction of the natural frequency.

## 5 CONCLUTIONS

Ambient vibration monitoring was conducted on full-scale bridge column specimens, constructed for a large-scale bridge experimental project at E-defense, to obtain the relation between seismic damage level and reduction of the natural frequency. When seismic damage of the column specimens is classified into safety, yield, and ultimate states from response ductility, evaluation of safety and yield states of reinforced concrete members, which is generally difficult in visual inspection, might be possible based on the ambient vibration data.

## ACKNOWLEDGMENTS

This paper presents a part of the results clarified in a cooperative research between Central Research Institute of Electric Power Industry and National Research Institute for Earth Science and Disaster Prevention. This project was supported from members of Executing Committee of Large-scale Bridge Experimental Program (Chair, Prof. Kawashima Kawashima, Tokyo Institute of Technology). Their strong support is greatly appreciated.

## REFERENCES

Housner, G.W., Bergman, L.A., Caughey, T.K., Chassiakos, A.G., Claus, R.O., Masri, S.F. Skelton, R.E., Soong, T.T., Spencer, B.F. & Yao, J.T.P. 1997. Special issue: structural control: past, present and future, *Journal of Engineering Mechanics*, ASCE, Vol. 123, No. 9, 897-971.

Japan Road Association. 1964. *Design specification of steel highway bridges*, Tokyo, Japan, Maruzen.

Japan Road Association. 2002. *Design specification of highway bridges –Part V Seismic design*, Tokyo, Japan, Maruzen.

Kanazawa, K. & Hirata, K. 2000. Modal identification for a multi degree of freedom system using cross spectrum method, *Journal of Structural & Construction Engineering*, AIJ, No. 529, 89-96 (in Japanese).

Kanazawa, K., Ogawa, K., Yabana, S. & Miyazumi, K. 2003. Modal characteristics variance of a tall reinforced concrete stack in a day, *Journal of Structural & Construction Engineering*, AIJ, No. 568, 67-74 (in Japanese)

Kawashima, K., Sasaki, T., Kajiwara, K., Ukon, H., Unjoh, S., Sakai, J., Takahashi, Y., Kosa, K. & Yabe, M. 2009. Seismic performance of a flexural failure type reinforced concrete bridge column based on E-defense excitation, *Journal of Structural Engineering/Earthquake Engineering*, JSCE, Vol.65, No.2, 267-285.

Kawashima, K., Sasaki, T., Ukon, H., Kajiwara, K., Unjoh, S., Sakai, J., Kosa, K., Takahashi, Y., Yabe, M. & Matsuzaki, H. 2010. Evaluation of seismic performance of a circular reinforced concrete bridge column designed in accordance with the current design code based on E-defense excitation, *Journal of Structural Engineering/Earthquake Engineering*, JSCE, Vol.66, No.2, 324-343 (in Japanese).

Kobayashi, H., Unjoh, S. & Kanoh, T. 2005. Development of an earthquake damage detection method for bridge structures with the acceleration sensor, *Journal of Earthquake Engineering*, JSCE, Vol.28 (in Japanese).

Petters, B. & De Reock, G. 2001. One year monitoring of the Z24-Bridge: environmental effects versus damage events, *Earthquake Engineering & Structural Dynamics*, Vol. 30, Issue 2, 149-171.
Rens, K.L., Wipf., T.J. & Klaiber, F.W. 1997. Review of nondestructive evaluation technique of civil infrastructure, *Journal of Performance Constructed Facilities*, ASCE, Vol. 11, No. 4.
Seki, M., Mizutani, K., Nishimura, A. & Nakano, S. 1996. Characteristic vibration of rigid frame bridges damaged by the Hyogo-ken-nanbu earthquake, *Journal of Structural Engineering/Earthquake Engineering*, JSCE, No. 550/V-33, 145-154 (in Japanese).
Seki, M., Nishimura, A., Sano, H. & Nakano, S. 2003. Study on the evaluation of damage levels of RC rigid frame railway bridges in the case of earthquakes, *Journal of Structural Engineering/Earthquake Engineering*, JSCE, No. 731/I-63, 51-64 (in Japanese).
Uehan, F. & Megro, K. 2003. Development of non-contact microtremor measuring method for vibration diagnoses of railway structure, *Journal of Earthquake Engineering*, JSCE, Vol.27 (in Japanese).
Ukon, H., Kajiwara, K., Kawashima, K. 2007. Large scale shake table experiments on bridges using E-defense, *Journal of Earthquake Engineering*, JSCE, Vol.29 (in Japanese).

# Uncertainty effects on seismic response evaluations of ground pavement system

K. Kawano and K. Nagafuchi

*Department of ocean civil engineering, Kagoshima University ,Japan*

ABSTRACT: The dynamic response evaluations of the surface ground layer play important roles on the seismic damage evaluations for the ground pavement system. A number of researches on seismic responses of the surface ground layer have been carried out to apply the seismic performance evaluation of structure. In the present study, the uncertainty effects on the seismic response evaluation of the ground pavement system are examined with the Monte Carlo Simulation (MCS). The ground pavement system is represented with the finite element method of two-dimensional plain strain situation. It is shown that the uncertainty effect on the maximum response evaluation can be effectively evaluated with the MCS to carry out the damage evaluation of the ground pavement system to the seismic motions.

## 1 INTRODUCTION

The dynamic response evaluation of surface layer of ground plays important roles on seismic damage evaluations for pavement system. From the seismic design point of views on structures, a number of researches on the seismic response of the surface layer have been carried out to clarify the dynamic characteristics. It is well known that the seismic performance evaluation of the structure is closely depended upon the ground situation and seismic motion characteristics. The ground condition of the surface layer can be represented with various quantities such as the shear wave velocity, friction angle, and density of soil, etc. While these quantities have been estimated by observation data and various experiments, it is likely to involve various uncertainties that are supposed to have important effects on the seismic responses. Especially, it is indicated that seismic motions, which have been observed in various ground conditions, have inherently the uncertainty on the maximum input acceleration. It is suggested that these uncertainties play important roles on the seismic response evaluation of the ground pavement system.

For the seismic damage evaluation of the ground pavement system, it is suggested that the second moment approach plays important roles on the maximum response evaluation. It is indicated that the seismic response evaluation of the ground pavement system can be effectively carried out with the MCS method on the uncertainty effects (Wakai et al 2005). If the uncertainty is limited within small variations, the sensitivity on uncertainty can be effectively evaluated by the perturbation method. However, if the uncertainty has relatively broad variations and the response of ground pavement system leads to be nonlinear, the MCS method can be very available to account for the influence (Kleiber, 1994, Marek et al 1998, Guan and Melches 2000, Kawano et al 2009). Since the uncertainty on the ground pavement system is supposed to be very different contributions on the seismic response evaluation, it is suggested that the second moment approach leads to considerably available method for the maximum response evaluation because of applying the result of the MCS simulation.

In the present study, the uncertainty effects on the seismic response evaluation of the ground pavement system are examined with the Monte Carlo Simulation (MCS). The ground pavement

system is represented with the finite element method of two-dimensional plain strain situation. The nonlinear dynamic characteristic of the ground and pavement are represented with a flow rule model. The uncertainty of the shear wave velocity of the ground is represented with a normal distribution. Otherwise, the uncertainty on the maximum acceleration of the seismic motion is possibly evaluated with a log normal distribution. It is demonstrated that applying the MCS on the dynamic response estimation of the ground pavement system, the damage evaluation can be carried out with the maximum response characteristics such as the maximum displacement, the maximum principal stress and shear strain. It is suggested that for the damage evaluation of the ground pavement system due to seismic forces, it is essential to clarify the effect of the uncertainty with respect to the maximum seismic response quantities.

## 2 FORMULATION

### *2.1 The governing equation of motion*

Considering stochastic properties of seismic forces to the ground pavement system, it is available for the random vibration approach to perform evaluation of the seismic response. If the uncertainty such as the seismic motion involves relatively broad variation, the MCS method can be applied to the seismic response estimation in spite of extent of the uncertainty. If severe dynamic response condition is brought about the ground pavement system, it is supposed that the response leads to possibly nonlinear situation. In such case, the time domain analysis plays significant roles for the seismic response evaluation. Moreover, there are many available seismic motion records obtained in the time domain. If seismic forces are denoted in the time domain, it can be very efficient to implement the seismic response evaluation of the ground pavement system.

For the idealized two-dimensional ground pavement system as shown in Figure 1, the seismic response analysis can be carried out in the time domain. The equation of motion of the ground pavement system is formulated with the finite element method and the finite boundary is evaluated with the viscous boundary. For the ground pavement system, the governing equation of motion can be expressed with

$$\begin{bmatrix} [M_{aa}] & [M_{ab}] \\ [M_{ba}] & [M_{bb}] \end{bmatrix} \begin{Bmatrix} \ddot{x}_a \\ \ddot{x}_b \end{Bmatrix} + \begin{bmatrix} [C_{aa}] & [C_{ab}] \\ [\tilde{C}_{ba}] & [C_{bb}] \end{bmatrix} \begin{Bmatrix} \dot{x}_a \\ \dot{x}_b \end{Bmatrix} + \begin{bmatrix} [K_{aa}] & [K_{ab}] \\ [K_{ba}] & [K_{bb}] \end{bmatrix} \begin{Bmatrix} x_a \\ x_b \end{Bmatrix} = \begin{Bmatrix} 0 \\ \{F_b\} \end{Bmatrix} \tag{1}$$

The suffix ‘a’ corresponds to the unconstrained nodal points and the suffix ‘b’ denotes the nodal points connecting to the boundary condition. $[M_{aa}]$ and $[C_{aa}]$ denote the mass matrix and damping matrix of the system, respectively. $[K_{aa}]$ denotes the stiffness matrix and $[K_{bb}]$ the stiffness matrix corresponding to the boundary condition. The vector $\{F_b\}$ denotes effective seismic force caused by the ground and the seismic motion and $\{x_a\}$ the displacement vector. The governing equation of motion as expressed with Equation 1 can be represented as follow:

$$[M_{ss}]\{\ddot{x}_s\} + [C_{ss}]\{\dot{x}_s\} + [K_{ss}]\{x_s\} = \{F_s\} \tag{2}$$

in which

$$\{F_s\} = -[M_{aa}][K_{aa}]^{-1}[K_{ab}]\{x_b\}\ddot{z}_g \tag{3}$$

and $z_g$ stands for the seismic motion. Given the seismic motion, the governing equation of motion can be solved by the time integration method.

The dynamic characteristics of the ground pavement system are closely related with nonlinear situation. The nonlinear characteristics of ground pavement system can be expressed with a stress strain relation in plain strain situation as follows:

$$\{d\sigma\} = [[D_e] - [D_p]]\{d\varepsilon\} \tag{4}$$

in which

$$[D_p] = \frac{[D_e]\left\{\frac{\partial f}{\partial \sigma}\right\}^T [D_e]\left\{\frac{\partial f}{\partial \sigma}\right\}}{g + \left\{\frac{\partial f}{\partial \sigma}\right\}^T [D_e]\left\{\frac{\partial f}{\partial \sigma}\right\}} \tag{5}$$

$$[D_e] = \frac{2G}{1-2\mu}\begin{bmatrix} 1-\mu & \mu & 0 \\ \mu & 1-\mu & 0 \\ 0 & 0 & \frac{1-\mu}{2} \end{bmatrix} \qquad g = \frac{1}{f}\lfloor \sigma \rfloor \left\{\frac{\partial f}{\partial \sigma}\right\} H'$$

in which G and $\mu$ denote the modulus of shear rigidity and poisson's ratio of the ground pavement system, respectively. The yield function *f* can be represented with the principle shear stress. Moreover, the strength of the ground pavement can be expressed with the Mohr coulomb relation in which c and $\phi$ denote cohesion and friction angle of ground pavement, respectively. The elastic and plastic situation of each time response is expressed with the yield function.

The seismic response is primarily governed by the dominant vibration mode. Generally, the dominant frequency of the seismic force is closely related with the natural frequency of the ground pavement system. For the dynamic response analysis of the ground pavement system, it is carried out using the step-by-step integration method because of the nonlinear situation. If the increment method is applied to Equation 2, the response at each time step can be expressed as follows:

$$\left[\tilde{K}(t)\right]\{\Delta x\} = \left\{\Delta \tilde{F}\right\} \tag{6}$$

in which

$$\begin{aligned} \left[\tilde{K}(t)\right] &= [K_{aa}] + (4/h^2)[M_{aa}] + (2/h)[C_{aa}] \\ \left\{\Delta \tilde{F}\right\} &= \{\Delta F\} + 2[M_{aa}]\{\ddot{x}_{aa}\} + ((h/4)[M_{aa}] + 2[C_{aa}])\{\dot{x}_a\} \end{aligned} \tag{7}$$

and *h* denotes a time increment. $\left[\tilde{K}_{(t)}\right]$ and $\left\{\Delta \tilde{F}\right\}$ are obtained by Equation 2 at each time step. The seismic response can be carried out Newton Raphson method.

### *2.2 Effects on uncertainties*

As previously mentioned, some uncertainties are involved inherently in seismic force estimations and ground pavement properties. Taking into account the uncertainty of the seismic motion, the exact response is not always evaluated by means of deterministic seismic motion. The uncertainty effect on the response quantities for the seismic motion can be examined with the MCS method in the present study. Namely, it is examined about the uncertainty effect on the dynamic response for the ground pavement property such as the shear wave velocity and intensity of seismic motion. Assumption is made for the distribution of these uncertain parameters being approximately represented with a normal distribution and log normal distribution, respectively. Assigning any uncertainty to the variable, the seismic response analysis can be carried out with Equation 6. Each uncertainty can be treated with independent variables for the simulation. The response quantities such as the maximum response and its variance can be determined with the results from simulation.

By the way, the reliability index is very helpful to evaluate the uncertainty contribution on the structural safety by means of very typical statistic quantities such as the mean value and its variance. The limit state function is closely related to the reliability evaluation. If the limit state function for the ground pavement system is evaluated with the most critical situation of the re-

sponse such as the maximum principal shear strain, the reliability index can be expressed as follows:

$$\beta = \left(\overline{R} - \overline{S}\right) \Big/ \sqrt{\sigma_S^2 + \sigma_R^2} \tag{8}$$

in which

$$\sigma_R = \delta_R \overline{R}, \qquad \sigma_S = \delta_S \overline{S} \tag{9}$$

$\overline{R}$ and $\overline{S}$ also denote the mean value and $\sigma_R$ and $\sigma_S$ its standard deviation. $\overline{R}$ denotes the allowable design quantity such as the principle shear strain and $\overline{S}$ the expected value of the maximum response quantity with respect to some uncertainties. Moreover, $\delta_R$ and $\delta_s$ stand for the coefficient of variation for the allowable design quantity and the response of the pavement. The limit state function may be estimated with appropriate expressions on the most critical situation of the pavement with respect to damages. The allowable principle shear strain at critical points of the pavement can be applied to the limit state function in the present study.

## 3 RESULTS AND DISCUSSIONS

### *3.1 Dynamic properties of ground pavement system*

For the two-dimensional ground pavement system, the seismic response analysis is carried out to examine the maximum response characteristics on the ground pavement system. From the design point of views, the pavement is usually treated with the static situation because the pavement damage due to seismic forces is considerably depended upon the ground response. However, it is important to estimate the damage situation of the pavement as well as the ground, because especially the damage of the pavement leads to severe vehicle accidents in spite of relatively light damage of the ground. It is suggested that the seismic response evaluation of the ground pavement system plays important roles on the reliable evaluation of the damage on the pavement. In the present study, the seismic response evaluation is carried out with the two-dimensional ground pavement system as shown in Figure 1.

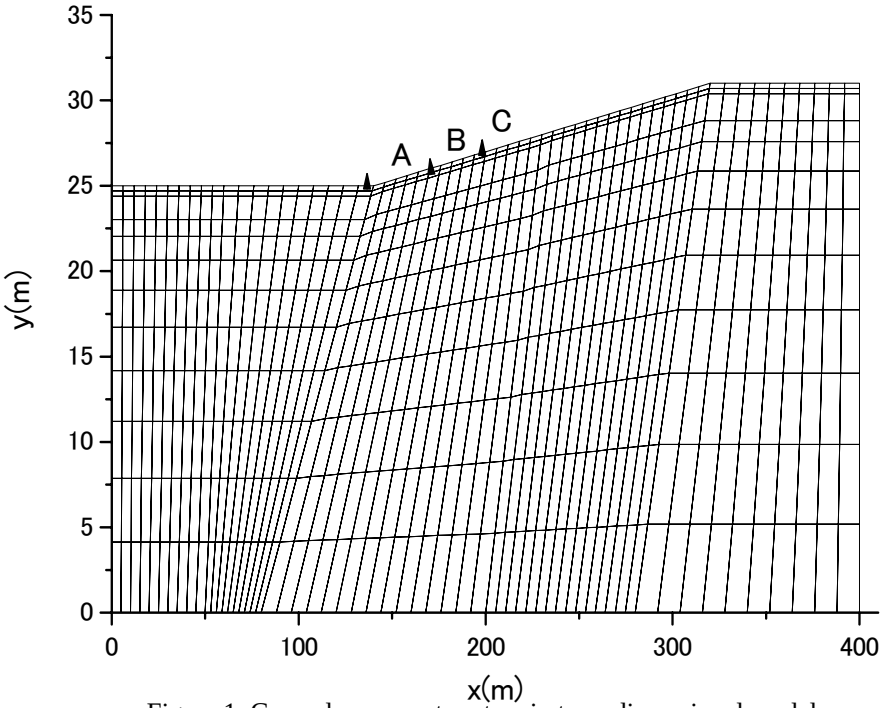

Figure 1. Ground pavement system in two- dimensional model.

The ground pavement system has horizontal width, 400m and depth of the ground about 25m. The pavement is settled on the surface layer between the points A and the point C as denoted in Figure 1. The seismic response evaluation on the pavement is carried out for the two cases of the ground conditions as shown in Figure 2. The pavement is treated with as asphalt concrete of which the dynamic properties such as the shear wave velocity and the strength of the shear stress are strongly depended upon temperature.

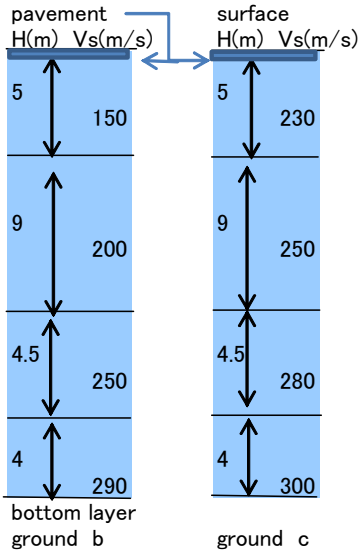


Figure 2. Property of ground pavement system.

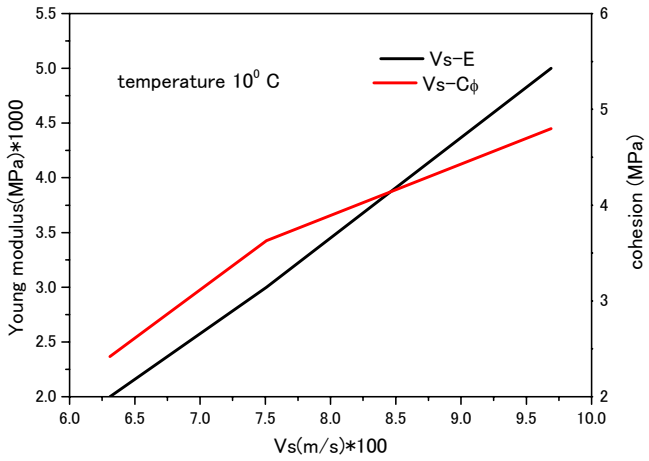


Figure 3. A example of property of asphalt of pavement

Figure 3 shows an example of the property of asphalt concrete of pavement. The abscissa denotes the shear wave velocity of pavement corresponding to the Young modulus $E$ and cohesion $C_\phi$ due to compression stress. These quantities, for example corresponding to 10˚C, are strongly depended upon temperature.

Figure 4 shows acceleration response spectra for seismic motions, kobe-ns component and taka-ns component, which are obtained in Kobe earthquake 1995, Japan. It is understood for the seismic motion to have different characteristics that are closely related with the ground condition. The designated points b and c stand for the dynamic characteristics of each ground as shown in Figure 2.

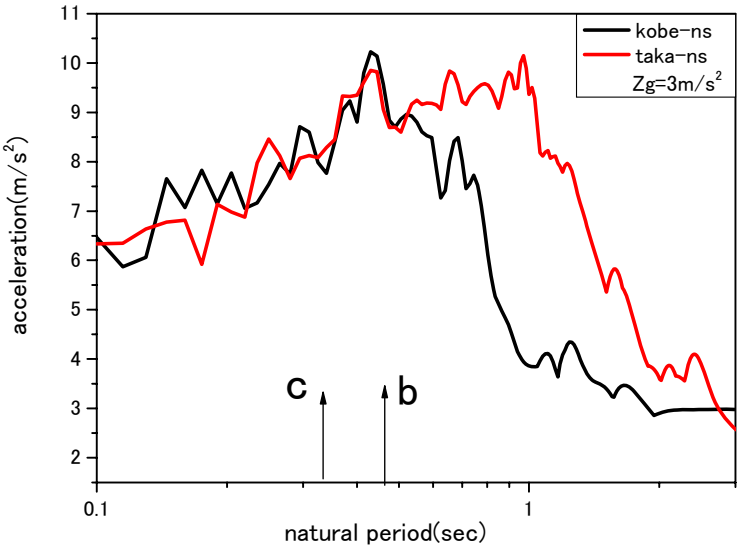


Figure 4. Acceleration response spectra for kobe-ns and taka-ns component.

*3.2 Seismic responses of ground pavement system*

For two cases of ground pavement conditions, the seismic response analysis is carried out with two seismic motions of which acceleration spectra are shown in Figure 4.

Figure 5 shows the time history of displacement response due to taka-ns component, the maximum acceleration of seismic motion, 3m/s$^2$, to the ground condition c. It is noted that the maximum displacement at point A, denoted at the pavement, is about 2.5cm, in the linear response.

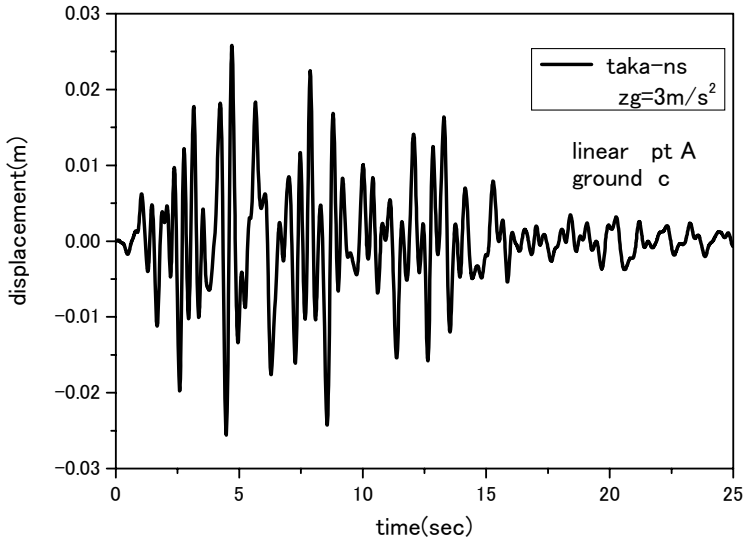


Figure 5. Time history of displacement response in the linear situation(taka-ns).

Figure 6 similarly shows the time history of displacement response due to kobe-ns component, for the same situation as previous case. It is noted that the maximum displacement at point A is about 2.5 cm in the linear situation. While the seismic motion involves different property on frequency characteristics, it is understood that the maximum displacement response is closely related to the dominant frequency due to the ground condition.

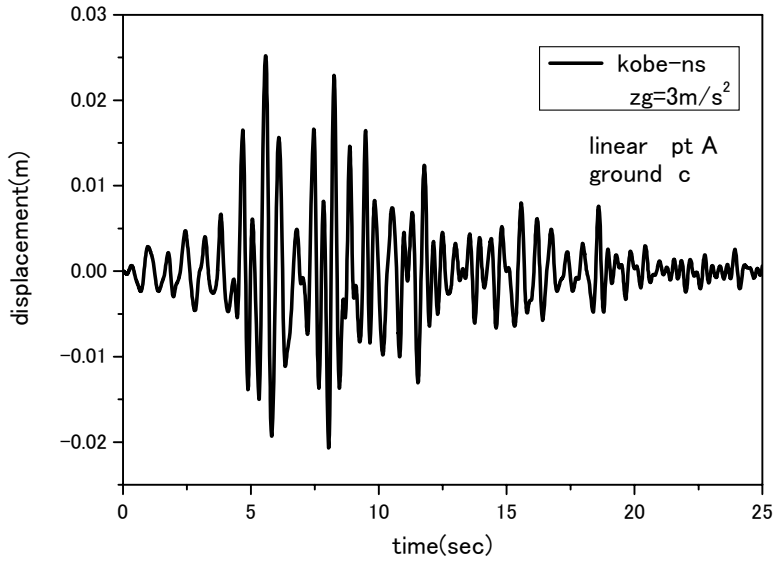


Figure 6. Time history of displacement response in the linear situation(kobe-ns).

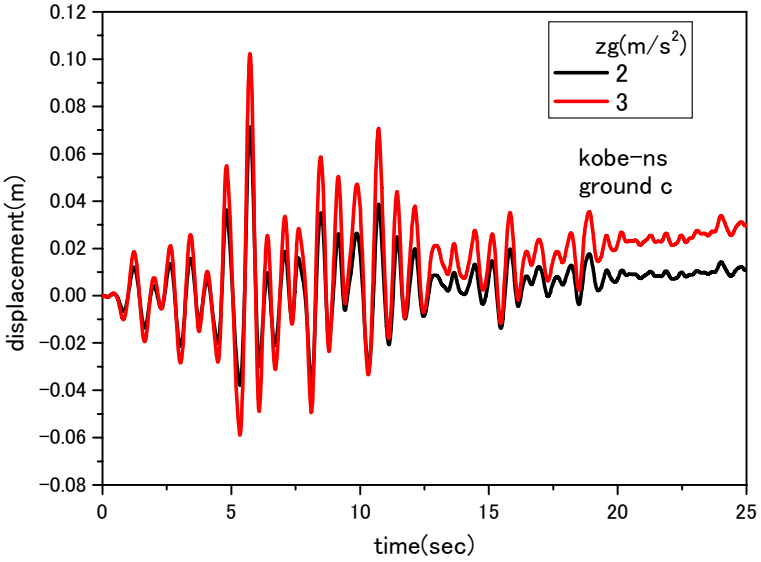


Figure 7. Time history of displacement responses in the nonlinear situation(kobe-ns).

Figure 7 shows the time history of seismic displacements in the nonlinear situation to kobe-ns component at the ground condition c. Comparison is made for the maximum acceleration of seisimc motion of 2 m/s$^2$ and 3 m/s$^2$, respectively. For the maximum acceleration of seisimc motion 3 m/s$^2$, it is understood that it leads to considerably increase of the displacement response and causes the drift displacement, which may be brought about some damages on the pavement system.

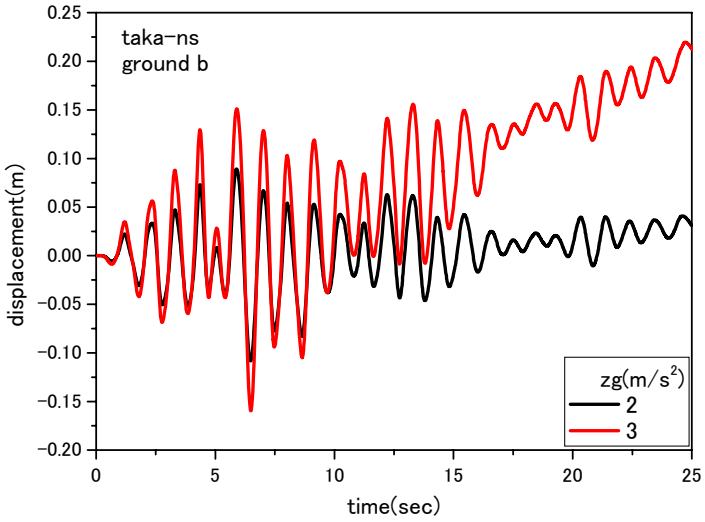


Figure 8. Time history of displacement response in the nonlinear situation.

Figure 8, moreover, shows the time history of seismic displacement in the nonlinear situation to taka-ns conponent at the ground condition b. Comparison is similarly made for the maximum acceleration of seismic motion 2m/s$^2$ and 3m/s$^2$, respectively. The response characteristic leads to the same tendency as the previous case. For the maximum acceleration of seismic motion 3m/s$^2$, it turns out considerably increase of the maximum displacement and causes the drift displacement as well. If the seismic response in nonlinear situation is compared with the response in linear one, the former leads to considerably increase of the response due to variation

of frequency characteristics. As known in acceleration response spectra in Figure 4, it is supposed that the response charateristic is closely related to the dominat frequency due to the nonlinear situation. It is understood that the nonlinear response plays important roles on the maximum response evaluation of the pavement sysytem due to seismic forces.

*3.3 Uncertainty effects on seismic responses of ground pavement system*

As understood in seismic responses, the maximum response properties are closely related to the maximum acceleration of seismic motion and the ground pavement condition. Since these quantities invole some uncetainties, it is suggested that the available seismic response evaluation could be carried out examining about the unertainty effects on the maximum response estimation. It is known that the MCS plays significant roles on the maximum response estimation for the nonlinear response with various uncertainties.

Figure 9 shows the convergence property on the displacement for the seismic motion kobe-ns of the maximum acceleration from $2m/s^2$ to $5m/s^2$. It is understood that the available convergence can be performed with the simulation more than about 300 times. Then, the response evaluation is carried out with simulation of 500 times of which computational time is about 70 hours in personal computer with Intel Core CPU(2.12GHz).

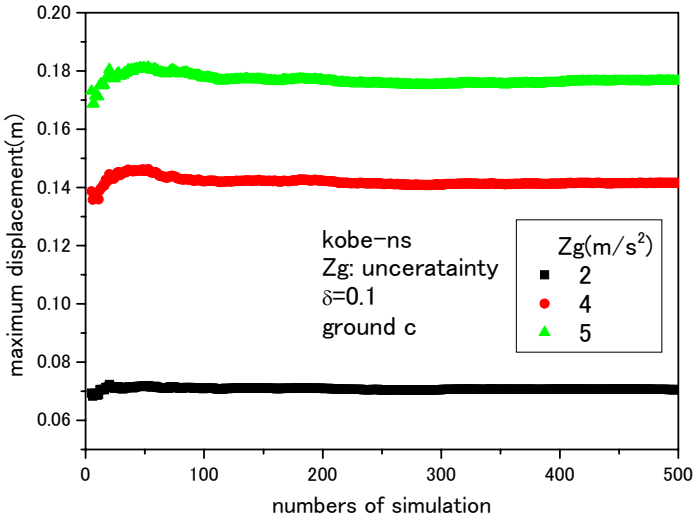


Figure 9. Converegence property of simulation.

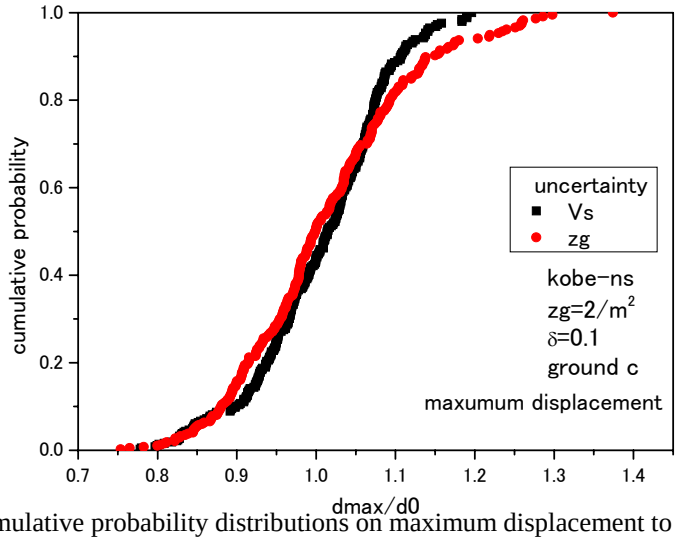


Figure 10. Cumulative probability distributions on maximum displacement to Vs and Zg.

Figure 10 similary shows the cumulative probability distribution on maximum displacement response of point A for the ground c. Two symbols stand for cumulative probability distributions on the maximum displacement for the unecertainty on the maximum acceleration of seismic motion and the shear wave velocity of the ground pavement system. The coefficient of variation is assumed to be 10% for each uncertainty. The unceratinty of the shear wave velocity of the ground pavement system is assumed to be a normal distribution. The abscissa denotes the ratio of the maximum displacement response to its mean value. It is noted that the distribution of the maximum displacement have the same tendency for the uncertainty on the shear wave velocity of ground and the maximum acceleration of seismic motion, but the extreme response due to the maximum acceleration of seismic motion leads to broader response than the response due to the shear wave velocity. The maximum response distributions become considerably different from the normal distribution due to the nonlinear situation.

Figure 11 similarly shows cumulative probability distribution of the maximum shear strain at point A of ground c. The situation on uncertainty is similar to the previous case. The abscissa denotes the ratio of maximum shear strain to its mean value of which the response is evaluated to the input seismic motion from $2m/s^2$ to $5m/s^2$. The extreme response leads to considerably broad distribution and turns out larger response than about two times of the mean value. Since the damage estimation of pavement system is closely depended upon the maximum shear strain, it is suggested that the evaluation of the uncertainty to the seismic response plays important roles on the damage evaluation.

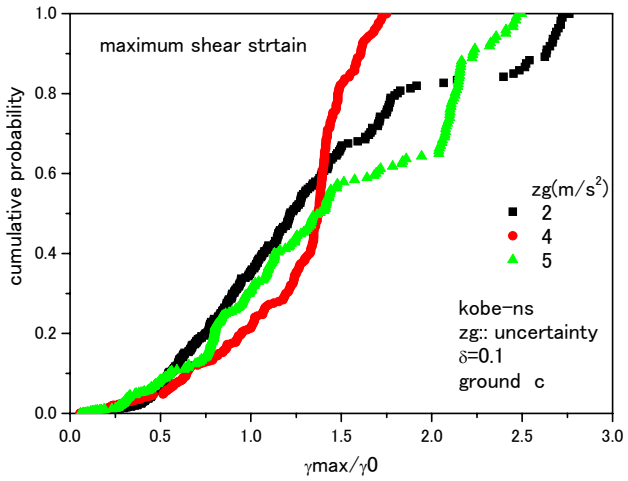


Figure 11. Cumulative probability distribution of maximum shear strain to ground C.

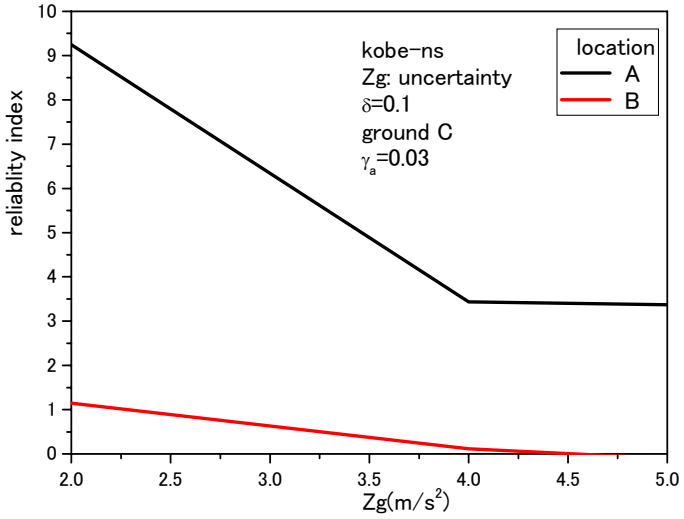


Figur 12. Reliability index for uncertainty on the maximum acceleration of seismic motion.

Figure 12 shows the reliablity index on the uncertainty of the maximum acceleration of the seismic motion. The abscissa denotes the mean value of the maximum acceleration of input seismic motion with the coeffcient of variation, 10%. Two lines denote the reliability index on the location A and B indicated in Figure 1. The limit state function is evaluated with the shear strain and the allowable shear strain is assumed to be 0.03, which may be suitable to severe damage on the pavement. The reliablity index is considerably related to location of the pavement because complicated response charateristics on shear strain are brought about nonlnearity. It is understood that the maximum acceleration of seismic motion leads to the different tendency for the reliablity index, especially it is considerably affected by the nonlinear response situation. In order to clarify the damage estimation due to seismic motions for the ground pavement system, it is significant to evaluate the uncertainty effects on the maxmum response evaluation in the nonlinear situation.

## 4 CONCLUSIONS

The effects of uncertainty on the seismic response are examined for the ground pavement system. The results from the analysis are summarized as follows:

(1) For the severe situation of the pavement system that could be estimated by the maximum shear strain for the seismic motion, it would be important for the available damage estimation to clarify the uncertainty effects due to the nonlinear seismic response. It is suggested that reliability index plays important roles on the damage estimation with nonlinear situation of ground pavement system for various seismic motions.
(2) In order to clarify the maximum response characteristics on the seismic response of the ground pavement system, it is essential to examine the uncertainty effects due to the maximum acceleration of seismic motion and shear wave velocity of the ground pavement system.
(3) The seismic response characteristics play important roles on damage evaluations for ground pavement system. Since useful evaluations with respect to the uncertainty effects in the nonlinear situation can be efficiently carried out with the MCS method in spite of its extent, it leads to available damage estimation of the ground pavement system with uncertainty.

## 4 REFERENCES


Guan,X.L. and Melchers, R.E, 2000. A comparison of some FOSM and Monte carlo results, *Applications of Statistics and probability, ICASP 8*, Vol.1, 65-71

Kawano,K., Kimura,Y., Ito,K. and Tanaka, N. 2009. Reliability of offshore platform with wind energy production to dynamic forces, *The Proceedings of the nineteenth international offshore and polar engineering conference*, Osaka, 617-624

Kleiber,M, 1994. Parameter sensitivity in nonlinear statistics and dynamics of solids and structures, *Proc. Of Third World Congress on Computational Mechanics, 2* , 1021-1023

Marek,P. et al,1998,Sensitivity analysis in simulation based reliability assessment of structure, *Structural Safety and Reliability*, Vol.2 715-721

Wakai,A, Ugai,K, Tani,S, 2005, Fundamental study for the reliability based design corresponding the residual settlement of a heterogeneous earth structure induced by earthquake (in Japanese), *Journal of Applied Mechanics,JSCE,Vol.8*, 663-672

# Development of MPS method for simulation of slope failure

I. Yoshida
*Tokyo City University, Tokyo, Japan*

**ABSTRACT:** Deformation is sometimes used to define ultimate limit state for geotechnical structure like a slope. MPS (Moving Particle Simulation) method is one of prospective method for estimation of deformation due to earthquake. The advantage of MPS method is that its formulation is derived mathematically from wave equation, and is very close to that of DEM. MPS method can be interpreted as an extended version of DEM that satisfies wave equation. The formulation of MPS method is illustrated to perform earthquake response simulation of slope. Viscous boundary for MPS method is proposed and verified through one dimensional wave propagation. Simulation of slope failure due to gravity is also shown.

## 1 INTRODUCTION

Needs for evaluation of ultimate limit state are increasing, partially because design earthquake motion is revised through the experience of large earthquakes occurred in Japan. The other reason is necessity to perform PSA (probabilistic safety assessment) of important structure such as nuclear power plant.

Deformation is sometimes used to define ultimate limit state for geotechnical structures like a slope. In some cases, Newmark method is used to estimate large deformation of slope caused by earthquake. It is very simple and convenient method, however many assumptions are involved. In order to estimate deformation more precisely, development of new simulation method is required. There are several prospective methods to estimate large deformation, such as SPH (Smoothed Particle Hydrodynamics), MPS (Moving Particle Simulation), DEM (Discrete Element Method), MPM (Material Point Method), which are still in the stage of research. DEM is most successful method to simulate the failure or collapse of slope, but its drawback is that it is an empirical method, which means that values of spring and dashpot to connect each particle must be determined empirically. In addition, theoretically DEM does not satisfy the wave equation. MPS method has advantage compared with DEM because it is derived mathematically from wave equation and it satisfies wave equation. Its formulation is very close to that of DEM, consequently MPS method has similar capability with respect to failure phenomenon as DEM. MPS method can be interpreted as extended DEM that satisfies wave equation. It was originally proposed for fluid analysis (Koshizuka et al. 1995, Koshizuka et al. 1996). The idea of the method was applied to elastic body (Chikazawa et al. 2001). MPS stands for Moving Particle Semi-implicit originally because semi-implicit scheme is used to solve the equation in fluid analysis. However, explicit scheme is used in elastic body analysis. The term, Moving Particle Simulation is sometimes used when the method for elastic body is referred.

The formulation of MPS method is illustrated to perform earthquake response simulation of slope. Viscous boundary is one of important function for earthquake response analysis and is often used in FEM (Finite Element Method). Viscous boundary for MPS method is proposed and verified through one dimensional wave propagation (Yoshida & Ishimaru 2010). Simulation of slope failure due to gravity is also shown.

## 2 OUTLINE OF FORMULATION OF MPS METHOD

### 2.1 *Formulation of stress and strain*

Initial and current vector $\boldsymbol{r}_{ij}^0, \boldsymbol{r}_{ij}$ from *i* to *j* are defined by using initial position vector $\boldsymbol{r}^0$ and current position vector $\boldsymbol{r}$.

$$\boldsymbol{r}_{ij}^0 = \boldsymbol{r}_j^0 - \boldsymbol{r}_i^0, \qquad \boldsymbol{r}_{ij} = \boldsymbol{r}_j - \boldsymbol{r}_i \tag{1}$$

MPS method has degree of freedom $\theta_i$ with respect to rotation of particle *i*. Deformation vector $\boldsymbol{u}_{ij}$ is obtained by removing the rigid deformation.

$$\boldsymbol{u}_{ij} = \boldsymbol{r}_{ij} - \boldsymbol{R}\boldsymbol{r}_{ij}^0, \quad \text{where, } \boldsymbol{R} = \begin{bmatrix} \cos\theta_{ij} & -\sin\theta_{ij} \\ \sin\theta_{ij} & \cos\theta_{ij} \end{bmatrix}, \quad \theta_{ij} = \frac{\theta_i + \theta_j}{2} \tag{2}$$

The current deformation vector $\boldsymbol{u}_{ij}$ is decomposed into normal direction $\boldsymbol{u}_{ij}^n$ (direction of $\boldsymbol{r}_{ij}$) and shear direction $\boldsymbol{u}_{ij}^s$ (perpendicular to normal direction).

$$\boldsymbol{u}_{ij}^n = \frac{\boldsymbol{u}_{ij} \cdot \boldsymbol{r}_{ij}}{|\boldsymbol{r}_{ij}|} \frac{\boldsymbol{r}_{ij}}{|\boldsymbol{r}_{ij}|} \tag{3}$$

$$\boldsymbol{u}_{ij}^s = \boldsymbol{u}_{ij} - \boldsymbol{u}_{ij}^n \tag{4}$$

Normal stress $\boldsymbol{\sigma}_{ij}^n$ related to Lame's constant $\mu$ is formulated with normal strain $\boldsymbol{\varepsilon}_{ij}^n$.

$$\boldsymbol{\sigma}_{ij}^n = 2\frac{(\mu_i + \mu_j)}{2}\boldsymbol{\varepsilon}_{ij}^n = (\mu_i + \mu_j)\frac{\boldsymbol{u}_{ij}^n}{|\boldsymbol{r}_{ij}^0|} = (\mu_i + \mu_j)\frac{c_{ij}^n}{|\boldsymbol{r}_{ij}^0||\boldsymbol{r}_{ij}|}\boldsymbol{r}_{ij} \tag{5}$$

$$\text{where, } c_{ij}^n = \frac{\boldsymbol{u}_{ij} \cdot \boldsymbol{r}_{ij}}{|\boldsymbol{r}_{ij}|}$$

Similarly, shear stress related to Lame's constant $\mu$ is formulated with shear strain.

$$\boldsymbol{\sigma}_{ij}^s = 2\frac{(\mu_i + \mu_j)}{2}\boldsymbol{\varepsilon}_{ij}^s = (\mu_i + \mu_j)\frac{\boldsymbol{u}_{ij}^s}{|\boldsymbol{r}_{ij}^0|} = (\mu_i + \mu_j)\frac{\boldsymbol{u}_{ij} - \boldsymbol{u}_{ij}^n}{|\boldsymbol{r}_{ij}^0|} \tag{6}$$

### 2.2 *Equilibrium of force*

The force acting on a particle is calculated separately for normal force (subscript *n*), shear force (subscript *s*) and pressure force (subscript *p*).

$$\rho_i\left[\frac{\partial \boldsymbol{v}_i}{\partial t}\right] = \rho_i\left[\frac{\partial \boldsymbol{v}_i}{\partial t}\right]_n + \rho_i\left[\frac{\partial \boldsymbol{v}_i}{\partial t}\right]_s + \rho_i\left[\frac{\partial \boldsymbol{v}_i}{\partial t}\right]_p \tag{7}$$

where, $\boldsymbol{v}_i = \frac{\partial \boldsymbol{r}_i}{\partial t}$, which means velocity of particle *i*, $\rho$ is mass density. The term as to normal force (subscript *n*) and shear force (subscript *s*) can be calculated as follows,

$$\rho_i\left[\frac{\partial \boldsymbol{v}_i}{\partial t}\right]_n = \frac{d}{n_i^0}\sum_{j\neq i}\frac{2\boldsymbol{\sigma}_{ij}^n}{|\boldsymbol{r}_{ij}^0|}w\left(|\boldsymbol{r}_{ij}^0|\right) = \frac{4d}{n_i^0}\sum_{j\neq i}\frac{(\mu_i + \mu_j)}{2}w\left(|\boldsymbol{r}_{ij}^0|\right)c_{ij}^n\frac{\boldsymbol{r}_{ij}}{|\boldsymbol{r}_{ij}||\boldsymbol{r}_{ij}^0|^2} \tag{8}$$

$$\rho_i\left[\frac{\partial \boldsymbol{v}_i}{\partial t}\right]_s = \frac{d}{n_i^0}\sum_{j\neq i}\frac{2\boldsymbol{\sigma}_{ij}^s}{|\boldsymbol{r}_{ij}^0|}w\left(|\boldsymbol{r}_{ij}^0|\right) = \frac{4d}{n_i^0}\sum_{j\neq i}\boldsymbol{b}_{ij}^s, \quad \text{where, } \boldsymbol{b}_{ij}^s = \frac{(\mu_i + \mu_j)}{2}w\left(|\boldsymbol{r}_{ij}^0|\right)\frac{\boldsymbol{u}_{ij}^s}{|\boldsymbol{r}_{ij}^0|^2} \tag{9}$$

Parameter *d* is determined based on dimension. In the case of two dimensional space, the parameter *d* is 2. Weighting function *w* is introduced in order to model the interaction of neighboring particles. In MPS method, following equation is used as the weighting function.

$$w(|\boldsymbol{r}_{ij}^0|) = \begin{cases} \dfrac{r_e}{|\boldsymbol{r}_{ij}^0|} - 1 & (0 < |\boldsymbol{r}_{ij}^0| < r_e) \\ 0 & (r_e \le |\boldsymbol{r}_{ij}^0|) \end{cases} \tag{10}$$

where $r_e$ is influence radius which expressess the distance of particle interaction. $n_i^0$ is particle number density which can be calculated by following equation.

$$n_i^0 = \sum_{i \neq j} w\left(\left|\boldsymbol{r}_{ij}^0\right|\right) \tag{11}$$

MPS method proposes use of constant value for particle number density $n_i^0$ irrespective of location. The pressure term is expressed by,

$$\rho_i \left[\frac{\partial \boldsymbol{v}_i}{\partial t}\right]_p = -\frac{d}{n_i^0} \sum_{j \neq i} \frac{2 p_{ij} \boldsymbol{r}_{ij}}{\left|\boldsymbol{r}_{ij}^0\right| \left|\boldsymbol{r}_{ij}\right|} w\left(\left|\boldsymbol{r}_{ij}^0\right|\right) \tag{12}$$

where, $p_{ij} = \dfrac{p_i + p_j}{2}$, pressure of particle $i$ $p_i$ is obtained by,

$$p_i = -\lambda_i \left(\varepsilon_{rr}\right)_i = -\lambda_i \left(div \boldsymbol{u}\right)_i = -\lambda_i \frac{d}{n_i^0} \sum_{j \neq i} \frac{\boldsymbol{u}_{ij} \cdot \boldsymbol{r}_{ij}}{\left|\boldsymbol{r}_{ij}^0\right| \left|\boldsymbol{r}_{ij}\right|} w\left(\left|\boldsymbol{r}_{ij}^0\right|\right) = -\lambda_i \frac{d}{n_i^0} \sum_{j \neq i} \frac{c_{ij}^n}{\left|\boldsymbol{r}_{ij}^0\right|} w\left(\left|\boldsymbol{r}_{ij}^0\right|\right) \tag{13}$$

where, $\lambda$ is Lame's constant.

## 2.3 *Conservation of Angular Momentum*

Angular momentum is not conserve by discretization procedure based on particle in MPS, though original differential equation of motion conserves angular momentum. Therefore it is necessary to activate torque to cancel the torque caused by shear stress. Shear stress between particles $i$ and $j$ causes force $F_{ij}$.

$$\boldsymbol{F}_{ij} = m_i \left[\frac{\partial \boldsymbol{v}_{ij}}{\partial t}\right]_s = \frac{m_i 2d\boldsymbol{\sigma}_{ij}^s}{\rho_i n_i^0 \left|\boldsymbol{r}_{ij}^0\right|} w\left(\left|\boldsymbol{r}_{ij}^0\right|\right) = \frac{4 m_i d}{\rho_i n_i^0} \frac{\mu_i + \mu_j}{2} w\left(\left|\boldsymbol{r}_{ij}^0\right|\right) \frac{\boldsymbol{u}_{ij}^s}{\left|\boldsymbol{r}_{ij}^0\right|^2} = \frac{4 m_i d}{\rho_i n_i^0} \boldsymbol{b}_{ij}^s \tag{14}$$

where, $m_i$ ($= \rho_i D^2$, $D$ is diameter of particle) is mass of particle $i$, the term $\partial \boldsymbol{v}_{ij} / \partial t$ is acceleration caused by shear stress between $i$ and $j$. An equal and opposite force acts on particle $i$ and $j$. Torque caused by the couple of force is expressed with outer product.

$$\boldsymbol{T}_{ij} = -\boldsymbol{r}_{ij} \times \boldsymbol{F}_{ij} \tag{15}$$

In order to cancel this torque, the half of torque is given to particle $i$ and $j$. This procedure is performed to every particle within influence distance of particle $i$.

$$I_i \left[\frac{\partial \omega_i}{\partial t}\right]_s = \sum_{j \neq i} \left[-\frac{1}{2} \boldsymbol{T}_{ij}\right] = 2d \sum_{j \neq i} \left(\frac{m_i}{\rho_i n_i^0} + \frac{m_j}{\rho_j n_j^0}\right) \left(\boldsymbol{r}_{ij} \times \boldsymbol{b}_{ij}^s\right) \tag{16}$$

where, $\omega_i (= \partial \theta_i / \partial t)$ is angular velocity, $I_i$ is assumed to be $\rho_i D^4/6$ which means rotary inertia of square with length D on a side.

## 2.4 *Time Integration Method, Verlet Method*

In this study, Verlet method is adopted. The algorithm is applied to the following equation of motion.

$$\boldsymbol{M} \ddot{\boldsymbol{r}}_k + \boldsymbol{g}(\boldsymbol{r}_k, \dot{\boldsymbol{r}}_k) = \boldsymbol{f}_k \tag{17}$$

$\boldsymbol{M}$ is diagonal mass matrix, $\boldsymbol{g}$ is restoring force, which is function of position vector $\boldsymbol{r}_k$, velocity vector $\dot{\boldsymbol{r}}_k$. The acceleration vector is approximated by,

$$\ddot{\boldsymbol{r}}_k = \frac{\boldsymbol{r}_{k+1} - 2\boldsymbol{r}_k + \boldsymbol{r}_{k-1}}{\Delta t^2}, \quad \text{where,} \quad \boldsymbol{r}_{k+1} = \boldsymbol{r}(t_k + \Delta t), \quad \boldsymbol{r}_k = \boldsymbol{r}(t_k), \quad \boldsymbol{r}_{k-1} = \boldsymbol{r}(t_k - \Delta t) \tag{18}$$

Substituting Eq.(18) into Eq.(17), we have,

$$\boldsymbol{M} \frac{\boldsymbol{r}_{k+1} - 2\boldsymbol{r}_k + \boldsymbol{r}_{k-1}}{\Delta t^2} + \boldsymbol{g}(\boldsymbol{r}_k, \dot{\boldsymbol{r}}_k) = \boldsymbol{f}_k \tag{19}$$

Arranging the equation, we have an equation to be solved.

$$\boldsymbol{r}_{k+1} = \left(2\boldsymbol{r}_k - \boldsymbol{r}_{k-1}\right) + \Delta t^2 \boldsymbol{M}^{-1}\left(\boldsymbol{f}_k - \boldsymbol{g}(\boldsymbol{r}_k, \dot{\boldsymbol{r}}_k)\right) \tag{20}$$

## 2.5 *Formulation for failure phenomenon*

Failure behavior is modeled by simple operation as to maximum shear stress and disconnection of particles like DEM. Mohr-Coulomb criteria gives maximum shear stress $\tau_{\max}$.

$$\tau_{\max} = c_{ij} + \sigma_{ij}^n \tan\phi_{ij} \tag{21}$$

where, $\sigma_{ij}^n$ is normal stress between particle $i$ and $j$, $c_{ij}$ is cohesion, $\phi_{ij}$ is internal friction angle. They express mean value of particles $i$ and $j$. When $\sigma_{ij}^n$ is negative (tensile stress), maximum shear stress is $c_{ij}$. It is noted that these parameters are given to each particle, and these parameters do not indicate micro strength obtained by compression test of soil. DEM has same problem that parameters given to each particle does not mean total strength. Therefore calibration analysis is necessary to determine input strength parameter to realize specific total strength.

Inter-particle stress $\sigma_{ij}^n$ can be estimated by the following equation.

$$\sigma_{ij}^n = 2\mu_{ij}\frac{\boldsymbol{u}_{ij}\cdot\boldsymbol{r}_{ij}}{\left|\boldsymbol{r}_{ij}\right|\left|\boldsymbol{r}_{ij}^0\right|} + p_{ij} = 2\mu_{ij}\frac{c_{ij}^n}{\left|\boldsymbol{r}_{ij}^0\right|} + p_{ij} \tag{22}$$

where, $\mu_{ij}$ is Lame's constant, $p_{ij}$ can be obtained by Eq.(13). Shear stress is,

$$\tau_{ij}^s = 2\mu_{ij}\frac{\boldsymbol{u}_{ij}^s}{\left|\boldsymbol{r}_{ij}^0\right|}, \qquad \text{where,} \quad \boldsymbol{u}_{ij}^s = \boldsymbol{u}_{ij} - \boldsymbol{u}_{ij}^n, \quad \boldsymbol{u}_{ij}^n = \frac{(\boldsymbol{u}_{ij}\cdot\boldsymbol{r}_{ij})\boldsymbol{r}_{ij}}{\left|\boldsymbol{r}_{ij}\right|\left|\boldsymbol{r}_{ij}\right|} \tag{23}$$

When $\tau_{\max} < |\tau_{ij}^s|$, rotation angles $\theta_i^{ij}$, $\theta_j^{ij}$ and initial vector $\boldsymbol{r}_{ij}^0$ corresponding to particles $i$, $j$ are updated as follows such that the condition $|\tau_{ij}^s| = \tau_{\max}$ is satisfied.

$$\boldsymbol{r}_{ij}^0 = \boldsymbol{r}_{ij}^0 - \frac{\tau_{\max}}{\left|\tau_{ij}^s\right|}\boldsymbol{u}_{ij}^s \tag{24}$$

$$\theta_i^{ij} = \theta_i - \tan^{-1}\left(\frac{\tau_{\max}}{\mu_{ij}}\right), \quad \theta_j^{ij} = \theta_j - \tan^{-1}\left(\frac{\tau_{\max}}{\mu_{ij}}\right) \tag{25}$$

The rotation angles $\theta_i^{ij}$, $\theta_j^{ij}$ are used in matrix $\boldsymbol{R}$ in Eq.(2) which removes rigid deformation.

$$\boldsymbol{R}_i = \begin{bmatrix} \cos\left(\theta_i - \theta_i^{ij}\right) & -\sin\left(\theta_i - \theta_i^{ij}\right) \\ \sin\left(\theta_i - \theta_i^{ij}\right) & \cos\left(\theta_i - \theta_i^{ij}\right) \end{bmatrix}, \qquad \boldsymbol{R}_j = \begin{bmatrix} \cos\left(\theta_j - \theta_j^{ij}\right) & -\sin\left(\theta_j - \theta_j^{ij}\right) \\ \sin\left(\theta_j - \theta_j^{ij}\right) & \cos\left(\theta_j - \theta_j^{ij}\right) \end{bmatrix} \tag{26}$$

The above mentioned operation with respect to shear stress does not disconnect interaction between particles. Normal stress is used for the disconnection of particles. When inter-particle normal stress $\sigma_{ij}^n$ is less than tensile strength $c_t$, the particles are disconnected. It is noted that tensile stress is negative.

$$\sigma_{ij}^n < c_t \tag{27}$$

In the following numerical example, we assume that tensile strength is equal to cohesion, namely, $c_t = -c_{ij}$.

Disconnection or large deformation causes contact of new pair of particle. When particles $i$ and $j$ are judged to be contact by distance between them, the position vector $\boldsymbol{r}_{ij}^0$ and angle $\theta_i^{ij}$, $\theta_j^{ij}$ at the moment are memorized. The reaction forces due to Lame's constant $\mu$, which are calculated by Eq.(8) and (9), are considered. This operation for new contact is perfectly same as that of DEM.

## 3 EXAMPLES OF NUMERICAL SIMULATION

### 3.1 *Elastic wave propagation*

Many operation adopted in FEM can be also used in MPS because above mentioned formulation is derived mathematically from governing equation. Viscous boundary condition is one of technique widely used in FEM, which is important in earthquake response analysis. The following stress is given to viscous boundary in order to cancel reflection wave.

$$\tau(t) = \rho V \dot{r}(t) \tag{28}$$

where $\rho$ is density, $V$ is wave propagation velocity, $\dot{r}$ is velocity of particle at the boundary. When upwardly propagated wave is specified as an input motion to a model (so-called 2E input), the following stress is given to the boundary.

$$\tau(t) = \rho V (2\dot{e}(t) - \dot{r}(t)) \tag{29}$$

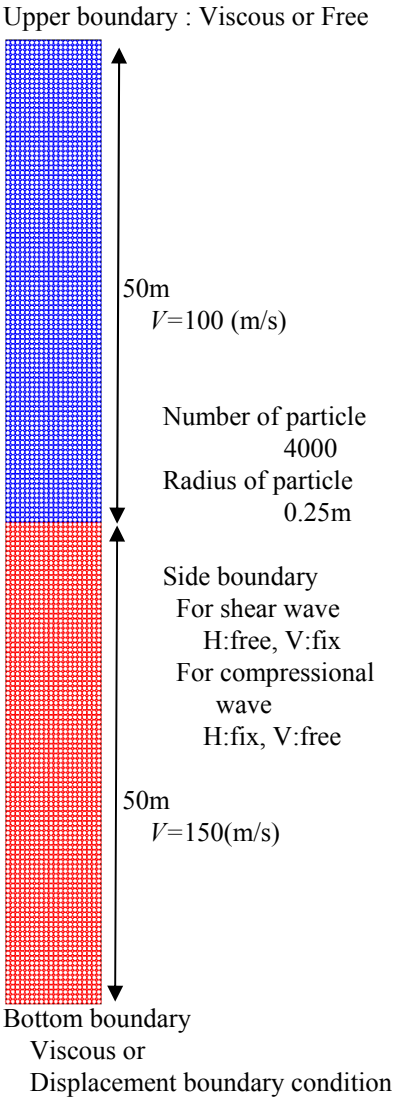


Figure 1 Model for wave propagation

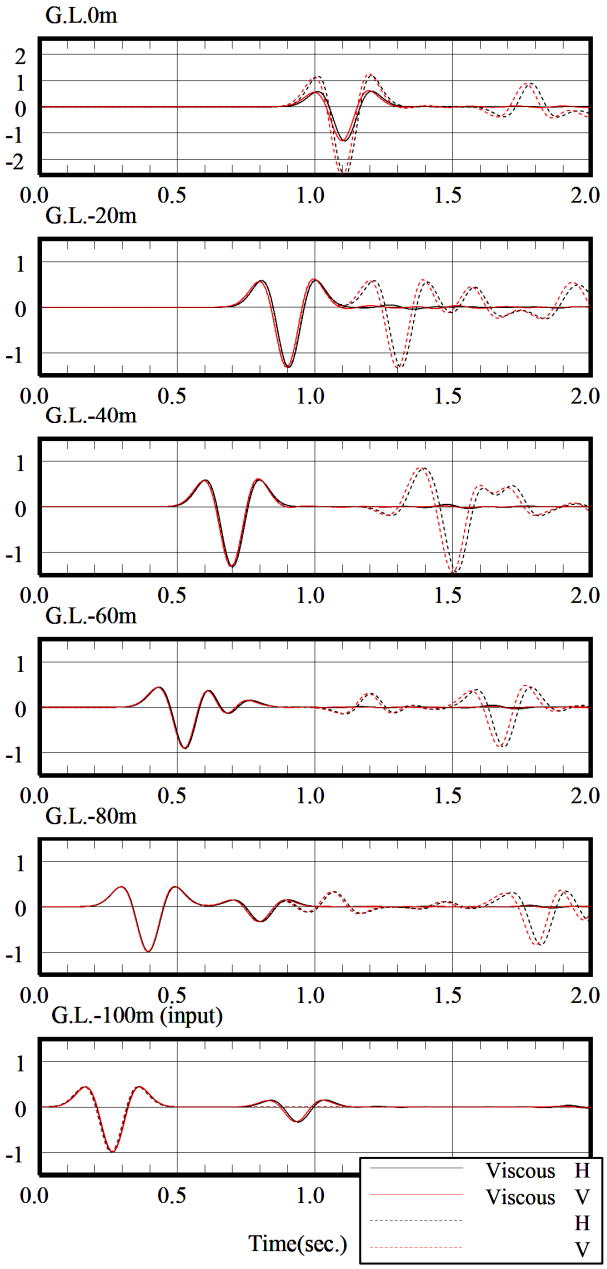


Figure 2 Response with viscous boundary or ordinary boundary for shear wave (H) and compressional wave (V)

where, $\dot{e}(t)$ is velocity time history of input motion. In MPS method with viscous boundary, the stress indicated in Eq.(28) or (29) is activated on particles at viscous boundary in addition to external force *f* and restoration force *g*.

$$m\ddot{r}_k^b = f_k - g(\dot{\boldsymbol{u}}_k, \boldsymbol{u}_k) + D\rho V(2\dot{e}_k - \dot{r}_k^b) \tag{30}$$

where *m* is mass of a particle which is assumed to be $\rho D^2$, *D* is particle diameter. We have following formulation to estimate acceleration of a particle at viscous boundary.

$$\ddot{r}_k^b = \frac{1}{D^2\rho}\left(f_k - g(\dot{\boldsymbol{u}}_k, \boldsymbol{u}_k)\right) + \frac{V}{D}\left(2\dot{e}_k - \dot{r}_k^b\right) \tag{31}$$

Figure 1 shows a model for wave propagation simulation. The number and radius of particle are 4000 and 0.25m respectively. Elastic wave velocity of the 1st layer and 2nd layer are 100, 150 m/s. Unit weight of them are 14.7, 19.6kN/m$^3$. The wave impedance ratio at the layer boundary is,

$$R = \frac{\rho_1 V_1}{\rho_2 V_2} = \frac{1.5 \times 100}{2.0 \times 150} = 0.5 \tag{32}$$

Magnification ratios *C* of transmission and reflection are,

$$C_{up} = \frac{2}{1+R} = \frac{4}{3} \tag{33}$$

$$C_{down} = \frac{1-R}{1+R} = \frac{1}{3} \tag{34}$$

Four cases of simulation, which are case-1 : shear wave (H) and viscous boundary, case-2 :compressional wave (V) and viscous boundary, case-3 shear wave (H) and ordinary boundary, case-4 : compressional wave (V) and ordinary boundary, are performed. Viscous boundaries are considered at both ends (top and bottom of the model) in case-1 and 2. Ricker wavelet is used as an input motion to the bottom of the model.

Figure 2 shows the simulation result of these four cases. The figures of shear and compressional wave indicate differences due to discretization error, when case-1 and 2, or case-3 and 4 are compared, though the differences are small. When the smaller particles are used, the better agreement is obtained. Reflection wave disappears in cases with viscous boundary. Transmission of the boundary of 1st and 2nd layer causes 4/3-fold magnification of wave amplitude. At the top of the model in cases with ordinary boundary condition, the amplitude is doubled in addition to the transmission magnification. Consequently the amplitude at the top becomes 8/3-fold of the input amplitude. Figure 2 shows almost compatible result with the theoretical amplitude.

### 3.2 *Slope Collapse due to gravity*

A model for collapse simulation due to gravity is shown in Figure 3. Model properties are Youg's modulus 389kPa, Poisson's ratio 0.466 (shear wave velocity 287m/s, compressional wave velocity 1137m/s), unit weight 15.8kN/m$^3$ and damping ratio 0.05. Cohesion and internal friction angle are 143kN/m$^2$ and 5.9 degree. After new contact, they are 0 N/m$^2$ and 30 degree respectively. The number of particle is 10800. The gravity is activated in first 0.01 second. It is noted that these input parameters for strength are not equivalent to total strength shown in simulation of compression test. The study of their relation is future topics.

It is known that initial alignment of particle affects a result calculated by DEM. Similarly the influence of initial alignment is confirmed in simulation by MPS method also. Initial random model is constructed by using random number, though explanation of the procedure is skipped in this paper.

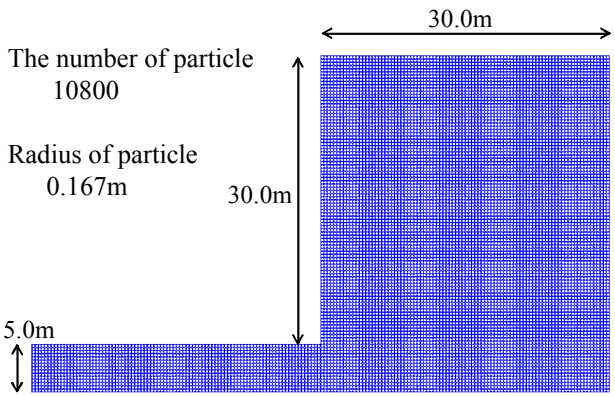


Figure 3 Slope model for collapse due to gravity

Figure 4 shows the collapse process. The failure is initiated from bottom of the slope. The failure line reaches to the top of slope at 2 second. The collapse is initiated along the line at 0.8 second. The collapse occurs along vertical line at the upper part and circular curve at the lower part of the slope.

## 4 CONCLUSIONTS

The formulation of MPS method is described and proposed for earthquake response analysis. MPS method can be interpreted as extended DEM (Discrete Element Method), which is derived mathematically from wave equation. Viscous boundary formulation is proposed for MPS method and its validity is demonstrated through one dimensional wave propagation problem. Collapse simulation is also shown to demonstrate the applicability of MPS method to highly nonlinear failure phenomenon. As future topics, quantitative study with collapse experiment is required to confirm the usefulness of MPS method. The determination of input strength parameters is also one of important problems in MPS method as same as in DEM.

## REFERENCES


Chikazawa, Y., Koshizuka, S. and Oka, Y. 2001. A Particle Method for Elastic and Visco-plastic Structures and Fluid-structure Interactions, Computational Mechanics, 27, pp. 97-106

Koshizuka, S., Tamako, H. and Oka, Y. 1995. A Particle Method for Incompressible Viscous Flow with Fluid Fragmentation, Comput. Fluid Dynamics J., 4, pp. 29-46

Koshizuka, S. and Oka, Y. 1996. Moving-Particle Semi-implicit Method for Fragmentation of Incompressible Fluid, Nucl. Sci. Eng., 123, pp. 421-434

Yoshida, I. and Ishimaru, M. 2010. Basic Study on Earthquake Response Analysis with Using MPS Method, J. of JSCE, A, Vol.66, No.2, pp.206-218 (in Japanese)


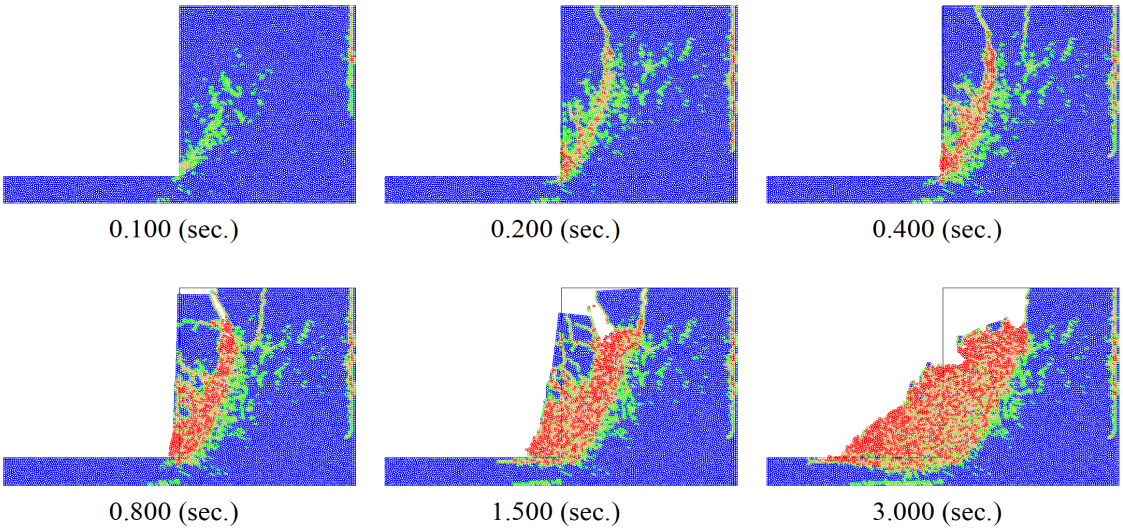


Figure 4 Process of slope collapse due to gravity,
number of disconnection of particle ○ 0, ○ 1, ○2, ○ 3, ○ more than 4

# Preliminary Study on Earthquake-induced Progressive Failure of Jointed Rock Foundation Supporting Arch Dam

H. Kimata
*Civil Engineering Division, Shimizu Corporation, Japan*

Y. Fujita
*Nuclear Project Division, Shimizu Corporation, Japan*

M.R. Okhovat
*Civil Engineering Division, Shimizu Corporation, Japan*

M. Yazdani
*Civil and Environmental EngineeringDepartment, Tarbiat Modares University, Iran*

ABSTRACT: A 2-dimensional nonlinear analysis has been carried out to simulate an experiment which has been performed by other researchers in order to evaluate the seismic performance of arch dams. The effect of jointed rock foundation is taken into consideration in both experiment and simulation and good agreement is found between their results. Therefore, it can be said that the proposed model can roughly simulate the progressive failure of jointed rock foundations and can be used in further similar researches.

## 1 INTRODUCTION

On December 2, 1959, the Malpasset dam failed explosively due to the shift of its left abutment caused by a thin clay filled seam in the rock behind the abutment. This displacement and the loss of support led to the cracking at the center and finally collapse of the dam as shown in Figure 1 (MA 1960). Since then, the study and prediction of the behavior of rock foundations of the dams have gained much attention. Authors already studied the behavior of RC gravity dams on jointed rock foundation using nonlinear analysis and could effectively evaluate the seismic performance of this type of dams (Kimata et al. 2009a, b and Kimata et al. 2010).

In this paper, a 2-dimensional nonlinear analysis has been carried out to simulate an experiment which has been performed by other researchers in order to evaluate the seismic performance of arch dams (Takano 1962). The effect of jointed rock foundation is taken into consideration in both experiment and simulation and therefore, by comparing the experiment data and analysis results, the validity of the constitutional model which is used in modeling of the joints at the rock foundation can be evaluated.

Figure 1. Malpasset dam (before and after the collapse, MA 1960).

## 2 OVERVIEW OF THE EXPERIMENT

### 2.1 *Experiment set-up and specimen*

The experiment set-up and loading frame can be seen in Figure 2. In order to assess the seismic safety of arch dams in the experiment, the abutment of arch dams is modeled as shown in Figure 2. The thickness of the specimen which includes both dam body and rock foundation is 50 mm. The specimen is placed inside a loading frame with a dimension of 1000mm×860mm and loading is applied using 13 jacks on the dam body in order to represent the water pressure (including increased dynamic water pressure due to seismic motions).

As for the rock foundation, it is constructed using square elements with a dimension of 20mm× 20mm made by mortar. In order to reproduce the joints and discontinuity inside the rock, a thin strip with a thickness of 2 mm made by the mixture of polyester with a certain shear property and diatomite is located between each two rock elements. Finally, the load is applied incrementally and the deflection of the model is measured.

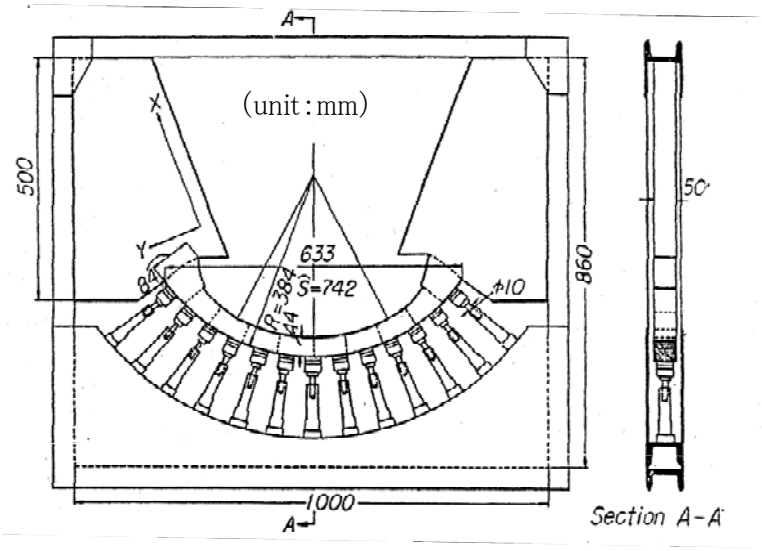


Figure 2. The Experiment setup to assess the seismic safety of arch dams (Takano, 1962).

### 2.2 *Failure pattern of the experiment*

The failure pattern of the experiment is shown in Figure 3. As it can be observed in this figure, the compressive load is applied to the rock foundation through the arch of the dam based on arch action. This pushing force would cause shear damage to the jointed rock foundation parallel to the load direction and make some openings between the rock elements which penetrates deeply inside the rock foundation. This damage pattern would make the rock foundation swell towards the inner part of the specimen which is not restraint. This swelling of rock foundation occurs not only at the vicinity of the connection with the dam, but also penetrates to almost deep parts of the foundation. Therefore, it can be said that if the thickness of the rock foundation which supports the dam at its inner side would not be sufficient, remarkable damage can happen which may lead to the collapse of the dam. Finally, it can be concluded that the failure of the model takes place when the openings between the rock elements spread through the foundation and result in a great loss of contact force which supports the dam model.

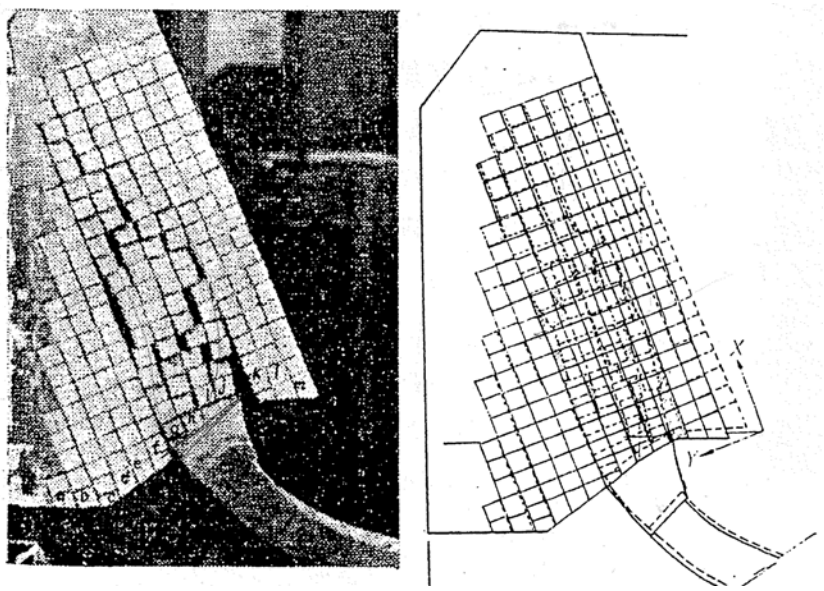

Figure 3. Failure pattern of the specimen.

## 3 OVERVIEW OF THE ANALYTICAL MODEL

A two dimensional plane strain Finite Element model which is shown in Figure 4 is used in this paper to simulate the above-mentioned experiment. 4-node quadrilateral elements with linear elastic properties are utilized to model the rock foundation since they do not suffer any damage during the experiment. Due to the symmetry of the experiment model, only half of that is modeled in the analysis as shown in Figure 4.

Boundary condition of the analytical model is considered to the same as that of the experiment, i.e. the nodes which are located next to the loading frame are fixed and leaving the other nodes free as shown in Figure 4. The incremental loading is also applied at the location of jacks in the experiment by some concentrated loads.

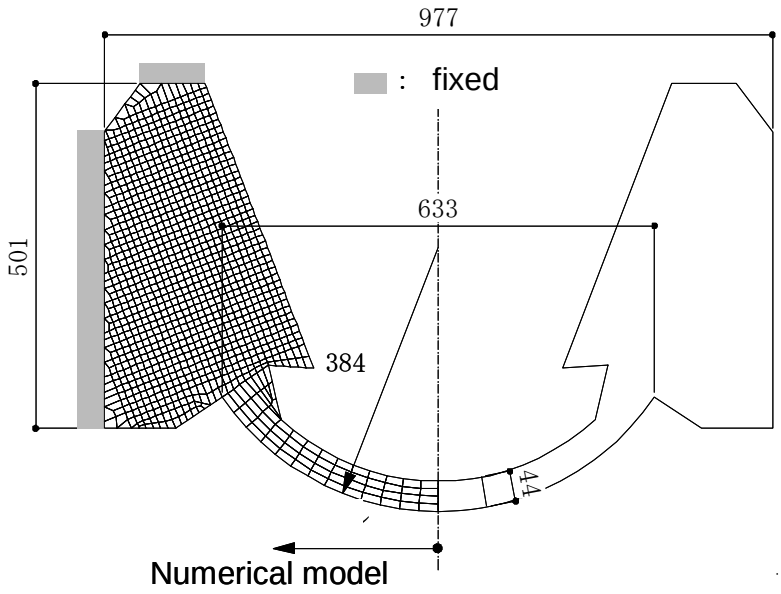


Figure 4. Analytical model.

The deformation properties of interface element which is used as joints are as follows:

(i) The relationship between shear stress τ and shear strain γ is assumed to be elasto-perfectly plastic hysteresis as shown in Figure 5a. The shear strength $\tau_f$ is defined by Mohr-Coulomb's failure criteria, Eq. (1). Tensile strength and shear stress at tensile normal stress are equal to zero as shown in Figure 5c.

$$\tau_f = \pm c \mp \sigma \tan\phi \tag{1}$$

where c: cohesion, φ: internal friction angle.

(ii) The relationship between normal stress σ and normal strain ε is elastic linear in compression side and the rigidity is zero in tension side as seen in Figure 5b. The interface elements are defined inside the rock elements as shown in Figure 5d.

(iii) In the stress- strain relationship shown by Eq. (2), matrix [D] is expressed by Eq. (3) for the elastic strain component and Eqs. (4a)–(4c) for the plastic strain component. As seen in the non diagonal term in Eq. (4a), shear stress increment due to the confining pressure is taken into consideration when the value of σ is positive in the plastic region. On the other hand, the influence due to the roughness of the joints, namely dilatancy, is disregarded. An extreme small value is given to $S_v$ in order to avoid numerical ill-conditioning when the value of diagonal component is zero. The material properties of rock foundation and interface elements which are assumed in the analysis are shown in Table 1.

$$\begin{Bmatrix} \tau \\ \sigma \end{Bmatrix} = [D] \begin{Bmatrix} \gamma \\ \varepsilon \end{Bmatrix} \tag{2}$$

where

$$[D] = \begin{bmatrix} G & 0 \\ 0 & E \end{bmatrix} \tag{3}$$

for elastic strain component, and

$$[D] = \begin{bmatrix} S_h & -S_v \cdot \tan\phi \cdot Sign(\tau) \\ 0 & S_v \end{bmatrix} \tag{4a}$$

$$S_h = 0 (= G/1\times10^4) \tag{4b}$$

$$S_v = \begin{cases} E(\sigma < 0) \\ 0(=E/1\times10^4)(\sigma \geq 0) \end{cases} \tag{4c}$$

for plastic strain component. where E: Young's modulus, G: shear modulus, Sign(τ): +1 (τ ≥ 0), –1 (τ ≤ 0).

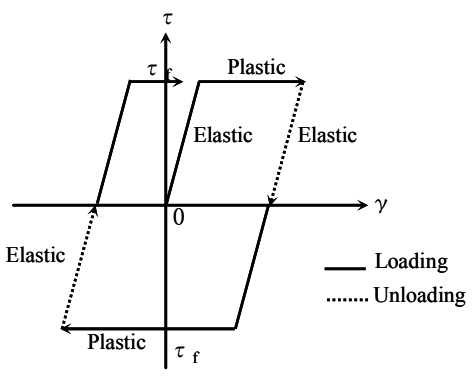


(a) Shear stress vs. shear strain

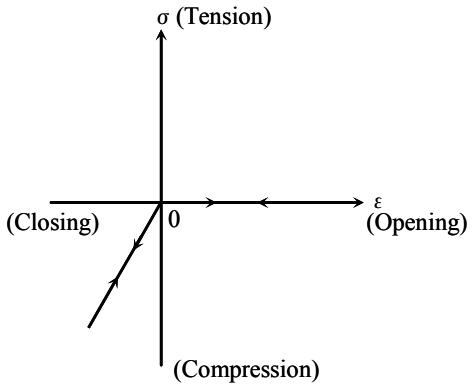


(b) Normal stress vs. normal strain

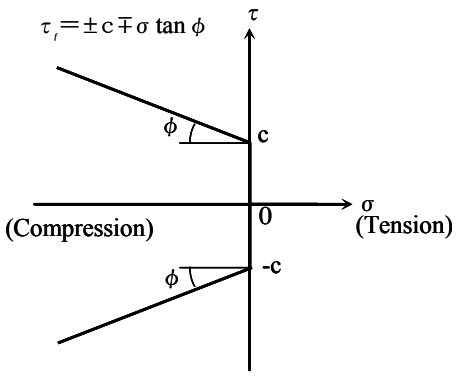


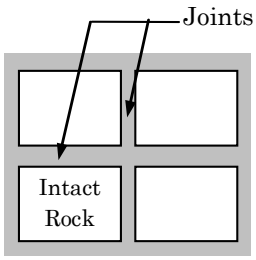


(c) Shear strength (Mohr-Coulomb failure criterion) (d) Arrangement of joint elements

Figure 5. Constitutive model for joint interface elements.

Table 1. Material properties assumed in the analysis.

| Material | Rock Foundation | Joint Interface |
|---|---|---|
| Young Modulus E(GPa) | 2.0 | — |
| Poison ratio ν | 0.2 | — |
| Density γ(kg/m3) | 2000 | — |
| Cohesion (MPa) | — | 0.12 |
| Internal friction angle (°) | — | 18 |

## 4 ANALYSIS RESULTS

The deflection pattern and minor principal stress of the rock foundation which are obtained by conducting two-dimensional nonlinear analysis are shown in Figures 6–7, respectively. It can be said that by increasing the applied load, the rock elements tend to deflect towards the inner part of the foundation as observed in the experiment. As shown in Figure 6, this trend can be easily seen when the load becomes large enough. Furthermore, Figure 7 shows that applied load would be transferred to the deep parts inside the rock foundations and finally both ends of the abutment would damage due to the incremental loading. Therefore, it can be said that the analytical results have the same trend as the experimental in general data and the shear damage and openings at the joints between the rock foundations are well simulated and observed in the analysis as well.

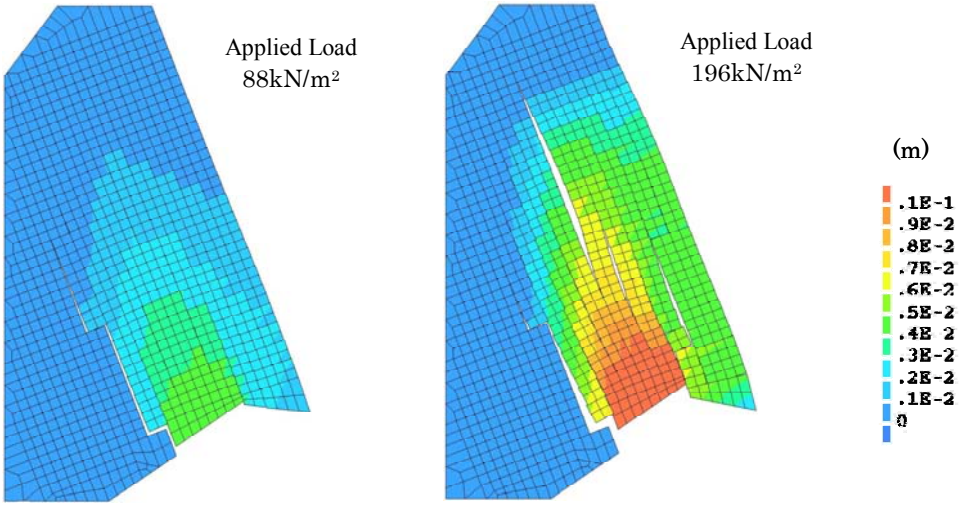


Figure 6. Deflection pattern of rock foundation in the analysis.

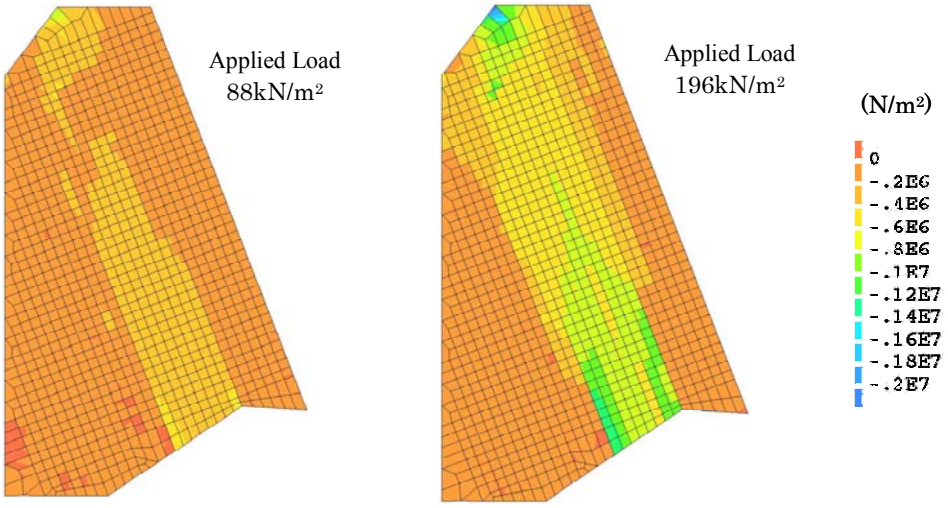


Figure 7. Minor principal stress pattern of rock foundation in the analysis.

In addition, the swelling of the rock foundation in the analysis is picked up as a damage index and is compared to that of the experimental data in terms of relative displacement in 5 locations inside the rock foundation as shown in Figure 8. At some certain level of loading, the relative displacement sharply starts to increase in the analysis results while experimental data show a smoother incremental trend. However, the relative displacement of the model roughly demonstrates the same trend in both experiment and analysis and therefore, the constitutive model used for simulating the joint elements proves to be accurate and acceptable.

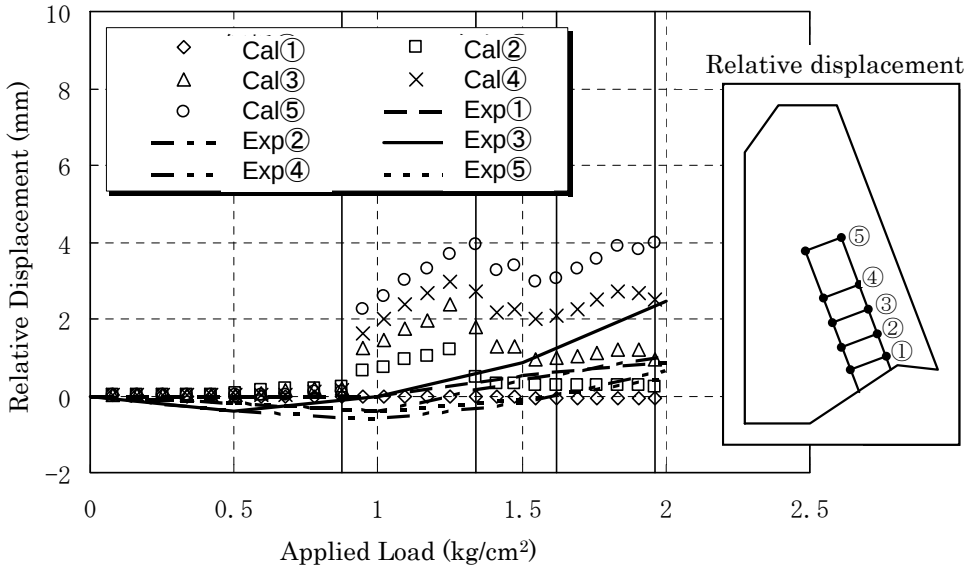


Figure 8. Comparison between the experimental and numerical results.

## 5 CONCLUSION

In this paper, a two-dimensional nonlinear Finite Element analysis is performed using joint interface elements with special deformation properties in order to simulate the progressive failure of jointed rock foundations of arch dams. Obtained results are compared with the data of an experiment under similar conditions and good agreement is found between them. Therefore, it can be concluded that the proposed model can roughly simulate the progressive failure of jointed rock foundations and can be used in further similar researches.

## REFERENCES


Kimata, H., Fujita, Y., Horii, H. and Yazdani, M. 2009. Dynamic crack propagation analysis of concrete gravity dams with jointed rock foundation. *64th Annual Conference of JSCE* (in Japanese).

Kimata, H., Fujita, Y., Horii, H. and Yazdani, M. 2009. Dynamic crack propagation analysis of concrete gravity dams with jointed rock foundation. *3rd Japan-Greece Workshop on Seismic Design, Observation, and Retrofit of Foundations,* proceedings of the workshop, pp.486-494.

Kimata, H., Fujita, Y., Tamai, S. and Okhovat, M.R. 2010. Nonlinear dynamic behavior of concrete gravity dams with jointed rock foundation. *65th Annual Conference of JSCE* (in Japanese).

Ministere de l'Agriculture (MA), 1960. Final Report of the Investigating Committee of the Malpasset Dam, France, pp. 166–172.

Takano, M. 1962. Experimental study on the safety of arch dam foundations. *Journal of JSCE*, No.78.

# Some notes on liquefaction analysis in simple two-dimensional formulation

N. Yoshida & Y. Ohya
*Department of Civil and Environmental Engineering, Tohoku Gakuin University*
*Port and Airport Research Institute*

ABSTRACT: A new formulation named a simple two-dimensional formulation is presented for the liquefaction analysis. When the effective mean stress is evaluated from the average of two normal stresses in the plane strain of analysis, the bulk modulus defined in the three-dimensional analysis cannot be used because the effective mean stress is obtained as an average of three normal stresses in the three-dimensional analysis and volumetric stress is same in both three- and two-dimensional analysis. This difference requires change of the overall structure of the stress-strain relationships. There are several different places compared with the conventional plane strain condition. For example, the Poisson's ratio is to be 1.0 under no volumetric change condition. Some other notes are also presented.

## 1 INTRODUCTION

Since the space is originally three-dimensional, the analysis of ground is to be ideally made by the three-dimensional analysis. There are several difficulties, however, in making the three-dimensional analysis. For example, computer power is not sufficient in the practical use, and the soil data for the three-dimensional analysis is difficult to obtain because it is costly. Therefore, a one-dimensional analysis is the most popular method and a two-dimensional analysis is carried out to a special case such as an important structure.

The plane strain condition and the plane stress condition are well known assumption to make the two-dimensional analysis. These methods work to reduce the number of unknown variables, but a constitutive model is to be the one developed in the three-dimensional space. In the plane strain condition, for example, normal stress perpendicular to the plane of analysis exists. Therefore, the constitutive model must consider this stress in the nonlinear analysis. The Mohr-Coulomb yield criterion is frequently used in the analysis of soil, and three normal stresses are necessary in defining the yield criterion. However, since this normal stress is generally a middle principal stress, it is frequently neglected, in which case constitutive models need not worry on this normal stress and two-dimensional formulation becomes possible.

In the liquefaction analysis, however, there is another factor that requires this normal stress. It is evaluation of the effective mean stress or the effective confining stress. Since it is an average stress in three normal stresses, evaluation of this normal stress is essential. It means that the constitutive model defined in the three-dimensional space is necessary. If one wants to use a constitutive model that is defined in the two-dimensional space, the definition of the effective mean stress is changed to the average of the two normal stresses working in the plane of interest[1)2)]. The model derived by this assumption is named a simple two-dimensional formulation in this paper.

There are several differences between the conventional two-dimensional analysis such as the plane strain and the plane stress analysis and the simple two-dimensional analysis. There exist

some differences in the definition of the elastic modulus. Some notes to convert conventional elastic modulus for the use of the simple two-dimensional analysis is also presented.

## 2 THREE-DIMENSIONAL FORMULATION

The stress-strain relationships are usually defined as follows by using the Young's modulus $E$ and the Poisson's ratio $\nu$.

$$\begin{Bmatrix}\sigma_x\\ \sigma_y\\ \sigma_z\\ \tau_{xy}\\ \tau_{yz}\\ \tau_{zx}\end{Bmatrix}=\frac{E}{(1-2\nu)(1+\nu)}\begin{bmatrix}1-\nu & \nu & \nu & 0 & 0 & 0\\ \nu & 1-\nu & \nu & 0 & 0 & 0\\ \nu & \nu & 1-\nu & 0 & 0 & 0\\ 0 & 0 & 0 & (1-2\nu)/2 & 0 & 0\\ 0 & 0 & 0 & 0 & (1-2\nu)/2 & 0\\ 0 & 0 & 0 & 0 & 0 & (1-2\nu)/2\end{bmatrix}\begin{Bmatrix}\varepsilon_x\\ \varepsilon_y\\ \varepsilon_z\\ \gamma_{xy}\\ \gamma_{yz}\\ \gamma_{zx}\end{Bmatrix} \tag{1}$$

where shear strain is not the tensor strain but the engineering strain. This equation is used as a fundamental equation in this paper. In the analysis of the ground, this equation is frequently expressed by using the bulk modulus $K$ and the shear modulus $G$, because both the volumetric change and the shear deformation are primary interest in the geometrical analysis. This equation is written as

$$\begin{Bmatrix}\sigma_x\\ \sigma_y\\ \sigma_z\\ \tau_{xy}\\ \tau_{yz}\\ \tau_{zx}\end{Bmatrix}=\begin{bmatrix}K+4G/3 & K-2G/3 & K-2G/3 & 0 & 0 & 0\\ K-2G/3 & K+4G/3 & K-2G/3 & 0 & 0 & 0\\ K-2G/3 & K-2G/3 & K+4G/3 & 0 & 0 & 0\\ 0 & 0 & 0 & G & 0 & 0\\ 0 & 0 & 0 & 0 & G & 0\\ 0 & 0 & 0 & 0 & 0 & G\end{bmatrix}\begin{Bmatrix}\varepsilon_x\\ \varepsilon_y\\ \varepsilon_z\\ \gamma_{xy}\\ \gamma_{yz}\\ \gamma_{zx}\end{Bmatrix} \tag{2}$$

In the liquefaction analysis, quantities related to the volumetric change (confining stress or mean stress $\sigma_m$ and volumetric strain $\varepsilon_v$), the one-dimensional rebound modulus B, the Poisson's ratio $\nu$, and the coefficient of earth pressure at rest $K_0$ are important. Here, as all the stresses in this paper is the effective stress, prime which is usually used to the effective stress in order to distinguish from the total stress is not used. In addition, $K_0$ is defined under the one-dimensional compression loading of the elastic material. They are defines as follows:

$$\sigma_m=(\sigma_x+\sigma_y+\sigma_z)/3 \tag{3}$$

$$\varepsilon_v=\varepsilon_x+\varepsilon_y+\varepsilon_z \tag{4}$$

$$\sigma_m=(\sigma_x+\sigma_y+\sigma_z)/3=K\varepsilon_v=K(\varepsilon_x+\varepsilon_y+\varepsilon_z) \tag{5}$$

$$B=K+4G/3 \tag{6}$$

$$\nu=(3K-2G)/2/(3K+G) \tag{7}$$

$$K_0=\frac{K-2G/3}{K+4G/3}=\frac{\nu}{1-\nu} \tag{8}$$

Here, the bulk modulus is important when considering the vertical motion as the P wave velocity $V_p$ is obtained by

$$V_p=\sqrt{B/\rho}=\sqrt{(K+4G/3)/\rho} \tag{9}$$

where $\rho$ denotes a density.

## 3 TWO-DIMENSIONAL FORMULATION

When considering a constitutive model for two-dimensional space, the volumetric change characteristics is to be expressed as

$$\sigma_m = (\sigma_x + \sigma_y)/2 = \tilde{K}\varepsilon_v = \tilde{K}(\varepsilon_x + \varepsilon_y) \tag{10}$$

This equation is derived by setting $\sigma_z$=0 and $\varepsilon_z$=0 in Eq. (3), but it is impossible because both stress and strain cannot be specified at the same time. Under the plane strain condition, for example, $\sigma_z$ is not zero although $\varepsilon_z$ is zero. This indicates that the framework of the constitutive model is different from the three-dimensional space. In order to emphasize it, "~" is put above the variable.

Then the problem occurs how to obtain the elastic moduli from the conventional elastic moduli. It is clear that the bulk modulus *K* defined in the three-dimensional space cannot be used instead of $\tilde{K}$. When deriving the conversion equation, it is important to consider what quantities are same between the three-dimensional space and the two-dimensional space. There are three elastic moduli that are frequently used in the engineering practice, which are *E*, *K*, and *G*. Among them, we assume that *E* and *G* are the same in the three- and two-dimensional analyses, in order to keep the S wave and the P wave velocities are same in two formulations.

The plane strain condition is assumed in this paper among the two assumptions for the two-dimensional formulation because this condition is close to the behavior of the ground during earthquakes.

Three strains are set zero in order to consider that displacement in the direction perpendicular to the plane of interest does not occur, i.e., $\varepsilon_z = \varepsilon_{yz} = \varepsilon_{zx} = 0$. The relationships that $\tau_{yz} = \tau_{zx} = 0$ are automatically derived. Then the stress-strain relationships yields,

$$\begin{Bmatrix} \sigma_x \\ \sigma_y \\ \sigma_z \\ \tau_{xy} \end{Bmatrix} = \begin{bmatrix} K + 4G/3 & K - 2G/3 & 0 \\ K - 2G/3 & K + 4G/3 & 0 \\ K - 2G/3 & K - 2G/3 & 0 \\ 0 & 0 & G \end{bmatrix} \begin{Bmatrix} \varepsilon_x \\ \varepsilon_y \\ \gamma_{xy} \end{Bmatrix} \tag{11}$$

Since $\sigma_z$ is not zero but changes in the plane strain condition, the constitutive model is essentially to be defined in the three-dimensional space.

The stress $\sigma_z$ is included in the confining stress and the yield condition. Under the assumption that the middle principal stress does not affect the yielding, however, $\sigma_z$ does not appear in the yield condition. This assumption is used in many constitutive models, and is accepted widely. Therefore, only the difference between Eq. (5) and (10) remains a problem.

The normal stress $\sigma_x$ is expressed from Eq. (1) as

$$\begin{aligned} \sigma_x &= \left\{ \frac{E(1-\nu)}{(1+\nu)(1-2\nu)} \right\} \varepsilon_x + \frac{E\nu}{(1+\nu)(1-2\nu)} \varepsilon_y \\ \sigma_y &= \left\{ \frac{E(1-\nu)}{(1+\nu)(1-2\nu)} \right\} \varepsilon_y + \frac{E\nu}{(1+\nu)(1-2\nu)} \varepsilon_x \end{aligned} \tag{12}$$

Then we obtain sum of the normal stresses as

$$\sigma_x + \sigma_y = \left\{ \frac{E(1-\nu)}{(1+\nu)(1-2\nu)} + \frac{E\nu}{(1+\nu)(1-2\nu)} \right\} (\varepsilon_x + \varepsilon_y) = \frac{E}{(1+\nu)(1-2\nu)} (\varepsilon_x + \varepsilon_y) \tag{13}$$

The relation among $\nu$, *E*, and *G* is known to be expressed as

$$G = \frac{E}{2(1+\nu)} \tag{14}$$

in the three-dimensional space. These terms including the Poisson's ratio yields

$$
\begin{aligned}
&\nu = \frac{E-2G}{2G}, \\
&1+\nu = 1+\frac{E-2G}{2G} = \frac{E}{2G}, \\
&1-\nu = 1-\frac{E-2G}{2G} = \frac{4G-E}{2G}, \\
&1-2\nu = 1-\frac{E-2G}{G} = \frac{3G-E}{G}
\end{aligned}
\tag{15}
$$

Substitution of this equation into Eq. (12) results in

$$
\begin{aligned}
&\sigma_x = \left\{ \frac{E\dfrac{4G-E}{2G}}{\dfrac{E}{2G}\dfrac{3G-E}{G}} \right\} \varepsilon_x + \frac{E\dfrac{E-2G}{2G}}{\dfrac{E}{2G}\dfrac{3G-E}{G}} \varepsilon_y = \frac{G(4G-E)}{3G-E}\varepsilon_x + \frac{G(E-2G)}{3G-E}\varepsilon_y \\
&\sigma_y = \frac{G(4G-E)}{3G-E}\varepsilon_y + \frac{G(E-2G)}{3G-E}\varepsilon_x
\end{aligned}
\tag{16}
$$

Therefore we obtain the sum of the normal stresses as

$$
\sigma_x + \sigma_y = \left\{ \frac{G(4G-E)}{3G-E} + \frac{G(E-2G)}{3G-E} \right\} (\varepsilon_x + \varepsilon_y) = \frac{2G^2}{3G-E}(\varepsilon_x + \varepsilon_y)
\tag{17}
$$

This is the fundamental equation in the simple two-dimensional analysis.

The bulk modulus $\tilde{K}$ in the simple two-dimensional formulation is obtained comparing Eq. (10) and Eq. (17) as

$$
\tilde{K} = \frac{G^2}{3G-E} = \frac{G^2}{3G-\dfrac{9KG}{3K+G}} = K + \frac{1}{3}G
\tag{18}
$$

and the Young's modulus is obtained by means of G and $\tilde{K}$ as

$$
E = \frac{G(3\tilde{K}-G)}{\tilde{K}}
\tag{19}
$$

Finally we obtain the coefficient of the normal stress-strain relationships in Eq. (17) as

$$
\begin{aligned}
&\frac{G(4G-E)}{3G-E} = \frac{G(4G-\dfrac{G(3\tilde{K}-G)}{\tilde{K}})}{3G-\dfrac{G(3\tilde{K}-G)}{\tilde{K}}} = \frac{4\tilde{K}-(3\tilde{K}-G)}{1} = \tilde{K}+G \\
&\frac{G(E-2G)}{3G-E} = \frac{G(\dfrac{G(3\tilde{K}-G)}{\tilde{K}}-2G)}{3G-\dfrac{G(3\tilde{K}-G)}{\tilde{K}}} = \frac{G(3\tilde{K}-G)-2G\tilde{K}}{3\tilde{K}-3\tilde{K}+G} = \tilde{K}-G
\end{aligned}
\tag{20}
$$

Then the stress-strain relationships are obtained as

$$
\begin{Bmatrix} \sigma_x \\ \sigma_y \\ \tau_{xy} \end{Bmatrix} = \begin{bmatrix} \tilde{K}+G & \tilde{K}-G & 0 \\ \tilde{K}-G & \tilde{K}+G & 0 \\ 0 & 0 & G \end{bmatrix} \begin{Bmatrix} \varepsilon_x \\ \varepsilon_y \\ \gamma_{xy} \end{Bmatrix}
\tag{21}
$$

The one-dimensional rebound modulus *B* is obtained as

$$
\tilde{B} = \tilde{K} + G = K + \frac{4}{3}G = B
\tag{22}
$$

This definition is same with the three-dimensional analysis. It means that the P wave velocity is same with that in three-dimensional analysis, which is the reason why we used the same Young's modulus $E$ for both three-dimensional and two-dimensional analyses.

The normal stress is written as

$$\begin{aligned}\sigma_x &= (\tilde{K}+G)\varepsilon_x + (\tilde{K}-G)\varepsilon_y \\ \sigma_y &= (\tilde{K}-G)\varepsilon_x + (\tilde{K}+G)\varepsilon_y\end{aligned} \tag{23}$$

Here, the following equation is obtained by putting $\sigma_x$=0

$$\begin{aligned}\varepsilon_x &= -\frac{\tilde{K}-G}{4\tilde{K}G}\sigma_y \\ \varepsilon_y &= -\frac{\tilde{K}+G}{\tilde{K}-G}\varepsilon_x = \frac{\tilde{K}+G}{4\tilde{K}G}\sigma_y\end{aligned} \tag{24}$$

Therefore, the Poisson's ratio for the simple two-dimensional formulation yields

$$\tilde{\nu} = -\frac{\varepsilon_x}{\varepsilon_y} = \frac{\tilde{K}-G}{\tilde{K}+G} = \frac{K-\frac{2}{3}G}{K+\frac{4}{3}G} = \frac{\nu}{1-\nu} \tag{25}$$

On the other hand, the following equation is obtained by putting $\varepsilon_x$=0,

$$\sigma_x = (\tilde{K}-G)\varepsilon_y,\ \ \sigma_y = (\tilde{K}+G)\varepsilon_y \tag{26}$$

Therefore, the coefficient of earth pressure at rest $K_0$ yields

$$K_0 = \tilde{\nu} \tag{27}$$

## 4 DISCUSSION

The stress-strain relation derived in this paper does not include the third stress $\sigma_z$ and the third strain $\varepsilon_z$. The final form of the stress-strain relation is obtained as Eq. (21). This formulation is called a simple two-dimensional formulation in order to distinguish from other formulations. As $G$ is kept constant between the three- and two-dimensional analyses, Lame's constant $\lambda$ changes keeping $\mu$ (=G) constant if the stress-strain relationships are written by means of the Lame's constants.

The S wave and the P wave velocities are hold in the new formulation. However, the bulk modulus includes shear modulus; it changes according to the nonlinear shear deformation of soil in exact sense. In the practical situation, however, this change may be neglected in order to make the analysis simple when the change of the shear modulus is not significant.

In the engineering practice, shear modulus is usually obtained with easy test, for example, the PS logging. On the other hand, the bulk modulus is difficult to evaluate. Therefore, it is frequently obtained by assuming a relevant Poisson's ratio and the bulk modulus is evaluated from the Poisson's ratio and the shear modulus. Here, the Poisson's ratio 1/3 is frequently assumed because the coefficient of earth pressure at rest becomes 0.5. However, in the simple two-dimensional formulation, the Poisson's ratio is to be 0.5 in order to make the coefficient of earth pressure at rest to be 0.5. The Poisson's ratio is close to 0.5 under nearly no volumetric change condition in the three-dimensional analysis whereas it is 1.0 under the simple two-dimensional analysis.

In the computer program in making the two-dimensional analysis, the normal stress perpendicular to the plane of analysis may not be output even when the plane strain condition is used. It means that the user cannot recognize whether the analysis is made by the plane strain condition or by the simple two-dimensional condition. The method to evaluate the elastic moduli is different between two formulations. Therefore, the engineer needs to check the formulation that he is going to use.

## 5 CONCLUDING REMAKRS

A new formulation named a simple two-dimensional formulation is presented. This formulation is necessary when the effective confining stress is evaluated from the two normal stresses working in the plane of analysis. It is essential for soil to consider the effective stress dependency of the elastic moduli as well as shear strength because of the effective stress principle. Therefore, three-dimensional formulation becomes necessary in the constitutive models that use three normal stresses in defining the effective confining stress. Therefore, the simple two-dimensional analysis presented here makes the development of the constitutive models very simple as it uses only two normal stresses working in the plane of the analysis.

The S wave velocity and the P wave velocity are same with that in the three-dimensional analysis in this formulation, but the bulk modulus includes shear modulus only in this formulation. There are some differences between two formulations. Therefore, some notes are necessary to use this formulation.

REFERENCE

1) S. Iai, Y. Matsunaga and T. Kameoka: Strain Space Plasticity Model for Cyclic Mobility, Report of the Port and Harbour Research Institute, Vol.29, No.4, pp.27-56, 1990.
2) Yoshida, N. (1993): STADAS, A computer program for static and dynamic analysis of ground and soil-structure interaction problems, Report, Soil Dynamics Group, The University of British Columbia, Vancouver, Canada

# Development of New Liquefaction Countermeasure Aimed for Old Existing Structures

K. Horikoshi, H. Ishii & H. Matsui
*Civil Engineering Research Institute, Taisei Corporation, Japan*

K. Higaki
*Taisei Service Corporation, Japan (Formerly belongs to Taisei Corporation)*

ABSTRACT: In the aftermath of a major earthquake that struck the city of Kobe in 1995, seismic design codes have often been revised so that structures can survive even after strong earthquakes. Seismic reinforcement of old existing structures has also become an urgent task for civil engineers to enhance the public safety. From a geotechnical point of view, soil liquefaction can be a cause of damage to structures, especially in the coastal areas of Japan. This paper presents an innovative technology, called 'Ground Flex Mole', which can strengthen the ground immediately beneath existing structures. The Ground Flex Mole technology consists of two processes, i.e. horizontal directional drilling and the subsequent chemical grouting. Details of the technology are described in this paper, as well as a case study where the ground beneath an actual oil storage tank was improved by using this new technology.

## 1 NECESSITY OF SEISMIC REINFORCEMENT OF OIL TANKS

### 1.1 *Background*

The Great Hanshin-Awaji earthquake, which struck the city of Kobe and surrounding area in 1995, led to the revision of seismic design codes to consider two types of earthquakes, i.e. earthquakes with a moderate intensity which often occur during the design period of the structure, and earthquakes of high intensity which rarely occur but may cause irreparable damage to structures. The Kobe earthquake has also made engineers keenly aware of the necessity of reinforcing a number of old existing structures which do not satisfy the latest seismic design codes.

There are a number of oil storage tanks along coastal areas in Japan, and these tanks are often located close to mega-cities such as Tokyo, Yokohama, Nagoya and Osaka. Since these tanks were constructed decades ago during the rapid economic growth period in Japan, all of them do not meet the latest design codes, and need to be seismically reinforced to increase their level of safety.

In Japan, the resistance of oil storage tanks against earthquakes has been regulated by the Fire Prevention Law. According to the law, oil storage tanks built before 1977, i.e. the year of the revision of the law, must be reinforced before a designated year.

Japanese regulations categorize oil tanks into two types. Tanks with a storage capacity of at least 1,000 $k\ell$ are defined as 'specified outdoor oil storage tanks', and those with a storage capacity of from 500 $k\ell$ up to 1,000 $k\ell$ are defined as 'quasi-specified outdoor oil storage tanks'. According to these regulations, all 'specified outdoor oil storage tanks' with a capacity of more than 10,000 $k\ell$ are to be reinforced by the end of 2009, those with a capacity from 1,000 $k\ell$ to 10,000 $k\ell$ are to be reinforced by the end of 2014. Quasi-specified outdoor oil storage tanks must be reinforced by the end of 2019. Tanks that fail to be reinforced by the designated year may not be used thereafter.

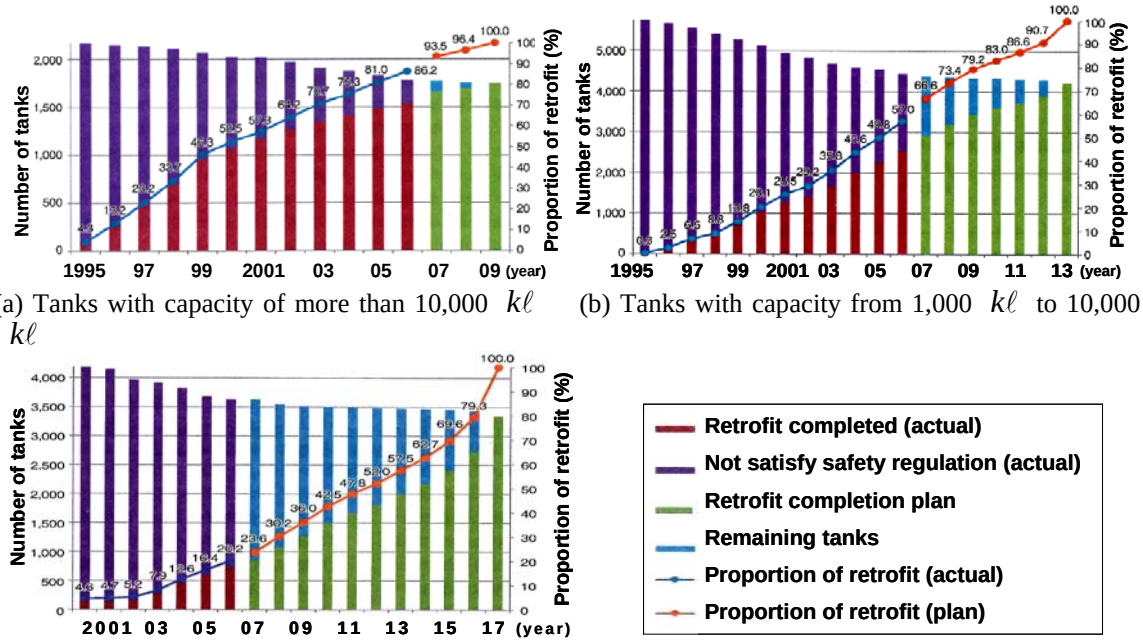


(a) Tanks with capacity of more than 10,000 $k\ell$ (b) Tanks with capacity from 1,000 $k\ell$ to 10,000 $k\ell$

(c) Tanks with capacity of less than 1,000 $k\ell$

Figure 1. Proportion of reinforced tanks by year (Hatakeyama, 2008)

Figure 1 shows the progress of the seismic reinforcement for each tank category, after Hatakeyama (2008). Reinforcement of tanks with a capacity of more than 10,000 $k\ell$ has already been completed. However, these figures show that many storage tanks in the other categories still need to be reinforced. For this purpose, an effective and economical method of seismic reinforcement is required. Preventing liquefaction of the ground beneath the tanks has been of special concern among geotechnical engineers.

### 1.2 *Approved methods of soil Improvement*

In Japan, the 'Hazardous Materials Safety Techniques Association' has been responsible for the safety of oil storage tanks. Based on the results of an intensive study, the association can authorize the following four types of liquefaction countermeasures for existing oil storage tanks. Schematic diagrams of these countermeasures are shown in Figure 2.

#### 1.2.1 *Groundwater lowering method*

This method prevents soil liquefaction by lowering the groundwater level through continuous pumping. As shown in the figure, a cut-off wall structure is necessary to effectively lower the groundwater level. The soil beneath the tank cannot liquefy in an unsaturated condition. This method is more feasible and economical when a group of tanks are seismically reinforced at the same time. It should be noted that although this method unquestionably prevents liquefaction in a condition without groundwater, it requires constant pumping during the design life of the tank, which increases operating costs.

#### 1.2.2 *Chemical grouting method*

This method has been the most popular method of reinforcement, since it can be applied while a tank is in operation. The method improves the soil strength beneath the tank by grouting solidification chemicals. Generally, a liquid glass solution is used as the grouting material. The unconfined strength of the solidification should be typically at least 60-100 kN/m$^2$. Since the grouting material needs to penetrate between the soil particles, the ratio of fine soil should be relatively low. Ground Flex Mole technology described later employs this chemical grouting method.

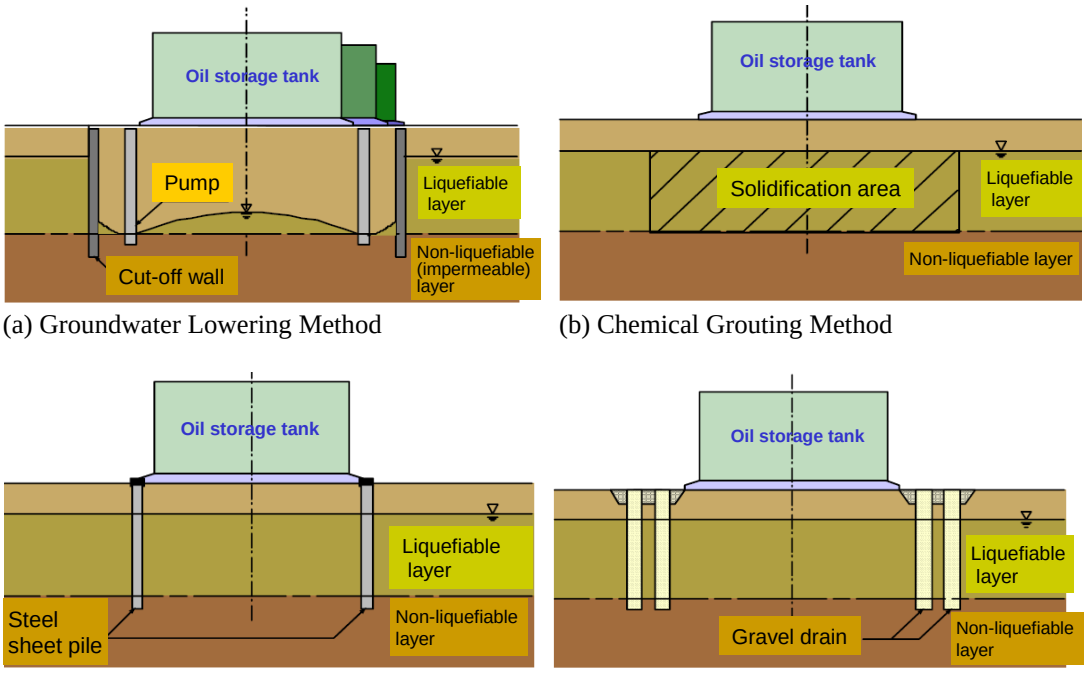


(a) Groundwater Lowering Method (b) Chemical Grouting Method

(c) Sheet Pile Ring Method (d) Gravel Drain Method

Figure 2. Methods approved for seismic retrofitting of tanks

### 1.2.3 *Sheet pile ring method*

This method prevents the settlement of a storage tank by preventing excessive ground deformation. Steel sheet piles are installed around the edge of the tank as shown in the figure. Pipe structures connected to the tank need to be removed temporarily during the installation of sheet piles. Therefore, this method cannot be applied while a tank is in operation.

### 1.2.4 *Gravel Drain Method*

This method prevents liquefaction by accelerating the pore water dissipation during and after an earthquake. Gravel columns are installed circumferentially along the outside edge of the tank as shown in the figure. However, the applicability of the method is limited since there is a possibility that pore water cannot be dissipated as quickly as it is generated during and after a strong earthquake.

## 2 DEVELOPMENT OF INNOVATIVE METHODS OF REINFORCEMENTGETTING

### 2.1 *The template file*

As mentioned above, solidification by chemical grouting has been the most popular method of seismic reinforcement against liquefaction. In the conventional chemical grouting method, drilling holes are made in a diagonal but straight direction, or perpendicular to a vertical shaft constructed near the tank (see Figure 3). In the former conventional method, it is difficult to reinforce the ground immediately beneath the central area of the storage tank, i.e. a non-improved area is often left. A new chemical grouting technology called ‘Ground Flex Mole’ has therefore been developed to solve this issue. The main characteristics of the new method are as follows:

1) ‘Ground Flex Mole’ applies HDD (Horizontal Directional Drilling) devices, which have already been used for lifeline pipe installation beneath existing structures. HDD devices enable the direction of the drilling to be changed at any point in the ground. As shown in Figure 4, the tip of the boring rod is tapered. When a straight drilling line is required, the rod is pushed into the soil as it rotates, whereas when a curved drilling line is required, the rod is pushed without rotation to make it proceed in a curved direction (see Figure 5).

Note that the drilling system has a percussion system that enables the rod to proceed even in hard ground.

2) The boring rod of the ‘Ground Flex Mole’ employs a double shaft system as shown in the right-hand photo of Figure 4. The double system was designed so that the proposed method can be used for various types of purposes other than soil improvement, such as soil decontamination, cavity filling and cement grouting. After the installation of both an inner and outer rod to a specified position, the inner rod is extracted along the drilled shaft. Then an inner system, such as a grouting system, is installed along the outer shaft depending on the objective of the method. Finally, the outer shaft is extracted along the line of the grouting tube (inner system).
3) For the grouting tube, the so-called ‘self-packer system’ was developed to simplify the grouting system and to minimize the diameter of the tube. In the ‘Ground Flex Mole’ method, packers are inflated by the pressure of the chemical grouting material itself, unlike the general method which employs independent air or water supply system for the inflation.

Figure 3. Conventional horizontal grouting from a vertical shaft

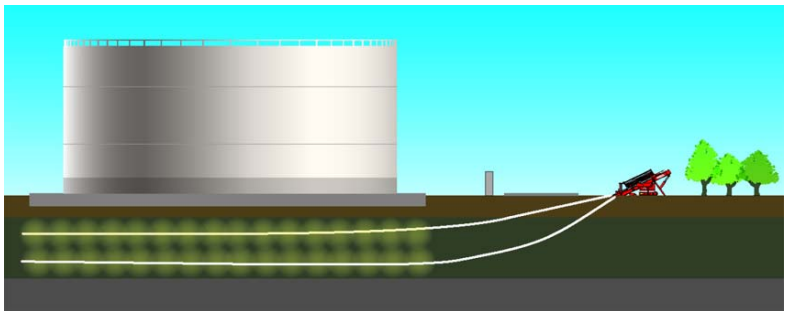

Figure 4. Outline of Grand Flex Mole Technology

Figure 5. Drilling machine and the tip structure of rods

## 3 APPLICATION TO EXISTING OIL TANKS

The developed technology was used to reinforce ground beneath existing oil storage tanks in western Japan against liquefaction. According to a preliminary soil investigation, two tanks with a capacity of 8,000 $k\ell$ and three tanks with a capacity of 2,000 $k\ell$ were considered to be in need of reinforcement in accordance with the Technical Manual on the Permeation Grouting Method (2008). A loose sand layer at a depth of 2-4 m was targeted for improvement. A planar view and a cross section of the ground improvement are illustrated in Figure 6 and Figure 7, respectively. Overall profiles of ground improvement are summarized in Table 1.

Note that at the site, before applying the Ground Flex Mole technology, a conventional horizontal grouting was applied from the temporary vertical shaft at the other tanks as already shown in Figure 3. A relatively large vertical shaft is required for the horizontal drilling. The figure clearly indicates the advantages of Ground Flex Mole technology, in terms of safety, work period, and cost, as well as adaptability to site constraints. Consequently, the fire authority allowed the application of Ground Flex Mole to tanks that were up to 60% filled with oil. The drilling machine was positioned outside the oil dike and the existing road so that their functions could be fulfilled (see Figure 8).

During the improvement work, the maximum allowable ground movement and the maximum allowable inclination were set at 17 mm and 1/430, respectively. The ground movement was observed periodically using fluid pressure type settlement gauges. Since the oil tanks were 60% full during the work period, a real-time warning system was employed for safety. Observations indicated that the maximum ground movement was at most about 7.4 mm at the final stage, and the inclination was negligible. These data show that the grouting caused almost no displacement of the surrounding soil.

The directional drilling was conducted for about three months using two machines. The comparison between the planned and the actual boring lines is shown in Figure 9. The large difference was attributed to the existence of cobbles and concrete brocks in the reclaimed ground at the site. The percussion drilling worked so effectively that the drilling work could be completed without changing the original lines.

The permeation grouting was conducted for about five months following the drilling work. The unconfined compressive strengths were checked using core samples collected from the improved ground. The measured strengths for individual tanks were well above the requirement, 60 kN/m$^2$ at 28 maturity days.

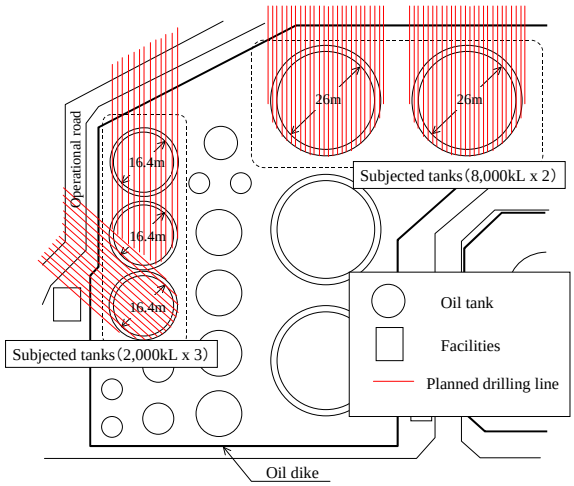


Figure 6. General plan of the case study site

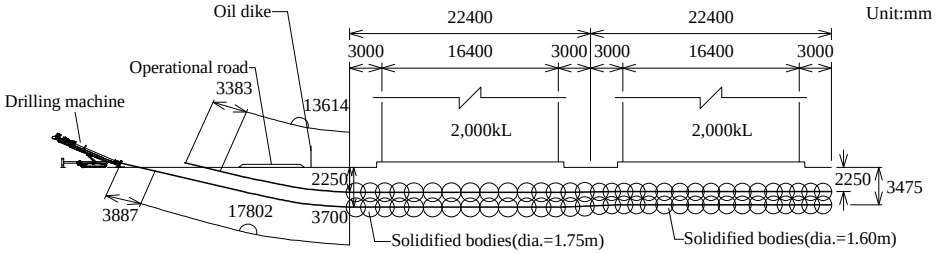


(a) Cross section for tanks with capacity 2,000 $k\ell$

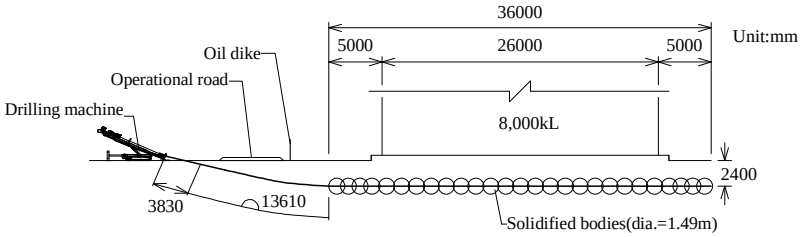


(b) Cross section for tanks with capacity 8,000 $k\ell$

Figure 7. Cross section of the ground improvement beneath existing oil tankS

Table 1. Overall profiles of ground improvement

| | |
|---|---|
| Total drilling length | 4,769 m |
| Number of holes drilled | 92 |
| Design volume of grout | 1,776,429 $\ell$ |
| Number of grouting points | 2,019 |

(a) Directional drilling towards the ground beneath the tank

(b) Installed grouting pipes

Figure 8. Reinforcement work beside a tank

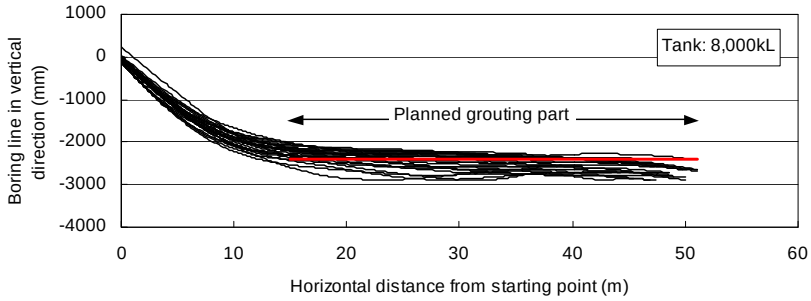


Figure 9. Planned and actual drilling lines

## 4 SUMMARY

As the seismic design codes are revised, seismic reinforcement of old existing structures and facilities is an important task for civil engineers to enhance public safety. This paper introduces an innovative technology which enables the ground beneath existing structures to be reinforced, and examines its applicability and advantages.

## REFERENCES


Coastal Development Institute of Technology 2008. Technical manual on permeation grouting method (revised) (in Japanese). *Coastal Technology Library*, No. 33.

Hatakeyama, T. 2008. Conformity of outdoor oil storage tanks to new regulations, and promotion of conformity for quasi-specified outdoor oil storage tanks (in Japanese). *Safety & Tomorrow*, Hazardous Materials Safety Techniques Association, No. 121, Sep.: 7-16.

Ishii, H., Matsui, H. & Higaki, K. 2010. Soil improvement beneath existing structures with use of directional drilling technology, Ground Flex Mole (in Japanese). *Plan of construction works*, Japan Construction Mechanization Association, No. 720, Feb.: 16-20.

# Seismic Performance of an Integrated Steel Pipe Bridge Pier by Multi Steel Pipes with Hysteretic Shear Damper

M. Shinohara & H. Kanaji
*Hanshin Expressway Company Limited, Osaka, Japan*

ABSTRACT: The research presented in this paper proposes the use of a basic structural unit comprised of four low-cost, off-the-shelf steel pipes, combined into a single structure (the steel pipe integrated pier) using shear panels that have a hysteretic damper function. The dynamic response characteristics of the new pier structure were evaluated and are presented in this paper. Comparisons were also made with conventional standard steel piers to consider the advantages of the proposed integrated pier.

## 1 INTRODUCTION

Since the Great Hanshin Earthquake, great efforts have been made to encourage research into seismic resistant designs and steel structures that can withstand Level 2 earthquakes, primarily by the Japan Society of Civil Engineers and the Japanese Society of Steel Construction (JSSC).

Because the design requirements for seismic retrofit were made more stringent following the Great Hanshin Earthquake, construction cost has become a major issue. One company dealing with the cost issue and the more stringent requirements for seismic retrofit is the Hanshin Expressway Company Limited, which has been designing seismic retrofit steel piers. The experience gained from the Great Hanshin Earthquake, as well as the new standards relating to seismic retrofit[1)] and steel pier design rationalization has been used as a basis.

This research proposes the use of a basic structural unit comprised of four low-cost, off-the-shelf steel pipes, combined into a single structure (the steel pipe integrated pier) using horizontal structural members (shear panels) that have a hysteretic damper function. The advantages of the proposed pier are its cheap structural materials, the effective use of the hysteretic damper function provided by these materials together with an abbreviation of an anchor frame, and the ability of the structure to respond differently to the vertical load (such as the dead load and the live load) and to horizontal forces during seismic events, which is part of the damage control design.

## 2 PROSED AND CONVENTIONAL PIER

The steel pipe integrated pier (hereafter referred to as the "proposed type") proposed in this research is shown in Figure 1. The depicted example is a pier of an average height (leg height 30 m) for a planned route. This is a Rahmen type structure that supports a cross beam is adequate for six lanes. An ordinary rectangular cross-section steel pier design is depicted in Figure 2 (hereafter referred to as the "conventional type"). A single column of the proposed type is made of four steel pipes, with shear panel between these steel pipe structures as depicted in Figure 3. A low yield strength steel LY225 web (shear) panel is used for the horizontal structural members, whereas steel material SM490Y is used in the flange sections, so that the cross-section is such that the horizontal structural members do not yield under the prescribed levels for a seismic event. The dimensions of Figures 3 and 4 were determined on the basis of the assumption that off-the-shelf spiral welded pipes would be used, since steel pipe piles have a proven track record. The steel pipes for the proposed type assume the following dimensions: diameter D = 1.5 m, thickness t = 25 mm, diametrical thickness ratio parameter Rt = 0.0781, and a net clearance between the steel pipes of the shear panels, L = 2.0 m.

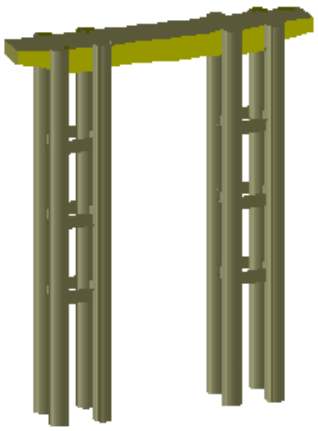

*Fig. 1: Steel pipe integrated Rahmen pier (Proposed Type)*

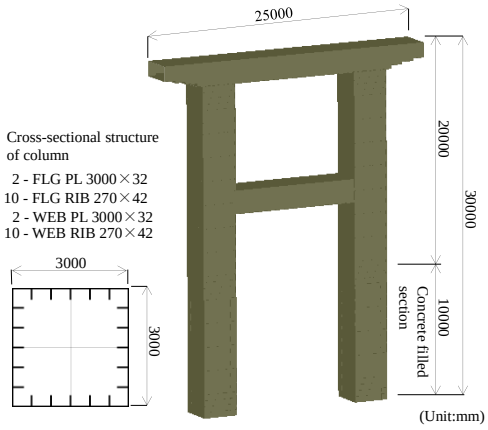


*Fig. 2: Rectangular cross-section steel Rahmen pier (Conventional Type)*

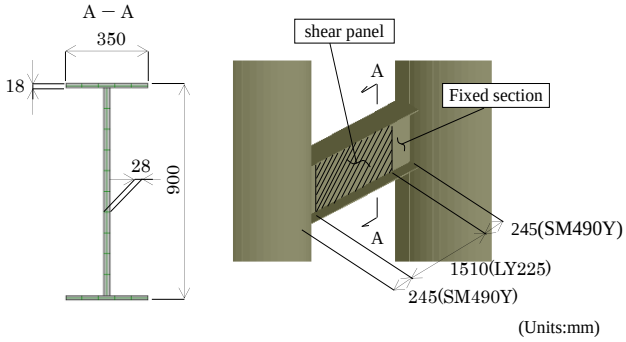


*Fig. 3: Structure of horizontal structural member*

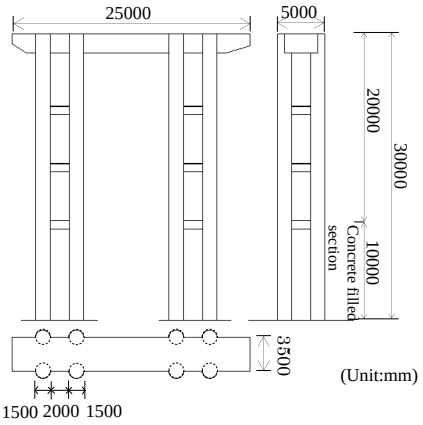


*Fig. 4: General diagram of steel pipe integrated Rahmen pier*

## 3 ANANALYSIS CONDITIONS

### 3.1 *Analysis model*

A comparative analysis was conducted with the conventional type in order to consider the seismic performance of the proposed type. A pushover analysis and a nonlinear time response analysis were used as analysis methods. These analyses were conducted in the longitudinal direction in which Rahmen structure type piers usually demonstrate a weaker seismic performance.

A model of the proposed integrated steel pipe Rahmen pier was created using a fiber model of the beam elements. The frame construction diagram for the model is shown in Figure 5 (a) and the fiber element division of the steel pipe cross-section is shown in Figure 5 (b). The structural stiffness of the upper rigid position between beams and pipes was created with an actual stiffness, whereas the lower stiffness was completely restrained. For comparison, a model of the rectangular cross-section conventional type was also made in a similar method using a fiber model of the beam elements.

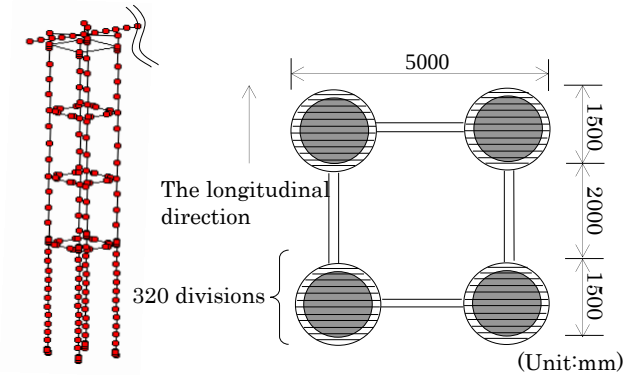


(a) Frame construction diagram (b) Cross-sectional division

*Fig. 5: Analysis model (framework diagram)*

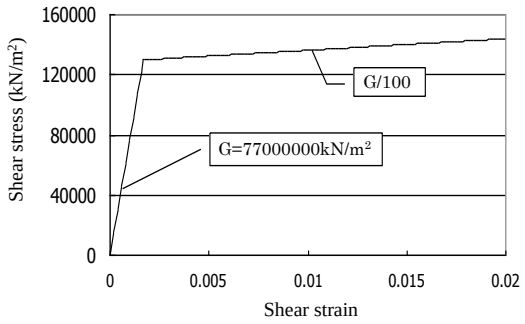


*Fig. 6: Relationship between shear stress and shear of shear panel*

### 3.2 *Material configuration rules*

With regards to the material configuration rules, those proposed in the document[2)] were used for SM490Y of the steel pipes, beams, horizontal structural member flanges, and the material of the filler concrete. For the dynamic analysis of the strain hardening of the steel materials, the bi-linear model, in which the secondary gradient should be 1% of the primary gradient, was used as the material configuration rule. A representation of the relationship between the shear stress and strain of LY225, used for the web plate of the horizontal structural members, is depicted as a bi-linear model in Figure 6.

### 3.3 *Analysis conditions*

A comparative analysis was conducted with the conventional type in order to consider the seismic performance of the proposed type. A pushover analysis and a nonlinear time response analysis were used as analysis methods. These analyses were conducted in the longitudinal direction in which Rahmen structure type piers usually demonstrate a weaker seismic performance.

A comparative analysis was conducted with the Conventional Type in order to consider the seismic performance of the Proposed Type. The pushover analysis and nonlinear time historical response analysis were used as analysis methods. Furthermore, these analyses were conducted in the longitudinal direction, which has a weaker seismic performance for Rahmen structure type piers.

#### 3.3.1 *Pushover analysis conditions*

A pushover analysis was conducted to investigate the deformation performance, load capacity, and plasticization rate. For the load, a dead load was applied in the vertical direction (axial force ratio P/Py = 0.08) and then a load was gradually increased in the horizontal direction. This horizontal load was applied in the longitudinal direction.

#### 3.3.2 *Nonlinear time response analysis conditions*

A response analysis was performed in the longitudinal direction, with the dead load acting in the vertical direction. This analysis was a time response analysis incorporating material nonlinearity. Three standard seismic waves, commonly used for road bridges, were used. Type III soil, a comparatively poor soil, was employed, while the Newmark-beta method of numerical integration ( $\beta = 1/4$) was adopted.

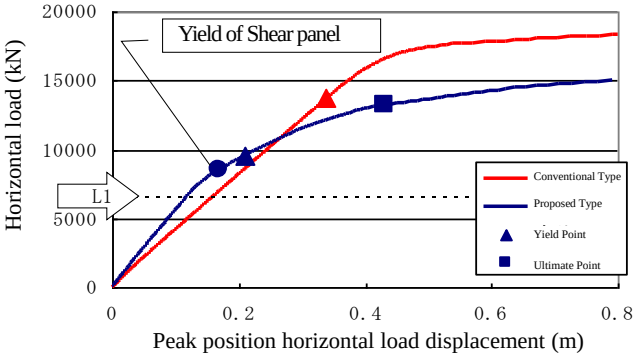


*Fig. 7: Pushover analysis result*

## 4 PUSHOVER ANALYSIS

The load–displacement curve resulting from the pushover analysis of the pier of the proposed type is shown in Figure 7. The design load for a Level 1 earthquake is also shown in the graph. The results are described below:

(1) The shear panels of the horizontal structural members did yield for the proposed type (blue line and markings), but only under a force larger than the load for a Level 1 earthquake. It was therefore shown that the proposed type will not yield when subjected to a Level 1 earthquake.

(2) The case of the conventional type is also shown in the graph (red line and markings). The initial rigidity of the proposed type is the same or exceeds that of the conventional type; this greater initial rigidity of the proposed type is because the external dimensions of the proposed type (Figure 5 (b)) were made larger than those of the conventional type (Figure 2), in order to satisfy the design load for a Level 1 earthquake, owing to the off-the-shelf steel pipes used in the proposed type, which have a limited range of available dimensions. The definition for the yield shown in the graph was determined when any part of the steel cross-section, other than the horizontal structural members, yielded.

(3) This diagram reveals that the ultimate load was approximately 13500 kN. Incidentally, in order to raise the ultimate load, either the rigidity of the shear panels had to be increased or the number of the shear panels had to be increased, whereas if the ultimate load had to be raised even further then a strategy to increase the thickness of the steel pipes could be conceived.

(4) The plasticization rate (ultimate displacement / yielded displacement) of the proposed type was 2.17, which was smaller than the 5.96 of the conventional type. The definition of ultimate points for the integrated steel pipes that comprise a single column is an issue for the future. The definition of ultimate points for a single circular cross-section steel pier, however, was adopted for this research. This became an evaluation for safety concerns. When considering the spread of ultimate points, the plasticization rate was believed to increase with an extension of the ultimate displacement due to the characteristics of the actual integrated steel pipe piers. The location of the critical strain on the cross-section when the pier reaches the ultimate point is shown in Figure 8, as a reference. This position is the entire width of the flange on one side with the conventional type, whereas with the proposed type this occurs in a small region on the circular cross-section.

(5) The condition of deformation at the ultimate point is shown in Figure 9 (a). The deformation diagram for the proposed type is shown with the actual deformation magnified ten times. The di-

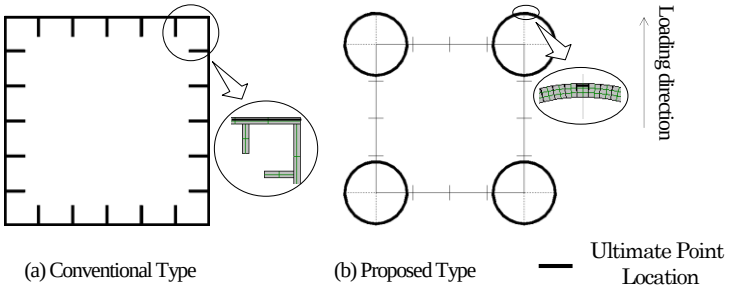


*Fig. 8: ultimate point locations*

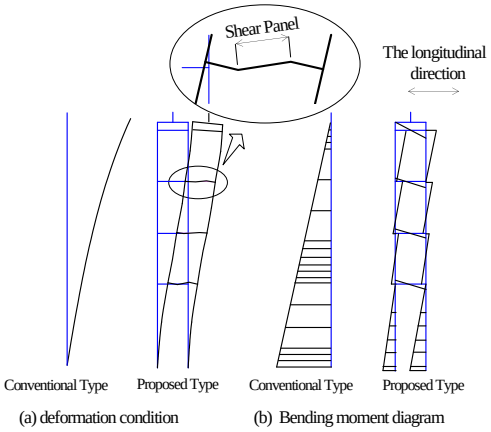


*Fig. 9: Behavior at ultimate point locations*

agram reveals that in comparison with the conventional type (with three times magnification, however), there was shear deformation as well and not only an overall bending deformation of the pier, which was due to the shear deformation of the shear panels.
(6) The bending moment distribution diagram for maximum deformation is shown in part (b) of the figure. The result of a separate calculation indicated that the bending moment affecting the base section was smaller than that of the conventional type steel pier.

## 5 NONLINEAR TIME RESPONSE ANALYSIS

### 5.1 *Natural period*

The natural periods of the conventional type and the proposed type are shown in Tables 1 and 2, respectively. A comparison of these tables reveals that the primary natural period of the proposed type is smaller. It also reveals that the secondary natural period of the conventional type is smaller than that of the proposed type, since there are intermediary beams with the conventional type. The dynamic behavior of the proposed type and the conventional type is in general quite similar with regard to the values and tendencies of their stimulation coefficients.

*Table 1: Natural period of the conventional*

| Mode Order | Period (s) | Frequency (Hz) | Stimulation coefficient | | |
|---|---|---|---|---|---|
| | | | transverse | longitudinal | Vertical |
| 1 | 1.482 | 0.675 | 0.0 | 49.1 | 0.0 |
| 2 | 0.435 | 2.297 | 49.2 | 0.0 | -0.9 |
| 3 | 0.364 | 2.746 | 0.0 | 1.8 | 0.0 |
| 4 | 0.104 | 9.653 | -5.1 | 0.0 | -39.8 |
| 5 | 0.088 | 11.389 | -5.5 | 0.0 | 29.7 |

*Table 2: Natural period of proposed type*

| Mode Order | Period (s) | Frequency (Hz) | Stimulation coefficient | | |
|---|---|---|---|---|---|
| | | | transverse | longitudinal | Vertical |
| 1 | 1.252 | 0.799 | 0.0 | 49.5 | 0.0 |
| 2 | 0.892 | 1.121 | 49.8 | 0.0 | 0.0 |
| 3 | 0.451 | 2.216 | 0.0 | 0.0 | 0.0 |
| 4 | 0.112 | 8.915 | 0.0 | 0.0 | -49.7 |
| 5 | 0.083 | 12.081 | 0.0 | 10.0 | 0.0 |

### 5.2 *Comparison of response displacements*

The maximum response displacements resulting from the nonlinear time response analysis conducted on the conventional type and the proposed type are shown in Table 3. The results of the analysis of the shear panels as linear components are also included in the diagram to show their damper effects in the proposed type. The location used for calculating the maximum response displacement was the site of the inertial impact on the superstructure. The table reveals that the maximum response displacement decreased with the proposed type from the conventional type down to 75%, in terms of the average for the three standard seismic waves. This is believed to

*Table 3: Comparison of maximum response displacement positions*

| Model | Seismic wave | Response displacement (m) | 3 waves average |
|---|---|---|---|
| Conventional Type | Ⅱ-Ⅲ-1 | 0.764 | 0.646 (1.00) |
| | Ⅱ-Ⅲ-2 | 0.670 | |
| | Ⅱ-Ⅲ-3 | 0.504 | |
| Proposed Type (No damper) | Ⅱ-Ⅲ-1 | 0.572 | 0.537 (0.83) |
| | Ⅱ-Ⅲ-2 | 0.783 | |
| | Ⅱ-Ⅲ-3 | 0.555 | |
| Proposed Type | Ⅱ-Ⅲ-1 | 0.504 | 0.483 (0.75) |
| | Ⅱ-Ⅲ-2 | 0.440 | |
| | Ⅱ-Ⅲ-3 | 0.507 | |

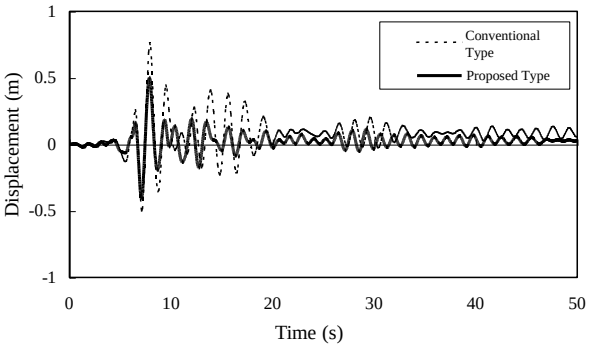


*Fig. 10: Displacement response history*

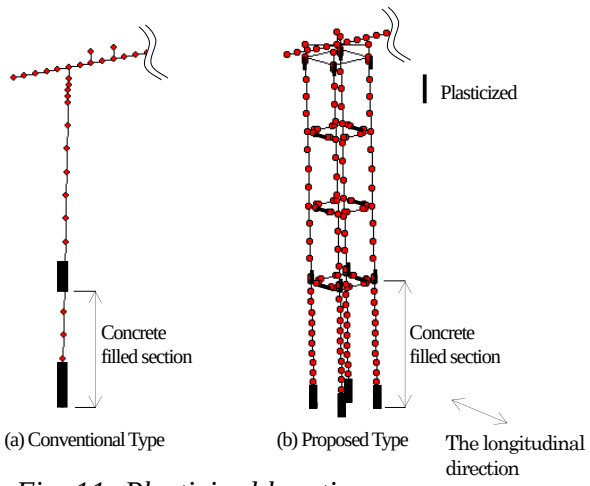


*Fig. 11: Plasticized locations*

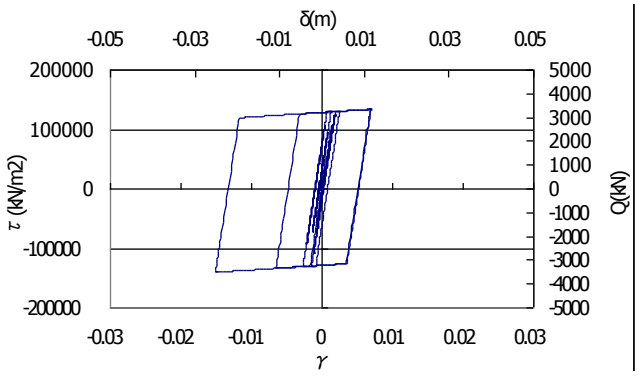


(a) Upper level shear panel

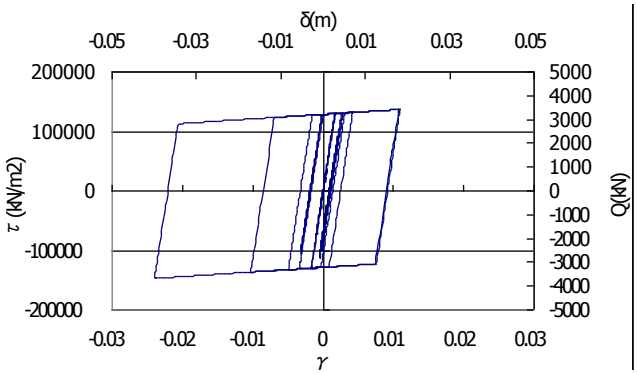


(b) Mid level shear panel

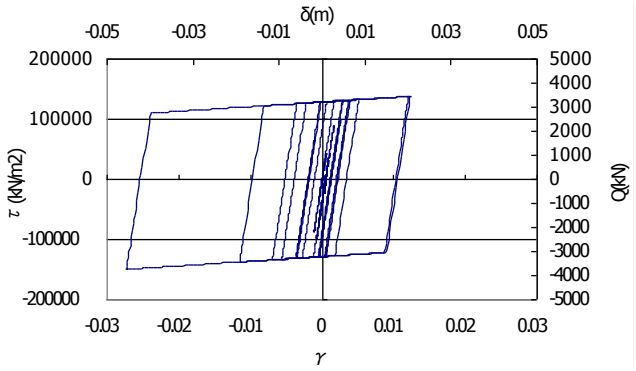


(c) Lower level shear panel

*Fig. 12: Hysteresis curve of shear panels*

have occurred due to two effects: (1) the proposed type had a higher rigidity than the conventional type and is therefore harder to deform; and (2) the energy was absorbed by the horizontal structural members. The response displacement positional history for the conventional type and the proposed type with a standard seismic wave II-III-1 is shown in Figure 10. This figure reveals that although the natural period varied (the natural period of the proposed type is smaller), the cyclical characteristics of the displacement response remained the same for the respective types. This is believed to be because the horizontal structural members and steel pipes of the proposed type yielded and increased the natural period, as described earlier.

### 5.3 *Plasticization conditions*

The plasticized locations for the proposed and conventional types are shown in Figure 11. Part (b) of the figure reveals that plasticization occurs at the base section of the proposed type pier, as well as at the steel cross-sections immediately above the concrete-filled segments, the upper sections of the pier, and the three shear panels. With the conventional type structure (Part (a) of the figure), the behavior is similar to a single-column structure, with plasticization occurring at the pier base section and the steel cross-section segments immediately above the concrete-filled segments. These imply that in comparison with the conventional type, the lesser plasticized structural elements are more widely distributed in the proposed type. This is because although Rahmen piers of the conventional type behave in a manner similar to a single-column pier in the bridge axis direction, the proposed type is, in fact, a Rahmen structure of a single column. The plasticization condition as described above is believed to be a reason why the proposed type has a smaller maximum response displacement than the conventional type.

### 5.4 *Analysis results of shear panels*

The response history curve for the shear stress and shear strain at the damper sections of the respective shear panels is shown in Figure 12. This figure reveals that each shear panels was plasticizing and absorbing energy. Plasticization had progressed even further with the damper installed in the lower section, where the maximum shear strain reached al-

most 3%. Plasticization of this extent is not considered to result in a fracture, even when a document3) is referenced. Furthermore, plasticization in the upper section is about half that of the lower section, indicating that plasticization was not taking place to the same extent. In this analysis, the optimum damper characteristics were not set for each horizontal structural member and the results were obtained with an identical damper with the same dimensions for all beams. This means that a further reduction in the response value is possible if the optimum characteristics are determined for the individual dampers.

### 5.5 *Comparison of absorbed energies*

The response histories of the energy absorbed by the individual segments of the conventional type and the proposed type are shown in Figure 13. This figure reveals that the dampers of the proposed type absorb about twice as much energy as absorbed by the main steel pipe body, demonstrating an efficient energy absorption by the dampers. Comparison of the proposed type with the conventional type, with a focus on the legs, indicates that the plasticity of the piers (i.e., the steel pipes) of the proposed type can be considered to be lower, being one-third that of the conventional type. A comparison of the hysteresis curves for the horizontal displacement and the horizontal load at the location of the inertial impact for the proposed type and the conventional type is shown in Figure 14. The maximum response displacement is smaller for the proposed type. Since bulging hysteresis curves are displayed, the area, which represents the absorbed energy, indicates that the energy absorption was relatively large for the response displacement. This can be considered to be resulting from the damper effects of the shear panels that are absorbing energy in an efficient method.

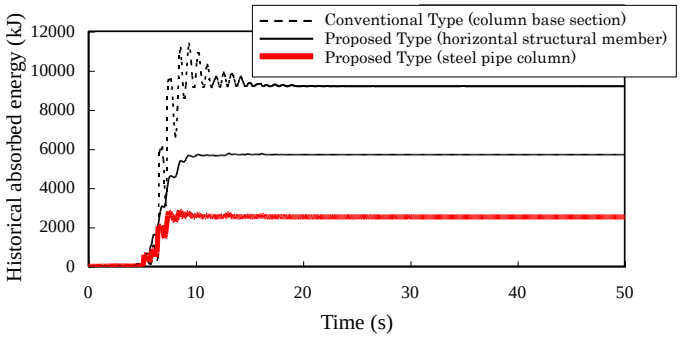


*Fig. 13: Historical absorbed energy*

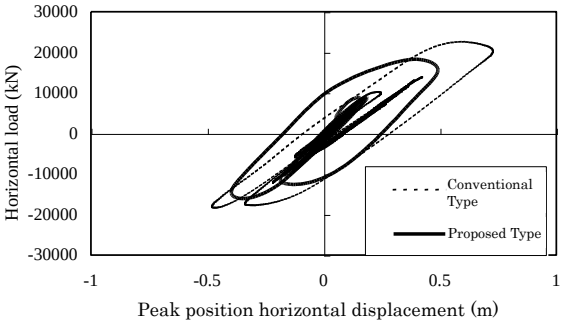


*Fig. 14: Hysteresis curve of entire pier sys-*

## 6 SUMMARY

The dynamic response characteristics of a new pier structure comprised of off-the-shelf steel pipes were evaluated. Comparisons were made with conventional standard steel piers so that the advantages could be fully considered. The following conclusions were made:

(1) A structure designed for damage control, preventing damage to steel pipes by the use of hysteretic damper effects is achievable using shear panels that join the pipes. Such a system has a basic performance equal to conventional steel piers with long legs.

(2) The steel pipe pier had a smaller response displacement at the top section during dynamic analysis, reduced down to about 75% of the conventional standard steel piers.

(3) Maximum shear deformation of the shear panels was about $\gamma = 3\%$ in the lower section, indicating stable hysteretic characteristics.

(4) Hysteresis damping of the shear panels significantly contributed to the response of the steel pipe piers and the steel pipe foundations, and significantly reduced the cumulative hysteretic energy.

## 7 REFERENCES


[1] Hanshin Expressway Company Limited: Guidelines for Seismic Resistant Design and Seismic Resistant Reinforcements for Steel Piers (Proposal), August 2003.

[2] Steel Bridge Seismic Resistance Subcommittee of the Performance-based Design Research Committee of the Japanese Society of Steel Construction: Fundamentals and Applications of Seismic Resistant Design for Piers, September 2002.

[3] Mai Amano, Tomohiko Watanabe, Tsutomu Usami and H. Ge: Strength and Ductility of Steel Plates Under Repeated Shear Force, Collection of Lectures from Third Collection of Papers on Nonlinear Numerical Analysis of Steel Structures and Application to Seismic Resistance Design, pp. 57 - 62, January 2000.

# Shake Table Experiment on Damage Free RC Bridge Column Using E-Defense

Manabu NAKAYAMA
*Principal Research Fellow, Hyogo Earthquake Engineering Research Center, National Research Institute for Earth Science and Disaster Prevention, Dr. Eng.*

Tomohiro SASAKI
*Research Fellow, Hyogo Earthquake Engineering Research Center, National Research Institute for Earth Science and Disaster Prevention, Dr. Eng.*

Richelle ZAFRA
*Grduate Sudent,* Tokyo Institute of Technology

Koichi KAJIWARA
*Deputy Director, Hyogo Earthquake Engineering Research Center, National Research Institute for Earth Science and Disaster Prevention, Dr. Eng.*

Kazuhiko KAWASHIMA
*Professor, Tokyo Institute of Technology, Dr. Eng.*

ABSTRACT: Now, the progress mechanism of failure that the covering concrete peeled out and the core concrete crushed is evaluated by the study about a typical flexural dominant column in the 1970s and typical column designed in accordance with the current design code based on the results of a large scale shake table experiments.

This paper presents preliminary results of a large scale shake table experiment for the development of high seismic performance RC bridge column using E-Defense.

## 1 INSTRUCTIONS

Serious damage occurred in RC bridge columns in the 1995 Great Hanshin-Awaji Earthquake. Bridge columns are important structures constituting transportation infrastructure in urban areas. They are also essential in reconstructing and assisting disaster areas.

In Hyogo Earthquake Engineering Research Center, National Research Institute for Earth Science and Disaster Prevention, shake table experiments on bridge columns has been carried out since fiscal 2007. In the experiment of fiscal 2007, a full-scale RC bridge column (bending-failure-type) designed by the former standard was used. In the experiment of fiscal 2008, a full-scale RC bridge column (shear-failure-type) designed by the former standard and the other one designed by the current standard were used.

According to the results of the experiments until now, earthquake motion significantly decreased the bridge column resistance because the concrete covering up from the reinforcing bar to the edge of the column (covering concrete) peeled out and the core concrete crushed.

Therefore, the experiment for fiscal 2009 aimed at developing a next-generation-type RC bridge column whose earthquake resistance exceeds that of the bridge column designed by the current standard. If bridge columns peel out, they will not fulfill their function, which will cause their users' inconvenience. Developing the next-generation-type bridge column will prevent such malfunction and inconvenience caused by a massive earthquake, which is beyond the simulation of the current standard.

In other words, the objectives of the experiment for fiscal 2009 are: keeping road service degradation to a minimum, approaching realization of a damage-free bridge column and putting the prototype of the next-generation-type bridge column into practical use.

## 2 OBJECTIVES

Since fiscal 2007, Hyogo Earthquake Engineering Research Center, National Research Institute for Earth Science and Disaster Prevention has carried out shake experiments on bridge columns in consideration of each objective and kind as shown in Table 1 and the relation between the objective and the kind.

As shown in Table 2, the shake table experiment for fiscal 2007 used a full-scale RC bridge column designed by the former standard (bending-failure-type) hereinafter called C1-1 (Photo 1). The experiment for fiscal 2008 used a full-scale RC bridge column designed by the former standard (shear-failure-type) and the other one designed by the current standard hereinafter called C1-5 (Photo 2).

Table1 : Objective of Experiments

| | |
|---|---|
| Component Experiments (C1) | to clarify the failure mechanism of reinforced concrete columns using models with as large section as possible |
| System Experiments (C2) | to clarify the system failure mechanism of a bridge consisting of decks, columns, abutments, bearings, expansions joints and unseating prevention devices |

Table2 : Full-scale Shake Table Experiments

| Fiscal Year | Specimen | Characteristic of Bridge Clolumns |
|---|---|---|
| 2007 | C1-1 | a typical flexure failure dominantcolumn which was built in the 1970s |
| 2008 | C1-2 | a typical shear failure dominant column which was built in the 1970s |
| | C1-5 | a typical column designed in accordance with the currrent design code |
| 2009 | C1-6 | an advanced column using polypropylene fiber reinforced cement composites(PFRC) for enhancing the damage control and ductility |

Damage at Kobe Earthquake

Cover concrete suffered and outer longitudinal bars buckled.

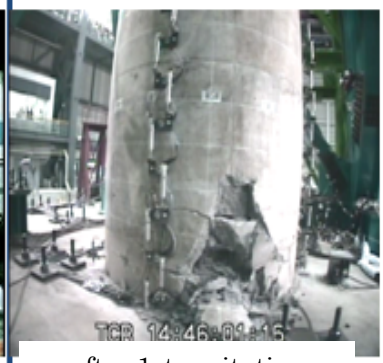

after 1st excitation

after 2nd excitation

Photo1: Damage progress of C1-1 at SW surface

According to the results of the above shake table experiments, the bridge columns' resistance against earthquakes was found to have decreased significantly because of the followings: peeling out of the concrete covering up from the reinforcing bar to the edge of the column (covering concrete) and crushing of core concrete.

Therefore, the experiment for fiscal 2009 aimed at developing a next-generation-type RC bridge column whose earthquake resistance exceeds that of the bridge column designed by the current standard. If bridge columns peel out, they will not fulfill their function, which will cause their users' inconvenience. Developing the next-generation-type bridge column will prevent such malfunction and inconvenience caused by a massive earthquake, which is beyond the simulation of the current standard.

The experimental subject was a full-scale bridge column designed by the current standard. In the column, fiber-reinforced mortar with high toughness, that is, mortar containing polypropylene fiber, was used in place of usual concrete so that strength in the base of a bridge column should increase. The column resistance was examined in the experiment.

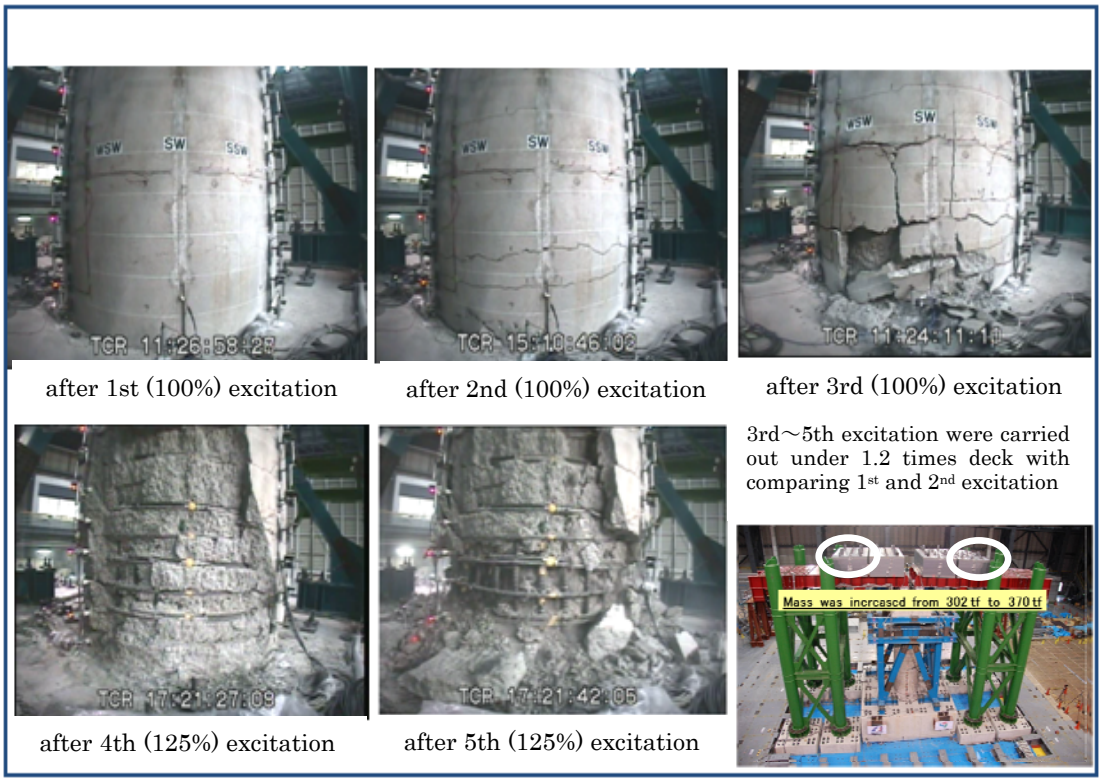


Photo 2：Damage progress of C1-5 at SW surface

## 3 BACKGROUND TO DECISION OF SPECIMEN

At first, the following three cases were mentioned as candidates. Using one-quarter-sized models in the three cases, preliminary experiments were performed in order to figure out their capacity.

- Case of using high-strength rebar (tensile strength: approximate 685N/mm$^2$) and high-strength concrete (60MPa at 28 days strength) in order to build a high-earthquake-resistant RC bridge
- The above case adding steel fiber reinforced concrete in the bridge basement
- The above case adding high-toughness fiber-reinforced cement composite in the bridge basement

As a result of the load experiments, the capacity was found to be the most excellent in the third case. So the results of the numerical analysis on the preliminary experiment were compared with the actual results of the preliminary experiment. As they were consistent, it was judged that the load experiment was reproduced well by the numerical analysis.

Next, simulation of a shaking experiment by numerical analyses was run. After reviewing the analysis results and the executability, it was concluded that the third case was the most excellent and executable.

Accordingly, a high-earthquake-resistant RC bridge shown in Fig. 1 (hereinafter called C1-6) was determined to be the experimental specimen in consideration of reduction of the whole cost expenses including those for construction.

## 4 EXPERIMENT

The specimen was a full-scale high-earthquake-resistant RC bridge (as shown in Fig. 2) , whose column measured 7.5m in height and whose base measured 7m long, 7m wide and 1.8m tall and whose gross weight was approximately 310t. As shown in Photo 3, the gross weight of the shake experiment unit on the table was over 1000t.

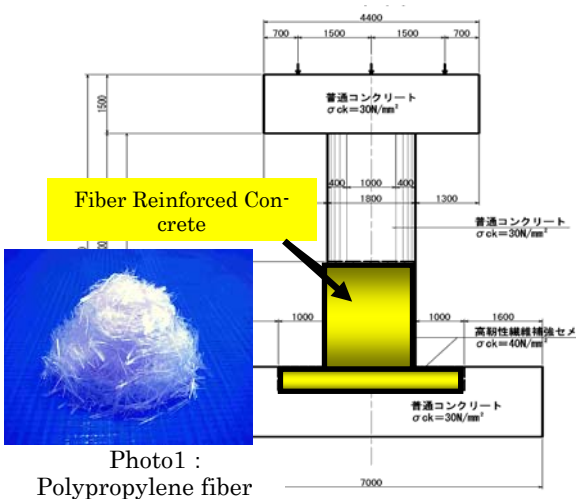


Photo1 : Polypropylene fiber

Fig 1 : Specimen C1-6

Photo3 : Experiment set-up on E-Defense shake table

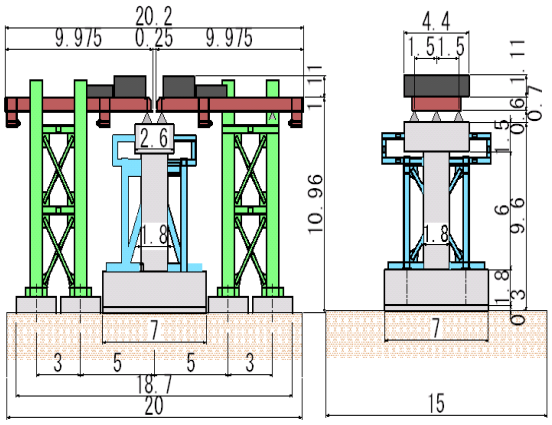


Fig2 : Set up of the model on E-Defense unit : m

The specimen was designed according to the current standard. It was also characterized by the followings: adopting fiber-reinforced mortar with high toughness, that is, mortar containing polypropylene fiber, with the purpose of increasing strength in the base of a bridge column, chamfering the corner of the column (R=400mm) and making the rectangle cross-section (Side=1.8m).

In order to reduce the gross experiment expenses, using fiber-reinforced mortar with high toughness, that is, mortar containing polypropylene fiber, was limited.

More specifically, the use of fiber-reinforced mortar with high toughness was limited to the yellow zone of Fig.1, on which damage will concentrate. Ordinary concrete ($\sigma_{ck}$ = 30N/mm$^2$) was used in the other places.

Furthermore, the design compressive strength of the fiber-reinforced mortar with high toughness containing polypropylene fiber was designed to be $\sigma_{ck}$ = 40N/mm$^2$. Compression tests, compression splitting tests and confined tension tests as shown in Photo 4 were conducted in order to figure out the characteristics of the materials. The results are illustrated in Table 3.

State of Test for Compressive strength of PFRC

State of Test for splitting tensile strength

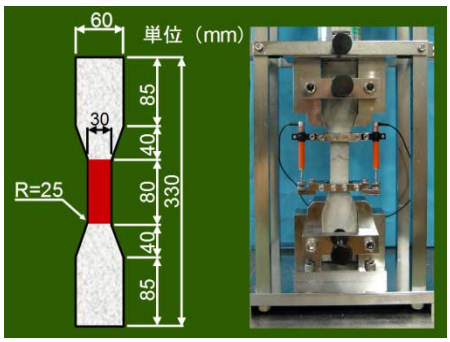


Specimen of test for tensile strength

Table 3：Results of TEST

| | | | |
|---|---|---|---|
| Compressive strength (N/mm2) | 7 days | 26.7 | |
| | 28 days | 38.4 | |
| Initial tangent modulus of elasticity (kN/mm2) | 7 days | 12.7 | |
| | 28 days | 15.5 | |
| Tensile strength (N/mm2) | 28 days | Cracking | 3.62 |
| | | Maximum | 5.64 |
| Tensile strength (N/mm2) | 28 days | yield | 2.00 |
| | | Tensile strength | 3.92 |
| | | final strain (%) | 2.52 |

| TEST | result | control value |
|---|---|---|
| Slump flow (mm) | 585 X 580 | 450～600 |
| Air (%) | 10.3 | 11±3 |
| Temp. of Mortar (℃) | 24 | 10～35 |

Photo 4：State of Test for PFRC

In addition, shaking tests on base isolation (high-damping rubber bearing as shown in Figure 3) were tried, too. In order to figure out the characteristics of base isolation, tension test were repeated before the shaking tests.

The specification of the base isolation used in this experiment is shown in Figure 4.

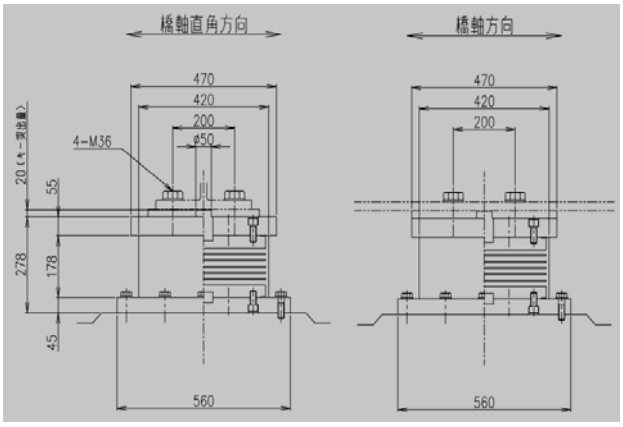


Fig.3：Section of Isolation Bearing　unit:mm

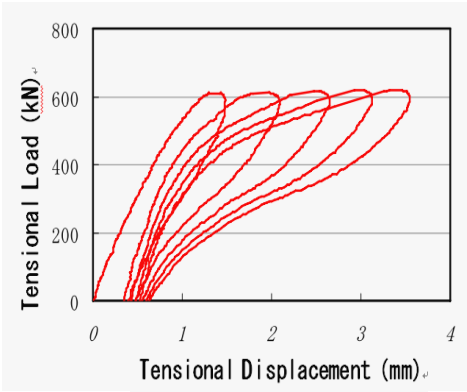


Fig：4　Results of Cyclic Stress-Strain Response Test

## 5 RESULTS

Testing equipment installed with the RC bridge column specimen shown in the center of Photo 3 was placed on the shaking table and shaken in three dimensions as shown in Table 4. Actual motion recorded at JR Takatori station during the 1995 Great Hanshin Awaji Earthquake was modified in consideration of its dynamic interaction effects. This 80% JR Takatori（E-Takatori）waves were used.

Next, the specimen was shaken using the 100 JR Takatori waves twice just as C1-5 was shaken. As a result, great damage didn't occur as shown in Photo 5.

After that, the maximum bearing force of the RC bridge column was examined. One shaking was carried out under the condition that the superstructure weight was increased by 21% and three shakings were carried out using the 125% Takatori waves. Though major cracks occurred as shown in Photo 6, mortar containing chemical fibers chipped little.

After shaking, the inside of the column marked by the red circle (as shown in Photo 7) was examined.

After all, cracking on the surface (10mm wide) didn't penetrate inside but just reached to the surface of the main reinforcement.

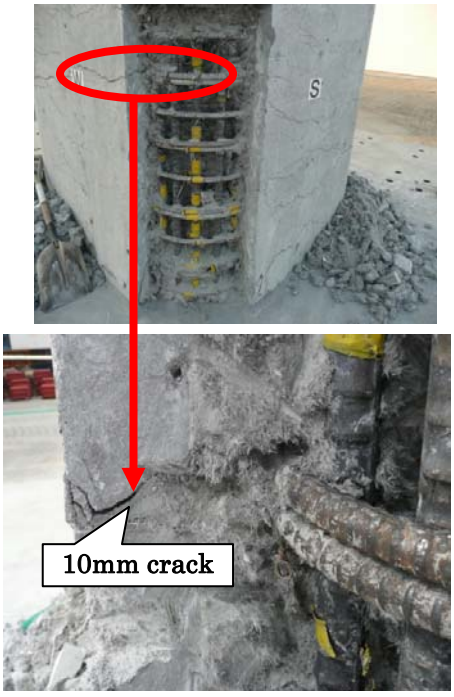


Photo 7 : Cut section and crack on PFRC cover

Table 4 : Summary of shake table excitations

| Condition of Bearing | Mass of Deck(tf) | Intensity of Excitation (vs E-Takatori) | | | | |
|---|---|---|---|---|---|---|
| Isolation | 302 | 10% | 20% | 30% | 40% | 50% |
| Fixed | 302 | 100% | 100% | | | |
| | 370 | 100% | 125% | 125% | 125% | |

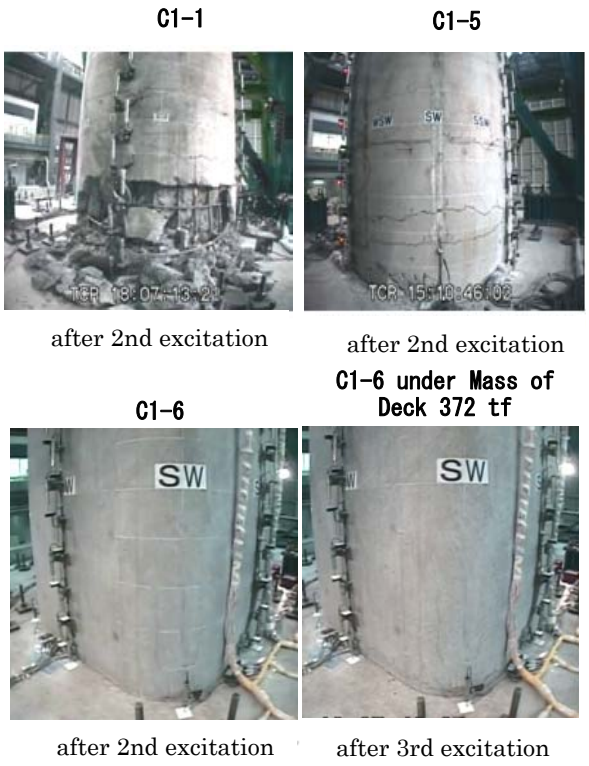


after 2nd excitation　　after 2nd excitation

after 2nd excitation　　after 3rd excitation

Photo 5 : Comparison between C1-1,C1-5


after 2nd (125%) excitation　　after 3rd (125%) excitation

Photo 6 : Results of excitations after adding Mass Deck to 372 tf

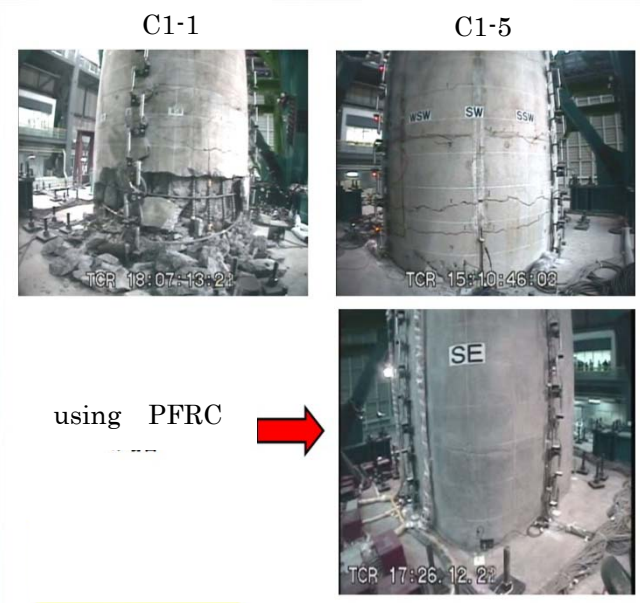


Table 5 : Comparison between C-1, C1-5 and C1-6 on relation of Lateral force and Lateral displacement

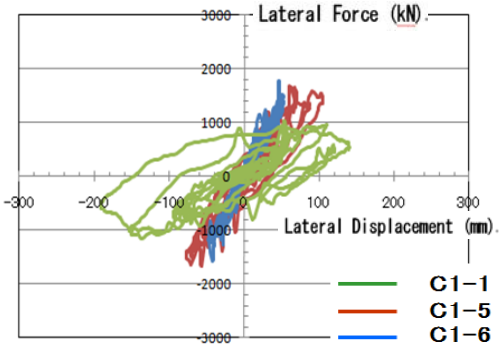


E-TAKATORI 100% 2nd (TR direction)

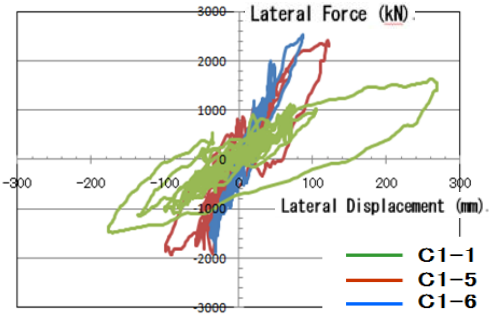


E-TAKATORI 100% 2nd (LG direction)


E-TAKATORI 125% 2nd

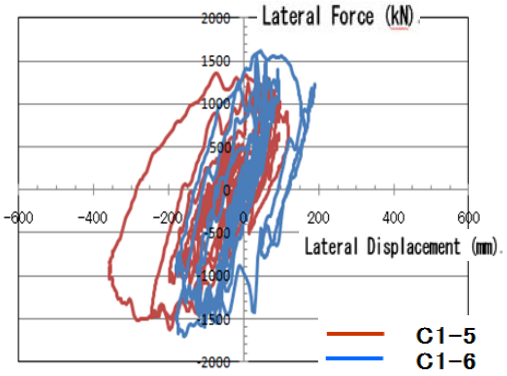


E-TAKATORI 125% 2nd (TR direction)


E-TAKATORI 125% 2nd

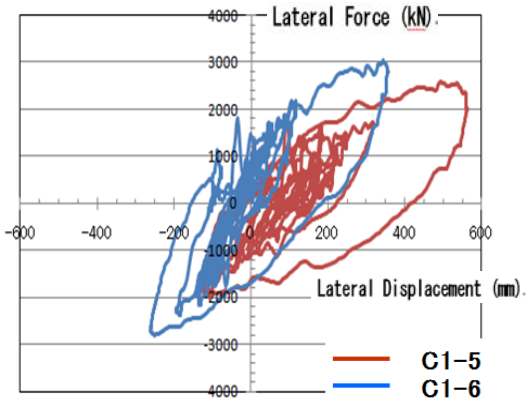


E-TAKATORI 125% 2nd (LG direction)

Table 6 : Comparison between C1-5 and C1-6 on relation of Lateral force and Lateral displacement after adding to 372 tf

## 6 CONCLUSION

The results of this experiment are summarized as follows;

1. Under the condition that the gross loading weight was 1.25 times as heavy as that during designing, the maximum shaking was repeated three times. After shaking, a crack appeared on the surface of the bridge column and was approximately 10mm wide. Deep penetration of the crack was not observed and the mortar containing chemical fibers chipped little.
2. Regarding the horizontal force shown in Table 5 and 6, the tilt which shows the time-history of the horizontal displacement was sharp, which means that the specimen in this experiment is closer to actual structures than those in the previous experiments (C1-1: Former standard. C1-5: Current standard).
3. Remarkable buckling of the main reinforcement wasn't observed. The buckling measured from 5mm to 8mm at a maximum. Judging from the situation of the main reinforcement, the bearing force of the structure is estimated to decrease little.
4. It was confirmed that the bridge column containing new materials in this experiment had high earthquake resistance, compared with commonly used RC structures.
5. The initial objective, that is, "developing a next-generation-type RC bridge column whose earthquake resistance exceeds that of the bridge column designed by the current standard", was fulfilled. As a result, the experiment established a milestone toward idealizing damage-free bridge columns.
6. From now on, it is necessary to reduce the cost of new materials, which is rather high, review equalization of the executability and consider bringing the column used in this experiment closer to a more reasonable one.

ACKNOWLEGMENTS : The E-Defense bridge project were formulated as a US-Japan cooperative research based on NEES and E-Defense collaboration.
These experiments were conducted based on the extensive support on over 80 personnel in the Overview Committee (Chair, Professor Emeritus Hirokazu Iemura, Kyoto University), Executing Committee of Large-scale Bridge Experimental Program (Chair, Kazuhiko Kawashima, Tokyo Institute o Technology), Analytical Correlation WG (Chair, Shigeki Unjoh, Research Coordinator for Earthquake Disaster Prevention Research Center for Disaster Risk Management National Institute for Land and Infrastructure Management), Measurements WG(Chair, Yoshikazu Takahashi, Kyoto University) and Dampers and Bearings WG (Chair, Masaaki Yabe, Chodai). Their strong support is greatly appreciated. Invaluable encouragement of Professor Stephen Mahin, University of California, Berkeley and Professor Ian Buckle, University of Nevada, Reno is also greatly appreciated.

REFERENCES

1) Kawashima, K., Sasaki, T., Kajiwara, K., Ukon, K. Unjoh, S., Sakai, J., Takahashi, Y., Kosa, K. and Yabe, M.: Seismic Performance of a Flexural Failure Type Reinforced Concrete Bridge Column based on E-Defense Excitation, Journal of JSCE, Vol. 65, No. 2, 2009, pp. 267-285
2) Nakayama,M., Kajiwara, K., Kawashima, K.: Shake Table Experiment on Damage Free RC Bridge Column using E-Defense, The 13th Japan Earthquake Engineering, Symposium (2010), pp.1322-1329
3) Zafra, R., Kawashima, K., Sasaki, T., Kajiwara, K. and Nakayama, M.: Stress-Strain Relation of Polypropylene Fiber Reinforced Cement Composites for use in Bridge Columns subjected to Earthquake Excitation, The 13th Japan Earthquake Engineering, Symposium (2010), pp.1298-1305

# Seismic Evaluation of a RC Rigid-Frame Arch Bridge Affected by Wenchuan Earthquake, May 12th, 2008, China

Z. Shi
*Graduate School of Kyushu Institute of Technology, Kitakyushu, Japan*

K. Kosa
*Kyushu Institute of Technology, Kitakyushu, Japan*

J. Zhang
*Jiangsu Transportation Research Institute, Nanjing, China*

H. Shimizu
*Nippon Engineering Consultants Co. Ltd., Fukuoka, Japan*

ABSTRACT: Xiaoyudong Bridge, a RC rigid-frame arch bridge, suffered enormous damage during the Wenchuan earthquake which occurred in Sichuan Province, China, on May 12th, 2008. According to the field damage survey conducted by the authors, structural information of Xiaoyudong Bridge is briefly summarized, as well as the information of nearby surface faults and the choice of seismic waves. Further, after presenting the characteristics of natural vibration, the results of dynamic analysis for single span (Span 4) are illustrated for the super structure and legs respectively. It has been found that the mid-span is the crucial point that will firstly suffer the yield, while the bottoms of inclined are also likely to suffer the yield due to the effect of axial force variation.

## 1 INSTRUCTIONS

The Wenchuan earthquake occurred in Sichuan Province, China, at 2:28 p.m. (Beijing time) on May 12th, 2008. It had the magnitude of 8.0 by CEA (China Earthquake Administration) and 7.9 by USGS (US Geographical Survey) (Kawashima et al. 2009). Reports have been published saying that nearly 1600 bridges suffered extensive damage due to this earthquake (Kawashima et al. 2009).

Authors conducted a detailed field damage survey of Xiaoyudong Bridge on September 27th, 2009, (as shown in Figure 1) which crossed Baishui River in Xiaoyudong Town on Peng-Bai Road. This bridge is a 189m long, 13.6m wide, 4 spans, rigid-frame arch bridge that was built in 1998. Rigid-frame arch bridge is a composite structural type of arch bridge and inclined rigid-frame bridge. According to Ren et al. (2008), this type of bridge is a high-order hyperstatic structure with horizontal thrust and has been abundantly built in China since 1980s, thanks to its advantages in construction, weight and appearance. Besides, the accumulative total span length of this type bridge is over 15,000 kilometers (Ren et al. 2008). However, the re-

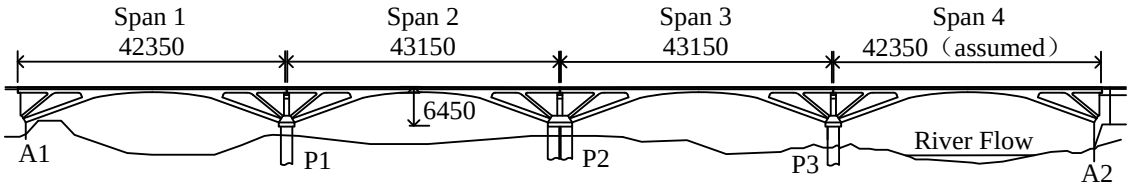


Figure 1. Overall elevation figure of Xiaoyudong Bridge (view from upstream before the earthquake, mm)

search for the behavior of rigid-frame arch bridges under natural disasters, as the earthquake effects, is still of great insufficiency.

Based on the field survey, bridge structure, bridge damage condition, and nearby surface faults, are presented in the following chapters. As well, dynamic analysis was conducted to examine the characteristics of seismic response of this type of bridge.

## 2 RESULT OF FIELD SURVEY

### 2.1 *Bridge structure*

Due to the lack of design drawings of Xiaoyudong Bridge, the detailed dimensions and the reinforcement information have been assumed based on the results of field survey by using measuring tape and total station, and referred from another rigid-frame arch bridge (Jinzhai No.6 Bridge, Anhui, China), which has almost the same characteristics with Xiaoyudong

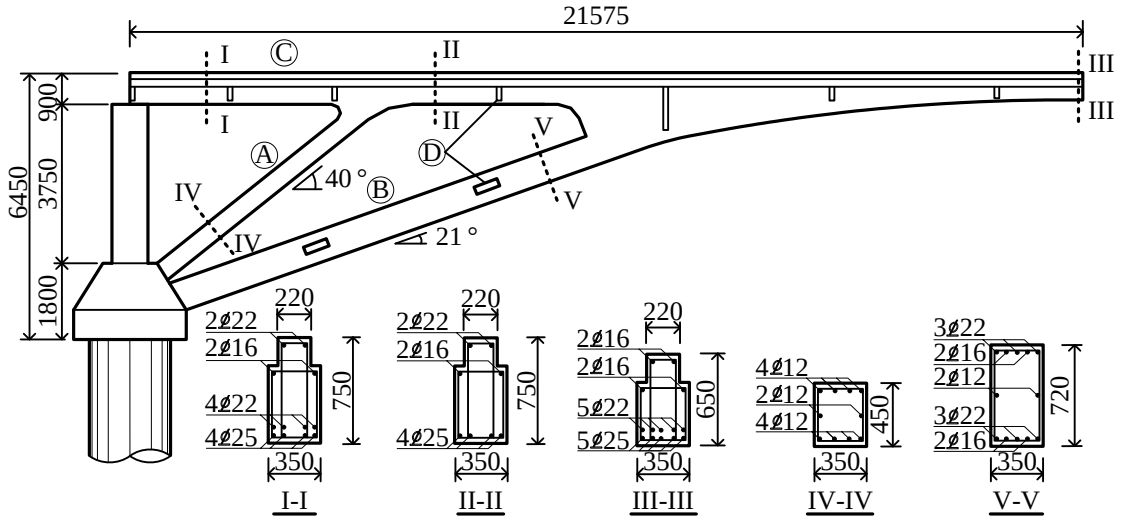


Figure 2. Elevation of half span and reinforcement in cross sections (mm)

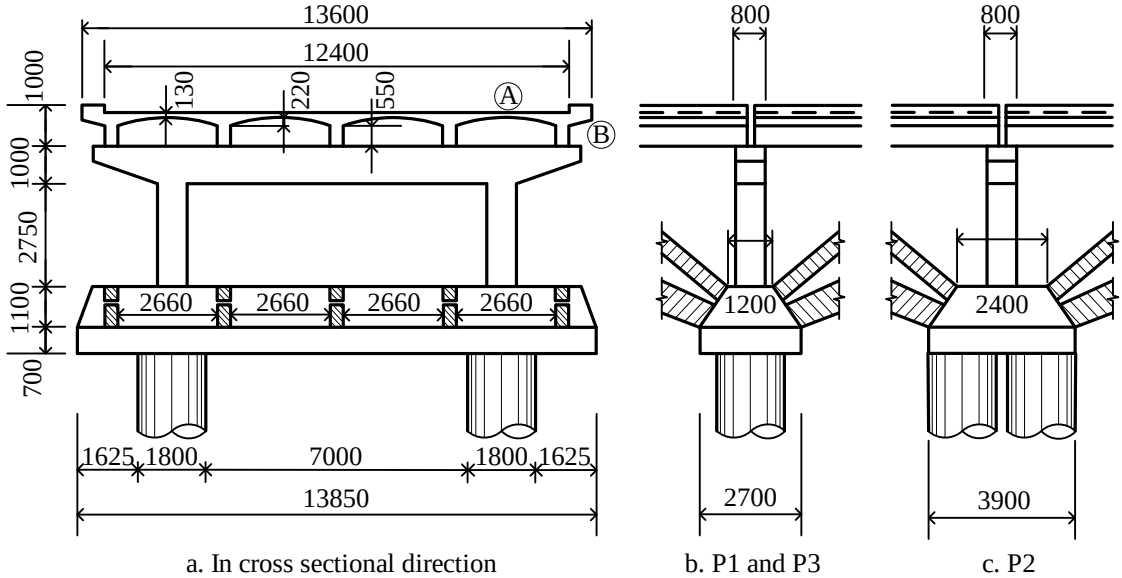


a. In cross sectional direction b. P1 and P3 c. P2

Figure 3. Elevation of piers in two directions (mm)

Bridge, as the span length, the rise, the width-girder ratio and the design seismic fortification (Anhui Communications Consulting & Design Institute, 2002). As shown in Figure 1, all abutments, piers and spans were numbered from the left bank. Therefore, Span 1 has a length of 42.35m, while Span 2 and Span 3 have the same length of 43.15m. However, because the river went through Span 4, and the girder fell into the water, it was impossible to measure Span 4. By noticed that Span 2 and Span 3 have a same length, we assumed Span 4 has same span length as Span 1 of 42.35m.

The detailed dimensions for half of Span 4 are illustrated in Figure 2 for instance. We can see that, the arch leg (Point A in Figure 2) and the inclined leg (Point B) has about 21 °and 40 ° slope respectively. The arch frame is formed by one arch leg from left pile cap, the corresponding one from the right cap, and the girder in the middle span. This arch frame composes one single rigid-frame, together with two inclined legs, and the girders (Point C) at the ends of deck. One span consists of five rigid-frames connected by several crossing beams (Point D in Figure 4), arch slabs (Point A in Figure 3), and extending slabs (Point B in Figure 3). Spans were connected by piers and abutments to form the entire bridge.

The detailed dimensions of piers are illustrated in Figure 3. A pier consists of a reinforced concrete moment resisting frame with two columns and a beam, upon which two decks were simply supported. The inclined legs and the arch legs from two decks next to each other were connected to a pile cap which was supported by reinforced concrete piles. There are two piles under Pier 1 and Pier 3 for each, and four piles under Pier 2, which causes that the capacity of Pier 2 is significantly greater than that of Pier 1 and Pier 3. Besides, because there was soil covering the bottom of abutments, whether there are piles under the abutments or not is still unable to know.

## 2.2 *Observed damage*

According to Hamada et al. (2010), there are two main surface faults after the earthquake as shown in Figure 4-a: Fault-1: Beichuan-Yingxiu Fault, and Fault-2: Guanxian-Jiangyou Fault.

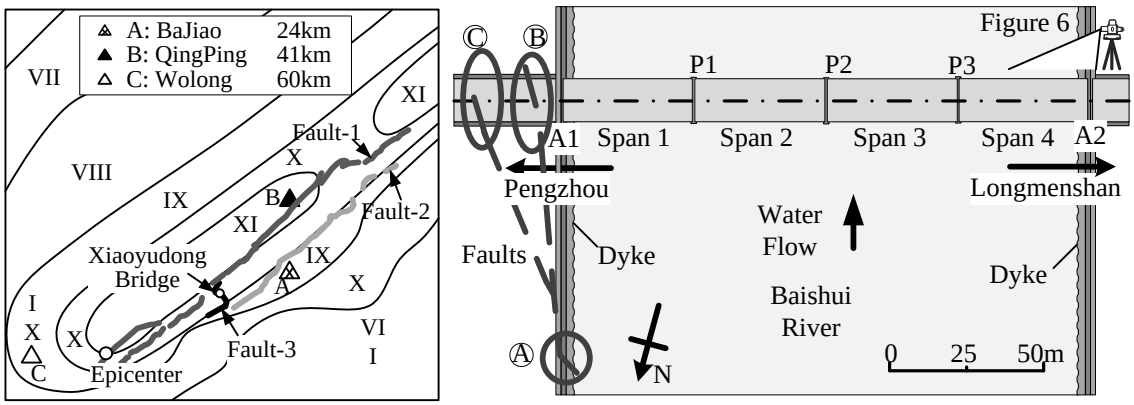


a. Nearby surface faults

b. Details of nearby surface faults

Figure 4. Surface faults nearby Xiaoyudong Bridge

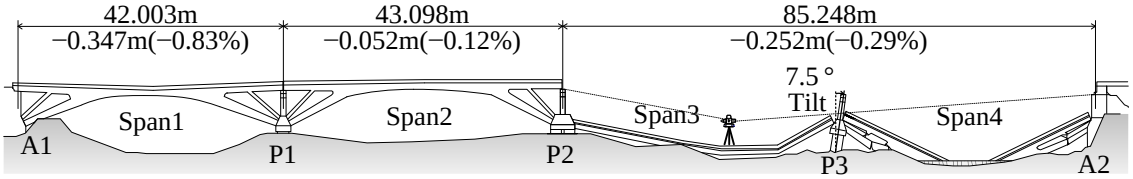


Figure 5. Changes of span length (view from upstream)

Another fault, Fault-3, named Xiaoyudong Fault connected these main two. Our objective bridge, Xiaoyudong Bridge was located between that two main surface faults and on this connecting Xiaoyudong Fault. Besides, according to Ma et al. (2009) and Kawashima et al. (2009), as shown in Figure 4-b, a surface fault went through the left dyke at about 70m upstream (Point A in Figure 4). This fault displacement extended to downstream along the left dyke and crossed the road at 10m (Point B) and 50m (Point C) behind A1. On the other hand, no obvious trace of surface fault has been found at the right dyke.

To confirm the influence of the surface faults, detailed field survey of the actual distance between P2 and A2 was observed by using electrical total station. Therefore, the change of span length was got as -0.252m (=85.248- 85.500). Thus, the average length change of Span 3 and 4 is about 12.6cm, which is relative small and may not have great influence to the failure. Similarly, the changes of span length were also got as -0.052m for Span 2, which is ignorable, and -0.347m for Span 1. Thus, it can be inferred that, the surface fault mainly effected on Span 1.

According to the field survey, shown in Figure 6-a (the position of observation is shown in Figure 4-b), Span 1 moved about 75cm downwards at middle span (Point A) and the girder collided into A1 (Point B) about 90cm, which consequently caused the shear failure of side wall (Point C). Because the settlement of A1, the arch legs collided with the revetment next to A1 (Point D), great shear failures occurred to the bottom of arch legs (Point E) and the top of inclined legs (Point F). Besides of this, some cracks occurred to the bottom of the legs (Point G) on Pier 1.

For Span 2, the damage is relatively slight that the middle span moved about 10cm upwards and some cracks have been observed at the bottoms of both inclined legs and arch legs.

As shown in Figure 6-b, Pier 3 (at Point A) tilted averagely 7.5 ° toward A2 (about 8.08 ° seeing from the upstream side and 6.85 ° seeing from the downstream side of the bridge, measured by the electronic total station). The piles under Pier 3 (at Point B) suffered great damage because of this tilt. Span 3 and Span 4 collapsed entirely, and the legs on them failed as well.

As shown in Figure 7, except the tilt of Pier 3, there is a 20cm permanent displacement of the support into backsoil (Point A) due to the collision between the girder and A2, and shear failure on the side wall (Point B). It should be noticed that at the joints of girder and arch legs, different types of failure occurred to left and right. On the left (view from downstream, Figure 8-a), by the negative moment, failure occurred because the reinforcement on the upside of girder resisted tension while the downside concrete resisted compression. Differently, the gird-

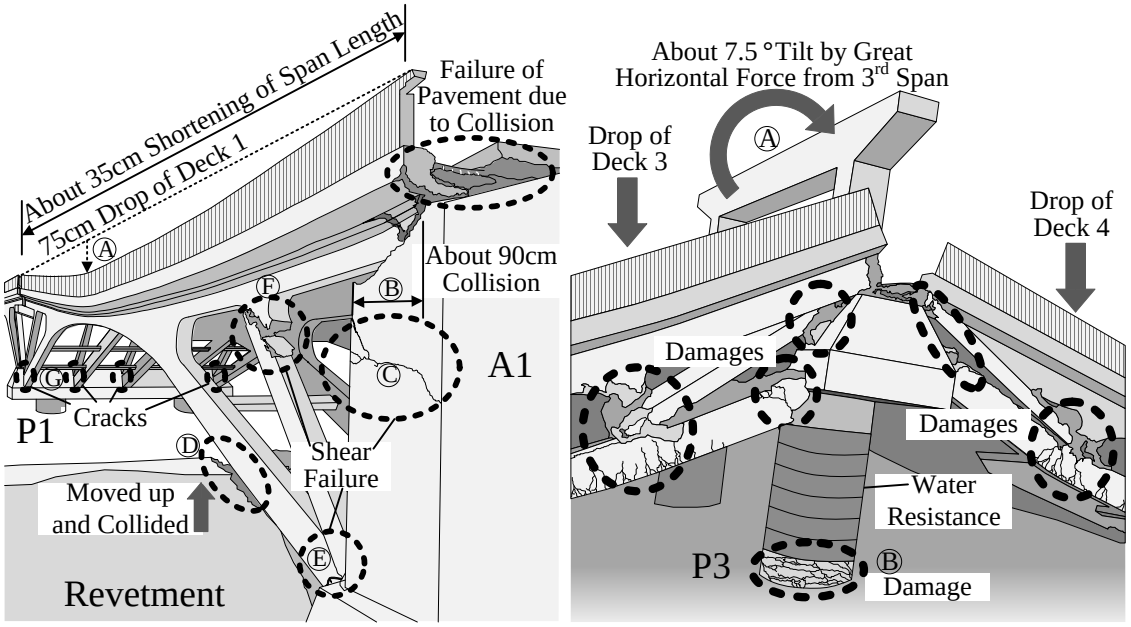


a. Joint at left (near to A2)

b. Joint at right (near to P3)

Figure 6. Damage condition of Span 1 and Pier 3

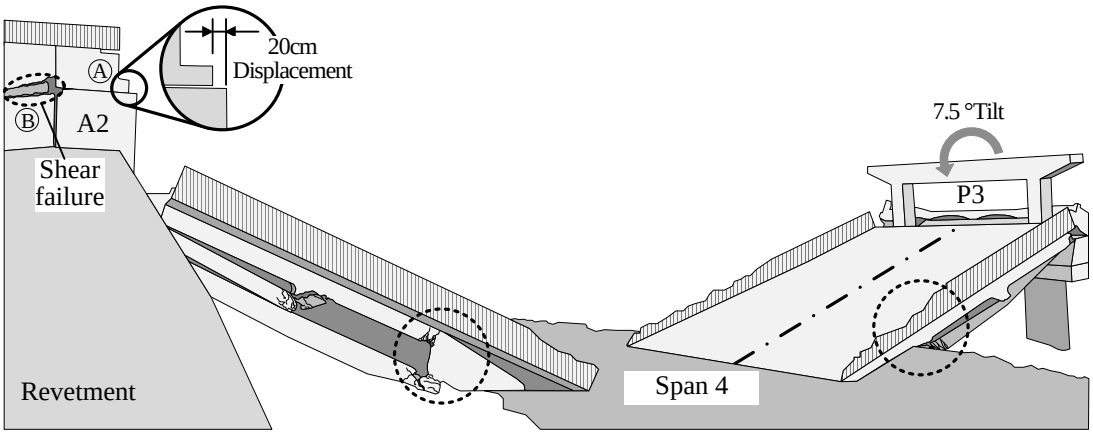


Figure 7. Damage condition of Span 4 (view from downstream)


a. Joint at left (near to A2) b. Joint at right (near to P3)

Figure 8. Details of failure at joints of girder and arch leg (view from downstream)

er on the right (Figure 8-b) was pulled by positive moment to separate from the joint, which caused extensive cracks at the joint.

## 3 ANALYTICAL CONDITION

### 3.1 *Analytical model*

The model has been made for Span 4 aiming at simulating its failure. As shown in Figure 9, noticing five arch frames on the right angle direction of the axis, here select one single arch frame, included the slab, to establish the two dimensional model.

Due to the insufficiency of the piles' information, a horizontal spring and a rotational spring with high rigidities have been directly set at the bottom of P3, ignoring the vertical displacement, and fix all three directions for A2, based on former researches. For the springs between girder and the pier, one frictional spring which is assumed to be comparatively weak, and one supporting spring are in use on P3. On the other hand, one collision spring with 5cm gap is used on A2, besides of the frictional and supporting springs as same as the ones on P3. Additionally, noticing relatively greater cross section area and greater amount of reinforcement, rigid elements have been set to the following parts: the footing, the beam on the top of the piers and the joints between legs and girder. Tri-linear M-Φ elements (defining the yield stage of the cross section as the tensile reinforcement reaches at $\varepsilon_y$, and the ultimate stage of the cross section as the compressive concrete reaches at $\varepsilon'_u$=0.0035) calculated based on Japanese Specifications

for Highway Bridges Part III Concrete Bridges (Japan Road Association, 2002) are used for the other parts.

### 3.2 *Characteristics of natural vibration*

The characteristics of natural vibration are listed in Table 1 and four dominant modes are shown in Figure 10. It can be found that the 1st and 7th modes are the dominant modes in the horizontal direction, while the 2nd, 3rd and 10th modes occupy over 84% of the effective mass in vertical direction.

Furthermore, the 1st mode has the natural period for the two dimensional model of Xiaoyu-dong Bridge is 0.6210s, and vibrates in the shape of first-order anti-symmetric with the mid-span point being the center of rotation. The vibration of the 2nd mode is controlled by the up-down movement at middle span. The vibration of the 3rd is mainly controlled by the movement of the arch legs and in the shape of second-order symmetric. The vibration of the inclined legs dominates the entire vibration of the 10th mode.

### 3.3 *Input seismic wave and analytical condition*

To choose the proper seismic wave for the following dynamic analysis, the locations of three seismic observing stations are illustrated in Figure 4-a as well. Firstly, since Station C (Wolong Station) was isolated from Xiaoyudong Bridge by two layers of surface fault, it is not suitable for the analysis. However, both Station A and Station B are located on the opposite side of

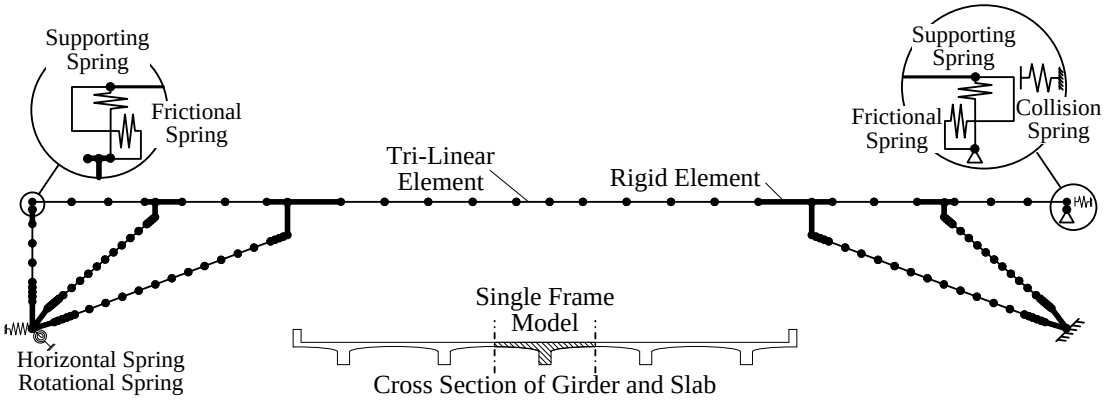


Figure 9. Analytical model for the side span

Table 1. Characteristics of natural vibration

| Order | | 1 | 2 | 3 | 4 | 5 | 6 | 7 | 8 | 9 | 10 |
|---|---|---|---|---|---|---|---|---|---|---|---|
| Natural Period | | 0.621 | 0.298 | 0.126 | 0.116 | 0.115 | 0.077 | 0.076 | 0.063 | 0.062 | 0.057 |
| Percentage of Effective Mass (%) | x | 20.8 | 0.0 | 0.0 | 1.1 | 4.0 | 1.3 | 13.9 | 9.7 | 1.6 | 2.9 |
| | z | 0.0 | 28.5 | 41.7 | 0.0 | 0.0 | 0.2 | 0.0 | 0.3 | 0.8 | 14.3 |

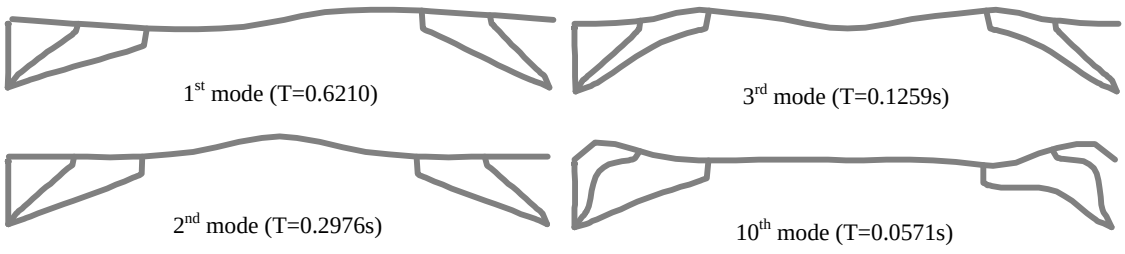


Figure 10. Dominant modes of natural vibration (deformation being 20 times enlarged)

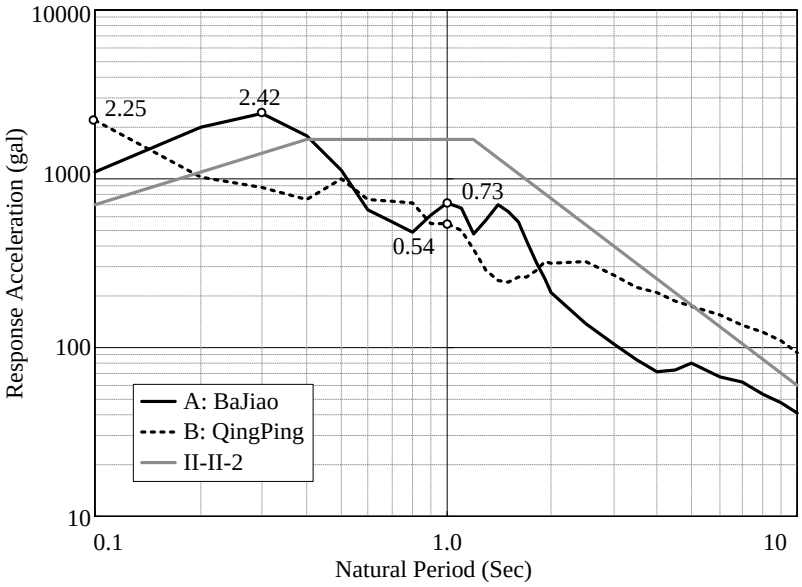


Figure 11. Responding acceleration spectra (E-W)

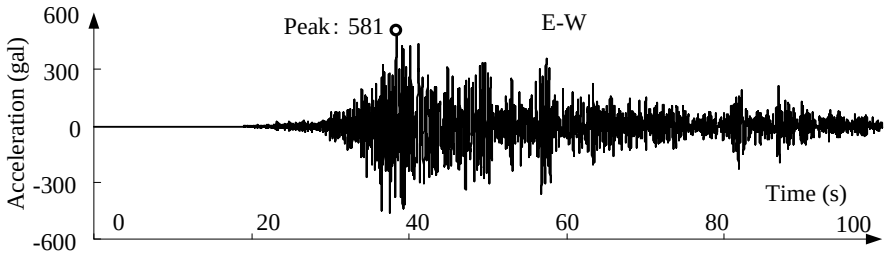


Figure 12. Input seismic wave data(E-W direction, by Bajiao Station)

Xiaoyudong Bridge by Fault-1 and Fault-2 respectively. Then the response acceleration spectra, as shown in Figure 11, are used to make comparison of the seismic wave by these two stations (since the direction of Xiaoyudong Bridge is approximately along East-West, only the E-W opponents of the response acceleration were presented). Thus, the choice of seismic wave by Station A is made considering the following reasons: (1) the seismic wave by Station A (Bajiao Station) has greater response accelerations (730gal) at 1.0 sec, and greater maximum response acceleration (2420gal), compared with the accelerations of 540gal and 2250gal by the seismic wave by Station B (Qingping Station); (2) smaller distance from the Xiaoyudong Bridge of 24km. Besides, compared with the standard seismic waves (Type II, Ground II, Level 2 for instance) by Japanese specification, the seismic wave by Station B will probably influence more strongly on the structures with lower natural period.

2% is used as the damping coefficient for all elements. Rayleigh damping is used for the structure of the 1st and the 10th modes. For the calculation, Newmark-β (β=1/4) method is applied in the numerical integration with the time step being 1/1000s.

## 4 ANALYTICAL RESULTS

### 4.1 *Examination of girder*

Based on the dynamic analysis, the sequence of yield stage is summarized and showed in Figure13-a, because no element reaches at its ultimate stage. We can see that, the girder near the

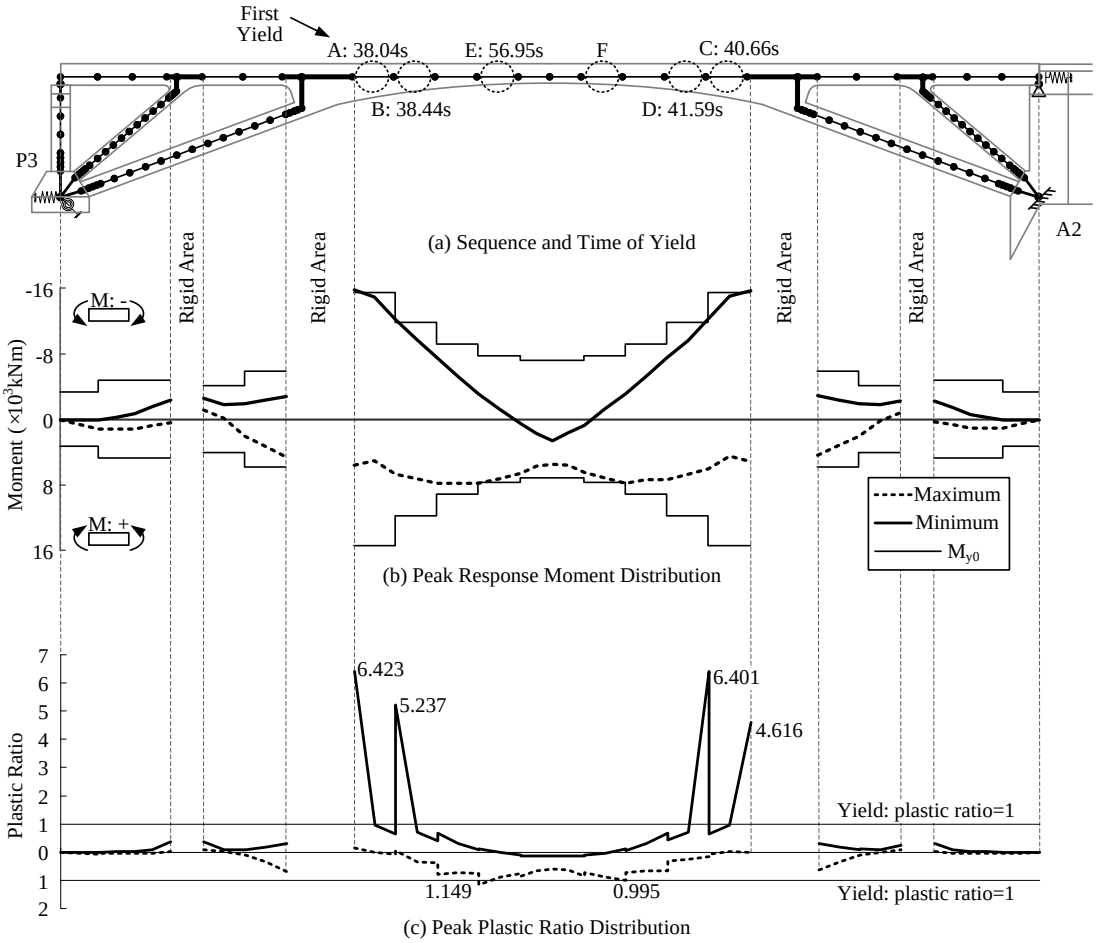


Figure 13. Analytical result of girder

joint with arch legs in the middle span are the weakest points where failures occur. Yield of cross section occurs to the girder next to the joint with left arch leg (Point A in Figure 13-a) at 38.04s at first, followed by the adjacent point at 38.44s (Point B). Then, yield occurs to the symmetrical points at the right side at 40.66s (Point C) and 41.59s (Point D). At last, the Point E, to the left the exact mid-span, reaches at yield stage by negative moment.

As the peak response moment distribution along the girder shown in Figure 13-b, we can see that the exact middle span point suffers negative moment continuously, while the other points in the middle span suffer changeable moment in both positive and negative direction. Furthermore, except that 5 points mentioned above which reach yield stage, Point F, the symmetrical

$$\mu_{\max} = \phi_{\max} / \phi_y \tag{1}$$

point to Point E is close to the yield stage as well.

where, $\mu_{max}$: peak plastic ratio; $\Phi_{max}$: peak response curvature; $\Phi_y$: yield curvature.

By using equation above, the distribution of the peak plastic ratio along the girder has been got and explained in Figure 13-c, from which following phenomena become obvious to us: (1) Point A suffers most serious failure beyond the yield stage, judged by its greatest plastic ratio of 6.423; (2) Point B, C and D also suffer extensive failure beyond the yield stage with the plastic ratios vary from 4.616 to 6.401; (3) Point E has the smallest plastic ratio of 1.149, which infers that the failure does not develop noticeably after the yield; (4) Point F, the symmetrical point to Point E, is considerably close to the yield stage as the plastic ratio reaches at 0.995 by negative moment.

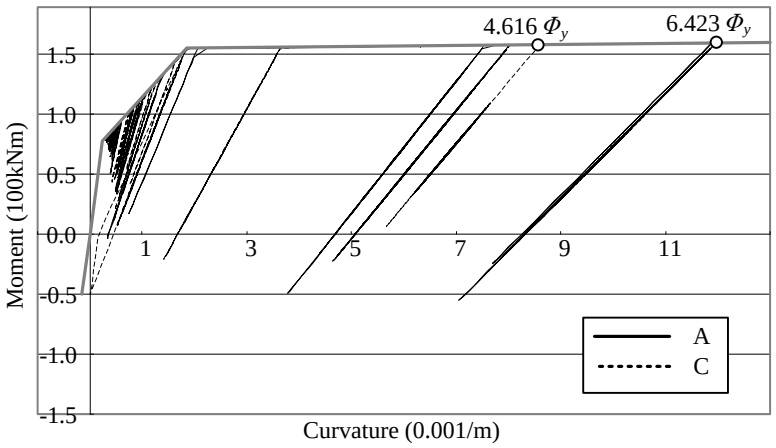


Figure 14. M-Φ Histories of Mid-Span Elements

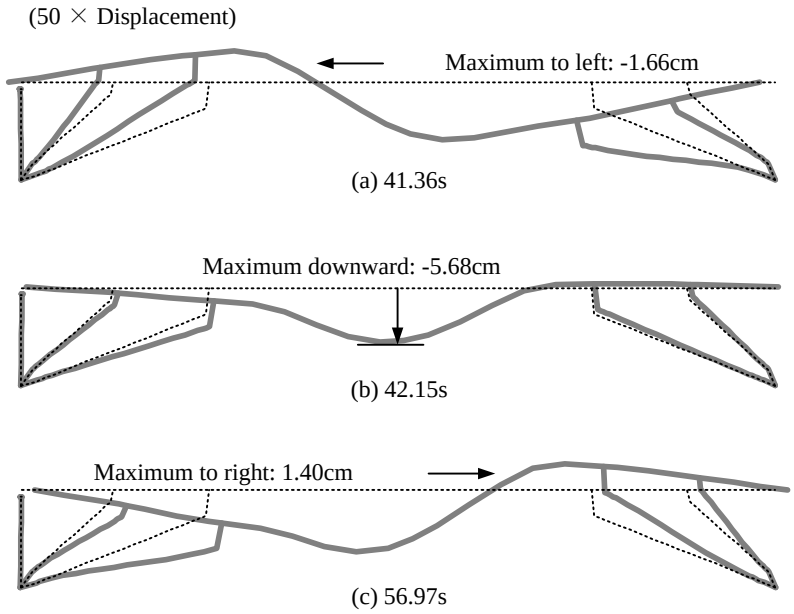


Figure 15. Deformation at peak displacements of mid-span

Besides, from the M-Φ histories of Point A and C, two symmetrical points next to the joints with arch legs, shown in Figure 14, the phenomenon that failures keep developing noticeably.

Equally important are the deformations of the structure, which are illustrated in Figure 15 at the peak displacement points. (a) and (c) show the maximum displacement in horizontal direction for the left side and right side respectively, from which we can see that the 1st mode mainly controls the deformation at peak horizontal displacement, but the displacement values (-1.66cm to the left and 1.40cm to the right) are too small even to reach the length of gap of 5cm between the girder and the abutment. On the other hand, as shown in Figure 15-b, the downward displacement of middle span point only reaches at 5.68cm at maximum, which suggests entire collapse does not occur to the bridge.

The axial force in the girder only changes slight in the range between -15% and +20%, which consequently has no considerable influence on the failure.

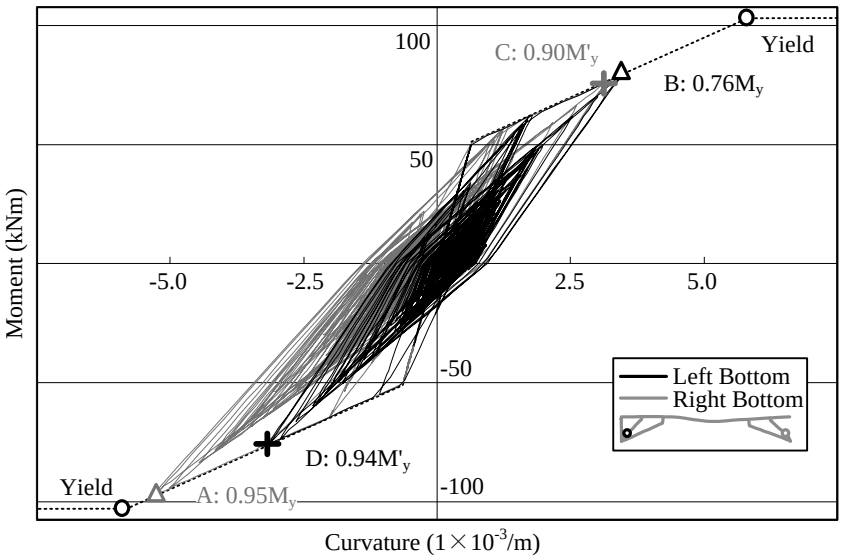


Figure 16. M-Φ Histories at Bottoms of Inclined Leg

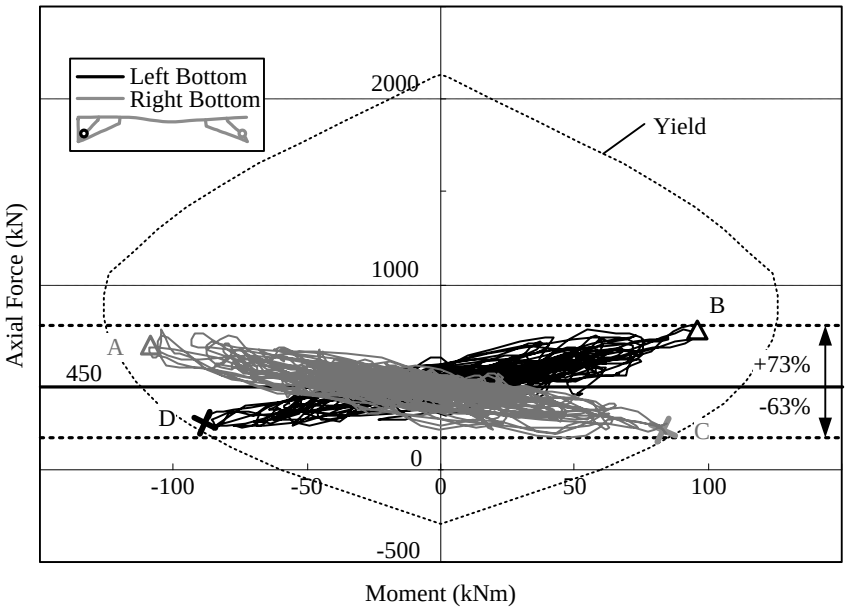


Figure 17. M-N Histories at Bottoms of Inclined Leg

## 4.2 *Examination of legs*

As to the inclined legs, it has been found that the bottoms of both sides suffer greater response moment than the tops. The M-Φ histories at bottoms are shown in Figure 16. According to this result, although no yield stage has been reached, the response moment of the inclined leg adjacent to A2 reaches at 0.95 My (Point A in Figure 16), which is more noticeable than that of the inclined leg adjacent to P3 of 0.76 My (Point B).

Nevertheless, during the horizontal seismic wave acts on the bridge, not only the response moment develops, but the axial force in the cross section of inclined legs varies considerably (from -63% to +73% compared with the axial force under only dead load, shown in Figure 17). For this reason, the effect of M-N relationship should be examined for them. The M-N histories at bottoms of inclined legs and the yield curve considering the M-N effect are illustrated in

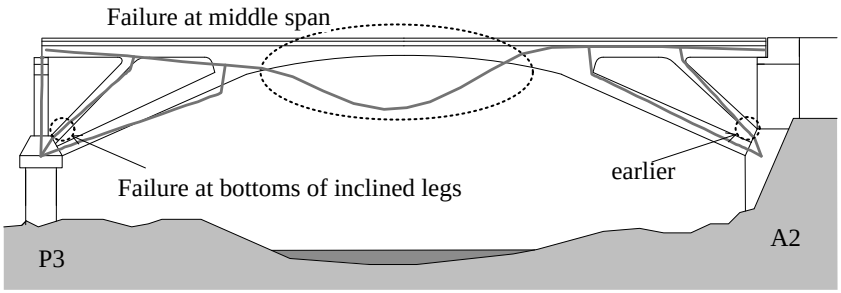


(a) Failure Based on Analytical Result

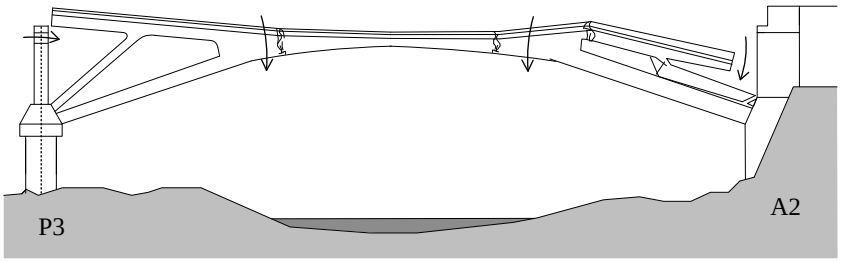


(b) Further Failure Imaged from Analytical Result

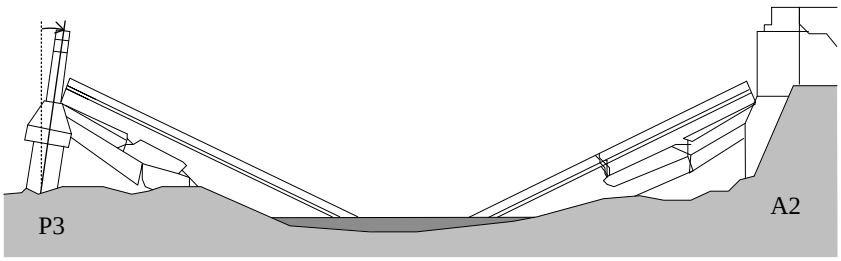


(c) Actual Failure

Figure 18. Geometrical relationship of rotation

Figure 17. For instance, at the left bottom of inclined leg, although the peak response moment is only about 0.76 My at the positive side (Point B), it reaches at 0.94 M'y (defined as the yield moment under the changed axial force) at the negative side (Point D). Similarly, the right bottom also reaches noticeable level about 0.90 M'y (Point C). Thus, the failure can be worsen by the variation of axial force, which makes the bottoms of inclined leg the weak point as well as the middle span where probably suffers failure. Besides, judged by positive and negative sides respectively, the failure at the right bottom of inclined leg is earlier and more serious than that of the left bottom (positive side: 0.90>0.76; negative side: 0.95>0.94).

On the other hand, although the axial force in the arch legs also changes obviously from -32% to +53%, both the top and the bottom of theirs still have not reached at 0.6 times of the yield moment.

### 4.3 *Comparison with actual failure*

As shown in Figure 18-a, from the examinations on the result of dynamic analysis, it becomes obvious to us that yield stage may firstly occur to the girder at middle span near the joint with the arch legs, and then trend to exceed towards middle. Bottoms of inclined legs also have high possibility to suffer yield, while the legs on A2 side may fail earlier. Then, imaged based on this, as being shown in Figure 18-b, if the seismic effect acts on the structure more strongly, further drop at middle span, and the downwards rotation of legs may occur. Meanwhile, the

earlier failure at the right bottom of inclined leg may cause the fall of girder at the right end before the middle span. Thus, the entire collapse may happen, similar to what has been found in the actual failure (in Figure 18-c).

However, the horizontal displacement of girder is relative small in the analysis, no greater than 2cm in both directions, which is even too small to reach the gap of 5cm between deck and abutment. This phenomenon can not coincide with the trace of the collision between the deck and the A2 and the 20cm permanent displacement, mentioned in Fig.6. If the horizontal displacement and the collision were caused mainly be the tilt of P3, the fail of the deck of Span 3 should be earlier than that of Span 4. Nevertheless, based on the eyewitness testimony of some local farmers, the deck of Span 4 dropped at first.

Following reasons may cause the analytical result differed from the actual failure: (a) Utilization of seismic wave: As a special type of arch bridge, vertical component of the seismic wave may probably have a great effect on Xiaoyudong Bridge, while only the horizontal seismic wave is being input in the current analysis. (b) Disregard of the foundation displacement: Since the pier and the abutment might have different response displacement due to the earthquake, it might influence on Span 4 as well.

## 5 CONCLUSIONS

From the field survey and the dynamic analysis, the following conclusions have been drawn:
(1) According to the field survey, the extensive collision occurred between A1 and the deck of Span 1, and between the revetment and the arch legs on A1. On the right side, Pier 3 tilted about 7.5 °averagely towards A2, and Span 3 and Span 4 collapsed entirely.
(2) The dynamic analysis shows that the girder at middle span is the weakest point of the structure. The variation of axial strongly influences on the failure at bottoms of inclined legs, that the failure is more likely to occur to them if take the M-N effect into consideration.
(3) The failure mechanisms based on the analytical result can roughly coincide with the actual failure. However, there is the gap about horizontal displacement of the girder between the result and the actual failure of Span 4, that no collision has been found in the analysis. The utilization of the seismic wave, as well as the disregard of foundation displacement, might be the possible reasons.

## REFERENCES


Kawashima, K., Takahashi, Y., Ge, H., Wu, Z., & Zhang, J. 2009. Reconnaissance Report on Damage of Bridges in 2008 Wenchuan Earthquake, China. *Journal of Earthquake Engineering*, Vol.13: 965-996

Ren, H., Li, W., Zhang, J. & Chen, H. 2008. Inspection and Design Suggestion on Rigid-Frame Arch Bridge. *the 1st Chinese-Croatian Joint Colloquium on Long Arch Bridge*: 309-315

Anhui Communications Consulting & Design Institute. 2002. *Design Drawings and Construction Illustration of Jinzhai No.6 Bridge*

Hamada, M. & Wu, X. 2010. The 2008 Wenchuan Earthquake Caused Damage and Japan-China Cooperation for the Recovery and Reconstruction. *Proc. of the 13th Japan Earthquake Engineering Symposium*: 55-59

Ministry of Construction; General Administration of Quality Supervision, Inspection and Quarantine of the People's Republic of China. 2002. *Code for Design of Concrete Structure, GB50010-2002*. Beijing

Ministry of Transport of the People's Republic of China. 2004. *Code for Design of Highway Reinforced Concrete and Prestressed Concrete Bridges and Culverts, JTG D62-2004*. Beijing

Ministry of Transport of the People's Republic of China. 2008. *Guidelines for Seismic Design of Highway Bridge, JTG/T B02-01-2008*. Beijing

Ma, G. Murata, Y. & Yashima, A. 2009. Damage Analysis of Geo-Structure in 2008 Wenchuan Earthquake. *Proc. of International Conference on Earthquake Engineering—the 1st Anniversary of Wenchuan Earthquake*: 607-614

Japan Road Association. 2002. *Specifications for Highway Bridges Part V Seismic Design*. Tokyo

Japan Road Association. 2002. *Specifications for Highway Bridges Part III Concrete Bridges*. Tokyo

# Method of Evaluating Average Shear Wave Velocity for Levees Based on Microtremor Measurement

A. Mikami
*The University of Tokushima, Japan*

ABSTRACT: This paper studies the feasibility of evaluating average shear wave velocity for levees by using microtremor measurement. Microtremor measurement is carried out on the crest and toe of the levee embankment simultaneously by placing servo-type velocity sensors perpendicular to the levee axis. Then, transfer functions are calculated using the horizontal motions. Finally, overall shear wave velocity structure is identified so that the peak frequency of the transfer function and the fundamental frequency of finite element model of the levee that has the same cross section coincide. The identified shear wave velocities are mostly consistent with shear wave velocities estimated based on SPT blow counts.

## 1 INTRODUCTION

The 2011 Tohoku earthquake caused a lot of damage to levees embankments. As of May 5, a total number of 2,115 levees were reportedly damaged among levees under jurisdiction of the Japanese Ministry of Land, Infrastructure, Transport and Tourism jurisdiction (2011). Damage occurred simultaneously in wide spread regions of Tohoku and Kanto.

We may have had an idea that damaged levee embankments may simply be fixed if they are damaged by an earthquake, since earth structures can be relatively easily restored. However, this idea is not applicable to the event since damage occurred over a wide spread area simultaneously. Therefore, it is utmost necessity to carry out seismic improvements of levees, evaluating seismic performance of levees when subjected to strong ground motions.

For long-extended earth structures such as levee embankments, seismic performance is usually evaluated for a representative cross section. An even better method is a simple method which is capable of evaluating its seismic performance at every section along the river.

A major cause of earthquake damage to levees is liquefaction of its foundation ground. Another cause is due to inertial force subjected to the levee embankments. In any case, it is important to know the inner structure of levee embankments for evaluation of seismic performance. Boring investigation is the most direct and simple method, however, it is expensive.

This study examines the feasibility of utilizing microtremors for the simple evaluation of seismic performance. Method of using microtremors is suitable for evaluating overall inner properties of levees, hence, this study attempts to evaluate overall shear wave velocity.

## 2 MICROTREMOR OBSERVATION

### 2.1 *Observation site*

Seven observation points were selected along the Yoshino River as shown in Figure 1. Yoshino River is one of the longest rivers in Japan, categorized as a class A river which has a length of

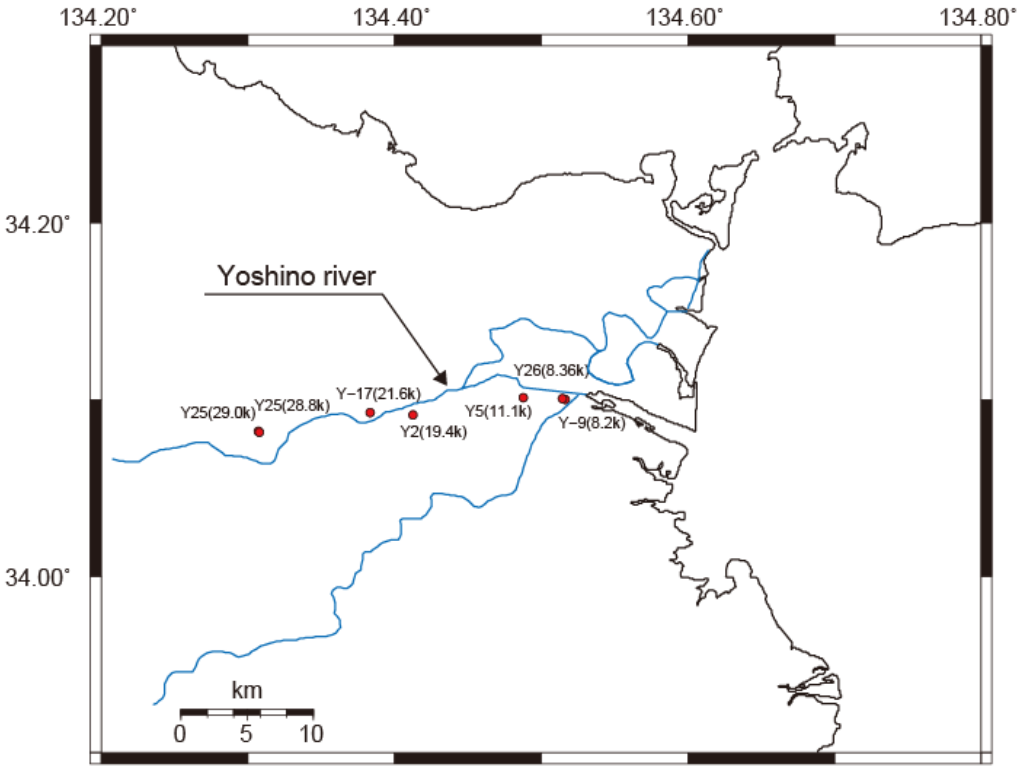


Figure 1. Yoshino River and observation locations

194km. Distances from the river mouth to the observation sites are approximately 8 km to 29 km.

### 2.2 *Cross sections*

Cross sections of levees at each observation point are shown in Figure 2, looking from the up-stream to downstream direction. Cross sectional shape is measured by a tape measure and a digital clinometer.

### 2.3 *Method of microtremor observation*

Microtremors were simultaneously observed at the crest and toe of the levee embankment as shown in Figure 3. Placing servo velocity-meter (Tokyo Sokushin, VSE-15D) perpendicular to the levee axis, horizontal component was observed in order to calculate the transfer function between the bottom and top of the levee embankment. Sampling frequency was 100(Hz), and each observation continued for 300 seconds. It is often the case that the crest area is used as a road for traffic, hence uncontaminated signal sections are carefully extracted from the unprocessed recorded signals in order to avoid traffic noise. Also, microtremor measurements were observed on the free-field near the toe. Although the free-filed condition is ideally situated far from the toe of the levee embankment, free-field sites in this observation was not so far from the toe (only several meters away) due to observational constraint conditions. Observations were carried out avoiding windy and rainy days.

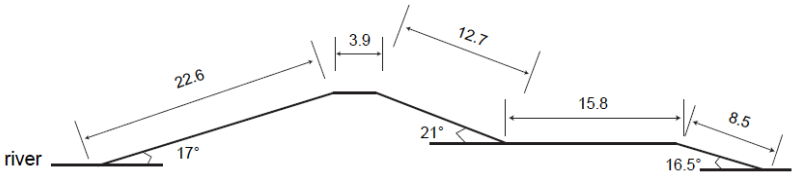


(1) Y-9

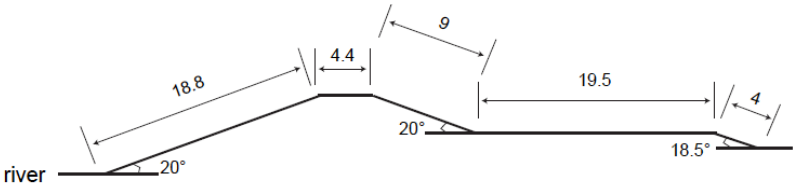


(2) Y-26

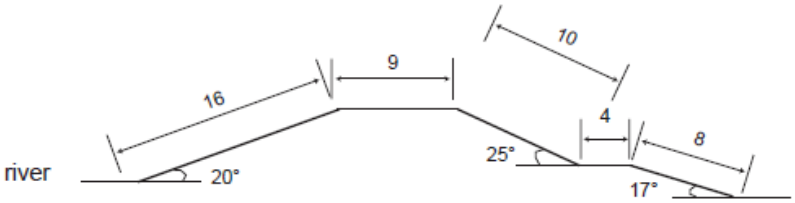


(3) Y-5

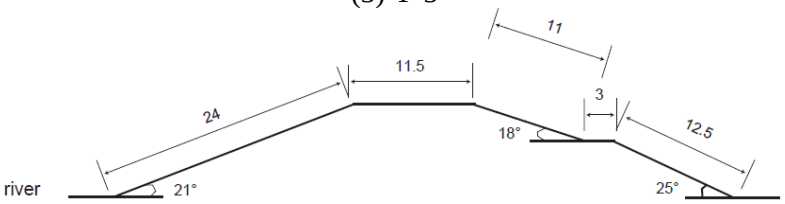


(4) Y-2

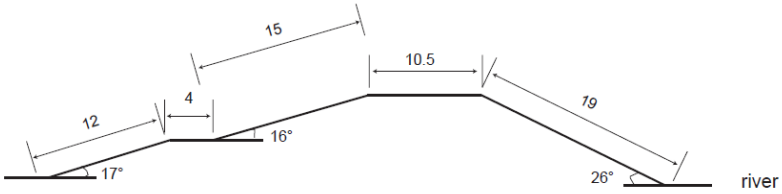


(5) Y-17

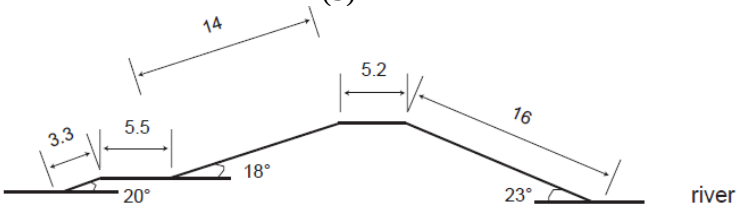


(6) Y-25a, 28.8k

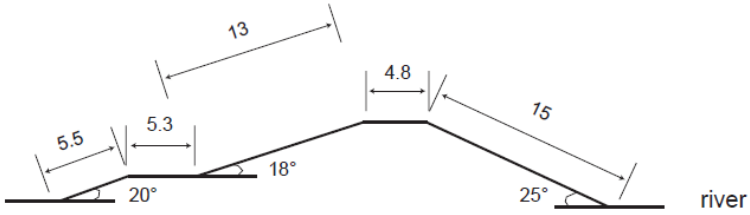


(7) Y-25b, 29.0k

Figure 2. Cross sections


Figure 3. Microtremor measurement

## 3 EVALUATION OF AVERAGE SHEAR WAVE VELOCITY

### 3.1 *Calculation of transfer function from spectral density functions*

The transfer function can be visualized as representing the characteristics of a system that receives and input *x* that is modified to an output *y*. In the context of levee-ground response system, input *x* would be ground motion at the toe of the levee and *y* would be levee crest motion. The transfer function can be calculated from spectral density functions as follows:

$$|H(f)| = \sqrt{S_{yy}(f)/S_{xx}(f)} \tag{1}$$

where $S_{xx}(f)$ and $S_{yy}(f)$ represent auto power spectral density functions of the input and output signals.

### 3.2 *coherence*

Coherence function is defined as follows:

$$\gamma^2(f) = \frac{|S_{xy}(f)|^2}{S_{xx}(f)S_{yy}(f)} \tag{2}$$

where $S_{xy}(f)$ is the cross spectral density function. Coherence function becomes smaller when it moves to a high frequency range and when two signals are less related to each other.

The average coherence of pairs of white noise signals is approximately $0.25 \pm 0.04$ for a type of smoothing (Mikami et al, 2008). For frequency beyond a certain frequency, coherence converges towards 0.2-0.3, as phase variations between the records in the pair are essentially stochastic. Transfer function amplitude would similarly be expected to be highly random for the same frequency range. Accordingly, I consider the transfer function at such frequencies to have little significance.

### 3.3 *Calculation of H/V spectral ratio*

Horizontal to vertical spectral ratio is called the H/V spectral ratio. By looking at the peak frequency of the H/V spectral ratio, predominant frequency of ground can be estimated. This information can be effectively referred when we need to choose inherent frequency of the levee from the peak frequencies of transfer functions.

### 3.4 *Identification using FE model*

Once significant peak frequency is found, we consider it to be the system frequency. When preparing the two dimensional FE model that has homogeneous shear wave velocity (Vs) with rigid base, the Vs value is identified so that the fundamental frequency of the FE model coincides with the peak frequency of the transfer function of levees. Due to the rigid base assumption of the levees, this method is expected to underestimate Vs.

## 4 RESULTS

Although there are seven sites (hence seven sets of microtremors), results are shown for the site Y-17 as an example. Other results are shown in the appendix.

### 4.1 *H/V spectral ratio of the ground*

Horizontal to vertical spectral ratio of the ground is shown in Figure 4. Predominant frequencies of the ground are approximately 2.44(Hz) and 5.66(Hz).

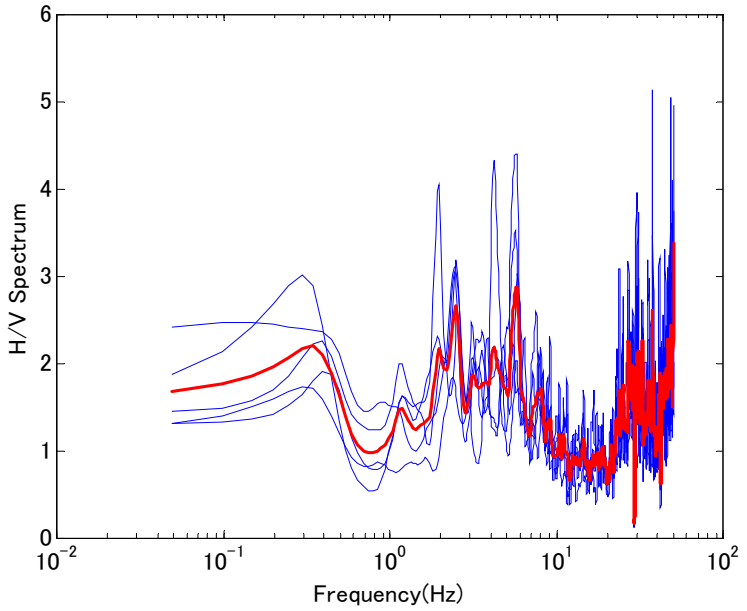


Figure 4. H/V spectrum of ground (Y-17)

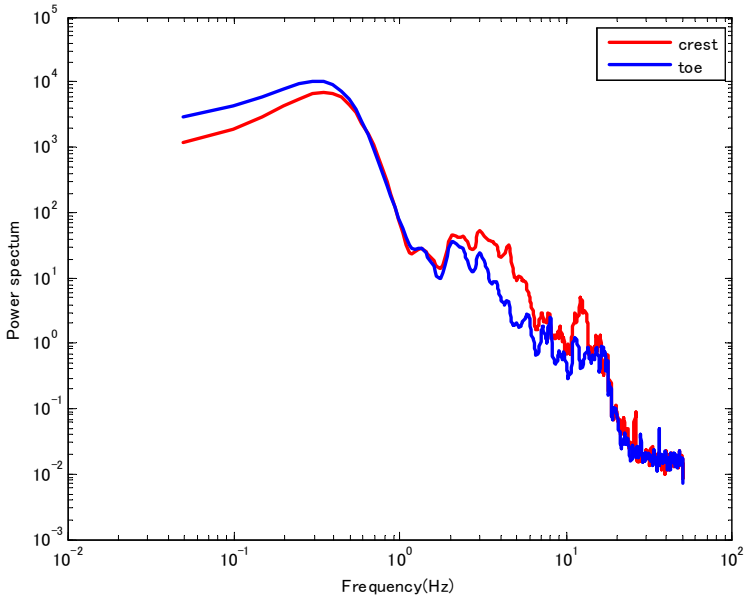


Figure 5. Power spectral density function (Y-17)

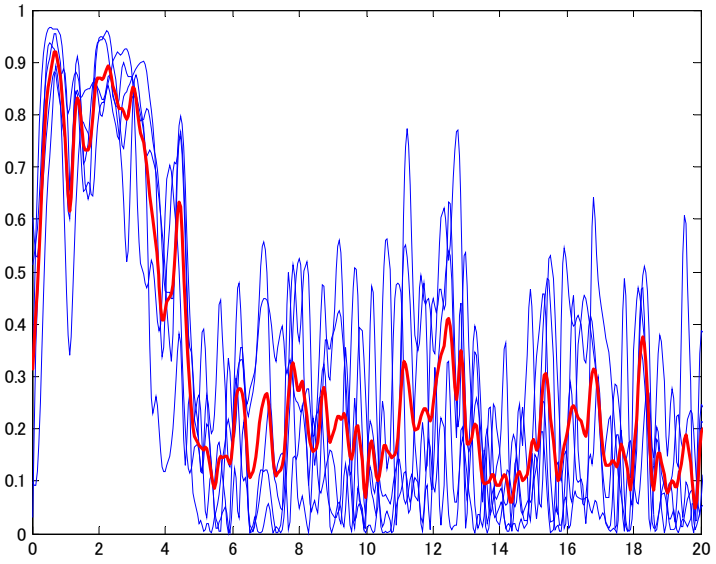

Figure 6. Coherence function (Y-17)

### 4.2 *Power spectrum and transfer function, coherence*

Power spectral density functions of microtremores obtained from the crest and the toe of the levee embankment are shown in Figure 5. Also shown in Figure 6 is coherence function. The thick line in Figure 6 is the averaged line of other thinner lines. Beyond approximately 6(Hz) in this case, the coherence function becomes almost constant, hence, two signals are considered to be stochastic in this frequency range.

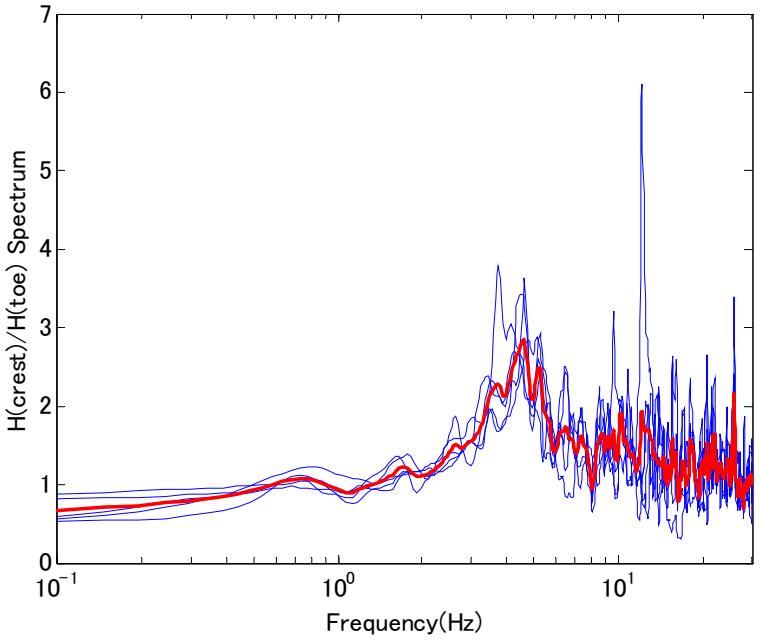


Figure 7. Transfer function (Y-17)

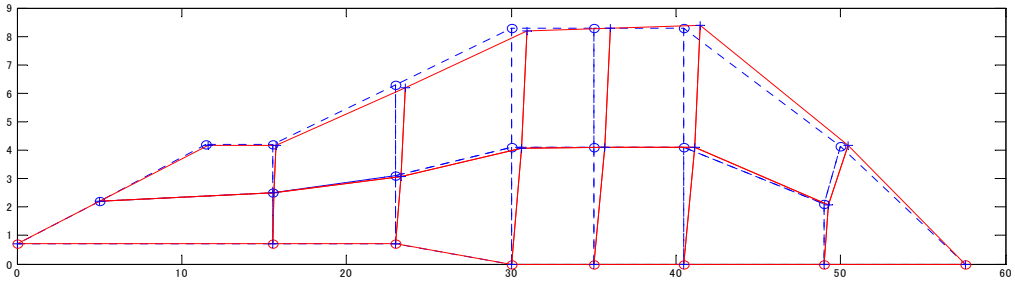

Figure 8. Identified finite element model (1st mode)

### 4.3 *Transfer function*

Transfer function of the signals between the crest and the toe is shown in Figure 7. The thick line is, as in the former section, represents averaged line of other thinner lines. A clear peak at 4.59(Hz) can be recognized, and I believe that this is the particular frequency that the system (levee embankment) has inherently.

### 4.4 *Identification using FE model*

The final process is to identify the overall Vs of the levee. Finite element model of site Y-17 is prepared as shown in Figure 8. As described before, inner shear wave velocity profiling of the levee is assumed to be constant (hence, identified Vs is overall Vs) on a rigid base. Vs of the levee is identified so that the fundamental frequency of the levee approximately coincides with the peak frequency obtained in the former section. Assuming soil density as 1800(kg/m$^3$) and Poisson's ratio as 0.45, Vs value of 121(m/sec) is obtained for the site Y-17. Although the obtained Vs provides approximate Vs value of the inner structure, the identified Vs may be underestimated as the numerical model used for the identification (FE model) assumed a rigid base.

Table 1. Summary of results

| Site | Distance from the river mouth | Predominant frequency of the ground (Hz) | Peak frequency of transfer function (Hz) | Identified shear wave velocity (m/sec) | SPT blow count & Soil |
|---|---|---|---|---|---|
| Y-9 | 8.2 km | 1.56 | 6.30 | 126 | 2 ~ 5 sandy silt |
| Y-26 | 8.36 km | 1.76 | 7.96 | 155 | 3 ~ 5 sandy silt |
| Y-5 | 11.1 km | 1.81 | 4.79 | 85 | 2 ~ 4 sandy silt |
| Y-2 | 19.4 km | 1.76*<br>2.15 | 4.93*<br>5.37 | 136*<br>148 | 5 ~ 12 sand and gravel |
| Y-17 | 21.6 km | 2.44, 5.66 | 4.59 | 121 | 5 ~ 8 sand and gravel |
| Y-25a | 28.8 km | 0.59 | 7.62 | 145 | 7 ~ 18 sand and gravel |
| Y-25b | 29.0 km | 0.63 | 6.10 | 117 | |

* windy condition

### 4.5 *Summary of the results*

Results for all sites are summarized in Table 1. Distribution of SPT blow counts along the depth of the levees are also shown in the figure. Vs values of the levee can be approximately estimated based on the correlation with N values as follows (Japan Road Association, 2002):

$$Vs = 80N^{1/3} \quad \text{for sand} \tag{3}$$

Vs values obtained from microtremor measurement are by and large consistent with the SPT evaluation.

## 5 CONCLUSIONS

This paper studies the feasibility of evaluating average shear wave velocity for levee embankments by using microtremor measurement. Microtremors are measured at the crest and toe of the levee simultaneously by placing velocity sensors perpendicular to the levee axis. Transfer functions are then calculated using the pair of horizontal motions. Finally, overall shear wave velocity structure is identified so that the peak frequency of the transfer function and the fundamental frequency of the finite element model of the levee that has the same cross section coincide. I found that the identified shear wave velocity is mostly consistent with the ones estimated by using SPT blow counts.

## ACKNOWLEDGMENTS

The author thanks Mr. Mitsuaki Yamamoto, Mr. Tatsuyuki Morita and Mr. Koichi Ikuta of Tokushima Office of River and National Highway, Shikoku Regional Development Bureau, Ministry of Land, Infrastructure, Transport and Tourism for providing data regarding Yoshino levee. This research was supported by a grant from the Shikoku Construction Association and Founda-

tion of River and Watershed Environment Management. The author also thanks Mrs. Noriko Tsujino for helping microtremor observation.

## REFERENCES

Japan Road Association, 2002. Specifications for Highway Bridges, Part V, Seismic Design.

Mikami, A., Stewart, J.P. and Kamiyama, M. 2008. Effects of time series analysis protocols on transfer functions calculated from earthquake accelerograms, Soil Dynamics and Earthquake Engineering, 28, 695-706.

Ministry of Land, Infrastructure, Transport and Tourism 2011. http://www.mlit.go.jp/

Wessel, P. and Smith, W. H. F. 1998. New improved version of the Generic Mapping Tools released, EOS Trans. AGU, 79, 579.

Wessel, P. and Smith, W. H. F. 1991. Free software helps map and display data, EOS Trans. AGU, 72, 441.

APPENDIX

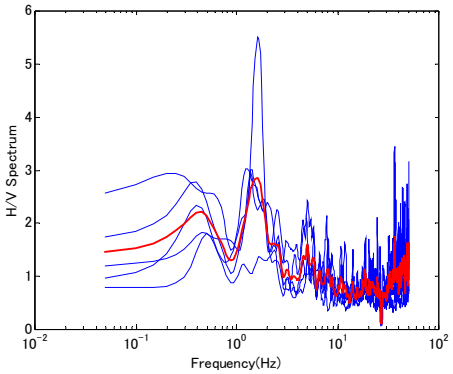


(a) H/V spectrum

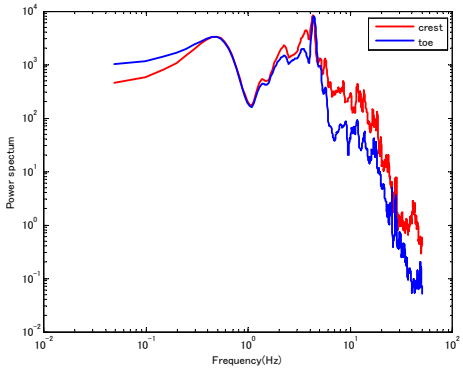


(b) Power spectral density function

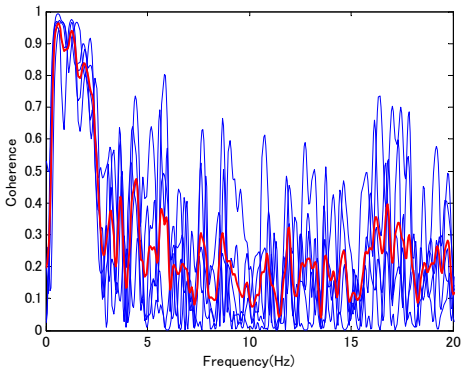


(c) Coherence function

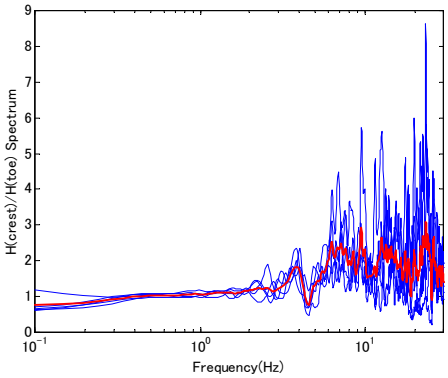


(d) Transfer function

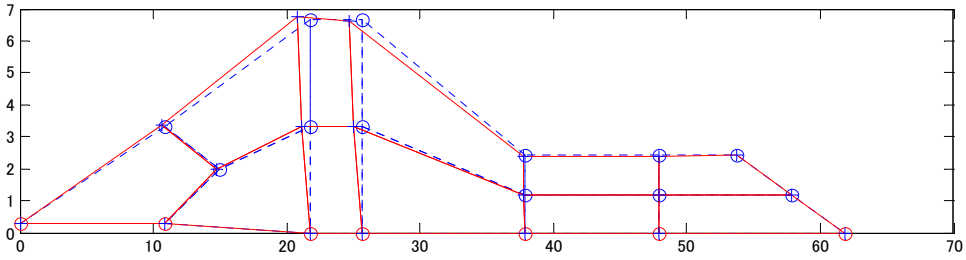

(e) Identified finite element model

Figure A1. Results for Y-9 (8.2 km)

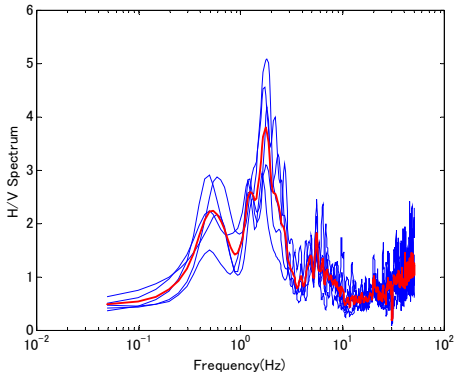


(a) H/V spectrum

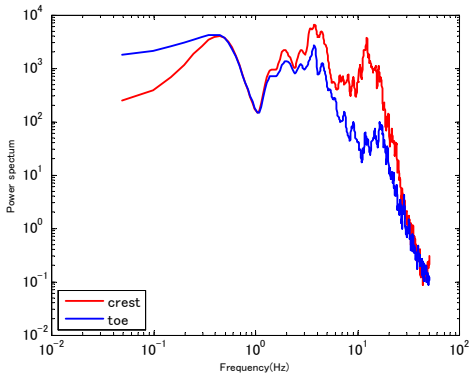


(b) Power spectral density function

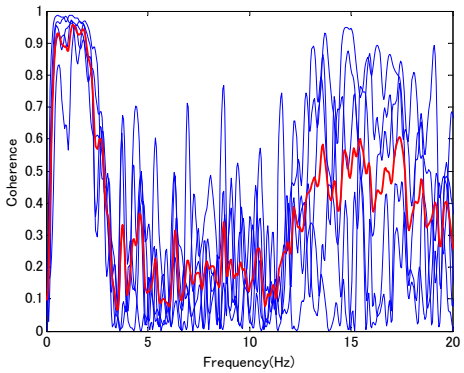


(c) Coherence function

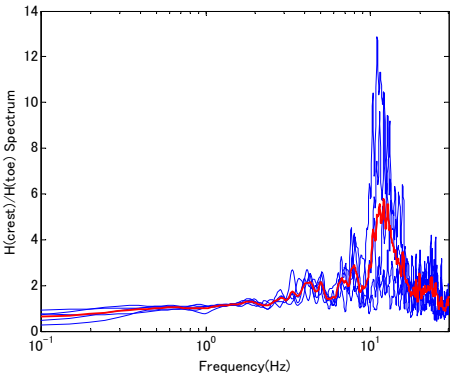


(d) Transfer function

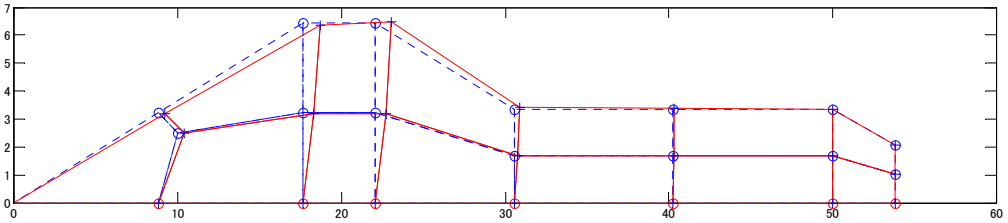

(e) Identified finite element model (1st mode)

Figure A2. Results for Y-26 (8.36 km)

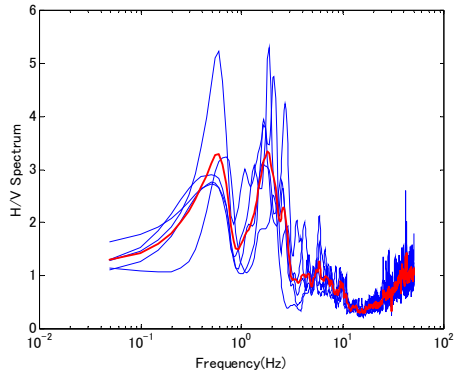


(a) H/V spectrum

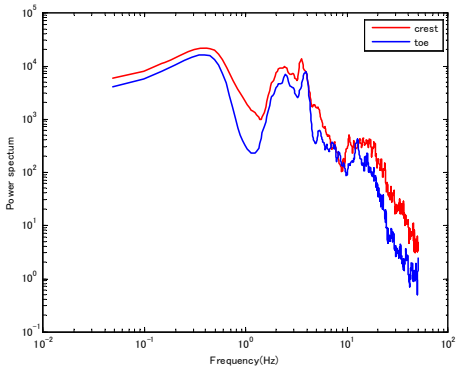


(b) Power spectral density function

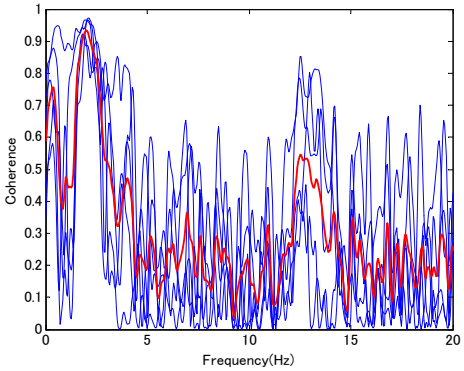


(c) Coherence function

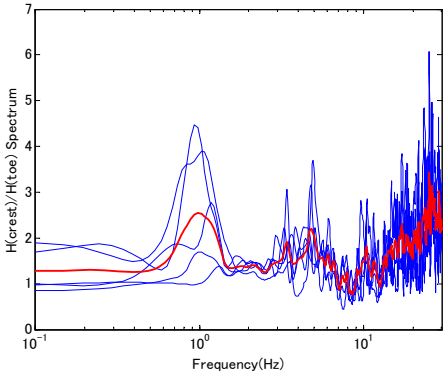


(d) Transfer function

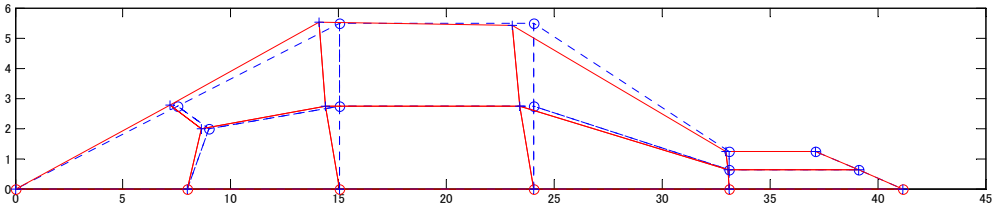

(e) Identified finite element model (1st mode)

Figure A3. Results for Y-5 (11.1 km)

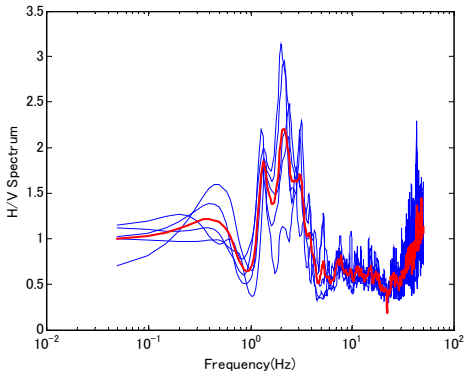


(a) H/V spectrum

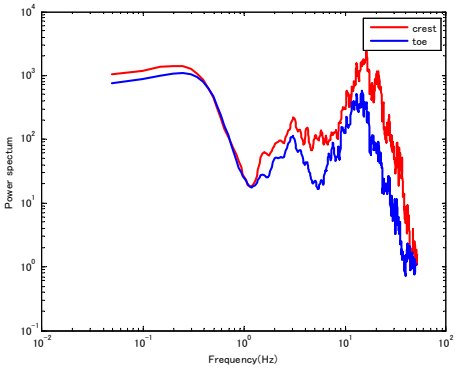


(b) Power spectral density function

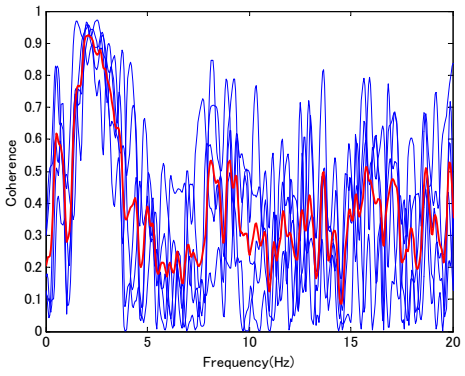


(c) Coherence function

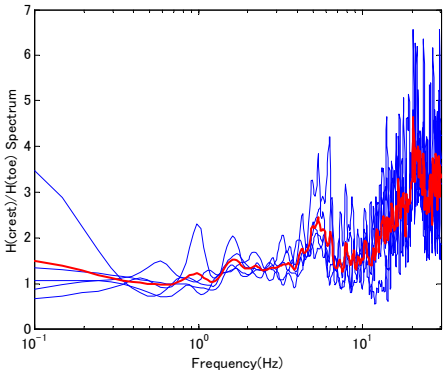


(d) Transfer function

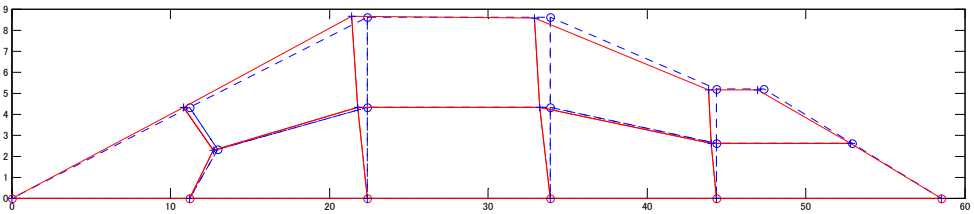

(e) Identified finite element model (1st mode)

Figure A4. Results for Y-2 (19.4km)

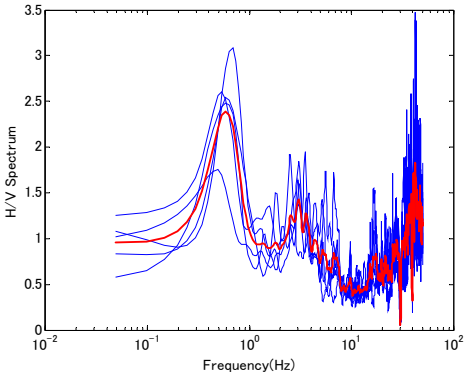


(a) H/V spectrum

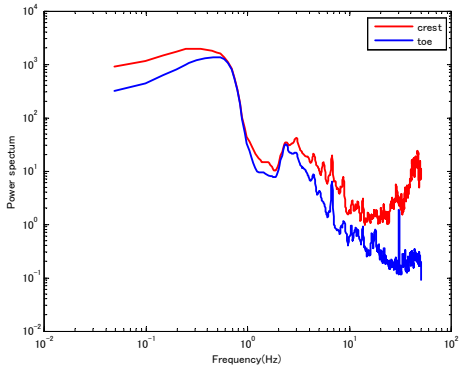


(b) Power spectral density function

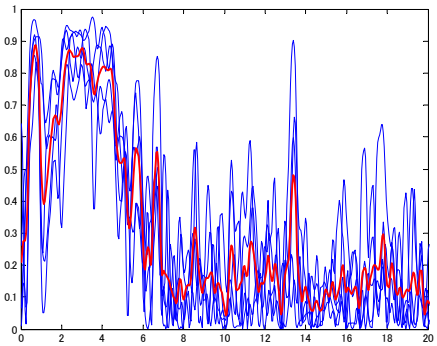

(c) Coherence function

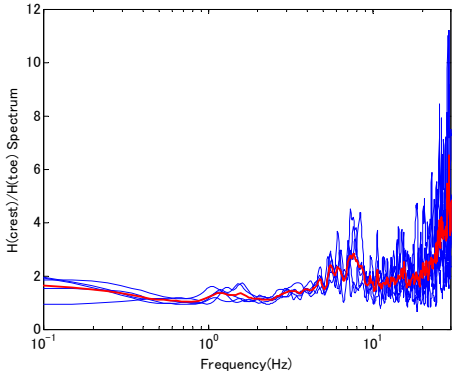


(d) Transfer function

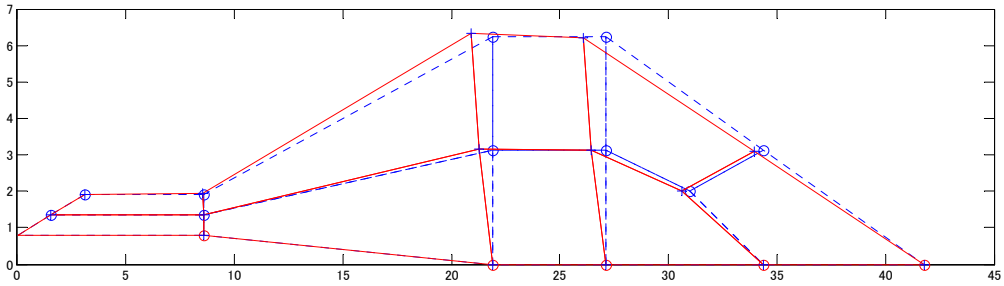

(e) Identified finite element model (1st mode)

Figure A5. Results for Y-25a (28.8 km)

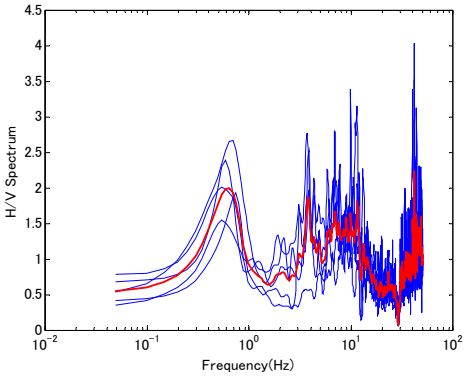


(a) H/V spectrum

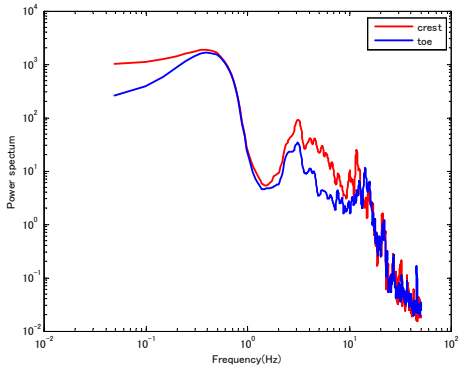


(b) Power spectral density function

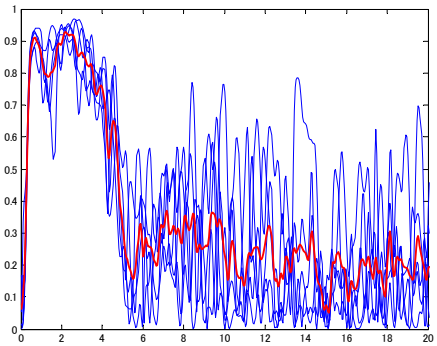

(c) Coherence function

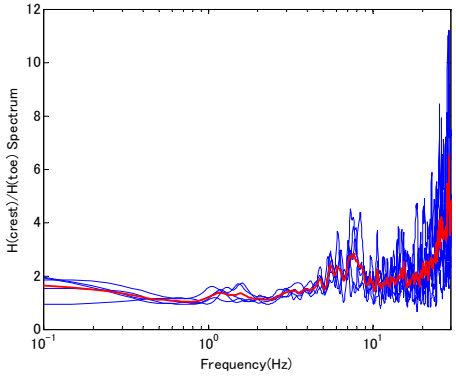


(d) Transfer function

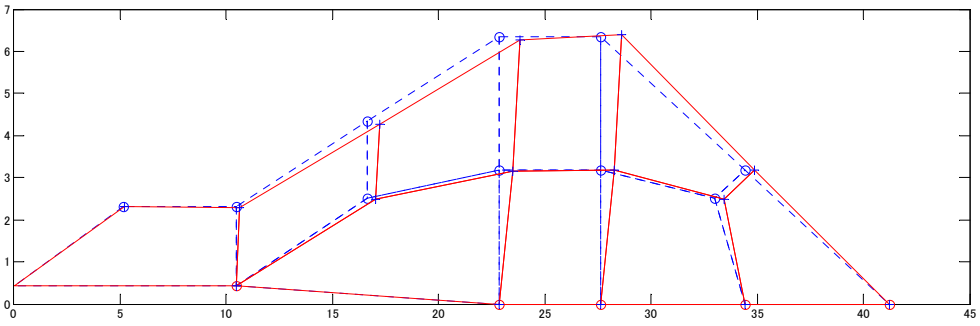

(e) Identified finite element model

Figure A6. Results for Y-25b (29.0km)

# Seismic Performance of Buried Steel Pipelines Crossing Strike-Slip Seismic Faults

P. Vazouras
*Dept. of Civil Engineering, University of Thessaly, Volos, Greece*

S. Karamanos
*Dept. of Mechanical Engineering, University of Thessaly, Volos, Greece*

P. Dakoulas
*Dept. of Civil Engineering, University of Thessaly, Volos, Greece, dakoulas@uth.gr*

ABSTRACT: The mechanical behaviour of buried steel pipelines, crossing active strike-slip tectonic faults is investigated. The interacting soil-pipeline system is modelled rigorously through finite elements, which account for large strains and displacements, nonlinear material behaviour and special conditions of contact and friction on the soil-pipe interface. Steel pipelines of various diameter-to-thickness ratios and typical steel material for pipeline applications are considered. The paper investigates the effects of various soil and pipeline parameters on the mechanical response of the pipeline, with particular emphasis on pipe wall failure due to "local buckling" and pipe wall rupture. The effects of soil shear strength and stiffness are also investigated. The results show the critical fault displacement at which the pipeline fails and the corresponding critical strain versus the pipe diameter-to-thickness ratio. The results can be used for efficient pipeline design in cases where active faults are expected to impose significant ground-induced deformation to the pipeline.

## 1 INTRODUCTION

Seismic events constitute a threat for buried pipeline structural integrity. In particular, permanent ground deformation applied on the pipeline in a quasi-static manner, and not necessarily associated with high seismic intensity, may cause serious pipeline damage, reported in numerous earthquakes, such as the 1995 Kobe earthquake (Nakata & Hasuda 1995), the 1999 Kocaeli earthquake (EERI 1999) and the 1999 Chi-Chi earthquake (Takada et al. 1999).

The present paper focuses on the mechanical response of continuous (welded) buried steel pipelines crossing active strike-slip seismic faults, a particular ground-induced action, associated with axial, shear and bending loads. High stresses and strains are developed in critical locations, which are well into the inelastic range of pipe material and may cause pipeline failure. In particular, high tensile stresses may cause fracture of the pipeline wall, especially at welds or defected locations, whereas high compression stresses may cause buckling, mainly in the form of pipe wall wrinkling, a shell-type instability referred to as "local buckling" or "kinking".

Newmark & Hall (1975) were the first to attempt prediction of pipeline mechanical response under fault displacement, using a simplified analytical model of a long cable with small displacements. Their work has been extended by Kennedy et al. (1977, 1983) considering non-uniform friction between the pipe and the surrounding soil, and further enhanced by Wang & Yeh (1985) to account for pipeline bending stiffness. Notable analytical works on the subject, based on a beam-type approach for pipeline modelling have been presented by Vougioukas et al. (1979), Wang and Wang (1995) and Takada et al. (2001).

Kokavessis & Anagnostidis (2006), presented a finite element methodology to simulate buried pipeline behaviour under permanent ground-induced actions, using contact elements to describe the soil-pipe interaction. Furthermore, Karamitros et al. (2007) presented an enhanced analytical beam-type methodology, supported by three-dimensional finite element models, which employed shell elements for describing the pipe and nonlinear springs to simulate soil

behavior. Liu et al. (2008) presented a numerical simulation of pipelines crossing active faults through a combination of shell elements and springs, similar to the model by Karamitros et al. (2007).

Experimental works on the effects of strike-slip faults on buried polyethylene (HDPE) pipelines have been reported by Ha et al. (2008a, 2008b) and Abdoun et al. (2009), based on centrifuge modelling of pipeline response and examined the influence of the type of faulting, the angle of strike-slip faults on the pipeline mechanical behaviour, as well as the effects of buried depth, pipeline diameter, and moisture content.

The work in the present paper is part of an extensive research effort aimed at investigating the response of buried steel pipelines crossing active faults for various soil conditions, using advanced numerical simulation tools and identifying possible failure modes, with emphasis on site conditions (i.e. the properties of the surrounding soil). The present work follows an integrated approach, which is based on modelling of the soil-pipeline system through nonlinear finite elements, accounting rigorously for (a) the inelastic behaviour of the surrounding soil, (b) the interaction and the contact between the soil and the pipe (including friction contact and the development of gap), (c) the development of large inelastic strains in the steel pipeline, (d) the distortion of the pipeline cross-section and possible local buckling formation, (e) the presence of internal pressure. The pipeline axis is assumed horizontal and crosses the fault plane at right angle. Considering a variety of soil parameters for both cohesive and non-cohesive soils, the influence of soil conditions on the pipeline structural response is examined in detail. Furthermore, the effects of pipeline diameter-to-thickness ratio $D/t$ and steel material on pipeline response are also investigated. The numerical results are employed to develop interaction diagrams of the fault displacement causing pipeline failure with respect to the value of pipe diameter-to-thickness ratio $D/t$, which could be used for practical design purposes.

## 2 NUMERICAL MODELING

The general-purpose finite element program ABAQUS (2010) is employed to simulate the mechanical behavior of the steel pipe, the surrounding soil medium and their interaction in a rigorous manner, considering the nonlinear geometry of the soil and the pipe (including the cross-sectional distortions of the pipeline cross-section), through a large-strain description of the pipeline-soil system and the inelastic material behavior for both the pipe and the soil.

Fig. 1 shows the elongated prismatic model considered for simulating this permanent ground-induced action, where the pipeline is embedded in the soil. The corresponding finite element mesh for the soil formation is depicted in Fig. 1a and Fig. 1b, and for the steel pipe in Fig. 1c. Four-node reduced-integration shell elements (type S4R) are employed for modeling the pipeline cylinder, whereas eight-node reduced-integration "brick" elements (C3D8R) are used to simulate the surrounding soil. The top surface represents the soil surface, and the burial depth is chosen equal to about 2 pipe diameters, which is in accordance with pipeline engineering practice. A short parametric study demonstrated that a 60-diameter length of the pipeline (in the $x$ direction) is adequate for the purposes of the present analysis. Furthermore, prism dimensions in directions $y, z$ equal to 10 and 5 times the pipe diameter, respectively, are also found to be adequate. The seismic fault plane crosses the pipeline axis at right angle and divides the soil in two equal parts (Fig. 1a). The analysis is conducted in two steps; gravity loading is applied first and, subsequently, fault movement is imposed. The vertical boundary nodes of the first block remain fixed in the horizontal direction (including the end nodes of the steel pipeline), whereas a uniform horizontal displacement due to fault movement is imposed in the external nodes of the second (moving) block (including the end nodes of the pipeline), except for the nodes in the fault zone (see below). A finer mesh was employed for the central part of the pipeline, where maximum stresses and strains are expected, with a total of 54 shell elements around the cylinder circumference in this central part, whereas the size of the shell elements in the longitudinal direction has been chosen equal to 1/26 of the pipeline outer diameter $D$.

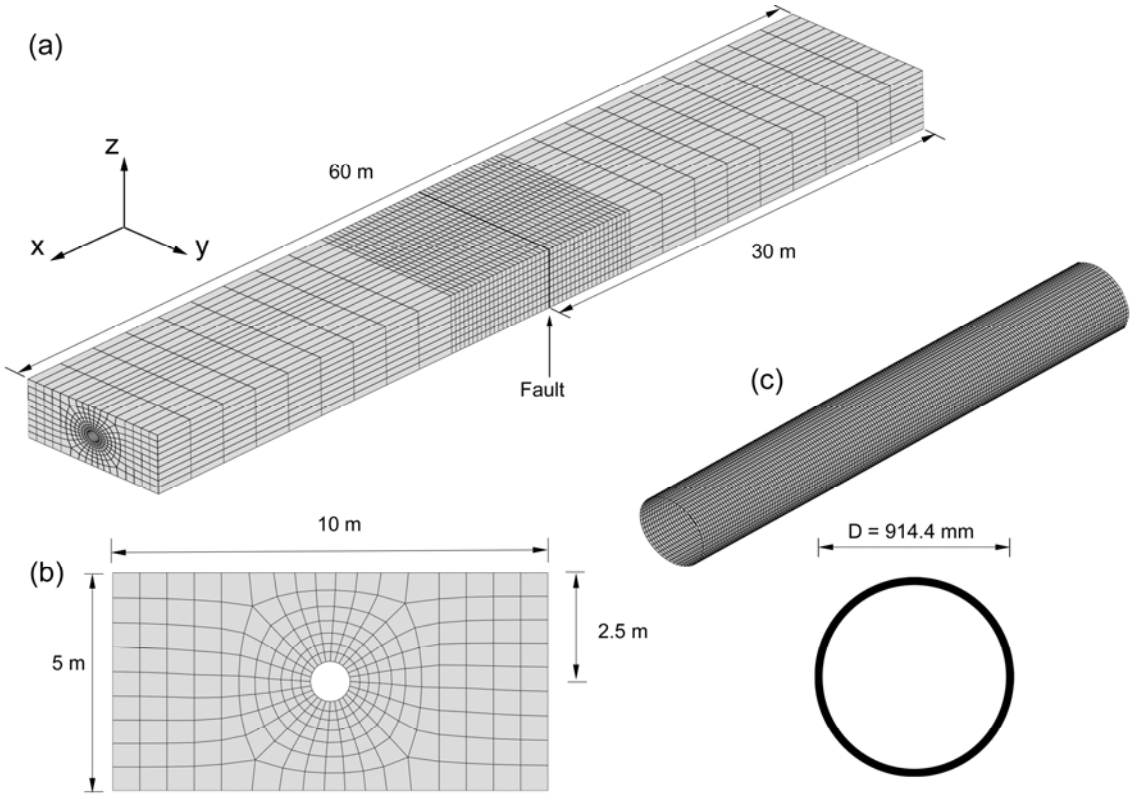


Figure 1. Finite element model of the (a) soil formation with tectonic fault, (b) soil cross-section and (c) steel pipeline.

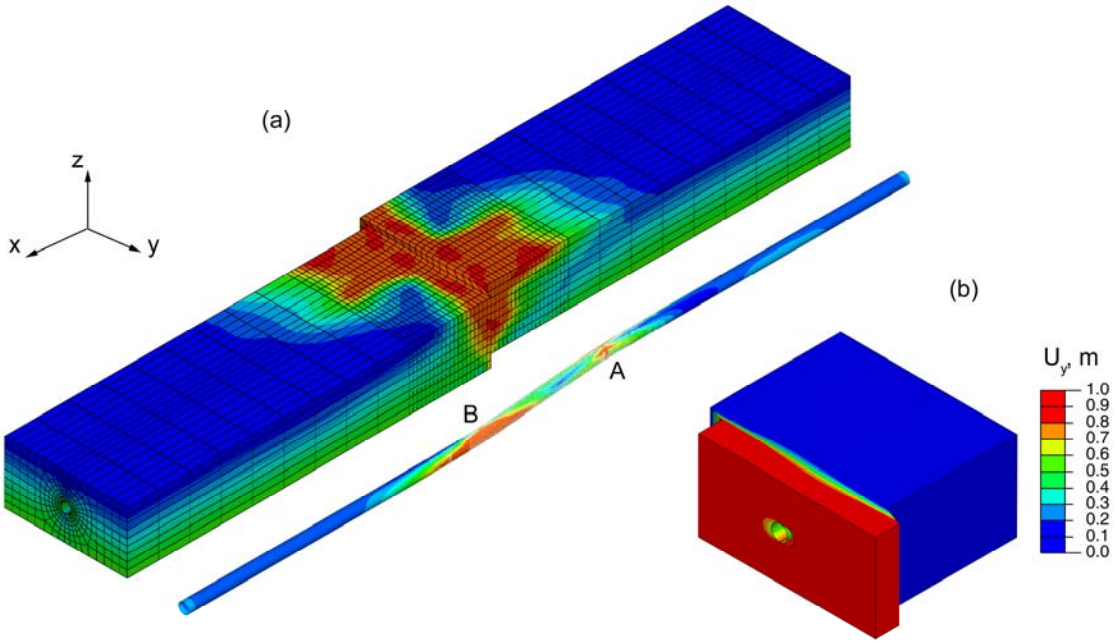


Figure 2. (a) Deformation of the pipeline-soil system after fault displacement; finite element results depict the von Mises stress. (b) Detail of fault displacement $U_y$ (X65 pipe, $D/t = 72$, Clay I, $w = 0.33$ m, $p = 0$).

Fig. 2a plots the soil – pipeline system response in terms of von Mises stress, after a seismic fault movement, for a plane perpendicular to the pipeline axis. The fault movement is considered to occur within a narrow transverse zone of width $w$, to avoid discontinuity at the vicinity of the fault, which sometimes causes numerical problems and corresponds to a more realistic representation of the fault displacement mechanism. Following a short parametric study, the value of $w$ has been considered equal to 0.33 m. Numerical analyses with value of $w$ up to 1 m showed a small influence on the results.

A large-strain $J_2$ flow (von Mises) plasticity model, with isotropic hardening is employed to describe the mechanical behavior of the steel pipe material, calibrated through an appropriate uniaxial stress-strain curve from a tensile test. Furthermore, an elastic-perfectly plastic Mohr-Coulomb model is considered for the soil behavior, characterized by the soil cohesiveness $c$, the friction angle $\phi$, the elastic modulus $E$, and Poisson's ratio $v$. The dilation angle $\psi$ is assumed to be equal to zero throughout this study. A contact algorithm is considered to simulate the interface between the outer surface of the steel pipe and the surrounding soil, which takes into account interface friction using of an appropriate friction coefficient $\mu$. In our analysis, the value of $\mu$ is considered equal to 0.3 for both non-cohesive and cohesive soils, to be able to have a more direct comparison of the effects of the other soil parameters on the behavior. The relatively low value of $\mu$ reflects the smoothness of the pipe surface. Previous parametric studies conducted by the authors have shown that the effect of $\mu$ ranging between 0.2 and 0.4 may not be significant for the pipeline structural behavior. The soil-pipe interface allows separation of the pipe and the surrounding soil. The analysis proceeds using a displacement-controlled scheme, which increases gradually the fault displacement $d$.

## 3 NUMERICAL RESULTS

### 3.1 *Parametric Studies*

Using the above numerical simulation tools, results are obtained for steel pipelines for various values of the diameter-to-thickness ratio, as well as for different soil conditions. In all cases considered in the present paper, the outer pipe diameter of the pipe $D$ is assumed equal to 914.4 mm (36 in), whereas the pipe wall thickness ranges from 6.35 mm (¼ in) to 19.05 mm (¾ in), so that a range of $D/t$ values between 48 and 144 is covered. This range of $D/t$ values is typical for onshore applications (oil, gas or water pipelines). The surrounding soil has dimensions 60m×10m×5m in directions $x$, $y$, $z$ respectively. In this section, the seismic fault plane is perpendicular to the pipeline axis and located at the middle cross-section of the pipeline. Particular emphasis is given on the effects of external pressure on the structural response. Both X65 pipelines and high-strength steel X80 pipelines are analyzed.

### 3.2 *X65 pipelines in cohesive soils*

A moderately thick-walled X65 pipeline is considered first, with diameter and thickness equal to 914.4 mm (36 in) and 12.7 mm (0.5 in) respectively, so that $D/t$ =72. The API 5L X65 steel material is a typical steel material for oil and gas pipeline applications, with a nominal stress-engineering strain curve shown with solid line in Fig. 3a, obtained from a uniaxial tensile test. The yield stress $\sigma_y$ is equal to 450 MPa (65 ksi) followed by a plastic plateau up to 3% strain and a strain-hardening regime with a hardening modulus equal to about $E_s/300$, where $E_s$ is the Young's modulus of the steel material. Assuming a safety (reduction) factor equal to 0.72 0, the maximum operating pressure $p_{\max}$ of this pipeline [ $p_{\max} = 0.72 \times \left(2\sigma_y\, t/D\right)$ ] can be readily calculated equal to 9 MPa (90 barr).

The pipeline is assumed to be imbedded in a cohesive soil and to be crossing a fault zone having a width $w$ equal to 0.33 m. At this stage, the internal pressure $p$ is equal to zero, and a soft-to-firm clay is considered, referred to as Clay I, which under "undrained" loading conditions has a cohesion $c$ = 50 kPa, friction angle $\varphi = 0^\circ$, Young's modulus $E$ = 25 MPa and Poisson's ratio $\nu$ = 0.5. Fig. 4a depicts the shape of the deformed pipeline at fault displacements $d$ = 1 m, 2 m, 3 m and 4 m in the area near the fault.

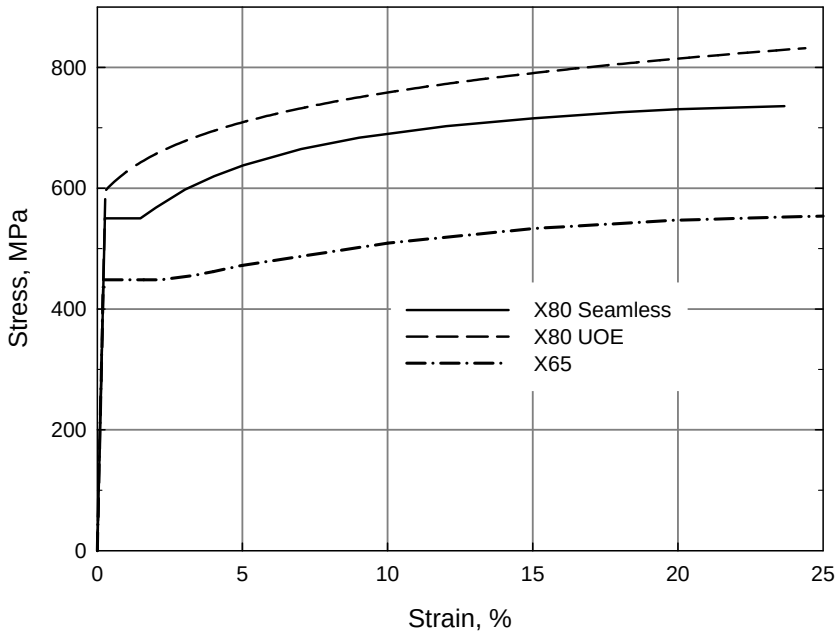


Figure 3. Uniaxial nominal stress-engineering strain curve for API 5L X65 , API 5L X80 steel.

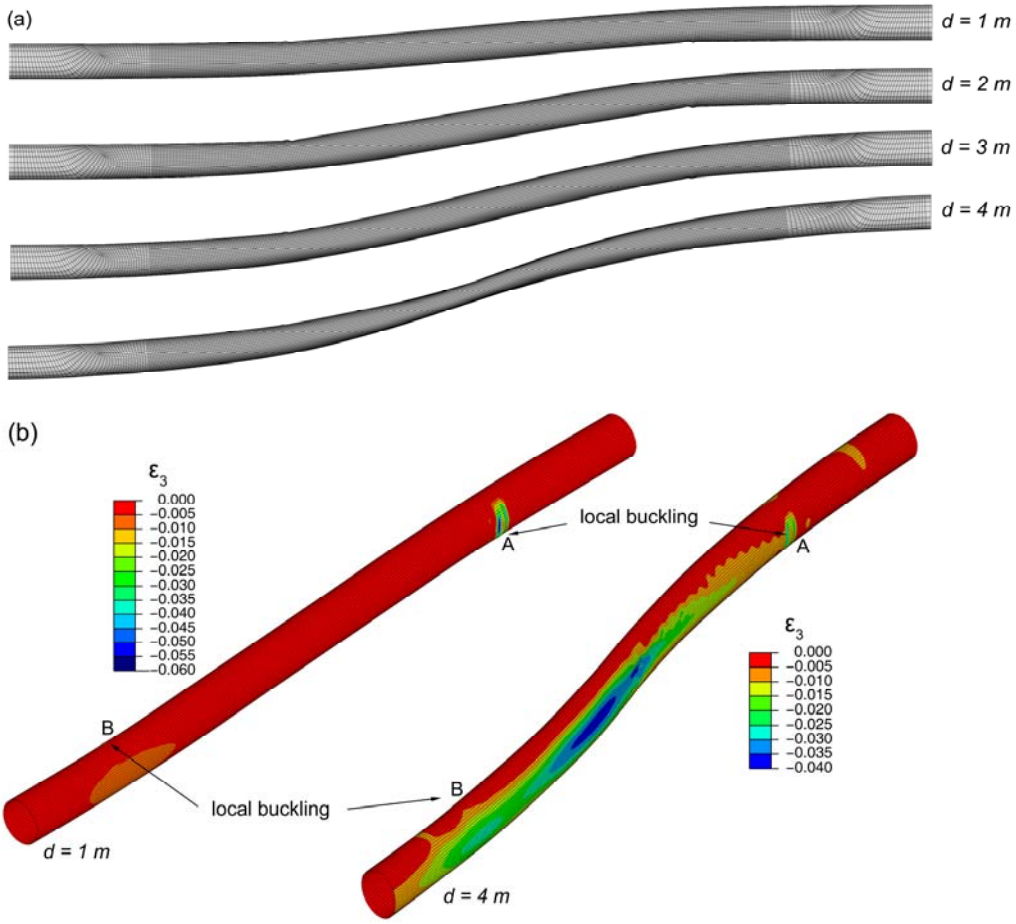


Figure 4.(a) Plan view of deformed shape of a pipeline for d = 1, 2, 3, and 4 m (b) Distribution of longitudinal normal strain $\varepsilon_x$ for seismic fault displacement equal to 1 m and 4 m. (X65 pipe, $D/t = 72$, Clay I, $w = 0.33$ m, $p = 0$).

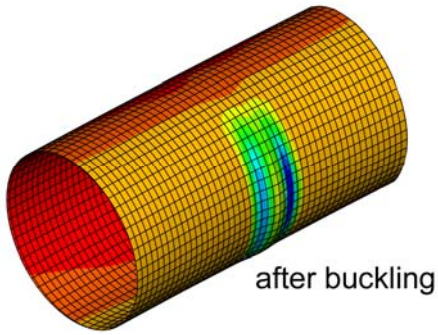


Figure 5. Details of the critical pipeline area: local buckling formation (X65 pipe, $D/t = 72$, Clay I, $w = 0.33$m, $p = 0$).

Fig. 4b depicts the shape of the deformed pipeline and the distribution of the longitudinal normal strain $\varepsilon_x$ on its outer surface at fault displacement equal to $d$ = 1 m and $d$ = 4 m. The deformed shape of the pipeline at $d$ = 1 m shows a localized deformation at point A, referred to as "local buckling" or "kinking", whereas point A is the "critical location" of the pipeline, at a distance of 5.45 m from the fault. Due to the skew-symmetry of the problem, a similar local deformation pattern occurs at point B, on the hidden side of the pipeline. Under increasing fault movement, a substantial development of this localized deformation pattern is observed, associated with the distortion of a significant part of the pipeline around this area, as shown in Fig. 4b, for a fault displacement of $d$ = 4 m. As the pipeline length increases with continued fault movement, it results to higher tensile and smaller compressive strains in the longitudinal direction. Fig. 4b, shows that for a fault displacement of $d$ = 4 m compressive longitudinal strains are significantly lower than those corresponding to a fault displacement of $d$ = 1 m.

Fig. 5 shows the deformed shape of the pipeline at fault displacements $d$ equal to 1 m, where a localized buckling pattern develops where the compressive stresses and strains reach a maximum value. It is also important to notice that, upon local buckling formation, the deformation of the pipeline localizes in the vicinity of the buckle, as shown in Fig. 5. The variations of longitudinal compressive and tensile strain $\varepsilon_x$ along the two outer (most stressed) generators of the pipe cylinder are shown in Fig. 6 and Fig. 7 for different values of the fault displacement and for a small segment of the pipeline about the critical area. The results for the compressive strain shown in detail in Fig. 6b, indicate that for a value of fault displacement greater than 0.67 m, significant distortion of the cross-section occurs due to the development of a localized wrinkling pattern (local buckling) on the pipe wall, on the compression side of the deformed pipeline. This stage is considered as the onset of local buckling.

One may notice that the value of fault displacement at which onset of localized buckling occurs ($d_{cr}$), referred to as "critical fault displacement", can be defined in many ways. In the present work, the onset of local buckling is considered at the stage where outward displacement of the pipe wall starts at the area of maximum compression. At that stage, bending strains due to pipe wall wrinkling develop (Fig. 6), associated with significant tensile strains at the "ridge" of the buckle, so that the longitudinal compressive strains at this location at the outer surface of the pipe wall start decreasing, forming a short wave at this location. In the present case, this stage corresponds to a fault displacement equal to 0.67m as shown in Fig. 6b.

At the above stage of local buckling onset, the longitudinal strain at the location of the buckle ($\varepsilon_{cr}$) is measured equal to $7.7\times10^{-3}$ .Furthermore, at this critical buckling stage, the maximum tensile strain on the opposite side of the pipe ($\varepsilon_{T,\max}$) is $5.2\times10^{-3}$, which is much less than the strain that would cause tensile failure in the form of rupture in a non-seriously-defected pipeline (Igi & Suzuki 2007). It is noted that the formation of a local buckle is undesirable because it is associated with the concentration of strain at the buckled area, which may lead to fatigue cracking under repeated loading (Dama et al. 2007). Upon formation of the local buckle, pipe deformation concentrates around the buckled cross-section. However, further continuation of the imposed deformation results in significant tensile strains at the buckled area, decreasing the compressive strains and resulting in high local tensile stresses, on either side of the pipeline cross-section, may lead to local fracture at welds or other locations where minor defects exist.

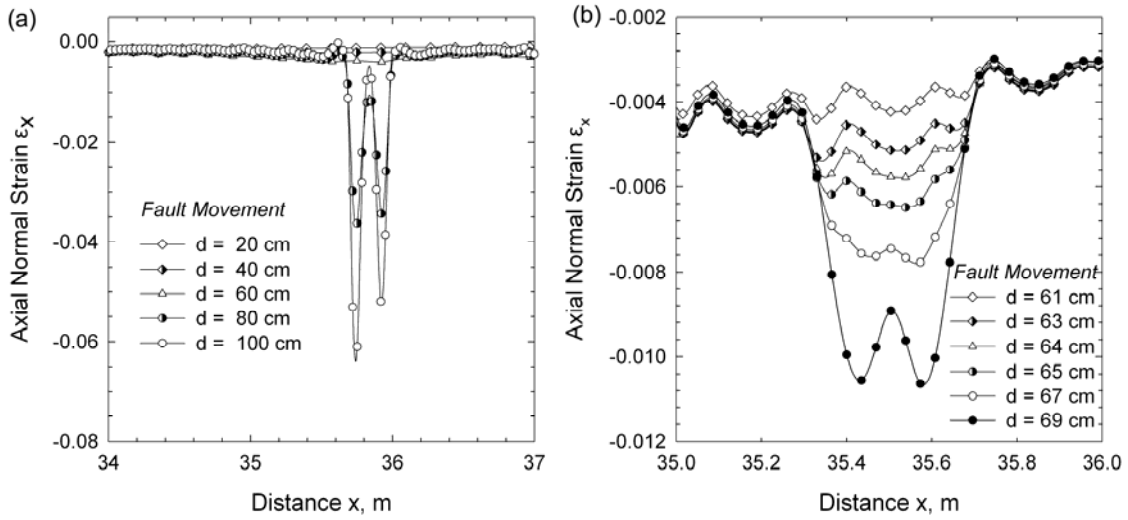


Figure 6. Details of the critical pipeline area: local buckling formation (X65 pipe, $D/t = 72$, Clay I, $w = 0.33$m, $p = 0$).

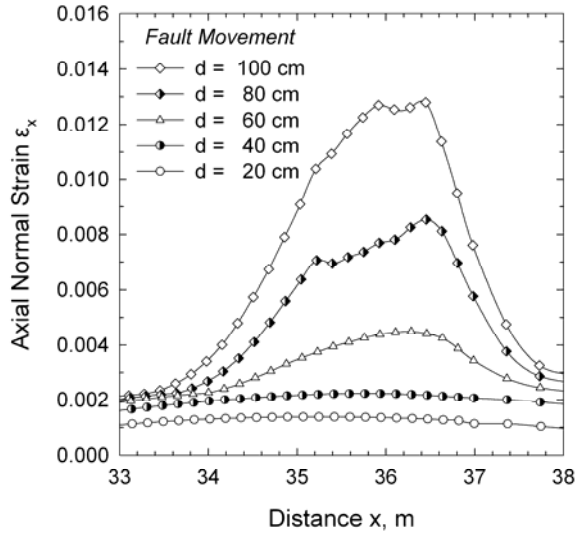


Figure 7. Variation of axial strain at the tension side of the buckled area for values of fault displacement from 0.2m to 1.0m (X65 pipe, $D/t = 72$, Clay I, $w = 0.33$m, $p = 0$).

The effects of internal pressure on pipeline mechanical behavior are investigated by considering internally pressurized pipelines imbedded in the same soil conditions (Clay I). Numerical results corresponding to a pressure level of 50 barr, which is equal to 56% of the maximum operating pressure $p_{\max}$ indicate that, despite the fact that the buckled shapes of pressurized cylinders are similar to the buckled shape of Fig. 5, the corresponding values of critical fault displacement $d_{cr}$ and the compressive strain along the critical generator of the steel pipeline are somewhat lower than the ones shown in Fig. 6b. Those results indicate that, in the case of buried (confined) pipes, the presence of internal pressure results in a decrease of critical fault displacement. The decrease is attributed to the development of additional stresses and strains in the pipeline wall that cause early yielding and lead to a premature local buckling failure. For the case of $p/p_{\max}$ =0.56, the maximum strain $\varepsilon_{cr}$ at buckling (critical strain) is equal to $8.3\times10^{-3}$, which is similar yet slightly higher than the critical strain for zero pressure.

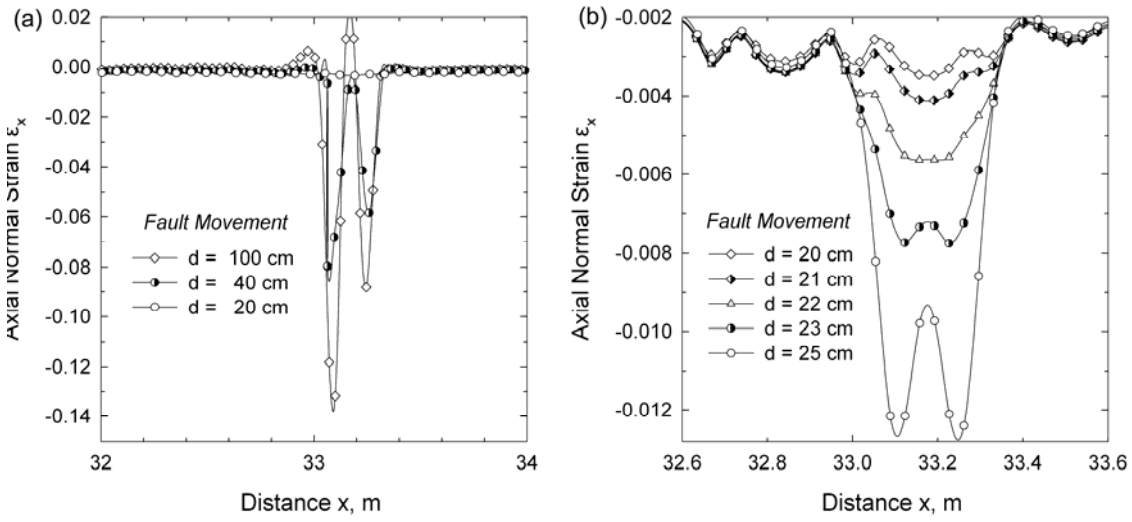


Figure 8. Variation of axial strain at the compression side of the buckled area for different values of fault displacement: (a) fault movement from 0.2m to 1.0m and (b) fault movement from 0.20m to 0.25m (X65 pipe, $D/t = 72$, Clay II, $w = 0.33$m, $p = 0$).

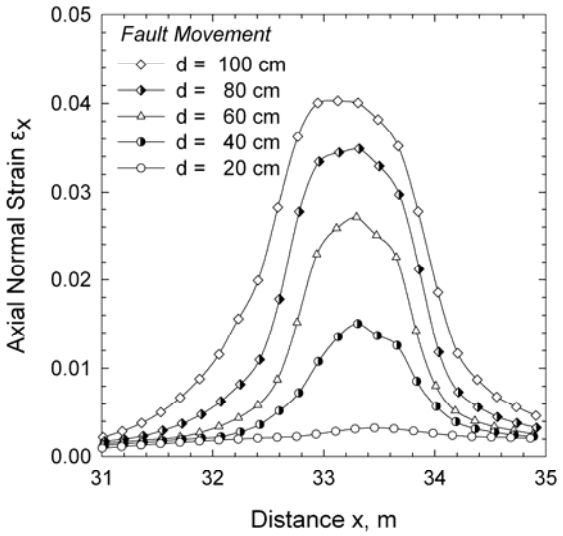


Figure 9. Variation of axial strain at the tension side of the buckled area in terms of fault displacement from 0.2m to 1.0m (X65 pipe, $D/t = 72$, Clay II, $w = 0.33$m, $p = 0$).

The numerical results in Figs. 8 and 9 refer to an X65 steel pipeline with $D/t$ ratio equal to 72, buried in stiffer cohesive soil conditions. The values of soil parameters $c$, $E$ and $\varphi$ are equal to 200 kPa, 100 MPa and $0^o$, respectively, and correspond to a stiff to hard clay under "undrained conditions", referred to as Clay II. The width of the fault zone is equal to 0.33 m. The numerical results indicate that pipe bending deformation in the stiff soil occurs within a shorter distance from the fault location, and the critical area is at 3.2 m from the fault. Comparison of those results with the results shown in Figures 6 and 7 demonstrates the significant effect of site conditions on the mechanical behavior of the steel pipeline. In other words, for the same fault displacement $d$, higher bending stresses and strains occur in the case of a stiff soil than those in the case of a soft soil. The numerical verification of the above observation is offered Figs. 8 and 9, which depict the variation of longitudinal (axial) normal strain along the compression generator. Local buckling occurs when the fault displacement becomes equal to 0.23 m, which is much less than the corresponding critical fault displacement for the case of soft clay (0.67 m).

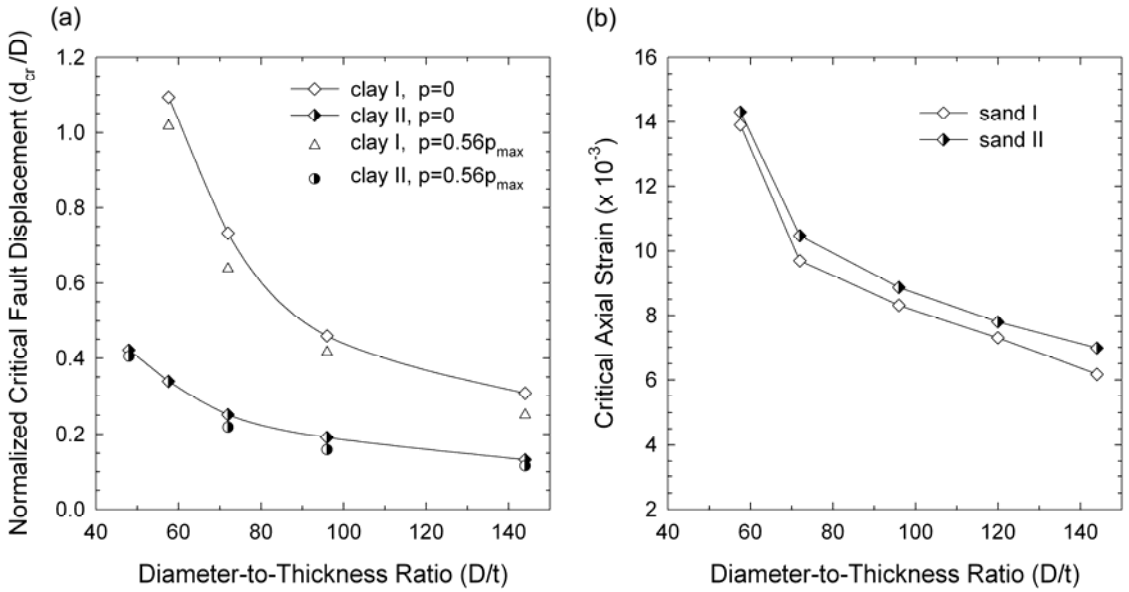


Figure 10. (a) Critical fault movement versus the diameter-to-thickness ratio $D/t$ for clay I, II and (b) Critical axial strain versus the ratio $D/t$ for clay I, II (X65 pipe, $w=$ 0.33m, $p$ =0 and $p = 0.56 p_{\max}$ )

The corresponding maximum compressive strain $\varepsilon_{cr}$ that causes local buckling is equal to $7.3\times10^{-3}$, whereas the maximum tensile strain $\varepsilon_{T,\max}$ along the opposite generator at the stage of local buckling onset is equal to $4.8\times10^{-3}$. The striking difference between softer and stiffer soil conditions is attributed to the fact that a steel pipeline in a softer soil, when subjected to a fault displacement, accommodates itself easier within the deformable soil, resulting in lower bending stresses and strains, which enable the pipeline to sustain larger ground-imposed displacements.

To investigate the effects of the diameter-to-thickness $D/t$ ratio in cohesive soils (Clay I, II), numerical results are obtained for 36-inch-diameter X65 steel pipelines with thickness ranging between ¼-inch and ¾-inch, corresponding to $D/t$ values between 48 and 144.

The numerical results are summarized in Fig. 10. In particular, Fig. 10a plots the fault critical displacement, $d_{cr}$, normalized by the pipe diameter $D$, in terms of the diameter-to-thickness ratio, $D/t$. The results show a substantial decrease of $d_{cr}$ with increasing value of the $D/t$ ratio, which means that thin-walled pipelines are more prone to buckling and fail at relatively small values of fault displacement. Furthermore, stiff soil conditions result in significantly lower deformation capacity of the pipeline. In Fig. 10b the corresponding critical compressive strain at the onset of local buckling, $\varepsilon_{cr}$, is plotted against the value of the diameter-to-thickness ratio, $D/t$. The results indicate that thinner pipes buckle at smaller critical strain, which is in accordance with test data and numerical results from non-confined pipes (Gresnigt & Karamanos 2009).

In the above results, no critical displacement or critical strain is shown for $D/t = 44$ and soft soil conditions (Clay I). In this particular case, the numerical results did not indicate local buckling; the pipeline exhibited significant ground-induced deformation without any wrinkling of the pipeline wall for fault displacements that exceed 2.5 m. The significant tensile strains developed in the pipeline due to longitudinal pipeline stretching after a certain fault movement are responsible for this behavior.

In Fig. 10, the effects of internal pressure are also depicted. The numerical results are obtained for a pressure level equal to 56% of the maximum operating pressure, $p_{\max}$, and show that the presence of internal pressure results to a small decrease of critical fault movement, $d_{cr}$ in Fig. 10a, due to the additional stresses and strains in the pipeline wall because of pressure. Furthermore, the corresponding critical strain in the presence of pressure is similar to the corresponding critical strain for the zero pressure case, as shown in Fig. 10b.

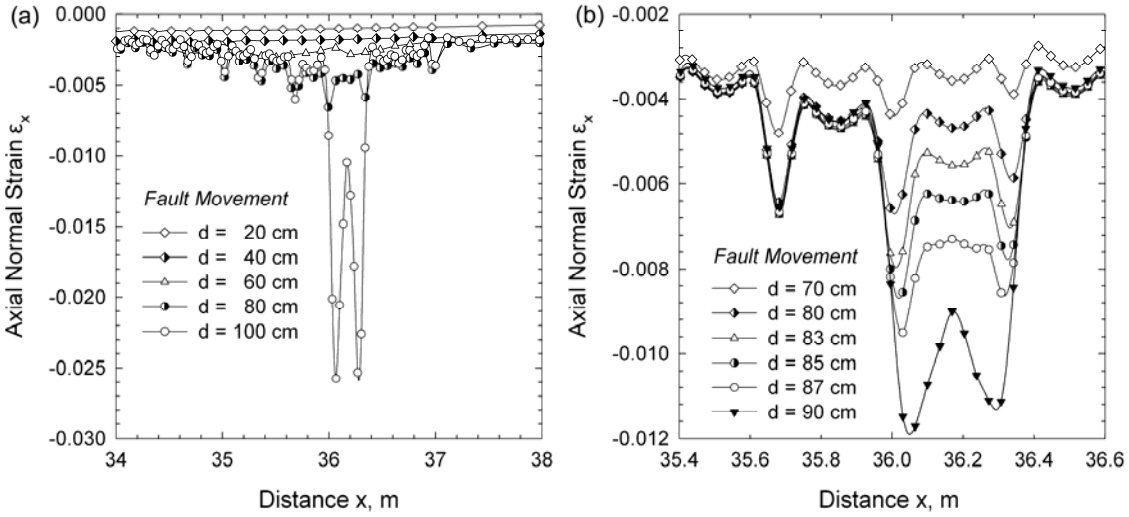


Figure 11. Variation of axial strain at the compression side of the buckled area for different values of fault displacement (a) fault movement from 0.2m to 1m and (b) fault movement from 0.7m to 0.9m (X65 pipe, $D/t = 72$, Sand I, $w = 0.33$m, $p = 0$).

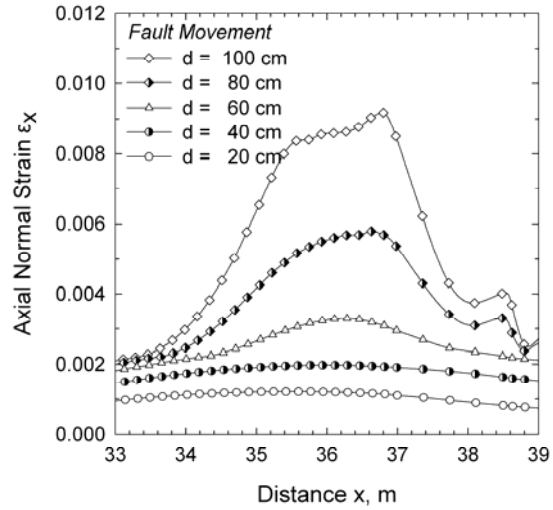


Figure 12. Variation of axial strain at the tension side of the buckled area for different values of fault displacement from 0.2m to 1.0m (X65 pipe, $D/t = 72$, Sand I, $w = 0.33$m, $p = 0$).

### 3.3 *X65 pipelines in non-cohesive soils*

The response of an X65 steel pipeline with $D/t$ = 72 embedded in non-cohesive soils is examined, by considering representative results for two frictional soils and comparing them to those obtained for the cohesive soils. First, a granular soil is considered with a friction angle $\varphi$=30°, Young's modulus $E$=8 MPa and Poisson's ratio $v$=0.3, corresponding to loose sand and referred to as "Sand I". The relatively small value of the stress-depended Young's modulus $E$ is justified by the shallow embedment depth of the pipeline. A small amount of artificial cohesion equal to $c$ = 5 kPa was also included to prevent numerical difficulties associated with the behavior of a purely frictional material at very small confining stress, such as in the case of a gap opening at the pipe-soil interface. Figs. 11 and 12 show the variation of the axial strain $\varepsilon_x$ along the compression and tension outer sides, respectively, of the buckled area for Sand I. The critical distance from the fault, corresponding to the point with maximum bending curvature along the pipe, is 6.1 meters. The results for the compressive strain shown in Fig. 11 indicate that at a value of fault displacement equal to 0.87 m, local buckling occurs, and beyond this stage, significant distortion of the cross-section occurs due to local buckling on the pipe wall on the compression side of the bent pipeline.

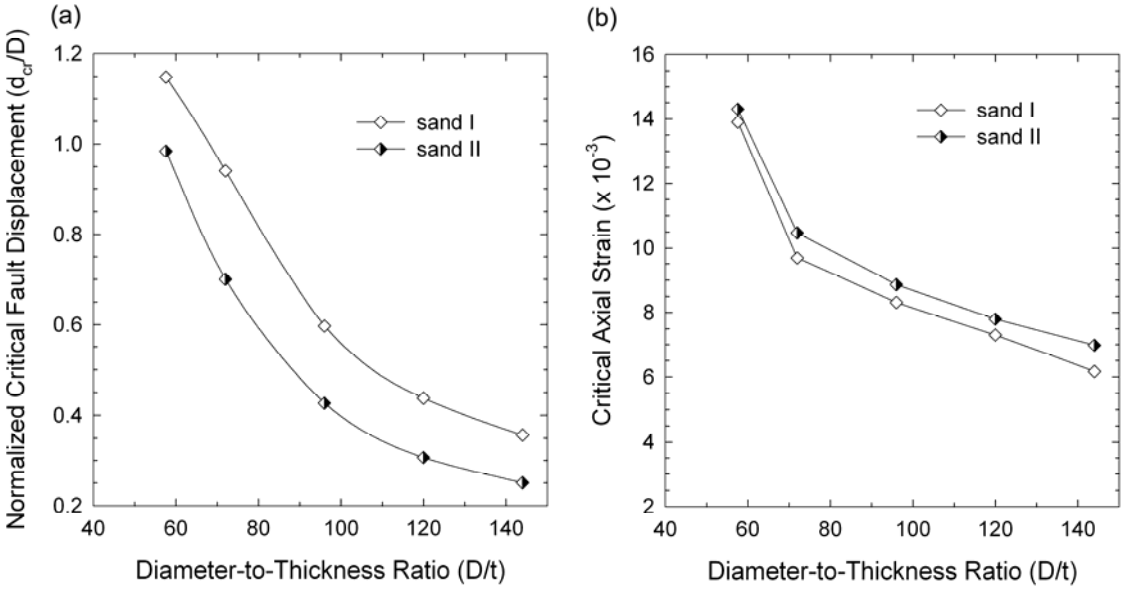


Figure 13. (a) Critical fault movement versus the diameter-to-thickness ratio $D/t$ for sand I, II and (b) Critical axial strain versus the diameter-to-thickness ratio $D/t$ for sand I, II (X65 pipe, $w = 0.33$m, $p = 0$).

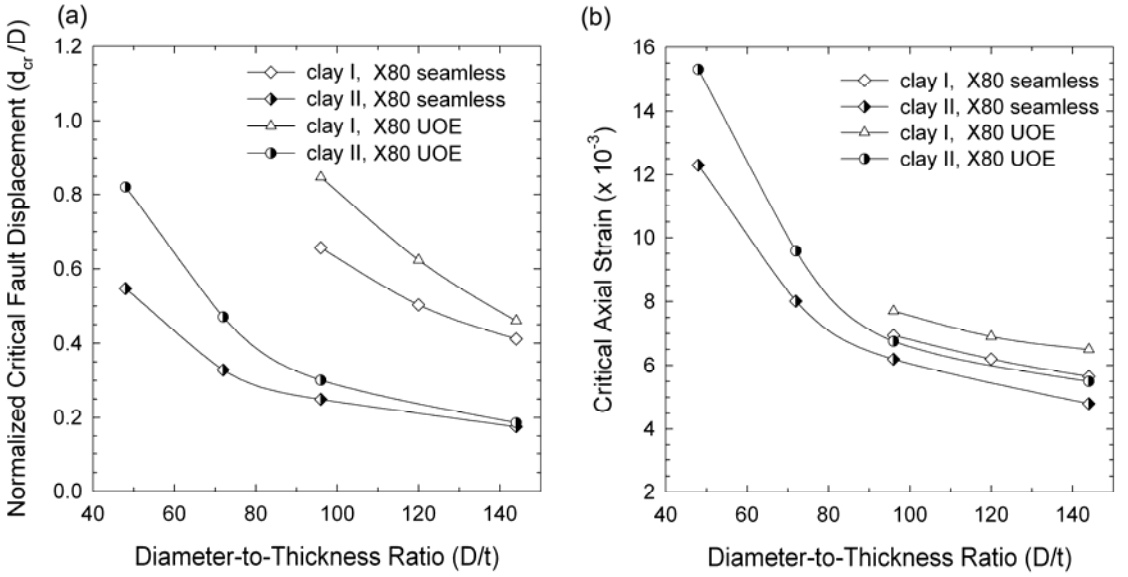


Figure 14. (a) Critical fault movement versus the diameter-to-thickness ratio $D/t$ for two different types of X80 pipelines and (b) Critical axial strain versus the diameter-to-thickness ratio $D/t$ for two different types of X80 (X80 pipe, $w = 0.33$m, $p = 0$).

The shape of the developing buckling is similar to that of Clay I. The longitudinal strain at the location of the buckle ($\varepsilon_{cr}$) is equal to $9.7\times10^{-3}$. Furthermore, at the critical buckling stage ($d$ =0.87 m), the maximum tensile strain on the opposite side of the pipe ($\varepsilon_{T,\max}$) is $6.8\times10^{-3}$, which is much less than the strain that would cause tensile rupture. Beyond the formation of the local buckle, pipe deformation concentrates around the buckled cross-section and the localized wrinkling pattern is further developed. Further continuation of the imposed deformation results in pipe-wall folding, which is accompanied by significant local strains (compressive and tensile) at the buckled area. Moreover, the maximum tensile strain on the opposite (tensile) side of the pipe is also significantly increased.

Similar results are obtained for an X65 steel pipeline with $D/t$ = 72, embedded in a more dense sand with values of $\varphi$ and $E$ equal to 40° and 50 MPa, respectively, referred to as "Sand II". The numerical results indicate that pipe bending deformation in Sand II occurs within a shorter distance from the fault location (5.1 m) due to the higher strength of this sand. Comparison of those results with the results in Figs. 11 and 12 demonstrates that for the same fault displacement $d$, higher bending stresses and strains occur in the case of Sand II. Furthermore, local buckling occurs when the fault displacement becomes equal to 0.70 m, which is less than the corresponding critical fault displacement for the case of loose sand (0.87 m). The maximum compressive strain $\varepsilon_{cr}$ that causes local buckling is equal to $10.47\times10^{-3}$, whereas the corresponding maximum tensile strain $\varepsilon_{T,\max}$ along the opposite generator is equal to $6.98\times10^{-3}$.
Finally, the numerical results for the mechanical behavior of X65 pipelines in non-cohesive soils (Sand I and II) are summarized in Fig. 13 in terms of the normalized fault critical displacement and the critical corresponding strain at buckling with respect to the diameter-to-thickness ratio, $D/t$. The results shown in Fig. 13a indicate that dense soil conditions (sand II) result in lower deformation capacity of the pipeline.

### 3.4 *Behavior of high-strength steel pipelines*

The behavior of buried high-strength steel (API X80) pipelines under normal fault-induced deformation is also analyzed, using the numerical tools described in the previous sections. The nominal uniaxial tensile stress-strain relationship of the X80 material is plotted Fig. 3. The dashed material curve, which has a yield stress of 596 MPa and does not have a plastic plateau, corresponds to a cold expanded (UOE) pipe. The solid material curve with a yield stress of 550 MPa and a plastic plateau up to a strain of 1.48% represents a seamless steel pipe material. Results are obtained for 36-inch-diameter X80 steel pipelines with $D/t$ ratios between 48 and 144.

Fig. 14a plots the value of the fault critical displacement, $d_{cr}$, normalized by the pipe diameter $D$, in terms of the diameter-to-thickness ratio, $D/t$, for the two types of X80 steel and for cohesive soil conditions (Clay I and II). As in the case of X65, the value of $d_{cr}$ decreases significantly with increasing value of $D/t$, indicating that thin-walled pipelines are more vulnerable to buckling and may fail at relatively small values of fault displacement. It should be noted that for the softer Clay I material, no values of $d_{cr}$ are given for $D/t$ = 44 and 72, as no wrinkling of the pipeline wall was observed in this case even for fault displacements exceeding 4 m. This is attributed to the beneficial effect of tensile deformation on the mechanical behavior of those relatively thick pipes. Naturally, the values of $d_{cr}$ for the high-strength steel X80 pipes in Fig. 14a are higher than those for the X65 pipes given in Fig. 10a. Similarly, Fig. 14b plots the corresponding critical axial strain, $\varepsilon_{cr}$, versus the diameter-to-thickness ratio, $D/t$, for zero internal pressure. Comparing the behavior of the two X80 materials, it is evident that both $d_{cr}$ and $\varepsilon_{cr}$ are higher for UOE pipe due to both increase of yield strength and higher initial post-yielding tangent modulus. The increase of buckling strength in UOE pipes is in accordance with the test data reported elsewhere (Gresnigt & Karamanos 2009).

## 4 CONCLUSIONS

Using advanced finite element simulation tools, the mechanical behaviour of buried steel pipelines crossing an active strike-slip fault was investigated. The pipeline is assumed horizontal and normal to the fault plane, an idealized case, which allows for the investigation of several soil and pipe parameters on pipeline deformation and strength. In particular, the effects of various cohesive and non-cohesive soil conditions [expressed through various values of soil cohesion, internal friction and stiffness parameters ($c$, $\varphi$, $E$)] on the structural response of the pipe are examined, with particular emphasis on pipe wall failure.

An extensive parametric study is conducted, and numerical results are obtained for various values of $D/t$ ratio and for X65 and X80 steel pipelines. In the majority of the cases analyzed, it is shown that the formation of local buckling due to excessive compressive strains at the pipeline wall is the governing mode of failure. The numerical results are presented in diagram form

for the critical fault displacement $d_{cr}$ and the corresponding critical strain $\varepsilon_{cr}$, and indicate a strong dependence in terms of the pipeline diameter-to-thickness ratio $D/t$.

It is concluded that in cohesive soils, softer ground conditions result in a large deformation capacity of the pipeline, whereas stiff ground conditions decrease the critical fault displacement. Similarly, in non-cohesive soils, loose sand conditions results in larger values of critical fault displacement than in dense soil conditions. It was demonstrated that the presence of internal pressure results in a small decrease of the deformation capacity, due to early yielding of the steel material. It was also concluded that high-strength X80 steel pipelines have a greater deformation capacity than X65 pipelines. Furthermore, cold-formed UOE X80 pipes exhibit better behaviour in terms of buckling than seamless X80 pipes due to strain hardening.

Finally, the numerical results show that thick-walled pipes may not exhibit buckling; in those pipelines wall fracture may occur due to the development of excessive tensile strains.

## 5 ACKNOWLEDGEMENTS

The authors would like to thank Arnoldus (Nol) M. Gresnigt, Associate Professor of Civil Engineering, Delft University of Technology, The Netherlands, for his valuable comments on the numerical results.

## 6 REFERENCES

Nakata T. & Hasuda K. 1995. Active fault I 1995 Hyogoken Nanbu earthquake. *Kagaku* 1995; 65:127–142

Earthquake Engineering Research Institute. 1999. “Kocaeli, Turkey Earthquake of August 17”, *EERI Special Earthquake Report*.

Takada S., Nakayama M., Ueno J., & Tajima C. 1999. Report on Taiwan Earthquake, *RCUSS, Earthquake Lab. of Kobe University*; 2–9

Newmark N.M. & Hall W.J. 1975. “Pipeline design to resist large fault displacement”. *Proceedings of U.S. National Conference on Earthquake Engineering*; 416–425.

Kennedy, R.P., Chow, A.W. & Williamson, R.A. 1977. “Fault movement effects on buried oil pipeline”, *ASCE Journal of Transportation Engineering*, Vol. 103, pp. 617-633.

Kennedy R. P. & Kincaid R.H. 1983. “Fault crossing design for buried gas oil pipelines”. *ASME, PVP conference*; 77:1–9

Wang, L.R.L. & Yeh, Y.A. 1985. “A refined seismic analysis and design of buried pipeline for fault movement”, *Earthquake Engineering & Structural Dynamics*, Vol. 13, pp. 75-96.

Vougioukas E.A., Theodossis, C., Carydis P.G. 1979. “Seismic analysis of buried pipelines subjected to vertical fault movement.”, *ASCE J. of Techn. Councils*, Vol. 105(TCI), 432– 441.

Wang L.L.R. & Wang L.J. 1995. Parametric study of buried pipelines due to large fault movement. *ASCE, TCLEE* 1995; (6):152–159.

Takada, S., Hassani, N. & Fukuda, K. 2001, “A new proposal for simplified design of buried steel pipes crossing active faults”, *Earthquake Engineering and Structural Dynamics*, 2001; Vol. 30: pp.1243–1257.

Kokavessis, N.K. & Anagnostidis, G.S. 2006. “Finite Element Modelling of Buried Pipelines Subjected to Seismic Loads: Soil Structure Interaction Using Contact Elements.”, *Proceedings, ASME PVP conference*, Vancouver, BC, Canada.

Karamitros, D.K., Bouckovalas, G.D. & Kouretzis, G.P. 2007. “Stress Analysis of Buried Steel Pipelines at Strike-Slip Fault Crossings.”, *Soil Dynamics & Earthquake Engineering*, Vol. 27, pp. 200-211

Liu, M., Wang, Y.Y. & Yu, Z. 2008, “Response of pipelines under fault crossing.”, *Proceedings, International Offshore and Polar Engineering Conference*, Vancouver, BC, Canada.

Ha, D., Abdoun T.H., O’Rourke, M.J., Symans, M.D., O’Rourke, T.D., Palmer, M.C. & Stewart, H.E. 2008a, “Buried high-density polyethylene pipelines subjected to normal and strike-slip faulting – a centrifuge investigation.”, *Canadian Geotechnical Journal*, Vol. 45, pp. 1733-1742.

Ha, D., Abdoun T. H., O'Rourke, M. J., Symans, M. D., O'Rourke, T. D., Palmer, M. C., Stewart, H. E. 2008b, "Centrifuge Modeling of Earthquake Effects on Buried High-Density Polyethylene (HDPE) Pipelines Crossing Fault Zones.", *ASCE Journal of Geotechnical and Geoenvironmental Engineering*, Vol. 134, No. 10, pp. 1501-1515.
Abdoun T.H., Ha, D., O'Rourke, M.J., Symans, M.D., O'Rourke, T.D., Palmer, M. C. & Stewart, H. E. (2009), "Factors influencing the behavior of buried pipelines subjected to earthquake faulting.", *Soil Dynamics and Earthquake Engineering*, Vol. 29, pp. 415– 427.
Lillig D.B., Newbury B.D. & Altstadt S. A. 2009. "The Second ISOPE Strain-Based Design Symposium-A Review.", *Int. Soc. of Offshore & Polar Engineering Conf.*, Osaka, Japan.
ABAQUS. 2010. *Users' Manual*, Simulia, Providence, RI, USA.
Anastasopoulos, I., Callerio, A., Bransby, M.F., Davies, M.C., Nahas, A.El, Faccioli, E., Gazetas, G., Masella, A., Paolucci, R., Pecker, A., Rossigniol, E. 2008. "Numerical analyses of fault foundation interaction.", *Bulletin of Earthquake Engineering*, Springer, 6(4), 645-675.
American Petroleum Institute.2007. *Specification for Line Pipe*, 44th Ed., ANSI/API Spec 5L.
American Society of Mechanical Engineers. 2007. *Gas Transmission and Distribution Piping Systems*, ANSI/ASME B31.8.
Igi, S. & Suzuki, N. 2007. "Tensile Strain Limits of X80 High-strain Pipelines.", *Proceedings of the 16th International Offshore and Polar Engineering Conference*, Lisbon, Portugal.
Dama, E., Karamanos, S.A. & Gresnigt, A.M. 2007. "Failure of Locally Buckled Pipelines.", *Journal of Pressure Vessel Technology,* ASME, Vol. 129, pp. 272-279.
Gresnigt, A.M. & Karamanos, S.A. 2009. "Local Buckling Strength and Deformation Capacity of Pipes.", *19th International Offshore and Polar Engineering Conference*, Osaka, Japan, pp. 212-223.

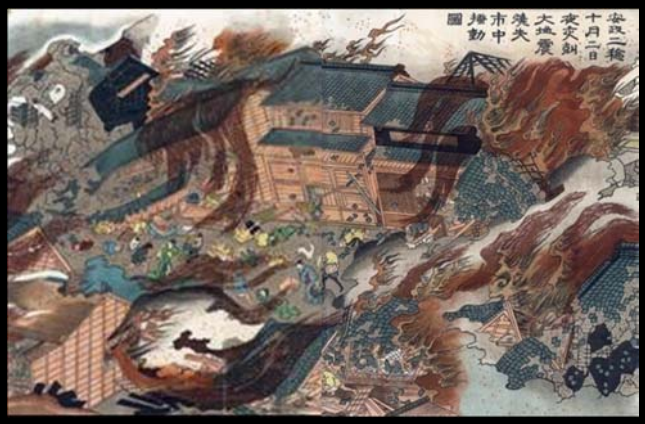
安政二乙卯
十月二日
夜亥剋
大地震
焼失
市中
騒動
圖